Transactions of the ASME, Journal of Turbomachinery (ISSN 0889-504X) is published quarterly (Jan., Apr., July, Oct.) by The American Society of Mechanical Engineers, Three Park Avenue, New York, NY 10016. Periodicals postage paid at New York, NY and additional mailing offices. POSTMASTER: Send address changes to Transactions of the ASME, Journal of Turbomachinery, c/o THE AMERICAN SOCIETY OF MECHANICAL ENGINEERS, 22 Law Drive, Box 2300, Fairfield, NJ 07007-2300.
CHANGES OF ADDRESS must be received at Society headquarters seven weeks before they are to be effective. Please send old label and new address.
STATEMENT from By-Laws. The Society shall not be responsible for statements or opinions advanced in papers or ... printed in its publications (B7.1, Par. 3).

INDEXED by Applied Mechanics Reviews and Engineering Information, Inc. Canadian Goods & Services Tax Registration #126148048

Journal of Turbomachinery

Published Quarterly by ASME

VOLUME 127 • NUMBER 1 • JANUARY 2005

SPECIAL SECTION—In Memoriam

ADDITIONAL TECHNICAL PAPERS

(**Contents continued on inside back cover**)

This journal is printed on acid-free paper, which exceeds the ANSI Z39.48-1992 specification for permanence of paper and library materials. ♾™
♻ 85% recycled content, including 10% post-consumer fibers.

Journal of Turbomachinery **Volume 127, Number 1** **JANUARY 2005**

ANNOUNCEMENTS AND SPECIAL NOTES

The ASME Journal of Turbomachinery is abstracted and indexed in the following:

Aluminum Industry Abstracts, Aquatic Science and Fisheries Abstracts, Ceramics Abstracts, Chemical Abstracts, Civil Engineering Abstracts, Compendex (The electronic equivalent of Engineering Index), Corrosion Abstracts, Current Contents, Ei EncompassLit, Electronics & Communications Abstracts, Energy Information Abstracts, Engineered Materials Abstracts, Engineering Index, Environmental Science and Pollution Management, Excerpta Medica, Fluidex, Fuel and Energy Abstracts, INSPEC, Index to Scientific Reviews, Materials Science Citation Index, Mechanical & Transportation Engineering Abstracts, Mechanical Engineering Abstracts, METADEX (The electronic equivalent of Metals Abstracts and Alloys Index), Metals Abstracts, Oceanic Abstracts, Pollution Abstracts, Referativnyi Zhurnal, Shock & Vibration Digest, Steels Alert

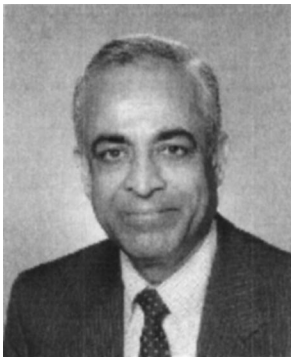

In Memory of Budugur Lakshminarayana (1935–2001)

by Robert Kunz and Chunill Hah

Budugur Lakshminarayana passed away in October in State College, Pennsylvania after a several-year battle with cancer. ''Bud,'' as he was known to his colleagues, received his doctorate from the University of Liverpool in 1963, having performed his thesis research under Sir John Horlock. He then joined the Aerospace Engineering Department at Penn State University, where his career spanned 37 years. During his career at Penn State, he published extensively in the area of turbomachinery fluid-thermal sciences and was the advisor for 21 Ph.D. and 25 M.S. graduate students. He was instrumental in developing the turbomachinery laboratory at Penn State, which comprised numerous experimental research facilities. He also developed a graduate and research program in computational fluid dynamics. He instructed many undergraduate and graduate courses in the Aerospace Engineering Department and authored a graduate-level textbook on turbomachinery.

Lakshminarayana was an Evan Pugh Professor of Aerospace Engineering, the highest academic rank bestowed on a Penn State faculty member. He was a Fellow of the American Institute of Aeronautics and Astronautics (AIAA) and the American Society of Mechanical Engineers (ASME). He was the recipient of numerous professional awards from the Society of Automotive Engineers, ASME, AIAA, and the National Science Foundation. He received the Fulbright Senior Professor Award for Research in Germany and the Distinguished Alumni Professor and Premier Research awards from Penn State. During his career, he traveled extensively and was a visiting advisor/professor in Germany, France, India, Japan, and the United States.

He had remained active in research, advising, and various philanthropic activities. At the time of his death, he was in the process of building an orphanage in Bangalore, India.

He is survived by his wife, Saroja Ramanujam; a daughter, Anita Silva of Virginia; a son, Arvind Narayana of Massachusetts; and two grandchildren.

Journal of Turbomachinery

Technology Review

The Jet Age, Continued

William H. Heiser
U.S. Air Force Academy,
Department of Aeronautics,
P.O. Box 428,
U.S. Air Force Academy, CO 80840
e-mail: heiser@propulsion.com

[DOI: 10.1115/1.1791278]

Introduction

I was pleased and honored to be invited to make the opening presentation of the International Gas Turbine Institute Budugur ''Bud'' Lakshminarayana Memorial Session. It has been a privilege to know and work with Bud for over 30 years, and the sole purpose of my talk is to celebrate his accomplishments and contributions, and a life well lived.

I have always thought of Bud primarily as a teacher, a title I hold in the highest regard. He taught through his lectures, writings, research, and, most of all, by example. My first professional contact with Bud occurred when I was working in the turbine technology group at Pratt & Whitney in the late 1960's, and we were striving to improve the cascade loss models in our performance procedures. We discovered that the end loss models published by Bud were perfect for our situation. They were fundamentally sound, intuitively appealing, broadly applicable, and easily incorporated. From that time on, we always paid attention to his publications.

During 1976–82 I had the opportunity to visit Bud periodically at the Pennsylvania State University as a member of the College of Engineering Industrial and Professional Advisory Council. This allowed me to witness first hand the deservedly famous turbomachinery laboratory he had created with his talent and dedication, as well as some of the outstanding students he nurtured (although it was not clear that they felt nurtured). As the years passed, I also discovered that he cared deeply about the professional societies, working tirelessly to improve their services, and felt passionately about providing the best possible educations for his own children.

My foremost intention is that this presentation would have interested and pleased Bud. It seeks to answer the implied question about what the Jet Age has in store for the turbine engine. We are all inhabitants of the Jet Age, many of us having known nothing else. Jet-propelled aircraft are so pervasive, and have such a strong hold on civilization, that it is impossible to envision a world not heavily influenced by their presence. But what will the future mean to jet propulsion, and the people who work in the field?

The best way I can answer that question is to examine what has motivated change in the past, and what is likely to motivate change in the future. In order to do that, I have divided the motivations I understand into three categories, and explore them in turn, as follows.

1 Evolution: The Main Sequence

There are many turbine engine technologies that are pursued because the laws of nature guarantee that they will improve specific thrust, specific fuel consumption, weight, reliability, and/or cost. The list below, which is neither exhaustive nor prioritized, illustrates this type of work, which might be called evolutionary because it produces continuous progress. It is worth noting that many of the papers in many of the sessions of this IJGPC Conference are dedicated to these, or closely related, subjects. This suggests that contemporary experts have many promising concepts that will continue the evolutionary process.

Evolutionary Technologies
- increase combustor entrance and exit temperatures;
- reduce structural weight;
- improve flowpath component efficiencies;
- increase fuel heating values;
- alter the cycle;
- reduce cooling and leakage flows;
- improve instrumentation and controls;
- reduce installation drag; and
- improve accessories.

It is easy to demonstrate that evolutionary improvements in the vehicle and engine plus fuel weight alone can significantly reduce the gross takeoff weight of aircraft of fixed mission and payload. Reductions of gross takeoff weight for conventional aircraft (e.g., commercial subsonic transports) of 35%–40%, and for advanced aircraft (e.g., supersonic bombers or transports) of 55%–60% are easily achievable within the next 20 years.

Since life cycle cost (i.e., acquisition, operation, and maintenance) depends strongly on gross takeoff weight, these potential gains are irresistibly tempting to the industry and society. The gross takeoff weight reductions can, of course, be traded for other improvements, such as greater payload and/or range. This leads us to the confident conclusion that the evolutionary path will continue to be followed for the foreseeable future.

2 Creation/Integration: New Engines and Cycles

The Robert J. Collier Trophy, awarded annually by the National Aeronautic Association, is the best indicator available of the forces that have motivated innovative changes of the whole engine. The Collier Trophy sets high standards for demonstrated achievement, as witnessed by its criterion: ''For the greatest achievement in aeronautics or astronautics in America, with respect to improving the performance, efficiency, and safety of air

Contributed by the Turbomachinery Division of THE AMERICAN SOCIETY OF MECHANICAL ENGINEERS for publication in the JOURNAL OF TURBOMACHINERY. Manucript received January 17, 2004; final revision February 8, 2004. Associate Editor: D. Wisler

or space vehicles, the value of which has been thoroughly demonstrated by actual use during the preceding year.''

It often surprises people to learn that aircraft engines have been the recipients of the Collier Trophy. The compilation below, which contains the entire citation for the selected awards, clearly demonstrates the importance of jet propulsion to modern aviation.

Collier Award Citations

1940: Dr. Sanford A. Moss and the Army Air Corps
For development of the turbo-supercharger.

1952: Leonard S. Hobbs of United Aircraft Corporation
For design, development, and production of the J-57 jet engine.

1958: The United States Air Force and Industry Team Responsible for the F-104 Interceptor.
Clarence L. Johnson of Lockheed Aircraft Corporation for the design of the airframe; Neil Burgess and Gerhard Neumann of the Flight Propulsion Division; General Electric Company, for development of its J-79 turbo jet engines; Major Howard C. Johnson, USAF for establishing a world land plane altitude record of 91,243 Feet; and Captain Walter W. Irwin, USAF, for establishing a world straightaway speed record of 1,404.09 miles per hour.

1970: The Boeing Company
As leader of the industry-airline-government team which successfully introduced the 747 into commercial service with particular recognition to Pratt and Whitney Division of United Aircraft Corporation and to Pan American World Airways.

1978: Sam B. Williams, Chairman and President, Williams Research Corporation
For conceiving and developing the world's smallest, high efficiency turbofan engine which was selected to power U.S. cruise missiles.

1987: NASA Lewis Research Center and the NASA/industry Advanced Turboprop Team
For the development of advanced turboprop propulsion concepts for single rotation, gearless counter rotation, and geared counter rotation inducted fan systems.

1999: The Boeing Company, GE Aircraft Engines, Northrop Grumman Corporation, Raytheon Company, and the United States Navy
For designing, manufacturing, testing and introducing into service the F/A-18E/F multi-mission strike fighter aircraft, the most capable and survivable carrier-based combat aircraft.

2001: Pratt & Whitney, Rolls-Royce, Lockheed Martin Corporation, Northrop Grumman Corporation, BAE SYSTEMS and the Joint Strike Fighter Program Office
For designing, developing, and demonstrating the Integrated LiftFan Propulsion System, the next generation in aviation propulsion performance, efficiency and safety.

The initial message inherent in this progression of awards seems to be that the turbine engine configuration has slowly changed in predictable directions through the years. The passage of time has witnessed the enhancement of the basic turbojet cycle with afterburning (to increase thrust), increasingly larger bypass ratios (to reduce fuel consumption), and combinations of these to provide flexibility. Interesting variants, such as very small engines and innovative turboprops have also appeared. Recently, however, the Joint Strike Fighter introduced a radical departure by combining the afterburning turbofan with a shaft-driven lift fan and a thrust-deflecting nozzle to enable short takeoff and vertical landing.

One may conclude that a period of innovation and experimentation has begun that will supplement the gradual alteration of engine cycles. The future is likely to bring many new forms of turbine engines that enable entirely new applications. This could well be a period of great challenge and accomplishment for propulsion engineers.

3 Revolution: Wild Cards

The undeniable truth is that unpredictable, external forces have driven much good technical work in the past. The partial list below illustrates the enormous range of technical demands that already have been encountered and satisfied. It is an interesting fact that solving these problems required improved analytical and experimental methods that were often capitalized upon for other purposes.

Take, for instance, the case of smoke and chemical emissions, all of which are generated in the main combustor. No one could possibly have foreseen the explosion of the public interest in environmental protection that followed from the original complaints in Newark, New Jersey. The sophisticated main combustor modeling techniques and instrumentation necessary for understanding and controlling chemical composition that resulted have allowed designers to meet increasingly stringent regulations, and have simultaneously made the combustion process virtually 100 percent efficient. Today, these methods are being used to further extend the operating range of main combustors and to advance the design of military afterburners.

Wild Cards Past

- sperm oil;
- inlet integration (drag/stability);
- nozzle integration;
- bird strike;
- the environment (noise/smoke/chemical emissions);
- sonic boom;
- ozone layer;
- low cycle fatigue;
- fuel heat sink requirements;
- high power requirements;
- engine life management;
- military stealth;
- high cycle fatigue; and
- engine health management.

The partial list below illustrates the equally enormous range of technical challenges that have just begun to make themselves known, and are realistic candidates to be the focus of intense future efforts. No one knows for certain which of these will mature into celebrity, or what other topics are about to emerge. It is certain, nevertheless, that things will happen, and that they will change their associated technologies for the better.

Take, for instance, the relatively recent recognition that CO_2 and H_2O, which have been the desired products of traditional hydrocarbon fuel combustion, contribute to the greenhouse effect and therefore to unwanted atmospheric heating. What could be done to reduce these newly undesirable turbine engine emissions? What could be done to eliminate them? How could the solution of this problem lead to the solutions of others?

Wild Cards Yet To Come

- greenhouse gases (CO_2 / H_2O);
- security;
- civilian stealth;
- variable cycles;
- ramjets/scramjets;
- fuel heating value;
- electric engines; and
- probabilistics.

The steadily increasing application of jet propulsion and the public awareness of its impact on the environment guarantee that the wild cards will continue to motivate dramatic change. The past has taught us, fortunately, that effective solutions will not only be found, but that they will be used to foster other advancements.

Conclusion

Bud Lakshminarayana continually adjusted to the motivations described above. We can easily see that through the many legacies he left for our benefit.

For example, the listing below of the chapter titles from his textbook, *Fluid Dynamics and Heat Transfer of Turbomachinery*, published by John Wiley and Sons, Inc., in 1996, follows the development of his technical interests. In the first four chapters he develops classical, foundational concepts, applies them to turbomachinery, and extends them to increasingly more complex and realistic situations. Chapter 5 reveals the enormous interest and expertise he developed in computational methods. One significant by-product of this work was that Bud spearheaded the development and directed the work of a computational fluid dynamics institute at Penn State. Chapter 6 collects the excellent experimental evidence of his career, including the end loss research that originally brought him to my attention. Finally, in Chapter 7, he provides a unique, comprehensive exploration of the profoundly bewildering and essential field of turbine cooling, proving that he kept up with the times, no matter how hard the problem.

Chapter 1: Classification and Basic Concepts of Fluid Mechanics
Chapter 2: Fundamental Principles, Analysis, and Performance of Turbomachinery
Chapter 3: Cascade Inviscid Flows
Chapter 4: Three-Dimensional Inviscid and Quasi-Viscid Flow Field
Chapter 5: Computation of Turbomachinery Flows
Chapter 6: Two- and Three-Dimensional Viscous Effects and Losses
Chapter 7: Turbine Cooling and Heat Transfer

Further, his many graduate students can be found in positions of influence throughout the turbomachinery community. His colleagues throughout academia, government, and industry remember the positive influence he had on them. His research endures to teach others in the changing world of the future. His many honors, awards, and visiting positions certify that he was recognized around the world, and that his curiosity was also boundless.

In closing, it is important to record that Bud had many tantalizing offers of positions that would have been commensurate withhis ability and embellished his resume. As one might expect, Bud studied them carefully and considered them seriously. Nevertheless, in the end he decided every time to stick with the things that interested him the most, and in which he had invested his personal energy. These are admirable and increasingly rare human traits that emphasize his special character. We are indeed fortunate to have known him.

A Review of Some Early Design Practice Using Computational Fluid Dynamics and a Current Perspective

J. H. Horlock

J. D. Denton

Cambridge University Engineering Department,
Whittle Laboratory,
Madingley Road,
Cambridge CB3 0DY, UK

In the early development of gas turbines, many empirical design rules were used; for example in obtaining fluid deflection using the deviation from blading angles, in the assumption of zero radial velocities (so-called radial equilibrium) and in expressions for clearance loss (the Lakshminarayana formulas). The validity of some of these rules, and the basic fluid mechanics behind them, is examined by use of modern ideas and computational fluid dynamics (CFD) codes. A current perspective of CFD in design is given, together with a view on future developments. [DOI: 10.1115/1.1650379]

1 Introduction

Dr Budugur Lakshminarayana graduated from Mysore University in India and came to Liverpool University as a research student in 1960. With one of the authors [JHH] he studied tip clearance effects in axial compressors, gaining his Ph.D. and becoming a Leverhulme Research Fellow of the University in 1963. He then moved to Pennsylvania State University to work with Dr. George Wislicenus, and enjoyed a most successful research career there for nearly 40 years, in recent years as an Evan Pugh Professor of Aerospace Engineering, the highest honor bestowed on a faculty member of the University.

Lakshminarayana's career thus spanned a period in turbomachinery research, performance and design which is remarkable in that this field of engineering changed from one largely of empirical methods, coupled with some simple analysis and experimental work, through to the modern day when computational fluid dynamics (CFD) plays a dominant role. Lakshminarayana made substantial contributions across the whole field (many but not all are referenced in his book on turbomachinery, [1]), so it is appropriate that this paper should attempt to a wide review of that changing scene.

2 The Early Post War Years

In the late 1940s and early 1950s, axial compressor and turbine design relied substantially on empirical correlations of data.

2.1 Compressors. For axial compressors these data came from cascade tests of blades with prescribed profiles, usually C4, C5, NACA series, double circular arc, coupled with some simple analytical methods. (Cumpsty [2] has illustrated how blading of these various profile shapes giving the same deflection can have substantially different pressure distributions, but this was to some extent ignored in the early compressor work.) The mean line design of axial compressors relied on cascade data for flow deviation and limiting deflections (the work of Howell [3] and Carter and Hughes [4] at the National Gas Turbine Establishment (NGTE), the NACA cascade data and Lieblein's diffusion factor, [5]). There was but a limited understanding of the physics of the flow, and the approach to compressor fluid mechanics was essentially incompressible.

For compressor stages of low hub-tip ratio requiring variation in blade geometry along the blade length, simple radial equilibrium theory (involving the assumption of zero radial velocity) was used, usually coupled with free vortex, forced vortex or ''half-vortex'' distributions of tangential velocity ($c_\theta = a/r$, $c_\theta = br$, and $c_\theta = a/r + br$, where a and b were constants). Cascade data also provided information on profile and secondary losses and reasonably efficient machines could be designed quite simply with this analytical/empirical combination. Difficulties arose when maximum permissible stage loadings were exceeded; other problems of stage matching were encountered off design.

2.2 Turbines. Gas turbine designs had almost always involved free vortex simple radial equilibrium theory (Whittle had an early influence here, see [6]), together with empirical information on blade section performance. In the UK, the latter was based less on comprehensive cascade data than on steam turbine experience with impulse and 50% reaction blading, and interpolation in between these (Ainley and Mathieson [7]). Efficiency was estimated using empirical expressions for basic two-dimensional loss, secondary loss, and clearance loss. Allowance was made in most turbine designs for onedimensional compressible flow (this was quite well understood, as subsequently presented by Shapiro [8] in his classic text). But we should note the early attempts at NACA in the early 1950s to provide sound analytical bases for two-dimensional design of turbine blade profiles in compressible flow. The work of Wu and Brown [9] in solving approximately the direct problem of the flow through cascades of given shape was developed into a full CFD solution much later by Novak (see Section 4.1). But Stanitz [10] provided an early basis for turbine blading design—the indirect (or inverse) problem of obtaining the required blade shape once the surface velocity distribution had been prescribed. This led to the so-called PVD (prescribed velocity distribution) method.

This was a remarkably sophisticated method which, coupled with a simple first approximation method also devised by Stanitz [11], was widely used in design of PVD turbine blading, particularly by Rolls Royce in the UK.

3 The Intermediate Period

Analytical research began to have greater impact on this largely practical design approach towards the end of the 1950s and the beginning of the 1960s. We discuss four particular areas here.

3.1 Blade to Blade Flows. Apart from the NACA research on the inverse (design) problem described above, there had been much work on the direct (analysis) problem of the two-dimensional potential flow in given compressor and turbine cascades. Lakshminarayana's book on turbomachinery, [1], gives a

Contributed by the International Gas Turbine Institute and presented at the International Gas Turbine and Aeroengine Congress and Exhibition, Atlanta, GA, June 16–19, 2003. Manuscript received by the IGTI Dec. 2002; final revision Mar. 2003. Paper No. 2003-GT-38973. Review Chair: H. R. Simmons.

useful review of work using conformal transformation, quoting names such as Howell, Carter, and Hughes, Weinig [12], Kraft [13], and Garrick [14]. But in truth such methods were rarely used directly in design, and by now singularity methods for computation of the twodimensional incompressible blade to blade flows were becoming available (e.g., Schlicting and Scholz [15], Martensen [16], but again see Lakshminarayana [1] for other references). Two analytical pieces of work, providing ''exact'' solutions for specific blade profiles, (Gostelow [17] for incompressible flow and Hobson [18] for compressible flow) were useful in checking these numerical solutions, which were later also developed to allow for boundary layer growth on the blade surfaces.

Some further attention was also given to profile design to give low profile loss (rather than deviation minimisation, which had no intrinsic advantage, since the camber could always be changed to give a required gas outlet angle). Two approaches may be mentioned here, those of Stratford [19] and le Foll [20]. The former suggested that if the boundary layer was taken to close to separation, and maintained in that condition, the profile loss should be small because the surface shear stress (and hence the blade drag) would be small. However, that argument neglected the dissipation in the boundary layer which continues, and even increases, as the shear stress falls to zero. Le Foll applied very advanced ideas to turbine blade design. He started by specifying the boundary layer parameters as a function of surface length, converted these to a surface velocity distribution, and then used inverse design to produce a blade with the specified boundary layer. Blades designed in this way were tested successfully by C. A. Parsons in the UK but the approach was too complicated to achieve general use.

3.2 Secondary Flow. Hawthorne [21,22] and L. H. Smith [23] made substantial progress in understanding the fluid mechanics of secondary flow, but attempts to integrate this work into design methods were not very successful; the problems of secondary and clearance loss were dominant and indeed remain so to this day. In compressors the classical secondary flow is not so strong because the blade turning is low. However, the end-wall boundary layers are thick and are prone to separate in the corner between the suction surface and the end-wall. This separation is greatly influenced by both secondary flows, which tend to exacerbate it, and tip leakage flows, which tend to prevent separation.

In turbines secondary flows are strong and very complex. The detailed flow pattern was first established by Langston et al. [24] who performed experiments on a large turbine cascade. With thick inlet boundary layers it was found that classical inviscid secondary flow theory does a remarkably good job in predicting the variations in exit flow angle. However, quite strong secondary flows persist even when there is no inlet boundary layer entering the blade, because of the growth of the end-wall ''boundary layer'' within the blade passage (see Section 4.4). Inviscid secondary flow theory clearly cannot predict these and viscous CFD calculations are necessary. Prediction of secondary loss is much more difficult than predicting the exit angle variations and for many years predictions were based on empirical correlation, e.g., Ainley and Mathieson [7] and Dunham and Came [25], which contained relatively little modelling of the underlying physics. The first successful CFD prediction of turbine secondary flow was performed by one of Lakshimarayana's students, Chunill Hah, in 1984, [26]. Nowadays such calculations have become routine (an example will be shown in Section 4.4); however, the accurate prediction of the loss arising from secondary flows in still not possible because of the limitations of turbulence and transition modeling.

3.3 Through-Flow Methods. In the late 1960s streamline curvature methods (e.g., see Smith [27] and Stubner [28], for possibly the first references to computer codes in use in the engine companies) and matrix through-flow methods (Marsh [29] following Wu [30]) started to replace the simple radial equilibrium calculations. These represented the start of the practical application of CFD to turbomachinery design. These methods still required empirical input for the blade row loss and deviation but they allowed designs with arbitrary vortex distributions to be developed. Their impact was substantial in low-pressure steam turbines where streamline curvature effects are very large and the earlier methods sometimes led to negative reaction at the rotor root. These through-flow methods remain the backbone of the modern compressor and turbine design process. They are used both in the design mode, where the enthalpy or angular momentum changes are specified and the flow angles are sought, and in the analysis mode where specified machine geometry is analyzed to predict its off-design performance. Streamline curvature methods have become dominant because they are better able to cope with transonic flow in the analysis mode. All methods still rely heavily on empirical input, but many have been developed to the stage where they model complex features such as end-wall boundary layers, secondary flows, tip leakage flows, and turbulent mixing.

3.4 Clearance Flows. Steam turbine designers had allowed for clearance losses in a simplified way. Now more detailed studies were undertaken for compressors, particularly by Rains [31] at Caltech and Dean at MIT [32].

Lakshminarayana's work at Liverpool (with JHH), on the fundamentals of tip clearance flows in compressor cascades, [33], was useful subsequently in two ways—in giving information on how blade lift varied along the blade span and on the magnitude of the tip clearance loss. In a fundamental experiment he studied the flow through a gap (2τ) equal to twice the simulated blade clearance cut at the midspan of a cascade of compressor blades, and in a set of comprehensive measurements showed how the clearance loss was created by the vorticity shed from the blades (he designed and used a ''vortometer''—a very small shrouded propeller which measured rotation directly). The experimental data (which also included pressure measurements round the blades along the span, right up to and including the tip section) led the authors to hypothesize that a finite lift remained at the end of the blade, which was termed the retained lift. This has been a matter of some controversy, it being argued that even with a small clearance space no lift should be retained in an inviscid flow. We investigate this further below in Section 4.2, using modern CFD.

Knowing the shed vorticity Lakshminarayana was able to make a fair assessment of the kinetic energy contained in the concentrated ''forced'' vortex and hence the induced drag associated with clearance.

Two equations are important in this formulation;

(a) for the retained lift fraction (K),

$$1-K=0.23+7.45(\tau/s), \tag{1}$$

which applies for $0.01<(\tau/s)<0.1$, where s is the blade pitch, and

(b) for the induced drag

$$C_D=(1-K)f(\tau/s,h/s)C_L^2=0.7C_L^2(\tau/s)/(AR), \tag{2}$$

where $AR=(h/c)$ is the blade aspect ratio (see Lakshminarayana [34]).

Both these expressions are open to the criticism that they were formulated for a uniform entry flow with no end-wall present; further the induced drag is essentially an inviscid phenomenon and so cannot be locally related to entropy creation. Lakshminarayana did other experiments introducing two other effects—a mild entry shear and with a shear created by an end-wall. But here he was mainly interested in calculating the outlet angle changes due to secondary flow and tip clearance; he did not modify Eqs. (1) and (2) for retained lift and loss.

Lakshminarayana's clearance loss expression has been widely used; and his expression for the retained lift has been used by other authors in end-wall flow calculations, as we shall discuss later below in Section 4.3.

4 A Retrospective View of These Two Periods Using CFD

We shall now look back at some of the analytical/empirical methods of the 1950–1970 periods in the light of the powerful computational methods now available. We consider four examples—flow deviation, annulus wall blockage, tip clearance flows, and secondary flows.

4.1 Deviation Rules. Deviation is mainly an inviscid phenomenon and can be thought of as the natural consequence of the divergence of the stream lines from the suction surface in a diffusing flow. For highly loaded blades it is significantly increased by the displacement effect of the rapidly growing boundary layer. The NGTE rule for nominal (near design) deviation in compressors was originally formulated by Constant [35] in the form

$$\delta = m\,\theta(s/c)^n, \tag{3}$$

where θ is the blade camber. Constant suggested $n=0.5$ and $m=0.26$ for compressor cascades, but Howell modified m to allow for a small variation with outlet angle α_2. Carter and Hughes used Howell's conformal transformation method of calculation to present m as a function of stagger ξ, for incompressible flow through blading with circular arc and parabolic centerlines. For circular arcs the value of m for compressor cascades dropped from about 0.32 for $\xi=50°$ stagger to 0.2 at zero stagger; for turbine cascades m dropped further, from 0.2 at zero stagger to about 0.18 at $\xi=60°$. The calculated values of m were lower for the parabolic blade centerlines, with maximum camber at 40% of the chord.

For heavily loaded turbine blades with a flat suction surface downstream of the throat, the usual steam turbine practice had been to take the outlet angle as $\alpha_2=\cos^{-1}(o/s)$, n where o is the throat width, s is the blade pitch, and subscript $_2$ indicates the flow downstream of the trailing edge. This implied that at sonic exit flow the deviation was zero for these blades; it was assumed to remain zero at subsonic exit speeds but increased as the blades were over expanded at pressure ratios above critical (see Taylor [36], quoted by Horlock [37]). Ainley and Mathieson [7] provided a more sophisticated correlation, showing how a (small) difference between α_2 and $\cos^{-1}(o/s)$ varied with α_2 for straight backed turbine blades; they also gave a correction for the curvature between throat and suction surface.

These deviation rules were striking in their simplicity. Indeed one would have thought they would follow from simple pitch averaged equations of continuity and momentum (see, for example, Horlock and Marsh [38]) but we have not been able to locate any convincing semi-analytical derivations. An attempt by one of the authors [JHH], in unpublished work with Novak, was based on a Taylor series expression for perturbation velocities across the pitch. This was an approach originally proposed by Wu and Brown [9] in their remarkable early paper leading to finite difference solutions for two-dimensional channel flows. A simple analysis, using only two terms in the Taylor series, leads to the following form for the deviation at the trailing edge (station 2) of a thin bladed cascade,

$$\delta=\alpha_2-\beta_2=\cos^2\beta_2(d^2\beta/dx^2)_2(s^2/8). \tag{4}$$

For a circular arc compressor cascade this expression becomes

$$\delta=\alpha_2-\beta_2=\tan\beta_2(\sin\beta_1-\sin\beta_2)^2(s/c)^2/8. \tag{5}$$

For a flat-backed turbine cascade $(d^2\beta/dx^2)_2$ will be zero at the trailing edge so from (4) the deviation would be predicted as zero, the old steam turbine assumption.

This analysis is attractive in its simplicity. But it is a channel flow solution and requires a hypothetical straight tail to be added to the blades to meet the Kutta condition. Further the power dependence $n=2$ for the space-chord ratio (which follows from using the two terms in the Taylor series) leads to low values of deviation and gives no valid comparison with the Howell and Carter rules.

It is apparent that there is no alternative to full numerical computation if deviation is to be obtained accurately. Several authors used early forms of CFD (e.g., Katsanis [39] and Wilkinson [40]) to calculate deviation for comparison with the design rules. Novak and Haymann-Haber [41] developed the Wu and Brown approach much more fully by allowing for four terms in the Taylor series for perturbations in velocity across the pitch and then solving the resulting equations numerically. They obtained results which were fully validated in comparison with Gostelow and Hobson, and with time-marching solutions developed by one of the authors [JDD], but made no direct comparison with the deviation rules.

Others applied singularity methods with various assumptions to allow for the Kutta condition at the trailing edge. Gostelow had originally allowed the rear stagnation point to move round a rounded trailing edge in his exact solutions, suggesting that the position giving equal surface velocities near the trailing edge would be a good approximation to a real flow with a realistic deviation. Smith [42] suggests that placing the downstream stagnation point on the end of the camber line gave a reasonably good answer. Gostelow also tried alternative hypotheses for the Kutta condition, extrapolating the pressure distribution to give equal pressures at the trailing edge; later, with colleagues, he allowed for an effective additional blade thickness due to boundary layer growth. Correct application of the Kutta condition remains a problem in many modern CFD calculations.

Miller and Serovy [43] fully explored these various hypotheses in a comprehensive set of calculations of two-dimensional cascade flow (involving finite difference solutions of the through-flow equations). Generally their calculated values of deviation gave low values in comparison with the NGTE rules and the NACA data (illustrating that the potential flow calculation, while giving the major part of the deviation, will not give completely accurate answers unless experimental data is fed in to fix the Kutta condition or viscous effects associated with the boundary layers are included in the calculation).

The importance of inclusion of viscous effects if deviation is to be calculated accurately was confirmed by subsequent work by Wang, Hetherington, and Goulas [44] who also used a finite difference approach to the solution of the partial differential equation for the Wu/S2 stream function. They included viscous effects by successively calculating the velocity field, the corresponding stress tensor, the viscous dissipative force, and the entropy generation, correcting the vorticity and then feeding this back into the partial differential equation for the stream function. This would appear to be a comprehensive and sophisticated CFD calculation of cascade flows and it suggested that deviation in compressor cascades could indeed be calculated accurately in comparison with the NACA correlation (less good agreement was obtained with the Carter rules). Such agreement is perhaps surprising as the number of grid points used by Wang et al. within the boundary layer would be far less than that used today.

The conclusion from this CFD work is that the direct problem, i.e., the solution of the two-dimensional flow in given cascades can be calculated reasonably well if the flow is steady, fully turbulent and if the viscous effects are included in a modern calculation method. We shall return to the question of steady or unsteady flow later.

4.2 Clearance Flows and Losses. A modern CFD code, derived from that described by Denton [45], has been used to calculate the flow in Lakshinarayana's cascade, Ref. [33]. The experiments with a central clearance region with no entry shear were modeled by calculating half the span with the central symmetry plane modeled as a solid wall with no shear stress acting on it. A normal boundary layer was specified at the other end-wall. The tip clearance was 2.05% of span (τ/c=0.047). A very closely spaced grid was used near the tip clearance region with eight grid points in the tip gap. The pressure distributions at different spanwise

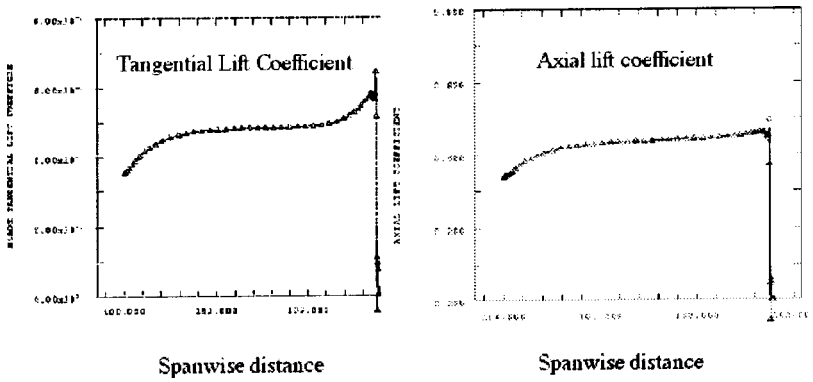

Fig. 1 Axial and tangential lift coefficients of Lakshimarayana's cascade

locations were found to be in close agreement with those observed by Lakshminarayana in his comprehensive experiments.

The components of blade lift along the span thus calculated (axial and tangential components, L_x and L_u) are shown in **Fig. 1**. It is seen that the lift increases slightly towards the blade tip, in agreement with Lakshminarayana's measurements. There is of course no retained lift across the clearance space but the lift force drops suddenly and very rapidly close to the blade end. This means that Lakshminarayana's observation of a concentrated shed vortex near the tip is confirmed, and by implication his model for calculating the induced drag has considerable validity.

Figure 2 shows the calculated losses for one half of the span of Lakshimarayana's cascade. The loss through the central clearance region can be compared with the normal secondary losses calculated at the end-wall of the cascade, where there is an inlet boundary layer but no clearance. The clearance loss is much greater than the normal secondary loss.

The actual details of the flow are shown in **Figs. 3** and **4**; it is here that CFD comes into its own, showing a degree of detail that it would be very difficult to measure experimentally. The clearance flow separates round the pressure side corner at the tip of the blade causing a sharp local suction with a length scale proportional to the very small radius of curvature of the corner. It is the small length scale of this corner flow that causes the lift to be retained so close to the tip. Towards the trailing edge the shed vorticity (present in the shear layer) in this clearance flow builds up into a strong vortex near the suction surface. It is the reduced static pressure on the blade suction surface due to this vortex, **Fig. 4**, that causes the lift to increase near the blade tip. Since the reduced static pressure occurs near the trailing edge where the camber line angle is near axial the effect on the tangential lift coefficient is greater than that on the axial one.

Lakshminaryana repeated his original experiment, firstly with (a) a weak shear flow and secondly (b) with a realistic end-wall boundary layer, both at entry to the central clearance region. The interaction between the secondary flow and the clearance flow became strong in the second of these experiments (b), the two loss regions joining together. Indeed Lakshminarayana argued that there was probably an optimum tip clearance for the clearance flow to counteract the normal secondary flow and minimize the combined loss, as he illustrated subsequently in his book, [1]. He did not modify his loss correlation expression for this combined flow case (b); his emphasis in 1962 was on trying to predict the outlet angle variation.

4.3 End-Wall Flows. Many papers in the literature are devoted to study of the ''boundary layers'' on the annulus walls. But it is now generally agreed that conventional boundary layer theory is inappropriate for describing these flows, as they are three-dimensional, often with areas of separation. However, the concept of the ''ultimate steady flow'' (USF) first described by Howell [46] and later by Smith [47]—that through an ''embedded'' stage in a multistage compressor or turbine where the flow changes little between entry and exit—has proved useful and enlightening.

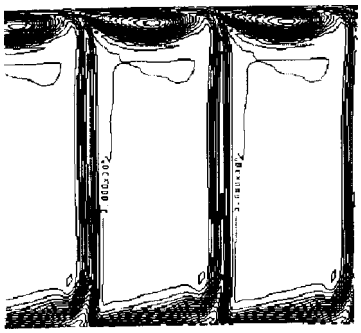

Fig. 2 Calculated stagnation pressure contours behind Lakshimarayana's cascade

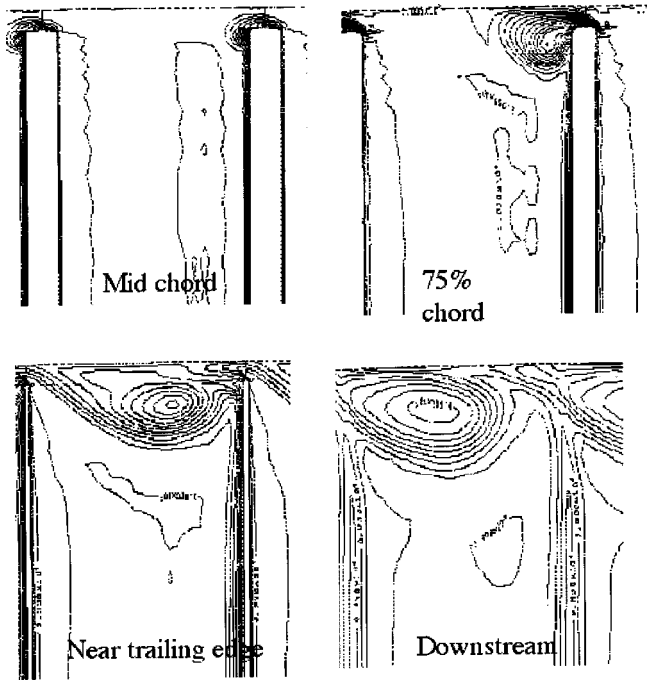

Fig. 3 The growth of tip leakage loss through Lakshimarayana's cascade

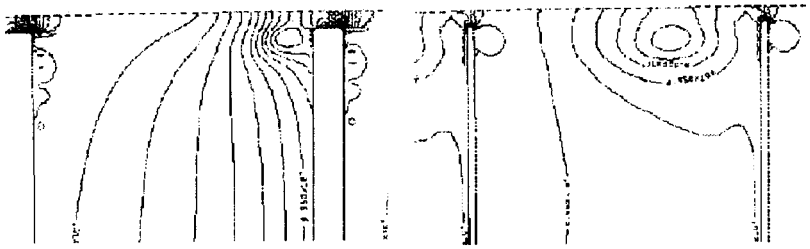

Fig. 4 Static pressure contours near the tip of Lakshimarayana's cascade

Smith made some penetrating observations about USF, three of which we reproduce here.

> "It is seen . . . in a twelve-stage compressor . . . that the flow does not actually deteriorate, but remains reasonably well behaved. Of course the flow details may be quite complex, particularly near the walls. Evidence that losses are larger near the walls than at mid-passage is given . . . . The excess total temperature near the blade ends is seen to increase as the flow proceeds through the compressor: the fluid near the walls is the receptacle of the energy dissipated by these losses."
>
> "As the flow passes through one (USF) stage all streamlines will experience the same increase in static pressure; this must be so because the same radial and circumferential distribution of velocities exist and hence radial and circumferential pressure gradients must be the same according to the momentum equation. Furthermore all streamlines experience the same increase in total pressure, which is the same as the static pressure because the dynamic pressure is the same at stage inlet and outlet from each streamline."
>
> "The momentum theorem tells us that the sum of the axial force on the rotor blades and the axial force on the stator vanes is equal to the static pressure rise across the stage multiplied by the annulus area . . . . Since this static pressure rise is constant over the annulus, the axial force per unit span varies as the radius, i.e. it does not fall off rapidly in the hub and casing boundary layers as we approach the wall. Actually the axial force component per unit span (divided by the radius) must increase slightly as we approach the wall to account for the fact that there is no blade surface to support a force in the tip clearance area. We are unable to make this statement for rotor blades and stator vanes individually, but only for the sum of their forces."

CFD was used by Bolger and Horlock [48], assisted by Denton, to study the flow in a four-stage compressor tested by Howard et al. at Cranfield [49]. This calculation showed the repeating stage phenomenon very clearly, casing blockage increasing across each rotor row (with tip clearance) and hub blockage across each stator row (with clearance). The blockages (displacement thicknesses) were then restored across the next rows (without clearance) to provide the repeating or ultimate steady flow. Developing Smith's arguments and using Lakshminarayana's concept of retained lift, Horlock [50] estimated the changes in the momentum deficit (and blockage) across rotor and stator rows in a fully developed USF stage (making the further assumption of a thin endwall region at large radius, so that static pressures near the endwall were virtually constant at rotor and stator exit). We have revisited and improved these CFD calculations (using more grid points) for Howard's four stage compressor, in order to look in more detail at the flow, particularly the lift variations. Broadly the calculations again confirm Smith's interpretation of the USF stage. The axial velocity and stagnation pressure profiles repeat quite well (the fourth stage is an exception as it has experiences no "upstream effect" from a downstream rotor). Smith's observation that the difference between the stagnation temperature near the walls and that at midspan increased continually through the machine is only partly confirmed. The work input per unit radius $\Delta W = L_u U = \rho c_x s c_p \Delta T_0$) repeats; its magnitude increases towards the walls as L_u increases, but the axial velocity drops so ΔT_0 increases. However, such a build up of higher stagnation temperature near the walls is opposed by heat transfer, through both conduction and (much more importantly) turbulent mixing, from the walls towards midspan. The rate of heat transfer will increase with stage number so that eventually the excess work may be cancelled by increased heat transfer. The calculated losses also increase towards the wall, balancing some of the excess work to deliver the approximately unchanging stagnation pressure profiles. Here, we show just three of the results from of these new CFD calculations.

(a) **Figure 5** shows the axial and tangential lift coefficients for the rotors and stators (lift components L_x and L_u per unit span divided by midspan relative dynamic head at stage entry). The forms of the lift coefficients are remarkably similar to those observed by Lakshminarayana in his cascade experiments and shown in **Fig. 1**. They also confirm Smith's arguments on lift in the USF stage; the tangential lift coefficients are substantially constant along the blade up to quite close to the tip clearance and then drop suddenly. The above expression for ΔW then implies that with a constant axial velocity the temperature rise in the mainstream is independent of span. At the nonclearance ends the lift drops in the end-wall region (as in the calculations of Lakshminarayana's cascade). The axial lift coefficient of the rotors increases almost linearly with radius as predicted by Smith in the discussion reproduced above.

(b) **Figure 6** gives the calculated flow angles, which indicate that at the clearance end the tip clearance flow swamps the effects of conventional secondary flow. At the nonclearance ends there is conventional secondary flow—overturning at the wall and underturning outside the end wall region in the mainstream. These angle distributions are similar to those observed by Howard et al. [49] at the stator casing, which were somewhat surprising. It might be expected that in a compressor the low velocity coming off the rotor tip clearance and casing boundary layer, with consequent high incidence (or skew) and "reverse" secondary vorticity for the flow into the stator, would lead to reduction in the secondary vorticity at stator exit).

(c) **Figure 7** shows contour plots of the axial velocity at stage 3 rotor exit and stator exit. These plots do not show much evidence of large low velocity separated flow areas; indeed in Smith's terms (and Howell's) the flow is quite well behaved. The similarity of the rotor flow to that in Lakshimarayana's cascade, **Fig. 2**, is quite remarkable. This tends to support the use of cascade testing which has sometimes been said to have little relevance to real compressor flow.

4.4 Computation of Secondary Flows. Modern numerical methods with more than about 200,000 grid points per blade row

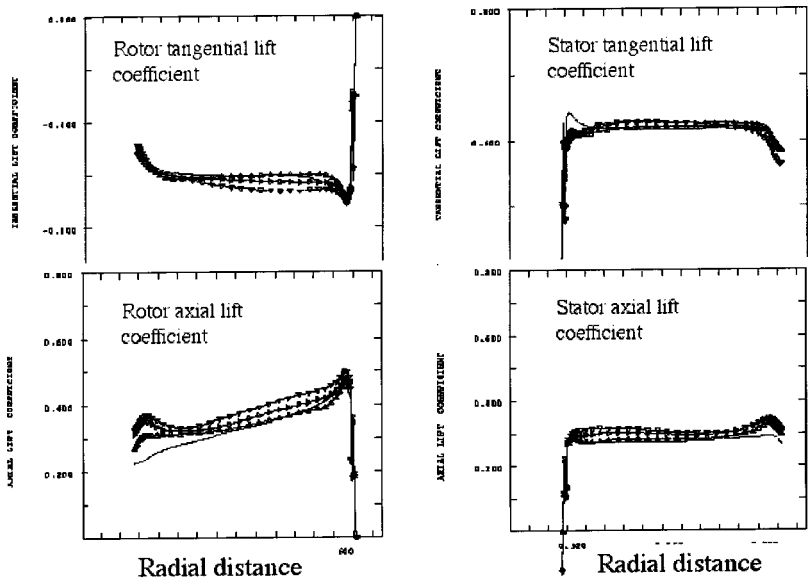

Fig. 5 Lift coefficients of the four stages

have negligible numerical errors and will predict an inviscid flow very accurately. Their limitation comes in the turbulence and boundary layer transition modelling needed to predict viscous effects. As a result such methods are probably more accurate when applied to turbines rather than to compressors because the viscous effects are less dominant.

A good example of the use of CFD is to predict complex secondary flows in turbine blades. However, in order to do this accurately the inlet boundary layer profiles on the endwalls must be known. This is usually available for cascades but unfortunately it is virtually never known in a real turbine. The importance of this is illustrated in **Fig. 8** which shows calculated stagnation pressure contours behind the turbine cascade tested by Harrison [51]. **Figure 8(*a*)** is the result of an inviscid calculation with the measured inlet boundary layer, **Fig. 8(*b*)** is a viscous calculation with no inlet boundary layer, **Fig. 8(*c*)** a viscous calculation with the inlet boundary layer. Also shown is the experimental result **Fig. 8(*d*)**. It can be seen that the inclusion of both the inlet boundary layer and

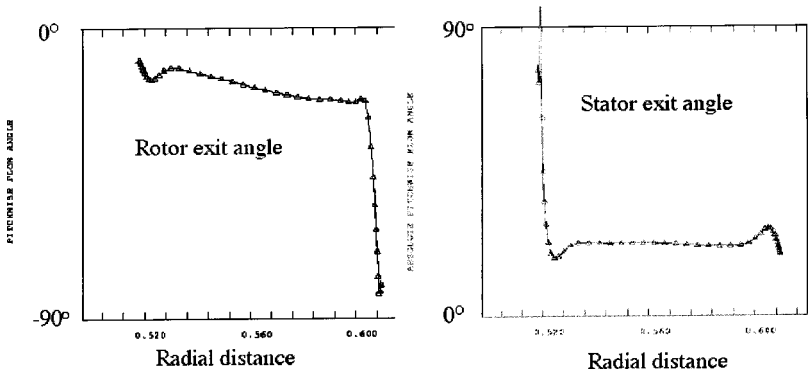

Fig. 6 Exit flow angles from stage 3, rotor and stator

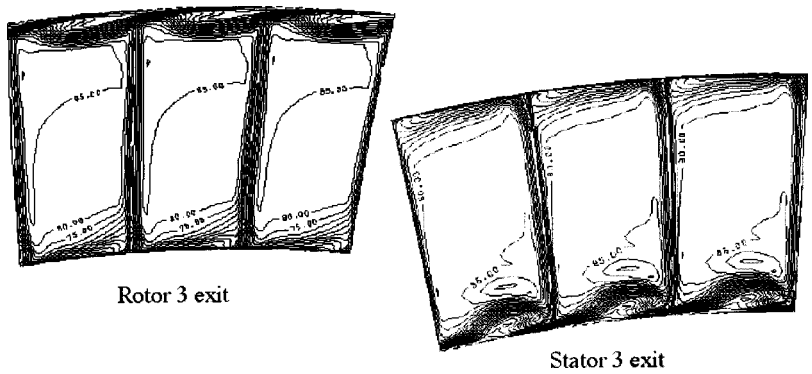

Fig. 7 (*a*) Axial velocities at rotor 3 exit, (*b*) axial velocities at stator 3 exit

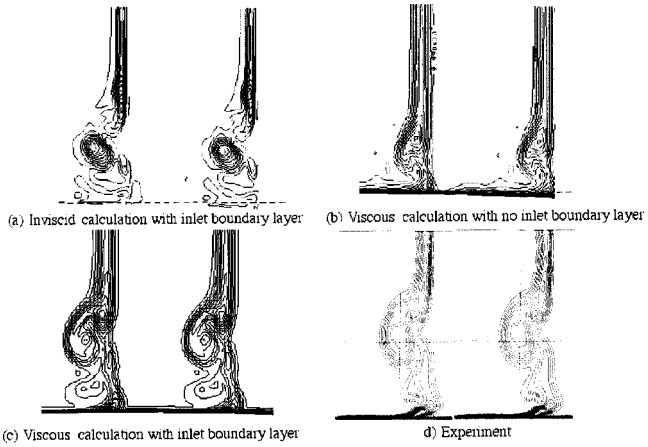

Fig. 8 Stagnation pressure contours behind Harrison's cascade; (*a*) inviscid calculation with inlet boundary layer, (*b*) viscous calculation with no inlet boundary layer, (*c*) viscous calculation with inlet boundary layer, (*d*) experiment

viscous effects on the endwall are necessary to obtain a reasonable prediction. Even the viscous calculation is of limited accuracy because it cannot model the state of the end-wall boundary layer within the blade passage. This was assumed to be fully turbulent because the inlet boundary layer was turbulent. Harrison showed the new endwall boundary layer downstream of the separation line was largely laminar and no CFD code is yet able to predict this relaminarization. However, the calculation does show clearly the formation and roll-up of the horseshoe vortices and the growth of the passage vortex. The total loss present just downstream of the blade row is reasonably well predicted, 4.8% compared to 5.4%, but what is not predictable from a steady calculation is the extra loss produced when the vortices mix out in the following blade row.

5 The Current Use of CFD in Design

Modern turbomachinery design relies almost completely on CFD to develop three-dimensional blade sections. Simple methods with empirical input are still needed for the mean-line design and for through-flow calculations and it is often emphasised by experienced designers that if the one-dimensional design is not correct (e.g., the blade diffusion factors and stage loading), then no amount of CFD will produce a good design. What CFD really provides is the ability to exploit the three-dimensional nature of the flow to control undesirable features such as corner separations in compressors or strong secondary flows in turbines.

Since loss predictions by CFD are still not accurate, interpretation of its results requires considerable skill and experience. Good physical understanding and judgement of when the flow has been improved remain very important. There are many reported examples of the successful use of CFD to improve designs but also many unreported failures. Examples of success are the use of bowed blades to control secondary loss in turbines and the use of sweep and bow to reduce corner separations in compressors; both of these techniques are now routinely used in production machines. Another example of three-dimensional design is the use of sweep to reduce the shock losses in transonic fans. This is a flow where experimental measurements of the shock structure are extremely difficult and our understanding of the flow is obtained almost entirely from CFD. However, in this case the author has shown (Denton and Xu [52]) that benefits are not so obvious. **Figure 9** shows that although the shock can be made swept over the outer part of the span, it must always intersect the casing perpendicularly, and so any benefits of shock sweep are lost in the region where shock losses are greatest.

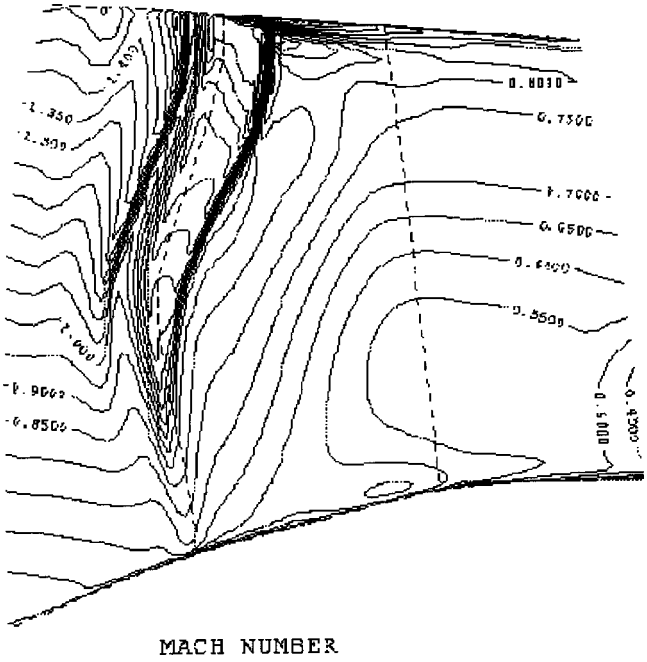

Fig. 9 Shock pattern in a swept fan. Mach number contours at midpitch.

6 Potential Developments and Conclusions

The capabilities of CFD are continually improving and there can be little doubt that future turbomachinery designs will rely even more heavily on it than they do at present. The current trend is to move to multistage and unsteady predictions, both of which require increased computer power, and to much more detailed consideration of secondary gas paths, such as cooling flows, leakage flows and cavity flows. Steady multistage calculations must inevitably model the unsteady interaction between blade rows by such techniques as mixing planes or deterministic stresses. These models are approximate and their limitations need to be explored by detailed flow measurements on multistage machines. Thus they create more rather than less need for experimental testing but much of this testing can be done on model and low-speed machines and the resulting validated CFD used to design real high-speed machines.

Unsteady calculations are still too time consuming to be used for routine design but they are starting to be used for specific investigations. Their results can be used to obtain the unsteady blade loading and hence to assess the mechanical limitations of blading. The implications of unsteady flow on the loss generation are just starting to be explored and questions such as whether the entropy generation is more or less when wakes and vortices mix out unsteadily in a downstream blade row, rather than in a steady flow, are starting to be answered by CFD rather than by experiment. Interpretation of unsteady CFD results can be almost as difficult as that of experimental results and good postprocessing techniques, such as obtaining the entropy generation rates, are needed. Again very high quality experimental data is needed to validate the predictions. In the long term unsteady techniques such as large eddy simulation and direct numerical simulation of turbulence will become practicable and these should remove many of the limitations of turbulence modeling.

The interaction of leakage flows, cooling flows and cavity flows with the main gas path flow has usually been neglected in the past but its importance is starting to be realized. Such flows can interact with the mainstream flow to produce shear layers which contain vorticity and hence generate additional secondary flows and losses. An example is shroud leakage flows in turbines; the leak-

age flow from one blade row enters the next downstream blade row at a high negative incidence and greatly increases the secondary flow and loss in that row. These flows are becoming amenable to CFD calculations using methods with unstructured or multiblock grids. However, because such flows are inevitably highly turbulent, their prediction is very dependent on the turbulence modelling in the codes, and so is of limited accuracy. Experimental measurement of these flows is difficult because their length scale is often very small; however, it is necessary if the turbulence models are to be improved so that future CFD predictions become quantitative rather than qualitative. The message from all of these areas is that both improved CFD and improved experimental measurements will be needed in the future. The function of experiments will be to calibrate CFD rather than to develop new designs. One message becomes very clear, however; it is that engineers with high analytical and computational ability, who are very familiar with experimental techniques and who have excellent physical understanding will be needed to produce the developments of the future. We need more engineers and teachers like Budugur Lakshminarayana.

Nomenclature

AR = blade aspect ratio (h/c)
c = blade chord
c_x = axial velocity
c_u = tangential velocity
c_p = specific heat at constant pressure
C_D = drag coefficient based in inlet dynamic head
C_L = lift coefficient based on inlet dynamic head
h = blade height
L_x = axial lift
L_u = tangential lift (in blade speed direction)
K = fraction of retained lift
o = blading throat width
s = blade spacing or pitch
T_0 = stagnation temperature
U = blade speed
W = work
a, b, m, n = constants
τ = tip clearance
α = gas angle (measured from axial)
β = blade angle (measured from axial)
δ = deviation
ξ = blade stagger
ρ = density
θ = blade camber

References

[1] Lakshminarayana, B., 1996, *Fluid Dynamics and Heat Transfer in Turbomachinery*, John Wiley and Sons, New York.
[2] Cumpsty, N. A., 1989, *Compressor Aerodynamics*, Longman, London.
[3] Howell, A. R., 1942, ''The Present Basis of Axial Flow Compressor Design: Part I—Cascade Theory and Performance,'' Aeronautical Research Council R. and M. No. 2095.
[4] Carter, A. D. S., and Hughes, H. P., 1950, ''A Theoretical Investigation of the Effect of Profile Shape on the Performance of Aerofoils in Cascade,'' Aeronautical Research Council R. and M. No. 2384.
[5] Lieblein, S., 1959, ''Loss and Stall Analysis of Compressor Cascades,'' ASME J. Basic Eng., **81**, p. 3.
[6] Whittle, Sir, Frank, 1945, ''The Early History of the Whittle Jet Propulsion Gas Turbine,'' Proc. Inst. Mech. Eng., **152**, pp. 419–535.
[7] Ainley, D. G., and Mathieson, G. C. R., 1955, ''An Examination of the Flow and Pressure Losses in Blade Rows of Axial Flow Turbines,'' Aeronautical Research Council R. and M. 2891.
[8] Shapiro, A. H., 1953, *The Dynamics and Thermodynamics of Compressible Fluid Flow*, Ronald Press, New York.
[9] Wu, Chung-hua, and Brown, C. A., 1952, ''A Theory of the Direct and Inverse Problems of Compressible Flow Past Cascade of Arbitrary Aerofoils,'' J. Aeronaut. Sci., pp. 183–196.
[10] Stanitz, J. D., 1952, ''Design of Two-dimensional Channels With Prescribed Velocity Distributions Along the Channel Walls,'' NACA Tech. Notes 2593, 2595.
[11] Stanitz, J. D., 1951, ''Approximate Design Method for High-Solidity Blade Elements in Compressors and Turbines,'' NACA Tech. Note 2408.
[12] Weinig, F., 1935, *Die Stromung um die Schaufeln von Turbomaschinen*, Joh. Ambr. Barth, Leipzig.
[13] Kraft, H., 1958, ''Development of a Laminar Wing Type Turbine Bucket,'' ZAMP, **404**.
[14] Garrick, J. E., 1944, ''On the Plane Potential Flow Past a Lattice of Arbitrary Aerofoils,'' NACA Report 778.
[15] Schlicting, H., and Scholz, N., 1951, *Uber die Theoretische Berechung der Stromungsverluste eines ebenen Schaufelgitters*, Ingen.-Arch. Bd. XIX Heft. 1.
[16] Martensen, E., 1959, ''The Calculation of the Pressure Distribution on a Cascade of Thick Aerofoils by Means of Fredholm Integral Equations of the Second Kind,'' Arch. Ration. Mech. Anal., **3**, pp. 251–270.
[17] Gostelow, J. P., 1962, ''Potential Flow Through Cascades-Extension to an Exact Theory,'' Aeronautical Research Council, CP 808.
[18] Hobson, D. E., 1979, ''Shock Free Transonic Flow in Turbomachinery Cascade,'' Cambridge University Report CUED/A Turbo 65 (also Ph.D. thesis Cambridge University).
[19] Stratford, B. S., 1959, ''The Prediction of Separation of the Turbulent Boundary Layer. An Experimental Flow With Zero Skin Friction Throughout Its Region of Pressure Rise,'' J. Fluid Mech., pp. 1–16,17–35.
[20] Le Foll, J., 1976, *Inverse Method for Optimised Blading Calculations*, VKI Lecture Series 84.
[21] Hawthorne, W. R., 1951, ''Secondary Circulation in Fluid Flow,'' Proc. R. Soc. London, Ser. A, **206**, p. 374.
[22] Hawthorne, W. R., 1955, ''Rotational Flow Through Cascades, Part I—The Components of Vorticity,'' Q. J. Mech. Appl. Math., **8**, p. 266.
[23] Smith, L. H., 1953, ''Secondary Flow in Axial Flow Turbomachinery,'' Trans. ASME, **77**, p. 1065.
[24] Langston, L. S., Nice, M. L., and Hooper, R. M., 1977, ''Three-Dimensional Flow Within a Turbine Passage,'' ASME J. Eng. Gas Turbines Power, **99**, pp. 21–28.
[25] Dunham, J., and Came, P. M., 1970, ''Improvements to the Ainley-Mathieson Method of Turbine Performance Prediction,'' ASME J. Eng. Gas Turbines Power, **A92**, p. 252.
[26] Hah, C. A., 1984, ''Navier-Stokes Analysis of Three-Dimensional Turbulent Flows Inside Turbine Blade Rows at Design and Off-Design Conditions,'' ASME J. Eng. Gas Turbines Power, **106**, pp. 421–429.
[27] Smith, L. H., 1962, discussion of Proc. Inst. Mech. Eng., **176**(30), p. 789.
[28] Stubner, A. W., 1962, discussion of Proc. Inst. Mech. Eng., **176**(30), p. 789.
[29] Marsh, H., 1968, ''A Computer Program for the Through Flow Fluid Mechanics in an Arbitrary Turbomachine Using a Matrix Method,'' Aeronautical Research Council R. and M. No. 3509.
[30] Wu, Chung-Hua, 1952, ''A General Theory of Three-Dimensional Flow in Subsonic and Supersonic Turbomachine in Radial, Axial and Mixed Flow Types,'' NACA Tech. Note 2604.
[31] Rains, D. A., 1954, ''Tip Clearance Flows in Axial Compressors and Pumps,'' California Institute of Technology, Hydrodynamics and Mechanical Engineering Laboratories, Report No. 5.
[32] Dean, R. C., 1954, ''Secondary Flow in Axial Compressors,'' Sc.D thesis, Gas Turbine Laboratory, M.I.T., Cambridge, MA.
[33] Lakshminarayana, B., and Horlock, J. H., 1967, ''Leakage and Secondary Flow in Compressor Cascades,'' Aeronautical Research Council, R. and M. 3483.
[34] Lakshminarayana, B., 1970, ''Predicting the Tip Clearance Flow in Axial Flow Turbomachines,'' ASME J. Basic Eng., **92**, pp. 467–482.
[35] Constant, H., 1939, ''Performance of Cascades of Aerofoils, Royal Aircraft Establishment,'' Note No. E3696, Aeronautical Research Council, Report No. 4155.
[36] Taylor, E. S., 1957, ''Problem of the Convergent Nozzle,'' Technical Note (unpublished) Gas Turbine Laboratory, M.I.T., Cambridge, MA.
[37] Horlock, J. H., 1973, *Axial Flow Turbines*, Krieger Publishing Company, Melbourne, FL.
[38] Horlock, J. H., and Marsh, H., 1971, ''Flow Models for Turbomachinery,'' J. Mech. Eng. Sci., **13**, pp. 358–368.
[39] Katsanis T., 1968, ''Computer Program for Calculating Velocities and Streamlines on a Blade-to-Blade Stream Surface of a Turbomachine,'' NASA TND 4525.
[40] Wilkinson, D. H., 1972, ''Calculation of Blade-to-Blade Flow in a Turbomachine by Streamline Curvature,'' Aeronautical Research Council, R. and M. 3704.
[41] Novak, R. A., and Haymann-Haber, G., 1982, ''A Mixed-Flow Cascade Passage Design Procedure Based on a Power Series Expansion,'' ASME Paper 82-GT-121.
[42] Smith, L. H., 2002, ''Axial Compressor Aerodesign Evolution at General Electric,'' ASME J. Turbomach., **124**, pp. 321–330.
[43] Miller, M. J., and Serovy, G. K., 1974, ''Deviation Estimation for Axial-Flow Compressors Using Inviscid Flow Solutions,'' ASME Paper 74-GT-74.
[44] Wang, L. C., Hetherington, R., and Goulas, A., 1983, ''The Calculation of Deviation Angle in Axial Flow Compressor Cascades,'' ASME J. Eng. Gas Turbines Power, **105**, pp. 474–479.
[45] Denton, J. D., 1991, ''The Calculation of Threedimensional Viscous Flow Through Multistage Turbomachines,'' ASME J. Turbomach., **114**.
[46] Howell, A. R., 1947, ''Fluid Dynamics of Axial Compressors,'' Proc. Inst. Mech. Eng., War Emergency Issue, 12.
[47] Smith, L. H., 1969, ''Casing Boundary Layers in Multistage Compressors, Flow Research in Blading,'' L. S. Dzung, ed., Elsevier, New York.
[48] Bolger, J. J., and Horlock, J. H., 1995, ''Predictions of the Flow in Repeating

Stages of Axial Compressors Using Navier-Stokes Solvers,'' ASME Paper 95-GT-199.
[49] Howard, M. A., Ivey, P. C., Barton, J. P., and Young, K. F., 1994, ''End Wall Effects at Two Tip Clearances in a Multi-Stage Axial Flow Compressor With Controlled Diffusion Blading,'' ASME J. Turbomach., **106**, pp. 635–647.
[50] Horlock, J. H., 2000, ''The Determination of End-Wall Blockage in Axial Flow Compressors—A Comparison Between Various Approaches,'' ASME J. Turbomach., **122**, pp. 218–224.
[51] Harrison, S., 1989, ''Secondary Loss Generation in a Linear Cascade of High-Turning Turbine Blades,'' ASME Paper 89-GT-47.
[52] Denton, J. D., and Xu, L., 2002, ''The Effects of Lean and Sweep on Transonic Fan Performance,'' ASME Paper GT-2002-30327.

Aerodynamics of Tip Leakage Flows Near Partial Squealer Rims in an Axial Flow Turbine Stage

Cengiz Camci
Professor of Aerospace Engineering
e-mail cxc11@psu.edu

Debashis Dey[1]
Research Assistant

Levent Kavurmacioglu[2]
Visiting Professor

Turbomachinery Heat Transfer Laboratory,
Department of Aerospace Engineering,
The Pennsylvania State University,
223 Hammond Building,
University Park, PA 16802

This paper deals with an experimental investigation of aerodynamic characteristics of full and partial-length squealer rims in a turbine stage. Full and partial-length squealer rims are investigated separately on the pressure side and on the suction side in the "Axial Flow Turbine Research Facility" (AFTRF) of the Pennsylvania State University. The streamwise length of these "partial squealer tips" and their chordwise position are varied to find an optimal aerodynamic tip configuration. The optimal configuration in this cold turbine study is defined as the one that is minimizing the stage exit total pressure defect in the tip vortex dominated zone. A new "channel arrangement" diverting some of the leakage flow into the trailing edge zone is also studied. Current results indicate that the use of "partial squealer rims" in axial flow turbines can positively affect the local aerodynamic field by weakening the tip leakage vortex. Results also show that the suction side partial squealers are aerodynamically superior to the pressure side squealers and the channel arrangement. The suction side partial squealers are capable of reducing the stage exit total pressure defect associated with the tip leakage flow to a significant degree. [DOI: 10.1115/1.1791279]

Introduction

Aerodynamic Character of Tip Clearance Flow: The gap required between the tips of rotating blades and the stationary casing of an axial flow turbine is a significant source of inefficiency. The leakage flow mainly induced by the pressure differential between the pressure side and suction side of a rotor tip usually rolls into a streamwise vortical structure. Total pressure losses of this flow structure measured at the exit of a turbine stage are directly proportional with the tip gap height. The leakage flow mixing with the rotor passage flow causes total pressure loss and significantly reduces turbine stage efficiency. Tip leakage related losses might account for as much as a third of the aerodynamic losses in a stage.

Early tip leakage flow visualization experiments in water led to the observation of the typical separation bubble near the entrance section of the gap. These studies concluded that viscous flow contributions could probably be ignored because of the magnitude of Reynolds number in the tip gap. Additional visualizations showed that the casing boundary layers changed the pressure field in the gap so much that rotational effects could not be ignored for an accurate determination of leakage losses. The rotation does have a very significant impact on the aerodynamic structure of tip clearance flows in turbomachinery systems.

The acceleration of the flow into the entrance region of the tip gap near the pressure side results in the relaminarization of an otherwise turbulent tip surface boundary layer. A number of investigators measured heat transfer coefficients on the tip surface by using a moving outer casing. They claimed that different rotational speeds imposed significant shear layer variations only near the outer casing. Flow features controlling the local tip heat transfer were not influenced from the rotation dependent shear layer near the outer casing. Heyes and Hodson [1] reported an iterative two-dimensional method of solving the mass flow through the tip gap. Their experimentally confirmed results showed that the chordwise pressure gradients had a significant influence on the separation zone and the mass flow rate through the gap region. Another set of experiments from Sjolander and Cao in Ref. [2] supported the Heyes and Hodson tip gap flow model, emphasizing the importance of having realistic chordwise pressure gradients. Their model was characterized by a vena-contracta forming a uniform isentropic jet along the endwall and a wake-mixing region along the blade tip surface downstream of the separation bubble. The main flow near the vena-contracta suffered very little loss. High losses were generated in the shear flow zone near the surface of the separation bubble.

Morphis and Bindon [3] performed an annular cascade experiment with a rotating outer casing. They found that the width of the separation bubble was directly controlled by the tip gap height. They experimentally confirmed that motion of the outer casing in the opposite direction to the tip gap flow reduced the leakage mass flow rate and momentum. The size of the separation bubble was reduced when the outer casing motion was imposed.

The effect of tip gap size and turbulence intensity on heat transfer distribution was investigated in a five bladed linear cascade by Azad, Han, Teng and Boyle [4]. They measured relatively high heat transfer near the entrance section of the gap near the pressure side because of the flow entrance effect. A larger tip gap generally resulted in a higher overall heat transfer coefficient because of the increase in the magnitude of the tip leakage flow. A 15–20% increase in heat transfer level along the leakage flow path resulted when the free stream turbulence intensity level was increased from 6.1% to 9.7%.

A new tip desensitization method based on a pressure side tip extension was discussed in Dey and Camci [5]. Phase-averaged total pressure maps downstream of the rotor showed the tip vortex leakage related local flow modifications. The rotating turbine study indicated that the momentum defect in the tip vortex of an untreated turbine blade tip could be effectively reduced by a suggested "*pressure side tip platform extension.*"

Squealer Tips: The function of a conventional squealer tip design is threefold. The squealer tip provides an effective reduction in tip gap flow. The specific approach also protects the blade tip from the full impact of high temperature leakage gases. A third function of this design approach is its protective ability against incidental rubs. A conventional full squealer approach forms an

[1]Presently at GE Global Research Center, Schenectady, NY.

[2]Currently at the Mechanical Engineering Department, Istanbul Technical University, Istanbul, Turkey.

Contributed by the International Gas Turbine Institute and presented at the International Gas Turbine and Aeroengine Congress and Exhibition, Atlanta, GA, June 16–19, 2003. Manuscript received by the IGTI Dec. 2002; final revision Mar. 2003. Paper No. 2003-GT-38979. Review Chair: H. R. Simmons.

enclosed cavity over the blade tip as shown by Anderson [6]. This is actually a simple labyrinth seal configuration between the turbine casing and rotating blade tip.

Azad, Han and Boyle [7] also investigated heat transfer and flow characteristics on the squealer tip of a gas turbine blade representative of E^3 design. They found a higher heat transfer coefficient on the rim surface because of the entrance and exit effects. The measured heat transfer coefficient is much lower in the mid-chord toward the pressure side and downstream end of the cavity when compared to the flat tip case. The heat transfer coefficient in a squealer tip is higher near the central upstream end of the cavity and the trailing edge region. They concluded that the squealer tip provides an overall lower heat transfer coefficient when compared to the flat tip case.

Heyes, Hodson and Daily [8] studied two squealer tip configurations in a cascade configuration and compared these to a flat baseline tip configuration. They showed the potential of squealer tip geometry to reduce tip clearance loss convincingly. Suction side squealer configuration provided the greatest gains in terms of eliminating leakage flow losses.

Variations of known squealer tip configurations may provide an effective aerodynamic seal in the turbine tip gap region. The implementation of chordwise sealing strips on a turbine tip was presented by Bunker and Bailey [9]. A numerical heat transfer investigation of a turbine tip section with a mean camber-line strip was investigated by Ameri [10] for a large power-generating turbine. A radiused-edge tip and a sharp-edge tip were investigated with a mean camber-line strip on the tip surface. The favorable conditions created by using a sharp edge tip were shown. Effects of a squealer tip covering the complete perimeter on rotor heat transfer and efficiency was presented in a numerical study by Ameri, Steinthorsson and Rigby [11].

A comprehensive investigation of the effect of squealer geometry on gas turbine blade tip heat transfer is presented in Azad, Han, Bunker and Lee [12]. In addition to tip heat transfer results in a five bladed linear cascade, stationary shroud wall static pressures were used for leakage flow field interpretation. They found that the location of the squealer could affect the leakage flow pattern and resulted in very different heat loads to the blade tip. A single squealer on the suction side provided a heat transfer benefit compared to that on pressure side or mid camber line. A single squealer arrangement performed better than a double squealer in reducing the overall heat transfer to the tip. When the squealer rim was located on the pressure side, a very low static pressure on the stationary shroud surface was observed near the mid suction side. When the squealer rim was located on the camber line, the low static pressure field in the middle of the suction side was reduced in size. The suction side squealer rim completely eliminated this low pressure field near the mid-suction side.

The current investigation deals with the aerodynamic features of tip leakage flow from ''full'' and ''partial-length'' squealer rims that are constructed separately on the pressure side and on the suction side in a rotating single stage turbine facility (AFTRF) as shown in **Fig. 1**. The lengths of these ''*partial squealer*'' rims are varied to find a configuration of optimal aerodynamic configuration. Current results indicate that the use of ''*partial squealer*'' arrangements can positively affect the local aerodynamic field by weakening the leakage vortex. The effectiveness of each suggested squealer rim arrangement is examined by using stage exit total pressure maps that have the capability of showing the size of the tip vortex dominated flow area and its momentum deficit. Since the high-resolution total pressure maps are obtained in a phase-averaged manner, the passage-to-passage flow field variations are effectively visualized. Results also show that the suction side partial squealers are capable of reducing the aerodynamic losses associated with the leakage flow to a significant degree.

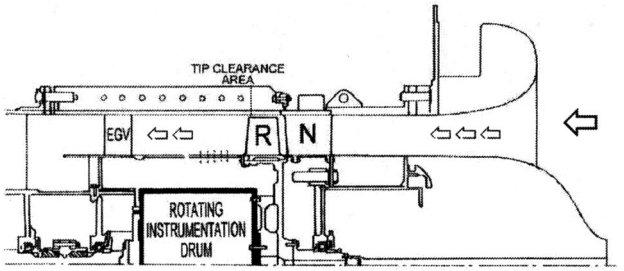

Fig. 1 Axial Flow Turbine Research Facility AFTRF of the Pennsylvania State University

Apparatus

Turbine Research Facility: The Penn State Axial Flow Turbine Research Facility, shown in **Fig. 1** is an open circuit rotating facility with a bell-mouth inlet of 1.1 m diameter which smoothly contracts the flow to a test section of 0.916 m (36 inch) diameter. The test section consists of a constant diameter outer casing, housing a single turbine stage with 23 nozzle guide vanes and 29 rotor blades. The flow passage height between the cylindrical hub surface and the outer casing is about 0.123 m. The rotor has an axial chord $c=0.129$ m at the tip. The total-to-total efficiency of the baseline turbine is 0.893. The nozzle efficiency is 0.994 and the rotor efficiency is 0.882. The stage inlet to exit total pressure ratio is 1.0778 at a mass flow rate of 10.53 kg/sec. The nominal rotational speed of the turbine rotor is 1320 rpm. Details about the stage, velocity triangles, blade design, as well as the turbine facility, are given in Lakshminarayana, Camci, Halliwell and Zaccaria [13].

Aerodynamic Instrumentation: Aerodynamic instrumentation available to the facility for steady state measurements includes sensors for the measurement of inlet temperature, total and static pressures, flow velocity and flow direction. The facility has provisions to perform aerodynamic shear stress, hot wire, hot film and dynamic pressure measurements in the stage. A probe traverse mechanism (radial and circumferential) is mounted inside the rotating instrumentation drum for the measurements to be performed in the rotating frame of reference.

Time Accurate Total Pressure Measurements: The present study uses a fast response, temperature compensated dynamic pressure transducer, XCS-062, made by Kulite Semiconductors. The transducer having a 150 kHz response time is flush mounted at the tip of the probe holder in order to eliminate the time response canceling effects of a cavity with finite volume. The diameter of the dynamic pressure transducer is 1.59 mm (0.063 inch). The transducer is housed in a probe tip section having a diameter of 2.4 mm. The total pressure probe is mounted on the outer casing in the stationary frame. The reference port of the differential transducer is open to atmospheric pressure in the lab. A mapping of the rotor including all twenty nine rotor passages, at the 30% chord (downstream) location is possible by using phase averaged total pressure measurements. A turbine shaft encoder triggers the data acquisition system. A total of 2000 samples, at an acquisition rate of 40 kHz, is collected once a trigger pulse is received. Hence, there are 62 data points in each blade passage. Slightly more than one revolution of the rotor is covered in a 2000 sample long data acquisition file. These data constitute an ensemble. Two hundred of such ensembles are averaged at a given radius, and radial position of the probe is changed by a computer-controlled system once the ensemble-averaged data are recorded. Other details of the time accurate total pressure probe and the data acquisition system is given in Dey [14].

Measurement Grid: The measurement grid extends from 0.17 h to 0.96 h in steps of 0.013 h (0.0016 m). The data acquisition board controls a stepper motor that actuates the probe traverse

mechanism in the radial direction. There is no need for a circumferential traverse because the probe in a stationary frame sees each one of the 29 tip vortices in each passage approximately 22 times a second. Signal conditioning is provided by a high-speed amplifier followed by an anti-aliasing filter which is set at about 15 times the blade passing frequency. A complete high-resolution mapping of the total pressure field requires only 30 minutes of turbine run time.

Tip Clearance: Although the turbine rotor tips are machined on a precision lathe there is a slight variation of tip clearance from one blade to another. The maximum measured tip gap size is 1.12 mm (t/h=0.91%) and the minimum gap size is 0.81 mm (t/h =0.66%). The nominal tip clearance of the rotor blades defined as the arithmetic average of 29 values from each blade is 0.98 mm (t/h=0.80%). A typical radius of the blade tip corners in AFTRF is about 0.10 millimeter.

Since the current tip desensitization study requires many tip region modifications, a special "*test blade*" was machined down to a relatively large tip gap of 1.65 mm (t/h=1.34%). Since the aerodynamic probe has a time response of about 150 kHz, the present method can easily differentiate the aerodynamic field of the "*test blade*" from the neighboring blades that have no tip treatment.

Measurement Uncertainties: The total pressure sensor used for the measurement of aerodynamic loss has a ±35 Pa absolute measurement uncertainty (±0.1% full scale). The dynamic pressure sensor Kulite XCS-062 did not have significant non-linearity error in the narrow range of dynamic pressure encountered in the turbine facility. The mean total pressure at the rotor exit is 94% of the inlet total pressure that is approximately 6 kPa or 17% full scale reading of the transducer. The rotor exit pressure varies between 0.935 an 0.945% of the inlet total pressure, which is a variation of the order of 1 kPa, or about 3% of full scale.

The rotational speed of the rotor in AFTRF was controlled within ±2 RPM by an eddy current brake. The stage entry temperature was measured by a K type thermocouple used in a total temperature probe located upstream of the nozzle guide vanes. This temperature measurement had an uncertainty of ±0.2 K. The tip clearance measurement uncertainty was about ±25.4 microns. A probe angle of 25 deg to the axial direction was maintained in all total pressure measurements reported in this paper. This angle corresponds to α_3 in the design velocity triangle for the tip region. Angular sensitivity studies were performed by rotating the probe with ±10 deg increments around the nominal value. The change in pressure data due to this rotation amounted to less than 0.1% of the data at the nominal value. Hence, within the limits of experimental error, the probe is insensitive to a flow angle change of ±10 deg. Wall interference was a concern for the tip measurements made close to the outer casing. Measurements indicated that data closer than 2.6% h from the tip endwall were unreliable. Hence, the last data point in the radial traverses was taken at 96.1% span. The information contained in this narrow radial band should be close to each other for most configurations studied in this paper.

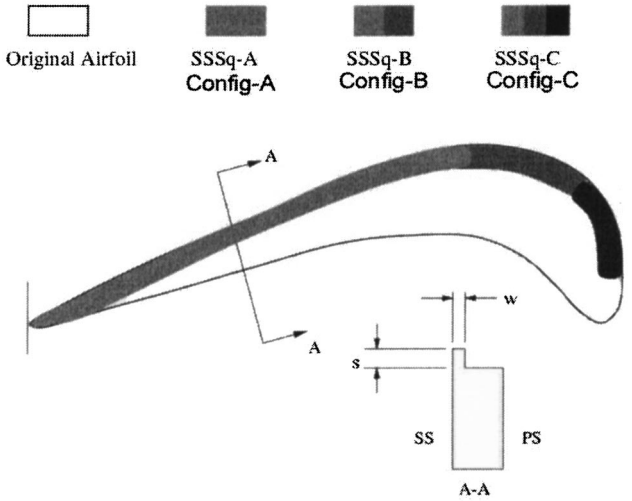

Fig. 2 Geometry of the suction side squealer tip, s=0.38 mm and 0.76 mm (t-s)/h=1.03% and 0.72%

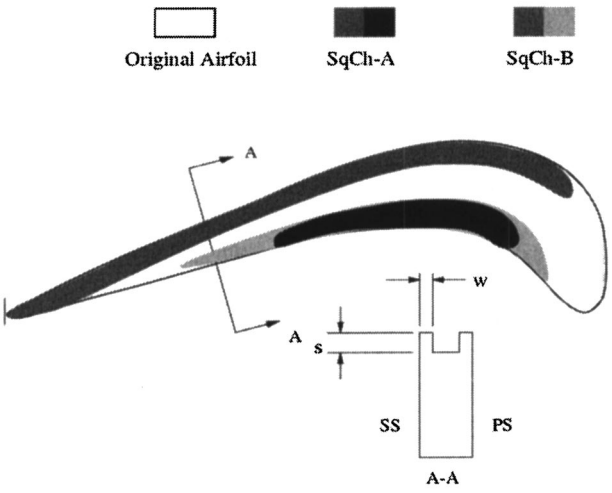

Fig. 3 Geometry of channel type squealer tip, s=0.76 mm (t-s)/h=0.72%

Squealer Tip Geometries: Squealer tips are currently used in production turbines for tip desensitization. A squealer tip is a blade tip treatment where the central part of the blade tip surface is recessed, leaving a thin rim which is much closer to the outer endwall than the center. Overall, a squealer tip resembles a cavity below a moving wall. The squealer tip geometries tested in AFTFR were obtained by attaching precision cut thermoplastic rim sections to regular/untreated tip on the test blade. Two geometries were tested:

The first one, shown in **Fig. 2**, would be termed as **S**uction **S**ide **Sq**uealer (SSSq). This configuration featured a constant width rim extending from the trailing edge to different lengths along the suction side of the blade tip. The rim width was 4 mm corresponding to 18% of the maximum blade thickness. SSSq-A was the shortest rim extending from the trailing edge of the blade to 22% axial chord measured from the leading edge. SSSq-B extended from the trailing edge to 4% chord and SSSq-C extended from the trailing edge to the leading edge as shown in **Fig. 2**.

The other one, shown in **Fig. 3**, was termed as **Sq**uealer **Ch**annel (SqCh). This geometry featured a channel formed by the suction side rim of SSSq-B configuration and a pressure side rim of varying length. SqCh-A had a pressure side rim extending from 25% to 62% axial chord. SqCh-B had a relatively longer pressure side rim extending from 22% to 66% axial chord. The pressure

Table 1 Test matrix for squealer configurations

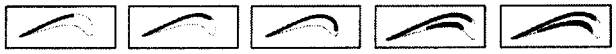

Squealer Type t=1.65 mm t/h=1.34 %	SSSq-A	SSSq-B	SSSq-C	SqCh-A	SqCh-B
Short rim (t-s)/h=1.03 % s=0.38 mm	✓	✓	✓		
Tall rim (t-s)/h=0.72 % s=0.76 mm	✓	✓	✓	✓	✓

side rim in both of these was slightly tapered in shape, and had a maximum thickness of 5 mm. Other details of the squealer rim configurations are described in Dey [14].

Experimental Matrix: Table 1 shows the test matrix for the squealer tip experiments performed in this study. Three configurations of SSSq were tried, as shown in **Fig. 5**. The thickness "*w*" of the squealer rim was 4 mm, with a maximum blade thickness of 22 mm. The rim was no more than 18% of the maximum blade thickness. The rim was made of thermoplastic shim that was attached to the blade surface using a double-sided tape manufactured by 3M Corporation. Configuration SSSq-A provided the shortest rim, extending from 22% to 66% chord. The pressure side rim in both of these was slightly tapered in shape and had a maximum thickness of 5 mm.

Turbine Passage Aerodynamics Without Squealer Rims

This section summarizes the general aerodynamic character of the AFTRF flow in the rotating frame of reference. The rotor inlet flow characteristics of the AFTRF, measured secondary flow patterns at the rotor exit and the measured static pressure values on the rotor tip platform are described in this section.

Rotor Inlet Flow Field: Measured and design values of the tangential, axial and radial components of the velocity vector in the exit plane of the nozzle guide vanes are shown in **Fig. 4**. The momentum deficit in the inner and outer endwall boundary layers is clearly shown in the circumferentially mass averaged axial velocity component V_θ. The radial components of the velocity vector before it enters into the rotor are extremely small.

The measured velocity components are in good agreement with the design values near the mid-span. The slight deviations from the design values are in the zones where secondary flows and other forms of passage vorticity are measurable. Details of the three-dimensional nozzle exit flow measurements using a subminiature five-hole probe are discussed in Zaccaria and Lakshminarayana [15].

Measured Secondary Flow and Tip Leakage Patterns at Rotor Exit: Ristic, Lakshminarayana and Chu [16] measured the secondary velocity field at the exit plane of the AFTRF rotor by using a three-component laser Doppler anemometer. The velocity field representations are based on the "average passage" derived from averaging the ensemble-averaged velocity across all the blade passages. The secondary velocity field was obtained by subtracting the measured velocity field from the design values of the velocity field. Five distinct regions of the flow exiting the rotor can be distinguished; passage core flow, hub passage vortex, casing passage vortex, rotor wake flow and the tip leakage vortex. Hub passage vortex is strong and well organized due to large blade turning angle in this region. The secondary flow near the casing is complex. The radially outward flow near the blade (tip) pressure side possesses significant radial outward velocity near the casing. The suction side corner of the blade tip flow has strong radially inward flow induced by the tip leakage vortex and passage vortex. The passage vortex tends to interact with the tip vortex and contains it in the vicinity of the suction surface. AFTRF rotor field measurements show that the leakage flow is different from those observed in cascades, e.g., Yamamoto [17]. The relative motion between the stationary wall and the moving blade tip tends to confine the leakage vortex to the suction side of the blade. In addition, the rotation effects prevent radial inward transport of the secondary flow core. In cascades, the secondary flow has a tendency to move much further away from the casing and away from the suction surface. Because of the leakage flow, the secondary flow pattern near the outer casing becomes much distorted compared to its counterpart near the hub surface. The leakage and secondary vortices entrain fluid from surroundings as confirmed by outward velocity near the pressure side and inward velocity on the suction side of the tip. It is also clear that the rotor wake is substantially influenced by the secondary flow and tip leakage flow from mid-radius to tip with secondary flow effects dominating over rotation effects in inducing radially inward flows.

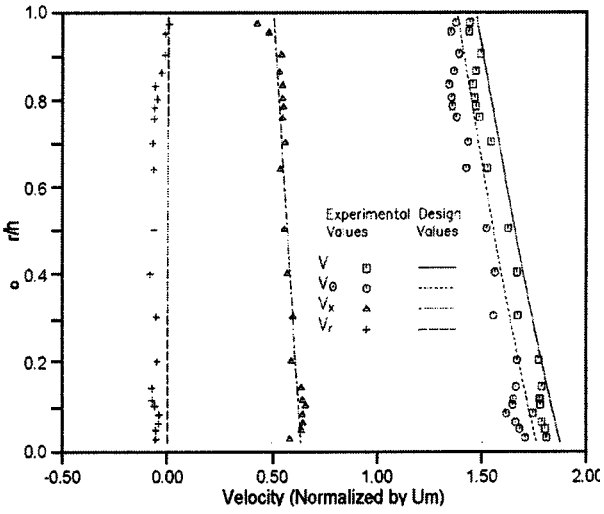

Fig. 4 Axial, tangential and radial velocity components at AFTRF rotor inlet plane (measured and design values) [15]

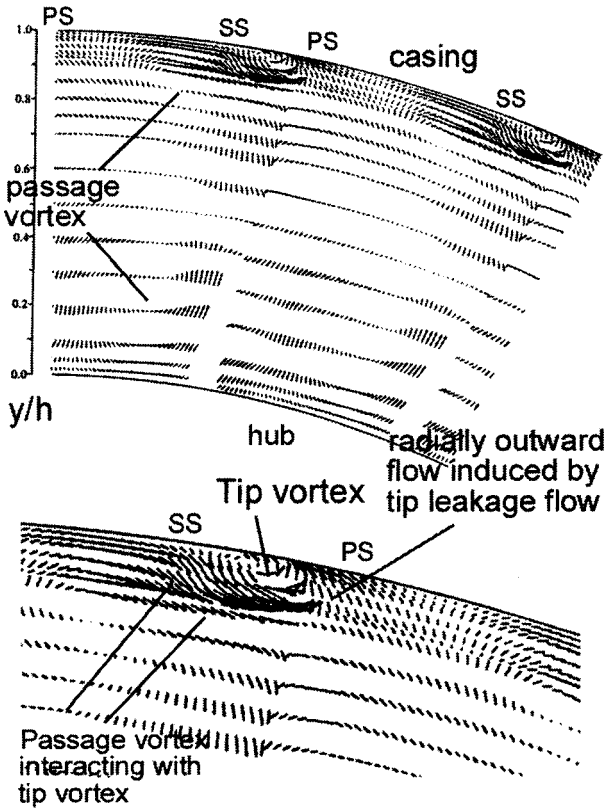

Fig. 5 Measured secondary flow patterns at AFTRF rotor exit plane without squealer rims. The observer is looking into the flow at rotor exit plane [16]. (Blade rotation is in CCW direction.)

Static Pressure on the Rotor Tip Surface: Detailed pressure distributions obtained on the rotating tip surfaces of turbine blades are helpful in explaining the physical aspects of tip leakage flows. A good understanding of the static pressure field on blade tips is essential in implementing new aerodynamic de-sensitization schemes. Tip static pressure measurements performed by Xiao, McCarter and Lakshminarayana [18] in AFTRF are shown in **Fig.**

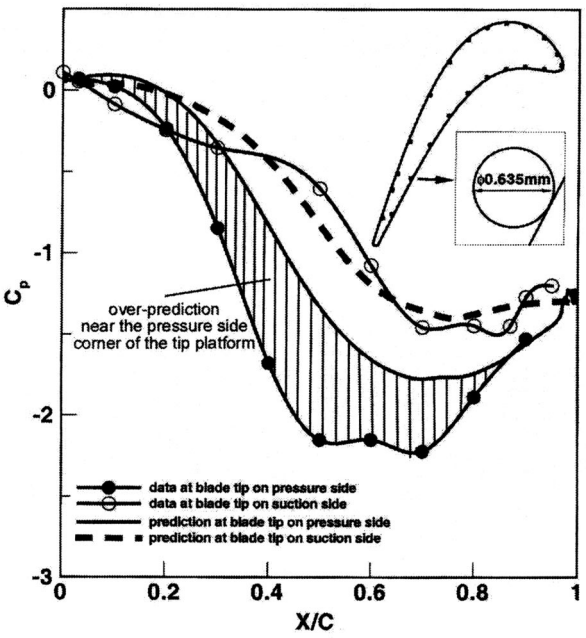

Fig. 6 Measured and predicted static pressure on the rotor tip platform of AFTRF [18]

5. The measurements are given for an average tip gap of 0.97 mm and a relative casing speed of 64 m/s. The tip platform static holes that are distributed around the perimeter of the tip airfoil are flush with the tip platform. The pressure measured at the corner between the pressure side and tip platform is extremely low. The pressure in this zone is even lower than the suction side corner. Morphis and Bindon [19,3] observed the same phenomenon in a turbine cascade. The ultra low pressure at the corner between the pressure surface and the tip is due to the sharp radius of the pressure side corner. A small separation bubble just downstream of the pressure side corner forms a vena-contracta effect at the entrance of the tip gap area. The width of the bubble depends on tip gap size and the corner radius. The separation bubble causes significant total pressure loss. The low-pressure zone is also because of the strong acceleration of the leakage flow into the vena-contracta dominated zone of the tip flow path. Sjolander [20] also came to similar conclusions in a cascade arrangement. **Figure 5** also shows the Navier-Stokes simulations performed by Luo and Lakshminarayana [21] using an algebraic Reynolds stress model of turbulence. The predicted static pressure shows a relatively low pressure near the pressure side corner in the tip gap when compared to the suction side corner. The suction side prediction of pressure is in very good agreement with the measurements. However, there is an over-prediction of the pressure near the pressure side corner. This over-prediction may be attributed to the relatively complex tip gap inlet velocity with radially outward components. The existence of a separation bubble near the pressure side corner complicates this highly three-dimensional leakage flow pattern.

The predictions match the measurements of tip platform pressure well in the last 20% axial chord of the blade where pressure side and suction side corner pressures are close to each other.

Experimental Results With Partial Squealer Rim Arrangements and Discussion

Chordwise Length of the Suction-side Partial Squealer Rim: Figs. 7, **8** and **9** show results from the experiments with suction side squealer rims. All three figures show the total pressure maps made at 0.3c downstream of the rotor. The stage exit total pressure

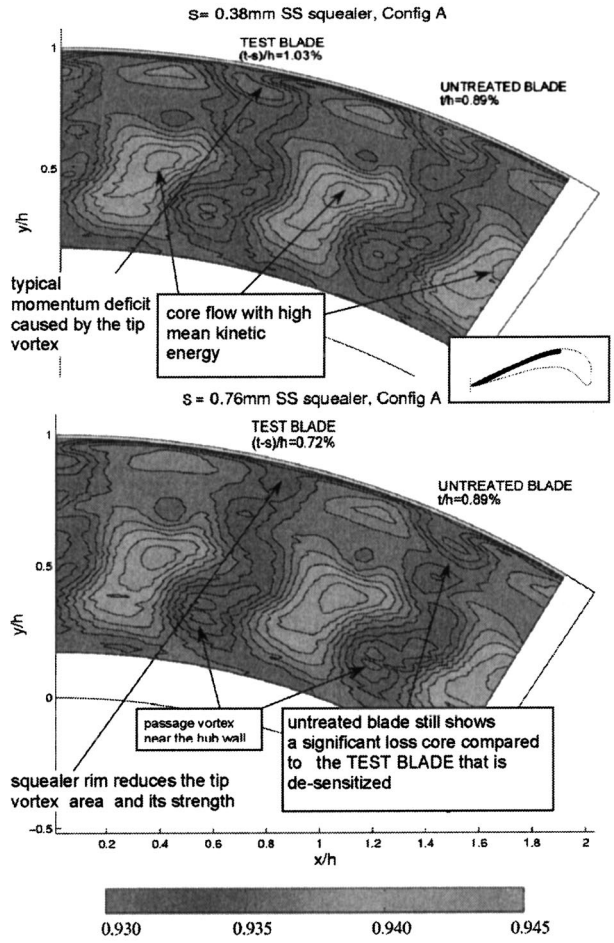

Fig. 7 P_o/P_{in} contours for two gaps, SSSq-A (the shortest squealer rim)

in a plane normal to the axis of rotation is contour plotted. The contour plots of total pressure from a test blade with partial squealer rims and a neighboring unaltered blade are presented side by side. The top sub-plot shows the total pressure map from a partial squealer rim that rises s=0.38 mm from the tip surface, while the lower sub-plot features a rim that is twice as tall, s=0.76 mm. The blade surface that is not covered by the partial squealer rim has the normal tip clearance of t=1.65 mm (t/h=1.34%). The top sub-plots are for an effective tip clearance of (t-s)/h=1.03%. The effective clearance (t-s)/h is 0.72% for the lower subplots. **Figures 7**, **8** and **9** are only different from each other in terms of the chordwise length of the squealer rim, as shown in **Fig. 2**. There seems to be little difference in stage exit total pressure between the three configurations for the same effective clearance (t-s)/h. The chordwise length of the partial squealer rim that is different in each one of the three configurations (A, B and C) does not affect the overall leakage flow pattern and the total pressure at the stage exit. The benefits of tip vortex desensitization for cases A, B and C are very similar to each other.

Influence of Squealer Rim Height: There is, however, a significant influence of effective clearance (t-s)/h on the flow structure of the tip vortex from the ''*test blade*'' that carries a partial squealer rim. The shorter rim with s=0.38 mm hardly performs any desensitization, while the taller rim with s=0.76 mm is quite effective in reducing both the size and the depth of the loss core due to the leakage vortex. If the shorter s=0.38 mm rim [(t-s)/h =1.03%] is compared to the baseline case having a clearance of t/h=1.03% (s=0 mm), a negligible difference is noticed in total pressure field.

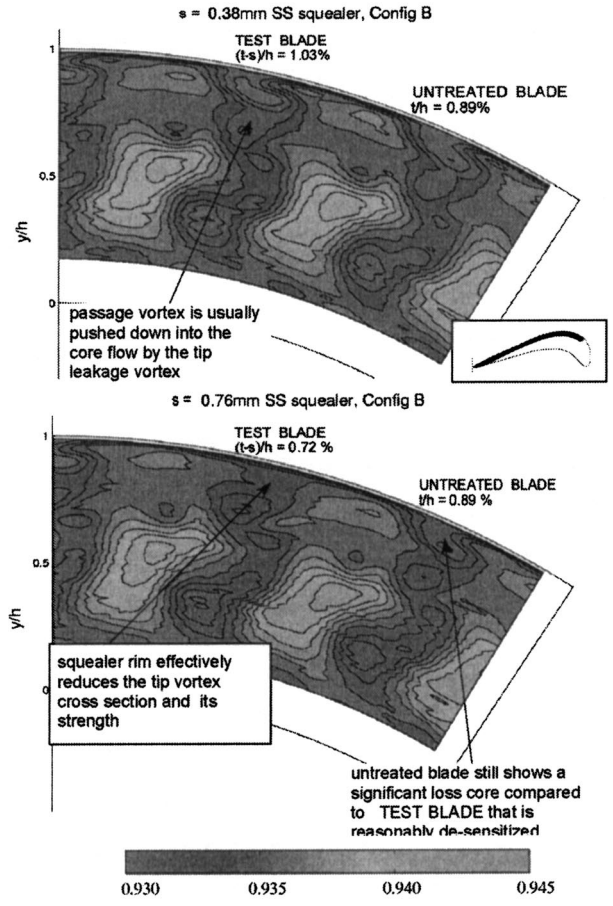

Fig. 8 P_o/P_{in} contours for two tip gaps, SSSq-B (middle length squealer rim)

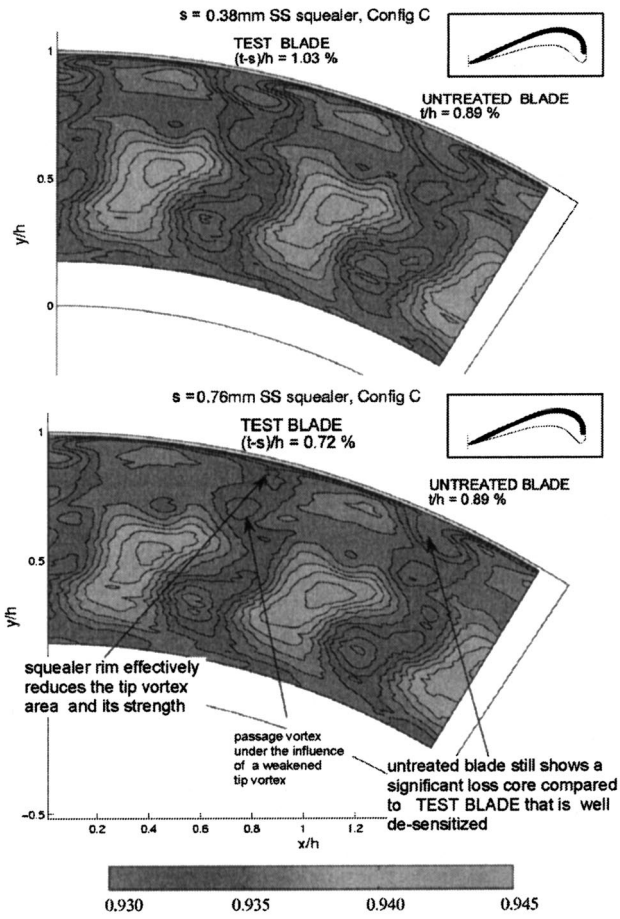

Fig. 9 P_o/P_{in} contours for two gaps, SSSq-C (the longest squealer rim)

This is, however, not the case with the s=0.76 mm rim that has an effective clearance of (t-s)/h=0.72%. In comparing this with the baseline which has a clearance of t/h=0.72% (s=0 mm), one notices a much smaller loss core when the rim is present. The taller rim with (t-s)/h=0.72% effectively weakens the tip vortex compared to a flat tip surface of the same effective clearance t/h=0.72% (s=0 mm). The influence of rim height s is shown clearly in **Figs. 10** and **11**, where ensemble averaged total pressure is plotted against the circumferential position of the rotor at two radial positions near the tip platform. The partial squealer tip configuration B termed as SSSq-B with s=0.38 mm rim [(t-s)/h =1.03%] is compared to a flat tip with the same effective clearance in **Fig. 10**. The flat tip is also termed ''*full cover*'' throughout this study. The r/h=89.7% location corresponds approximately to the core of the leakage vortex and the 79.3% location corresponds to the passage vortex location. The SSSq-B with a shorter rim height of s=0.38 mm results in an almost identical total pressure distribution when compared to the full cover tip at r/h=89.7% and r/h=79.3%. **Figure 11** presents the results from the case with a taller rim height of s=0.76 mm. This time the tall partial squealer rim that has (t-s)/h=0.72% is compared against the flat tip with the same effective clearance of t/h=0.72% (s=0 mm). The chordwise length of the rim is defined as SSSq-B in **Fig. 2**. It is clear that the SSSq-B performs significantly better than the flat cover with the same clearance in the leakage vortex zone near r/h =92.2%. At r/h=81.9%, the performance of SSSq-B with s=0.76 mm (**Fig. 11**) is similar to that of the flat tip with the same effective clearance as shown in the lower sub-plot.

The partial squealer rim attached to the suction side of the tip platform is effective only when the rim is relatively high. **Figure 11** shows that the taller s=0.76 mm rim desensitizes much better than does the 0.38 mm rim. The shaded area in **Fig. 11** represents the total pressure gain because of the leakage reducing influence of the partial squealer rim SSSq-B.

Leakage Mechanisms with a Partial Squealer Rim on the Suction Side: An attempt to explain why the taller squealer rim is more effective is made in **Fig. 12**. In this figure, a cross section of the turbine blade tip is shown in a direction approximately normal to the blade camber line. The observer is attached to the rotating blade (TEST BLADE) and the outer casing moves in the opposite direction to the mean tip leakage flow, with a velocity of U_{casing}.

When the flow from the pressure side enters the clearance gap, a separation bubble ''A5'' forms. A little upstream, the flow encounters a forward facing step as it meets the squealer rim of height ''s''. A second separation bubble ''A4'' forms at this corner. The flow then moves radially upwards as it tries to negotiate the squealer rim. However, next to the moving outer casing, a near wall flow pointing from the suction side towards the pressure side, is induced (U_{casing}). A high level of turbulent shear stress is applied to the leakage jet by the casing. Some of the radially upward flow might roll up in a vortex ''A3'' as it encounters the ''backward'' flow near the moving wall. The rest of the radial outward flow manages to climb on top of the squealer rim and escapes to the suction side of the tip. The leakage flow, upon meeting the passage flow, rolls into a leakage vortex. Of key importance in this description is the formation of the vortex ''A3'' which tends to sit on the central portion of the blade tip surface. This vortex forms a barrier to the gap leakage flow. The leakage mass that manages to form the leakage vortex from a squealer rim is the

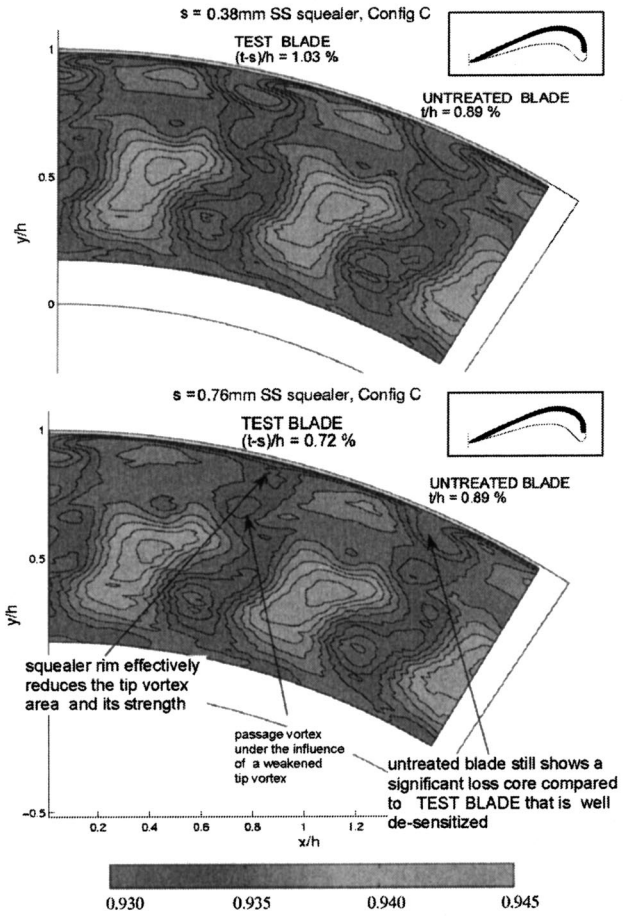

Fig. 10 Plots of P_o/P_{in} for s=0.38 mm SSSq-B and full cover

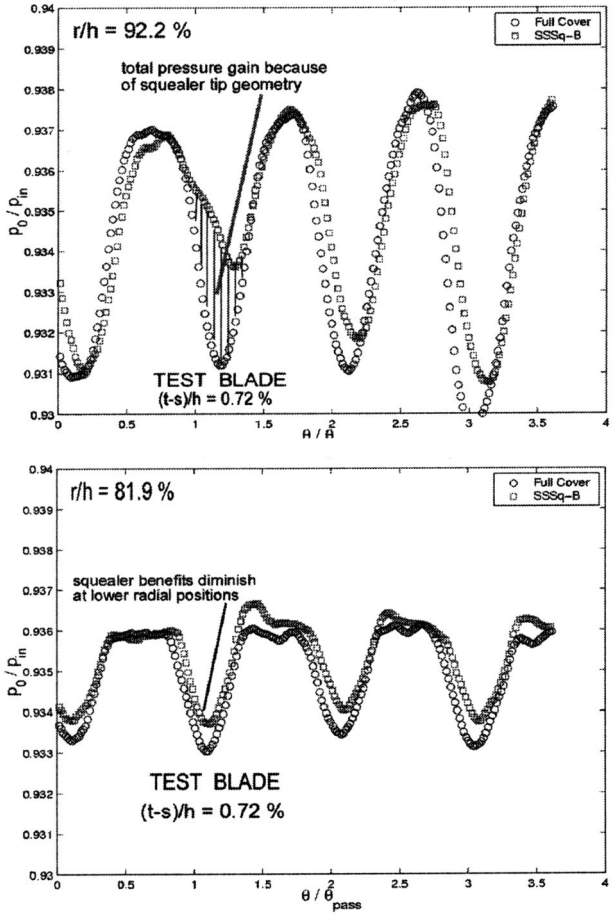

Fig. 11 Plots of P_o/P_{in} for s=0.76 mm SSSq-B and full cover

relatively small fluid mass that escaped below the vortex ''A3''. Not only is this mass flow rate small, but the momentum associated with it is small as it escapes to the suction side.

The partial squealer rim height s could be related to the formation of the vortical structure ''A3''. It is expected that the vortex ''A3'' forms only when ''s'' is large. For lower ''s'', the leakage mass does not have a significantly large radially outward momentum near the separation bubble ''A4'', and the vortex ''A3'' may not form. The leakage jet may go straight through the tip gap, and emerges as a relatively strong leakage vortex on the suction side. Thus, the flow in the tip gap region behaves quite like a flat tip of the ''*full cover*'' configuration.

Influence of Partial Squealer Rims on Total Pressure at Different Radial Positions Near the Tip: Fig. 13 compares the three SSSq configurations with s=0.38 mm rim, at two radial positions. The top and the bottom sub-plots correspond to the locations for the core of the leakage vortex (r/h=89.7%) and passage vortex (79.3%), respectively. It is obvious from this figure that all three configurations perform similarly at (t-s)/h=1.03%. **Figure 13** needs to be compared to **Figs. 14** and **15** which show the performance of the three SSSq configurations with s=0.78 mm rim, at four radial locations, r/h=94.8%, 92.2%, 89.7% and 79.3%. The first three locations correspond to approximately the leakage vortex core location while the last one corresponds to the passage vortex core location. All four plots show that configuration SSSq-B performs better than SSSq-A or SSSq-C. The superior performance is evident near the leakage vortex core at, but it is also felt near the passage vortex. This means that the chordwise length of the squealer rim is important for the purpose of tip desensitization. The squealer tip configuration performs better as its length is increased from that of SSSq-A to that of SSSq-B. However, further increase in the chordwise length does not serve to make the desensitization effort any better. The rim does not need to extend all the way to the leading edge, but there is an optimal length of the squealer tip.

Figure 16 tries to explain the reason why SSSq-B performs better than SSSq-A and SSSq-C. This figure shows the tip airfoil with the squealer rim installed near the suction side, along with possible flow paths from the pressure side to the suction side. As explained previously, the squealer rim blocks part of the mass flow trying to pass through the clearance gap. Which part of the tip gap region passes the maximum amount of leakage jet is a question directly related to the static pressure distribution of the specific airfoil tip design. Local viscous flow conditions near the pressure side corner and the suction side corner of the tip section also contribute to the amount of leakage flow passing from the tip gap. It is also known that most streamlines turn very sharply as they enter the clearance gap, and thus the mass originating near region **X**, near the leading edge of the airfoil leaks through the front part of the airfoil to form the leakage vortex. Obviously, any obstructions in the forward part of the airfoil would increase the effectiveness of the desensitization effort, and this is what SSSq-B offers. The fluid particles following the streamlines from both region **X** and **Y** are effectively blocked by SSSq-B, and that is why SSSq-B performs better than SSSq-A that is the shortest rim used in this study.

However, SSSq-C, that is the longest rim configuration, does not perform as well as SSSq-B. This is possibly because in SSSq-C, the rim is located right in front of the fluid following the

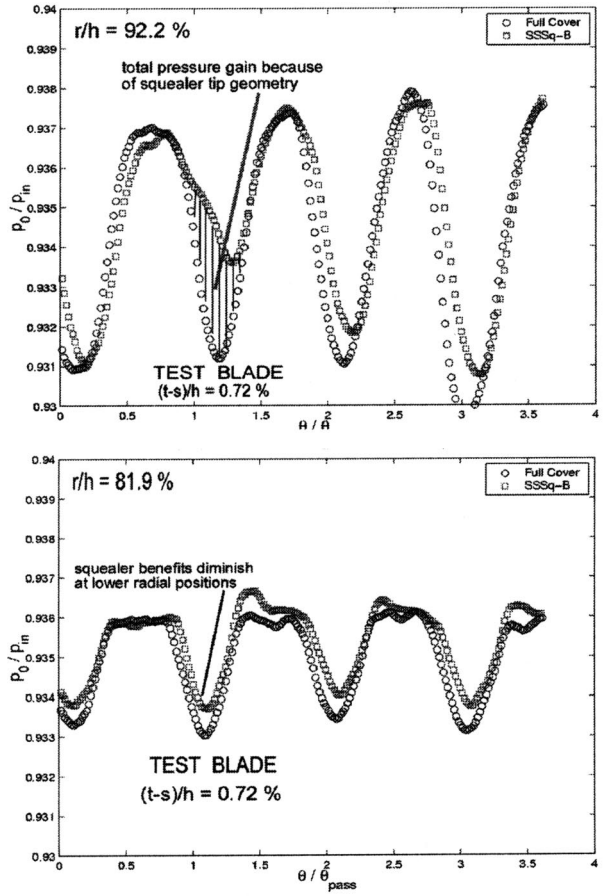

Fig. 12 A representation of flow field near a partial squealer tip on the suction side

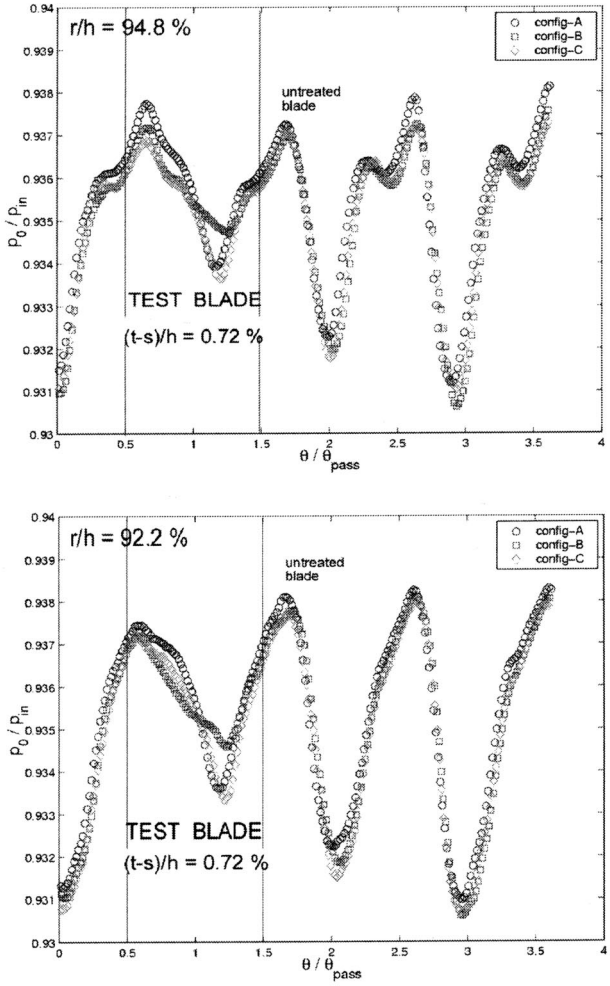

Fig. 14 Plots of P_o/P_{in} for three s=0.76 mm SSSq configurations (r/h=94.8% and 92.2%)

streamlines from region **X**. The partial rim section very near the leading edge may act as an unnecessary channeling device sending more leakage fluid into the tip vortex, forming near the suction side corner of the airfoil. When this feature is considered together with the extra aerodynamic losses imposed by the leading edge section of the partial rim, the slightly better performance of the configuration SSSq-B (middle length rim) when compared to the longest length rim SSSq-C could be explained.

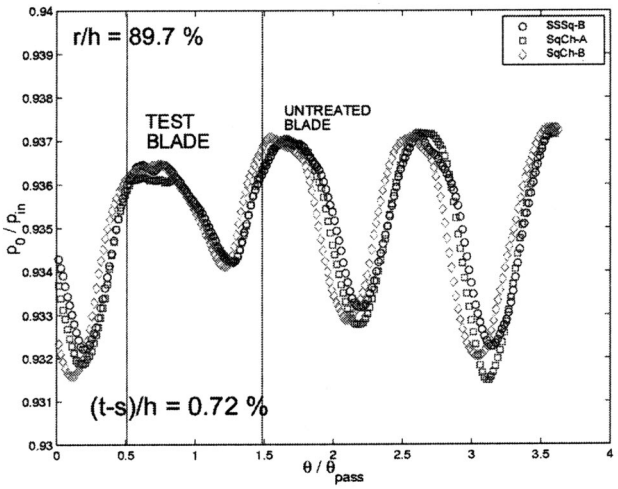

Fig. 13 Plots of P_o/P_{in} for three s=0.38 mm SSSq configurations (r/h=89.7% and 79.3%)

Squealer Channel Configurations: Fig. 17 shows the total pressure results for the squealer channel arrangement. The channel geometry was shown in **Fig. 3**. Two configurations were tried. SqCh-A, with a shorter pressure side squealer rim, is shown in the top sub-plot, while SqCh-B, with the longer pressure side rim, is shown in the bottom sub-plot. The rim height was s=0.76 mm for both channel configurations. The total pressure maps presented in the two figures are extremely similar, meaning that the length of the pressure side squealer rim does not seem to affect the aerodynamic desensitization process.

More light is shed to the channel configurations from **Fig. 18** in which three s=0.76 mm high squealer configurations are compared, SSSq-B, SqCh-A and SqCh-B. It could be seen that the performance of the SSSq-B and SqCh-A and SqCh-B configurations are almost identical in the passage defined by the test blade. Thus the pressure side squealer rims are hardly contributing to the desensitization process. A typical squealer tip arrangement used in gas turbine practice would have a rim occupying the full circumference of the blade tip. It seems that the portion of the rim near the pressure side corner is not an effective contribution to aerodynamic desensitization. It appears that the pressure side part of the

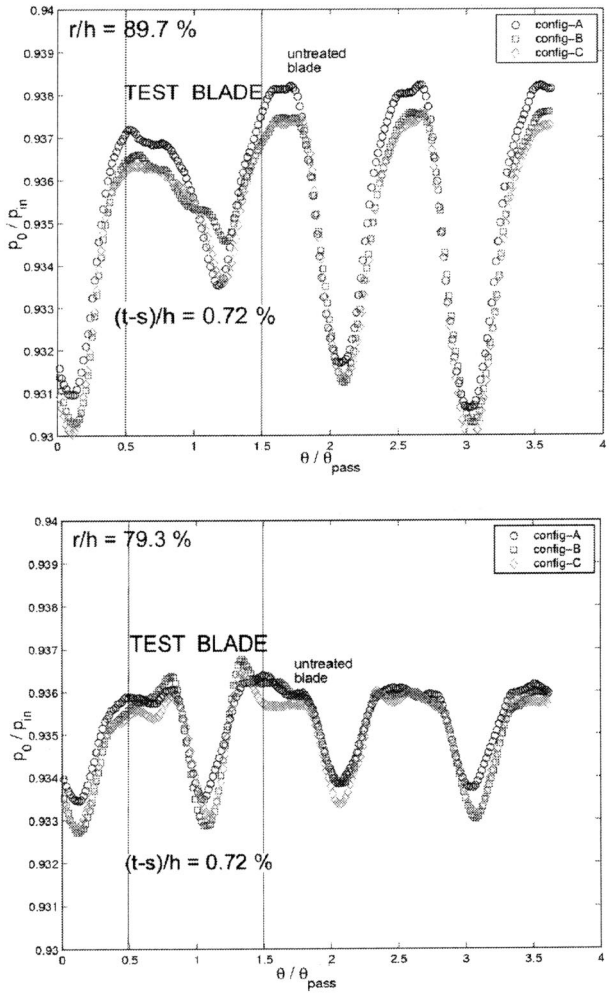

Fig. 15 Plots of P_o/P_{in} for three s=0.76 mm SSSq configurations (r/h=89.7% and 79.3%)

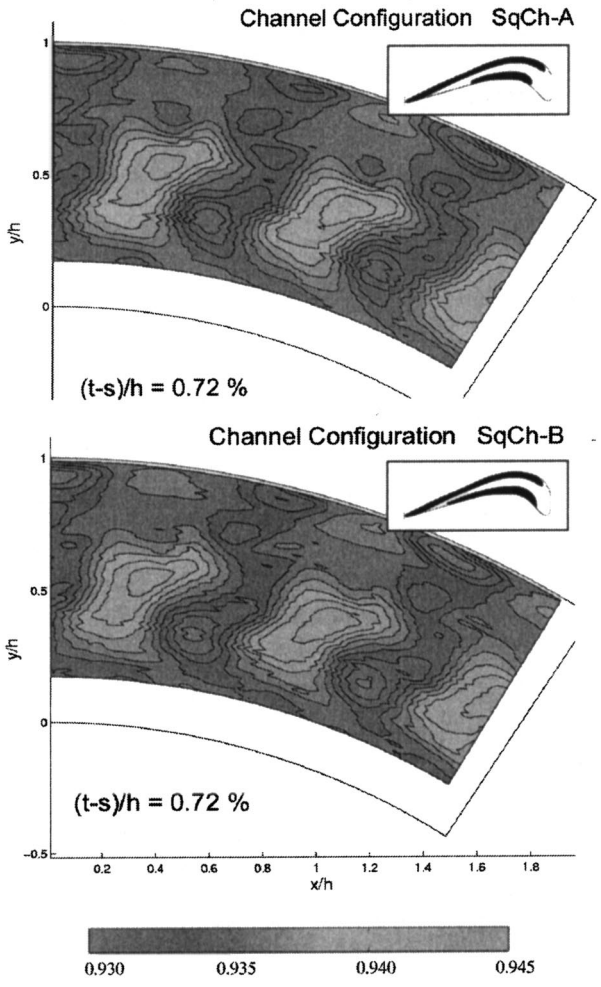

Fig. 17 P_o/P_{in} contours of channel configurations, SqCh-A and SqCh-B, s=0.76 mm

squealer rim is redundant, and does not contribute to the blockage of the leakage fluid that tends to eject from the suction side of the blade.

Aerodynamic Efficiency Change due to Partial Squealer Tips: The current experimental results were obtained in a cold turbine facility (AFTRF). The rotor tip Mach number is about 0.18 and the relative rotor exit Mach number near the outer casing is about 0.24. The cold airflow in the nozzle guide vane and the rotor passages is incompressible everywhere. The total-to-total efficiency of an axial flow turbine stage is defined as follows:

$$\eta_{tt} = \frac{1-(T_o/T_{in})}{1-(P_o/P_{in})^{(\gamma-1)/\gamma}}. \tag{1}$$

The circumferentially averaged total pressure ratio between the stage exit and inlet under nominal conditions is about $P_o/P_{in} = 0.945$ at the mid span. The corresponding mid-span temperature ratio is $T_o/T_{in} = 0.986$. A typical total temperature drop in the stage is approximately 5°K. The corresponding total-to-total efficiency is about $\eta_{tt} = \%87.3$. The sensitivity of the total-to-total efficiency to the stage pressure and temperature ratio could be obtained by chain differentiating Eq. (1) as follows:

$$\delta\eta_{tt} = \left(\frac{\partial\eta_{tt}}{\partial p_r}\right)\cdot\delta p_r + \left(\frac{\partial\eta_{tt}}{\partial T_r}\right)\cdot\delta T_r \tag{2}$$

where $p_r = P_o/P_{in}$ and $T_r = T_o/T_{in}$. The variation of the total-to-total efficiency in function of the change in stage total pressure ratio and temperature ratio could be obtained from Eqs. (1) and (2).

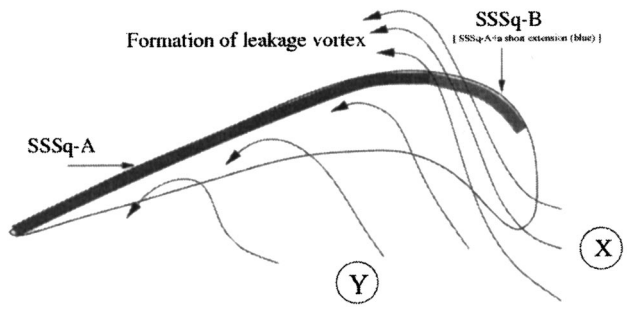

Fig. 16 Streamlines near partial squealer rims located at the suction side

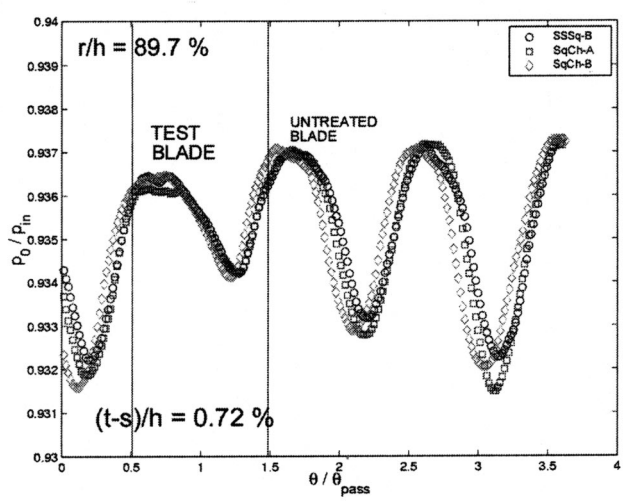

Fig. 18 Comparison of the two squealer channels with the partial squealer rim (SSSq-B) on the suction side, s=0.76 mm

$$\delta\eta_{tt} = -\frac{[1-(T_o/T_{in})]\cdot[(\gamma-1)/\gamma](P_o/P_{in})^{-(1/\gamma)}}{[1-(P_o/P_{in})^{(\gamma-1)/\gamma}]^2}\cdot\delta p_r \hookleftarrow$$

$$\rightarrow -\frac{1}{[1-(P_o/P_{in})^{(\gamma-1)/\gamma}]}\cdot\delta T_r \qquad (3)$$

Equation (3) is helpful in evaluating the change in the efficiency of the stage due to the implementation of a specific tip de-sensitization scheme. **Figure 11** shows a significant gain in the total pressure ratio measured at a radius corresponding to the core of the tip vortex with and without de-sensitization. δp_r in Eq. (3) could be obtained from the shaded area of **Fig. 11**. The total pressure distribution for the baseline tip shown with circular symbols is notably improved by the implementation of the partial squealer arrangement SSSq-B. A measurable gain in local p_r because of de-sensitization is shown by square symbols in the shaded area for r/h=92.2%. This area corresponds to the flow zone originally occupied by a tip vortex that had a significant amount of secondary kinetic energy and total pressure loss. The leakage reduction and the subsequent elimination of strong streamwise vorticity because of the squealer tip SSSq-B could be quantified from Eq. (3). By assuming that "the local temperature change δT_r due to squealer tip implementation is not significant in this cold turbine rig," one could use the first term of Eq. (3) for the calculation of efficiency improvement $\delta\eta_{tt}$. The temperature change δT_r is with respect to the case where no tip treatment is applied. The measurement of the time accurate total temperature at the exit of the turbine is not currently possible at a temporal resolution that is compatible with that of the current dynamic pressure measurements. Although the temperature change with respect to the baseline case (full cover/flat tip) is not available from the current experiments, it is expected that the turbine passage flow generates more work in this zone (r/h=92.2%). This is because of the significant improvements in local total pressure distribution in the tip vortex dominated area. Although small in magnitude in AFTRF, the second term in Eq. (3) always adds to $\delta\eta_{tt}$ when δT_r is negative which is the case for a successful aerodynamic de-sensitization attempt. If the maximum measured total pressure gain δp_r (as shown in the shaded area of **Fig. 11**) is used in Eq. 3, a local maximum η_{tt} improvement of $\delta\eta_{tt}=+5.01\%$ is obtained for r/h=92.2%. When η_{tt} improvements are area averaged in the shaded area, the overall de-sensitization improvement for the specific passage is about $\delta\eta_{tt}=+3.2\%$. The current dynamic total pressure measurements at stage exit show that the favorable improvements in total-to-total efficiency are clearly observable from r/h=79% to 94% blade height.

Conclusions

The aerodynamic characteristics of partial squealer rims of varying lengths and heights were studied in a single stage cold turbine research facility. Two different channel arrangements were also examined.

Phase-locked time accurate total pressure measurements at rotor exit plane can be effective in determining if a tip desensitization scheme is aerodynamically acceptable or not.

A (150 Khz) dynamic pressure transducer in a total pressure probe arrangement can be used in the phase-averaged mapping of total pressure at the exit of a turbine stage. A complete high-resolution mapping of all blade passages at the rotor exit plane is an effective way of determining the aerodynamic impact of tip leakage vortices. In this approach, subsequent modifications made in the tip area can be visualized with respect to a baseline clearance in the rotor assembly.

Experimental results show that partial squealer configurations seal the tip effectively. The current study shows that, when effective squealer clearance between the top surface of the squealer rim and the outer casing "(t-s)/h" is about 0.72%, a favorable tip desensitization level is achieved.

The chordwise length of a partial squealer rim near the suction side is an important parameter in defining the sealing effectiveness of the rim. The shortest rim (Config-A) and the longest rim (Config-C) were less effective than (Config-B) (mid-size) in reducing the leakage flow through the tip gap. Every tip profile may have an optimal rim length in terms of the effectiveness of aerodynamic de-sensitization.

The suction side squealer is by itself capable of significant aerodynamic tip desensitization. The squealer rims extending from the trailing edge to about 6% axial chord location near the leading edge perform best amongst suction side squealers of different chordwise lengths.

Two different channel arrangements that have partial squealers both near the suction side corner and pressure side corner were investigated. SqCh-A with a shorter pressure side rim produced a desensitization performance very similar to SqCh-B with a longer rim on the pressure side.

A comparison of the two channel arrangements with (Config-B) indicated that the sealing performance of the partial rim on the suction side is even better than the channel arrangements. The portion of the rim near the pressure side corner of the channel arrangement did not contribute to the sealing action.

The influence of the tip vortex area total pressure ratio on the total-to-total efficiency of the turbine stage was evaluated for cold turbine flow conditions. If the maximum measured total pressure gain δp_r is used, a "*local maximum*" η_{tt} improvement of $\delta\eta_{tt}=+5.01\%$ is obtained in the tip vortex dominated zone. When η_{tt} improvements are "*area averaged*" in the circumferential direction, the overall de-sensitization improvement is about $\delta\eta_{tt}=+3.2\%$ at r/h=92.2%.

The current dynamic total pressure measurements at stage exit show that the favorable improvements in total-to-total efficiency are clearly observable from r/h=79% to 94% blade height.

Although the current experiments demonstrate the aerodynamic gains obtained from partial squealer tips, a much detailed understanding of the leakage flow in the gap is needed.

A numerical visualization effort in the tip gap area using a 3D, steady, viscous and turbulent flow system based on Reynolds-averaged Navier-Stokes equations is under progress with and without the relative motion of the outer casing.

Acknowledgments

Our research subcontract was sponsored by the U.S. Department of Energy ''National Energy Technology Laboratory'' through a cooperative agreement with the South Carolina Institute for Energy Studies at Clemson University. The authors are thankful to Drs. Wenglarz and Golan at SCIES/HEET for their program monitoring efforts. The authors are also indebted to the late Prof. Lakshminarayana for his constructive criticism and suggestions over the years the AFTRF was developed into a fully operational turbine research facility.

Nomenclature

- c = Rotor axial chord length at tip=0.129 m
- C_p = Pressure coefficient $(p-\overline{p_l})/(0.5\rho U_m^2)$
- (t-s)/h = Effective clearance height between squealer rim top plane and outer casing
- h = Rotor blade height=0.123 m
- p, p_{atm} = Static pressure, atmospheric pressure
- P_o/P_{in} = Total pressure (stage exit to inlet) ratio
- p_l = Passage averaged local mean pressure at the rotor inlet
- r/h = Non-dimensional radial position measured from hub surface (also y/h in contour plots)
- r, θ, z = Radial, tangential and axial coordinates
- s = Height of the squealer rim measured from the base of the untreated tip section (see **Figs. 2**, **3** and **12**)
- SSSq-A = The shortest partial squealer tip on the suction side
- SSSq-B = The most optimal partial squealer tip on the suction side
- SSSq-C = The longest partial squealer tip on the suction side
- SqCh-A = Channel type squealer tip-A (or B) (see **Fig. 3**)
- t = Rotor tip clearance height without a squealer rim
- T_o/T_{in} = Total temperature (stage exit to inlet) ratio
- U_m = Mean wheel speed at rotor mid-span
- V_{sec} = Secondary velocity (V_{design}-$V_{measured}$)
- x, y, z = Coordinates (x is also axial direction)

References

[1] Heyes, F. J. G., and Hodson, H. P., 1993, ''Measurement and Prediction of Tip Clearance Flow in Linear Turbine Cascades,'' ASME J. Turbomach., **115**, pp. 376–382.

[2] Sjolander, S. A., and Cao, D., 1994, ''Measurements of the Flow in an Idealized Turbine Gap,'' ASME paper 94-GT-74.

[3] Morphis, G., and Bindon, J. P., 1988, ''The Effects of Relative Motion, Blade Edge Radius and Gap Size on the Blade Tip Distribution in an Annular Turbine Cascade With Tip Clearance,'' ASME paper 88-GT-256.

[4] Azad, Gm. S., Han, J. C., Teng, S., and Boyle, R. J., 2000, ''Heat Transfer and Pressure Distributions on a Gas Turbine Blade Tip,'' ASME paper 2000-GT-194.

[5] Dey, D., and Camci, C., 2001, ''Aerodynamic Tip De-Sensitization of an Axial Turbine Rotor Using Tip Platform Extensions,'' ASME paper 2001-GT-484.

[6] Anderson, R. H., 1979, ''Tip Cooling for Turbine Blades,'' U.S. Patent #4,142,824, March 6, 1979.

[7] Azad, Gm. S., Han, J. C., and Boyle, R. J., 2000, ''Heat Transfer and Flow on the Squealer Tip of a Gas Turbine Blade,'' ASME paper 2000-GT-195.

[8] Heyes, F. J. G., Hodson, H. P., and Dailey, G. M., 1992, ''The Effect of Blade Tip Geometry on the Tip Leakage Flow in Axial Turbine Cascades,'' ASME J. Turbomach., **114**, pp. 643–651.

[9] Bunker, R. S., and Bailey, J. C., 2000, ''Blade Tip Heat Transfer and Flow With Chordwise Sealing Strips,'' International Symposium on Transport Phenomena and Dynamics of Rotating Machinery (ISROMAC), Honolulu, Hawaii, pp. 548–555.

[10] Ameri, A. A., 2001, ''Heat Transfer and Flow on the Blade Tip of a Gas Turbine Equipped With a Mean Camber-Line Strip,'' ASME J. Turbomach., **123**, pp. 704–708.

[11] Ameri, A. A., Steinthorsson, E., and Rigby, L. D., ''Effects of Squealer Tip on Rotor Heat Transfer and Efficiency,'' ASME paper 1997-GT-128.

[12] Azad, Gm. S., Han, J. C., Bunker, R. S., and Lee, C. P., 2001, ''Effect of Squealer Geometry Arrangement on Gas Turbine Blade Tip Heat Transfer,'' ASME/IMECE 2001/HTD-24314, HTD-Vol. 369-5, pp. 297–305.

[13] Lakshminarayana, B., Camci, C., Halliwell, I., and Zaccaria, M., 1992, ''Investigation of Three Dimensional Flow Field in a Turbine Including Rotor/Stator Interaction. Part I: Design Development and Performance of the Research Facility,'' AIAA paper 92-3326, presented at the ASME-AIAA Joint Prop. Conf., Nashville, Tennessee.

[14] Dey, D., 2001, ''Aerodynamic Tip Desensitization in Axial Flow Turbines,'' Ph.D. Thesis, 2001, The Pennsylvania State University.

[15] Zaccaria, M., and Lakshminarayana, B., 1995, ''Investigation of Three Dimensional Flow Field at the Exit of a Turbine Nozzle,'' J. Propul. Power, **11**(1), pp. 55–63.

[16] Ristic, D., Lakshminarayana, B., and Chu, S., 1998, ''Three-Dimensional Flow Field Downstream of an Axial Flow Turbine Rotor,'' AIAA paper 98-3572, presented at the 34th AIAA/ASME/SAE/ASEE Joint Propulsion Conference and Exhibit, Cleveland, Ohio.

[17] Yamamoto, A., 1989, ''Endwall Flow/Loss Mechanisms in a Linear Turbine Cascade With Blade Tip Clearance,'' ASME J. Turbomach., **111**, pp. 264–275.

[18] Xiao, X., McCarter, A. A., and Lakshminarayana, B., 2000, ''Tip Clearance Effects in a Turbine Rotor, Part I: Pressure Field and Loss,'' ASME paper 2000-GT-476.

[19] Bindon, J. P., 1987, ''Pressure Distribution in the Tip Clearance Region of an Unshrouded Axial Turbine, as Affecting the Problem of Tip Burnout,'' ASME paper 87-GT-230.

[20] Sjolander, S. A., 1997, ''Overview of Tip Clearance Effects in Axial Turbines,'' VKI Lect. Series, Sec. and Tip Cl. Flows in Axial Turbines, dir. by Sieverding, C. H., the von Karman Institute for Fluid Dynamics, Belgium.

[21] Luo, J., and Lakshminarayana, B., 1997, ''3D Navier-Stokes Analysis of Turbine Rotor and Tip Leakage Flow-Field,'' ASME paper 97-GT-421.

Review of Centrifugal Compressor's Application and Development

Hartmut Krain
German Aerospace Center,
Linder Hoehe,
51147 Cologne, Germany

The paper historically describes the application and development of the centrifugal compressor from the very beginning of its introduction until today. It focuses on selected practical and theoretical examples that—to the author's opinion—pushed the centrifugal's standard from simple, low efficiency designs to its current high level status. The main events related with this development like the impact of the industrial revolution and the introduction of jet propulsion are pointed out. The implication of improved theoretical tools becoming available with raising computer capacity and the impetus of advanced measurement techniques on the centrifugal's improvement are described. A considerable number of references offers the possibility to engross the thoughts.
[DOI: 10.1115/1.1791280]

Ancient Designs

The centrifugal compressor belongs to a class of pressure producing machines known as turbo compressors. Like in other turbomachines energy is transferred by dynamic means from a rotating component (impeller) to the continuously flowing working fluid. Therefore the centrifugal compressor's evolution was always closely related to the development of turbomachinery in general.

One of the first documented turbomachinery applications dates back to about 60 A.D. At that time Heron of Alexandria (Greek origin) presumably designed his first steam engine, Fig. 1. He described a sphere which was rotated by the principle of jet propulsion. Water was heated in the lower boiler, forming steam which was guided through a hollow leg into a sphere. Two bent outlet pipes were attached to the sphere that moved when boiled steam expanded through the outlet pipes: A radial flow reaction steam engine was invented! The device was very similar to modern reaction water sprinklers. Heron also described a design driven by hot air instead of steam which was probably one of the first machines using gas turbine principles. At that time, however, there was no real need for labor saving machines because a large number of slaves was available who built the basis of ancient economy.

Nevertheless, historically the Romans seemed to make first practical use of turbomachinery principals. About 100–200 A.D. they used water wheels as mills for grinding flour. There was no fundamental improvement on the basic device which disappeared with the decline of the Roman Empire. The next water powered flour- and sawmills were described in the 12th century. These mills were simple overshot or undershot wheels depending on the landscape, i.e., on the position and head of the water stream available.

Simple windmills were another early day turbomachinery application already described by Heron, the Greek inventor. They are also mentioned in documents dealing with ancient Iranian culture. It is not clear whether Heron succeeded to build one and to get it into operation. Next time they appear in the middle-ages where they were used in North West Europe, in the Netherlands, Belgium and the northern parts of Germany [2]. Around 1500 A.D. Leonardo da Vinci sketched a machine rotating due to hot gases raising through a chimney where a fan was mounted. These machines were designed by observation only and without any fluid mechanic background which was not developed until the 19th century. Around 1750 A.D. Leonhard and Albert Euler analyzed Heron's steam turbine and made several basic experiments which resulted 1754 in ''Newton's Law on Turbomachinery'' also simply called ''Euler's Equation.'' In the first part of the 20th century engineers like Stodola [3] started to make systematic use of the fundamental fluid dynamic rules developed by Bernoulli and Euler.

Industrial Applications

A widespread industrial application of centrifugal compressors evolved at the end of the 19th century when industry began to need a lot of pressurized air: For example in mines for ventilation, in pneumatic conveyors for grain-, malt-, and cotton wool transportation. At that time there was also need for drying and sucking systems used for example for dust transportation and oil firing. Later on, centrifugals were used for a variety of technical applications: In metallurgy, chemical and petrochemical engineering and refineries, in the gas and pipeline industry, for refrigeration and in armored vehicles.

Figure 2 shows a single stage centrifugal compressor with pressure ratio of about 2. Similar machines were used to pressurize gases in coking plants, to compress blast furnace, lime kiln and synthetic gases. They were built for volume rates of 400–40000 m^3/h. Compressor and gear box were one unit. Lubricant and oil cooling were located in the gear box casing. The unit was driven by an electric motor. For sealing reasons journals were used on both sides of the rotor, sealing was obtained by coal stuffing boxes. For diesel motors compressors of this type were used for turbocharging and scavenging the motor. They were built as single and multistage devices. For scavenging pressure ratios were in the range of 1.2–1.5, for turbocharging four stroke engines pressure ratios are today between 4–6.

The earliest gas turbine experiments in which centrifugals were involved came up in the period 1900–1910. During that decade research projects like that on

1. the constant pressure hot air turbine of Stolze 1900/1904,
2. the explosion gas turbine of Holzwarth 1906/1908,
3. the constant pressure gas turbine of Armengaud/Lemale 1903/1905,
4. the constant pressure gas turbine of Moss 1903/1904,
5. and the early gas turbine of Aegidius Elling 1903

were carried out. The machine of Stolze never moved, the projects

Contributed by the International Gas Turbine Institute and presented at the International Gas Turbine and Aeroengine Congress and Exhibition, Atlanta, GA, June 16–19, 2003. Manuscript received by the IGTI December 2002; final revision March 2003. Paper No. 2003-GT-38971. Review Chair: H. R. Simmons.

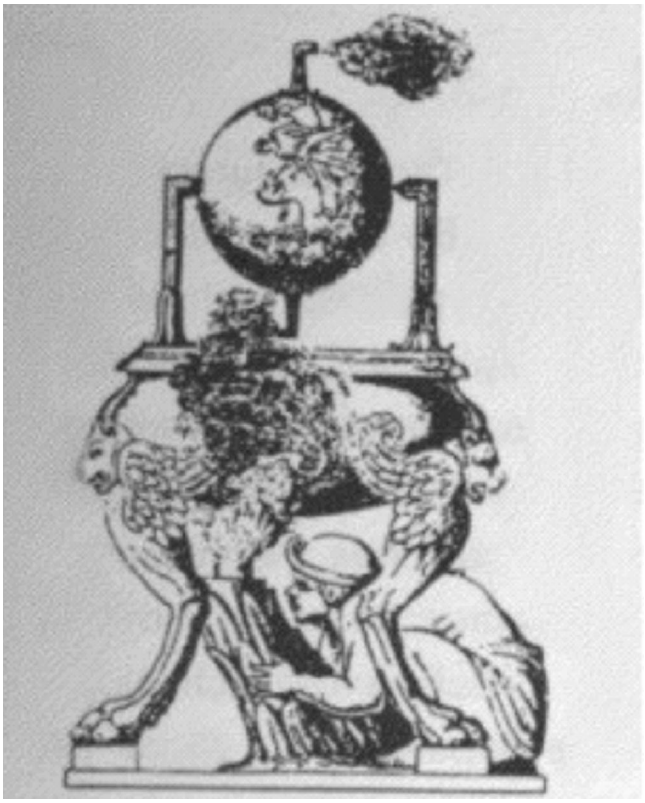

Fig. 1 Heron's steam rotor (about 60 A.D. [1])

of Holzwarth, Armengaud/Lemale, and Moss were abandoned after a short period of operation. The machine of Aegidius Elling, however, for which he filed his first gas turbine patent in 1884 delivered positive power already in 1903 [5]. Several modifications went into operation later on (last rebuilt 1932). Figure 3 shows a principle sketch of Elling's first successful gas turbine. Air entered through the centrifugal compressor B. Part of that air was bled off at C, constituting the net power output of the whole device. The remaining part of the air passed the combustion chamber D where fuel E was injected.

The hot gases passed the cooler F where the turbine inlet temperature was limited to 400°C before entering the Turbine T. A six stage centrifugal compressor with water injection between the stages was applied by Elling. Aft of the impellers vaned diffusers

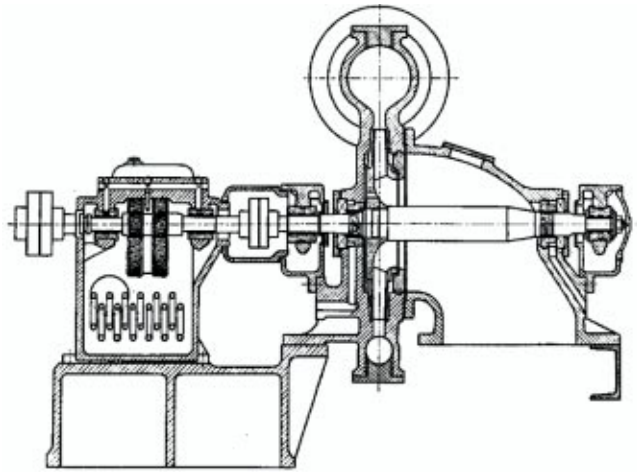

Fig. 2 Radial blower for gas compression (Demag) [4]

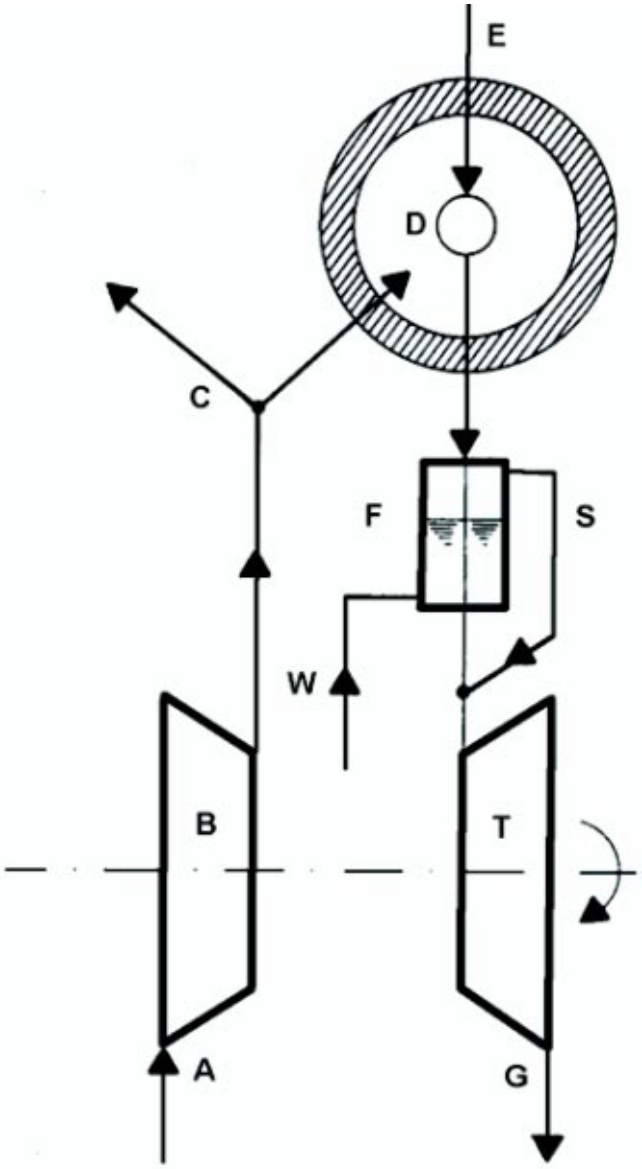

Fig. 3 Sketch of Elling's first gas turbine design [5]

with variable geometry were used which was a very advanced design for that time. A radial type turbine (centripetal) was also applied by Elling. He estimated the efficiencies of both components to be 70%. The results pointed to higher values which seemed to be the main reason for the net power output of 11 hp in 1903. In 1933, Aegidius Elling wrote: ''When in 1882, I started work on the gas turbine, it was with aeronautics in mind and I firmly believe that aeronautics is still waiting for the gas turbine.'' As we know today Aegidius Elling was an engineer of wide vision.

Impetus From Aircraft Propulsion

Strong impetus for further development of centrifugal compressors came from the introduction of aircraft propulsion. Frank Whittle (England) and Hans Joachim Pabst von Ohain (Germany), Fig. 4, developed almost independently of one another the world's first jet engine (1928–1941). Both pioneers used the same principle of air compression: Centrifugal compression. Von Ohain's HeW 3B engine installed in the Heinkel He178 made the world's first turbojet flight on 27 August 1939, Whittle's W1 engine installed in the Gloster E28/39 first flew 15 May 1941.

Fig. 4 Frank Whittle (left) and Hans Joachim Pabst von Ohain, inventors of turbo-jet propulsion

Fig. 6 Rotor assembly of the Whittle's W1 engine

Frank Whittle applied for his first patent in January 1930. A cross section of his first engine in flight and the rotor assembly used are shown in Figs. 5 and 6. The engine was a simple jet propulsion gas turbine having a single stage centrifugal compressor with bilateral intakes, driven by a single stage axial turbine directly coupled to the compressor. The double sided compressor rotor was probably used to avoid supersonic flow at the tip of the rotor inlet and to reduce axial thrust. He already aimed at stage pressure ratios of about 4:1 which was beyond all previous engineering experience. At that time pressure ratios of 2.5:1 had not been exceeded.

In contrast to Whittle, von Ohain used a fully radial engine for his first design, i.e., a radial compressor and a radial turbine, back to back to each other, Fig. 7. After the first flight Whittle devoted much of his effort to the further development of the centrifugal, whereas von Ohain switched to the axial compressor, which due to his smaller frontal area and larger flow capacity became the essential component of large aircrafts. Nevertheless, the centrifugal compressor still finds widespread application in the aviation field for small aircraft engines, most significantly for helicopters and APUs for all type of aircrafts.

Helicopter performance is critically dependent on the engine's weight plus fuel. Helicopters, especially for military applications, are outstanding examples for the need to have very compact engines with high power/weight ratio. Therefore the development in this area significantly attributed to the further development of centrifugal compressors in the decades after the first jet propulsion flight. The most favorable compressor arrangement for helicopter applications is the single stage centrifugal compressor, because it is rather simple, robust and resistant to erosion. However, if a simple gas turbine process, without heat exchanger, is used, high cycle pressure ratios and turbine inlet temperatures are necessary. For single stage designs pressure ratios in the range of 8:1–12:1 are required at efficiencies of about 80% for rather small components running at reasonable tip clearance.

As an alternative very often a combination of several axial stages with a centrifugal end stage, or a two stage centrifugal compressor is used. Such designs are quite often used in the engines of propeller driven business aircrafts. Figure 8 shows a shaft engine built by Garrett Engine Devision, generating 1.100 shp at

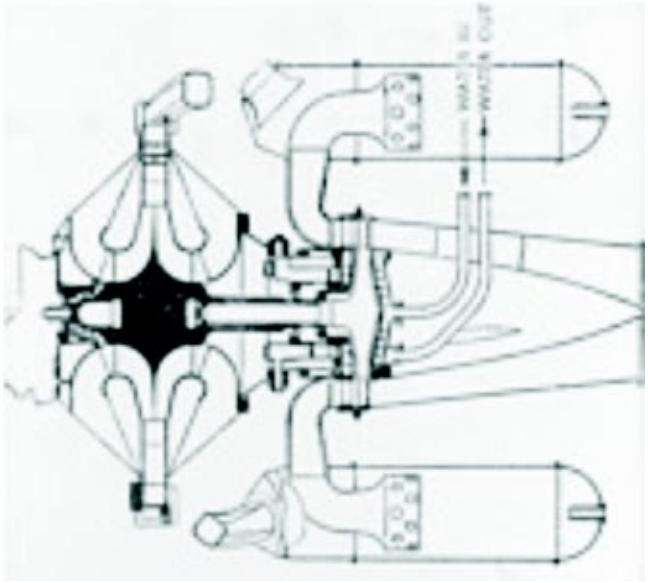

Fig. 5 Assembly of Whittle's W1 engine

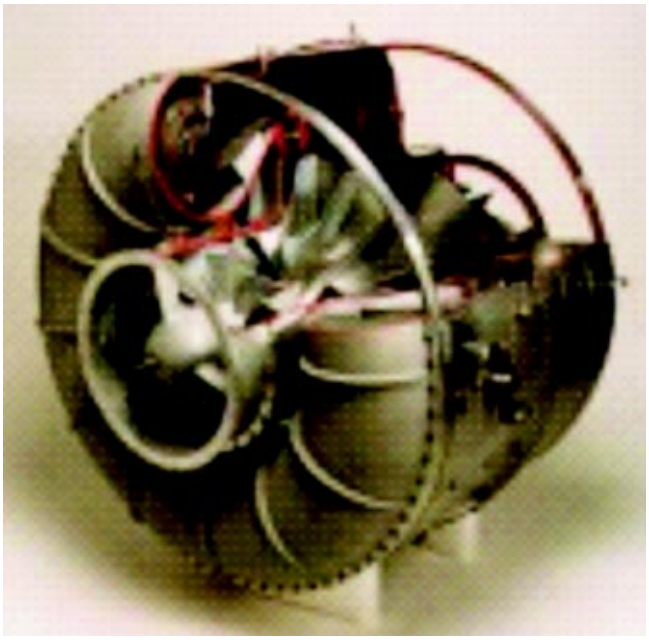

Fig. 7 Von Ohain's engine He S3B

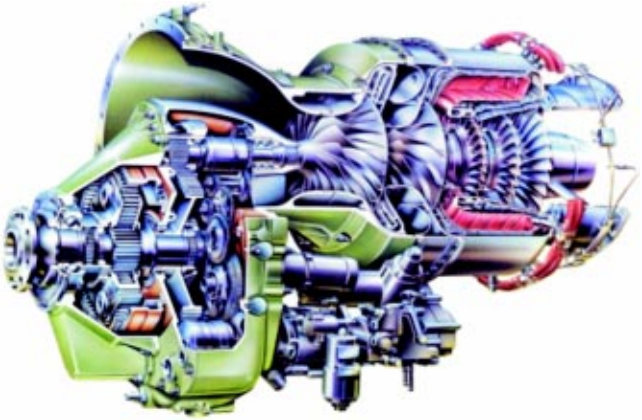

Fig. 8 Honeywell shaft engine (formerly Garrett Engine Devision, TPE331-12U)

the time of its introduction (1984). It was used to power Jetstream Super 31, CASA 212-400, MetroIII and Metro23, scaled-up-models for larger aircrafts followed with power output up to 1750 shp.

During the last 5 decades centrifugal compressor stage pressure ratios were boosted more and more so that single stage compressors with pressure ratios larger than 8:1 came into practical use. There are strong demands to build these compressors with high efficiencies. To fulfill these requirements the development and application of sophisticated measurement and calculation techniques were necessary to get better insight into the complex flow structure of these machines. The combined use of these tools in the aircraft field also stimulated the development of centrifugal compressors in the stationary turbomachinery field.

Approaches Towards Improvement of Centrifugal Compressors

The introduction of the jet engine boosted the further development of centrifugal compressors significantly. Many activities date back to the middle of the 20th century. The improvement, however, was not straight forward. Contributions towards a better aerodynamic compressor design came from different disciplines, from empirical, theoretical and experimental approaches.

Empirical Approaches. The most important components of a centrifugal compressor stage are the rotor and the diffuser, Fig. 9.

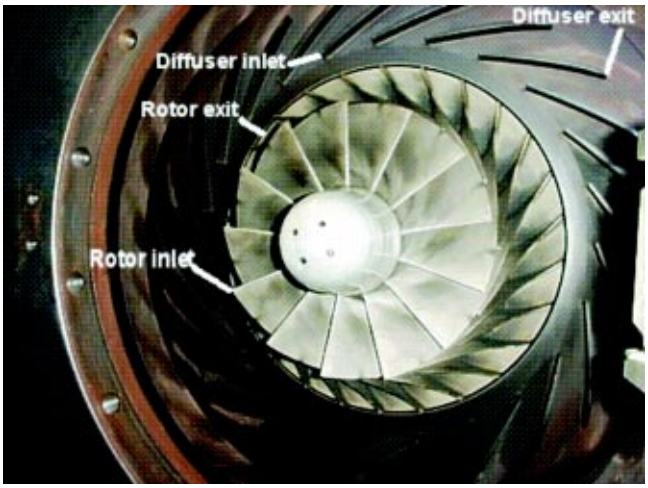

Fig. 9 Components of a centrifugal compressor stage

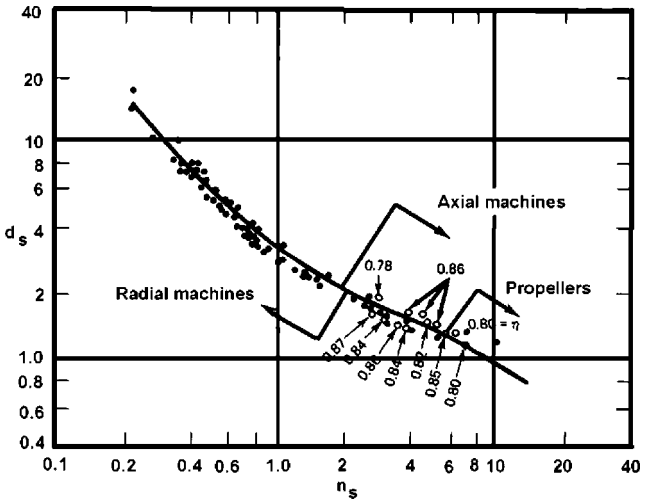

Fig. 10 "Cordier line" in the NsDs-diagram [8]

Energy is transferred to the fluid via the rotor blades resulting in an increase of static pressure and kinetic energy at the rotor exit. Depending on rotor design, 30% (backswept blades) to 50% (radial ending blades) of the total energy input is contained in the kinetic energy at rotor discharge, a large fraction of which is recovered in the succeeding vaneless or vaned diffuser. The aerodynamic design of these components was always based to a wide extend on empirical knowledge available in the companies and in the open literature.

Satisfactory rotor designs without knowing very much about the internal flow character of centrifugals were possible with the similarity concept [4,6–8], which offers a convenient and exact method to recognize important characteristics of turbomachinery. The result of similarity considerations is, that machines,

1. which are geometrically similar,
2. have similar velocity triangles at similar points in the flow path,
3. have the same ratio of gravitational to inertia forces,
4. operate with fluids having the same thermodynamic quality

will have equal fluid dynamic characteristics, i.e., equal efficiencies.

The concept provides design and performance information on compressors based on state-of-the-art knowledge. From similarity considerations it can be concluded that the impeller efficiency is mainly a function of the similarity parameters specific speed (Ns), specific diameter (Ds), Reynolds (Re)- and Mach number (M), so that lines of constant efficiency and optimum geometry can be presented as functions of Ns and Ds for constant values of M and Re. NsDs-diagrams for compressors are obtained by computing them on the basis of empirical loss considerations or by plotting test data as a function of specific speed and specific diameter.

A famous diagram of that type, derived by Cordier [8] for different types of turbomachines is shown in Fig. 10. The solid line shows the location of efficient compressor designs. This line is frequently referred to as the ''Cordier line'' and indicates that axial machines dominate the high specific speed regime whereas radial machines are more efficient in the low specific speed regime. The plotted test points belong to efficient turbomachines and demonstrate that they are clustered close to the ''Cordier line.'' A variety of geometrically similar, high efficient compressors can be designed with this information as long as Reynolds- and Mach number effects can be neglected. Reynolds number effects on centrifugal compressor performance were studied carefully by Wiesner [9], Simon et al. [10], and Casey [11]. If the designer stays close to the ''Cordier line'' taking simultaneously care of Reynolds number corrections, he can easily derive the

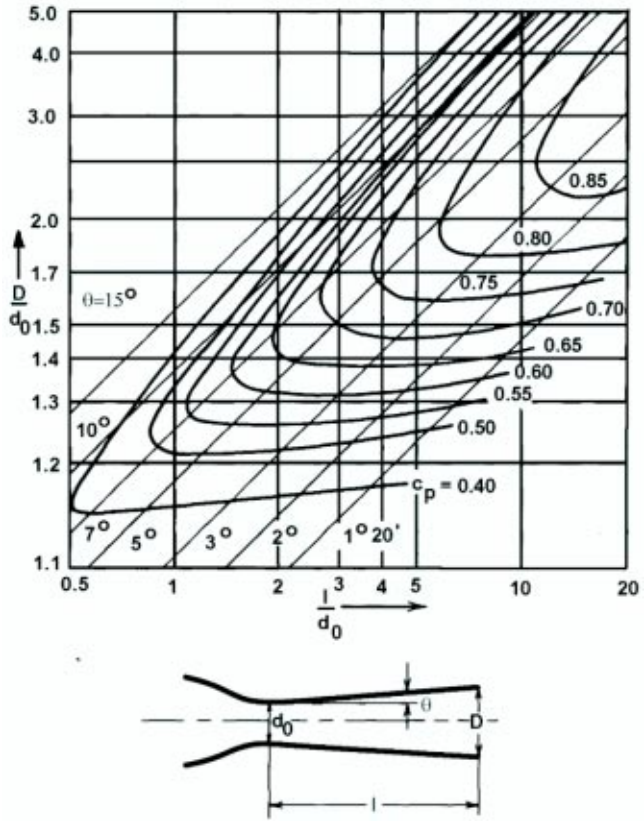

Fig. 11 Conical diffuser performance map [12]

main dimensions of a suitable and rather efficient centrifugal compressor rotor. However, fine tuning of the meridional contour, blade shape etc. will be necessary to come up with a design which is beyond state-of-the-art knowledge represented by the ''Cordier line.''

Concerning the flow character inside centrifugal compressor rotors researchers and developers very early became aware of the fact that the flow in an impeller is not completely guided by the vanes and hence the effective fluid outlet angle does not equal the vane outlet angle. To account for this deviation, a factor known as the ''slip factor'' is introduced to correct the energy transfer calculated from one dimensional theory. Several theoretical and empirical equations have been derived for the slip factor to allow calculation of the energy transfer during the design of a new impeller. Widely used equations were published by Stodola [3], Busemann [13], Stanitz [14], and Wiesner [15].

From the 1950s until now vaned diffusers for high performance compressors were very often designed on the basis of diffuser performance maps deduced from experimental procedures. In 1955 S.J. Kline [16,17] started to investigate diffuser flow character with the help of a water table. Much of his work has been done at Stanford University. With his data it was possible to identify separation criteria for ''first separation,'' ''appreciable stall,'' ''fully developed two-dimensional stall,'' ''hysteresis flow,'' and ''jet flow.'' Another major discovery was that of Sovran and Klomp [18] who identified the key fluid variable impacting diffuser performance: Throat boundary layer blockage! Later on Runstadler et al. [19] and Albering [12] contributed to a better understanding of the diffuser world by testing flat and conical diffusers. A typical diffuser performance map is shown in Fig. 11. Lines of constant diffuser pressure recovery are plotted for a conical diffuser versus length/diameter ratio with divergence angle as a parameter. Such charts, which were the basis for diffuser design, were submitted for constant Reynolds-, Mach number, blockage and aspect ratio. From experiments it was found, that boundary layer blockage at the diffuser inlet has major influence on diffuser recovery.

A centrifugal compressor stage built from empirical data for optimum rotor and diffuser components will not necessarily be the optimum stage with respect to flow range and stage efficiency. Very often this is due to the effects of rotor/stator matching that generates diffuser inlet conditions far away from the inlet conditions present in the experiments carried out for isolated flat or conical diffusers. An improvement of vaned diffuser inlet conditions generally results in higher diffuser recovery, more flow range and better stage efficiency. The ''pipe diffuser'' suggested by Vrana [20] is believed to generate better flow conditions at the diffuser throat when coupled with a centrifugal compressor impeller than its cambered counter parts that are generally derived from measured diffuser performance maps [21]. The pipe diffuser is a low cost diffuser based on discrete pipe drillings inserted into a flat plate. The drillings are arranged in such a way that a gradual transition from the vaneless space at rotor exit to the individual throat of each pipe is implicitly defined. The three-dimensional shape of the diffuser leading edge is better accommodated to the rotor discharge flow than the leading edges of two-dimensional diffusers, thus allowing these diffusers to swallow a highly non uniform flow much better than the 2D-diffusers. In many cases, however, cascade type diffusers need less radial extension and are therefore preferred in favor of pipe diffusers. A diffuser with very small radial extension is the low solidity diffuser (LSD) which due to its low blade number has no throat and thus generally ensures a wide flow range on the expense of efficiency [22]. Improvement of diffuser inlet/rotor exit conditions seemed to be the key for a further improvement of centrifugal compressor performance. This recognition motivated many researchers to look deeper into the internal flow character of centrifugal compressors.

Theoretical Approaches. Very early it was found that the flow leaving the impellers of centrifugal machines is rather irregular and loss effected across the exit area of each impeller passage [23,24]. Nevertheless, in the 1950s researchers at first produced a number of theoretical solutions for isentropic flow through radial and mixed flow impellers [25–28]. These solutions delivered insight into the internal flow behavior with regard to blade loading, compressibility effects, eddy formation and slip factor in absence of viscosity. Experimental studies of viscous effects, however, showed that in general a low velocity area (wake) occurred in the shroud suction side area whereas a high velocity region (jet) appeared in the hub pressure side area [29,30]. Strong through flow and flow angle variations were found from hub to shroud and from pressure to suction side of the blade. This condition leads to an unsteady asymmetric flow pattern in the diffuser. Dean and Senoo [31] attempted to describe the influence of the phenomena on the flow in a vaneless diffuser by a two-dimensional inviscid approach taking mainly care of the distortion between pressure to suction side. At the impeller exit they assumed for the relative frame a step-type velocity distribution for the jet/wake flow like that shown in Fig. 12. The wake was located close to the suction side, the jet covered the area in the vicinity of the pressure side.

Their main findings were:

1. The diffuser inlet flow distortions generated by the jet/wake structure in the rotor exit area (Fig. 12) have significant influence on vaneless diffuser flow behavior.
2. It is impossible to predict the behavior of a diffuser receiving a distorted inlet flow from information on axissymmetric flow.
3. A rotating distorted flow in a vaneless diffuser leads to a significant pressure work transfer between high and low relative velocity regions.

Later on, Japikse [32,33] used the same Jet/Wake model as a basis for the development of his ''Two-Zone-Model'' taking care of compressibility effects. In this model, the jet flow was assumed

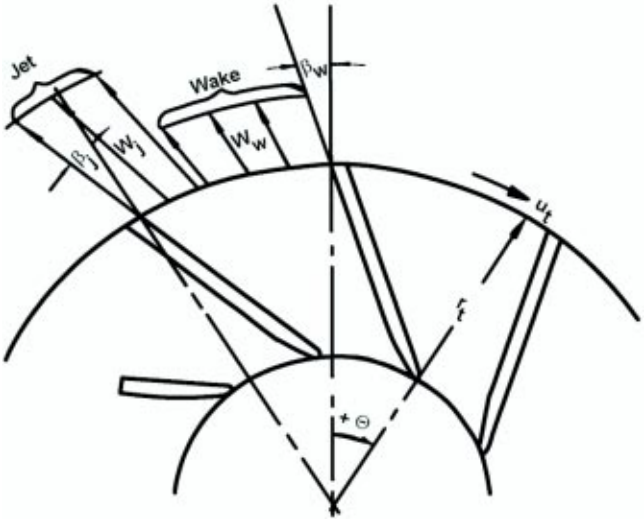

Fig. 12 Model of impeller exit flow, Dean and Senoo [31]

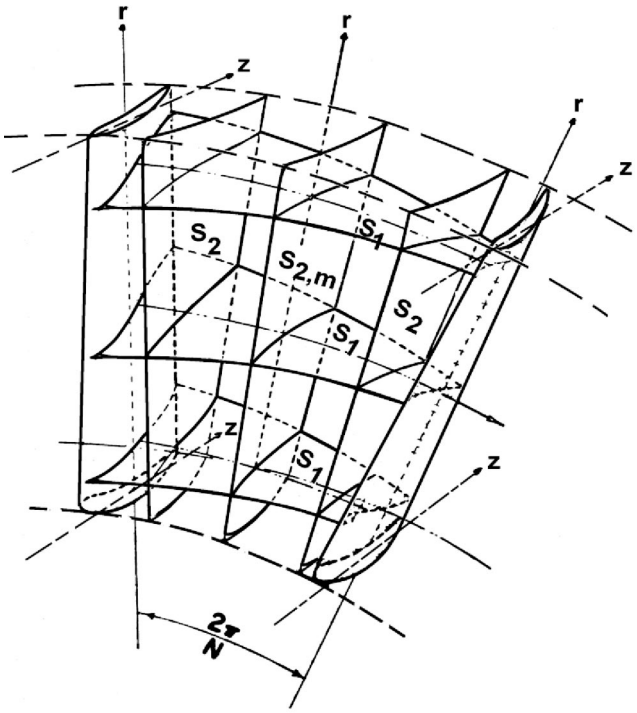

Fig. 13 Orientation of S_1 and S_2 surfaces according to Wu [35]

to be isentropic and the losses were attributed to the wake. The impeller flow process was described by the ''Two-Zone-Model'' using one-dimensional equations.

A significant impulse towards a clarification of the real flow character in axial as well as in centrifugal turbomachines came in the middle of the last century with the introduction of the ''Quasi-Three-Dimensional Calculation Methods'' and with raising computer capacities. In 1950 Hamrick et al. [34] published the stream line curvature method, in 1952 Wu [35] followed with his matrix method. The main difference between both methods was the handling of the equations of motion and continuity. Wu coupled both equations via a stream function whereas Hamrick handled them separately. Therefore the stream line curvature method needed an iterative solution between both equations resulting in more computer time. Both methods introduced stream surfaces of the first (S_1) and second (S_2) type thus tackling the actual three dimensional flow problem in a mathematically two dimensional way. According to Wu [35], S_1 surfaces extended from the pressure to the suction side whereas S_2 surfaces extended from hub to shroud, Fig. 13. It was assumed that the flow would follow the stream surface and that there would occur no cross flow perpendicular to the surface which was a significant restriction of these methods. But this was the only way to handle 3D-problems on computers of that time and in the following two decades. The idea was to iterate between the solutions obtained on both types of stream surfaces to come close to the real three-dimensional flow. The procedure was therefore called ''Quasi-Three-Dimensional Calculation Method.''

For centrifugal compressors the calculation usually started on a mean S_{2m}-stream surface, located at mid-pitch. Here, flow quantities like relative velocity, pressure, density etc. and stream lines were calculated. To continue the calculation on S_1 surfaces the streamlines obtained on the S_{2m} surface were rotated until intersecting with the pressure and suction side of the neighboring blades, which delivered axis symmetric S_1-surfaces. In most cases the calculation stopped at this point because it was rather difficult to generate in a next step appropriate S_2 stream surfaces from the streamlines of the S_1 solution.

Calculations of this type were carried out by the authors listed in Refs. [36–41], a detailed overview was given in 1976 by Japikse [42]. Losses were generally taken into account by making use of a prescribed entropy increase taken from empirical equations.

Figure 14 displays the influence of irreversibility on the calculated flow field development within the impeller passage. The viscous effects introduced have strongest influence on the flow field near impeller discharge, whereas nearly identical flow patterns are predicted for the inducer as well as for the radial impeller entry region with both the inviscid and loss-effected calculation. The comparison with inviscid results—particularly near impeller discharge—shows decreasing static pressures, associated with a shift of high static pressure regions from hub to shroud pointing to a rather irregular impeller discharge flow.

About 1980 a new impetus towards better understanding of centrifugal compressor flow phenomena arose from the introduction of fully 3D-calculation methods for turbomachinery components like rotors or stators. As with the 2D and quasi-3D calculation methods, inviscid approaches were initially applied for the 3D procedure. Several of these methods were described by Meauze et al. [43]. At the beginning the most commonly used methods were time dependent solutions of the 3D-Euler equations, sometimes coupled with viscous interaction methods [44]. They were developed to a stage where acceptable solutions were obtained in a few minutes of computer time on modern supercomputers of that time. The main limitation of inviscid methods in predicting the real flow is their neglect of boundary layer block-

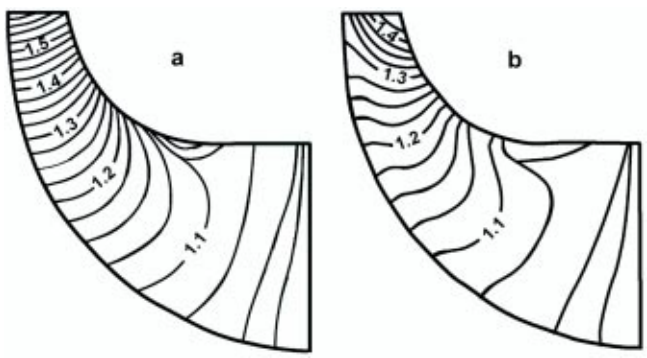

Fig. 14 Q3D-solution: Calculated isobars p/p_{t1}

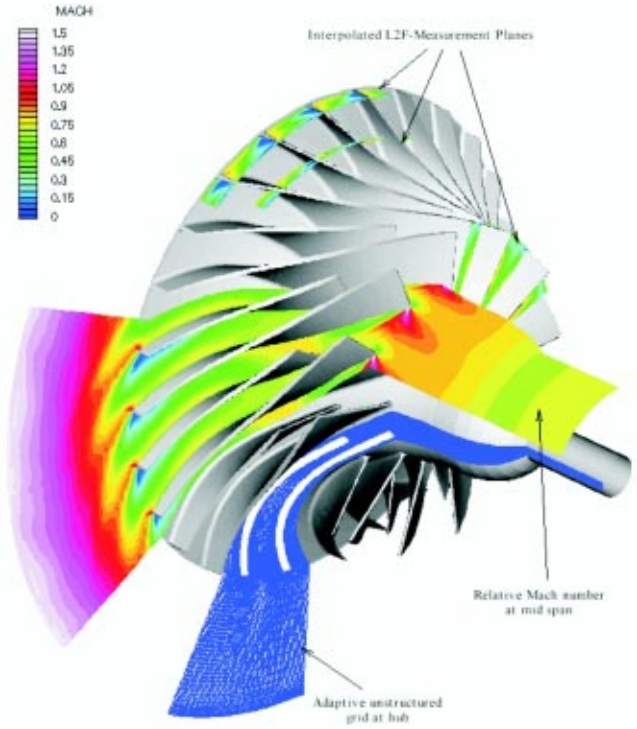

Fig. 15 Calculated 3D-flow field for a transonic centrifugal impeller [45,46]

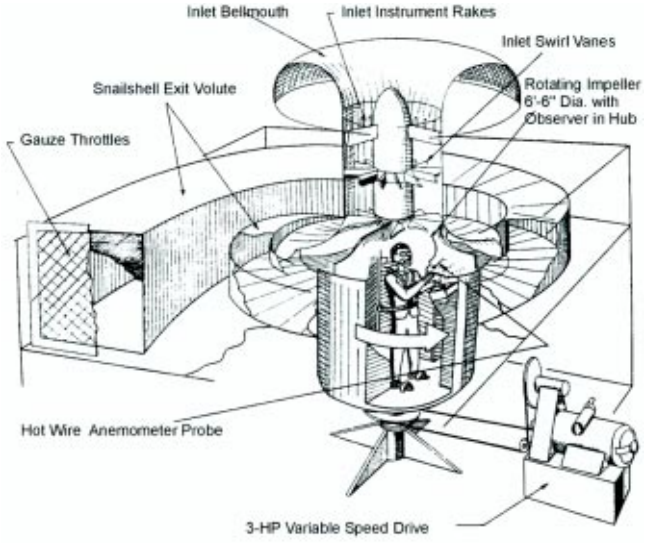

Fig. 16 Observer inside the shaft of a rotating centrifugal impeller

age, which was especially severe for centrifugal compressors where boundary layer blockage, wake development and secondary flow are dominant factors.

A few time consuming 3D viscous solutions, sometimes limited in their application to subsonic flows and blade rows without back-flow were developed rather early [47,48]. But the accuracy obtained from early generation turbulence models did not permit the solutions to be used for quantitative predictions of blade row losses. At the end of the 1980s the first viscous 3D codes became available showing the capability to predict satisfactory the main complex flow characteristics of centrifugals like jet/wake and secondary flow development [49–51]. They solved the 3D Navier–Stokes equations, turbulence modeling was carried out via mixing length closure by using either a one-equation (Baldwin Lomax) or two-equation turbulence model $(k\text{-}\varepsilon)$.

A result produced by Hoffmann [45] at DLR with the code described by Dawes [46] is shown in Fig. 15. Here the grid topology used and the relative Mach number distribution calculated at mid span is plotted for a transonic centrifugal compressor rotor from a station ahead of the rotor leading edge up to the vaneless diffuser region. The supersonic flow region at rotor leading edge and the wake flow in the suction side/exit area of the rotor exit area are clearly seen. Meanwhile a large number of similar solutions have been generated world wide with a variety of codes many of which are nowadays available on a commercial basis [52–57]. Tools like this are now routinely used by industry for solving more difficult aerodynamic design tasks. The methods originally developed to study steady 3D-flows have been meanwhile extended to handle 3D unsteady flows so that many of them are now capable to solve simultaneously the flow passing successively rotating and stationary components like rotors and stators, thus offering the possibility to study unsteady effects like rotor/stator interactions [58]. Presently the qualitative results produced are already very impressive, the quantitative reliability for centrifugal compressors, however, has to be checked in many cases against measurement data that are today still rare [59].

Experimental Approaches. At the middle of last century experimenters also put a lot of emphasis on the clarification of the internal flow character of centrifugals. They mainly used measurement techniques like hot wire, photography, pressure measurements, etc. Their results were used for validating the theoretical tools under development. From 1950 to 1960 a series of experiments on the internal flow in centrifugals was conducted at Lewis Flight Propulsion Laboratory (today NASA Glenn), Cleveland [24,29,30,60–62]. Many measurements were carried out on a large scale (48 in.) compressor.

All investigations with internally instrumented impellers showed an accumulation of comparatively low energy air in the vicinity of the trailing edge that could not be attributed to boundary layer separation because no steep pressure loss gradient was found. Therefore the researchers attributed the development of the low energy to secondary flows that were defined as ''cross currents'' normal to the potential flow streamline, caused by hub-to-shroud gradients in total pressure also normal to the potential streamlines [24].

Rather spectacular experiments were carried out by Fowler [63] at the National Research Council of Canada (NRC) who run even larger model impellers than those tested in Cleveland. They were models of actual aero engine compressors operated at low speed to simulate the true Reynolds and Rotation number effects. The experimental rig, consisting basically of a rotating drum with $6\frac{1}{2}$ ft. (about 2m) diameter impeller blades mounted on it, housed an observer with experimental equipment (hot wire anemometer, smoke generator and camera), Fig. 16. Simple traverse arrangements allowed the observer to move a probe over grids of points in various planes in one of the impeller channels to explore the flow quantitatively. After overcoming some medical problems mainly related with the observer's dizziness, Fowler succeeded to carry out half-hour runs at 70 rpm and to detect the relative rotor flow field by means of hot wire probes.

He plotted the measured through flow velocities for 7 measurement planes from rotor inlet to rotor exit, Fig. 17. By comparing his experimental results with 2D Stanitz solutions [25,26] he noticed: ''That there was a systematic disagreement between the measured and calculated velocity profiles.'' He wrote: ''The calculation predicts higher radial flow speeds near the suction wall of the channel with lower speeds on the pressure wall whereas the experiments show, that additional effects cause the opposite to be the case, with higher speed flow on the pressure wall.'' Actually

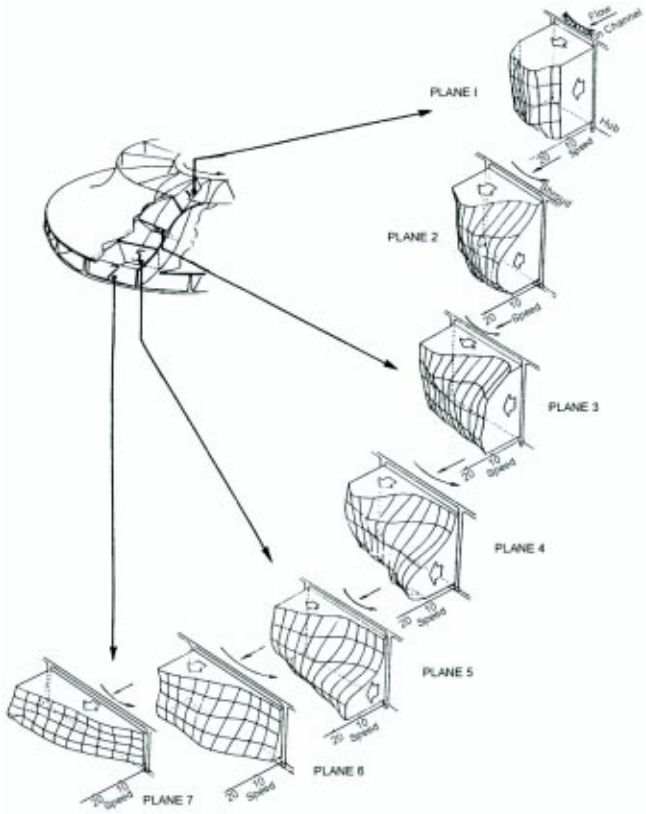

Fig. 17 Development of velocity pattern inside the rotor [63]

his results were indicating the development of the classical jet/wake pattern, very similar to that predicted reliably by today's viscous 3D calculation methods, Fig. 15.

Testing large scale, low speed compressor models, of cause, was appropriate for the application of the measurement technique available in 1950–1960. These tests fulfilled similarity parameters

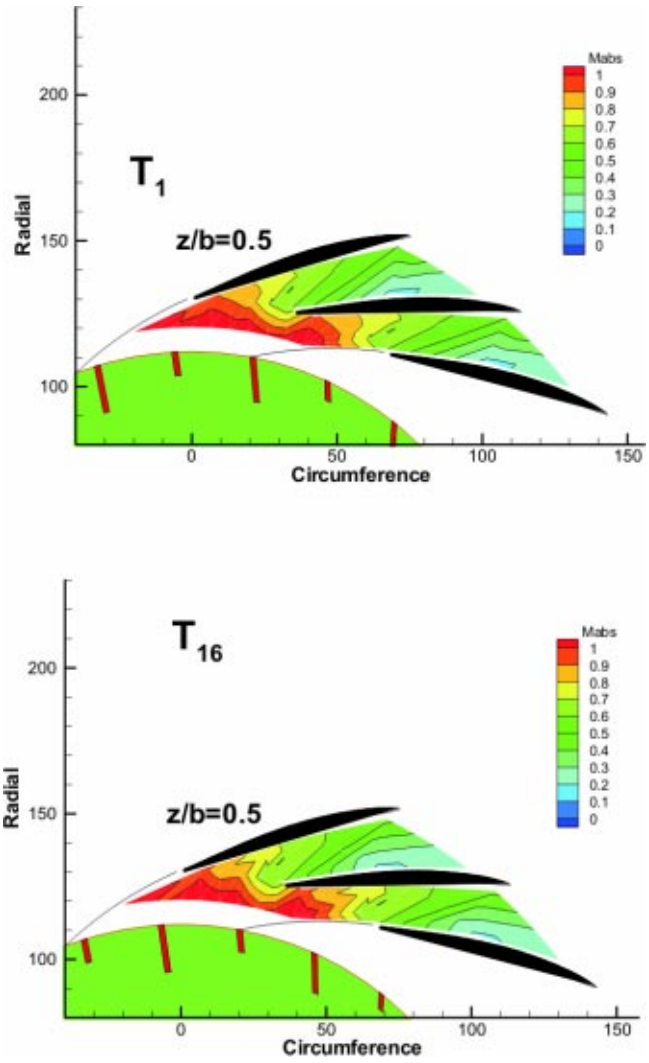

Fig. 19 Laser measured unsteady flow in the diffuser inlet region

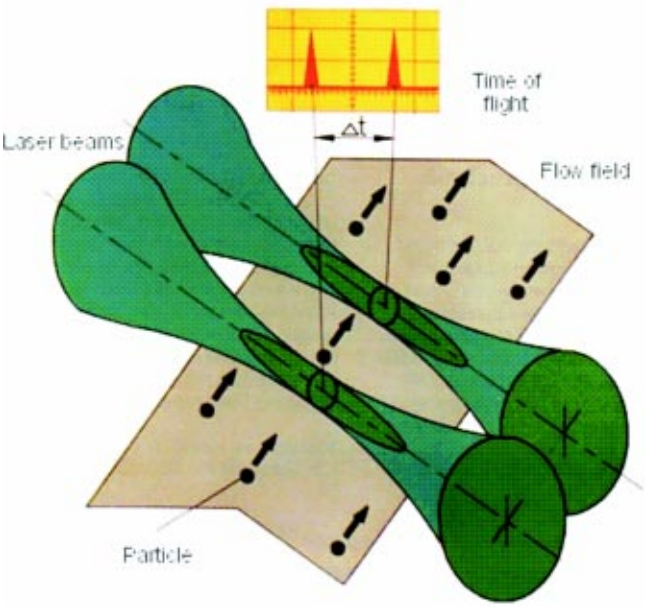

Fig. 18 Principal of L2F-velocimetry

like specific speed, specific diameter and Reynolds number which ensured a reliable transfer of the results to similar low pressure ratio designs of that time. For high performance compressors, however, the main opportunities for further efficiency improvement lay in a carefully controlled diffusion in rotors and diffusers on a rather high Mach number level. Consequently there was much interest to investigate the internal flow field of centrifugals at real operating conditions, and to clarify the problem of separation onset, jet/wake development and secondary flow. Various dynamic measurement systems of high time and space resolution like pressure transducers and hot wire anemometry were especially built for the extraordinary operating conditions of centrifugals [64].

A very helpful breakthrough in testing the internal flow fields of centrifugal compressors running under real operating conditions arose with the successful development of laser velocimetry. About 1970 Schodl [65] developed the Laser-2Focus-Velocimeter used by Eckardt [66] to study the flow field of a 3:1 pressure ratio compressor [64]. The Laser Doppler Velocimetry appeared in the early 1960s and was demonstrated for centrifugal compressor applications almost at the same time as the L2F measurement technique [67]. Both systems measured the velocity of small light-scattering particles seeded into the fluid that followed the streamlines. The L2F-system replaced the LDV fringe pattern in the probe volume by two discrete, highly focuses light beams, Fig.

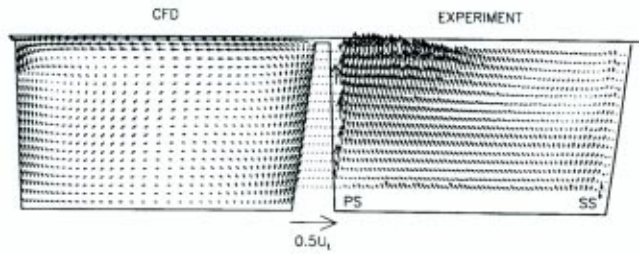

Fig. 20 Secondary flow velocity vector plots for rotor exit [73]

18, thus creating an about 100 times greater light concentration and much higher signal/noise ratio than the LDV-system. This was advantageous for resolving the flow in compact centrifugals where a laser system, due to difficult access conditions has generally to work in a back scattering mode. This is especially difficult when the reduced signal intensity is additionally superimposed by considerable background radiation due to laser light reflections in the vicinity of channel surfaces. The L2F system generates two laser beams and works like a light gate. The absolute velocity component perpendicular to the laser beam axis is derived from the time a particle needs to pass the two beams and from the known distance between the beams. The flow direction is obtained by turning the system around the laser axis until most particles pass the two spots in the probe volume. Turbulence intensity is obtained from a statistical evaluation. Actually it is a 2D measurement system, but by orienting the laser beam axis almost perpendicular to the main flow direction, the most important 3D flow effects can be resolved. Meanwhile the system has been further developed to resolve additionally the third velocity component [68].

Eckardt [66] was the first to apply the 2D-system in a centrifugal rotor. He carried out detailed measurements at 5 through flow positions and found a pronounced wake at the rotor exit that covered 35% of the flow channel. The wake comprised of 15% of the total mass flow rate and was characterized by low flow velocity and very high fluctuation intensity. These measurements were used by many theoreticians to validate their theoretical models. The further developed measurement technique was afterwards used to study the subsonic, unsteady flow character occurring in the narrow flow channels of a wedged type vaned diffuser [69], in backswept 4:1 pressure ratio rotors [70] and at least to analyze the steady and unsteady flow in very compact transonic centrifugal compressors running with 600 m/s rotor tip speed [59,71,72], Fig. 19.

Laser anemometry has been used by a number of investigators to obtain measurements of the flow fields in centrifugal compressors [74]. Hathaway et al. [73] reported results from a study in a large low-speed compressor obtained with an LDV-system and compared them to the results of a 3D-Navier-Stokes simulation [49], Fig. 20. Skoch et al. [75] applied the LDV measurement technique to a 4:1 pressure ratio impeller with splitter blades. Today Particle Image Velocimetry (PIV), generally much faster than laser measurements, are going to be applied for analyzing centrifugal compressor aerodynamics [76]. Compared with laser velocimetry, however, its main shortcoming is related to the limited applicability in complex geometries like centrifugal impellers and cascade-type diffusers.

Further Development Potential

Quite a few aerodynamic secrets of centrifugal compressors have been revealed during the last 50 years. But many machines having moderate efficiency are still in operation and could certainly be improved by making use of today's knowledge. The flow phenomenology of centrifugals is meanwhile impressively described by most 3D codes available, but not all of them have been seriously validated with experimental data.

Very high pressure ratio compressors ($\pi_t > 5:1$) are still seldom used because of their low efficiencies and limited flow range. A lot of effort is required to overcome these problems. A success in this field, however, will result in a significant expansion of centrifugal compressor's application and will additionally result in reduced manufacturing costs. Modern 3D solvers are showing the potential to close this gap. The improvement of operating conditions close to surge seems also to be possible with the help of fast field measurement techniques like PIV, probably in combination with 3D codes having the potential to resolve unsteady flow effects in the rotating stall regime. A great deal has been achieved, but much has to be done!

References

[1] Fransson, T. H., Hillon, F., and Klein, E., "An International, Electronic and Interactive Teaching and Life-Long Learning Platform for Gas Turbine Technology in the 21st Century," ASME Paper 2000-GT-0581, p. 10.
[2] Kenny, D. P., 1984, "The History and Future of the Centrifugal Compressor in Aviation Gas Turbines," SAE SP 602, p. 15.
[3] Stodola, A., 1924, *Dampf-und Gasturbinen*, Springer, Berlin.
[4] Eckert/Schnell 1961, *Axial-und Radialkompressoren*, Springer-Verlag, Berlin/Göttingen/Heidelberg.
[5] Johnson, D. G., 1985, "*The Norwegian Gas Turbine Pioneer: Aegidius Elling*," Energy World, pp. 10–13.
[6] Balje, O. E., 1962, "A Study on Design Criteria and Matching of Turbomachines: Part B—Compressor and Pump performance and Matching of Turbocomponents," ASME J. Eng. Gas Turbines Power, **84**, pp. 103–114.
[7] Balje, O. E., 1981, *Turbomachines: A Guide to Design, Selection and Theory*, John Wiley and Sons, New York, p. 513.
[8] Cordier, O., 1955, "Similarity Considerations in Turbomachines," VDI Report 3, 85.
[9] Wiesner, F. J., 1979, "A New Appraisal of Reynolds Number Effects on Centrifugal Compressor Performance," ASME J. Eng. Gas Turbines Power, **101**, pp. 384–396.
[10] Simon, H., and Bülskämper, A., 1983, "On the Evaluation of Reynolds Number and Relative Surface Roughness Effects on Centrifugal Compressor Performance based on Systematic Experimental Investigations," ASME-Paper 83-GT-118, p. 10.
[11] Casey, M. V., 1984, "The Effects of Reynolds Number on the Efficiency of Centrifugal Compressor Stages," ASME-Paper 84-GT-247, p. 8.
[12] Albering, W., 1978, *Applied Fluid Mechanics*, 5th ed., Akademie-Verlag, East Berlin.
[13] Wislicenus, G. F., 1947, *Fluid Mechanics of Turbo-Machinery*, McGraw-Hill Book Co., New York.
[14] Stanitz, J. D., 1952, "Some Theoretical Aerodynamic Investigations of Impellers in Radial and Mixed Flow Centrifugal Compressors," Trans. ASME, **74**, p. 473.
[15] Wiesner, F. J., 1967, "A Review of Slip Factors for Centrifugal Impellers," ASME J. Eng. Gas Turbines Power **89**, pp. 558–592.
[16] Kline, S. J., Abbott, D. E., and Fox, R. W., 1959, "Optimum Design of Straight-Walled Diffusers," ASME J. Basic Eng., **81**(3), p. 321.
[17] Waitman, B. A., Reneau, L. R., and Kline, S. J., 1961, "Effects of Inlet Conditions on Performance of Two-Dimensional Subsonic Diffusers," ASME J. Basic Eng., Series D, **83**(3), pp. 349–360.
[18] Sovran, G., Klomp, E. D., 1965, "Experimentally Determined Optimum Geometries for Rectilinear Diffusers with Rectangular, Conical and Annular Cross-Section," General Motors Corp., Research Publication GMR-511, Nov. 16.
[19] Runstadler Jr., P. W., Dolan, F. X., and Dean, R. C., 1975, *Diffuser Data Book*, Creare TN-186, p. 88.
[20] Vrana, J. C., 1967, "Diffuser for Centrifugal Compressors," U.S. Patent No. 3 333 762, August 1.
[21] Kenny, D. P., "A Novel Low cost Diffuser for High Performance Centrifugal Compressors," ASME-Paper 68-GT-38, p. 12.
[22] Hayami, H., Senoo, Y., and Utsunomiya, K., 1990, "Application of a Low Solidity Cascade Diffuser to Transonic Centrifugal Compressor," ASME J. Turbomach., **112**, pp. 125–129.
[23] Fischer, K., and Thomas, D., 1932, "Investigation of the Flow Conditions in a Centrifugal Pump," Trans. ASME, **54**, p. 141.
[24] Hamrick, J. T., 1956, "Some Aerodynamic Investigations in Centrifugal Impellers," Trans. ASME, **78**, pp. 591–602.
[25] Stanitz, J. D., and Ellis, G., 1950, "Two-Dimensional Compressible Flow With Straight Blades," NACA Report 954.
[26] Stanitz, J. D., and Prian, V. D., 1951, "A Rapid Approximate Method for Determining Velocity Distribution on Impeller Blades of Centrifugal Compressors," NACA TN 2421.
[27] Hamrick, J. T., Ginsburg, A., and Osborn, W. M., 1952, "Method of Analysis for Compressible Flow Through Mixed Flow Centrifugal Impellers of Arbitrary Design," NACA Report 1082.
[28] Stanitz, J. D., and Ellis, G., 1952, "Comparison of Two-and Three-dimensional Potential Flow Solutions in a Rotating Impeller Passage," NACA TN 2086.
[29] Michel, D. J., Ginsburg, A., and Mizisin, J., 1951, "Experimental Investigation

of Flow in the Rotating Passages of a 48-inch Impeller at Low Speed,'' NACA RM E51D20.
[30] Hamrick, J. T., Mizisin, J., and Michel, D. J., 1954, ''Study of Internal flow distribution Based on Measurements in a 48-inch Radial-Inlet Centrifugal Impeller,'' NACA TN 3101.
[31] Dean, R. C., and Senoo, Y., 1960, ''Rotating Wakes in Vaneless Diffusers,'' ASME J. Basic Eng., **82**, pp. 563–574.
[32] Japikse, D., 1985, ''Assessment of Single- and Two-Zone Modeling of Centrifugal Compressors. Studies in Component Performance. Part 3,'' ASME-Paper 85-GT-73.
[33] Japikse, D., 1992, ''Centrifugal Compressor Design and Performance. Course Proceedings,'' pp. 2.55–2.73.
[34] Hamrick, J. T., Ginsburg, A., and Osborn, W., 1950, ''Method of Analysis for Compressible Flow through Mixed Flow Centrifugal Impellers of Arbitrary Design,'' Lewis Flight Laboratory, Cleveland, Ohio.
[35] Wu Chung Hua, ''A General Theory of Three-Dimensional Flow in Subsonic and Supersonic Turbomachines of Axial-, Radial- and Mixed-Flow Types,'' NACA TN 2604.
[36] Katsanis, T., 1964, ''Use of Arbitrary Quasi-Orthogonals for Calculating flow Distribution in the Meridional Plane of a Turbomachine,'' NASA TN D-2546.
[37] Marsh, H., 1968, ''A Digital Computer Program for the Through-Flow Fluid Mechanics in an Arbitrary Turbomachine using a Matrix Method. Her Majesty's Stationary Office,'' R.&M. No. 3509, London, p. 32.
[38] Howard, J. H. G., and Osborne, C., 1977, ''Centrifugal Compressor Flow Analysis Employing a Jet-Wake Passage Flow Model,'' ASME J. Fluids Eng., **99**, pp. 141–147.
[39] Hirsch, C. H., and Warzee, G., 1976, ''A Finite Element Method for Through-Flow Calculations in Turbomachines,'' ASME-Paper 76-FE-12, p. 13.
[40] Bosman, C., and El-Shaarawi, M. A. I., 1977, ''Quasi-Three-Dimensional Numerical Solution of Flow in Turbomachines,'' ASME J. Fluids Eng., **99**, pp. 132–140.
[41] Krain, H., 1975, ''Contribution to the Calculation of Quasi-Three-Dimensional Flow in Centrifugal Compressor Rotors,'' thesis Technical University of Aachen, p. 185 (in German).
[42] Japikse, D., 1976, ''REVIEW-Prograss in Numerical Turbomachinery Analysis,'' ASME J. Fluids Eng., **98**, pp. 592–606.
[43] Meauze, G. et al., 1985, ''3D Computation Techniques Applied to Internal Flows in Propulsion Systems,'' AGARD-LS-140.
[44] Denton, J. D., ''The Use of Distributed Body Forces to Simulate Viscous Effects in 3D Flow Calculations,'' ASME-Paper 86-GT-144.
[45] Krain, H., and Hoffmann, B., 1998, ''Flow Physics in High Pressure Ratio Centrifugal Compressures ASME-SUMMER MEETING,'' FEDSM98-4853.
[46] Dawes, W. N., 1991, ''The Simulation of Three-Dimensional Viscous Flow in Turbomachinery Geometries Using a Solution Adaptive Unstructured Mesh Methodology,'' ASME Paper 91-GT-124.
[47] Moore, J., and Moore, J. G., 1979, ''A Calculation Procedure for 3D Viscous Compressible Duct Flow,'' ASME J. Fluids Eng., **101**.
[48] Hah, C., 1983, ''A Navier–Stokes Analysis of 3D Turbulent Flows inside Turbine Blade Rows at Design and Off-Design Conditions,'' ASME-Paper 83-GT-34.
[49] Dawes, W. N., ''Development of a 3D Navier–Stokes Solver for Application to all Types of Turbomachinery,'' ASME-Paper 88-GT-70.
[50] Hah, C., Bryans, A. C., Moussa, Z., and Tomsho, M. E., 1988, ''Application of Viscous Flow Computations for the Aerodynamic Performance of a Back-Swept Impeller at Various Operating Conditions,'' ASME-Paper 88-GT-39.
[51] Hirsch, Ch., Kang, S., and Pointel, G., 1996, ''A Numerically Supported Investigation of the 3D Flow in Centrifugal Impellers. Part I and II,'' ASME-Papers 96-GT-151 and 96-GT-152.
[52] AEA GmbH: CFX-TASCFlow: www.cfx.aeat.com
[53] Fluent Inc.:www.fluent.com
[54] NUMECA International: FINE/TURBO:www.numeca.com
[55] Star-CD: Advanced CFD-Solver: www.cd-adapco.com
[56] Flow Science: Flow-3D:www.flow3d.com
[57] DLR: TRACE: www.dlr.de/en-at/numsim
[58] Dawes, W. N., 1994, ''A Simulation of the Unsteady Interaction of a Centrifugal Impeller with its Vaned Diffuser: Flow Analysis,'' ASME-Paper 94-GT-105.
[59] Krain, H., 2001, ''Unsteady Flow of a Transonic Centrifugal Compressor, in Proceedings of the 15th International Symposium on Air Breathing Engines,'' Bangalore, India, p. 9.
[60] Prian, V. D., and Michel, D. J., 1951, ''An Analysis of Flow in Rotating Passage of Large Radial Inlet Centrifugal Compressor at Tip Speed of 700 Feet per Second NACA TN 2584.''
[61] Michel, D. J., Mizisin, J., and Prian, V. D., 1952, ''Characteristics of a 48-Inch Centrifugal Compressor. I-Change in Blade Shape,'' NACA TN 2706.
[62] Mizisin, J., and Michel, D. J., 1952, ''Effect of Changing Passage Configuration on Internal Flow Characteristics of a 48-Inch Centrifugal Impeller. Change in Hub-Shape,'' NACA TN 2835.
[63] Fowler, H. S., 1969, ''Research on the internal Aerodynamics of the Centrifugal Compressor,'' 11th Anglo-American Aeronautical Conference, London 8–12, Paper No. 19, p. 14.
[64] Eckardt, D., 1975, ''Instantaneous Measurements in the Jet-Wake Discharge Flow of a Centrifugal Compressor Impeller,'' ASME J. Eng. Power, **97**, pp. 337–346.
[65] Schodl, R., 1975, ''A Dual focus Velocimeter for Turbomachine Applications,'' Von Karman Institute, LS 78, p. 39.
[66] Eckardt, D., ''Detailed Flow Investigations Within a High-Speed Centrifugal Compressor Impeller,'' ASME-Paper 76-FE-13.
[67] Osborne, C., Runstadler, P. W., and Dodd, W., 1975, ''Aerodynamic and Mechanical Design of an 8:1 Pressure Ratio Centrifugal Compressor,'' NASA CR-134782, Creare TN-204, p. 139.
[68] Förster, W., Karpinski, G., Krain, H., Röhle, I., and Schodl, R., 2000, ''3-Component-Doppler-Laser-Two-Focus Velocimetry Applied to a Transonic Centrifugal Compressor, 10th International Symposium on Application of Laser Techniques to Fluid Mechanics.''
[69] Krain, H., 1981, ''A Study on Centrifugal Impeller and Diffuser Flow,'' ASME J. Eng. Power, **103**, pp. 688–697.
[70] Hah, C., and Krain, H., 1990, ''Secondary Flows and Vortex Motion in a High Efficiency Backswept Impeller at Design and Off-Design Conditions,'' ASME J. Turbomach., **112**, pp. 7–13.
[71] Krain, H., Hoffmann, B., and Pak, H., ''Aerodynamics of a Centrifugal Impeller With Transonic Inlet Conditions,'' ASME-Paper 95-GT-79, p. 9.
[72] Eisenlohr, G., Dalbert, P., Krain, H., Pröll, H., Richter, F. A., and Rohne, K. H., 1998, ''Analysis of the Transonic Flow at the Inlet of a High Pressure Ratio Centrifugal Impeller,'' ASME 98-GT-24.
[73] Hathaway, M. J., Chriss, R. M., Wood, J. R., and Strazisar, A. J., 1993, ''Experimental and Computational Investigation of the NASA Low-Speed Centrifugal Compressor Flow Field,'' ASME J. Turbomach., **115**, pp. 527–542.
[74] Ahmed, N. A., and Elder, T. L., ''Flow Investigations in a Small High Speed Impeller Passage Using Laser Anemometry,'' ASME-Paper 90-GT-233.
[75] Skoch, G. J., Prahst, P. S., Wernet, M. P., Wood, J. R., and Strazisar, A. J., ''Laser Anemometer Measurements of the Flow Field in a 4:1 Pressure Ratio Centrifugal Impeller,'' ASME-Paper 97-Gt-342.
[76] Wernet, M. P., Bright, M. M., and Skoch, G. J., 2001, ''An Investigation of Surge in a High Speed Centrifugal Compressor Using Digital PIV,'' ASME J. Turbomach., **123**, pp. 418–428.

Response of a Laminar Separation Bubble to an Impinging Wake

J. P. Gostelow

R. L. Thomas

Department of Engineering,
University of Leicester,
Leicester, LE1 7RH, UK

Laminar separation and transition phenomena were investigated experimentally in the wake-disturbed flow over a 2.4 m long flat plate. A controlled diffusion pressure distribution, representative of that on a compressor blade, was imposed but with sufficiently strong loading to cause laminar separation. Boundary layer velocity traverses were performed at several longitudinal stations. Wakes were generated upstream by a single rod, parallel to the leading edge, attached to a rotating disk mounted flush in the sidewall of the working section. Data are presented in the form of velocity traces and contours of velocity and turbulent intermittency. The results highlight the interaction between the incoming wake and the natural boundary layer, which features a long and thin laminar separation bubble; they demonstrate that wind tunnel experiments provide a good representation of boundary layer behavior under wake disturbances on turbomachinery blading. The calmed region behind the disturbance is a feature that is even stronger behind a wake interaction than behind a triggered turbulent spot. Intermittency values for the undisturbed flow in the separation bubble reattachment region are well represented by Narasimha's universal intermittency distribution, lending support to the use of intermittency-based predictive routines in calculations of blade boundary layers.
[DOI: 10.1115/1.1829729]

Introduction

The aerodynamic performance of turbomachinery blades operating at Reynolds numbers of less than one million is dependent on the transition modes occurring on the suction surface of the blade. For these low Reynolds numbers, characteristic of aircraft cruise conditions, laminar flow is present over a significant portion of the blade surface and the general nature of the flow is both unsteady and transitional.

Under a strong adverse pressure-gradient transition is likely to occur in the separated boundary layer, which, assuming appropriate conditions, reattaches further downstream. Luo and Lakshminarayana [1] undertook extensive computational studies of turbine blade boundary layers and heat transfer and assessed the performance of different low Reynolds number turbulence models under these conditions. The various k-ε models used captured the location of separation-induced transition very well. It was reported that separation-induced transition resulted in a much sharper increase in local heat transfer rate than bypass transition. Findings such as this have made it important to study separation-induced transition in more detail.

The periodic passage of wakes from upstream blade rows also affects transition and could cause the boundary layer to undergo transition ahead of any laminar separation. This has been documented in many studies, such as those of Halstead et al. [2] and Mayle [3].

Meticulous work by Hughes and Walker [4] on the identification of instability phenomena in periodic transitional flows on compressor blades has shown that, in this type of flow, transition is likely to be predominantly a natural growth process, rather than of the bypass type.

This interpretation was supported by the measurements of D'Ovidio et al. [5–7] who studied the development of turbulent spots under a strong adverse pressure gradient. The observed transition process was characterized by the development of instabilities of the Tollmien-Schlichting (T-S) variety. These experiments were based on the similarities in the transition process between wake-induced turbulent patches on turbomachinery blades and triggered turbulent spots on a wind tunnel flat plate [8]. The aim of testing on a flat plate is to simulate the transition phenomena occurring in turbomachines, but on a larger scale, in more detail than is possible in turbomachinery blading.

In the present experiments, the flow conditions reported in [5] have been replicated; the main difference lies within the imposed disturbance. In earlier work, wave packets and turbulent spots were triggered by a small loudspeaker that perturbed the flow by the injection of a small jet of air into the boundary layer. In this work the disturbance consists of wake generation by a spanwise rod rotating in the upstream flow.

The data gathered are intended to provide further evidence on the similarities in the transition process between turbomachinery and wind tunnel flows. This would justify the use of spot propagation and spreading rates, measured through wind tunnel experimentation, in numerical computations or transition length predictions for unsteady flows. In the model of Solomon, Walker, and Gostelow [9], explicit account is taken of turbulent spot formation as a part of the transition modeling.

In ongoing investigations the influence of the spacing between wakes and the resulting interactions with the attached boundary layer and the laminar separation bubble are being examined. The results should extend the current fundamental investigations to provide data directly applicable in the turbomachinery environment.

Test Conditions

The experiments were carried out in the 1.0×1.15 m test section of the low-speed wind tunnel at the University of Leicester. For all tests the Reynolds number, based on the flat plate length of $L=2.41$ m, was maintained constant and equal to $1.4\times10^6 \pm 0.7\%$, generating working-section inlet freestream flow speeds of 9.1 m/s with a turbulence level below 0.3%. Wakes were introduced to the flow by a tapered spanwise rod, of average radius 4.5 mm, cantilevered from a disk having an axis 0.5 m upstream of the leading edge (Fig. 1). The rod was mounted at a radius of 270

Contributed by the International Gas Turbine Institute and presented at the International Gas Turbine and Aeroengine Congress and Exhibition, Atlanta, GA, June 16–19, 2003. Manuscript received by the IGTI Dec. 2002; final revision Mar. 2003. Paper No. 2003-GT-38972. Review Chair: H. R. Simmons.

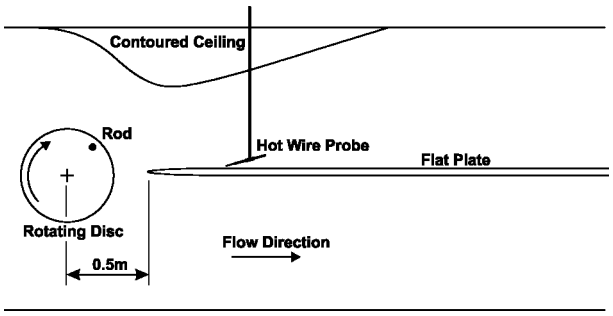

Fig. 1 Schematic view of flat plate and wake generator

mm on the disk and was rotated at a rate of 60 rpm, resulting in the introduction of two dissimilar wakes per second.

The top wall of the test section was contoured to provide the desired strong adverse pressure gradients. The measured static pressure distribution on the flat plate was of a self-similar type and gave a value for the Hartree pressure-gradient parameter β of -0.221 (Fig. 2). The pressure distribution was typical of a controlled-diffusion compressor blade, but having sufficient imposed loading to cause flow separation. For such a controlled diffusion distribution, this took the form of a long, and thin, laminar separation bubble.

The bubble was so thin that its displacement effect on the flow was small, and it had little of the ''plateau'' effect usually observed on separated-flow pressure distributions.

Data were acquired continuously using a single-wire hot-wire probe mounted on a computer-controlled traverse mechanism. Centerline phase-averaged velocity traces were determined at 27 x locations along the plate and y distances up to 50 mm normal to the flat plate surface. A photodiode circuit, mounted beside the rotating disk of the wake generator, acted as a triggering mechanism for the purposes of activation of data acquisition routines and continuous signal discretization.

Results

Phase averaging was performed over 128 repetitions, each record consisting of one full rotation of the wake generator producing two individual wakes, one as the rotating rod passes close to the leading edge of the flat plate (near wake) and another further upstream at 180 deg out of phase (far wake). Since the far wake has to travel slightly further before reaching the leading edge, there are approximately 650 ms between them.

A representative axial compressor blade-wake interaction should be simulated well by the near wake case, which gives a modest velocity deficit as the wake passes and also a modest

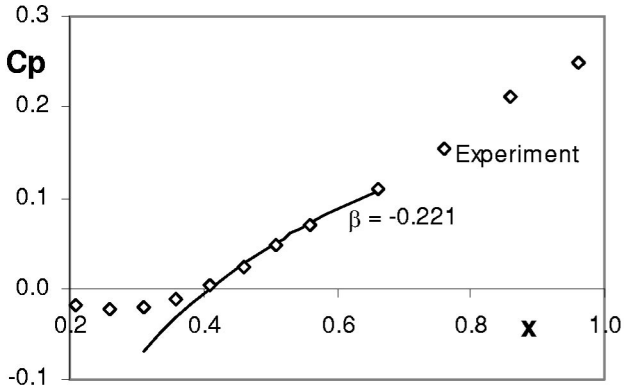

Fig. 2 Measured pressure distribution compared with self-similar distribution

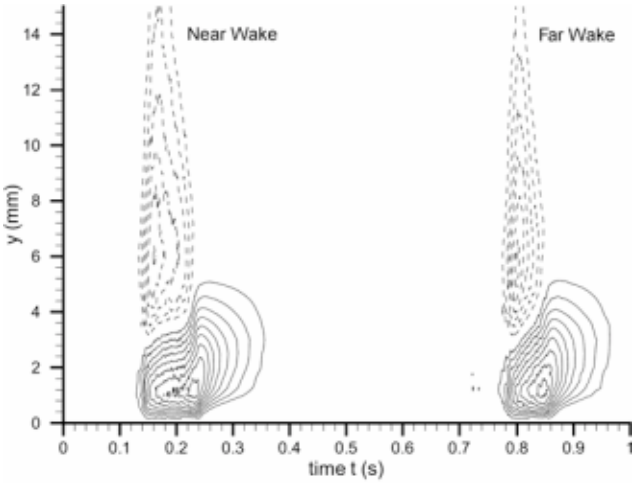

Fig. 3 Velocity perturbation contours at $x=0.65$ m

increase in incidence. Most turbine velocity triangles are not well represented by this arrangement, a higher disk rotational speed would be needed. The best role for the far-wake data might be in assessing the relative importance of velocity triangles and wake turbulence for the wake interaction behavior. This question is not fully resolved, but regardless of the velocity triangles both near-wake and far-wake results should be relevant to the question of the role of wake turbulence in promoting transition.

Disturbance Interaction. Contours of the velocity perturbations, $(\langle u\rangle - u_{nat})/U_\infty$, and rms levels, $\sqrt{\Sigma(u-\langle u\rangle)^2/n}$, are presented in the plots of Figs. 3 and 4 for a representative streamwise station. For Fig. 3, both the positive and negative (indicated by dashed lines) contours commence at 0.05 and are spaced at 0.05 intervals. From both figures, the wakes and the induced turbulent spots are clearly identifiable. The existence of the calmed regions, following the passage of the spots can be seen in the reattaching flow of Fig. 4. These regions of laminarlike flow are characterized by very low rms levels and extremely stable velocity profiles.

Contour plots of ensemble-averaged velocity and rms of velocity (Figs. 5 and 6) in a centerline plane normal to the blade surface show the progression and interactive effects of the wake with the natural boundary layer. Both figures synchronously demonstrate the passing of one wake, as it convects downstream. The plots of

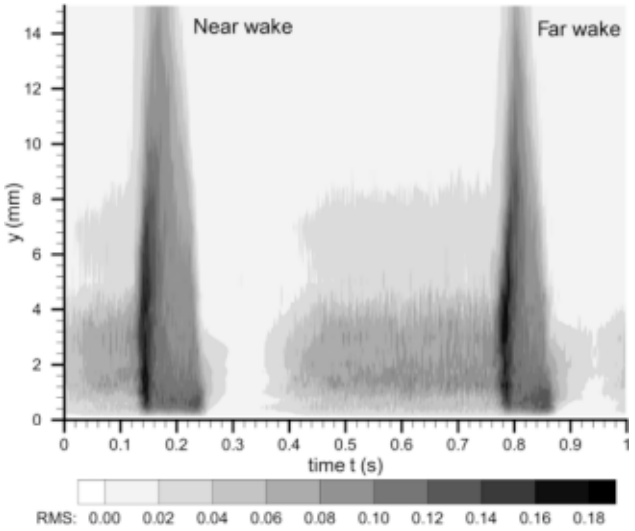

Fig. 4 RMS of velocity at $x=0.65$ m

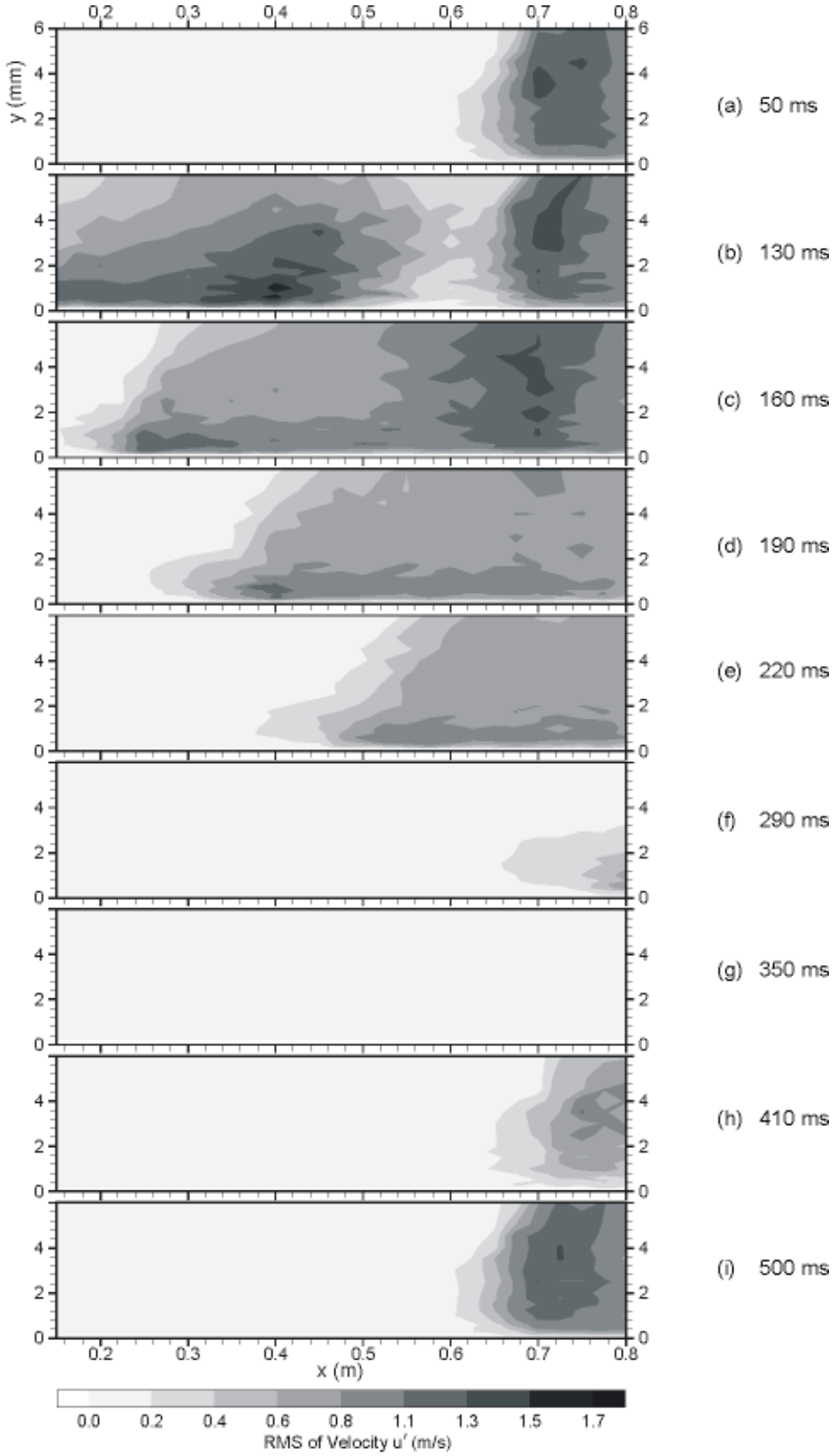

Fig. 5 Contours of rms of velocity for 9 phases of the cycle

rms of velocity (Fig. 5) best represent regions of turbulence and demonstrate the propagation of the wake through the transition zone; the natural undisturbed mode of transition to turbulence can be studied in Figs. 5(*a*) and 5(*i*). The extreme severity of the fluctuations in the reattachment region and immediately downstream is clear, and this is consistent with the computational findings of Luo and Lakshminarayana [1]. The incoming wake is seen in Fig. 5(*b*) as the large region of high rms that merges with the

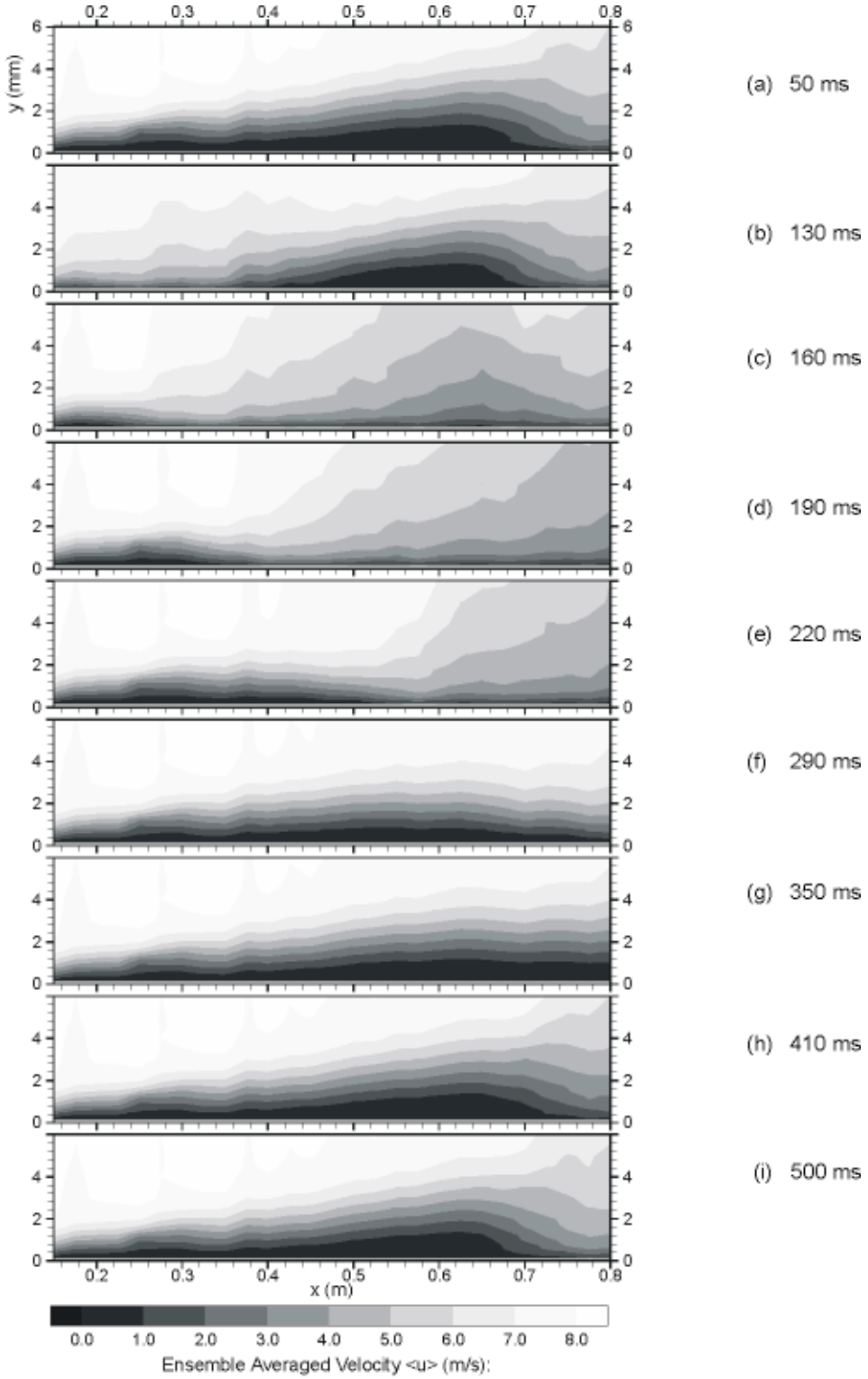

Fig. 6 Ensemble-averaged velocity contours for 9 phases of the cycle

existing region of transition as it progresses downstream [Fig. 5(*c*)]. This resulting, longer, turbulent region is swept downstream with the wake, leaving behind a more stable region of flow, very much like laminar flow [Figs. 5(*f*) and 5(*g*)]. This region corresponds to the calmed region, normally observed behind a turbulent spot, as seen by Schubauer and Klebanoff [10] and Gostelow et al. [11]. In comparison with previously conducted work on turbulent spots, a calmed region produced by an imposed wake is stronger, with a more stable velocity profile, and persists for a longer time. In the same way as the calmed region produced by a triggered turbulent spot, it is ultimately overrun and supplanted by the encroaching naturally turbulent boundary layer.

The plots of ensemble-averaged velocity (Fig. 6) are used here to show the distribution of velocity through the boundary layer. They, therefore, highlight well the fate of the bubble under the influence of the disturbances, such as the impingement of wakes

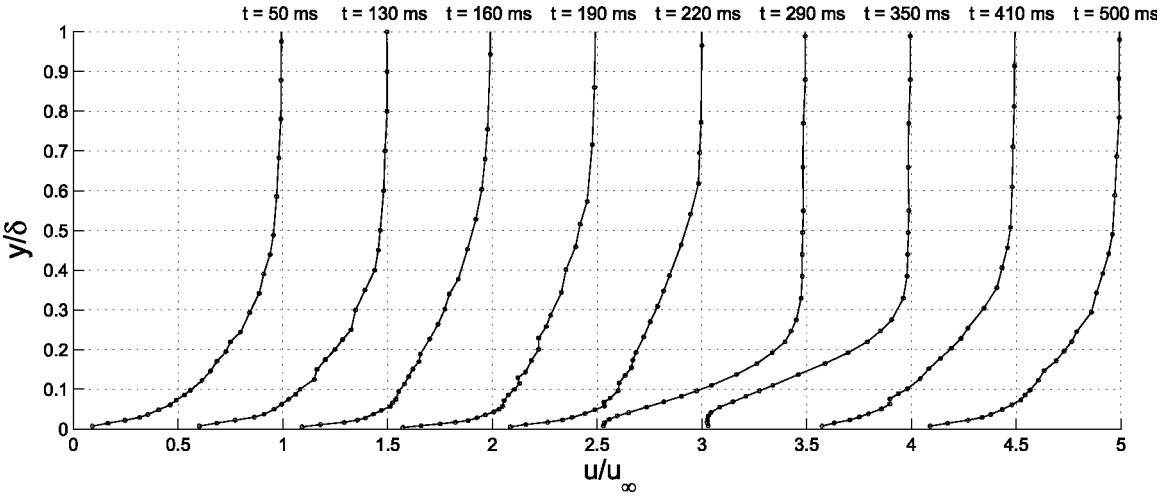

Fig. 7 Boundary layer velocity profiles at different phases for $x=0.750$ m

from upstream blade rows. In the undisturbed flow, the long and thin laminar separation bubble exists between chord locations 0.425 and 0.700 m, with a maximum height of approximately 1.5 mm toward its end. Figure 5 gives the corresponding wake locations in each frame as it interacts with the boundary layer. The wake suppresses the bubble as it convects downstream, causing a reattachment of the boundary layer and the removal of the bubble. The calmed region that follows demonstrates an elevated shear stress at the wall [2], which has the effects of delaying transition and stabilizing the boundary layer against separation [11]. It can be seen from Figs. 6(*f*) and 6(*g*) that the prominent calmed region has a more stable laminarlike velocity profile. The adverse pressure gradient promotes separation, and, in a natural mode of separated transition, the amplification of instabilities in the shear layer causes reversion to the natural turbulent boundary layer [Figs. 6(*h*) and 6(*i*)]. Boundary layer velocity profiles at $x=0.75$ m are provided for varying phases of the cycle in Fig. 7. These show the expected turbulent profile in regions of attached flow, except in the calmed region, where a laminarlike flow that eventually separates is indicated by the inflectional profile.

Instabilities. Figure 8 shows representative instantaneous velocity traces in the free shear layer at a height of 2 mm above the surface ($y=2.0$ mm) at four streamwise locations. From these raw velocity traces, transient instabilities can be observed that are lost in the ensemble-averaging process. It can be seen that low-amplitude instabilities matching predicted Tollmien-Schlichting (T-S) frequencies are evident in the undisturbed flow. These T-S waves are amplified as they are convected downstream, resulting in the development of harmonics and their subsequent breakdown to turbulence.

Lou and Hourmouziadis [13] have conducted somewhat similar experiments, but using a periodically oscillating velocity field rather than a convected wake. They interpret their instabilities as of the inflectional shear layer (Kelvin-Helmholtz) type rather than the viscous (T-S) type. There is not seen to be a contradiction here since quite small differences in Reynolds number and pressure distribution can result in significant differences in velocity profile and have a decisive influence on the stability outcome. It is worth noting that the calmed region directly following the turbulent patch strongly suppresses the development of instabilities and has a retarding influence on this growth process, including the development of harmonics and the breakdown to turbulence [8].

Walker [12] developed an equation that predicted the most probable T-S frequencies

$$\frac{\omega \nu}{U_\infty^2} = 3.2\,\mathrm{Re}_{\delta^*}^{-1.5} \tag{1}$$

Walker advocated the use of a compensation factor when dealing with adverse pressure gradients [4] because of the broader range of instability frequencies evident as compared to a favorable pressure gradient. Estimated values using this approach closely match the measured frequencies for instability occurrence observed in the data.

Intermittency. The approach to intermittency pioneered by Narasimha [14] has proved a robust means of determining the extent of the transition region [15]. In earlier work on transition

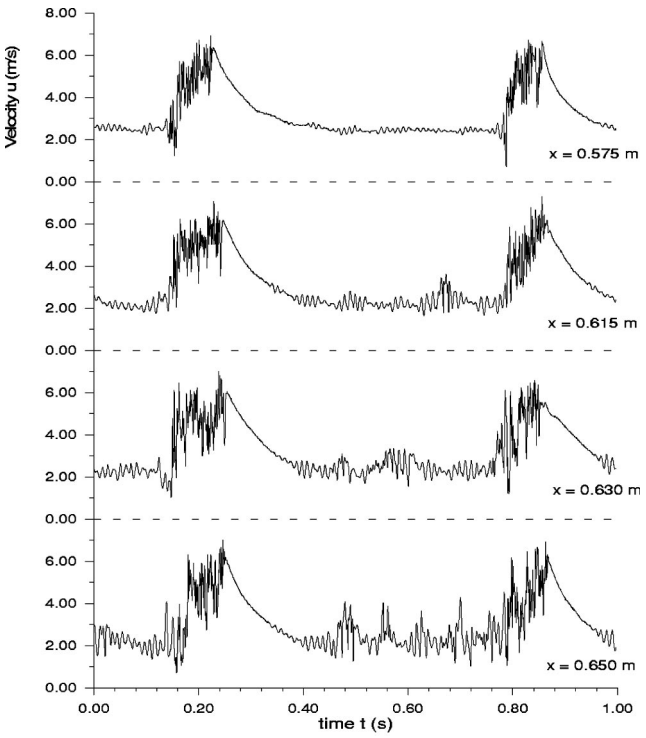

Fig. 8 Representative velocity traces at $y=2.0$ mm

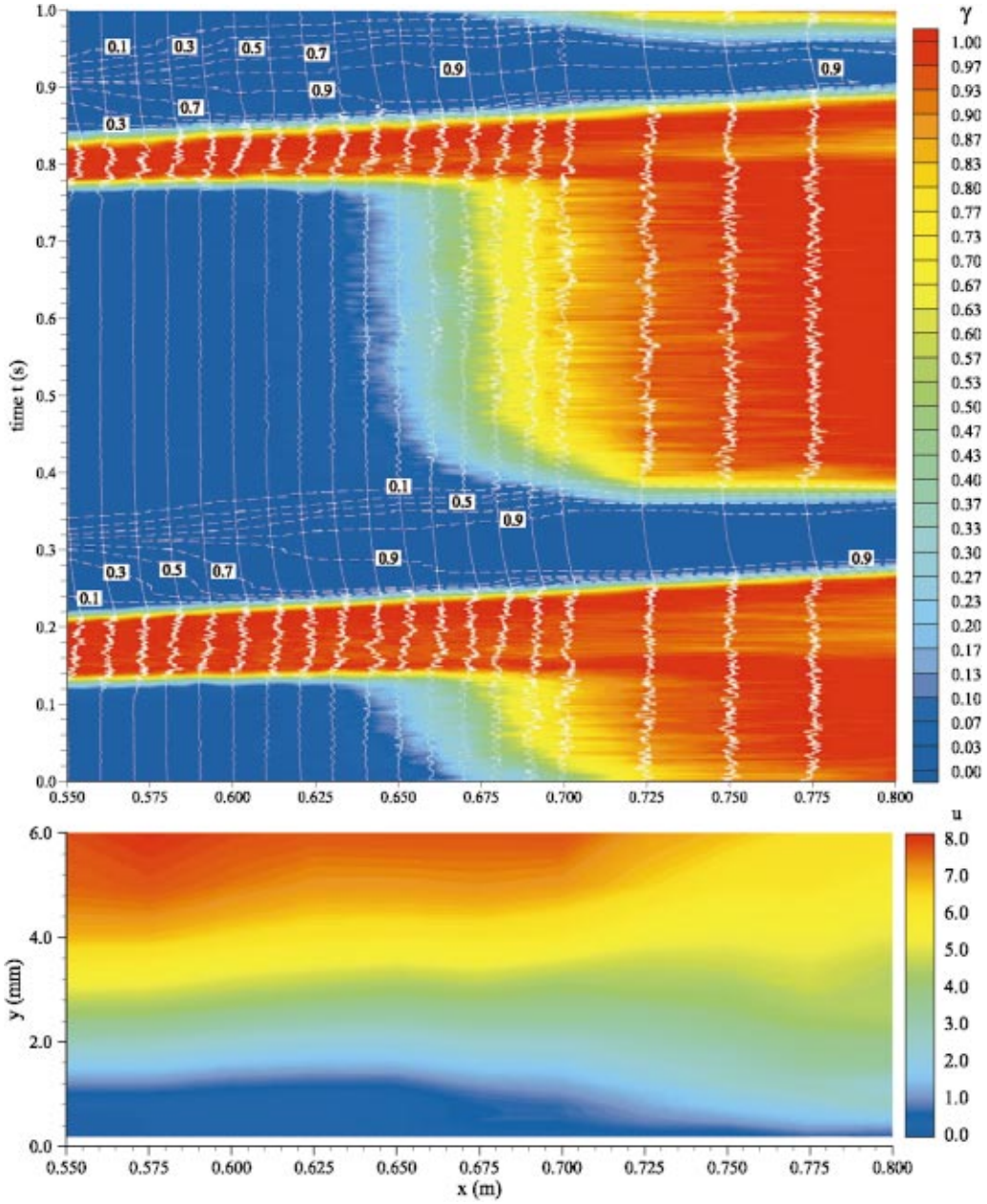

Fig. 9 (**Color**) (***a***) (**upper**) **Measured** $x \sim t$ **diagram for intermittency with velocity traces and relaxation parameter superimposed and** (***b***) (**lower**). **Measured** $x \sim y$ **diagram of ensemble-averaged velocity contours in undisturbed boundary layer showing outline of separation bubble.**

and turbulent spots, the TERA routine of Falco and Grendrich [16], which is based on $(u \times \partial u/\partial t)$ as a discriminant, has proved to be versatile and robust. However, in the present investigation it failed to accurately discriminate the calmed region following each turbulent patch. This is due to the high velocities with steep gradients that exist at the beginning of the particularly strong calmed regions following a wake (see Fig. 8). Accordingly, for these experiments on wakes, with particularly strong velocity gradients in stable flows, the temporal velocity gradient alone $(\partial u/\partial t)$ was used to promote detection of high gradients only. The calmed region itself has a high gradient, but very little velocity fluctuation; a high pass filter was therefore applied to the data, retaining the high-frequency content of the turbulent regions while reducing the aggressive gradient of the calmed region. A moving average with a smoothing window of eight samples was introduced to improve the continuity of the detected regions. Calibration of the routine was performed through visual selection of turbulent regions from velocity traces to derive the correct threshold.

Figure 9(*a*) gives intermittency variations in the wake-disturbed flow in an $x \sim t$ diagram at a height of 1.25 mm above the flat plate. The range of x covered in this plot is 0.550–0.800 m. This does not cover the early part of the long laminar separation bubble because the focus of the investigation is on the growth of instabilities and the transition process that eventually results in bubble closure. Representative individual velocity traces from the same height are superimposed. For each trace, the velocity is highest to the right-hand side of the plot. In addition the relaxation parameter κ (the probability that following a region of turbulent flow the flow is in a relaxing state) has been evaluated and is represented by dashed contours. The single cycle of data contains two dissimilar wakes, the near wake followed by the far wake, each preceding a calmed region and regions of laminar separation terminated by

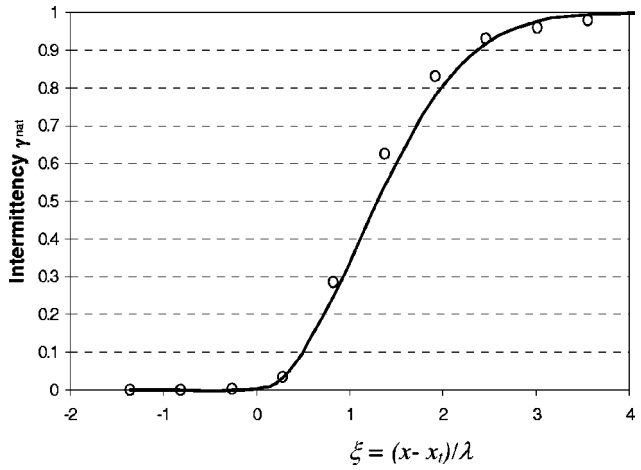

Fig. 10 Measured intermittency distribution (○) compared to Narasimha's universal distribution

transition in the shear layer. The strongly turbulent regions initiated by the wake passage are clearly visible, showing dissimilar leading- and trailing-edge propagation speeds. The strongly laminar calmed region persists for a length of time comparable to that of the disturbance and, as time increases, is seen to be replaced by a natural transition to turbulence. The extent of the laminar separation bubble is best judged in the $x \sim y$ plane velocity contour plot of Fig. 9(*b*).

Figure 9(*a*) may usefully be compared with Figs. 1 and 4 of Ref. [8]. These show $x \sim t$ data from a triggered turbulent spot and an operating compressor stage, respectively. Immediate similarities can be highlighted. The prominent calmed region is apparent, following the trailing edge of each disturbance region, as a region of very low intermittency that displays laminarlike properties. The calmed region delays restoration of the natural boundary layer, but after initiation it can be seen to take place rapidly.

The universal intermittency distribution of Narasimha [14] has proved to be an accurate and robust approach to predicting transition rates in boundary layer flows. Figure 10 shows the intermittency of the flow for the undisturbed transition region averaged across the period $0.5 \leqslant t \leqslant 0.7$ s. The curve fit derived from Eq. (2) shows that transitional flow in the reattachment region of a laminar separation bubble accurately follows Narasimha's intermittency distribution:

$$\gamma = 1 - \exp(-0.412\xi^2) \tag{2}$$

where

$$\xi = (x - x_t)/\lambda$$

The value for x_t is determined from intermittency, plotted as

$$F(\gamma) = [-\ln(1-\gamma)]^{1/2} \tag{3}$$

as a function of x, by equating the left-hand side of a straight line fit to zero to find the x-axis intercept. The flow had separated at $x = 0.425$ m, and transition commenced at $x_t = 0.612$ m. λ is the distance between the two x locations for $\gamma = 0.25$ and $\gamma = 0.75$, and for this case $\lambda = 0.046$ m.

This finding confirms an earlier finding of Malkiel and Mayle [17], who also observed agreement with the universal intermittency distribution in the reattachment region of a laminar separation bubble. It also justifies the extension of intermittency-based transition-region prediction procedures, such as those of Solomon, Walker, and Gostelow [9], to flows having laminar separation bubbles. A good example of such a practice is given in the work of Sanz and Platzer [18].

Conclusions

Strong similarities between results from wake-disturbed boundary layer flows in wind tunnel experimentation and from compressor blading have been described. This evidence supports the direct application of data from wind tunnel experiments in numerical computations for predicting the behavior of unsteady flows, with special regard to the use of spot propagation and spreading rates in predicting the transition process.

An aim of this paper is to enable the reader to judge the relative importance of the separate influences of wake-induced turbulence, the calmed region, and the natural transition region on the inception and development of transition. In practice, each turbomachinery condition will have a differing mix of these and the time-averaged behavior will vary accordingly.

The adverse pressure gradient causes strong amplification of instabilities, first detected upstream of the separation region. Driven at a particular frequency, matching those of the predicted T-S waves, these instabilities grow into turbulent spots that develop in the shear layer of the separation bubble. This ultimately progresses into fully three-dimensional turbulence. The traces clearly indicate that the undisturbed flow experiences a natural transition, and, at this low free-stream turbulence level, transition inception is predicted best by methods developed for natural growth transition. As indicated by Luo and Lakshminarayana [1], the most violent fluctuations occur in the reattachment region of the laminar separation bubble.

Each wake passing heralds a calmed region of flow that stabilizes the boundary layer and suppresses the growth of instabilities. This has the effect of delaying transition sufficiently to maintain a lasting laminarlike velocity profile. This is eventually overrun by the surrounding turbulence to return the boundary layer to its natural state. By careful manipulation of blade properties, advantages can be realized through the exploitation of wake-induced calmed regions to increase the loading of turbomachinery blades and thus reduce the blade count, weight, and cost.

Universal intermittency distributions for predicting the distribution of intermittency through a boundary layer have proven to accurately estimate the rate of turbulent spot development over a laminar separation bubble under an adverse pressure gradient. This relationship provides support for the use of intermittency-based predictive boundary layer routines, such as that of Solomon, Walker, and Gostelow [9], even in flows involving separation bubbles.

Acknowledgments

This paper is dedicated to the memory of Bud Lakshminarayana, a dear friend and supportive colleague of J. P. Gostelow since their student days in Liverpool. A research grant from Engineering and Physical Sciences Research Council is gratefully acknowledged. Richard Thomas is indebted to the same research council for a studentship.

Nomenclature

k = turbulent kinetic energy
L = plate length
n = number of records in ensemble
Re_{δ^*} = displacement thickness Reynolds number
t = time
$u_{x,y,t}$ = instantaneous velocity in space and time
x = chordwise distance
x_t = point of transition inception (Narasimha)
y = distance normal to plate surface
U_∞ = freestream velocity
β = Hartree pressure gradient parameter
γ = intermittency
δ = boundary layer absolute thickness
ε = turbulent kinetic energy dissipation rate
κ = relaxation parameter

ν = kinematic viscosity
ω = circular frequency

Superscripts, Subscripts

$'$ = rms of value
$\langle\ \rangle$ = ensemble average value
nat = of the undisturbed flow

References

[1] Luo, J., and Lakshminarayana, B., 1997, ''Numerical Simulation of Turbine Blade Boundary Layer and Heat Transfer and Assessment of Turbulence Models,'' ASME J. Turbomach., **119**, pp. 794–801.

[2] Halstead, D. E., Wisler, D. C., Okiishi, T. H., Walker, G. J., Hodson, H. P., and Shin, H. W., 1997, ''Boundary Layer Development in Axial Compressors and Turbines: Part 1–4,'' ASME J. Turbomach., **119**(1), pp. 114–127; pp. 128–139; **119**(2), pp. 234–246; **119**(3), pp. 426–444.

[3] Mayle, R. E., 1991, ''The Role of Laminar-Turbulent Transition in Gas Turbines,'' ASME J. Turbomach., **113**, pp. 509–537 (1991 IGTI Scholar Lecture).

[4] Hughes, J. D., and Walker, G. J., 2001, ''Natural Transition Phenomena on an Axial Compressor Blade,'' ASME J. Turbomach., **123**, pp. 392–401.

[5] D'Ovidio, A., Harkins, J. A., and Gostelow, J. P., 2001, ''Interaction Between a Laminar Separation Bubble and a Turbulent Spot Under a Strong Adverse Pressure Gradient,'' *Proc. of 4th European Conference on Turbomachinery Fluid Dynamics and Thermodynamics*, ATI-CST-077/1.

[6] D'Ovidio, A., Harkins, J. A., and Gostelow, J. P., 2001, ''Turbulent Spot in Strong Adverse Pressure Gradients, Part I: Spot Behavior,'' ASME Paper No. 2001-GT-0194.

[7] D'Ovidio, A., Harkins, J. A., and Gostelow, J. P., 2001, ''Turbulent Spot in Strong Adverse Pressure Gradients. Part II: Spot Propagation and Spreading Rate,'' ASME Paper No. 2001-GT-0406.

[8] Gostelow, J. P., Hodson, H. P., and Walker, G. J., 1999, ''Comparisons Between Triggered Turbulent Spots and Unsteady Transition Phenomena on Compressor and Turbine Blading,'' *Laminar-Turbulent Transition*, Proc. IUTAM Symposium, H. F. Fasel and W. S. Saric, eds., Sedona, AZ, pp. 365–370.

[9] Solomon, W. J., Walker, G. J., and Gostelow, J. P., 1996, ''Transition Length Prediction for Flows With Rapidly Changing Pressure Gradients,'' ASME J. Turbomach., **118**, pp. 744–751.

[10] Schubauer, G. B., and Klebanoff, P. S., 1955, ''Contributions on the Mechanics of Boundary Layer Transition,'' NACA Report 1289.

[11] Gostelow, J. P., Walker, G. J., Solomon, W. J., Hong, G., and Melwani, N., 1997, ''Investigation on the Calmed Region Behind a Turbulent Spot,'' ASME J. Turbomach., **119**, pp. 802–809.

[12] Walker, G. J., 1989, ''Transitional Flow on Axial Turbomachine Blading,'' AIAA J., **27**(5), pp. 595–602.

[13] Lou, W., and Hourmouziadis, J., 2000, ''Separation Bubbles Under Steady and Periodic-Unsteady Main Flow Conditions,'' ASME Paper No. 2000-GT-0270.

[14] Narasimha, R., 1957, ''On the Distribution of Intermittency in the Transition Region of the Boundary Layer,'' J. Aeronaut. Sci., **24**, pp. 711–712.

[15] Gostelow, J. P., Blunden, A. R., and Walker, G. J., 1994, ''Effects of Free-Stream Turbulence and Adverse Pressure Gradients on Boundary Layer Transition,'' ASME J. Turbomach., **116**, pp. 392–404.

[16] Falco, R. E., and Grendrich, C. P., 1990, ''The Turbulence Burst Detection Algorithm of Z. Zaric,'' *Near-Wall Turbulence*, 1988 Zoltan Zaric Memorial Conference, Hemisphere, New York, Kline, S. J., and Afgan, N. H., eds., pp. 911–931.

[17] Malkiel, E., and Mayle, R. E., 1996, ''Transition in a Separation Bubble,'' ASME J. Turbomach., **118**, pp. 752–759.

[18] Sanz, W., and Platzer, M. F., 1996, ''On the Navier-Stokes Calculation of Separation Bubbles,'' ASME Paper 96-GT-487.

Experimental Investigation of a High Pressure Ratio Aspirated Fan Stage

Ali Merchant

Jack L. Kerrebrock

Gas Turbine Laboratory,
Massachusetts Institute of Technology,
Cambridge, Massachusetts 02139

John J. Adamczyk

Edward Braunscheidel

NASA Glenn Research Center,
Cleveland, Ohio 44135

The experimental investigation of an aspirated fan stage designed to achieve a pressure ratio of 3.4:1 at 1500 ft/s is presented in this paper. The low-energy viscous flow is aspirated from diffusion-limiting locations on the blades and flowpath surfaces of the stage, enabling a very high pressure ratio to be achieved in a single stage. The fan stage performance was mapped at various operating speeds from choke to stall in a compressor facility at fully simulated engine conditions. The experimentally determined stage performance, in terms of pressure ratio and corresponding inlet mass flow rate, was found to be in good agreement with the 3D viscous computational prediction, and in turn close to the design intent. Stage pressure ratios exceeding 3:1 were achieved at design speed, with an aspiration flow fraction of 3.5% of the stage inlet mass flow. The experimental performance of the stage at various operating conditions, including detailed flowfield measurements, are presented and discussed in the context of the computational analyses. The stage performance and operability at reduced aspiration flow rates at design and off-design conditions are also discussed. [DOI: 10.1115/1.1812323]

Introduction

The work reported here constitutes one element of a program being conducted by the MIT Gas Turbine Laboratory and its collaborators to develop and validate the technology for design of axial compressors that incorporate control of flow separation by aspiration (or suction) of the viscous flows at diffusion-limiting locations. These include points of impingement of passage shocks, just ahead of diffusion due to flow turning on the blade suction surface, and in corners of the flow path.

The intent of this particular element of the aspirated compressor program was to assess the limit of pressure ratio attainable with aspiration in a single stage, within conventional tip speed limits as set by structural considerations. Preliminary calculations indicated that aspiration should enable an approximate doubling of the work of a stage, while maintaining attached flow [1]. Prior to the work reported here, a moderately aggressive aspirated transonic fan stage, with a pressure ratio of 1.6 and tip speed of 750 ft/s, was designed and tested at MIT as a first step in demonstrating the utility of aspiration [2]. Consistent with the more aggressive design space of supersonic high through-flow fans, the design objective for the present stage was set as a pressure ratio of approximately 3.4 at a tip speed of 1500 ft/s. A rotor-tip shroud was included in the design to ensure that tip-clearance effects did not limit the aerodynamic performance. Detailed design calculations using a MISES-based approach developed at MIT, followed by 3D viscous analyses carried out at NASA Glenn Research Center, confirmed the viability of the initial choice of pressure ratio [3].

While the principal emphasis of this work was on attaining high work per stage, careful attention was also paid to minimizing the aspiration requirement and achieving acceptable through-flow efficiency, which is the adiabatic efficiency of the compressor based on the stator (or rotor) outflow. This through-flow efficiency includes the effects of shock losses in the core flow and viscous losses that influence the entropy of the outflow of the compressor. It does not embrace the effects of losses that raise the entropy of the aspirated flow, or the pumping work associated with it. The overall impact of these (secondary) effects of aspiration can be properly quantified only in the context of a complete engine design, in which the handling of the aspirated flows is explicated. Such an overall evaluation of the effect of aspiration on engine efficiency is outside the scope of this paper.

The structure of this paper is as follows. The aerodynamic design is summarized first, followed by a description of the mechanical design of the stage. The experiment test package, instrumentation, and data reduction procedure are briefly described. The experimental results are discussed next and compared with the multi-stage CFD analyses. Lastly, the important conclusions and implications of the results of the test program are enumerated.

Aerodynamic Design

The computational system assembled to design the aspirated fan stage consists of the quasi-3D MISES integral boundary layer solver [4] coupled with an axisymmetric solver described by Merchant [5]. The blade shapes incorporate several unique design features, which enable the high loading. The details of the aerodynamic design and design procedure can be found in Merchant [5].

Three-dimensional viscous analysis of the stage, using the multi-stage average passage APNASA code developed by Adamczyk [6], was a critical component in the design process. The high supersonic Mach numbers in the blade rows, and close blade row spacing, coupled with the very high blade loading demanded more accurate blade row matching than is possible with mixing-plane approaches. While the blade design was carried out using the quasi-3D design system, modifications to blade geometry, primarily incidence changes, were made using information extracted from the 3D APNASA solution.

In addition to the design point analysis, an off-design study along the operating lines was also performed using APNASA in order to assess the performance of the stage at lower tip speeds, and to develop a test plan for the experiment. Two such operating lines were calculated: one close to stall (high op line) and one sufficiently away from stall (low op line). The computational mesh used for all the analyses consists of 389 axial points from rotor inlet to stator exit, 51 circumferential points and 51 spanwise

Contributed by the International Gas Turbine Institute (IGTI) of THE AMERICAN SOCIETY OF MECHANICAL ENGINEERS for publication in the ASME JOURNAL OF TURBOMACHINERY. Paper presented at the International Gas Turbine and Aeroengine Congress and Exhibition, Vienna, Austria, June 13–17, 2004, Paper No. 2004-GT-53679. Manuscript received by IGTI, October 1, 2003; final revision, March 1, 2004. IGTI Review Chair: A. J. Strazisar.

Table 1 Aerodynamic design summary

Tip speed	1500 ft/s (457 m/s)
Pressure ratio	3.4
Mass flow/Area	42.5 lbm/s-ft^2
Rotor face axial Mach no.	0.65
Stage exit Mach no.	0.5
Rotor peak Mach no. (rel.)	1.5
Stator peak Mach no. (abs.)	1.5
Peak diffusion factor (rot./sta.)	0.76/0.68
Rotor work coefficient ($\Delta H/U^2$)	0.7

Table 3 Design aspiration requirement

Aspiration location	Designation	Aspiration fraction (%)
Rotor shroud	B2	1.0
Rotor spanwise	B3	1.5
Stator spanwise	B5	2.0
Stator hub (circumferential)	B7	1.0
Stator hub (chordwise)	B7	1.0

grid points. The APNASA code was modified with a transpiration boundary condition on the blade and flowpath surfaces to model the effect of aspiration.

The aerodynamic design characteristics of the stage are summarized in Table 1, and the geometric characteristics are summarized in Table 2. The diffusion factors were calculated using the definition of Lieblein et al. [7]. The choice of tip speed, specific flow, and inlet/exit Mach numbers are consistent with modern supersonic high through-flow fans [8,9]. The aspect ratio and average solidities of the stage are also similar to such modern fans. The peak Mach numbers, noted in Table 1, occur at the rotor tip and the stator hub. The rotor was designed to achieve a free vortex work profile, and the stator was designed to turn the flow to axial conditions at the stage exit.

The aspiration scheme is illustrated in Fig. 1, and the design aspiration fractions are given in Table 3. The designations refer to the experiment setup and will be discussed in the section describing the test package. The aspiration scheme consists of primary aspiration slots on the rotor and stator suction surfaces, and secondary aspiration on the hub and shroud surfaces. The location and flow fraction of the primary aspiration was optimized in the quasi-3D design process. The secondary aspiration consists of slots on the rotor shroud and stator hub surfaces to prevent shock-induced separation and control the growth of secondary flows. The location and flow fractions of these were determined by examining the 3D solution. However, no attempt was made to optimize the secondary aspiration locations and flow fractions. Bleeds B1, B4, and B6 were present only in the experiment, and were not included in the CFD analysis. It should be noted that the stator hub circumferential and chordwise bleed have the same designation (B7) since they are discharged into the same cavity in the experiment.

Table 2 Stage geometry characteristics

Rotor inlet (r_{hub}/r_{tip})	0.40
Stator exit (r_{hub}/r_{tip})	0.81
Blade count (rot/stat)	26/31
Average solidity (rot/sta)	2.5/2.5
Aspect ratio (rot/sta)	1.2/0.8

Mechanical Design

As the main purpose of the experiment was to assess the viability of aspiration from the aerodynamic standpoint, the mechanical design became a matter of devising a configuration that would meet the mechanical requirements, while providing the shape and tip speed capability dictated by the aerodynamic design. This is a different logical structure than is usual for compressor stages, where the structural considerations generally play a larger role in the overall design optimization. The desire for as clean an aerodynamic design as possible led to the use of a tip shroud in order to eliminate the tip clearance flow. In addition, the tip shroud was attractive as a means for transporting the aspirated flow from the blades to the rotor housing.

The features dictated by the aerodynamic design posed an unusual set of constraints for the mechanical design of the rotor in particular. Finite element calculations showed that the blade stresses due to the high tip speed and large camber and twist of the blades were so high as to be unacceptable, except for the highest

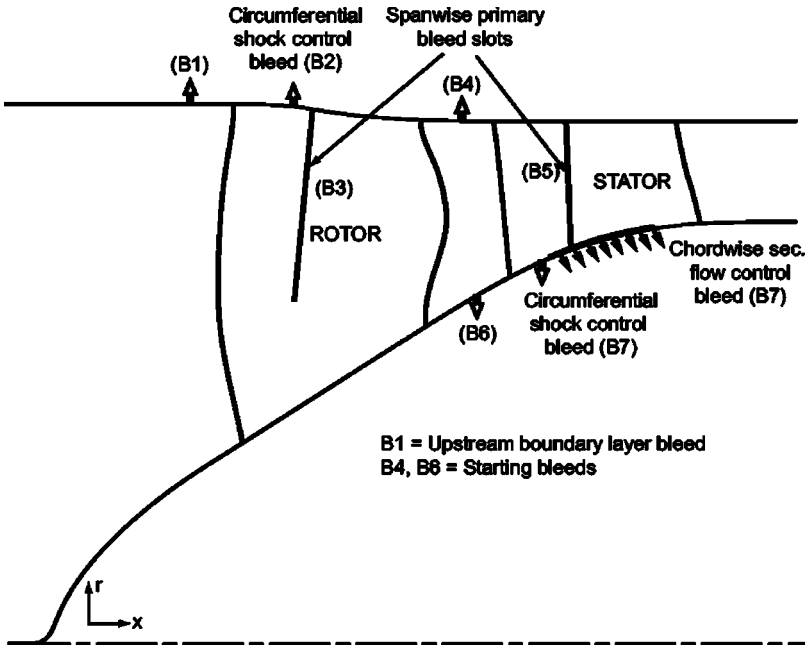

Fig. 1 Stage aspiration scheme

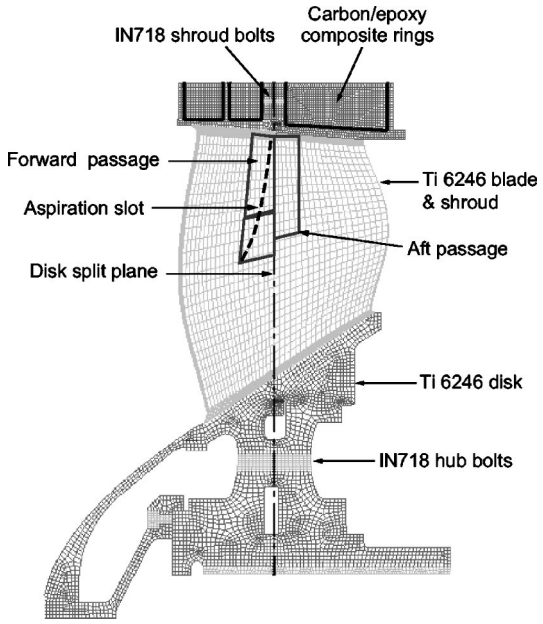

Fig. 2 Rotor structural concept

strength-to-weight ratio titanium alloys such as Ti-6246, which was selected for the rotor. Welding was ruled out by the choice of this alloy. Stress calculations also indicated that the shroud, at the design tip speed of 1500 ft/s, was beyond its self-supporting limit, and given the already high stresses in the blades, it was not feasible to carry much of the centrifugal load of the shroud on the blades. This led to the decision to use a graphite-polymer composite winding on the shroud to make it essentially self-supporting. The amount of composite was chosen so that the average radial growth of the shroud would match that of the blade tips (without the shroud). This would result in only local radial load transfer from the blades to the shroud. The shroud does, however, greatly increase the torsional stiffness of the blades in the tip region, essentially eliminating flutter issues, and potential structural problems due to the bleed passages in the blades.

Machining the high solidity rotor and stator blades, bleed passages, and bleed slots as bladed disks posed another set of challenges. These were met by dividing the blade rows into forward and aft disks on a plane perpendicular to the axis of rotation. Halving the blade chord enabled machining of the high solidity blades from single disks, and the suction passages were then machined into the two halves from the separation plane. The assembly of the blade rows involved bolting the forward and aft disks together at the shroud and at the hub. This concept is illustrated for the rotor in Fig. 2.

The composite winding of the shroud was implemented as three separate rings in channels in the titanium shroud as shown in Fig. 2. The front disk carried two rings separated by a land for the rotor shroud bleed, and the aft disk carried a single composite ring. The primary aspirated flow was taken from the suction surface of the blade through slots into the radial passages and discharged from the tip at an angle of 45 deg, against the direction of rotation. This was done to minimize the pumping work for the bleed flow, and consequently the temperature rise of the aspirated flow circulating in the rotor casing.

The stator suction surface aspirated flow was carried through the radial passage into the casing manifold shown in Fig. 3.

Test Package

The aspirated compressor test package consisted of the rotor, stator, and a specially designed casing. The casing sealed the rotor bleed flows from the core flow and collected the high swirl flow from the rotor shroud. The test package installed in the rig is shown in Fig. 3. Seven independently controlled, and metered, boundary layer bleed lines were also key elements of the system. These include, in addition to the five design bleeds shown in Fig. 1, an inlet boundary layer bleed slot (B1) approximately 1 chord upstream of the rotor, an interblade casing bleed slot (B4), and an interblade hub bleed slot (B6). The stator hub pitchwise and chordwise bleeds were combined into a common bleed line (B7). Bleeds B1, B4 and B6 were not modeled in the aerodynamic analysis of the stage. Bleeds B4 and B6 were added to ensure that the stage could be operated at part speeds. The bleed exhaust system was designed to keep the rotor and stator bleed slots operating in a choked condition. A vacuum source was used for all the bleed lines to achieve this condition. Figure 4 shows the rotor with the spanwise aspiration slot (B3), circumferential shock control bleed (B2), and shroud surface indicated. The NASA Glenn Research Center Multistage Compressor Test Facility, which includes a 15,000 hp drive motor and a 5.21:1 gearbox, was used for this experiment.

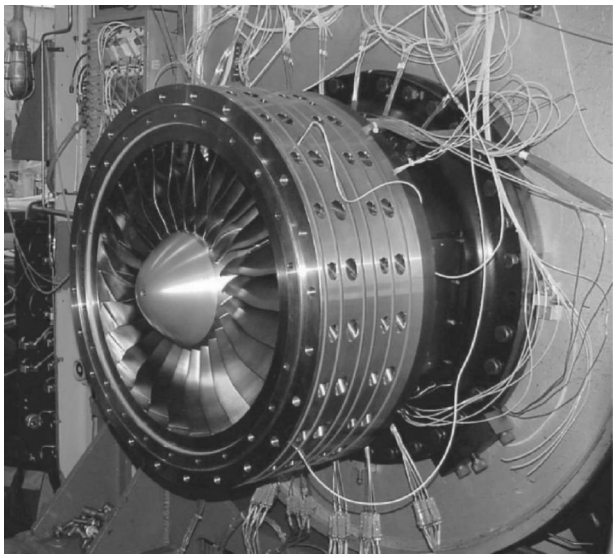

Fig. 3 Test package installed in the compressor rig

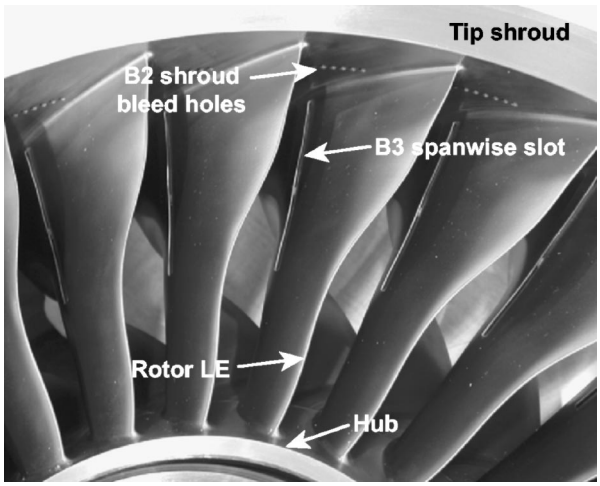

Fig. 4 Rotor aspiration scheme

Instrumentation

The performance of the stage was measured by an array of total pressure and total temperature rakes located 4 in. downstream of the stator trailing edge. Rake designs with a wide acceptance flow angle were chosen to give accurate measurements at a fixed orientation. The temperature rakes were calibrated for temperature recovery versus Mach number. The rakes provided seven spanwise measurements at six equally spaced pitchwise locations covering one blade pitch, resulting in a total of 42 measurements at the stage exit. Wall static taps were the only instrumentation located between the rotor exit and stator inlet. There were ten pitchwise static taps, on the hub and casing surfaces, covering 1.5 blade pitches, and located 0.125 in. upstream from the stator leading edge. Stator leading edge instrumentation was not implemented in this experiment, so the rotor spanwise performance could not be measured. Bleed flow rates (B1–B7) were measured using an independently metered and controlled bleed system. Dynamic pressure measurements to detect stall were obtained from the flow path casing approximately one chord upstream of the rotor. Pressure and temperature near the rotor shroud labyrinth teeth rub areas were measured to monitor the shroud condition, and an infrared thermocouple was installed to directly monitor the temperature of the shroud composite material. Rotor shroud radial growth and axial positions were closely measured. Inlet airflow was determined from an upstream ASME orifice. The health of the facility during the test was constantly monitored via the measured pressures, temperatures, flow rate, and vibration levels.

Data Reduction Procedure

Orifice weight flow, total pressures, rotor RPM, and temperature were all corrected to standard day conditions based on inlet plenum conditions. The Mach number at each rake port was determined by a linear interpolation of the inner and outer flowpath walls static pressures and the total pressure obtained from that rake port. The pressures and temperatures were area averaged to obtain the overall performance and throughflow efficiency. At the higher operating speeds from 90% to 100%, total temperature rake elements were damaged during the experiment and were not replaceable. Measurements from sister rake elements located at the same radial position one pitch apart were substituted in place of the lost measurements and used in the area averaging procedure. In some cases, where these redundant measurements were also not available, the total temperature was substituted by judiciously interpolating between measured data points. The overall area-averaged total temperature and efficiency were calculated with and without this substitution, and the effect on the overall result was found to be negligible.

Results and Discussion

The aspirated fan stage was tested from 50% to 100% of the design speed. Speedlines from choke to stall were obtained from 50% to 85% speed, and from choke only to the predicted low op line at 90%, 95%, and 100% speed. The experimental results presented and discussed in this section include: (1) the overall stage performance, (2) sensitivity of the stage performance to design aspiration flows, stage upstream bleeds, and starting bleeds, and (3) measurements at the stage exit and between the rotor and stator. The experimental results are compared to CFD calculations carried out using APNASA on the two operating lines, which represent fixed exit corrected mass flow boundary conditions in the code. The bleed flows are presented as fractions of the inlet corrected flow.

1 Overall Stage Performance. The measured pressure ratio and efficiency of the stage are shown in Figs. 5 and 6. The overall measured pressure ratios and mass flows are seen to be in good agreement to the predicted performance of the stage.

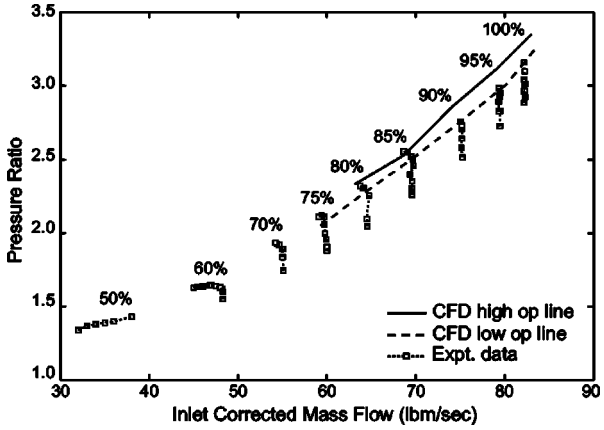

Fig. 5 Compressor pressure ratio performance map

On the 50%, 60%, and 70% speedlines, the inlet boundary layer bleed B1 was set to approximately 1% of the stage inlet flow, no interstage bleed was used, and all other bleeds were flowing at their individual maximum capacities (wide open). The stalling flow rate was difficult to determine on 50% and 60% speedlines as indicated by the measurements. At 70% speed, the stage exhibited a well-defined and repeatable stall point, and the total mass flow range for this speed was 1 lbm/s. A peak pressure ratio of 1.93, at a corrected mass flow of 54.2 lbm/s, and adiabatic efficiency of 89% were recorded.

On the 75%, 80%, and 85% speedlines, the inlet boundary layer bleed B1 was also set to approximately 1% of stage inlet flow. At 75% speed, the stage could not be operated without the casing starting bleed B4, and stalled when the bleed was closed. Bleed B4 was therefore set to 1% of the stage inlet flow, and hub starting bleed B6 was turned off, to obtain the speedline data. The measured pressure ratio closely matches the APNASA calculation, but the measured mass flow rate is 0.8% higher than the calculated value. This can be attributed to the effect of bleeds B1 and B4 that were not included in the APNASA calculation. A peak pressure ratio of 2.12, at 59.4 lbm/s and an adiabatic efficiency of 88.6% were recorded. The stage behaved similarly at 80% speed, and a peak pressure ratio of 2.32 at 63.7 lbm/s and an adiabatic efficiency of 88.5% were recorded. The measured pressure ratios closely match the calculated low and high op line points; however, the measured mass flow rate is 1.2% higher than the calculation due to the presence of additional bleeds B1 and B4. At 85% speed,

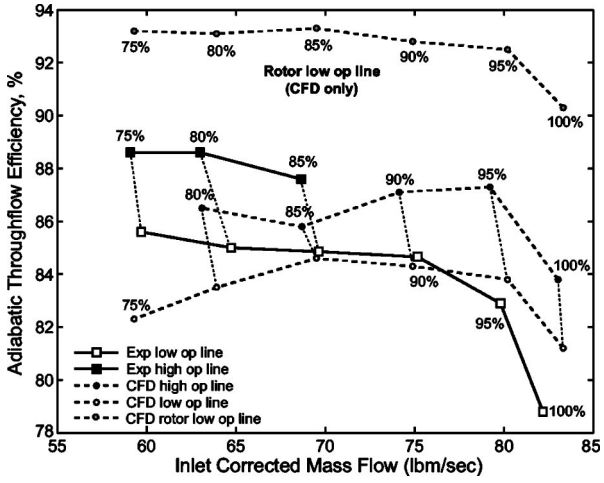

Fig. 6 Measured and calculated efficiencies on the low and high op lines

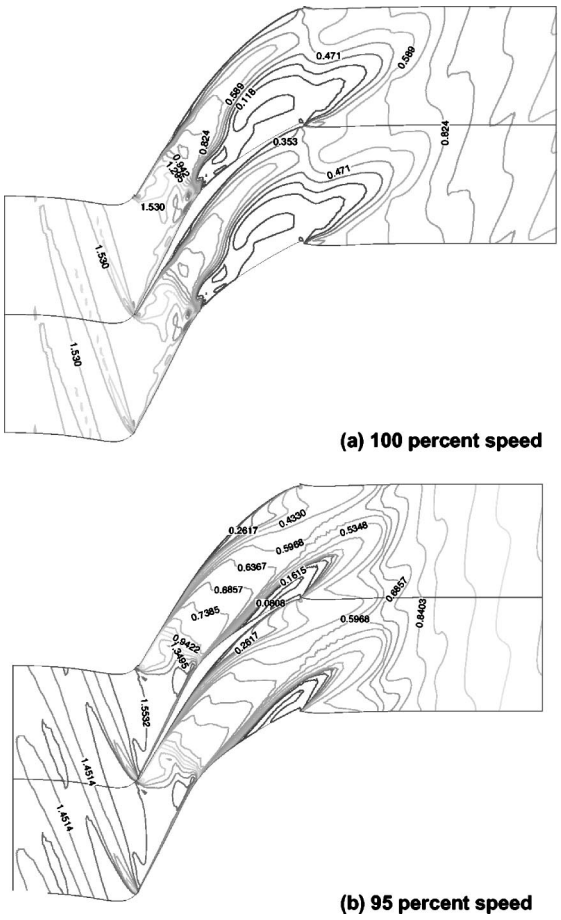

Fig. 7 Rotor tip flow field (relative Mach number). (*a*) 100% speed, (*b*) 95% speed.

the starting bleeds B4 and B6 were required initially to achieve stable operation and were subsequently turned off. Once again the measured pressure ratio on the low and high op lines closely matches the CFD prediction. The stalling pressure ratio is 1% higher than the predicted point on the high op line. The difference between the measured and predicted mass flow is negligible despite the presence of 1% bleed B1 in the test. A peak pressure ratio of 2.55 at 69 lbm/s and adiabatic efficiency of 87.6% were recorded at this speed.

On the 90%, 95%, and 100% speedlines, starting bleeds were not required to maintain steady-state operation of the stage, and the upstream bleed B1 was also not utilized. At 90% speed excellent agreement is seen between the measured pressure ratio and mass flow and the CFD calculation at the low op line point. A pressure ratio of 2.76 at 75.2 lbm/s and adiabatic efficiency of 84.7% were recorded. At 95% and 100% speed, the pressure ratios lie on the predicted low op line, but the measured mass flows are 0.91 lbm/s (1.1%) and 1.2 lbm/s (1.5%) lower than the predicted mass flow rates, respectively. At 95% speed, a pressure ratio of 2.99 at 79.3 lbm/s and adiabatic efficiency of 82.8% were recorded. At the design speed, a pressure ratio of 3.17 at 82.1 lbm/s and adiabatic efficiency of 78.7% were recorded. The lower than predicted mass flows and pressure ratios at these speeds can be attributed primarily to the lower measured aspiration flow fractions than the design intent.

The measured efficiencies, shown in Fig. 6, are at least two points higher than the predicted efficiencies along the high op line. Similarly, higher efficiencies were also measured along the low op line up to 90% speed. The higher measured efficiencies may be attributed in part to the presence of the upstream bleed B1

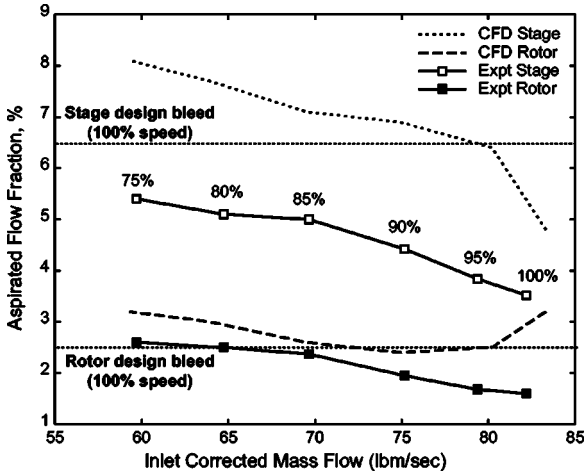

Fig. 8 Measured and calculated aspirated flow

and starting bleeds B4 and B6 at the lower operating speeds. However, at 90% speed, even without these additional bleeds, the measured efficiency is 0.5% higher than the CFD prediction.

In Fig. 6, a gradual decrease is observed in the measured stage efficiency with increasing operating speed. However, at 95% and 100% speeds a rapid decrease occurs in both the measured and predicted efficiencies. An examination of the CFD calculation at these speeds suggests that this may be related to the flow behavior in the high diffusion and high Mach number regions near the rotor shroud and near the stator hub. At the design speed, the rotor tip flow shows a large region of low momentum flow Figure 7(*a*). A similar region of low momentum flow is also present in the stator hub region. Both these regions contribute to the loss and flow blockage, consequently lowering the stage efficiency and mass flow. Unstarting of the shock system in the presence of this low momentum flow is prevented solely due to the aspiration downstream of the shock. At 95% speed, Fig. 7(*b*) shows a significant reduction in the size of this low momentum flow region and increase in diffusion in the rotor passage. There is also a 6% reduction of the inlet relative Mach number and attendant reduction in the strength of the shock system. The CFD calculation also shows a similar degree of improvement in the flow quality in the stator hub region. The cumulative effect of these changes is an improvement in stage performance observed between 100% and 95% speeds. The larger drop in the measured efficiency compared to the CFD predictions at these speeds can be attributed to the significantly lower measured aspiration flow fractions (see Fig. 8) than the design intent.

Figure 6 also shows the calculated rotor efficiency along the low op line. The rotor efficiency is seen to be over 92% along the entire low op line and decreases to 90% at the design tip speed. This can be attributed to the changes in the flow behavior discussed above and shown in Fig. 7.

2 Bleed Sensitivity. The sensitivity of the stage performance to bleed flow rates is discussed first in the context of the design aspiration requirement given in Table 3 followed by the effect of the additional starting and upstream bleeds. Figure 8 shows the measured and calculated aspiration flow rates, as fractions of the stage inlet corrected flow, along the low and high op lines. The variation in aspiration flow along a speedline at a fixed operating speed was found to be negligible. The rotor aspiration includes bleeds B2 and B3, and the stage aspiration includes, in addition to the rotor, bleeds B5 and B7 consistent with the CFD calculation. The upstream and starting bleed flow fractions are not included. The measured aspirated flow fraction is almost 30% lower than the flow fraction imposed in the CFD calculation. The dashed line indicates the design intent aspiration fractions of 2.5%

for the rotor and 6.5% for the stage. At the design speed, the measured rotor aspiration was 1.6% and total stage aspiration was only 3.5%, which is at almost half the design aspiration requirement.

The sensitivity of the stage performance to aspiration was studied at 90% speed using CFD, where the rotor aspiration was decreased to 1.1% and the stage aspiration to 3%. This resulted in a 2% decrease in the rotor and stage pressure ratios, a 6% decrease in the stage mass flow, and a 1% point decrease in stage efficiency. The measured performance, in comparison, at 90% speed is almost identical to the CFD prediction at an aspiration fraction 30% below the design intent. At 95% speed, the measured efficiency is 1 point lower, and mass flow 1.1% lower, than the CFD prediction at aspiration fraction 40% below the design intent. The experimental data therefore indicates robust performance and a lower sensitivity to decrease in the aspiration flow than observed in the CFD study.

The starting bleeds were required to operate the stage at 70%, 75%, and 80% percent speed. At 85% speed the casing bleed B4 was required to initially stabilize the stage, but was not required continuously. At 75%, 80%, and 85% speed, both the starting bleeds were required in addition to opening the throttle valve to recover from stall. The stage, in general, was found to be more sensitive to the casing starting bleed B4 at these speeds.

At 80% speed, several points were also taken with the inlet boundary layer bleed turned on. At similar pressure ratios, the efficiency of the stage with inlet boundary layer bleed on was about 1.2 points higher, and the stage mass flow rate increased by 1.3 lbm/s (2%). At 85% speed, several points were also taken with the inlet boundary layer bleed off ($B1=0$). At similar pressure ratios, the efficiency of the stage with inlet boundary layer bleed off was about 0.6 points lower, and the stage mass flow rate was decreased by about 1 lbm/s (1.4%).

3 Stage Exit Profiles. Figure 9 shows the measured and predicted stage exit total pressure profiles on the low operating line. The profiles were obtained by area averaging the experimental total pressure measurements in the pitchwise direction. The experimental profiles are seen to be more uniform in the spanwise direction than the profiles predicted by CFD. Reasonable agreement is seen between the measured and calculated profiles at 85% and 90% speeds. At 95% and 100% speeds, while the overall pressure ratio is lower, the spanwise variation is in qualitative agreement with the CFD prediction. The predicted total pressure profiles show a defect in the hub region which increases with rotor tip speed. In contrast, the experimental data do not show a defect in the hub region. The experimental profiles indicate the presence of a total pressure deficit around mid-span which appears to increase with rotor tip speed. This is also seen in the CFD calculation at 95% speed, but it is not very apparent at the other speeds.

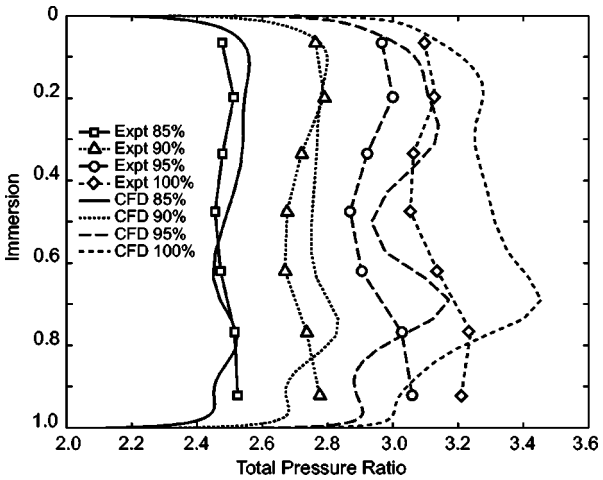

Fig. 9 Stage exit measured and calculated total pressure profiles

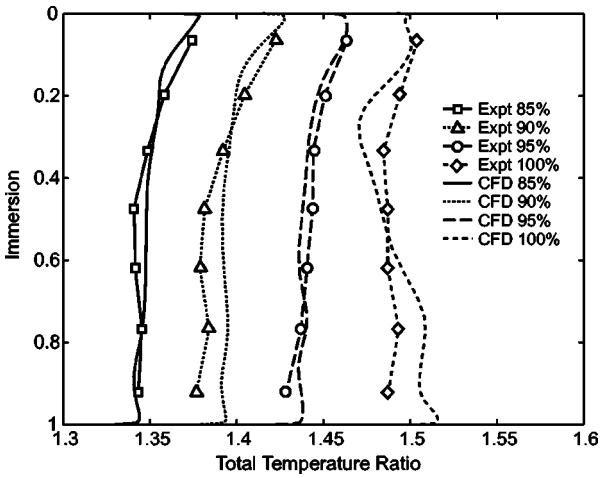

Fig. 10 Stage exit measured and calculated total temperature profiles

The measured and predicted total temperature profiles, shown in Fig. 10, are seen to be in reasonable agreement at 85%, 90%, and 95% speeds. At the design speed, the measured total temperature is lower than the CFD prediction below mid-span and higher than the CFD prediction above mid-span. This is indicative of greater throttling of the rotor in the experiment and has been observed in earlier experiments on supersonic rotors [9]. It is interesting to note that the rotor exit relative flow angle is close to 0 at mid-span. This implies a flat work versus flow coefficient characteristic (0 slope) at mid-span. The rotor spanwise work output is seen to be nearly uniform as per the design intent. The CFD calculation captures the total temperature increase near the casing, which can be attributed to the additional temperature rise due to the rotating shroud.

Figure 11 shows the efficiency profiles calculated from the measured total pressure and temperature profiles along with the CFD predictions.

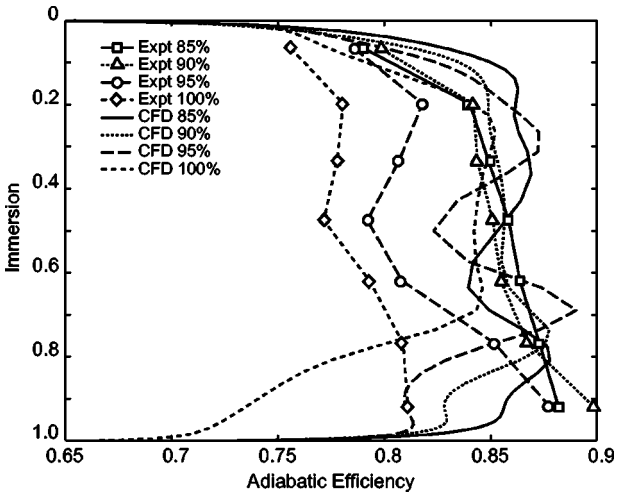

Fig. 11 Stage exit measured and calculated adiabatic efficiency profiles

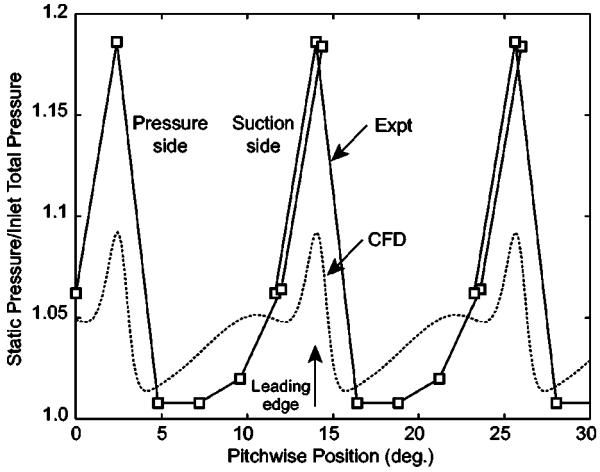

(a) Stator Hub

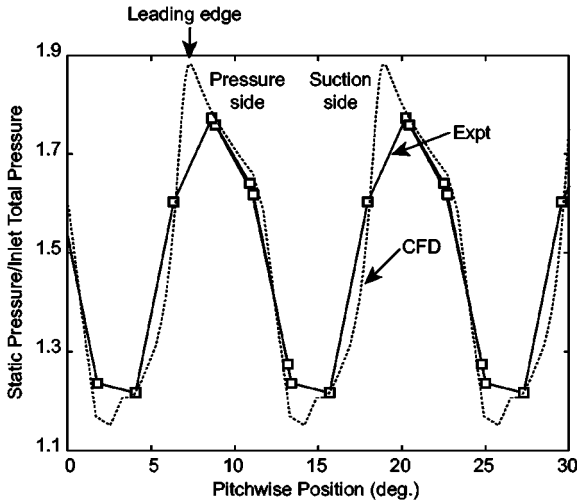

(b) Stator Casing

Fig. 12 Pitchwise static pressure variation at the stator leading edge (85% speed). (*a*) Stator hub. (*b*) Stator casing.

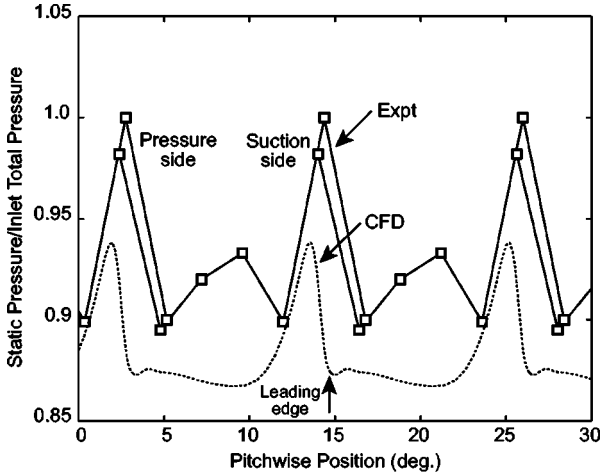

(a) Stator Hub

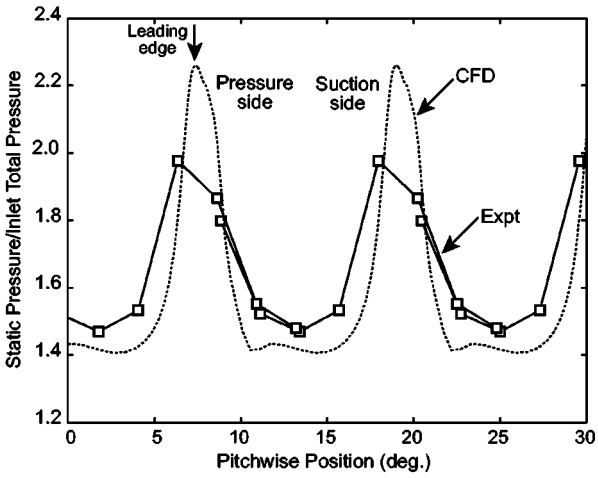

(b) Stator Casing

Fig. 13 Pitchwise static pressure variation at the stator leading edge (100% speed). (*a*) Stator hub. (*b*) Stator casing.

4 Stator Static Pressure Measurements. Figures 12(*a*) and 12(*b*) show the pitchwise variation of static-to-inlet total pressure ratio just upstream of the stator leading edge at 85% speed. The peak static pressure is approximately 10% higher in the experiment than in the CFD calculation. The minimum pressure on the pressure side is well predicted, but the pressure rise at mid-passage, due to crossing of the leading edge bow shock, is higher in the CFD calculation. The lower mid-passage pressure may indicate a higher Mach number and a bow shock that is deeper in the blade passage in the experiment compared to the CFD calculation. It should be noted that the starting bleed B6 is located 0.4 in. upstream of the stator leading edge static taps. Although this bleed was nominally turned off, interference from the slot may be contributing to some of the observed differences. The measured and predicted static pressure variations at the casing at 85% speed are in good agreement (Fig. 12*b*). The CFD solution shows that the pressure rise from 14 deg to 12 deg on the pressure side is due to crossing of the stator passage shock, and the agreement with measured pressure suggests that the shock positions are consequently in good agreement.

Figures 13(*a*) and 13(*b*) show the pitchwise variation of static-to-inlet total pressure ratio near the stator leading edge at the design speed. Similar to the comparison at 85% speed, the measured static pressure at the hub (Fig. 13(*a*) is observed to be higher than the CFD prediction. As noted above, the starting bleed B6 may be contributing to some the observed pressure differences. The observed pressure peak at mid-pitch in the measured pressure indicates that the bow shock may be located further upstream of the stator leading edge in the experiment. The pitchwise static pressure variation at the casing is seen to be in reasonable agreement with CFD, and the minimum pressure and overall variation are reasonable agreement with the CFD prediction. The pressure peak in the measured data is not adequately captured since none of the casing static taps were aligned with the stator leading edge.

Figures 14(*a*) shows the mid-pitch static pressure rise along the stator hub. The approximate locations of the stator leading edge, bleed slot B5, and trailing edge are indicated on the plot. Due to the large pressure tap spacing the experimental profile does not resolve the initial pressure rise across the bow shock seen in the CFD profile. However, the measured pressure rise from the leading edge to just downstream of the slot is in good agreement with the CFD prediction. The measured exit pressures at 85% and 90% speeds are also seen to be in excellent agreement with the predicted value. At 95% and 100% speeds, the measured value is lower than the CFD consistent with the overall reduction in pressure ratio and mass flow of the stage at these speeds.

Figure 14(*b*) shows the mid-pitch static pressure rise along the stator casing. The measured pressure rise in the leading edge re-

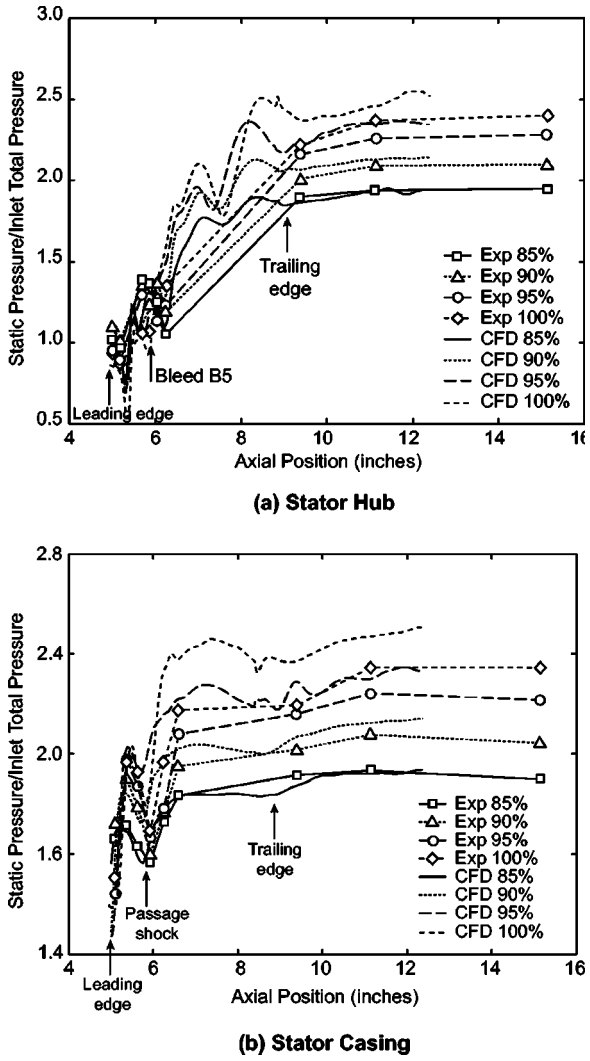

Fig. 14 Stator mid-pitch static pressure rise. (*a*) Stator hub. (*b*) Stator casing.

gion, passage shock position, and pressure rise across the shock are in good agreement at 85% speed. At 90% and 100% speeds, the measured static pressures indicate that passage shock may be downstream of the CFD prediction, and moves upstream in going from 90% to 100% speed. The measured exit pressure rise at 85% and 90% speeds are in good agreement with CFD, but fall below the CFD prediction at 95% and 100% speeds as seen in the case of the hub surface measurements. The measured stator hub and casing mid-pitch static pressure rise coefficients are approximately 0.66 at the design speed.

Conclusions and Recommendations

This program, comprising the design, analysis and test of a very high pressure ratio compressor stage enabled by aspiration, leads us to the following conclusions and recommendations:

1. Removal of the low energy flow in the amount of a percent of the stage inlet mass flow per bleed location does in fact result in an increase in low-loss diffusion, such as to enable designs with approximately double the compressor work at a given tip speed.

2. The CFD flowfield shows that aspiration fixes the passage shock position, particularly in the tip region. The agreement between the measured and predicted performance suggests that, along with enhancing the diffusion of the stage, aspiration is also effective in controlling the shock position and achieving a started shock system at operating speeds above 90%, which is necessary for achieving the desired inlet mass flow and pressure ratio.

3. Although the stage design and aspiration were optimized for the design point, good performance was obtained at off-design conditions. The measured throughflow efficiency of the stage was higher than the CFD prediction on the low and high operating lines up to 90% speed.

4. The measured stage performance was found to be less sensitive to reduction in aspiration flow than predicted by the 3D CFD calculation. Performance close to the design intent, and in good agreement with the CFD predictions, was obtained at aspiration flow rates significantly lower than the design intent.

5. The starting bleeds were required for stable operation only from 70% to 85% speeds. These were also necessary to recover from stall in addition to opening the throttle valve (the stage was not operated to stall above 85% speed). The stage exhibited a well-defined entry and recovery from stall once the starting bleeds were opened.

6. The effects of aspiration are quantitatively represented in the computational quasi-3D design system in which the aspiration is modeled by a prescribed mass flux into the wall at the location of a flush slot or hole. The effect of aspiration can therefore be integrated into the blade design process.

7. The quasi-3D design system can be used effectively to design blade shapes at high loading levels (with flow conditions extracted from a fully 3D viscous calculation). The independent design of the blade shapes and design features incorporated in the aspirated stage are essential ingredients in achieving the high loading while maintaining good throughflow efficiency and minimizing the aspiration requirement.

8. The 3D viscous analyses using APNASA yielded performance predictions for the compressor stage that were very close to the experimentally observed performance. This has important implications for design of highly loaded stages since an accurate 3D viscous analysis can augment the quasi-3D design system by providing critical flow information that can be used to refine the design and achieve good blade row matching.

9. The novel mechanical structure devised for the aspirated stage, including a rotor split fore and aft into two integrally bladed halves, with a graphite-polymer wound tip shroud, proved to be mechanically sound and expeditious for the purposes of the experiment.

10. Relaxing the design objectives set forth for this stage, such as the pressure ratio, radial work profile, and stator exit angle, could result in a stage with higher efficiency, lower bleed requirements, a less demanding structure, and lower stator Mach number, the last being a major challenge in this design.

11. In the present design, major effort was focused on optimizing the blade shapes and minimizing the required blade surface aspiration. There are clearly additional opportunities to enhance the performance of future designs, particularly with respect to managing the endwall flows through three-dimensional design features, and developing more effective endwall flow control schemes.

Acknowledgments

The authors wish to acknowledge the support provided by DARPA and the AFOSR, which respectively funded and monitored this work. Pratt & Whitney Aircraft Engines collaborated in the early phases of the design and Honeywell Aircraft Engines carried out the detailed mechanical design and structural analysis of the stage. TURBOCAM of Dover, NH fabricated the stage, and Wilson Composites of Folsom, CA executed the composite winding of the rotor. Individuals who made large contributions include Professor Alan Epstein and Professor Mark Drela of MIT, and Dr. Anthony Strazisar, Dr. Randall Chriss, and Scott Thorp of NASA Glenn Research Center.

References

[1] Kerrebrock, J. L., Drela, M., Merchant, A. A., and Schuler, B. J., 1998, ''A Family of Designs for Aspirated Compressors,'' ASME paper no. 98-GT-196.

[2] Schuler, B. J., Kerrebrock, J. L., and Merchant, A. A., 2002, ''Experimental Investigation of an Aspirated Fan Stage,'' ASME paper no. 2002-GT-30370, ASME IGTI Conference.

[3] Merchant, A. A., Drela, M., Kerrebrock, J. L., Adamczyk, J. J., and Celestina, M., 2000, ''Design and Analysis of a High Pressure Ratio Aspirated Compressor Stage,'' ASME paper no. 2000-GT-619, ASME IGTI Conference.

[4] Youngren, H. H., and Drela, M., 1991, ''Viscous/Inviscid Method for Preliminary Design of Transonic Cascades,'' AIAA paper no. AIAA-91-2364.

[5] Merchant, A. A., 1999, ''Design and Analysis of Axial Aspirated Compressor Stages,'' PhD. thesis, Massachusetts Institute of Technology, Cambridge, MA.

[6] Adamczyk, J. J., 1985, ''Model Equation for Simulating Flows in Multistage Turbomachines,'' ASME paper no. 85-GT-226.

[7] Lieblein, S., Schwenk, F. C., and Broderick, F. L., 1953, ''Diffusion Factor for Estimating Losses and Limiting Blade Loadings in Axial Flow Compressor Blade Elements,'' Technical Report RME53D01, NACA.

[8] Wennerstrom, A. J., 1984, ''Experimental Study of a High-Throughflow Transonic Axial Compressor Stage,'' Water Policy, **106**, pp. 553–559.

[9] Wadia, A. R., Szucs, P. N., and Crall, D. W., 1998, ''Inner Workings of Aerodynamic Sweep,'' ASME J. Turbomach., **120**, pp. 671–682.

Computational Fluid Dynamics Study of Wake-Induced Transition on a Compressor-Like Flat Plate

D. Keith Walters[1]

James H. Leylek

Advanced Computational Research Laboratory,
Department of Mechanical Engineering,
Clemson University,
Clemson, SC 29634 USA

Recent experimental work has documented the importance of wake passing on the behavior of transitional boundary layers on the suction surface of axial compressor blades. This paper documents computational fluid dynamics (CFD) simulations using a commercially available general-purpose CFD solver, performed on a representative case with unsteady transitional behavior. The study implements an advanced version of a three-equation eddy-viscosity model previously developed and documented by the authors, which is capable of resolving boundary layer transition. It is applied to the test cases of steady and unsteady boundary layer transition on a two-dimensional flat plate geometry with a freestream velocity distribution representative of the suction side of a compressor airfoil. The CFD results are analyzed and compared to a similar experimental test case from the open literature. Results with the model show a dramatic improvement over more typical Reynolds-averaged Navier–Stokes (RANS)-based modeling approaches, and highlight the importance of resolving transition in both steady and unsteady compressor aerosimulations. [DOI: 10.1115/1.1791650]

1 Introduction

Boundary layer transition plays an important role in compressor aerodynamic performance. The location and type of transition (bypass, separation-induced, natural) depends on both the airfoil geometry and the freestream conditions. This includes the effects of Reynolds (Re) number, freestream turbulence, curvature, and pressure gradient. In real machines, the freestream conditions are often not steady, but undergo periodic behavior due to the presence of upstream bladerows in the compressor. Recent studies have demonstrated that unsteady effects significantly alter the time-averaged boundary layer behavior, and as such have considerable impact on the compressor aerodynamics.

Previous experimental studies [1–7] have documented the physics of unsteady boundary layer development. At low freestream turbulence intensities, the boundary layer has a tendency to remain laminar over much of the airfoil surface, and to separate in regions of strong adverse pressure gradient. At higher turbulence intensities, the boundary layer may undergo transition near the leading edge, leading to a suppression of separation and an attached boundary layer. With incident wake passing, the boundary layer may undergo a periodic behavior, in which the passing wake induces a turbulent strip to develop near the leading edge and to convect downstream. The turbulent strip removes the separation region as it passes, and is followed by a calming region in which the boundary layer remains attached. For low enough wake passing frequency, the region between wakes eventually relaxes toward the steady low-turbulence condition, and the separation bubble re-forms. For higher frequencies, the next wake may pass before the separation region can develop, resulting in an attached boundary layer at all times.

Clearly, the ability to accurately predict boundary layer development and transition using computational fluid dynamics (CFD) represents an important challenge. Numerical tools can help designers make rapid evaluations of new compressor blade geometries and significantly reduce overall design cycle time. The key to successful prediction rests in the turbulence and/or transition modeling employed by the simulations.

Current numerical approaches typically either adopt low-Re versions of fully turbulent models or include empirical transition functions in the simulations. The primary advantage of the first approach is that it requires no user input in terms of nonlocal or integral parameters—such as Re_x, Re_θ, or Tu_∞—and can therefore be easily implemented into general-purpose, elliptic CFD solvers. In general, however, these models require prescription of the starting condition of the laminar boundary layer, and show a high degree of sensitivity to both initial and freestream conditions [8–10]. This is likely due to the fact that low-Re models rely on a ''diffusion-controlled'' transition concept, in which transition occurs due to the transport (diffusion) of freestream turbulence into the boundary layer, where steep mean velocity gradients lead to turbulent production. Recent experimental, numerical, and analytical studies indicate that the dynamics of disturbance growth in pretransitional boundary layers is considerably more complex, and that the diffusion-controlled concept may be insufficient to describing the physics of bypass transition [11–16].

In the second approach, the effect of transition is included into the turbulence model through some type of additional damping function, most often taken to be the intermittency. This function may be prescribed algebraically, although more recent approaches incorporate transport equations for its determination [17–19]. In either case, calculation of transition onset and eddy-viscosity damping invariably depends on integral and/or nonlocal parameters. This method is most accurately described as a combination of CFD and empirical correlations, and is therefore not well suited for single-point implementation into general-purpose CFD solvers for use on arbitrary geometries.

A recent paper by the current authors [20] presented a turbulence modeling technique for prediction of boundary layer transition with Reynolds-averaged Navier–Stokes (RANS)-based CFD, and applied it to the test cases of a flat-plate [21] and a highly loaded turbine airfoil [22,23], both under varying levels of free stream turbulence. The major goal of the model is to provide a framework that is independent of integral or nonlocal inputs, as well as intermittency factors, and can be implemented with the same ease-of-use as currently popular eddy-viscosity models for fully turbulent flows. At the same time, the approach seeks to

[1]Current Address: Department of Mechanical Engineering, Mississippi State University; electronic mail: walters@me.msstate.edu

Contributed by the International Gas Turbine Institute and presented at the International Gas Turbine and Aeroengine Congress and Exhibition, Atlanta, GA, June 16–19, 2003. Manuscript received by the IGTI Dec. 2002; final revision Mar. 2003. Paper No. 2003-GT-38680. Review Chair: H. R. Simmons.

avoid the necessity of prescribing initial boundary layer profiles, and avoiding artificial sensitivity to initial and boundary conditions. The model is intended to be "hands off" for the user, requiring no modification for different application cases. The model specifically addresses the development of pretransitional fluctuations in the developing boundary layer, and their subsequent breakdown to turbulence. The development was based on considerations of the physics of transition, and relies on recently published advances, including experimental studies [11,12], analytical treatments [13,14], direct numerical simulations [15], and previous modeling proposals [16,24].

The present study presents a more advanced version of the model in Ref. [20], intended to more accurately reproduce the transition breakdown process, especially in the presence of adverse pressure gradients. The model is applied to the test case of a developing boundary layer on a flat plate, with a loading similar to the suction surface of a compressor airfoil. The test case is similar to that considered by Ottavy et al. [25], including freestream velocity distribution, Reynolds number, and inlet turbulence intensity. The model is applied to both steady and unsteady flow cases. Steady results are obtained at low and high freestream turbulence intensities. Unsteady results are obtained with incident wakes passing at two different frequencies. The performance of the model is analyzed in terms of its ability to reproduce the correct boundary layer behavior in both a steady and unsteady framework.

2 Turbulence Model

The concept and development of the modeling approach has been documented in detail by the current authors [20] and will not be repeated here. This section simply presents the model equations used in the present study with minimal explanation. Differences between this model form and that in Ref. [20] are discussed.

The model is a three-equation eddy-viscosity type, including transport equations for turbulent kinetic energy (k_T), laminar kinetic energy (k_L), and inverse turbulent time scale (ω)

$$\frac{Dk_T}{Dt} = P_{k_T} + R + R_{\mathrm{NAT}} - \varepsilon - D_T + \frac{\partial}{\partial x_j}\left[\left(\nu + \frac{\alpha_T}{\sigma_k}\right)\frac{\partial k_T}{\partial x_j}\right], \quad (1)$$

$$\frac{Dk_L}{Dt} = P_{k_L} - R - R_{\mathrm{NAT}} - D_L + \frac{\partial}{\partial x_j}\left[\nu\frac{\partial k_T}{\partial x_j}\right], \quad (2)$$

$$\frac{D\omega}{Dt} = P_\omega + C_{\omega R}\frac{\omega}{k_T}(R + R_{\mathrm{NAT}}) - C_{\omega 2}\omega^2 + C_{\omega 3} f_\omega \alpha_T \left(\frac{\lambda_{\mathrm{eff}}}{\lambda_T}\right)^{4/3}\frac{\sqrt{k_T}}{d^3} + \frac{\partial}{\partial x_j}\left[\left(\nu + \frac{\alpha_T}{\sigma_\omega}\right)\frac{\partial \omega}{\partial x_j}\right]. \quad (3)$$

The laminar kinetic energy k_L represents the magnitude of nonturbulent streamwise fluctuations in the pretransitional boundary layer, following the recommendation of Mayle and Schulz [16]. Note that the original model [20] used the turbulence farfield dissipation rate ε as the turbulence scale-determining variable. Use of the inverse turbulent time scale leads to a better representation of the breakdown of laminar kinetic energy to turbulence. The scalar farfield turbulent dissipation rate is simply obtained as

$$\varepsilon = \omega k_T. \quad (4)$$

The influence of turbulent and laminar fluctuations on the mean flow and energy equations is included through prescription of a total eddy viscosity and total eddy thermal diffusivity, respectively,

$$-\overline{u_i u_j} = \nu_{\mathrm{TOT}}\left(\frac{\partial U_i}{\partial x_j} + \frac{\partial U_j}{\partial x_i}\right) - \frac{2}{3}k_{\mathrm{TOT}}\delta_{ij} \quad (5)$$

$$-\overline{u_i \theta} = \alpha_{\theta,\mathrm{TOT}}\frac{\partial \theta}{\partial x_i}. \quad (6)$$

The effective length scale is defined as

$$\lambda_{\mathrm{eff}} = \mathrm{MIN}(C_\lambda d, \lambda_T), \quad (7)$$

where λ_T is the turbulent length scale

$$\lambda_T = \frac{k^{3/2}}{\varepsilon}. \quad (8)$$

Small-scale and large-scale energies are then calculated assuming the Kolmogorov inertial range spectrum applies over all wave numbers greater than $1/\lambda_T$

$$k_{T,s} = k_T\left(\frac{\lambda_{\mathrm{eff}}}{\lambda_T}\right)^{2/3}, \quad (9)$$

$$k_{T,1} = k_T\left[1 - \left(\frac{\lambda_{\mathrm{eff}}}{\lambda_T}\right)^{2/3}\right]. \quad (10)$$

The sum of the small-scale energy (Eq. (9)) and large-scale energy [Eq. (10)] is the turbulent kinetic energy k_T.

The first term on the right-hand side of Eq. (1) is the production of turbulence by turbulent fluctuations

$$P_{k_T} = \nu_{T,s} S^2. \quad (11)$$

The small-scale turbulent viscosity $\nu_{T,s}$ is defined as

$$\nu_{T,s} = \mathrm{MIN}\left(f_\nu f_{\mathrm{INT}} C_\mu \sqrt{k_{T,s}}\lambda_{\mathrm{eff}}, \frac{2.5\cdot\varepsilon_{\mathrm{TOT}}}{S^2}\right). \quad (12)$$

The limit on turbulent viscosity is imposed to prevent too rapid production in the case of boundary layer separation and in highly strained freestream regions. Other terms in the definition of turbulent viscosity include:

$$C_\mu = \frac{1}{A_0 + A_s\left(\frac{Sk_T}{\varepsilon}\right)}, \quad (13)$$

$$f_\nu = 1 - \exp\left(-\frac{\sqrt{\mathrm{Re}_{T,s}}}{A_\nu}\right), \quad (14)$$

$$f_{\mathrm{INT}} = \mathrm{MIN}\left(\frac{k_T}{C_{\mathrm{INT}}k_{\mathrm{TOT}}}, 1\right), \quad (15)$$

and

$$\mathrm{Re}_{T,s} = \frac{k_{T,s}^2}{\nu\varepsilon}. \quad (16)$$

Equation (15) defines a damping function on turbulent production due to intermittency, and is a modification to the original model [20]. This term helps to prevent overprediction of momentum and scalar transport in the latter stages of bypass transition, a weakness of the original model.

The first term on the right-hand side of Eq. (2) is the production of laminar kinetic energy by large-scale turbulent fluctuations

$$P_{k_L} = \nu_{T,1} S^2. \quad (17)$$

The large-scale turbulent viscosity $\nu_{T,1}$ is modeled as:

$$\nu_{T,1} = \mathrm{MIN}\left(\nu_{T,1}^*, \frac{0.5\times k_{T,1}}{S}\right), \quad (18)$$

where

$$\nu_{T,1}^* = f_{\tau,1} C_{11}\left(\frac{\Omega\lambda_{\mathrm{eff}}^2}{\nu}\right)\sqrt{k_{T,1}}\lambda_{\mathrm{eff}} + \beta_{\mathrm{TS}} C_{12}\varphi_{\mathrm{NAT}} d^2\Omega. \quad (19)$$

The limit introduced in Eq. (18) ensures that realizability is not violated in the two-dimensional (2D) developing boundary layer. The time-scale-based damping function $f_{\tau,1}$ is

$$f_{\tau,1}=1-\exp\left[-C_{\tau,1}\left(\frac{\tau_m}{\tau_{T,1}}\right)^2\right], \tag{20}$$

$$\tau_{T,1}=\frac{\lambda_{\text{eff}}}{\sqrt{k_{T,1}}}, \tag{21}$$

$$\tau_m=\frac{1}{\Omega}. \tag{22}$$

The second term on the right-hand side of Eq. (19) includes the following:

$$\beta_{\text{TS}}=1-\exp\left(-\frac{\text{MAX}(\varphi_{\text{NAT}}-C_{\text{TS,crit}},0)^2}{A_{\text{TS}}}\right), \tag{23}$$

$$\varphi_{\text{NAT}}=\frac{d^2\Omega}{\nu}. \tag{24}$$

Near-wall dissipation is given by

$$D_T=2\nu\frac{\partial\sqrt{k_T}}{\partial x_j}\frac{\partial\sqrt{k_T}}{\partial x_j}, \tag{25}$$

$$D_L=2\nu\frac{\partial\sqrt{k_L}}{\partial x_j}\frac{\partial\sqrt{k_L}}{\partial x_j}, \tag{26}$$

and the total dissipation rate of fluctuation energy, ε_{TOT}, is defined as

$$\varepsilon_{\text{TOT}}=\varepsilon+D_T+D_L. \tag{27}$$

The term R that appears in Eqs. (1)–(3) represents the averaged effect of the breakdown of streamwise fluctuations into turbulence during bypass transition, and has been modified from its original form to

$$R=C_R\beta_{\text{BP}}k_L\omega\left(\frac{\lambda_T}{\lambda_{\text{eff}}}\right)^{2/3}. \tag{28}$$

The threshold function β_{BP} controls the bypass transition process

$$\beta_{\text{BP}}=1-\exp\left(-\frac{\varphi_{\text{BP}}}{\text{A}_{\text{BP}}}\right), \tag{29}$$

$$\varphi_{\text{BP}}=\text{MAX}\left[\left(\frac{\sqrt{k_T}d}{\nu}-C_{\text{BP,crit}}\right),0\right]. \tag{30}$$

The breakdown to turbulence due to instabilities is included as a separate natural transition "production" term

$$R_{\text{NAT}}=C_{R,\text{NAT}}\beta_{\text{NAT}}k_L\Omega, \tag{31}$$

$$\beta_{\text{NAT}}=1-\exp\left[-\frac{\text{MAX}(\varphi_{\text{NAT}}^{0.75}\varphi_{\text{MIX}}^{0.25}-\text{C}_{\text{NAT,crit}},0)}{A_{\text{NAT}}}\right], \tag{32}$$

$$\varphi_{\text{MIX}}=\frac{\sqrt{k_L}d}{\nu}. \tag{33}$$

The coefficient $C_{\omega\text{R}}$ in Eq. (3) enforces a reduction of turbulent length scale during the transition breakdown, and takes the functional form

$$C_{\omega\text{R}}=1.5*\left(\frac{\lambda_T}{\lambda_{\text{eff}}}\right)^{2/3}-1. \tag{34}$$

The first term on the right-hand side of Eq. (3) is the increase in inverse turbulent time scale due to either turbulence production mechanisms or flowfield instabilities. It takes the form

$$P_\omega=(C_{\omega1}\nu_{T,\omega}S^2+f_{\Delta P}C_{\Delta P}k_{T,1}\Omega)\frac{\omega}{k_T}, \tag{35}$$

the first term inside the parenthesis is due to turbulent production, where the effective turbulent viscosity corresponds to that in Eq. (12) without any imposed limits

$$\nu_{T,\omega}=f_\nu f_{\text{INT}}C_\mu\sqrt{k_{T,s}}\lambda_{\text{eff}}. \tag{36}$$

The second term represents the increase in inverse turbulent time scale in unstable regions of the boundary layer subjected to an adverse pressure gradient. The damping function $f_{\Delta P}$ takes the form

$$\begin{aligned} f_{\Delta P}&=f_{\tau,1}, \quad \text{if } \frac{\partial\Omega}{\partial d}>0 \\ f_{\Delta P}&=0, \quad \text{if } \frac{\partial\Omega}{\partial d}\leqslant 0. \end{aligned} \tag{37}$$

In Eq. (3), the coefficient $C_{\omega2}$ is assigned the following functional form:

$$C_{\omega2}=0.92\cdot\left(\frac{\lambda_{\text{eff}}}{\lambda_T}\right)^{4/3}. \tag{38}$$

This enforces a decrease in the turbulent length scale close to the wall.

The use of ω as the scale-determining variable can lead to a reduced intermittency effect in the outer region of a turbulent boundary layer, and consequently an elimination of the wake region in the velocity profile. The third term on the right-hand side of Eq. (3) is included to rectify this. The term includes the following damping function:

$$f_\omega=1-\exp\left[-0.41*\left(\frac{\lambda_{\text{eff}}}{\lambda_T}\right)^4\right]. \tag{39}$$

The total eddy viscosity and eddy diffusivity included in Eqs. (5) and (6) are given by

$$\nu_{\text{TOT}}=\nu_{T,s}+\nu_{T,1}, \tag{40}$$

$$\alpha_{\theta,\text{TOT}}=\left(\frac{\lambda_{\text{eff}}}{\lambda_T}\right)^{2/3}\left(\frac{k_T}{k_{\text{TOT}}}\right)\frac{\nu_{T,s}}{\text{Pr}_\theta}+\left[1-\left(\frac{\lambda_{\text{eff}}}{\lambda_T}\right)^{2/3}\right]C_{\alpha,\theta}\sqrt{k_T}\lambda_{\text{eff}}. \tag{41}$$

The form of α_{TOT} given in Eq. (41) differs from the original model. The changes are intended to more accurately represent the fundamental differences in thermal energy transport in a pretransitional versus fully turbulent boundary layer. Finally, the turbulent scalar diffusivity in Eqs. (1)–(3) is given by

$$\alpha_T=f_\nu C_{\mu,\text{std}}\sqrt{k_T}\lambda_{\text{eff}}. \tag{42}$$

The inlet boundary conditions for k_T and ω are set as for any form of a two-equation model, in order to reproduce the desired turbulence intensity and scale. If the inlet is located in the freestream, far from any solid boundary, then k_L is set to zero. At solid walls, the model equations use zero-flux boundary conditions

$$\frac{\partial k_T}{\partial\eta}=0, \tag{43}$$

$$\frac{\partial k_L}{\partial\eta}=0, \tag{44}$$

$$\frac{\partial\omega}{\partial\eta}=0. \tag{45}$$

During processing of the simulation, the wall values of k_T and k_L used to compute the gradients in Eqs. (25) and (26) are set to zero. The above model equations and boundary conditions yield the correct asymptotic behavior at solid boundaries, i.e., $k_{\text{TOT}}\sim d^2$ and $\varepsilon_{\text{TOT}}\rightarrow 2\nu k_{\text{TOT}}/d^2$ as $d\rightarrow 0$.

Table 1 Summary of model constants

$A_0 = 4.04$	$C_{INT} = 0.75$	$C_{\omega 1} = 0.44$
$A_s = 2.12$	$C_{TS,crit} = 1000$	$C_{\Delta P} = 0.15$
$A_\nu = 6.75$	$C_{R,NAT} = 0.04$	$C_{\omega 3} = 0.3$
$A_{BP} = 3$	$C_{11} = 3.4*10^{-6}$	$C_\lambda = 2.495$
$A_{NAT} = 60$	$C_{12} = 1.0*10^{-9}$	$C_{\mu,std} = 0.09$
$A_{TS} = 200$	$C_R = 0.08$	$Pr_\theta = 0.85$
$C_{BP,crit} = 12$	$C_{\alpha,\theta} = 0.035$	$\sigma_k = 1$
$C_{NAT,crit} = 440$	$C_{\tau,1} = 4360$	$\sigma_\omega = 1.17$

The model constants are summarized in Table 1. These constants were determined based on comparison with direct numerical simulations of fully turbulent channel flow [26] and flat plate boundary layer experiments [21]. Note that some constants have been modified from the original version of the model [20].

Figure 1 shows the heat transfer distribution for a flat plate boundary layer, using the current version of the turbulence model. Results are compared to an experimental test case [21] and the details of the numerical method are documented in Ref. [20]. The figure demonstrates the ability of the model to resolve transition over a range of freestream turbulence intensities for this simple but crucial reference case.

3 Test Case

The test case to be examined in this study is that of flow over a highly loaded compressor-like flat plate. It is intended to mimic the experimental study by Ottavy et al. [25]. This test case includes the essential characteristics of boundary layer development on the suction surface of a compressor airfoil. Most notably, the experimental results show that the boundary layer is separated under steady, low-turbulence conditions and responds strongly to unsteady wake effects, making it a challenging test for the new turbulence model presented above.

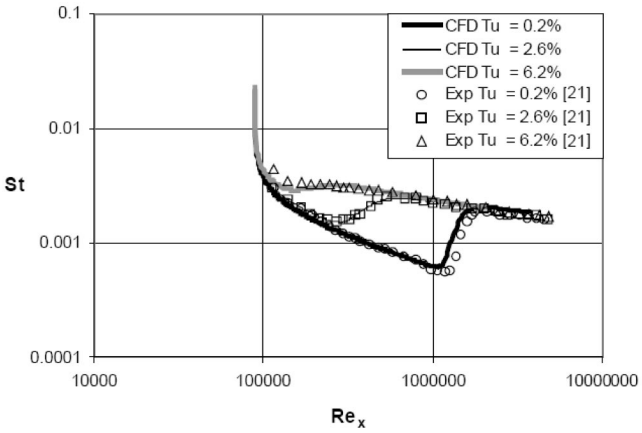

Fig. 1 Stanton number distribution for flat plate boundary layer test case, showing good agreement between model predictions and experiments

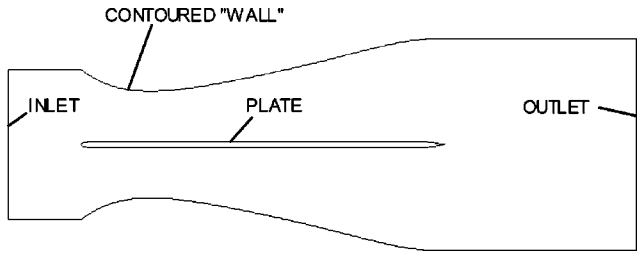

Fig. 2 Two-dimensional model geometry for compressor-like flat plate

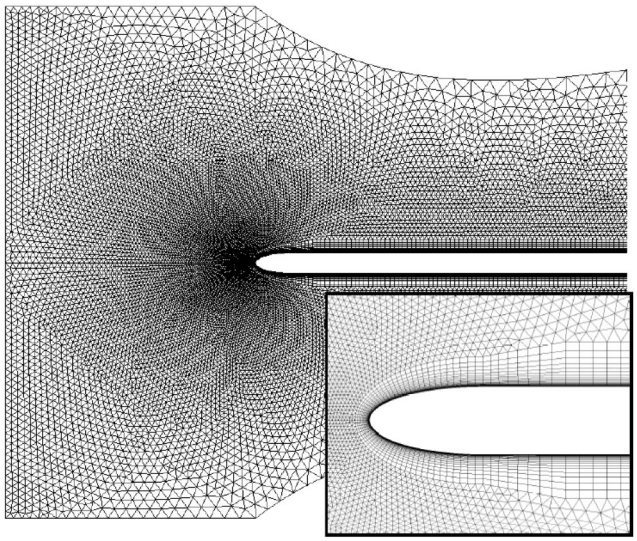

Fig. 3 Illustration of 2D mesh used in the current study, including the upstream and near leading edge regions

Figure 2 shows the computational geometry. It was intended to match as closely as possible shape 02 documented in Ref. [25]. The outer walls were contoured in order to impose the proper freestream acceleration over the flat plate. The outer wall geometry was obtained by digitizing Fig. 2 in Ref. [25], and so is not an exact reproduction of the experimental reference case. Nonetheless, it is considered adequate to demonstrate the resolution of the transitional behavior of the airfoil boundary layer. The inlet and outlet height were 0.443*C and 0.625*C, respectively. The throat occurred at approximately 20% of the plate chord, with a height of 0.318*C. The flat plate length-to-thickness ratio was 56.4. The plate had an elliptic leading edge, which comprised 3% of the overall plate chord length. Not included in the definition of plate chord was an attached wedge-shaped trailing edge region, as shown. This had a length equal to 5.54% of the chord length, and prevented unsteady vortex shedding at the plate trailing edge.

For the steady simulations, the inlet velocity was constant, and set to yield $Re_C = 350,000$. This matched one set of experiments in Ref. [25]. The inlet turbulence intensity for the low-turbulence reference case was 1.2%. No length scale information was available in Ref. [25], and it was assumed in the computations that $\lambda_{T,inlet} = 0.03*C$. Doubling of the length scale to determine the sensitivity showed negligible change in the steady results. A separate steady simulation was run with turbulence inlet conditions equal to those likely to be found in the wake of an upstream airfoil. Inlet turbulence intensity was 6.4%, and $\lambda_{T,inlet} = 0.015*C$. These two simulations provided a steady reference for comparison to the unsteady cases with incident wakes.

Two unsteady simulations were run. For each, a periodic wake profile was implemented as the inlet boundary condition. Since detailed wake profiles were not available in Ref. [25], approximations were used. The conditions outside of the wake were identical to those in the low-turbulence steady simulations, and the conditions at the wake center included $U/U_\infty = 0.9$, Tu=6.4%, and $\lambda_T = 0.015*C$. A simple linear variation was assumed between the freestream and wake centerline conditions, and the centerline conditions occupied one-half of the total wake width. The total wake width was approximately 8% of the plate chord length, and numerical experiments indicated that the qualitative behavior of the unsteady transitional boundary layer was insensitive to variations of wake width and shape. Two wake frequencies were considered, $f_{red} = 0.75$ and $f_{red} = 1.5$. For both cases, the vertical wake velocity V_{wake} was taken as equal to the inlet velocity U_{in}.

4 Numerical Method

The 2D mesh for this case is shown in Fig. 3. The simulations made use of multitopology grid capability, so that a quadrilateral mesh aligned with the flow streamlines was placed in the plate boundary layer, and an unstructured triangle mesh was placed in the remainder of the passage. This technique allows accurate resolution of the boundary layer while maintaining a relatively low cell count. The mesh for all cases contained 80,000 cells, and subsequent refinement did not yield any appreciable change in the steady results. It was therefore assumed that both steady and unsteady simulations were grid independent. The first-cell wall distance was such that the y^+ was less than one at every location on the plate. The current turbulence model is designed to be implemented with y^+ values of approximately one or less.

The outer contoured walls were actually implemented as symmetry conditions, i.e., no flow across the boundary and normal gradients of all primary variables equal to zero. This approach was recommended in Ref. [25] in order to match the experimental case, which used boundary-layer suction to ensure that separation did not occur on the outer walls. It also reduced the meshing requirement considerably.

The inlet boundary conditions were prescribed as either constant values or periodic profiles in times of mean velocity components (U_i), turbulence kinetic energy (k_T), and inverse turbulence time scale (ω). As discussed in Sec. 2, the inlet condition for k_L was taken to be constant and equal to zero. The outlet was set to atmospheric pressure, with all other variables upwinded. The wall boundary conditions on the plate were set to no slip for the mean velocities. The turbulence quantities (k_T, k_L, and ω) were all set to zero flux conditions at the wall, as described in Sec. 2.

The solution was processed with FLUENT VERSION 6.0.20 from Fluent, Inc., Lebanon, NH. The simulations used the segregated solver, which is an implicit pressure-correction scheme. The pressure-velocity coupling was implemented via the SIMPLE algorithm (Patankar [27]). The spatial discretization used was a second-order linear reconstruction scheme for convective terms, and central differencing for diffusion terms. The transport equations for k_T, k_L, and ω were implemented as user-defined scalars, and source terms for these equations were supplied through user-defined functions (UDF) written by the authors. The turbulent viscosity and effective diffusivities were supplied as UDFs in a similar manner. Model implementation via UDF has been extensively validated at Clemson University, Clemson, SC [20]. All steady cases required approximately 2000 iterations for convergence. For the unsteady cases, the time-dependent terms used second-order time discretization. The time step was taken as approximately 0.177% of a single wake passing period. The solution required 30 iterations for full convergence at each time step, with under-relaxation values of 0.8 for each of the turbulence quantities.

5 Results and Discussion

5.1 Steady Test Cases. This section presents results obtained for the steady cases, with two different levels of freestream turbulence intensity. Results with the model are compared to those obtained with two other eddy-viscosity models, currently available in FLUENT. The first is the realizable k-ε (RKE) model of Shih et al. [28], which is intended for use in fully turbulent flows only. The second is a variation of the k-ω shear-stress transport (SST) model [29] that includes a low-Re correction for use in transitional flows. The comparison is meant to highlight the importance of using a model properly sensitized to boundary layer transition.

Figure 4 shows contours of turbulence intensity for the low-turbulence ($Tu_{in}=1.2\%$) and high-turbulence ($Tu_{in}=6.4\%$) test cases using the model. In the low turbulence case, the boundary layer is initially laminar over the flat plate, as indicated by the low levels of turbulence. Transition is seen to initiate at approximately 45% of the plate chord, due to the presence of a separation region. This is qualitatively similar to the experimental results reported by Ottavy et al. [25] for low freestream turbulence. For the high turbulence case, on the other hand, the turbulence levels are indicative of a turbulent boundary layer over the majority of the plate

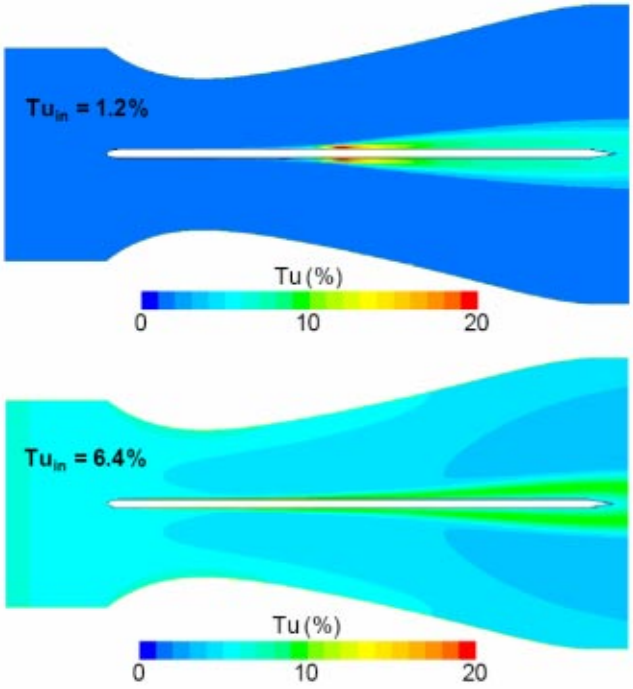

Fig. 4 Contours of turbulence intensity for low- and high-turbulence steady test cases with the model

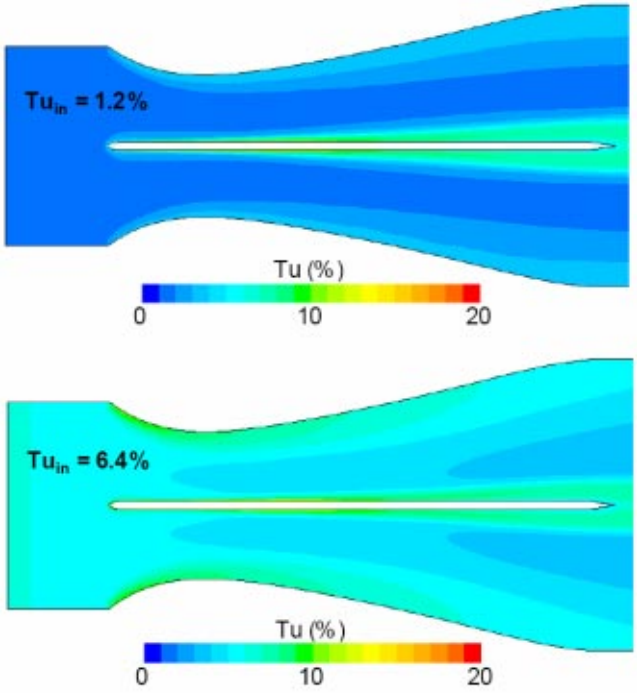

Fig. 5 Contours of turbulence intensity using the RKE turbulence model [28], showing fully turbulent boundary layer from leading edge onward, for both cases

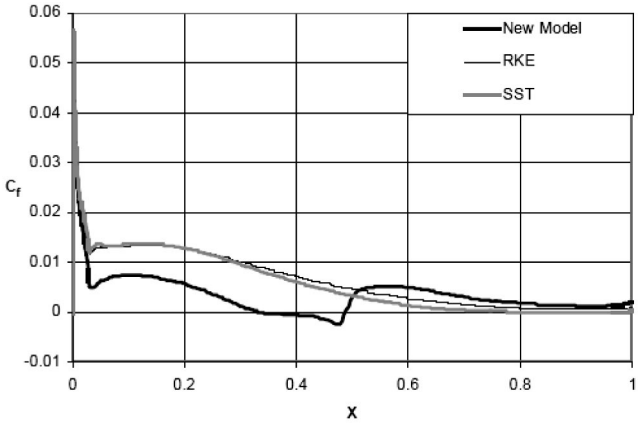

Fig. 6 Wall shear stress distribution using three different turbulence models for low-turbulence steady test case (Tu_{in} = 1.2%)

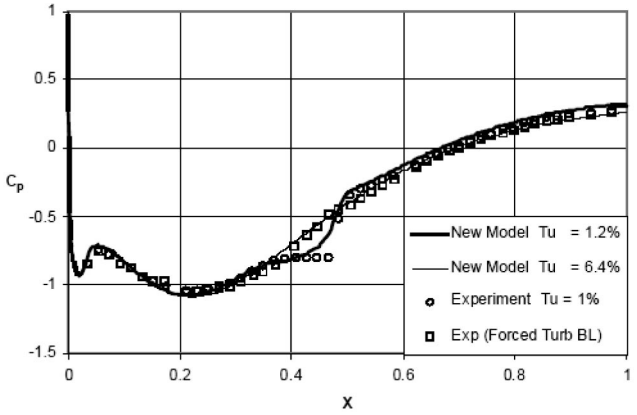

Fig. 8 Static pressure distribution comparison between the model and experiments, indicating separation at low turbulence level, and attached flow for the high-turbulence case

surface. Recall that this case uses freestream turbulence quantities comparable to those found in upstream wakes, as reported in Ref. [25].

By comparison, Fig. 5 shows the results using the RKE turbulence model. In both low- and high-turbulence cases, the boundary layer is clearly turbulent from the leading edge onward. Although not shown, the results with the SST model showed almost identical behavior. Neither one of these currently available models properly captured the boundary layer behavior, including separation, for the low-turbulence test case.

Figure 6 helps to illustrate the performance of each of the models in the low-turbulence case. The figure shows the distribution of friction coefficient using the model and each of the currently available models. The separation bubble reported in Ref. [25] is apparent with the model, beginning at approximately $X=0.35$ and ending at approximately $X=0.48$. Both of the other models indicate that the boundary layer is fully turbulent from the leading edge onward, resulting in elevated shear stress levels on the leading half of the plate, and suppression of the separation region. Figure 7 shows the friction coefficient distribution for the high-turbulence steady case. The model indicates transition shortly downstream of the leading edge, but still farther downstream than indicated by either of the other two models. For their part, the other models yield results almost identical to the low turbulence case in Fig. 6.

The pressure coefficient distribution on the flat plate is shown in Fig. 8. Comparison is made between the model and the experimental data reported in Ref. [25]. For the low-turbulence case, the computations and experiments are directly comparable. For the high-turbulence case, the comparison is between the computations with inlet Tu of 6.4%, versus experiments in which the boundary layer was forced to transition upstream of the throat using a trip wire. For the low-turbulence case, the separation of the boundary layer is clearly apparent in both the simulations and the measured data. Both indicate the familiar pressure plateau, although the simulations show pressure recovery beginning sooner than the experiment and occurring more gradually. For the high-turbulence case, no separation is observed for either set of results, and the model accurately resolves the pressure distribution over the entire surface. Though not shown, the results with the other two eddy-viscosity models are almost identical to those for the high-turbulence case with the new model, regardless of freestream conditions. Despite some quantitative discrepancy, the model correctly resolves the response of the boundary layer to changes in the freestream turbulence conditions, including the change in regime from a separation-induced transition to attached transition as Tu increases. This is especially encouraging given that the model is truly single-point, and does not rely on intermittency functions or non-local parameters.

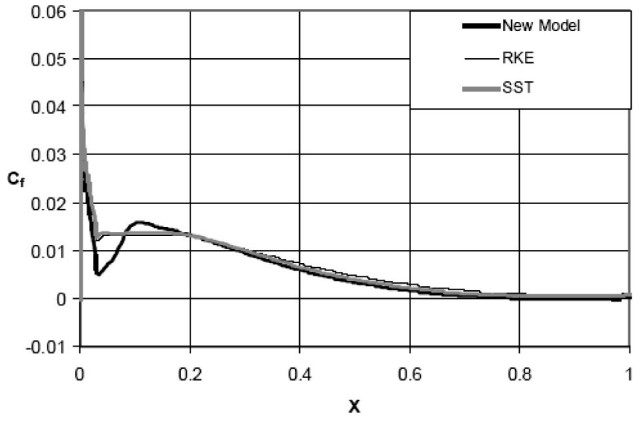

Fig. 7 Wall shear stress distribution using three different turbulence models for high-turbulence test case (Tu_{in}=6.4%)

5.2 Unsteady Test Cases

5.2.1 Instantaneous Results. The unsteady cases were run using the new model only. Since the other two tested models showed almost identical boundary layer results for low- and high-turbulence steady cases, it is apparent that there would be negligible response to unsteady wake passing. The model, on the other hand, shows considerable response. Figures 9 and 10 are time traces of the minimum local wall shear stress on the flat plate at any given instant, normalized by the wake passing period. At any time when the minimum shear stress is negative, there is boundary layer separation on the plate. If the minimum stress is positive, the boundary layer is attached over the entire length of the plate. Figure 9 shows the time trace for the low frequency case, $f_{red}=0.75$. Two curves are shown, for the top and bottom plate surfaces, respectively. Only a slight difference is noticeable, near where the shear stress reaches a minimum. The figure indicates that the boundary layer is separated about 50% of the time during a single wake passing period. The sudden elimination of the separation bubble is apparent at about $t/T=0.4$, 1.4, etc. This is followed by an attached turbulent boundary layer, and a relaxation to laminar levels. The separation bubble reappears at about $t/T=0.9$. This behavior agrees well with that reported in Ref. [25]. Figure 10 shows the time trace for the high frequency case ($f_{red}=1.5$), and indicates that the boundary layer remains attached at all times. This is due to the more frequent passing of the high

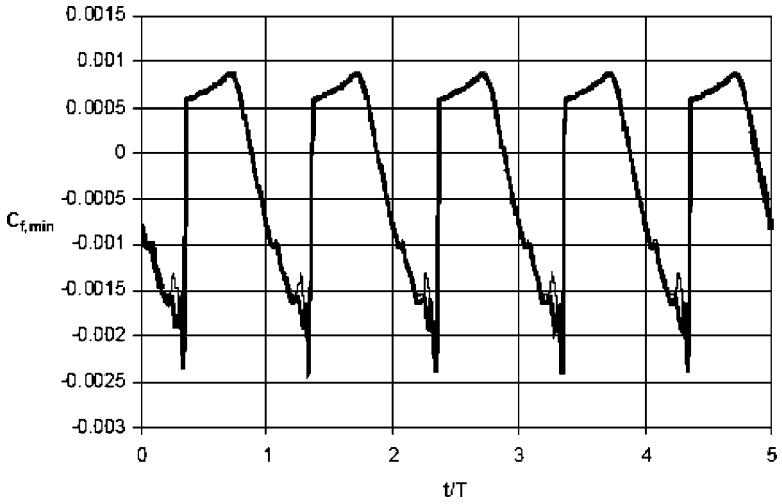

Fig. 9 Time trace of minimum shear stress on top- and bottom-plate surfaces for $f_{red}=0.75$. The boundary layer is separated for approximately half of each wake passing period.

turbulence wake, which does not allow time for the flow to fully relax. The plate top and bottom curves are indistinguishable. Again, the predicted behavior agrees well with that reported in [25].

Figure 11 highlights the response of the turbulence field to the wake passing, and shows the corresponding response of the wall shear stress. The figure shows contours of turbulence intensity at ten equally spaced times during a single wake passing period. Alongside each contour plot is a line plot indicating the instantaneous wall shear stress distribution with a thick black line. Also shown on each line plot are the low- and high-turbulence steady results as reference. The first three times show the approaching wake passing over the plate leading edge. During this time period, the shear stress indicates separation of the boundary layer downstream. Note that the separation occurs slightly farther downstream than for the low-turbulence steady case. The formation of a turbulent strip downstream of the leading edge and slightly upstream of the wake is seen at the fourth time. The presence of the strip is also apparent in the shear stress plot, which shows increased levels between about $X=0.11$ and $X=0.21$. By the fifth time, the turbulent strip has merged with the downstream turbulence, and the separation bubble has been suppressed. The remaining times show the continued path of the wake over the airfoil surface, and the relaxation of the boundary layer back toward the low turbulence steady case. By the final time shown, the boundary layer is almost ready to separate once more, and the shear stress and turbulence levels upstream of the separation point indicate a laminar boundary layer. The next wake is seen to be approaching the leading edge of the plate.

For the higher frequency case ($f_{red}=1.5$), similar behavior was observed, in that a turbulent strip is formed downstream of the passing wake, and this strip suppresses boundary layer separation. However, for this case the next wake strikes the plate quickly enough that there is no time for the boundary layer to relax far enough to the low-turbulence steady result so that separation occurs. This matches the unsteady behavior reported in Ref. [25].

5.2.2 Time-Averaged Results. The unsteady wake effect leads to time-averaged behavior for each of the two cases different from either of the steady cases discussed above. The time-averaged wall shear stress distribution is shown in Fig. 12, for

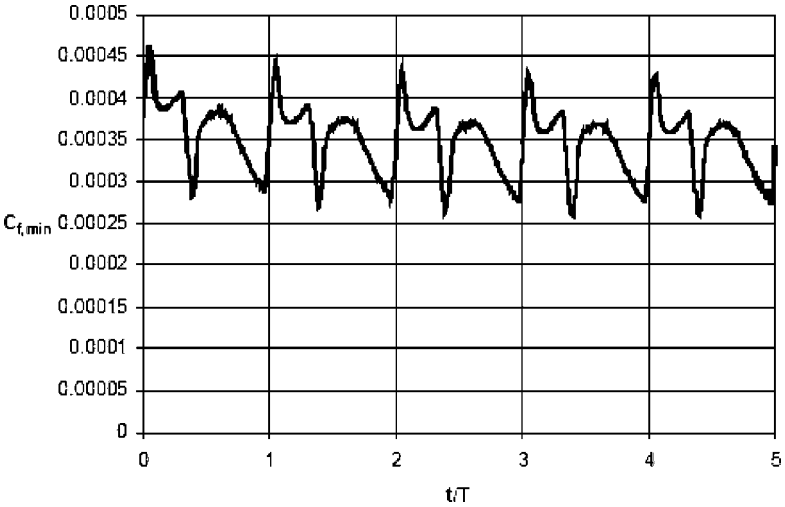

Fig. 10 Time trace of minimum shear stress for case $f_{red}=1.5$. The boundary layer remains attached at all times.

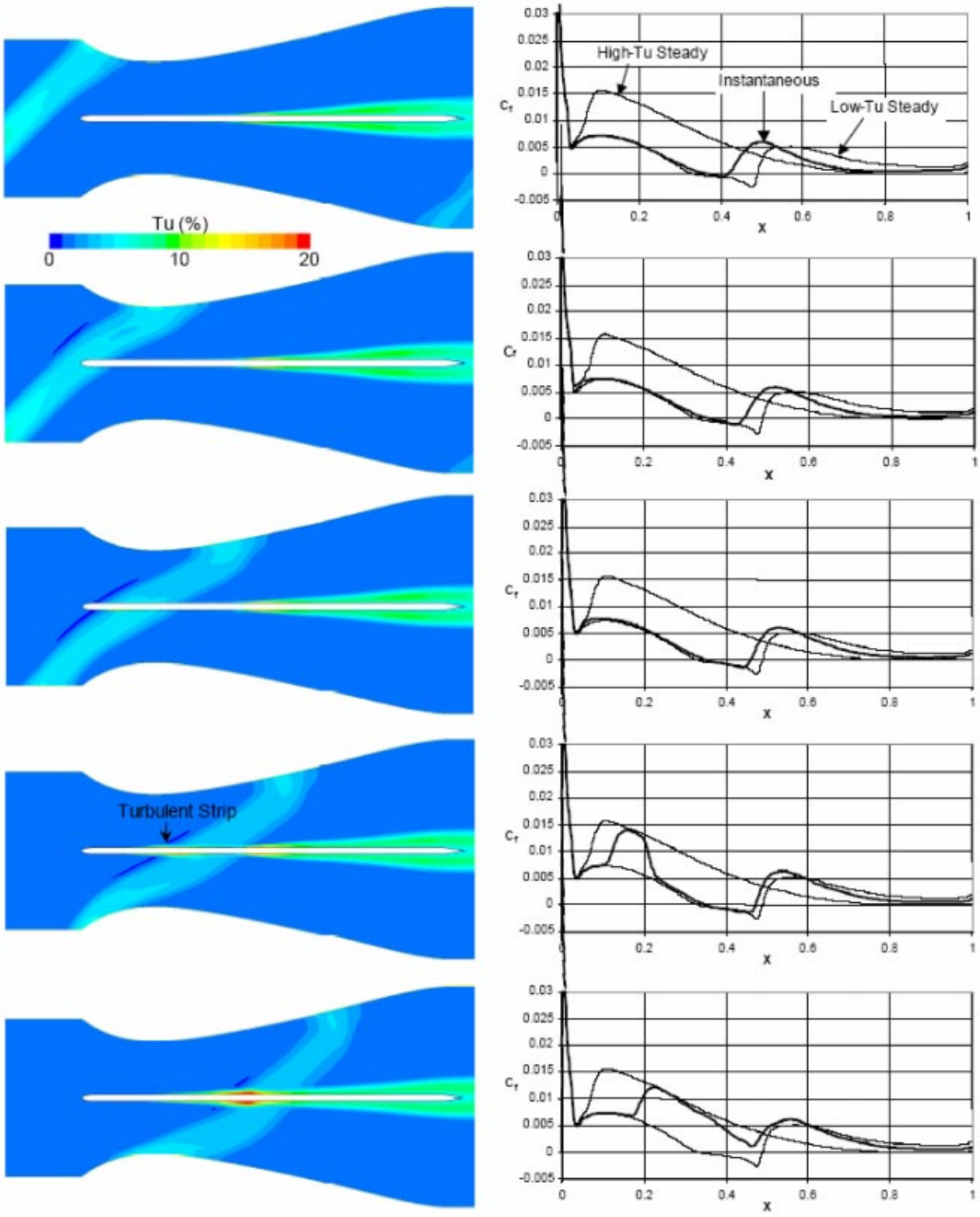

Fig. 11 Contours of instantaneous turbulence intensity and corresponding wall shear stress distributions for ten equally spaced times during a single wake passing period. Thick lines indicate instantaneous values, thin lines show low- and high-turbulence steady results.

both wake passing frequencies, along with the steady references. It is seen that the time-averaged boundary layer is attached for both frequencies. Furthermore, the lower frequency result more closely resembles the low-turbulence steady result, although both lie ''between'' the steady cases.

The time-averaged pressure distribution is shown in Fig. 13 for the two unsteady cases, and compared to the experimental data [25]. Comparison to Fig. 8 shows that neither of the unsteady simulations indicates a significant time-averaged separation region. The low-frequency case shows only a small hint of a sepa-

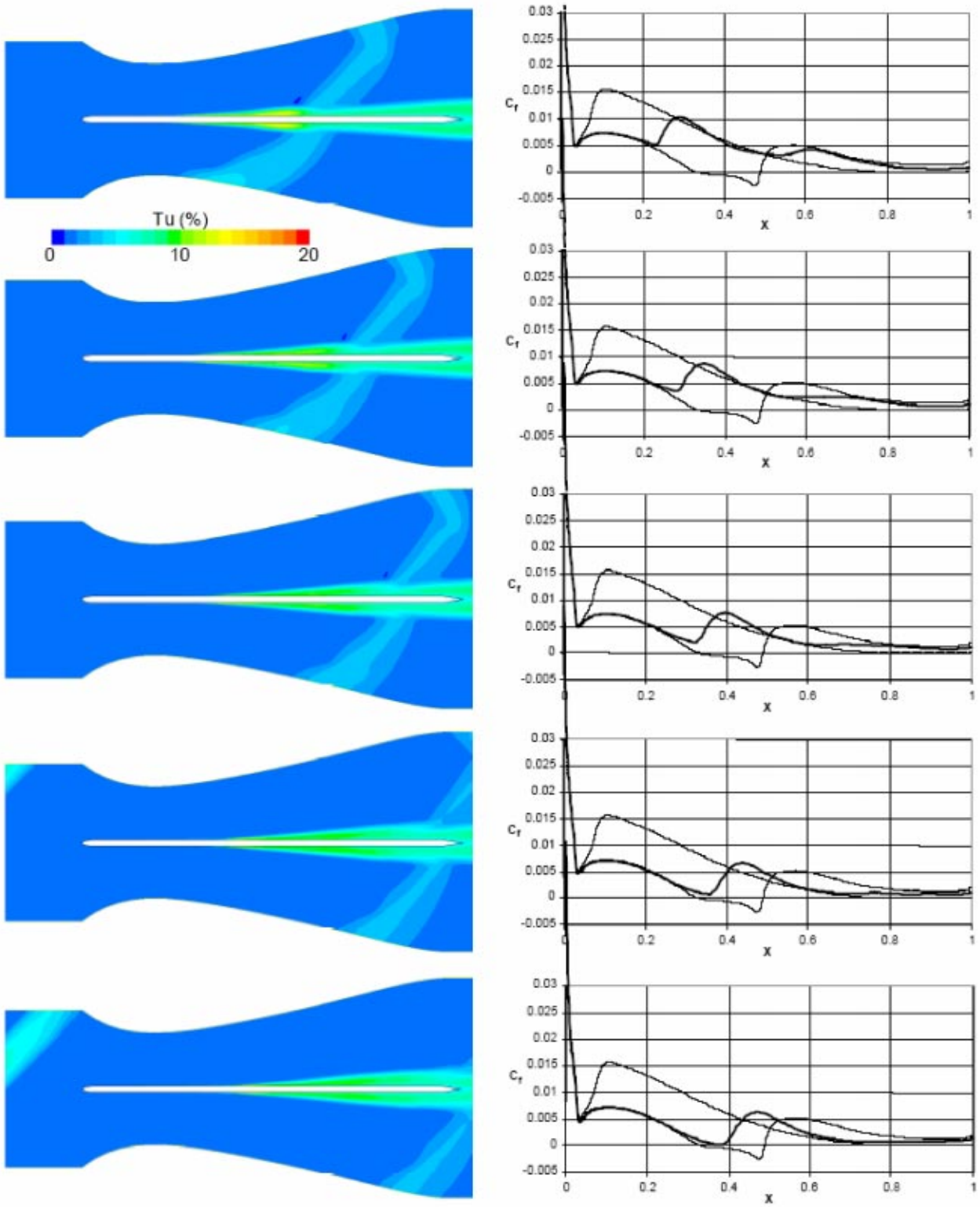

Fig. 11 (*continued*) **Contours of instantaneous turbulence intensity and corresponding wall shear stress distributions for ten equally spaced times during a single wake passing period. Thick lines indicate instantaneous values, thin lines show low- and high-turbulence steady results.**

ration bubble, as opposed to the experiments, which clearly show a perturbation in the pressure distribution at this frequency. Since the model does in fact indicate periodic separation of the boundary layer, it is likely that this discrepancy is related to the differences observed for the steady cases in Fig. 8. That is, the instantaneous pressure profiles due to separation are less distinct with the model than in the data, and the effect of time averaging is to make separation even less apparent. For the high-frequency case, on the other hand, both simulation and experiment show behavior similar to the high-turbulence steady case above.

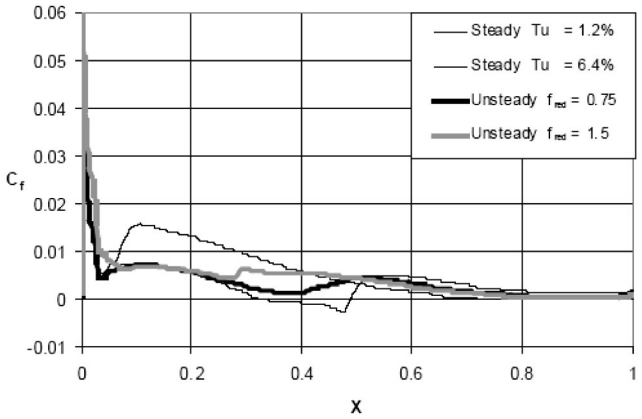

Fig. 12 Time-averaged wall shear stress distribution for steady and unsteady test cases

The time-averaged normalized velocity profiles near the trailing edge of the plate ($X=0.975$) are shown in Fig. 14. The unsteady wake passing impacts the boundary layer shape factor as shown. For the steady low-turbulence case, the boundary layer has a shape factor of 1.68. This is close to that for a flat plate turbulent boundary layer. The shape factor is relatively low in this case because the ''new'' turbulent boundary layer generated by separation-induced transition does not respond to the pressure gradient effects over the entire length of the blade. By comparison, the high-turbulence steady case has a shape factor of 2.07, due to the effects of adverse pressure gradient on this ''old'' turbulent boundary layer. The two unsteady cases have shape factors of 1.94 and 2.02, respectively. Both are much closer to the high-turbulence steady case, which is to be expected since the time-averaged shear stress distributions indicated attached boundary layers for these cases. It should be noted that in the experiments, the shape factor for the low-turbulence steady case was approximately 1.6, and the maximum instantaneous shape factor during the unsteady cases was approximately 2.1, which is similar to the steady results obtained with the model.

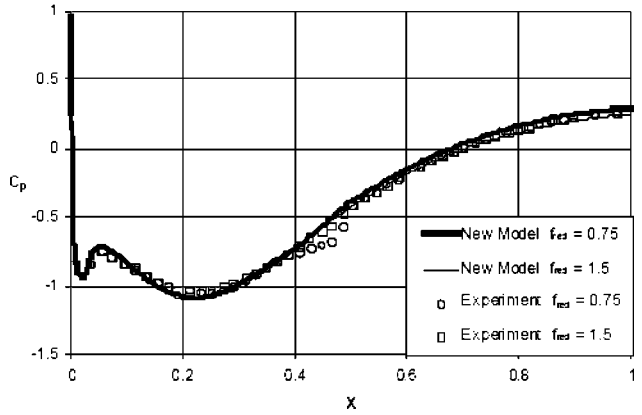

Fig. 13 Time-averaged pressure distribution for unsteady cases, showing suppression of separation region relative to low-Tu steady result in Fig. 8

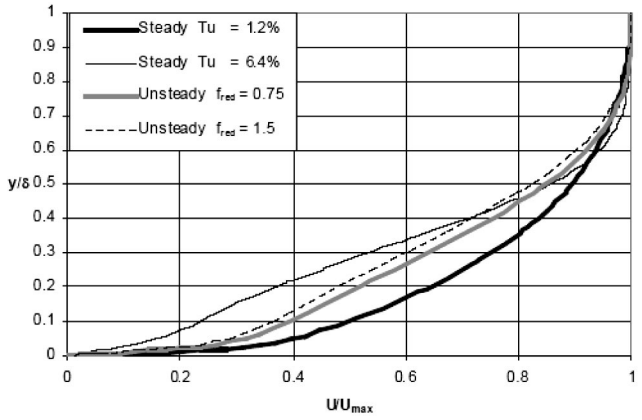

Fig. 14 Time-averaged streamwise velocity profiles for each of the four test cases, at $X=0.975$. The figure highlights the influence of steady and unsteady transition on boundary layer characteristics.

6 Summary and Conclusions

Results have been presented for steady and unsteady boundary layer development on a compressor-like flat plate, using a transition-sensitive eddy-viscosity turbulence model. The new modeling approach is implemented as a ''hands-off'' approach, in which no integral or nonlocal inputs are required for different cases. This is considerably different from most approaches adopted in the open literature. The test case is similar to an experimental study documented in the open literature [25], and was chosen to highlight the unsteady response of the developing boundary layer to passing wakes.

Steady results indicate that the model reproduces the correct trends in response to different levels of freestream turbulence intensity. At low turbulence levels ($Tu_{in}=1.2\%$), the boundary layer remains laminar over the initial portion of the plate, separates at about 35% of the chord, transitions to turbulence, and reattaches at about 48% of the chord. However, at high turbulence levels ($Tu_{in}=6.4\%$), altogether different behavior is predicted. The boundary layer transitions to turbulence shortly downstream of the leading edge, and remains attached over the remainder of the airfoil. This matches behavior reported in Ref. [25]. Neither of the two commercially available eddy-viscosity models used for comparison could reproduce this behavior.

The unsteady results with the model show that the passing wakes induce localized transition of a turbulent strip in the developing boundary layer. This strip propagates downstream accompanied by elevated levels of wall shear stress. Eventually, the turbulence suppresses the separation region near the midchord of the plate, and the boundary layer remains attached for some time. For low wake passing frequency ($f_{red}=0.75$), the boundary layer relaxes toward the low-turbulence steady state, and separation reappears during part of the wake passing period. For high frequency ($f_{red}=1.5$), the next wake arrives too quickly for separation to reappear between wakes.

In the case of boundary layer separation, comparison with experiments indicates that the model, while correctly resolving the qualitative response, does not show as strong a deviation of the pressure distribution due to the separation. This is apparent in both the low-turbulence steady case and the low-frequency unsteady wake-passing case, and should be addressed in future model development if the new model is to be considered as a simulation tool for compressor analysis and design.

Overall, these results indicate that the model shows potential for development as a predictive method for steady and unsteady transitional boundary layer flows. The ability to resolve the correct behavior for different freestream conditions, as well as the unsteady boundary layer response to passing wakes, is encouraging. Future work will include further refinement and testing of the model, including application to a broad range of steady and unsteady compressor aerodynamics applications.

Acknowledgments

Special thanks to Satish Undapalli, for his assistance in much of the background research for this work. The authors gratefully acknowledge the continued support of Fluent, Inc. personnel, with special thanks to Rick Lounsbury, John Straus, and Evangelos Koutsavdis. Thanks as well to Will Robinson, Clemson University College of Engineering and Science Computer & Network Services, for excellent support of computing systems.

Nomenclature

C = flat plate chord length
C_f = friction coefficient, $\tau_w/1/2\rho U_\infty^2$
C_p = pressure coefficient, $(P-P_{\text{in}})/1/2\rho U_\infty^2$
C_μ = turbulent viscosity coefficient
D = wake separation distance
d = wall distance
D_L = laminar kinetic energy near-wall dissipation
D_T = turbulent kinetic energy near-wall dissipation
f_{red} = reduced wake frequency, $(V_{\text{wake}}\times C)/(U_{\text{in}}\times D)$
f_ν = viscous damping function
f_{INT} = intermittency damping function
$f_{\tau,1}$ = time-scale damping function
k_L = laminar kinetic energy
k_T = turbulent kinetic energy
k_{TOT} = total fluctuation energy, $k_{\text{L}}+k_{\text{T}}$
P = mean (Reynolds-averaged) static pressure
P_{TOT} = mean total pressure
P_L = laminar kinetic energy production term
P_T = turbulent kinetic energy production term
PS = airfoil pressure surface
Pr_T = turbulent Prandtl number
R = bypass transition production term
R_{NAT} = natural transition production term
Re_T = turbulence Reynolds number
Re_C = Reynolds number based on chord length and inlet velocity
Re_θ = momentum thickness Reynolds number
S = magnitude of mean strain rate tensor, $\sqrt{2S_{ij}S_{ij}}$
S_{ij} = strain rate tensor, $1/2(\partial U_i/\partial x_j+\partial U_j/\partial x_i)$
SS = airfoil suction surface
St = Stanton number based on inlet velocity
T = unsteady wake passing period
t = time
Tu = turbulence intensity, u'/U_{in}
U = mean (Reynolds-averaged) streamwise velocity
U_i = mean (Reynolds-averaged) velocity vector
V_{wake} = vertical wake velocity
X = nondimensional downstream distance, x/C
x = axial downstream distance from plate leading edge
$-\overline{u_iu_j}$ = kinematic Reynolds stress tensor
$-\overline{u_i\theta}$ = kinematic heat flux vector
$-\overline{uv}$ = turbulent shear stress
u' = average streamwise fluctuation
u_τ = friction velocity
v' = wall-normal fluctuation
y^+ = nondimensional wall distance, yu_τ/ν
α_T = turbulent diffusivity for turbulent quantities
$\alpha_{\theta,\text{TOT}}$ = total (laminar+turbulent) diffusivity for θ
β_{BP} = bypass transition threshold function
β_{TS} = Tollmien-Schlichting threshold function
β_{NAT} = natural transition threshold function
$\beta_{\Delta P}$ = inviscid instability threshold function
δ = 99% boundary layer thickness
ε = farfield dissipation
ϕ_{BP} = bypass transition parameter
ϕ_{NAT} = natural transition parameter
η = local wall-normal coordinate direction
λ_{eff} = effective (wall-limited) length scale
λ_T = turbulent length scale
ν = molecular kinematic viscosity
ν_T = turbulent kinematic viscosity
ν_{TOT} = total (laminar+turbulent) eddy viscosity
Ω = magnitude of mean rotation tensor, $\sqrt{2\Omega_{ij}\Omega_{ij}}$
Ω_{ij} = rotation rate tensor, $1/2(\partial U_i/\partial x_j-\partial U_j/\partial x_i)$
ω = inverse turbulent time scale, $\varepsilon/\text{k}_\text{T}$
θ = mean (Reynolds-averaged) temperature
ρ = density
τ_m = mean flow time scale
τ_T = turbulent time scale
τ_w = streamwise direction wall shear stress

Subscripts

i, j = indices
s = small scale
l = large scale
∞ = local freestream condition
in = inlet value

References

[1] Dong, Y., and Cumpsty, N. A., 1990, "Compressor Blade Boundary Layers: Part 1—Test Facility and Measurements With No Incident Wakes," ASME J. Turbomach., **112**, pp. 222–230.
[2] Dong, Y., and Cumpsty, N. A., 1990, "Compressor Blade Boundary Layers: Part 2—Measurements With Incident Wakes," ASME J. Turbomach., **112**, pp. 231–240.
[3] Walraevens, R. E., and Cumpsty, N. A., "Leading Edge Separation Bubbles on Turbomachine Blades," ASME J. Turbomach., **117**, pp. 115–125.
[4] Cumpsty, N. A., Dong, Y., and Li, Y. S., 1995, "Compressor Blade Boundary Layers in the Presence of Wakes," ASME paper no. 95-GT-443.
[5] Halstead, D. E., Wisler, D. C., Okiishi, T. H., Walker, G. J., Hodson, H. P., and Shin, H., 1997, "Boundary Layer Development in Axial Compressors and Turbines: Part 1 of 4—Composite Picture," ASME J. Turbomach., **119**, pp. 114–127.
[6] Halstead, D. E., Wisler, D. C., Okiishi, T. H., Walker, G. J., Hodson, H. P., and Shin, H., 1997, "Boundary Layer Development in Axial Compressors and Turbines: Part 2 of 4—Compressors," ASME J. Turbomach., **119**, pp. 426–444.
[7] Halstead, D. E., Wisler, D. C., Okiishi, T. H., Walker, G. J., Hodson, H. P., and Shin, H., 1997, "Boundary Layer Development in Axial Compressors and Turbines: Part 4 of 4—Computations and Analyses," ASME J. Turbomach., **119**, pp. 128–139.
[8] Savill, A. M., 1993, "Some Recent Progress in the Turbulence Modelling of By-Pass Transition," In *Near-Wall Turbulent Flows*, So, R. M. C., Speziale, C. G., and Launder, B. E. (eds.), Elsevier Science, New York, pp. 829–848.
[9] Yang, Z., and Shih, T. H., 1993, "A k-ε Model for Turbulent and Transitional Boundary Layers," *Proceedings of the International Conference on Near-Wall Turbulent Flows*, Tempe, AZ, p. 165.
[10] Biswas, D., and Fukuyama, Y., 1994, "Calculation of Transitional Boundary Layers With an Improved Low-Reynolds-Number Version of the k-ε Turbulence Model," ASME J. Turbomach., **116**, pp. 765–773.
[11] Volino, R. J., and Simon, T. W., 1997, "Boundary Layer Transition Under High Free-Stream Turbulence and Strong Acceleration Conditions: Part 2—Turbulent Transport Results," ASME J. Heat Transfer , **119**, pp. 427–432.
[12] Matsubara, M., and Alfredsson, P. H., 2001, "Disturbance Growth in Boundary Layers Subjected to Free-Stream Turbulence," J. Fluid Mech., **430**, pp. 149–168.
[13] Andersson, P., Berggren, M., and Henningson, D. S., 1999, "Optimal Disturbances and Bypass Transition in Boundary Layers," Phys. Fluids, **11**, pp. 134–150.
[14] Leib, S. J., Wundrow, D. W., and Goldstein, M. E., 1999, "Effect of Free-Stream Turbulence and Other Vortical Disturbances on a Laminar Boundary Layer," J. Fluid Mech., **380**, pp. 169–203.
[15] Jacobs, R. G., and Durbin, P. A., 2001, "Simulations of Bypass Transition," J. Fluid Mech., **428**, pp. 185–212.
[16] Mayle, R. E., and Schulz, A., 1997, "The Path to Predicting Bypass Transition," ASME J. Turbomach., **119**, pp. 405–411.
[17] Michelassi, V., Martelli, F., Denos, R., Arts, T., and Sieverding, C. H., 1999, "Unsteady Heat Transfer in Stator-Rotor Interaction by Two-Equation Turbulence Model," ASME J. Turbomach., **121**, pp. 436–447.
[18] Suzen, Y. B., and Huang, P. G., 2000, "Modeling of Flow Transition Using an Intermittency Transport Equation," ASME J. Fluids Eng., **122**, pp. 273–284.
[19] Steelant, J., and Dick, E., 2001, "Modeling of Laminar-Turbulent Transition for High Freestream Turbulence," ASME J. Fluids Eng., **123**, pp. 22–30.
[20] Walters, D. K., and Leylek, J. H., 2004, "A New Model for Boundary-Layer Transition Using a Single-Point RANS Approach," ASME J. Turbomach., **126**, pp. 193–202.
[21] Blair, M. F., 1983, "Influence of Free-Stream Turbulence on Turbulent Boundary Layer Heat Transfer and Mean Profile Development, Part I—Experimental Data," ASME J. Heat Transfer , **105**, pp. 33–40.

[22] Radomsky, R. W., and Thole, K. A., 2000, "Flowfield Measurements for a Highly Turbulent Flow in a Stator Vane Passage," ASME J. Turbomach., **122**, p. 255.
[23] Radomsky, R. W., and Thole, K. A., 2001, "Detailed Boundary-Layer Measurements on a Turbine Stator Vane at Elevated Freestream Turbulence Levels," ASME paper no. 2001-GT-0169.
[24] Volino, R. J., 1998, "A New Model for Free-Stream Turbulence Effects on Boundary Layers," ASME J. Turbomach., **120**, pp. 613–620.
[25] Ottavy, X., Vilmin, S., Opoka, M., Hodson, H., and Gallimore, S., 2002, "The Effects of Wake-Passing Unsteadiness Over a Highly-Loaded Compressor-Like Flat Plate," ASME J. Turbomach., **126**, pp. 13–23.
[26] Kim, J., Moin, P., and Moser, R. D., 1987, "Turbulence Statistics in Fully Developed Channel Flow at Low Reynolds Number," J. Fluid Mech., **177**, pp. 133–186.
[27] Patankar, S. V., 1980, *Numerical Heat Transfer and Fluid Flow*, Taylor & Francis, London.
[28] Shih, T.-H., Liou, W. W., Shabbir, A., Yang, Z., and Zhu, J., 1995, "A New k-ε Eddy Viscosity Model for High Reynolds Number Turbulent Flows," Comput. Fluids, **24**, pp. 227–238.
[29] Menter, F. R., 1994, "Two-Equation Eddy-Viscosity Turbulence Models for Engineering Applications," AIAA J., **32**, pp. 1598–1605.

Unsteady Aerodynamics and Aeroacoustics of a High-Bypass Ratio Fan Stage

Anil Prasad

Dilip Prasad

Aerodynamics Division,
Pratt & Whitney Aircraft Engines,
East Hartford, CT 06108

A numerical investigation of the unsteady aerodynamics of a fan stage comprised of a transonic rotor, swept fan exit guide vane (FEGV), and low-pressure compressor inlet guide vane (IGV) is described, with emphasis on acoustics. It is shown that the effects of the two downstream stator rows on the time-mean blade flow field are negligible, permitting its investigation using isolated rotor calculations. Simulations of this type are carried out along the engine operating line to quantify the acoustic sources associated with the upstream shock field and wake turbulence-stator interaction. The shock noise achieves its maximum value near the flyover acoustic certification condition, while the wake turbulence is least at this condition owing to its proximity to the design point. The behavior of these noise sources is explained physically by carrying out a detailed examination of the rotor flow field. The unsteady interaction between the rotor and stator rows at a high-power setting is investigated next. It is shown that the time-mean IGV flow is significantly affected by this interaction. Moreover, the unsteady loading on the IGV is found to be large. The behavior of the upstream-propagating acoustic field generated by rotor-IGV interaction is examined. The interaction between the rotor and FEGV is found to be linear in nature. The FEGV surface unsteady pressure and far-field acoustic field behavior are investigated. [DOI: 10.1115/1.1811103]

Introduction

The challenges encountered in the design of the fan of a modern commercial aircraft engine are manifold. Specifically, it is essential that performance (e.g., thrust and efficiency), operability (e.g., surge and flutter margin), and mechanical criteria (e.g., weight and foreign-object damage resistance) be satisfied. More recently, a requirement of increasing concern is that of low noise. Although this latter constraint has a bearing on the design of several components, the large bypass ratio of current and future engines results in the fan being a dominant source of noise.

The noise emitted from the fan possesses both tonal and broadband character, and the essential features have been admirably reviewed by Cumpsty [1]. Tone noise is characterized by the presence of well-defined peaks in the power spectrum and is related to the turbomachinery. On the other hand, the acoustic energy associated with broadband noise is spread over a large portion of the spectrum and is generated by random processes, such as jet mixing. One source of fan tone noise is the unsteady aerodynamic interaction between the rotor and downstream stator rows, viz., the fan exit guide vane and low-pressure compressor inlet guide vane. In addition, tone noise is generated by the direct rotor field at supersonic rotor tip relative speeds. Under these conditions, shocks formed at the rotor blade leading edges propagate through the inlet and are radiated to the far field.

The broadband component of fan noise has been attributed [1,2] to several mechanisms, all of which feature the interaction of turbulence with an aerodynamic surface. These mechanisms include rotor wake turbulence interacting with the downstream stators and the interaction of turbulence generated in the blade boundary layer with the rotor trailing edge. The latter is usually referred to as self-noise. In addition, interaction of turbulence ingested through or generated by the inlet with the rotor can also generate noise. It would appear from the study of Morin [3] that turbulence-stator interaction is the dominant source of aft broadband noise, although the matter is far from closed.

The present investigation employs steady and time-domain numerical analyses to examine the noise generation mechanisms associated with the direct rotor field, wake turbulence, and rotor-stator interaction in the fan stage of a modern commercial engine. Unlike most previous studies, the complete fan stage is simulated, including the core splitter, low-pressure compressor inlet guide vane (IGV), and fan exit guide vane (FEGV). It is shown that the time-mean flow in the rotor is unaffected by the presence of the downstream stators. This permits investigation of the mean blade flow using isolated rotor computations. In the present study, simulations of this type are carried out over engine operating conditions ranging from approach to maximum power.

The acoustic power associated with the propagating shock waves that comprise the direct rotor field first increases with the tip relative Mach number and decreases thereafter. It is shown that this behavior can be understood in terms of the variation of the shock strength with the engine operating condition and the supersonic span fraction of the blade.

The turbulence generated in the rotor wake is examined and found to be largest at the low-power engine setting. As the engine power is increased, the wake turbulence drops, but rises again at high power. This behavior is investigated in detail and shown to be associated with blade separation mechanisms.

The interaction between the rotor and downstream stator rows is studied next using coupled unsteady and isolated steady calculations at the acoustic sideline condition. The IGV mean flow is found to be strongly affected by the rotor. In particular, the mean loading obtained using the two computational procedures differs significantly as a consequence of the large blockage associated with the rotor wakes as they pass through the IGV passage. In addition, the magnitude of the unsteady loads on the IGV is found to be quite large. The acoustic waves generated as a consequence of the large IGV unsteady loading are shown to not propagate through the rotor at this condition and to be reflected into the bypass duct.

Unlike the interaction of the rotor with the IGV, that with the

Contributed by the International Gas Turbine Institute (IGTI) of THE AMERICAN SOCIETY OF MECHANICAL ENGINEERS for publication in the ASME JOURNAL OF TURBOMACHINERY. Paper presented at the International Gas Turbine and Aeroengine Congress and Exhibition, Vienna, Austria, June 13–17, 2004. Paper No. 2004-GT-53955. Manuscript received by IGTI, October 1, 2003; final revision, March 1, 2004. IGTI Review Chair: A. J. Strazisar.

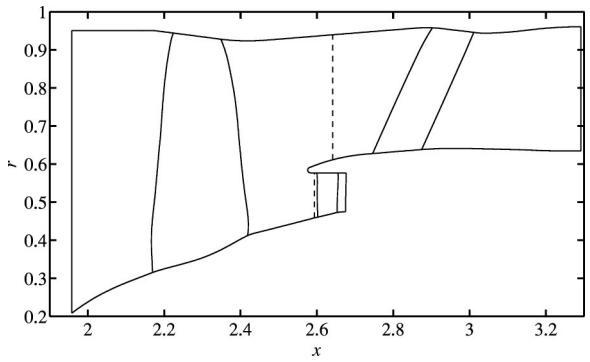

Fig. 1 Meridional view of the flow configuration for coupled simulations of the fan system. The broken lines indicate the locations of the sliding interface planes.

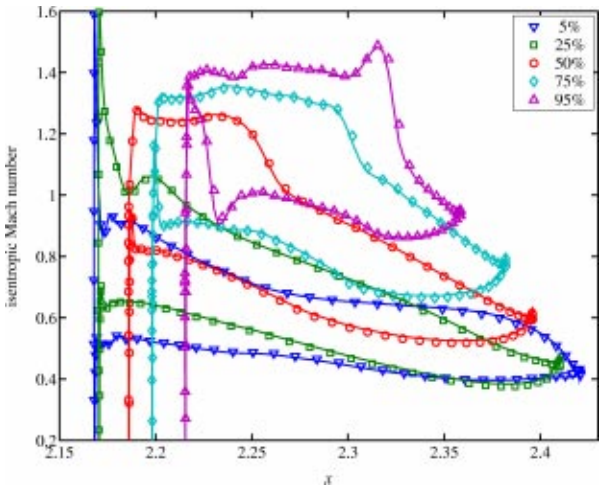

Fig. 2 Comparison of rotor isentropic Mach number distributions at various spanwise locations for a high-power engine setting. Lines: isolated calculation; symbols: coupled calculation (for clarity, only every other point is shown).

FEGV is found to be linear, demonstrating that the use of linearized approaches [4] to determine the noise generated by this mechanism is justified. The spanwise structure of the unsteady pressure field at the fundamental frequency downstream of the FEGV reveals that the peak value lies away from the duct endwalls so that the effectiveness of acoustic liners located along these endwalls may be limited.

Computational Details

In this study, the Reynolds-averaged Navier-Stokes equations are solved numerically using the methods described in [5,6]. The algorithm is based on the Lax-Wendroff multiple grid scheme of Ni [6] and utilizes dual-time stepping for the time-accurate unsteady calculations. Turbulence closure is achieved using the $k-\omega$ model of Wilcox [7] and the quasi-two-dimensional nonreflecting conditions of Giles [8] are applied at the inflow and outflow boundaries. The present problem, where large computational grids are employed, is made tractable through the use of domain decomposition and parallel-processing capability. The solver has been extensively validated for use in turbomachinery applications, details of which are to be found in [9–12].

We study here a fan stage representative of modern commercial engines, comprised of a transonic rotor, swept FEGV, and low-pressure compressor IGV. Unsteady fully coupled simulations as well as steady isolated airfoil row calculations are carried out. The flow configuration for the coupled simulations is depicted in meridional view in Fig. 1. In this figure and in the development that follows, the axial (x) and radial (r) coordinates are normalized by the radius of the nacelle highlight, while the axial origin is arbitrary. The unsteady calculations are carried out in the relative frame of each blade row, and sliding interface planes are inserted between the rotor and stator domains. These interfaces are illustrated in Fig. 1 by the broken lines. The tangential extent of the computational domain of Fig. 1 corresponds to a 1/12 sector of the wheel and consists of 2 rotor passages and 5 FEGV and IGV passages each. An O-H grid topology is used to resolve the details of the flow around each airfoil. Similarly, the flow in the vicinity of the splitter leading edge is resolved using a local C-grid. The overall grid resolution employed is significantly higher than that used in typical performance predictions so as to maintain the numerical dissipation at low levels. Specifically, the grid density was chosen such that the propagating acoustic disturbances were resolved in the axial and tangential directions by at least 25 points per wavelength. The time step for the unsteady simulation was chosen such that a complete rotor revolution occurred in 6000 steps; convergence to a stationary state was typically achieved over about half a rotor revolution period. The solution was deemed converged when flow field variables differed by less than 0.25% between successive periodic cycles.

The isolated rotor calculations were carried out on a computational domain similar to that in Fig. 1, but with the core and bypass downstream boundaries placed 2 blade-tip chord lengths downstream of the rotor trailing edge. For this purpose, the core region was extended downstream as a constant-area annular duct. Comparison of results from the steady isolated rotor calculation and the time-accurate coupled calculation are made by converging both simulations to the same bypass and core mass flow rates. Radial equilibrium of static pressure was imposed at the two exit boundaries of the isolated rotor computational domain. The isolated FEGV and IGV calculations were each converged to their respective mass flow rates in the bypass and core ducts, thus allowing direct comparisons with results from the time-accurate coupled simulation. The isolated FEGV and IGV calculations were supplied with circumferentially averaged inlet profiles from the isolated rotor calculations. In all simulations, the no-slip condition is imposed at the solid boundaries, which are also adiabatic.

The fan operating condition is characterized here in terms of a tip relative Mach number at the fan face. This quantity, denoted by M_f, is determined as follows. The corrected mass flow rate per unit area at the fan face is used to define an axial Mach number M_x. Imposing conservation of stagnation temperature and making use of its value far upstream, the fan face sonic speed and thereby the rotor tip Mach number M_t, is determined. The fan face tip relative Mach number is then given by $M_f=\sqrt{(M_x^2+M_t^2)}$. It should be noted that this is based only on one-dimensional quantities and the condition $M_f=1$ does not denote the precise operating condition at which the rotor tip relative flow first becomes supersonic.

Rotor Flow Field

The meridional geometry in Fig. 1 illustrates that the distance between the rotor and two stator rows is quite large when measured in terms of the axial chords of the two stators. Since the stator flow is designed to remain subsonic, the potential field of the stators is expected to exert minimal influence on the rotor. In order to verify that this is the case, we compare the rotor blade loading distributions determined using the previously described coupled unsteady and isolated steady procedures at a high-power engine setting, where the stator Mach number and thus the upstream influence is largest. We illustrate in Fig. 2 isentropic Mach number distributions along various spanwise blade sections at a high-power setting corresponding approximately to takeoff. The splitter leading edge is located approximately at 30% blade span.

The isentropic Mach number is based on the local static pressure and the blade leading-edge relative stagnation pressure. The coupled airfoil-row loading distributions, determined by averaging over one periodic unsteady cycle, are observed to be in excellent agreement with their isolated counterparts, indicating that the two downstream stator rows are all but invisible to the rotor, in the steady sense. This observation is further supported by verifying that the circumferentially averaged profiles of total temperature, total pressure, and flow angle from the two sets of calculations are also in close correspondence.

The negligible upstream influence of the downstream stators on the rotor flow field suggests that the latter can be examined using isolated rotor calculations instead of the considerably more expensive coupled analysis, with little loss in fidelity. In what follows, we carry out such simulations over a range of engine power settings, which are referred to here in terms of the acoustic certification condition. Thus, the lowest power setting corresponds to approach power while the highest, referred to as ''sideline,'' corresponds approximately to the takeoff setting. A third power setting examined is that corresponding to a typical cutback condition, known more precisely in the acoustic terminology as ''flyover.'' Further details pertaining to acoustic certification are found in the ICAO document [13].

We examine the rotor flow, focusing on two aspects that are relevant to engine acoustics: the behavior of the upstream-propagating shock field and the turbulence generated in the wake downstream of the blade. The former is of interest because it is the mechanism by which inlet tone noise is generated at supersonic blade tip relative speeds, while the latter is believed to be a significant source of fan broadband noise [3].

Upstream Shock Behavior. The fan relative flow is transonic at the design condition, as is the case in most modern commercial engines. Thus, at the typical operating condition, the relative Mach number past the tip section is supersonic while that past the hub section is subsonic. The advantage of this type of design is that it provides the desired pressure ratio and flow capacity with a relatively small penalty in efficiency [14] in a compact mechanical configuration. The flow structure in a two-dimensional supersonic cascade at high-power conditions is described in [15] and [16] and consists of leading-edge and in-passage shocks. At supersonic tip relative speeds, the periodic array of shocks generated at the rotor leading edges propagates upstream through the inlet. The propagation of the shocks is accompanied by a decay in their strength, brought about by nonlinear effects [17]. This behavior has recently been examined in the context of transonic compressor flows by Prasad [12], who demonstrated the capability of the present solver to correctly capture the shock decay, provided the grid is sufficiently fine. The grid resolution employed in the present study exceeds the recommendations in [12], thus ensuring that numerical dissipation is controlled.

The rotor-locked upstream shock field may be characterized in terms of the acoustic power that it carries. Following Morfey [18], the acoustic intensity vector **I** is defined as

$$\mathbf{I}=\left(\frac{\tilde{p}}{\bar{\rho}}+\mathbf{v}\cdot\mathbf{V}\right)\left(\bar{\rho}\mathbf{v}+\frac{\tilde{p}}{c^2}\mathbf{V}\right) \tag{1}$$

where **V** and **v** are the mean and fluctuating velocity fields, $\bar{\rho}$ is the mean density, $\tilde{p}$ is the pressure fluctuation, and c is the local sonic speed. The power $P(x)$ crossing an axial plane is obtained by integrating the expression in Eq. (1) over the duct

$$P=R_t^2\int_{\mu}^{1}\int_{0}^{2\pi} I_x\ r\,dr\ d\theta \tag{2}$$

where I_x is the axial component of the acoustic intensity flux vector defined on the plane, μ is the hub-tip ratio, θ is the circumferential coordinate, and r is the radius normalized by its value at the outer casing R_t.

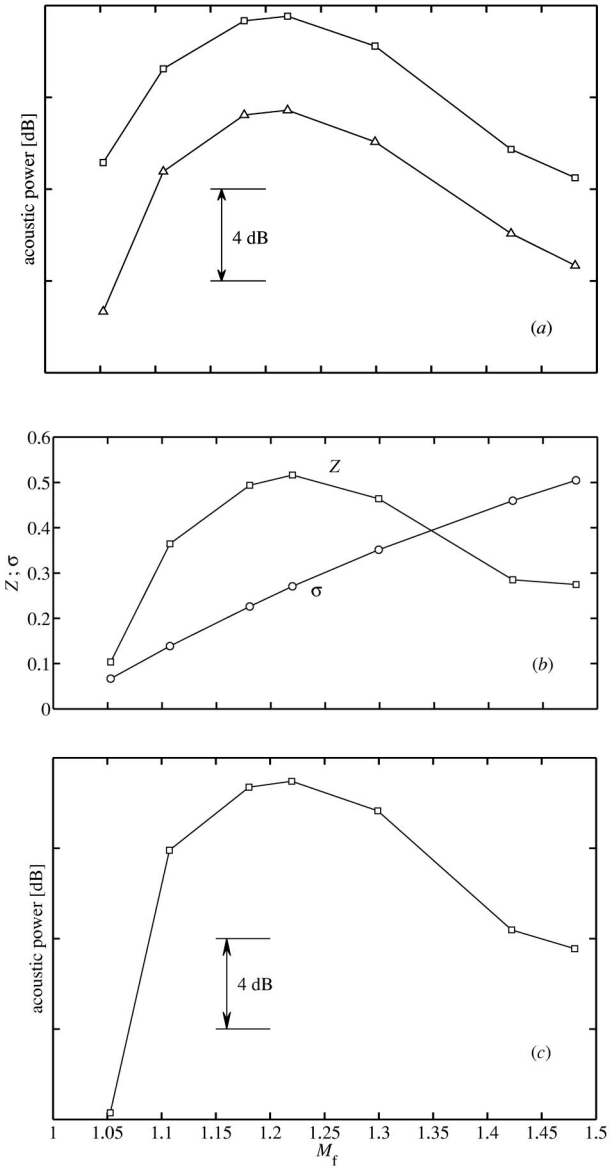

Fig. 3 Variation with fan face tip relative Mach number M_f of (*a*) computed acoustic power level at 1.25 (□) and 2.05 (△) tip chords upstream of fan tip leading edge, and (*b*) shock strength *Z*, and supersonic span fraction σ. The approximate prediction of acoustic power using a one-dimensional analysis is shown in (*c*).

For linear waves propagating through a uniform mean flow, the acoustic power as defined by Eq. (2) is a conserved quantity and, therefore, invariant with distance from the source. This is not true for a shock wavetrain for which the amplitude and power decay with distance from the source as a consequence of dissipation across the shocks. Although the power is not conserved, we use its value at a given axial station to quantify the shock-generated noise propagating away from the fan.

We examine in Fig. 3(*a*) the variation of P with M_f at axial stations located 1.25 and 2.05 tip chord lengths upstream of the fan tip leading edge. The blade leading-edge shocks propagate upstream for $M_f \gtrsim 1.05$. At both axial stations, it is observed that the power grows rapidly with M_f, attaining a maximum value at $M_f \approx 1.2$. At higher values of M_f, the power decays, albeit at a relatively slow rate. The two curves in Fig. 3(*a*) are observed to be

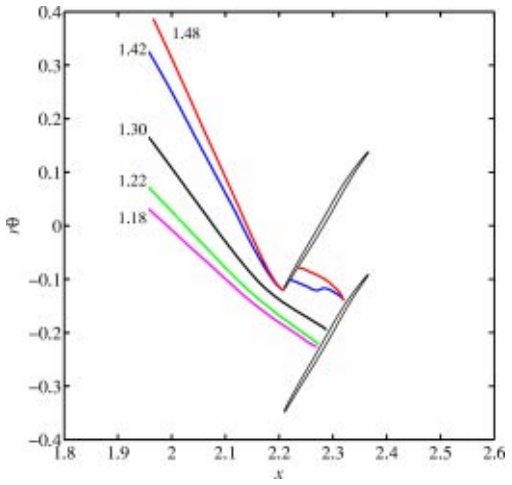

Fig. 4 Position of the rotor leading-edge shock for several values of fan face tip relative Mach number M_f

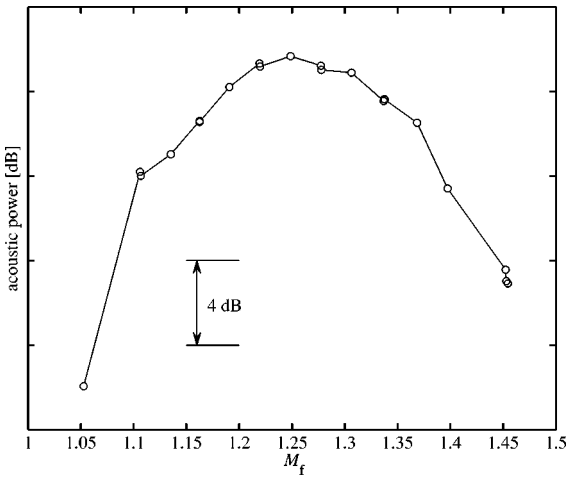

Fig. 5 Variation of measured inlet shock noise power level with fan face tip relative Mach number M_f

nearly parallel, suggesting that the trend with M_f is determined by the nature of the shock generated at the blade rather than that of the dissipation which occurs in the duct.

In order to understand the reason for this behavior, we note first that increases in M_f occur due to increases in both the axial and tangential Mach numbers M_x and M_t, respectively. The growth of M_t, which corresponds to that of the wheel speed, results in an increasing fraction of the blade span operating under supersonic relative flow conditions. This is quantified by making use of radial profiles of the circumferentially averaged relative Mach number to extract the supersonic span fraction σ, the variation of which is plotted in Fig. 3(*b*) as a function of M_f.

The variation of M_f with the fan operating condition also results in changes in the structure of the blade leading-edge shock. This is illustrated in Fig. 4 for different values of M_f, where the spatial variation of the relative Mach number field was used to identify the location of the shock. For $M_f=1.18$, the shock is almost normal to the relative flow and detached from the blade leading edge. The angle of the shock relative to the tangential direction is quite large. Increases in M_f cause the shock to move closer to the blade leading edge. Moreover, the shock begins to assume an increasingly oblique character relative to the blade, and its angle relative to the tangential direction decreases. This is accompanied by a decrease in the shock strength Z defined as

$$Z=\frac{\Delta p}{p_m}$$

where p_m and Δp represent, respectively, the mean pressure and pressure rise across the shock. We illustrate in Fig. 3(*b*), the variation of Z with M_f on a midpassage plane at the spanwise location corresponding to that of maximum rotor loading. The shock strength is observed from Fig. 3(*b*) to increase between $1.05<M_f<1.2$ and to decrease rapidly thereafter.

Based on the variation of Z and σ with operating condition, the acoustic power can be estimated using the quasi-one-dimensional expression of Morfey and Fisher [17]. The resulting approximate power shown in Fig. 3(*c*) as a function of M_f is observed to exhibit a behavior rather similar to that in Fig. 3(*a*). In particular, the rapid increase toward the peak that occurs at $M_f=1.2$ and the gradual decrease thereafter is reproduced. This shows that the variation in power level is primarily governed by the shock strength, and that the rapid decrease of this quantity at the higher Mach numbers is compensated for by the larger span fraction of supersonic flow.

In order to substantiate the predicted acoustic power variation with M_f, measurements were carried out with the engine placed on a standard acoustic test stand. A hard-walled flight inlet was used, with microphones placed 45.7 m away from the test stand in a 180°-arc circular array. Spectra were recorded and a proprietary acoustic source-separation procedure was applied to extract the shock noise in the forward arc. The test data, plotted in Fig. 5, are seen to feature a maximum at $M_f=1.25$, which is in good agreement with the numerical prediction. For $1.25<M_f<1.35$, the dropoff in the test data is in reasonable agreement with the prediction but becomes more pronounced for $M_f>1.35$. Similarly, for $M_f<1.18$, the numerical predictions fall off more slowly than the test data. There are several possible reasons for these discrepancies. Foremost among these is the fact that the effects of the inlet on the shock field is not accounted for in the present model. Furthermore, the use of a flight inlet causes excessively large attenuation of the shock field at the nacelle leading edge. Both of these aspects have been examined in a recent study by Prasad and Feng [19]. Another source of difference between the numerical results and test data is that the model employed here assumes identical blading. In reality, imperfections in the blades due to manufacturing tolerances result in dissimilar shocks, so that weaker shocks are overtaken by their stronger counterparts, and the spatial evolution of the flow field differs from the symmetric case considered here. We note, parenthetically, that this also results in the generation of buzz-saw noise [1,20]. Despite these discrepancies between the tests and predictions, the essential features of the unsteady flow associated with the upstream shocks appear to be well captured.

Wake Turbulence Behavior. We now turn our attention to noise sources associated with the rotor wake. Specifically, the fan exit guide vane is subjected to excitations due to the mean momentum deficit in the rotor wake as well as random turbulent fluctuations generated by the rotor. The response of the FEGV to tonal excitations falls in the category of classical rotor-stator interaction and is addressed later in this paper. Turbulence convected downstream of the rotor is dominated by that contained in the wake, although some contribution may result from that produced by the rotor shock structure at supersonic relative Mach numbers. These unsteady turbulent velocity perturbations induce pressure fluctuations on the FEGV, which are propagated to the far field as broadband noise. Another source of broadband noise is the convection of turbulence past the blade trailing edge, commonly referred to as self-noise.

Disregarding for the purposes of this study the acoustic aspects of broadband noise generation by the turbulence interaction mechanism, we examine here the dependence of the rotor wake turbulence quantities on the operating condition. In particular, we

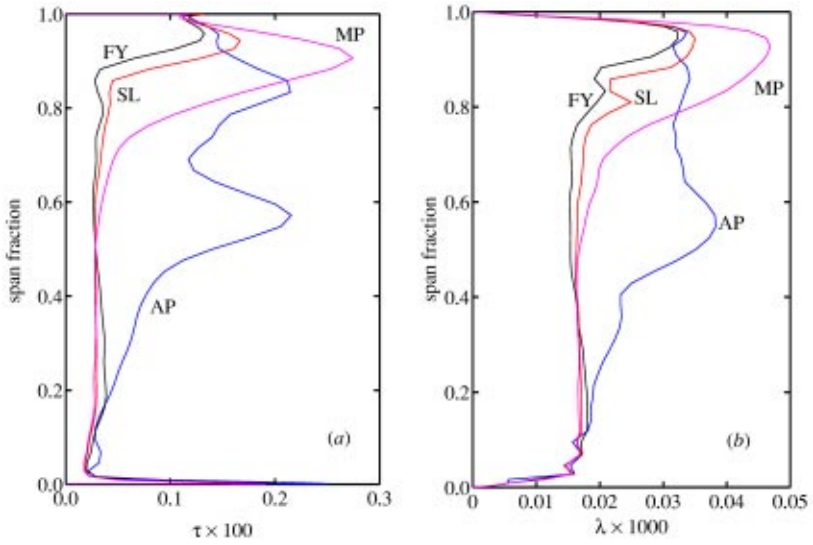

Fig. 6 Radial profiles at $x=2.7$ of (*a*) normalized turbulent kinetic energy and (*b*) normalized turbulent length scale at the approach (AP), flyover (FY), sideline (SL), and maximum power (MP) conditions

study the behavior of the turbulent kinetic energy and that of the integral length scale. These quantities are determined from the parameters of the two-equation turbulence model utilized in the present numerical procedure. In what follows, the turbulent kinetic energy is normalized by U^2, where U is the wheel tip speed and the length scale is normalized by the blade tip chord.

Radial profiles of the normalized circumferentially averaged turbulent kinetic energy τ and length scale λ are shown in Fig. 6 at conditions corresponding to approach, flyover, and sideline as well as a maximum power condition. The profiles are extracted from the flow field on an axial plane that lies at $x=2.7$, about 0.25 stator chord lengths upstream of the FEGV leading edge. It is immediately apparent that the τ and λ distributions at the approach condition differ fundamentally from the three high-speed conditions. Specifically, whereas τ and λ at the higher speeds are dominated by its value near the blade tip, the approach condition exhibits large values near the midspan location.

Focusing on the high-speed conditions, it is observed from Fig. 6 that an increase in engine power from the flyover to the sideline condition and beyond, to that of maximum power, causes the value of τ to increase rapidly in the outer span. This is a consequence of the blade shock structure and may be understood as follows. Returning to Fig. 4, we note that at $M_f=1.30$, which corresponds to the flyover condition, a normal shock forms upstream of the blade leading edge, as observed earlier. The streamlines near the blade suction surface corresponding to this condition are shown in Fig. 7(*a*): the slight displacement of the streamlines in the outer 50% of span reflects the position of the detached shock. For $M_f>1.3$, the normal shock is replaced by an oblique shock with its downstream leg contained in the throat region of the passage, as seen in Fig. 4. This passage shock induces a local separation on the blade suction surface as is evident in the streamlines depicted in Fig. 7(*b*). At this condition, the shock-induced separation extends over about 10% of the outer span. At still higher values of M_f, the passage shock strengthens and extends to lower blade spans, yielding the streamline pattern shown in Fig. 7(*c*). We observe from Fig. 7(*c*) that the shock-induced separated region now occupies nearly 35% of the outer span. These variations with M_f of the shock location and strength are apparent in Fig. 7(*d*), which depicts the change in blade surface isentropic Mach number as the engine operating point is progressively changed from the flyover condition to that of maximum power. Since the occurrence of separation is known to be associated with an increase in turbulent kinetic energy, it is evident that the observed variation of this quantity at the higher speeds in Fig. 6 is due to the behavior of the passage shock. It may be noted that the streamline patterns in Fig. 7 also indicate the existence of secondary flow near the hub that gradually intensifies with increasing wheel speed due to increased loading in this region.

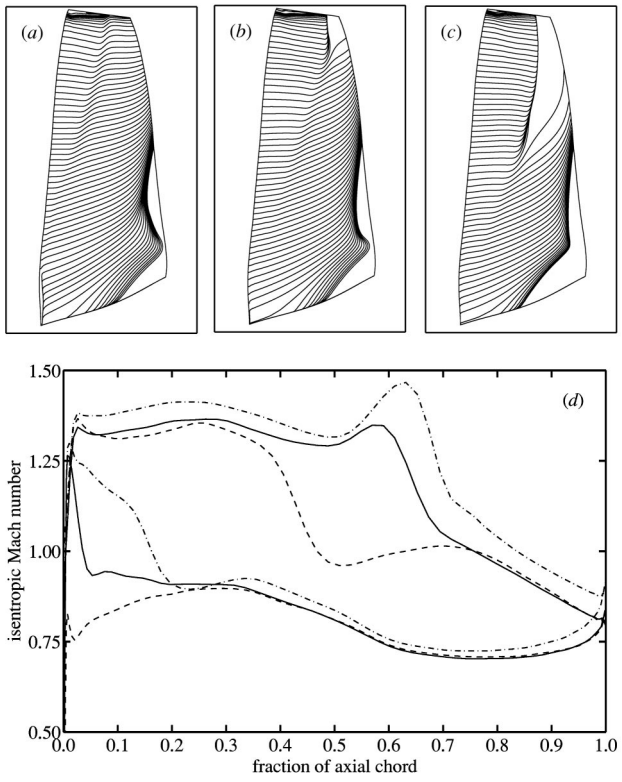

Fig. 7 Streamline patterns near the blade suction surface at the (*a*) flyover, (*b*) sideline, and (*c*) maximum power acoustic conditions. (*d*) Isentropic Mach number distributions at 80% span for the flyover (- - -), sideline (—) and maximum power (-·-·-) conditions.

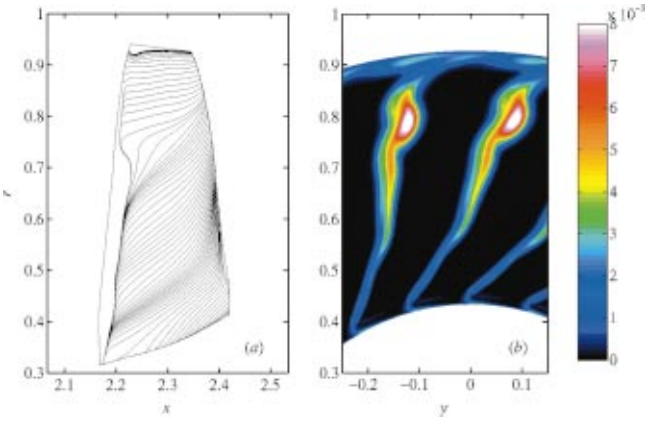

Fig. 8 Flow features associated with the rotor at the approach condition: (*a*) Streamline pattern near blade suction surface and (*b*) contours of normalized turbulent kinetic energy at $x=2.5$

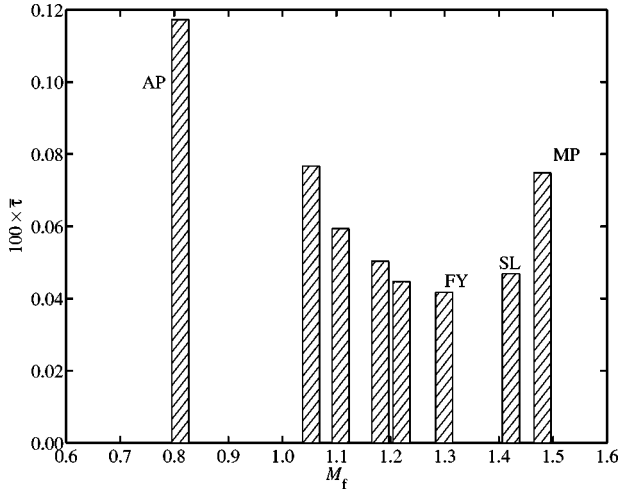

Fig. 9 Average normalized turbulent kinetic energy at $x=2.7$ as function of fan face tip relative Mach number M_f. The approach (AP), flyover (FY), sideline (SL), and maximum power (MP) conditions are indicated.

However, values of τ and λ associated with the secondary flow are not significantly affected by the operating condition.

The values of τ at the approach condition are found to be larger over the entire span than at the other acoustic conditions. For most transonic fans, at the low wheel speeds characteristic of approach, the blade operates at a severely off-design condition. The fan is subjected to high flow incidence causing separation and/or thick boundary layers on the blade suction surface. The separation zones are typically localized near the leading edge as is evident in Fig. 8(*a*), which depicts streamlines near the blade suction surface at the approach condition. The presence of this separation leads to the maxima in the normalized turbulent kinetic energy at the 55% and 80% span locations, while the occurrence of thick boundary layers leads to overall elevated levels of turbulent kinetic energy over the remainder of the span, as illustrated in Fig. 8(*b*).

In the above discussion, it has been implicitly assumed that the FEGV has little or no influence on the turbulence exiting the rotor. In order to verify that this is the case, the sideline radial profile of τ from the isolated rotor calculation was compared with its time-averaged analog from the coupled simulation. The agreement between the two profiles was found to be excellent, thus justifying our use of isolated rotor calculations in the present context.

We now examine the variation of the excitation source for broadband noise over the operating range of the fan. The area-averaged value of τ, denoted by $\bar{\tau}$ is used for this purpose and shown in Fig. 9. As before, the operating point is characterized by the fan face tip relative Mach number M_f. At near-design conditions, $1.2 \lesssim M_f \lesssim 1.35$ and in the vicinity of the flyover condition ($M_f \approx 1.3$), thin boundary layers develop on the blade surfaces, yielding low values of $\bar{\tau}$. At $M_f \approx 1.42$, corresponding to the sideline condition, the inception of a passage shock discussed previously, causes an increase in the average turbulence impinging on the FEGV. When the Mach number is increased further, the development of a strong passage shock extending over the outer 35% of the blade span results in higher turbulence levels in the now wider wakes, causing a sharp increase in the value of $\bar{\tau}$. The somewhat more gradual increase in $\bar{\tau}$ as M_f is decreased from 1.3 is the result of the increased blade incidence as the fan operating point moves farther away from design. The variation of the broadband excitation shown in Fig. 9 is in some ways optimal from the standpoint of noise. Specifically, at the flyover condition, it is advantageous to have a low level of broadband noise, since this reduced power level is selected specifically to alleviate the noise signature of an aircraft after takeoff when it is still in close proximity to the community. A moderate increase in the broadband source toward sideline, although not desirable, is acceptable because it adds only minimally to the already high levels of broadband noise from the jet. The higher level of broadband noise excitation at the approach condition unfortunately worsens a situation already dominated by strong tones generated by rotor-stator interaction in the fan, and from other sources, such as the turbine.

The present results concerning the behavior of the wake turbulence may be viewed in the light of a recent study by Morin [3]. In this study, experimentally measured radial profiles of the turbulent kinetic energy and length scale were used in conjunction with an acoustic model based on the unsteady response of a flat-plate cascade [21]. Despite the simplicity of the model, predictions of the spectra and overall broadband noise levels were found to be in very good agreement with the data. It is then natural to inquire whether the experimentally measured wake data can be replaced with analogous quantities obtained from computations, enabling the creation of a truly predictive system. The present study may be viewed as the first step in this direction.

Unsteady Stage Aerodynamics

An important component of the overall acoustic signature of an engine is the tone noise that is generated at multiples of the blade-passing frequency (BPF) by rotor-stator interaction. Although this aspect of the noise is expected to be dominated by the interaction between the rotor and FEGV, there are frequently flow conditions where the rotor-IGV interaction contributes significantly. Since the FEGV is usually located at a relatively large distance from the rotor, the perturbations due to the latter at the FEGV location are expected to be sufficiently small, so that linearized methods (see, for example [4]) may be applied. The fundamental assumption in these methods is that the perturbations do not alter the mean flow field, which may then be determined independently. The linearized governing equations are solved in the frequency domain for a single blade row subjected to incoming excitations. The determination of the overall unsteady behavior of a stage would therefore require multiple linearized calculations, in addition to those required to determine the mean states in the two airfoil rows. The case of the fan stage is further complicated by the presence of two sets of stators and a region between the rotor and stator that is not a simple annulus owing to the presence of the splitter.

In this study, we determine the unsteady stage behavior in the time, rather than frequency, domain. The time-domain simulation includes the fan rotor, IGV, and FEGV, as indicated previously. Although the numerical model can be applied to study the behav-

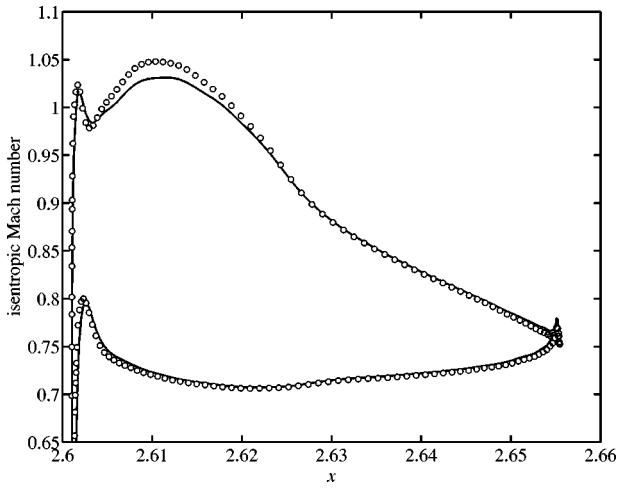

Fig. 10 Isentropic Mach number distribution on the IGV at midspan: the time-averaged coupled calculation result (○) is compared with that of the isolated rotor simulation (—).

ior over all operating conditions, we focus here on an engine setting corresponding to the sideline acoustic certification condition, with the objective of gaining some insight into the unsteady behavior of the flow at high power.

Rotor-IGV Interaction. We begin our study of the unsteady aerodynamics of the fan stage by examining the interaction between the rotor and low-pressure compressor IGV. The IGV is usually designed in isolation of the fan rotor, and the question of whether the mean IGV flow is affected by the unsteady interaction between the two airfoil rows does not appear to have been addressed. Since the IGV is usually in close proximity to the fan, it is to be expected that rotor-stator interaction cannot be neglected, in general. In order to resolve this issue, numerical simulations for both the coupled system and the isolated IGV were carried out in the manner described previously. The resulting blade-loading distributions at the midspan location are illustrated in Fig. 10, where the surface isentropic Mach number is shown as a function of the axial coordinate, at the midspan location. The time-averaged isentropic Mach number obtained from the coupled calculation is observed to be markedly different ($\sim 3\%$) from that corresponding to the isolated simulation, especially near the $\frac{1}{4}$-chord location on the suction surface where the maximum velocity occurs. This may have implications for the veracity of compressor performance parameters determined using a steady isolated blade-row computation. More importantly, the alteration of the mean loading indicates that perturbations in the IGV cannot be regarded as being small and, therefore, that the unsteady response cannot be accurately predicted using linearized methods.

In the context of the present simulations, since the perturbations induced by the rotor on the stator must occur at harmonics of the blade-passing frequency (BPF), it is natural to study the IGV response at these frequencies. The real and imaginary parts[1] of the IGV surface pressures corresponding to the first harmonic of BPF are illustrated in Fig. 11. Here, the unsteady pressure is nondimensionalized by the total pressure far upstream of the fan. The largest pressures occur close to the leading edge, as expected, but the pressure amplitude further downstream is not particularly small. In fact, it is evident from Fig. 11 that unsteady pressures as high as 3% of the upstream total pressure are generated even at the midchord location. The existence of this large unsteady loading has a bearing on noise generation, high-cycle fatigue life, and on the loss characteristics of the IGV.

[1]The real and imaginary parts represent quantities that are temporally 90° out of phase with each other.

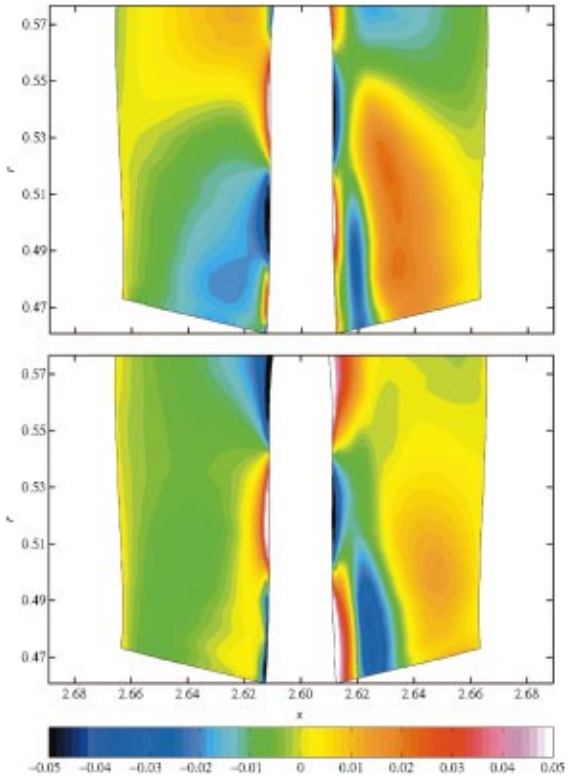

Fig. 11 Unsteady pressure distribution on the IGV. The real part (upper panel) and imaginary part (lower panel) are shown on the pressure (left) and suction (right) surfaces.

The highly swirling flow that leaves the blade trailing edge causes the wakes to become skewed as they enter the IGV. The rotor wakes, identified by contours of normalized turbulent kinetic energy τ, are depicted in Fig. 12 at the entrance plane of the IGV. The wake skew is evident, and any given IGV is intersected by multiple wakes, which is responsible for the four-lobed pattern in the unsteady pressure at the vane leading edge in Fig. 11.

Another aspect of the wakes that is apparent from Fig. 12 is that they occupy a large portion of the vane passage. The presence of a velocity deficit in the wake region results in a lower transported mass flux through the IGV than would have been transported in

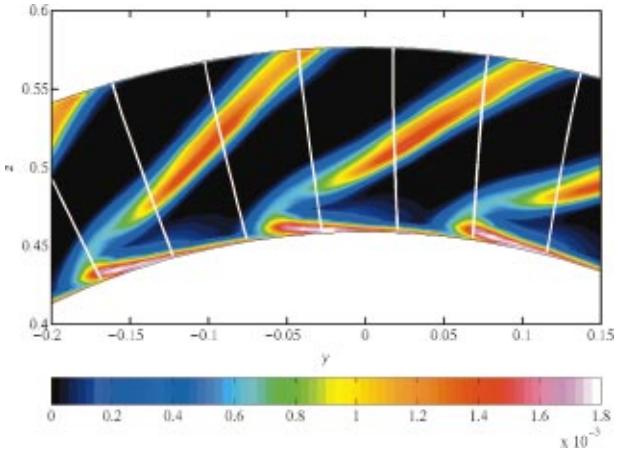

Fig. 12 Normalized turbulent kinetic energy τ associated with the rotor wakes entering the IGV. The IGV leading edges are indicated. The view shown is from downstream and rotor motion is counterclockwise.

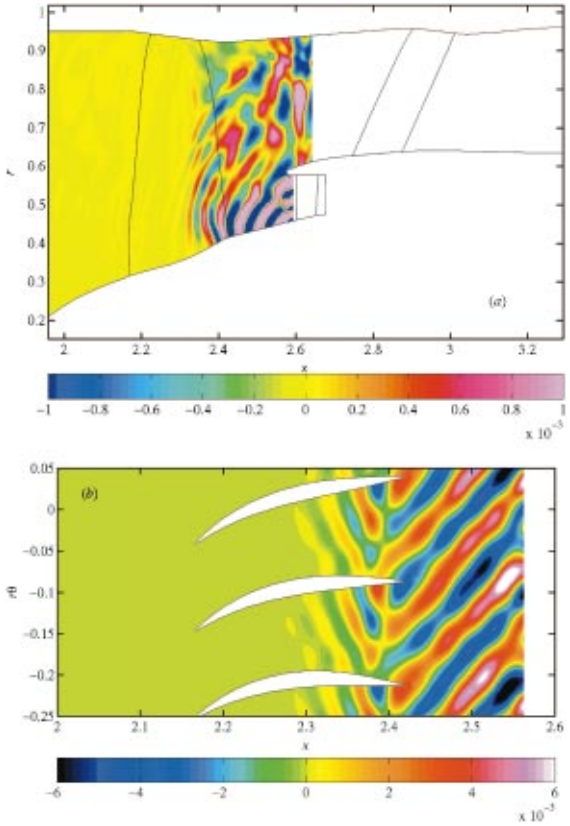

Fig. 13 Real part of the rotor-frame unsteady pressure field at the vane passing frequency on (*a*) a meridional midrotor passage plane and (*b*) radial plane located at the IGV midspan

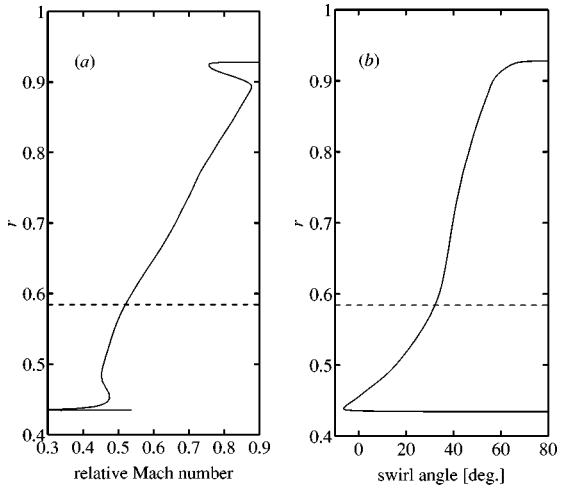

Fig. 14 Radial profiles of (*a*) relative Mach number and (*b*) relative swirl angle at $x=2.5$. The splitter location is indicated by the broken line.

its absence, thus introducing a flow blockage. Using concepts from boundary layer theory, Khalid et al. [22] have developed a method for calculating of the blockage caused by endwall flows. Employing their method and considering the wake deficit to be comprised of two adjoining boundary layer-like velocity profiles, the blockage introduced by the rotor wakes in the IGV passage was computed. Results from the time-accurate simulations at the interfacial plane (shown by the broken line in Fig. 1) are used to calculate the blockage due to the rotor wakes outside the hub endwall boundary-layer region. Excluding the latter so as to ascertain blockage due to the wakes alone, it is found that the wakes result in a blockage of about 4% of the rotor passage, which is a typical value for moderate to strongly loaded airfoil rows [22]. However, the disparity of scale between the rotor and IGV passages causes the blockage to be magnified by the blade count ratio, in this case a factor of 5/2. This leads to the somewhat surprising result that the rotor wake causes a blockage of nearly 10% of the average IGV passages, as can be confirmed by estimating the relative area occupied by the wake in Fig. 12. Such elevated levels of rotor wake blockage, which are usually not accounted for during the design of the low pressure compressor, can have implications on its performance characteristics.

As alluded to earlier, the large unsteady loads on the IGV can be expected to generate a strong acoustic response. The upstream-propagating acoustic waves generated by the rotor-stator interaction are examined on a midpassage computational plane in Fig. 13(*a*). Since the plane is phase locked to the rotor, any unsteadiness in the rotating reference frame can be decomposed into harmonics of the vane-passing frequency. Contours of the real part of the unsteady pressure at the first harmonic of this frequency demonstrate the evolution of these disturbances at they propagate upstream. The four-lobed pattern, referred to earlier, is again visible at $x=2.58$. The pressure perturbations generated by the rotor-stator interaction propagate upstream of the IGV in a configuration that is initially an annular duct. At the splitter leading edge, the annular duct ceases to exist and the waves are radiated into the space between the blade trailing edge and splitter leading edge. The flow in the neighborhood of the splitter leading edge is rather complex, and it appears that the IGV-generated acoustic field undergoes some diffraction there. The wave crests emanating from the short duct upstream of the IGV rapidly become curved. In addition to the natural tendency for the wave fronts to spread as they propagate into the space between the rotor and stator, this curvature is also caused by the variation of the mean flow in this region. This is exemplified in Fig. 14, where radial profiles of the circumferentially averaged relative frame Mach number and swirl angle on an axial plane located at $x=2.5$ are depicted. The radial variation of both quantities is not insignificant, and results in a refraction of the acoustic field [23]. This issue has been emphasized by Cumpsty [24], who also showed that the root section of the blade, by virtue of its smaller stagger angle, is more conducive to wave propagation through the passage. Indeed, we observe from Fig. 13(*a*) that although no disturbance is transmitted through the rotor, the acoustic waves generated via rotor-IGV interaction travel farthest upstream near the root. We examine this in more detail in Fig. 13(*b*), which depicts a blade-to-blade view of the perturbation pressure field on a computational plane near the IGV midspan location. The acoustic disturbance is observed to propagate into the blade passage to a distance of approximately 25% of the rotor chord before it is completely reflected. Thus, the acoustic energy generated by the rotor-IGV interaction will be radiated to the far field through the aft duct, after undergoing interaction with the FEGV. It is also conceivable that other compressor tones may be perceived in the aft far field by a similar mechanism.

Although we have focused on the acoustic waves scattered by the IGV, it is evident from Fig. 13(*a*) that similar disturbances scattered by the FEGV are present, especially in the bypass duct. Like their IGV counterparts, these waves also are completely reflected by the rotor and, upon reflection, impinge on the FEGV. The interaction between the rotor and FEGV is examined next.

At the sideline condition considered here, with high inlet and blade passage Mach numbers, no transmission of acoustic waves occurs through the rotor. However, it is entirely possible that at a low-power setting, such as that corresponding to approach, the acoustic waves generated by the rotor-IGV interaction may propagate upstream through the rotor to be perceived as inlet noise.

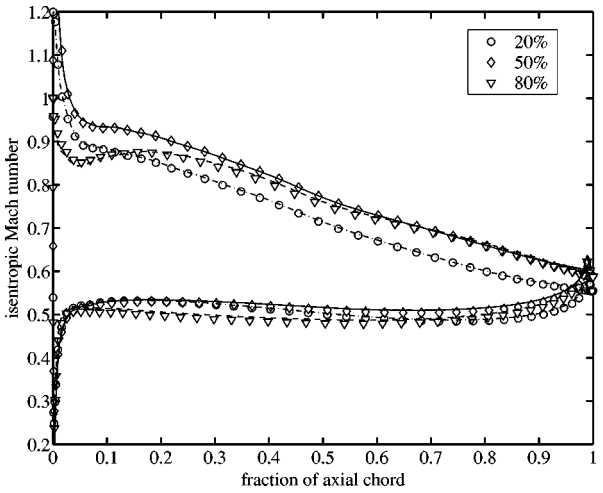

Fig. 15 Isentropic Mach number on the FEGV at three spanwise locations obtained from the coupled time-averaged simulation (symbols) and the isolated calculation (lines)

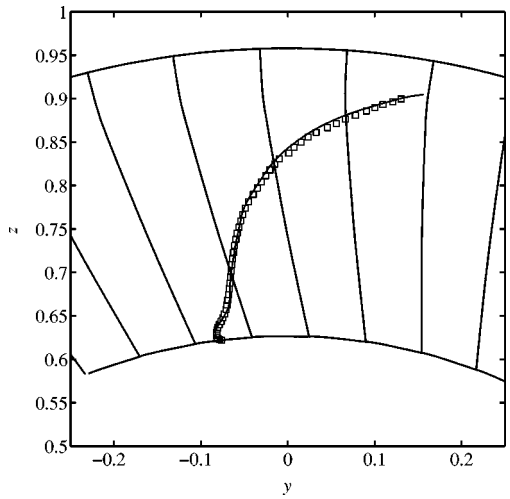

Fig. 16 Comparison of the locus of maximum rotor wake velocity deficit from the coupled (□) and isolated rotor (—) simulations at $x=2.75$

Rotor-FEGV Interaction. We now turn to the unsteady interaction between the FEGV and rotor, which is expected to be the dominant source of tone noise, as indicated earlier. The spacing between the FEGV and rotor is therefore usually large so as to reduce this unsteady interaction and thereby the noise that is generated.

Coupled unsteady and isolated steady simulations were carried out in a manner similar to that described earlier for the IGV. The time-averaged vane surface isentropic Mach number obtained from the unsteady calculation is compared with the analogous steady quantity in Fig. 15 at three spanwise locations. Unlike the IGV case, the two loading distributions are in very good agreement with each other, demonstrating that the mean flow through the vane is not altered by the perturbations, justifying the use of linearized methods for this interaction.

We have shown previously that the mean rotor flow is not affected by the presence of the stator, and it is of interest to inquire whether this is true for the perturbation field as well. To this end, we examine in Fig. 16 the locus of the maximum wake deficit on an axial plane located 0.2 FEGV chord lengths upstream of the FEGV hub leading edge. The loci obtained from the coupled calculation and isolated rotor simulation are shown and were determined using profiles of the velocity deficit, vorticity, and turbulent kinetic energy in the blade-to-blade direction. Also shown in Fig. 16 are projections of the FEGV leading edges on the axial plane. We observe that the wake locus obtained from the isolated computation agrees very well with that of the coupled simulation, indicating that the wakes, like the blade mean flow, are not affected to any significant extent by the upstream influence of the FEGV.

The locus of maximum wake deficit in Fig. 16 is observed to be highly skewed, especially in the outer span. This is a result of the spanwise rotor loading distribution. Specifically, the large stagger of the rotor in the outer span results in the swirl angle shown in Fig. 14(*b*) and causes the wake fluid there to lag that at the inner diameter, yielding the shape in Fig. 16 for the locus of maximum wake deficit. The highly skewed wakes result in a given vane being intersected by multiple wakes, which is beneficial from the point of view of noise generation. In particular, it has been shown [25,26] that for uniform mean flows, the effect of multiple wake intersections is to couple the unsteady response more efficiently to higher-order duct modes, which tend to be evanescent, i.e., exponentially decaying along the axial direction. In the case of nonuniform flows, the benefits are diminished by the fact that the pressure field is distributed into other radial modes that may propagate [24]. The blade spanwise loading distribution does, nonetheless, offer the engine designer a means to control the tone noise generated by rotor-stator interaction.

In view of the fact that the time-mean rotor field is unaffected by the presence of the FEGV, the excitation due to the rotor may be determined from an isolated rotor calculation. Then, denoting the azimuthal coordinate by θ and the rotor angular speed by Ω, and decomposing the (deterministic) excitation field as a Fourier series, we obtain

$$(\rho,\mathbf{v},p)^T=(\overline{\rho},\overline{\mathbf{V}},\overline{p})^T+\sum_{n=1}^{\infty}(\tilde{\rho}_n,\tilde{\mathbf{v}}_n,\tilde{p}_n)^T e^{inN_B(\Omega t-\theta)} \tag{3}$$

where ρ, $\mathbf{v}$, and p represent the density, velocity and pressure, N_B is the number of rotor blades, and the overbars represent circumferential averages. The flow quantities on the right-hand side of Eq. (3) are functions of x and r. When the rotor excitation impinges on a stator row comprised of N_V vanes, the linear response field consists of multiple scattered modes [27] and may be written as

$$\sum_{n=1}^{\infty}\sum_{m=-\infty}^{\infty}(\hat{\rho}_{nm},\hat{\mathbf{v}}_{nm},\hat{p}_{nm})^T e^{i(mN_V-nN_B)\theta}e^{inN_B\Omega t} \tag{4}$$

where $\hat{\rho}_{nm}$, $\hat{\mathbf{v}}_{nm}$, and $\hat{p}_{nm}$ are functions of x and r. The integer m is usually referred to as the scattering index. The nth harmonic $(\tilde{\rho}_n,\tilde{\mathbf{v}}_n,\tilde{p}_n)^T$ of the excitation field can be determined from the steady isolated rotor calculation by performing a spatial Fourier transform.

The normalized magnitude and phase of the excitation fields $(\tilde{\rho}_n/\rho_*,\tilde{\mathbf{v}}_n/v_*,\tilde{p}_n/p_*)^T$ for the fundamental component $(n=1)$ are shown in Fig. 17(*a*) as functions of the radial coordinate at the axial station corresponding to the FEGV hub leading edge. The reference values ρ_*, v_*, and p_* are the plane-averaged values of the density, axial velocity, and pressure at this axial station, respectively. The velocity perturbation is dominated by its axial component $(\tilde{v}_{x,1})$ in the outer span and by the radial component $(\tilde{v}_{r,1})$ in the inner span of the annulus. The tangential component of perturbation velocity $(\tilde{v}_{\theta,1})$ is nearly uniform over the span and has a value about half that of the other two components. The relatively large magnitude of $(\tilde{v}_{r,1})$ and the strong variation of the perturbation velocity over the height of the annulus demonstrates that the excitation is highly three-dimensional in nature and, therefore, that stripwise approaches [28,29] for computing the unsteady response are likely to be inaccurate. The perturbation pressure

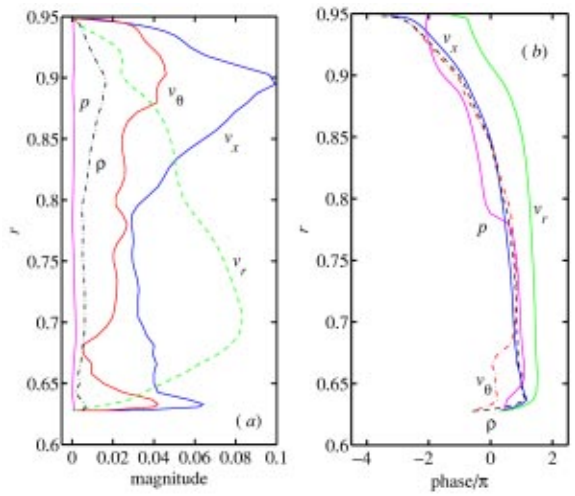

Fig. 17 Radial profiles at $x=2.7$ of the (*a*) magnitude and (*b*) phase of the normalized gust excitation components at BPF

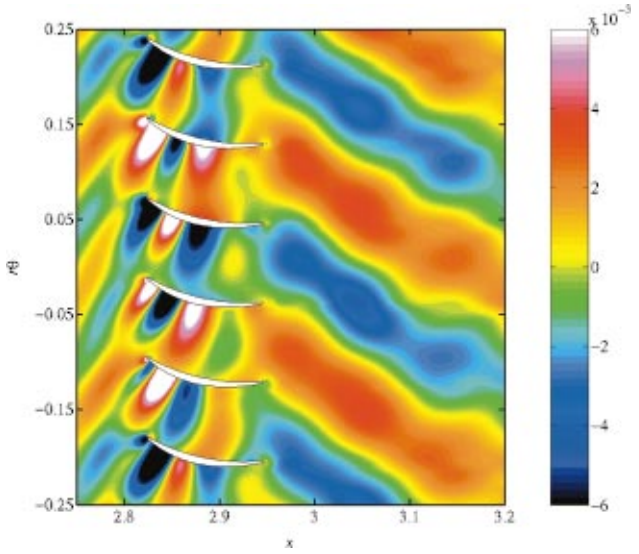

Fig. 19 Real part of unsteady pressure at BPF on a midspan plane through the FEGV

associated with the wake is observed to be quite small; this indicates that although vortical and pressure disturbances in a swirling flow are coupled [30], this coupling is weak for the present flow. The phase variation of all the perturbation quantities, shown in Fig. 17(*b*), is similar and decreases from hub to tip. This is consistent with our previous observation concerning radial differences in the wake transport caused by the blade stagger.

Next, we study the FEGV response by examining in Fig. 18 the real and imaginary parts of the surface unsteady pressure (normalized by the far upstream total pressure) corresponding to the fundamental excitation. As in the case of the IGV, the unsteady pressure is greatest at the leading edge, but the magnitude remains large at a distance of 0.3 chord lengths downstream of the leading edge. The intersection of the FEGV by multiple wakes is manifested by the presence of several lobes in the unsteady pressure on the suction surface, where the magnitude is as high as 3%. The pressure surface response is much smaller than that on the suction surface, but also displays a strongly three-dimensional character.

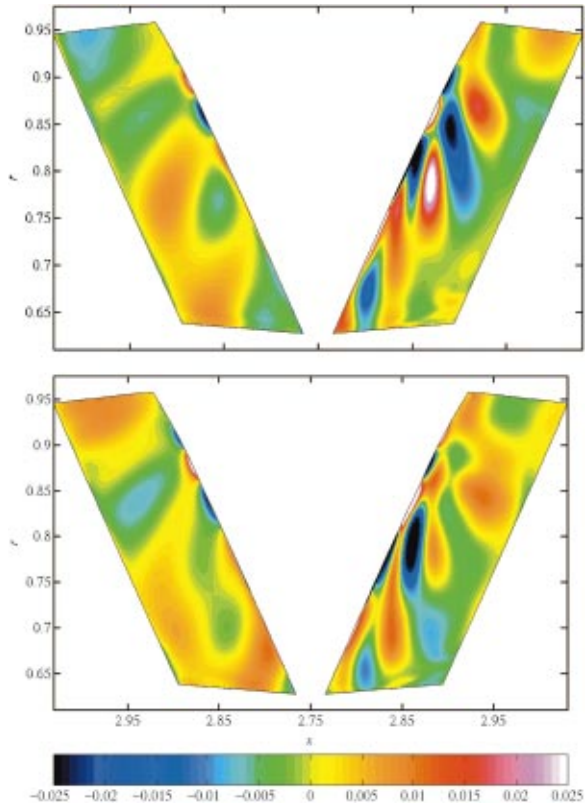

Fig. 18 Unsteady static pressure perturbation on the FEGV at BPF. The real part (upper panel) and imaginary part (lower panel) are shown on the pressure (left) and suction (right) surfaces.

The noise generated by rotor-stator interaction consists of two interlinked processes: response of the stator to incoming rotor-induced disturbances and the coupling of this stator response to the duct in which the stator row lies. The real part of the unsteady pressure field corresponding to the fundamental frequency on a computational plane located at the midspan of the FEGV is illustrated in Fig. 19. Acoustic waves generated by the rotor-stator interaction are observed to propagate away from the stator both upstream and downstream. A significant portion of the FEGV appears to participate in the generation of these waves, consistent with the surface pressure response in Fig. 18. An approximate eigenanalysis of the circumferentially averaged inlet and exit flow fields based on the procedure of Verdon et al.[4] reveals that the propagating modes at the FEGV inlet and exit boundaries possess scattering indices $m=0$ and $m=1$ respectively, which is in accord with the circumferential structure in Fig. 19.

The propagating disturbances are associated with a specific radial structure as well. The magnitude of the unsteady pressure at the fundamental frequency is illustrated in Fig. 20(*a*) on a computational plane that lies one chord length downstream of the FEGV trailing edge and approximately perpendicular to the axial direction. We observe that the maximum value occurs near the midspan location, relatively far from both the inner and outer radii of the duct. This is in contrast to the low radial-order pressure eigenfunctions for a uniform flow [27], which achieve their maximum values at or near the outer wall. This is a consequence of the radial gradients in the mean flow, which are evident in the radial Mach number profile at this location, shown in Fig. 20(*b*). The radial structure of the pressure field in Fig. 20 has implications for the design and deployment of acoustic liners in the fan duct. The liner is most effective when it lies in close proximity to regions of large pressure excursions. Therefore, liners placed at either of the duct walls, as is conventional, are not likely to attenuate the blade-passing frequency perturbation to any significant extent at this operating condition.

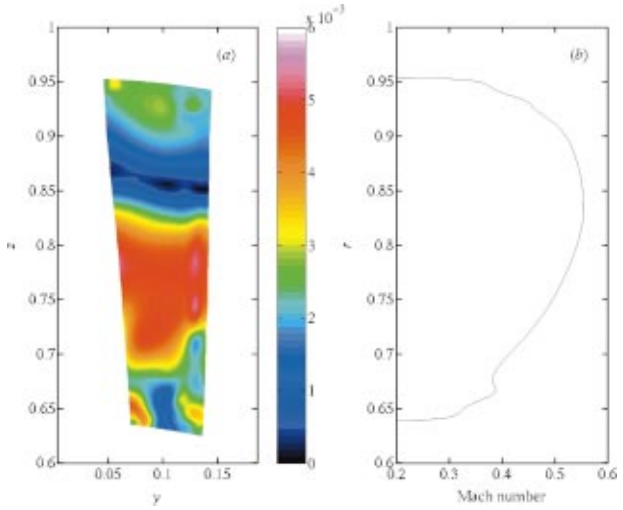

Fig. 20 (*a*) Magnitude of unsteady pressure at BPF and (*b*) radial profile of absolute Mach number on a plane downstream of the FEGV

Conclusions

A numerical investigation of the unsteady flow in a fan stage consisting of rotor, fan exit guide vane (FEGV) and the inlet guide vane (IGV) of the low-pressure compressor is conducted. The time-mean rotor loading is found to be virtually unaffected by the presence of the downstream airfoil rows, allowing the use of isolated rotor calculations to examine the variation of shock noise and wake turbulence over the operating range of the fan.

The variation of the shock noise with engine power was examined and found to achieve a maximum close to the flyover acoustic certification condition. This behavior was shown to be the result of the competing effects of increasing supersonic blade span fraction and decreasing shock strength with increasing engine power. An important aspect of shock noise not addressed here is the influence of the inlet. Specifically, the shape of the inlet contour and the nature of the acoustic treatment have a significant effect on magnitude and directivity of the radiated noise.

The wake turbulence entering the FEGV was also quantified as a function of the engine power setting and found to be lowest at the flyover condition. This is not surprising, since the condition is aerodynamically similar to the design intent. As the power is lowered to the approach condition, the wake turbulence increases greatly due to the development of a leading-edge separation zone. When the engine power is increased to the maximum power condition, the turbulence increases again, albeit to a lesser degree. This increase is caused by the formation of a separated region induced by the strong passage shock.

The unsteady interaction between the rotor and the two downstream stator rows was investigated next at the sideline condition. Owing to the close proximity of the IGV and rotor, the wake excitation due to the latter causes a change in the IGV mean flow. Specifically, it was shown that the mean IGV loading obtained using coupled unsteady and isolated steady analyses differs significantly. This violates the fundamental assumption on which linearized methods are based, thus precluding estimation of the unsteady response using such methods. Moreover, the rotor wakes were found to cause a blockage corresponding to about 10% of the IGV passage. These results have implications for the design of the low-pressure compressor, which is usually conducted independently of the fan. However, it would appear from the present results that, by properly accounting for the effects of the fan rotor, the performance and, possibly, the operability of the low-pressure compressor can be enhanced. The unsteady surface pressures on the IGV caused by the rotor wake excitation were also found to be quite large. In view of the fact that these surface pressure values are likely to induce large unsteady loads on the IGV, the fatigue life of this component can be affected by its close proximity to the rotor. The upstream acoustic waves generated by the rotor-IGV interaction are found to propagate into the rotor passage, where they are reflected into the bypass duct.

The unsteady interaction between the rotor and FEGV was found to be well represented as a linear process, which justifies the application of linearized analyses to estimate the acoustic response. The unsteady pressure on the FEGV at the blade-passing frequency was found to possess significant spanwise variation, a feature that may be attributed to both the strong wake skew and the three-dimensional nature of the swept FEGV geometry. Downstream of the FEGV, the propagating acoustic response at the blade-passing frequency was shown to be dominant away from the duct walls, suggesting that conventionally placed acoustic liners may be of limited effectiveness in attenuating this harmonic.

Acknowledgment

The authors are grateful to Pratt & Whitney for granting permission to publish the present work. In particular, they wish to express their gratitude to Dr. Jayant Sabnis for his encouragement and support during the course of this study. They are also indebted to Dr. Wesley Lord, Dr. Jinzhang Feng, and Dr. Bruce Morin for several fruitful discussions.

References

[1] Cumpsty, N. A., 1977, ''A Critical Review of Turbomachinery Noise,'' ASME J. Fluids Eng., **99**, pp. 278–293.
[2] Smith, M. J. T., 1989, *Aircraft Noise*, Cambridge University Press, Cambridge, England.
[3] Morin, B. L., 1999, ''Broadband Fan Noise Prediction System for Gas Turbine Engines,'' AIAA Paper No. 99-1889.
[4] Verdon, J. M., Montgomery, M. D., and Chuang, H. A., ''Development of a Linearized Unsteady Euler Analysis With Application to Wake/Blade-Row Interactions,'' NASA CR-1999-208879.
[5] Ni, R.-H., 1982, ''A Multiple-Grid Scheme for Solving Euler Equations,'' AIAA J., **20**, pp. 1565–1571.
[6] Davis, R. L., Ni, R.-H., and Carter, J. E., 1986 ''Cascade Viscous Flow Analysis Using the Navier-Stokes Equations,'' AIAA Paper No. 86-0033.
[7] Wilcox, D. C., 1998, *Turbulence Modeling for CFD*, DCW Industries, La Cañada, CA.
[8] Giles, M. B., 1990, ''Non-Reflecting Boundary Conditions for Euler Equation Calculations,'' AIAA J., **28**, pp. 2050–2058.
[9] Ni, R.-H., and Bogoian, H., 1989 ''Predictions of 3-D Multi-Stage Turbine Flow Fields Using a Multiple-Grid Euler Solver,'' AIAA Paper No. 89-0233.
[10] Ni, R.-H., and Sharma, O. P., 1990 ''Using a 3-D Euler Flow Simulation to Assess Effects of Periodic Unsteady Flows,'' AIAA Paper No. 90-2357.
[11] Davis, R. L., Shang, T., Buteau, J., and Ni, R.-H., 1996, ''Prediction of 3-D Unsteady Flow in Multi-Stage Turbomachinery Using an Implicit Dual Time-Step Approach,'' AIAA Paper No. 96-2565.
[12] Prasad, A., 2003, ''Evolution of Upstream Propagating Shock Waves from a Transonic Compressor Rotor,'' ASME J. Turbomach., **133**, pp. 133–140.
[13] International Civil Aviation Organization, ''Environmental Protection, Aircraft Noise,'' Annex 16, Vol. 1.
[14] Calvert, W. J., and Ginder, R. C., 1999, ''Transonic Fan and Compressor Design,'' Proc. Inst. Mech. Eng., Part C: J. Mech. Eng. Sci., **213**(C5), pp. 419–436.
[15] Kantrowitz, A., 1950, ''The Supersonic Axial-flow Compressor,'' NACA Report 974.
[16] Ferri, A., 1964, ''Aerodynamic Properties of Supersonic Compressors,'' *High Speed Aerodynamics and Jet Propulsion, Volume X: Aerodynamics of Turbines and Compressors*, W. R. Hawthorne (ed.), Princeton University Press, Princeton, NJ.
[17] Morfey, C. L., and Fisher, M. J., 1970, ''Shock-wave Radiation from a Supersonic Ducted Rotor,'' J. R. Aeronaut. Soc., **74**, pp. 579–585.
[18] Morfey, C. L., 1971, ''Acoustic Energy in Non-uniform Flow,'' J. Sound Vib., **74**, pp. 159–170.
[19] Prasad, D., and Feng, J., 2003 ''Propagation and Decay of Shock Waves in Turbofan Inlets,'' ASME J. Turbomach., **127**, pp. 117–126.
[20] Pickett, G. F., 1972, ''Prediction of the Spectral Content of Combination Tone Noise,'' J. Aircr., **9**, pp. 658–663.
[21] Hanson, D. B., 1999, ''Influence of Lean and Sweep on Noise of Cascades With Turbulent Inflow,'' AIAA/CEAS Paper No. 99-1863.
[22] Khalid, S. A., Khalsa, A. S., Waitz, I. A., Tan, C. S., Greitzer, E. M., Cumpsty, N. A., Adamczyk, J. J., and Marble, F. E., 1999, ''Endwall Blockage in Axial Compressors,'' ASME J. Turbomach., **121**, pp. 499–509.
[23] Goldstein, M. E., 1976 *Aeroacoustics*, McGraw-Hill, New York.
[24] Cumpsty, N. A., 1972, ''Tone Noise from Rotor/Stator Interactions in High Speed Fans,'' J. Sound Vib., **24**, pp. 393–409.

[25] Namba, M., 1977, ''Three-dimensional Analysis of Blade Force and Sound Generation for an Annular Cascade in Distorted Flows,'' J. Sound Vib., **50**, pp. 479–508.
[26] Schulten, J. B. H. M., 1982, ''Sound Generated by Rotor Wakes Interacting with a Leaned Vane Stator,'' AIAA J., **20**, pp. 1352–1358.
[27] Tyler, J. M., and Sofrin, T. G., 1962, ''Axial Flow Compressor Noise Studies,'' Trans. ASAE, pp. 309–332.
[28] Topol, D.A., 1998, ''TFaNS Tone Fan Noise Design/Prediction System, Vol. 1: System Description, CUP3D Technical Documentation and Manual for Code Developers,'' NASA CR-1999-208882.
[29] Meyer, H. D., and Envia, E., 1996 ''Aeroacoustic Analysis of Turbofan Noise Generation,'' NASA CR-4715.
[30] Kerrebrock, J. L., 1977, ''Small Disturbances in Turbomachine Annuli with Swirl,'' AIAA J., **15**, pp. 794–803.

Suppression of Unstable Flow at Small Flow Rates in a Centrifugal Blower by Controlling Tip Leakage Flow and Reverse Flow

Mashiro Ishida
e-mail: hiro@net.Nagasaki-u.ac.jp
Mem. ASME

Taufan Surana

Hironobu Ueki

Daisaku Sakaguchi

Department of Mechanical Systems Engineering,
Graduate School of Science and Technology,
Nagasaki University,
Nagasaki 852-8521, Japan

The effects of the inlet recirculation arrangement on inducer stall and the diffuser width on diffuser stall in a high-specific-speed-type centrifugal impeller with inducer were analyzed by numerical simulation and also verified experimentally. It was found that the incipient unstable flow occurs due to a rolling-up vortex flow, resulting from an interaction between the tip leakage flow and the reverse flow accumulated at the pressure side immediately downstream of the inducer tip throat, in which a strong streamwise component of vorticity is included. By forming the inlet recirculation flow, the tip leakage vortex is effectively sucked into the suction ring groove, and the flow incidence is decreased simultaneously. The unstable flow range of the test blower was reduced significantly by about 45% without deteriorating the impeller characteristics by implementing optimally both the ring groove arrangement and the narrowed diffuser width.
[DOI: 10.1115/1.1811092]

Introduction

In a high specific speed-type open shrouded centrifugal impeller, a periodic unstable flow occurs at small flow rates mainly due to inducer stall, sometimes due to diffuser stall. According to experimental studies conducted previously by the authors (Ishida et al. [1,2] and Ueki et al. [3]), the unstable flow in a centrifugal impeller with short inducer blades was identified as being due to inducer stall, and the three-dimensional (3D) turbulent flow analyses [4–6] showed that this stall inception was mainly due to a blade-leading separation that resulted from the excessive flow incidence at small flow rates. In order to suppress this kind of unstable flow and to improve both surge and choke margins, Fisher [7] suggested a bypass arrangement in which a recirculation flow was formed from the inducer throat to compressor inlet based on the pressure difference between these two regions through the bypass. Ishida et al. [5] also proposed a similar ring-groove arrangement that consisted of two ring-shaped grooves and an annulus connecting the two grooves, functioning as a bypass. The front groove was located upstream of the impeller inlet, and the rear one was at the inducer tip throat. The widths of the front and rear grooves were adjusted independently in the experiment to obtain the maximum effect on the inducer stall suppression.

In order to clarify further the mechanism of unstable flow due to inducer stall, Sun et al. [8], Ishida et al. [9], Sun et al. [10], and Taufan et al. [11] have investigated the effect of a blade-leading shape on unstable flow inception. The 3D turbulent flow simulation was performed to analyze the effect of the inducer blade-leading shape on the blade-leading separation bubble as well as the reverse flow along the shroud wall. The shape of blade leading was changed in two types: the flat blade-leading edge and the rounded one, without changing the overall blade profile in both cases. The 3D flow simulation and experiment showed that the unstable flow occurred when a large separation bubble appeared near the blade leading on the suction surface in the case of the flat blade-leading edge. In the case of the rounded one, the unstable flow occurred without appearance of a separation bubble at the corresponding flow rates. These results indicate that the blade-leading separation is not always the cause of unstable flow, but it might be one of the triggers of the unstable flow inception.

The unsteady flow simulation was performed by Furukawa et al. [12,13] in an axial compressor rotor at near-stall conditions. The results showed that the spiral-type breakdown of the tip leakage vortex occurs inside the rotor passage at near-stall conditions, and downstream of the breakdown onset, the tip leakage vortex twists and turns violently with time, thus interacting with the pressure surface of the adjacent blade. These results are very suggestive for understanding the mechanism of unstable flow inception due to inducer stall.

With respect to the unstable flow due to diffuser stall in centrifugal blowers, various devices for suppression of diffuser stall have been investigated: throttling at the diffuser exit [14], reduction of diffuser inlet width [15], circular cascade diffuser with a low solidity [16], variable diffuser guide vane in combination with impeller inlet guide vane [17], a swirl breaker consisting of many shallow radial grooves distributed properly on the diffuser wall [18], and jet injection in the counterdirection of impeller rotation [19]. Ishida et al. [20] have implemented a completely rough-wall condition only on the hub side wall downstream of $R=1.20$. As the result, the 3D separation was suppressed remarkably as the turbulent intensity increased, and the flow rate of the unstable flow inception was successfully decreased by 42% with a small pressure drop of less than 1%.

In the present study, 3D turbulent flow simulations and experimental works were performed in a high-specific-speed-type open shrouded centrifugal impeller with a radial vaneless diffuser to clarify the mechanism of the unstable flow inception and to analyze the effect of the inlet recirculation on inducer stall and the effect of the diffuser width on diffuser stall. A ring-groove arrangement has been adopted again in the present study with some modifications. The ring groove was located on the shroud wall near the inducer tip throat, which was connected with an enlarged suction pipe upstream of the impeller inlet through an annular bypass. The computational results show that the inlet recirculation flow rate is strongly dependent on both the location of the ring groove and the through-flow rate, and that the occurrence of the reverse flow in the impeller is suppressed by forming the inlet

Contributed by the International Gas Turbine Institute (IGTI) of THE AMERICAN SOCIETY OF MECHANICAL ENGINEERS for publication in the ASME JOURNAL OF TURBOMACHINERY. Paper presented at the International Gas Turbine and Aeroengine Congress and Exhibition, Vienna, Austria, June 13–17, 2004, Paper No. 2004-GT-53400. Manuscript received by IGTI, October 1, 2003; final revision, March 1, 2004. IGTI Review Chair: A. J. Strazisar.

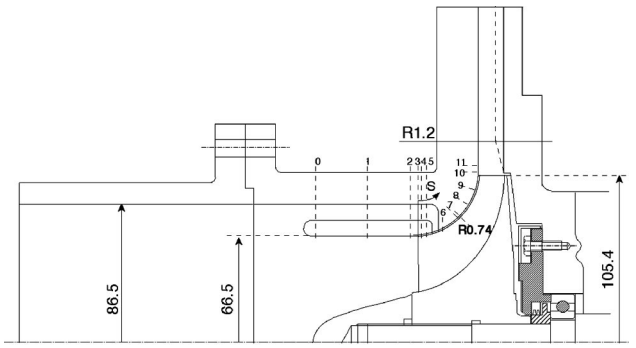

Fig. 1 Meridional section of test blower with $S_G^*=0.21$ groove and $b_e=15$ or 10 [mm]

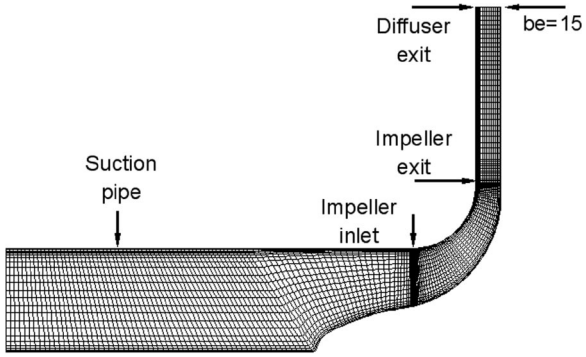

Fig. 2 Computational grid for test blower; STD casing with $b_e=15$ [mm]

recirculation flow. The effects of the ring-groove arrangement and the diffuser configuration on the impeller characteristics are investigated numerically and experimentally for both suppression of the inducer and diffuser stalls without deteriorating the blower performance, even at the design flow rate.

Experimental Apparatus

Figure 1 shows the meridional section of the test blower. The centrifugal blower consists of a high-specific-speed-type impeller and a parallel wall vaneless diffuser with the exit radius ratio of about $R=2.0$. The impeller is an unshrouded and inducer integrated one with 20 inducer blades and radial blades; the exit diameter is 210.8 mm and the inlet diameter is 132 mm. The blade-leading edge is vertical to the impeller rotation axis, and the inlet blade angles are 34 and 55 deg at the blade tip and blade root, respectively, from the circumferential direction. The blade heights are 35 and 15 mm at the inlet and exit, respectively, and the clearance between the impeller blade tip and the shroud wall is 0.5 mm. The air is sucked into the blower through a straight suction pipe and discharged axisymmetrically into the atmosphere through the vaneless diffuser. The diffuser width is a constant of 15 mm in the standard case, but it is reduced to 10 mm downstream of $R=1.2$ in order to suppress diffuser stall as shown by the broken line in Fig. 1. A 4 mm wide ring-shaped suction groove is located on the shroud wall near the inducer tip throat, which is connected through the annular bypass, with the enlarged suction pipe of 173 mm dia upstream of the impeller inlet. Furthermore, the suction pipe is 133 mm dia in the standard case. In the experiment, the impeller was operated at a constant speed of 4000 rpm, and the flow rate was decreased to the surge limit from the larger side. The specific speed defined by $\phi^{1/2}\psi_{S2}^{-3/4}$ was 0.58 at the design flow coefficient of $\phi_d=0.36$. The time-mean wall static pressure was measured at 12 pressure taps along the shroud wall; each tap was placed at four positions, circumferentially. The pressure fluctuation was measured on the shroud-casing wall at two points apart, circumferentially, on the radial position of $R=0.74$ ($S^*=0.49$), downstream of the inducer tip throat by using a small semiconductor pressure transducer made by Kulite.

Numerical Calculation Method

In the numerical simulation, the flow was assumed to be incompressible and steady with reference to the relative frame. The 3D turbulent flow in the impeller was calculated by using the commercial CFD code of the ANSYS-TASCflow together with the k-ω turbulence model. In the calculation, one of the impeller passages is selected, and the number of computational grid in the main frame shown in Fig. 2 is $199\times28\times24$ in the streamwise, pitchwise, and spanwise directions, respectively, and the grid-point total is 184,947, including the grid points of the annular passage shown in Fig. 3. The calculation was performed in the whole rotating domain, not in the stationary frame.

As shown in Figs. 2 and 3, the inlet boundary was set at 250 mm far upstream from the impeller inlet, where a uniform and no prewhirl inflow could be assumed. The outlet boundary was set at 110 mm downstream of the impeller exit. A periodic condition was imposed on the spatially periodic boundaries, and no slip condition was set on all stationary wall surfaces. In the first simulation, the diffuser was a parallel wall with a constant width of 15 mm. In the second simulation, in order to suppress the diffuser stall, it varied linearly from 15 to 10 mm between the diffuser inlet and $R=1.2$ and is a parallel wall downstream of $R=1.2$ as shown by the broken line in Fig. 1.

The groove width of 4 mm was selected as an optimum size in the present study according to the authors' previous work [5]. In order to optimize the groove location, the flow simulation was performed in three kinds of groove location with a different meridional distance along the shroud wall from the blade-leading edge as shown in Fig. 4. Figure 4(a) shows the case with the groove center location of $S_G^*=0.31$, Fig. 4(b) shows the $S_G^*=0.21$ case and Fig. 4(c) shows the $S_G^*=0.13$ case, where the inducer tip throat locates at $S_t^*=0.25$.

Effect of Inlet Recirculation

Figures 5(a) and 5(b) show the numerical simulation results of the inlet recirculation flow zone in the suction ring groove and the annular passage, and the reverse flow zone along the shroud-casing wall and in the vaneless diffuser. They are defined by the

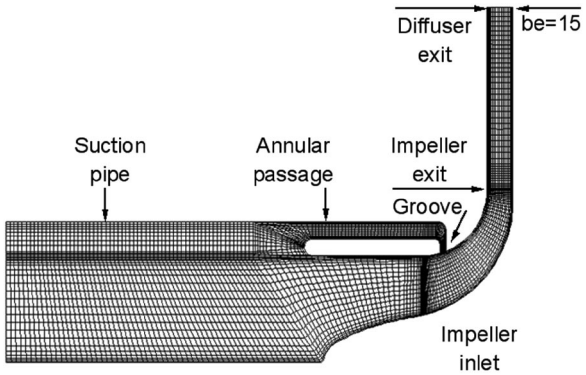

Fig. 3 Computational grid for test blower; $S_G^*=0.21$ groove with $b_e=15$ [mm]

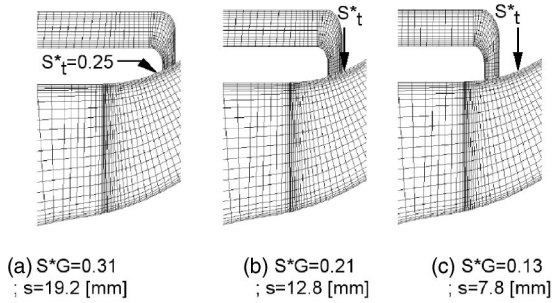

Fig. 4 Variation of ring groove location: (*a*) $S_G^*=0.31$; $s=19.2$ [mm], (*b*) $S_G^*=0.21$; $s=12.8$ [mm], and (*c*) $S_G^*=0.13$; $s=7.8$ [mm]

region with the negative meridional velocity. Figure 5(*a*) is the case of the design flow rate of $\phi_d=0.360$, and Fig. 5(*b*) is that of $\phi=0.250$ at which the developed unstable flow occurs. The parameter is the ring groove location S_G^* and the standard case STD without the ring-groove arrangement. In both flow rates of $\phi=0.360$ and 0.250, the reverse flow near the inducer tip throat almost disappears by the formation of inlet recirculation. Figure 6 shows the numerical results of the static pressure at the impeller exit ψ_{S2} and the inlet recirculation flow rate ϕ_{IR} due to a change in the through-flow rate ϕ. In the $S_G^*=0.31$ case shown by the thin solid line, the impeller characteristic ψ_{S2} is deteriorated in almost whole flow-rate range because of the excessive inlet recirculation flow rate; whereas in the $S_G^*=0.13$ case, the bypass flow through the annular passage toward the ring groove appears in a flow rate smaller than $\phi=0.28$, which corresponds to the negative ϕ_{IR}, and is injected into the impeller passage. The dead zone is formed behind the jet as shown in the bottom of Fig. 5(*a*), resulting in a marked decrease in ψ_{S2}. In the case of $S_G^*=0.21$, ψ_{S2} is improved in the small flow-rate range remarkably compared with that of the standard casing, and also, ψ_{S2} at $\phi_d=0.36$ is not deteriorated. The ring groove location of $S_G^*=0.21$ was selected as the optimum condition.

Experimental verification was performed for the cases with and without the ring-groove arrangement of $S_G^*=0.21$, where the diffuser width of $b_e=15$ mm was adopted. Figure 7 shows a comparison of the static pressures at the impeller exit ψ_{S2} and at the diffuser exit ψ_{Se}, respectively. The solid marks in Fig. 7 denote the flow-rate range where the periodic pressure fluctuation is observed showing a peak frequency of about 5~7 Hz (as shown in Fig. 8). The frequency power spectra of the wall static pressure

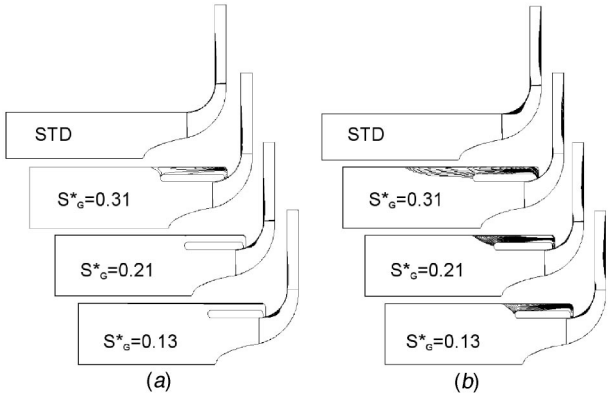

Fig. 5 Effect of ring-groove location on inlet recirculation flow zone in the ring-groove arrangement and reverse flow zones in the midpitch plane of impeller passage and vaneless diffuser: (*a*) $\phi=0.360$ and (*b*) $\phi=0.250$

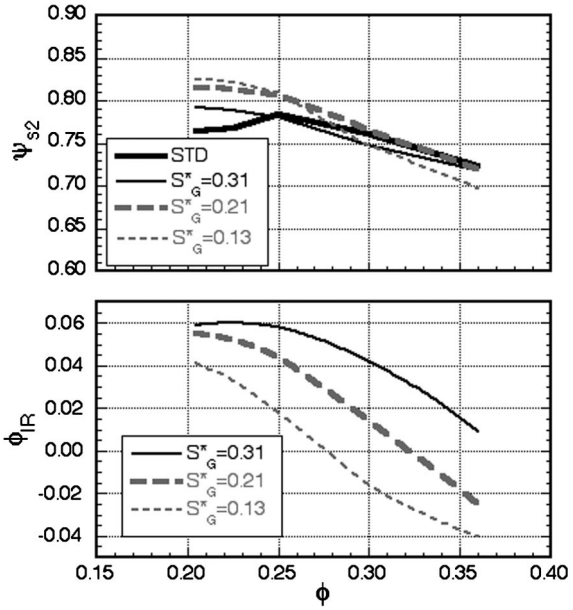

Fig. 6 Numerical results of impeller characteristics ψ_{S2} and inlet recirculation flow rate ϕ_{IR}

fluctuation were measured at $S^*=0.49$ downstream of the inducer tip throat, and compared the cases of STD and $S_G^*=0.21$ in the frequency range between 0 and 20 Hz lower than the shaft rotation frequency of 66.7 Hz.

The unstable flow appears between $\phi=0.316\sim0.204$ in the STD case, on the other hand, between $\phi=0.274\sim0.204$ in the $S_G^*=0.21$ case, respectively. It is found that the unstable flow range is reduced by about 13% by the formation of the inlet recirculation flow. In the STD case, the peak spectrum appears at 6.5 Hz at $\phi=0.300$, while it completely disappeared in the $S_G^*=0.21$ case. At a flow rate of $\phi=0.249$, the peak power spectrum appears at 5.5 Hz, which is markedly low in the $S_G^*=0.21$ case in comparison to the STD case. At the surge flow rate of $\phi=0.204$, a high-peak power spectrum appears near 5 Hz in both cases. It was confirmed by the measurements of pressure fluctuation at two points apart circumferentially on the same radial position, that these unstable flow phenomena were not the rotating stall, but a fluctuationlike surge.

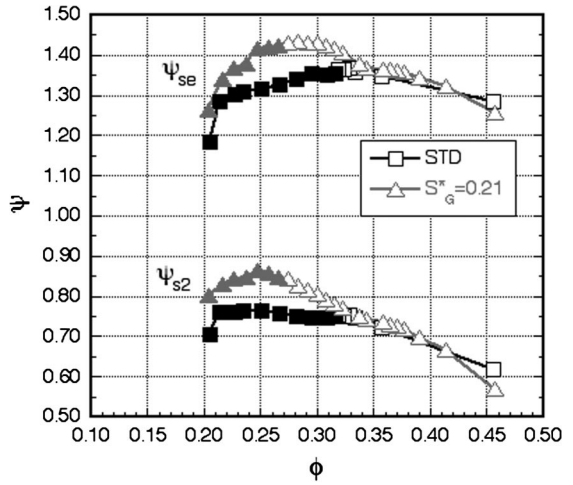

Fig. 7 Experimental characteristics of test blower; comparison between STD casing and $S_G^*=0.21$ groove

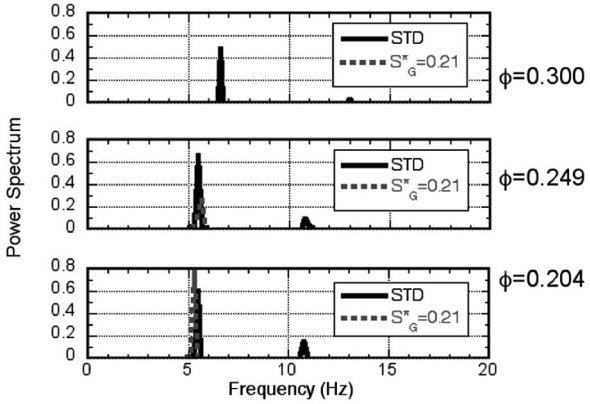

Fig. 8 Frequency power spectrum of wall static pressure at $S^*=0.49$ ($R=0.74$); comparison between STD casing and $S^*_G=0.21$ groove

Figures 9(*a*) and 9(*b*) show a comparison of the numerical simulation results between the cases of STD and $S^*_G=0.21$, and the parameter is the through-flow rate ϕ. Figure 9(*b*) shows that the reverse flow zone on the shroud wall in the inducer portion is successfully suppressed by the formation of inlet recirculation except for the case of $\phi_d=0.360$. However, the reverse flow zone remains at the hub side in the vaneless diffuser and extends to the diffuser exit at flow rates of $\phi=0.250$ and 0.205; it does not at $\phi=0.300$ in both cases. The reverse flow extended to the diffuser

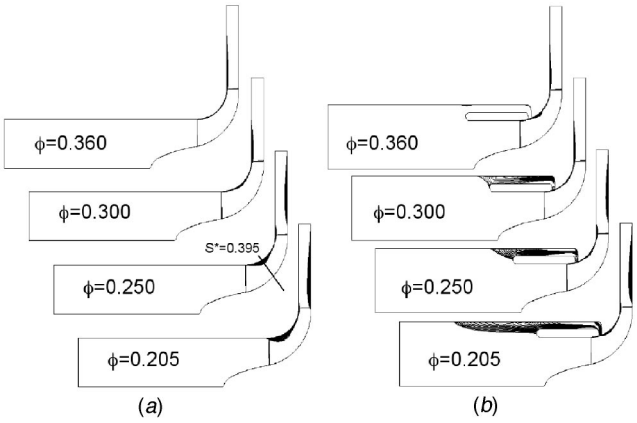

Fig. 9 Effect of through-flow rate on reverse flow zone and inlet recirculation flow zone: (*a*) STD casing and (*b*) $S^*_G=0.21$ groove

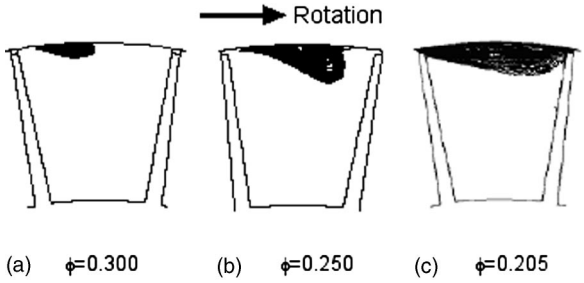

Fig. 11 Reverse flow zone in the impeller passage section of $S^*=0.395$ downstream of inducer tip throat; Case of STD casing with $b_e=15$ [mm]: (*a*) $\phi=0.300$, (*b*) $\phi=0.250$, and (*c*) $\phi=0.205$

exit could be the cause of unstable flow that appeared at flow rates smaller than $\phi=0.274$. In other words, the incipient unstable flow in the STD case is due to the reverse flow near the inducer tip throat.

Mechanism of Unstable Flow Inception

In order to clarify the mechanism of the unstable flow inception due to inducer stall, the behavior of the reverse flow formed in the inducer tip region and an interaction between the reverse flow and the blade tip leakage flow are investigated by comparing the two cases with and without inlet recirculation, as shown in Figs. 10–12. Figure 10 shows contour lines of the reverse flow area on the surface of revolution of the midtip clearance space, and Fig. 11 shows the reverse flow zone in the impeller passage section of $S^*=0.395$, downstream of the inducer tip throat; both are cases without inlet recirculation. In the case of $\phi=0.300$ at which the incipient unstable flow appears, the reverse flow is formed locally between blades; it is at the suction side of the blade near the blade tip leading, then, expands in the pitchwise direaction and moves to the pressure side, downstream. The reverse flow is accumulated in the pressure side, downstream of the inducer tip throat, as shown in Fig. 11(*a*). As the flow rate decreases to $\phi=0.250$ and 0.205, the reverse flow zone grows wider in both pitchwise and spanwise directions, covering the blade pitch as shown in Figs. 10(*b*) and 10(*c*) and 11(*b*) and 11(*c*).

Figures 12(*a*) and 12(*b*) show the behavior of a streak line that forms the tip leakage flow as indicated by five streak lines at $\phi=0.300$, in cases without and with inlet recirculation, respectively. The blade-to-blade contour lines of reverse flow zone on the revolution surface of the midtip clearance space are superimposed in the figure. In the case without inlet recirculation [see Fig. 12(*a*)], it is clearly seen that the tip leakage flow streak lines form a rolling-up vortex flow near the pressure side of the adjacent blade, resulting from the interaction between the tip leakage flow and the accumulated reverse flow zone, in which the streamwise

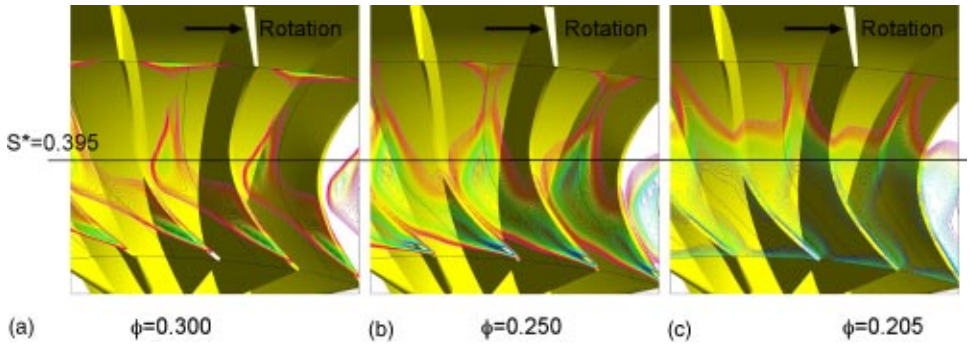

Fig. 10 Contour lines of reverse flow zone on the surface of revolution of the midtip clearance space; case of impeller without inlet recirculation: (*a*) $\phi=0.300$, (*b*) $\phi=0.250$, and (*c*) $\phi=0.205$

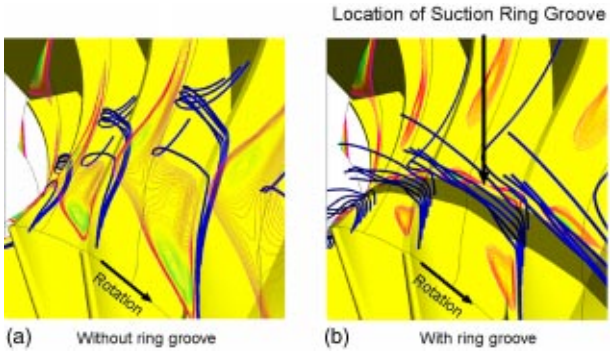

Fig. 12 Effect of suction ring groove on tip leakage flow streak lines (ϕ=0.300). (*a*) Without ring groove and (*b*) With ring groove.

component of vorticity seems to be included due to the tip leakage vortex [12]. By the formation of inlet recirculation flow as shown in Fig. 12(*b*), the tip leakage flow is sucked together with the reverse flow into the ring-groove arrangement. The reverse flow zone mostly disappears, then, the complete suppression of the unstable flow at ϕ=0.300 results, as shown in Figs. 7 and 8. These results, in addition to the result that the flow incidence near the blade tip is lower than the critical one, convince us that the incipient unstable flow is caused by the rolling-up vortex motion of the tip leakage flow at the pressure side of the blade downstream of the inducer tip throat.

Effect of Diffuser Width on Diffuser Stall

The occurrence of unstable flow at flow rates smaller than ϕ=0.274 seems to be due to diffuser stall, judging from the result that the reverse flow zone extends to the diffuser exit at ϕ=0.250 in both cases with and without inlet recirculation [see Figs. 9(*a*) and 9(*b*)]. The simulation and experiment were performed by changing the diffuser configuration; the diffuser width is reduced from b_e=15 to 10 mm downstream of R=1.2 (see Fig. 13).

The experimental blower characteristics are shown in Fig. 14 in cases with a standard diffuser width of b_e=15 mm and the narrowed one of b_e=10 mm, under the condition without the ring-groove arrangement, where the solid marks denote the unstable flow range. In the case of the narrowed diffuser width, the unstable flow is suppressed in the flow-rate range between ϕ=0.278 and 0.213 (see Fig. 14); however, it is not between ϕ=0.316 and 0.278. And the surge flow rate is decreased from ϕ=0.204 in the case of b_e=15 mm to ϕ=0.165 in that of b_e=10 mm by the suppression of diffuser stall. These results, in addition to the result that it is suppressed between ϕ=0.316~0.274 by the inlet recirculation (see Fig. 7), surely convince us that the incipient unstable flow is due to the rolling-up vortex motion of the tip leakage flow downstream of the inducer tip throat.

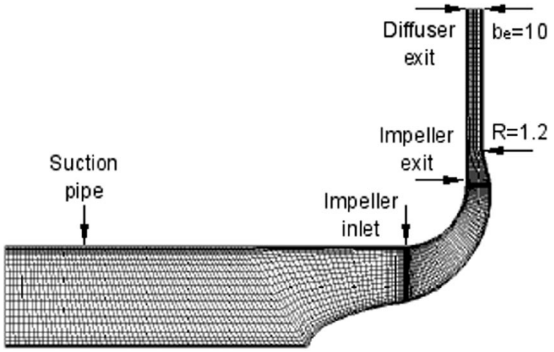

Fig. 13 Computational grid for test blower; STD casing with b_e=10 [mm] (R>1.2)

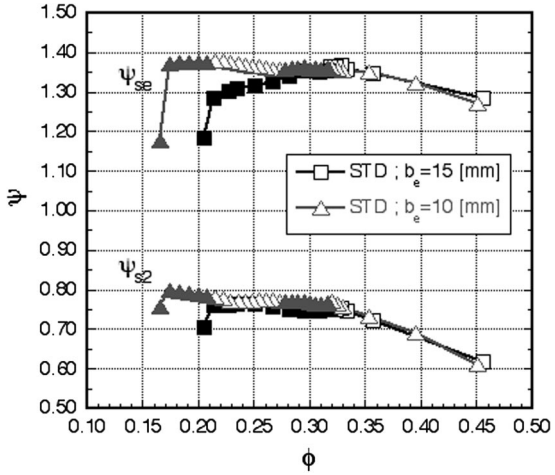

Fig. 14 Characteristics of test blower; comparison between b_e=15 and 10 [mm] in STD casing

Figure 15 shows numerical simulation results of the reverse flow zone in the vaneless diffuser as well as along the shroud wall in the impeller; the parameter is the flow rate. The reverse flow zone disappears at both hub and shroud side walls by means of the narrowed diffuser width in all flow rates (see Fig. 15); then, the unstable flow due to diffuser stall is suppressed in the flow-rate range between ϕ=0.278 and 0.213. The unstable flow appearing at flow rates smaller than ϕ=0.213 is caused by excessive flow incidence at the inducer blade-tip leading edge, which will be shown later in Fig. 21.

In the experimental characteristics shown in Fig. 14, the pressure recovery in the diffuser, which is the difference between the pressures of ψ_{Se} and ψ_{S2}, is improved significantly in a flow-rate range smaller than ϕ=0.278 by the suppression of diffuser stall. It is noted that the diffuser pressure recovery at the design flow rate is not deteriorated even though the diffuser width is decreased

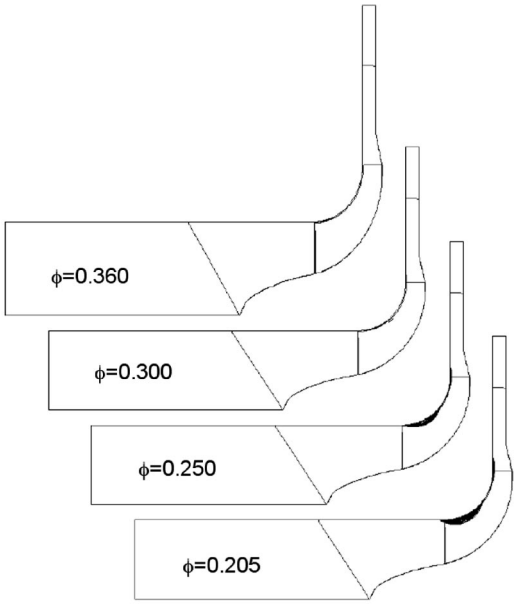

Fig. 15 Effect of through-flow rate on reverse flow zone in STD casing with b_e=10 [mm]

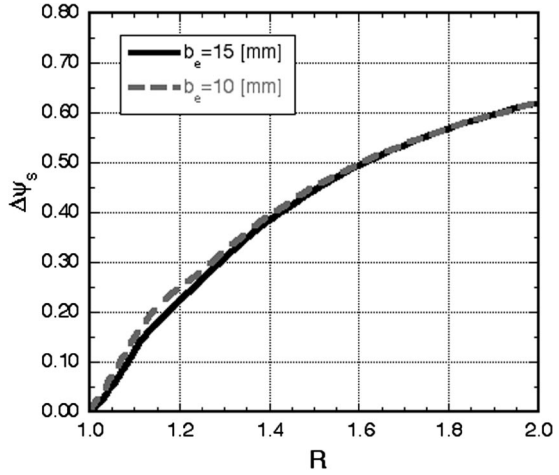

Fig. 16 Effect of diffuser width on pressure rise in vaneless diffuser at the design flow rate of $\phi_d=0.360$

from 15 to 10 mm. Figure 16 shows a comparison of the pressure rise $\Delta\psi_S$ in the diffuser in cases with $b_e=15$ and 10 mm. It is confirmed from Fig. 16 that the pressure recovery at the design flow rate is not deteriorated by the reduction of diffuser width because the higher pressure rise is obtained between $R=1.0 \sim 1.2$ in the $b_e=10$ mm case compared to the $b_e=15$ mm case. This is due to the fact that the tangential velocity component (see Fig. 17), which is the dominant factor of the pressure rise, is higher at the shroud side in $b_e=10$ mm than $b_e=15$ mm. In the case of $b_e=15$ mm, the tangential velocity component is decreased due to the local reverse flow at the shroud side as shown by the negative meridional velocity component Vm in Fig. 17.

Simultaneous Suppression of Inducer Stall and Diffuser Stall

Taking advantages of the results shown in Figs. 7 and 14, the numerical simulation and experiment were performed in the combined case with both the ring-groove arrangement and the narrowed diffuser width as shown in Fig. 18. Figure 19 shows a comparison of the experimental blower characteristics of the three cases; the squares denote the original standard case, the triangles denote the case with the narrowed diffuser width but without inlet recirculation, and the diamonds denote the case with both the inlet recirculation and narrowed diffuser width. The implementation of

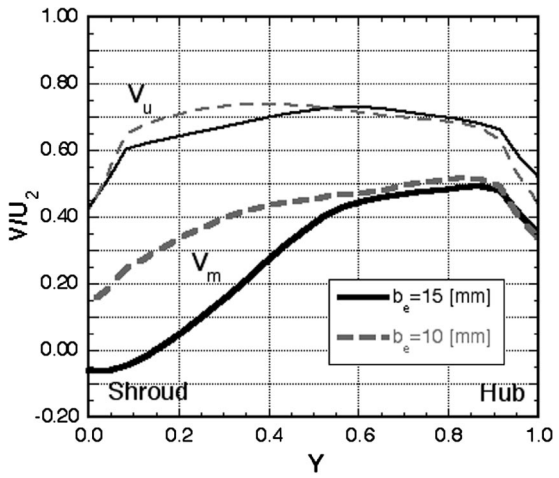

Fig. 17 Effect of diffuser width on hub-to-shroud velocity distribution at $R=1.20$; the design flow rate of $\phi_d=0.360$

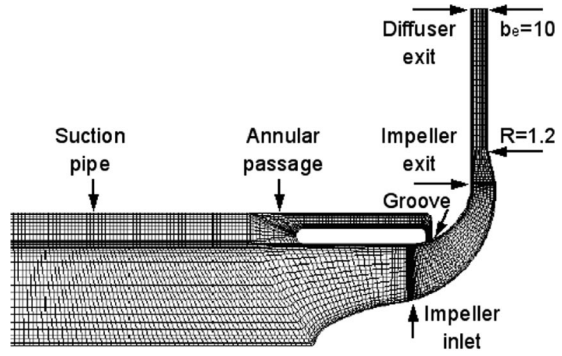

Fig. 18 Computational grid for test blower; $S_G^*=0.21$ groove with $b_e=10$ [mm] ($R>1.2$)

the inlet recirculation device can suppress the inducer stall, while the reduction in the diffuser width can suppress the diffuser stall (see Fig. 19). As shown in Fig. 20, the reverse flow zone disappears successfully in the impeller passage as well as in the diffuser passage. This combination gives marked improvements in the pressure rise of the impeller, and in the surge margin of the test blower up to about 45% without deteriorating the blower characteristics even at the design flow rate (see Fig. 19). Furthermore, according to the measured shaft torque data, blower characteristics were little affected by the formation of inlet recirculation because the recirculation flow is limited only in part of the impeller entrance region; then, the blower efficiency was not deteriorated.

Figure 21 shows the hub-to-shroud distribution of the flow incidence averaged between blades. The thin black lines denote the standard case, the thin gray lines denote the standard casing with the narrowed diffuser width, and the thick black lines denote the revised case shown in Fig. 18, where $\phi_1(=\phi+\phi_{IR})$ denotes the incoming flow rate. As the inlet recirculation flow rate ϕ_{IR} increases with the decreasing through-flow rate, the flow incidence is decreased. It is clearly seen in Fig. 21 that the flow incidence is slightly decreased in almost the whole region between the hub and shroud by reducing the diffuser width, as shown by the gray lines, and is markedly decreased by the formation of inlet recirculation, as shown by the thick black lines. This large reduction in flow incidence is mainly due to the increase in the incoming flow rate and partly due to a prewhirl of the inlet recirculation flow. The

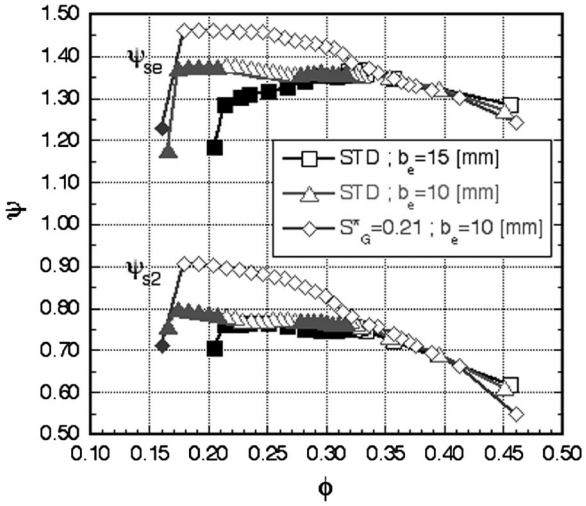

Fig. 19 Experimental characteristics of test blower; Comparison between STD casing with $b_e=15$ [mm], STD casing with $b_e=10$ [mm], and $S_G^*=0.21$ groove with $b_e=10$ [mm]

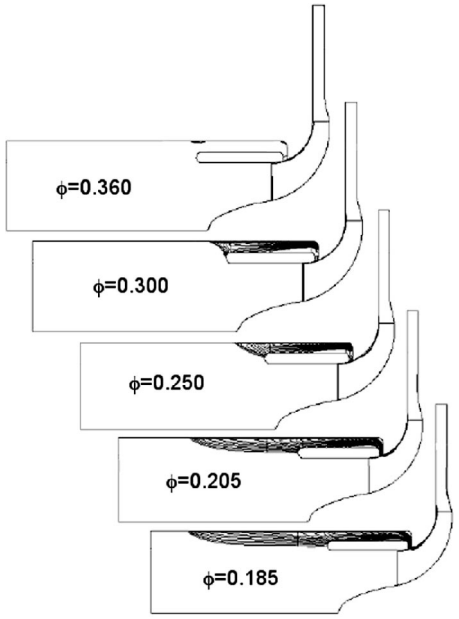

Fig. 20 Effect of through-flow rate on inlet recirculation flow and reverse flow; $S_G^*=0.21$ groove with $b_e=10$ [mm]

critical flow incidence $\Delta\beta_{crt}$ is about 14 deg in the present inducer, which is about twice that of $\Delta\beta_{crt}=7.4$ deg for the two-dimensional cascade case [21], which might be due to a strong secondary flow in the inducer portion.

Conclusions

In order to clarify the mechanism of the unstable flow inception in a high-specific-speed-type open shrouded centrifugal impeller and to analyze the effect of the ring-groove arrangement on inducer stall and/or that of the diffuser width on diffuser stall, a 3D turbulent flow simulation and experiment were performed. It was found that the steady flow simulation was very helpful for understanding unsteady stall phenomena, and the following concluding remarks were obtained.

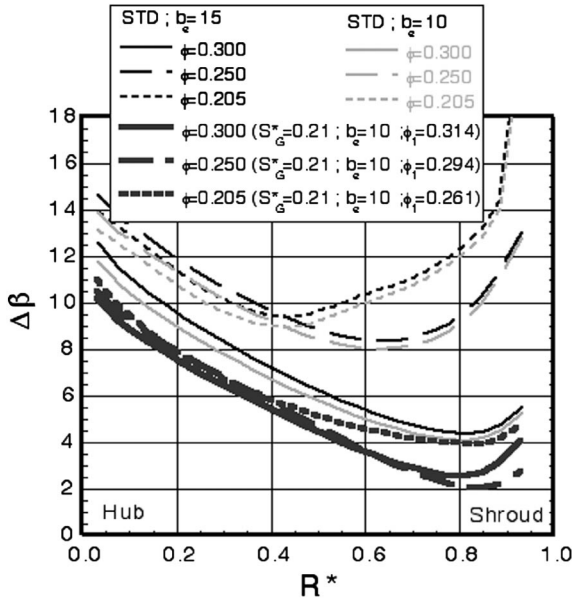

Fig. 21 Comparison of hub-to-shroud distribution of flow incidence ($S^*=0$)

1. The incipient unstable flow is caused by the rolling-up vortex flow near the pressure side of the adjacent blade, resulting from the interaction between the tip leakage flow and the accumulated reverse flow zone, in which the strong streamwise vorticity component seems to be included due to the tip leakage vortex.
2. The formation of inlet recirculation is very effective for suppression of unstable flow due to inducer stall; one factor is the suction of the tip leakage vortex together with the reverse flow, and another is a decrease in the flow incidence due to an increase in the inlet recirculation flow rate, which increases with a decrease in the through-flow rate.
3. The optimum location of the suction ring groove is in the region near the inducer tip throat, resulting in suppression of inducer stall without deterioration of the impeller characteristics, even at the design flow rate.
4. The unstable flow due to diffuser stall occurs when the reverse flow zone extends to the diffuser exit.
5. The unstable flow occurring between $\phi=0.278$ and 0.213 was suppressed by reducing the diffuser width from the impeller exit height to two-thirds between the diffuser inlet and $R=1.2$, by which the pressure recovery in the diffuser is not deteriorated.
6. The unstable flow range of the test blower was reduced significantly by about 45% in total from $\phi=0.316$ to 0.174 by implementing the ring-groove arrangement for the inducer inlet as well as the narrowed diffuser width for the diffuser exit.

Acknowledgments

This research was financially supported by the Grants-in-Aid from the Ministry of Education, Science and Culture of Japan. The authors also would like to thank T. Sakaguchi, a graduate student of Nagasaki University, for securing the experimental data.

Nomenclature

b = diffuser width (mm)
p = static pressure (Pa)
P_0 = total pressure in suction plenum tank (Pa)
Q = through-flow rate (m^3/s)
Q_{IR} = inlet recirculation flow rate (m^3/s)
r = radial distance (mm)
R = radius ratio ($=r/r_2$)
R^* = dimensionless radial distance along the blade leading from the blade root ($=[r-r_h]/[r_s-r_h]$)
s = meridional distance along the shroud from the blade leading (mm)
S_G^* = dimensionless groove center location ($=s_G/s_2$)
U_2 = impeller tip speed (m/s)
V_m = meridional velocity component (m/s)
V_u = tangential velocity component (m/s)
$\Delta\beta$ = flow incidence (deg)
ϕ = through-flow rate coefficient ($=Q/2\pi r_2 b_2 U_2$)
ϕ_{IR} = flow coefficient of inlet recirculation ($=Q_{IR}/2\pi r_2 b_2 U_2$).
ϕ_1 = incoming flow rate coefficient ($=\phi+\phi_{IR}$)
ψ_S = static pressure coefficient ($=2(p-P_0)/\rho U_2^2$)
ρ = fluid density (kg/m^3)

Subscripts

1, 2 = inlet and exit of impeller
e = diffuser exit
h, s = hub and shroud sides

References

[1] Ishida, M., Sakaguchi, D., Ueki, H., and Sun, Z., 1997, ''Relationship Between Rotating Stall Inception and 3-D Flow Separation on Vaneless Diffuser Walls in Centrifugal Blowers,'' *Proc. of JSME International Conference on Fluid Engineering*, JSME, Toyko, Paper No. 97-203, Vol. II, pp. 1097–1102.

[2] Ishida, M., and Sakaguchi, D., 1997, ''Behavior of Separation Ring on Shroud Casing Wall of a Centrifugal Blower (Visualization of Separation Ring by Oil Film Technique),'' J. Visualization, **117**(64), pp. 46–50 (in Japanese).

[3] Ueki, H., Ishida, M., Sakaguchi, D., and Sun, Z., 2000, ''Suppression of Inducer Stall Based on Inlet Recirculation in a Centrifugal Blower (1st Report, Improvement in Stall Limit by Ring Groove Arrangement),'' Trans. Jpn. Soc. Mech. Eng., Ser. B, **66**(647), pp. 1706–1711 (in Japanese).

[4] Sun, Z., Ishida, M., Sakaguchi, D., and Ueki, H., 1998, ''Flow Analysis and Surge Suppression in a Centrifugal Blower,'' *Proc. of 3rd International Conference on Pumps and Fans*, Tsinghua University Press, Beijing, pp. 204–214.

[5] Ishida, M., Sun, Z., Sakaguchi, D., Ueki, H., and Masuzawa, C., 1999, ''Numerical Analysis and Experimental Verification of Inlet Recirculation for Unstable Flow Suppression in a Centrifugal Blower,'' *Proc. of 3rd ASME/JSME Joint Fluid Engineering Symposium*, Paper No. FEDSM99-6844.

[6] Sun, Z., Ishida, M., Sakaguchi, D., and Ueki, H., 2000, ''Suppression of Inducer Stall Based on Inlet Recirculation in a Centrifugal Blower (2nd Report, Numerical Analysis of Stall Suppression Effect),'' Trans. Jpn. Soc. Mech. Eng., Ser. B, **66**(647), pp. 1712–1718; (in Japanese).

[7] Fisher, F. B., 1988, ''Application of Map Width Enhancement Devices to Turbocharger Compressor Stages,'' SAE Paper No. 880794.

[8] Sun, Z., Ishida, M., and Masuzawa, C., 2000, ''A Computational Study on Optimum Inducer Leading Geometry for Stall Suppression in a Centrifugal Blower,'' ASME Paper No. FEDSM2000-11059.

[9] Ishida, M., Sun, Z., Taufan S., and Sakaguchi, D., 2002, ''Numerical Investigation of Inducer Stall at Small Flow Rates in a Centrifugal Blower (Effect of Blade Leading Shape on Flow Separation),'' *Proc. of 4th International Conference on Pumps and Fans* (4th ICPF), China Science and Technology Press, Beijing, pp. 206–212.

[10] Sun, Z., Taufan S., Ishida, M., and Ueki, H., 2002, ''Numerical Simulation on Flow Separation Behavior in a Centrifugal Blower Under Time-Periodic Inflow Condition,'' *Proc. of 4th International Conference on Pumps and Fans* (4th ICPF), China Science and Technology Press, Beijing, pp. 315–321.

[11] Taufan, S., Ishida, M., Ueki, H., and Sakaguchi, D., 2002, ''Effect of Inducer Blade Leading Shape on Unstable Flow Inception in a Centrifugal Blower (Comparison of Numerical Analysis and Experiment),'' *Proc. (CD-ROM) of 5th JSME-KSME Fluids Engineering Conference*, JSME, Tokyo, OS16-4, Paper No. 2, pp. 1–6.

[12] Furukawa, M., Inoue, M., Saiki, K., and Yamada, K., 1999, ''The Role of Tip Leakage Vortex Breakdown in Compressor Rotor Aerodynamics,'' ASME J. Turbomach., **121**(3), pp. 469–480.

[13] Furukawa, M., Saiki, K., Yamada, K., and Inoue, M., 2000, ''Unsteady Flow Behavior Due to Breakdown of Tip Leakage Vortex in an Axial Compressor Rotor at Near-Stall Condition,'' ASME Turbo Expo, Munich, Germany Paper No. 2000-GT-0666.

[14] Abdelhamid, A. N., 1982, ''Control of Self-Excited Flow Oscillations in Vaneless Diffuser of Centrifugal Compressor System,'' ASME Paper No. 82-GT-188.

[15] Fukushima, Y., Nishida, H., and Miura, H., 1989, ''Rotating Stall of Centrifugal Compressors,'' Turbomach., **17**(3), pp. 149–159 (in Japanese).

[16] Senoo, Y., Hayami, H., and Ueki, H., 1983, ''Low-Solidity Tandem-Cascade Diffusers for Wide-Flow-Range Centrifugal Blowers,'' ASME Paper No. 83-GT-3.

[17] Harada, H., 1996, ''Non-Surge Centrifugal Compressor With Variable Angle Diffuser Vanes,'' Turbomach., **24**(10), pp. 600–608 (in Japanese).

[18] Kurokawa, J., Matsui, J., Kitahora, T., and Saha, L., 1997, ''A New Passive Device to Control Rotating Stall in Vaneless and Vaned Diffusers by Radial Grooves,'' *Proc. of JSME Intl. Conf. on Fluid Engineering*, Vol. II, JSME, Tokyo, Paper No. JSME ICFE-97-716, pp. 1109–1114.

[19] Tsurusaki, H., and Kinoshita, T., 1999, ''Flow Control of Rotating Stall in a Radial Vaneless Diffuser,'' *Proc. of 3rd ASME/JSME Joint Fluids Engineering Conference*, ASME, New York, Paper No. FEDSM99-7199, pp. 1–6.

[20] Ishida, M., Sakaguchi, D., and Ueki, H., 2001, ''Suppression of Rotating Stall by Wall Roughness Control in Vaneless Diffusers of Centrifugal Blowers,'' ASME J. Turbomach., **123**(1), pp. 64–72; also ASME Paper No. 2000-GT-0461.

[21] Nishizawa, T., and Takata, H., 1999, ''Numerical Study on Stall Flutter of A Compressor Cascade (1st Report, Numerical Method and Numerical Example),'' Trans. Jpn. Soc. Mech. Eng., Ser. B, **65**(635), pp. 2293–2300 (in Japanese); also ASME 94-GT-258.

A Study of Impeller-Diffuser-Volute Interaction in a Centrifugal Fan

Tarek Meakhail
e-mail: mina_tarek@hotmail.com

Seung O. Park
e-mail: sopark@sop1.kaist.ac.kr

Korea Advanced Institute of Science and Technology,
Yuseong-gu,
Daejeon 305-701, Korea

This paper reports velocity measurement data in the interaction region between the impeller and vaned diffuser and the results of numerical flow simulation of the whole machine (impeller, vaned diffuser and volute) of a single stage centrifugal fan. Two-dimensional instantaneous velocity measurement is done using particle image velocimetry (PIV). Numerical simulation of impeller-diffuser-volute interaction is performed using CFX-Tascflow commercial code. A frozen rotor simulation model is used for the steady calculation and a rotor-stator simulation model is used for the unsteady calculation using the steady results as an initial guess. The simulation results show that the separated flow regime near the diffuser hub extends to the volute. Comparison between the unsteady computation and those of measurement indicates that the rotor/stator model employed in the simulation predicts essential characteristics of unsteady flow in the centrifugal fan. However, quantitative agreement remains rather poor. [DOI: 10.1115/1.1812318]

Introduction

There has been steady progress in the field of turbomachinery flow computations during the past decade. These advances have made it possible for turbomachinery designers to carry out analysis of various flow phenomena occurring inside turbomachines. To improve design of centrifugal machines, a better understanding of the flow of such machines is required. This paper deals with an experimental and theoretical study of the flow in a low specific-speed centrifugal fan.

A number of authors have treated the problem of the interaction of the impeller and its surroundings numerically and experimentally. Inoue and Cumpsty [1], Sideris and Braembussche [2] and Arndt et al. [3,4] have been concerned with the action of the diffuser. Paone et al. [5] at VKI have used particle image displacement velocimetry (PIDV) to measure the flow field inside the vaneless diffuser of a centrifugal pump made of plexiglass with a shrouded impeller. They compared the PIDV measurements and the corresponding LDV measurement data and found that they were different in the wake. They believed that the information available from PIDV could largely contribute to a better understanding of the flow in centrifugal machines. Also, at VKI, Hillewaert and Van den Braembussche [6] have studied numerically the problem of impeller-volute interaction in a centrifugal compressor. So far, the measurement of the instantaneous whole flow field in the interaction region between the impeller and the diffuser or numerical simulation of the whole machine could not be found in the literature. The purpose of this paper is to introduce a numerical simulation of the whole machine and to compare the numerical results to those obtained by PIV measurement at the interaction region between the impeller and the diffuser at different relative location.

The Centrifugal Fan

Figure 1 shows a single stage centrifugal fan made of plexiglass. It consists of impeller, diffuser (vaned or vaneless) and volute. More details of the test rig, performance and PIV measurement data can be found in Meakhail et al. [7,8]. Steady and unsteady numerical simulation of the whole fan is performed using CFX-Tascflow commercial Code, using a HP-Unix workstation. A ''frozen rotor'' simulation is used first to find the preliminary steady flow field. A ''rotor-stator'' simulation is used to find final unsteady flow, using the steady results as an initial guess.

Numerical Technique

The commercially available CFD code, CFX-Tascflow [9], is employed for this study. The validation of this code for the turbomachinery flows can be found, for example, in the work of Gernot et al. [10], Peter and Donald [11] and Mihael et al. [12]. The code solves the Reynolds averaged Navier–Stokes equations in primitive variable form. The effects of turbulence were modeled using the standard K-ε turbulence model. To make the simulation time economical, wall function is used to resolve the wall flows.

Grid Generation

A high quality mesh is produced using a single block H-grid through the main blade and the passage (for both impeller and diffuser) using CFX-Turbogrid software [13]. CFX-Tascgrid is used for volute grid generation. This type of grid generation gives better minimum skew angle, which should not be less than 20 deg, and better maximum aspect ratio, which should not be more than 100. The blades are defined by blocking off grid elements. The entire grid size for one blade is

For the impeller		
Entire grid:	42*32*23=30,912	(I, J, K)
Blade block off	24*8*23=4416	(I, J, K)
For the vaned diffuser		
Entire grid:	46*27*23=28,566	(I, J, K)
Blade block off	22*5*23=2530	(I, J, K)

For the volute, the grid consists of several blocks and the total number of nodes is 230,000 nodes

Figure 2 shows the grid system of the present calculation. The total number of grid nodes is around 1,000,000 nodes for the whole impeller, diffuser and volute.

Transient Rotor/Stator and Frozen-Rotor Simulation

The frozen rotor simulation is used to get the steady state solution for different components of the machine. That is, the interface condition is in steady state and the geometry remain fixed across the interface.

Contributed by the International Gas Turbine Institute (IGTI) of THE AMERICAN SOCIETY OF MECHANICAL ENGINEERS for publication in the ASME JOURNAL OF TURBOMACHINERY. Paper presented at the International Gas Turbine and Aeroengine Congress and Exhibition, Vienna, Austria, June 13–17, 2004, Paper No. 2004-GT-53068. Manuscript received by IGTI, October 1, 2003; final revision, March 1, 2004. IGTI Review Chair: A. J. Strazisar.

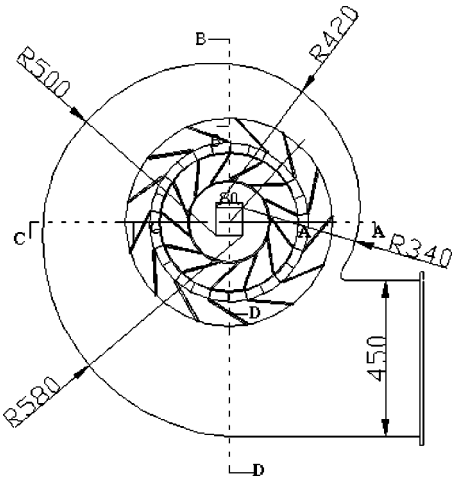

Fig. 1 The centrifugal fan

A transient rotor/stator simulation can be used any time when it is desired to account for transient interaction effects at a sliding (frame change) interface. By nature, these simulations are always transient, never achieving a steady state condition. The components on each side of a transient sliding interface are always in relative motion with respect to each other. Pitch change is automatically dealt with at a transient sliding interface in the same manner as at frozen rotor interfaces: the profiles in the pitch-wise direction are stretched or compressed to the extent that there is pitch change across the interface. As with the frozen rotor condition, the computational accuracy degrades rapidly with increasing pitch change.

Boundary Conditions

There are several different types of boundary condition that can be applied at the inlet boundary. For example, the velocity (or mass flow rate) can be specified or total pressure can be specified.

The velocity is specified over the entire inlet face of the impeller for most computational cases. The average inlet velocity is 5 m/s at the outlet, the measured static pressure applied as an average value over the outlet area of the volute ($P_{out}=102{,}200$ Pa). However, for the computations to evaluate performance parameter, total pressure is applied at the inlet. The diffuser and volute are stationary and the impeller is rotating with a rotational speed of 1000 rev/min. A sliding interface model is set between the impeller and diffuser. Additionally, the K-ε turbulence model in Tascflow requires an inlet value for the turbulence intensity (Tu) and the eddy length (L), which can be calculated as the cubic root of the volume of the calculation domain. The computations for the present work run in fully turbulent mode with Tu$=5\%$ and $L=0.5$ and the Reynolds number is 4.5E4.

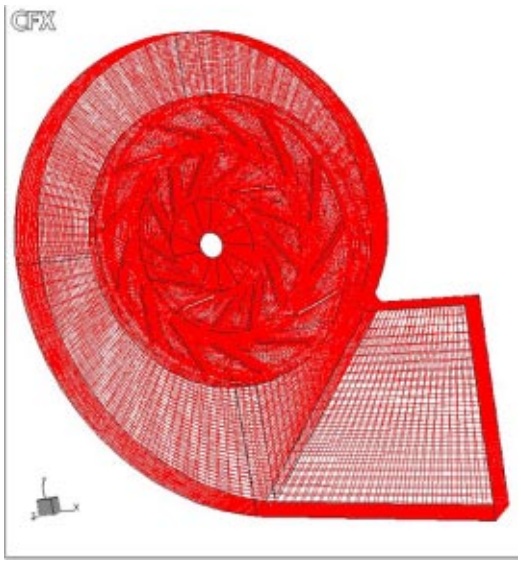

Fig. 2 The grid system

Solution Procedures

The frozen rotor simulation is obtained first using a larger time step ($\Delta t=1E-3$ s). The transient simulation is done using a smaller time step ($\Delta t=1.5E-4$ s) with using the frozen rotor simulation as an initial guess. The number of iteration per time step is 10. The calculation results discussed here were run on HP-UNIX workstation with 512 Mbytes of memory, which can be extended to a virtual memory of 1Gbyte. Typical CPU times were around 2 days for 200 iterations for frozen rotor simulation and 5 days for 60 time steps for transient simulation necessary for a run to converge down to maximum residuals of less than $E-04$.

Results and Discussion

Frozen Rotor Simulation. The flow leaving the rotating impeller is very complex and presents nonuniformities between the hub and the shroud as well as in the circumferential direction. These nonuniformities result from the secondary flow that develops in the machines. Under the action of the centrifugal and Coriolis forces low momentum fluid accumulates in the shroud-suction side corner. This migration of the low momentum fluid led to the so-called *jet-wake* model. This model was very popular in the past, but as detailed measurements became available, it appears that the model is too idealized. Therefore, in view of the complexity of the outflow, it appears doubtful that a simple model can be used to construct the flow entering the downstream blade row, making the uncoupled unsteady approach not practical for designing any new rotating machine. Also, it must be pointed out here that the jet/wake structure is a complicated flow phenomenon. Each impeller has its own jet/wake structure. For example, Eckardt [14] has found the wake region near the shroud suction side, while Kirtley and Beach [15] have found the wake region near the shroud pressure side. Hamkins and Flack [16] showed a migration of vortex from suction side to the pressure side. On the other hand, Krain and Hoffman [17] found that there was no jet/wake characteristics at all but the flow went smoothly at the impeller exit.

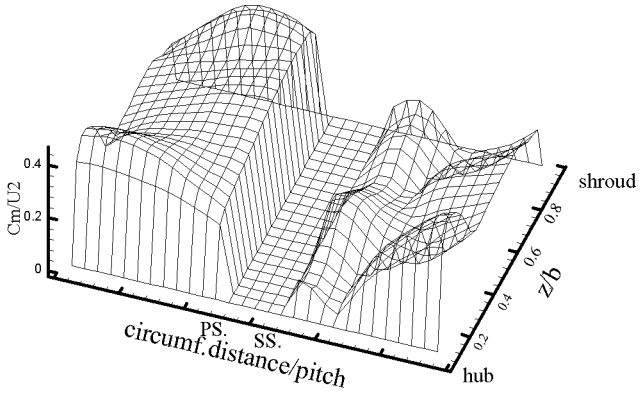

Fig. 3 Normalized meridional velocity profile at the exit plane of the impeller

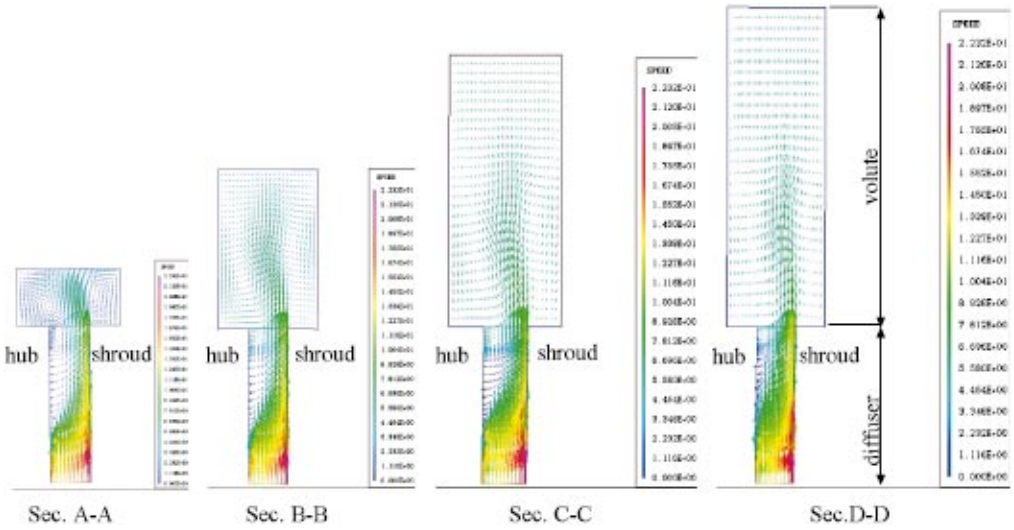

Fig. 4 Velocity vectors at design flow rate for diffuser and volute at different sections

The predicted impeller flow exhibits a jet/wake structure. Figure 3 shows a relief plot of the steady state-predicted meridional flow velocity normalized by impeller tip speed (C_{mer}/U_2) at the exit plane of the impeller at medium flow rate. C_{mer} is calculated from the equation:

$$C_{mer} = \sqrt{C_{rad}^2 + C_{tan}^2 + C_{ax}^2}$$

The figure shows a clear jet-like flow (of high meridional flow velocity) at the pressure side and a wake-like flow (of lower velocity) near the hub suction side. Apart from this low velocity region near the hub, another low velocity region around $z/b = 0.7$ is also found.

Figure 4 shows the velocity vectors in the meridional plane, sections A-A, B-B, C-C and D-D for vaned diffuser and volute at best efficiency point (BEP), close to the design point. The figure shows a detached flow region in the hub side starting at a location of 40% of the diffuser length. The hub detachment seems to arise from a disturbance generated at the moving impeller hub/stationary diffuser wall interface. This hub separation extends to the volute and a high swirl flow zone is found at the volute, especially at the section near the tongue. Also, due to sudden expansion of the diffuser-volute interface, a high circulation region is found also at the shroud side. Because the fan was made of plexiglas, it was too difficult to make the cross section of the volute rounded. The diffuser hub separation is also seen by Kirtley and Beach [15] for NASA Lewis Low Speed Centrifugal Compressor. At off-design conditions, at a flow rate 150% of the design mass flow, Fig. 5 shows that, due to high flow momentum in the diffuser, the separation is very small near the hub, and that a high swirl flow zone occurs at the volute section near the tongue. This swirl flow zone is gradually attenuated from section B-B to section D-D. At flow rate 40% of the design mass flow, Fig. 6 shows a high separation region occurs at the beginning of the diffuser near the hub and that a massive recirculation zone is somewhat larger than the throughflow zone. This blockage near the hub deviates the flow towards the shroud to pass through a small area, which results in increasing the flow velocity near the shroud of the diffuser.

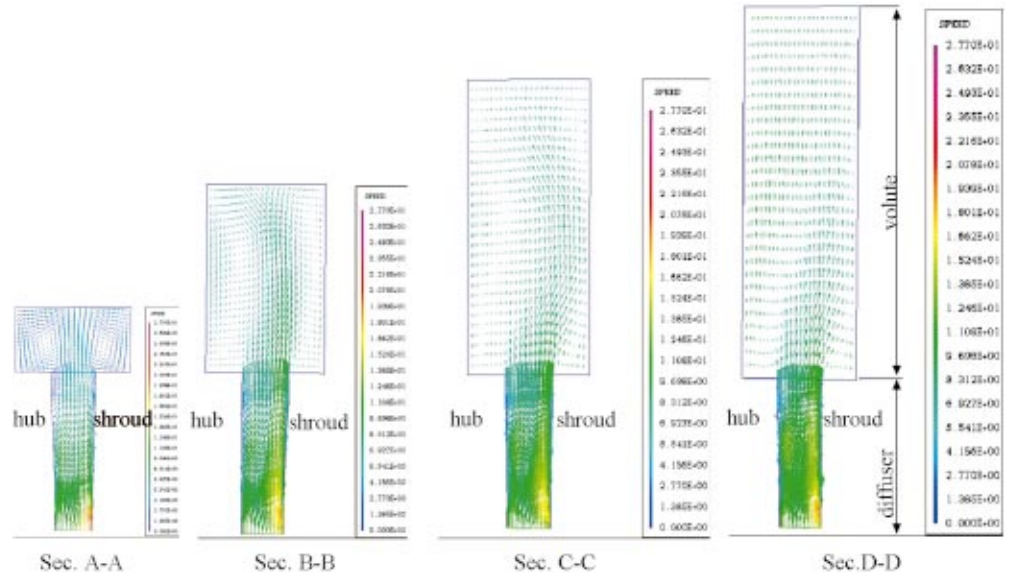

Fig. 5 Velocity vectors at 150% design flow rate for diffuser and volute at different sections

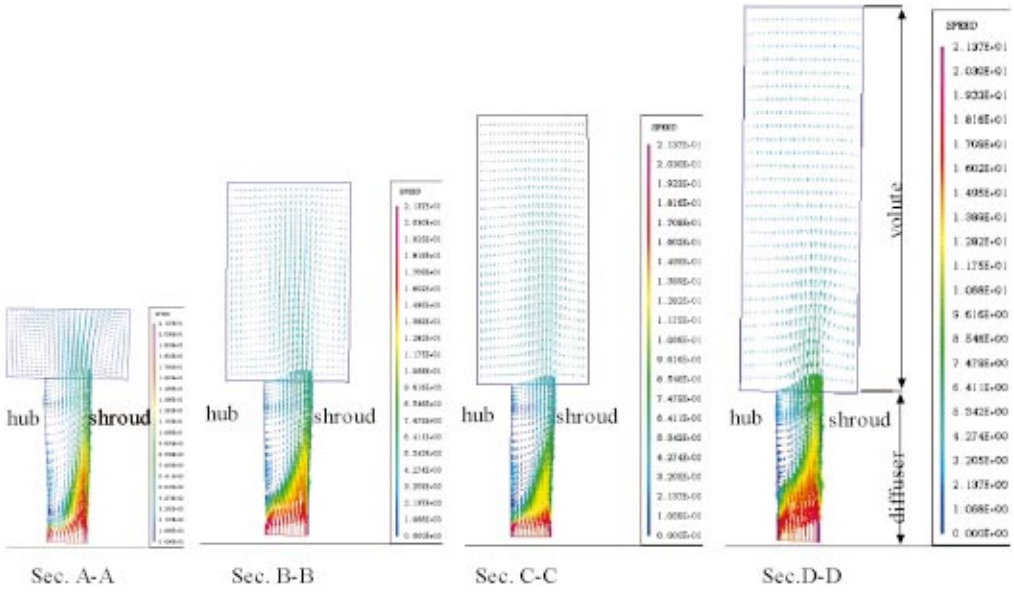

Fig. 6 Velocity vectors at 40% design flow rate for diffuser and volute at different sections

2 Transient Rotor-Stator-Volute Simulation. A huge amount of data has been obtained during a cycle of the transient simulation process. One cycle is divided into 20 timesteps; each timestep requires ten iterations and a converged solution is obtained after three cycles (where the initial guess for the transient simulation is taken as the converged solution of the frozen rotor simulation). Due to the large amount of data, all of the impeller positions could not be presented here; only one position (when the impeller blade matches the diffuser blade) is selected and presented for each case.

Figure 7 shows the instantaneous pressure field at (BEP) at midspan from the impeller inlet to the volute outlet. The potential effect, when the impeller trailing edge passes in front of the diffuser vane leading edge, is clearly visible. Pressure perturbations due to the vortex shedding behind the impeller blades can be observed also. In a small band around the vaneless space between the impeller blades and diffuser blade, complex pressure structures can be observed. These pressure structures are well correlated with the unsteady part of the relative velocity at the exit of the impeller. Outside this band, the pressure field is smoother and it can be observed that the pressure unsteadiness in the impeller is well synchronized. These global pressure variations are due to potential effects. It can also be noted that in the diffuser the pressure is changing with time only in the semi-vaneless space. Inside the diffuser and volute, the pressure variation is very small because the rotational speed of the impeller is very small.

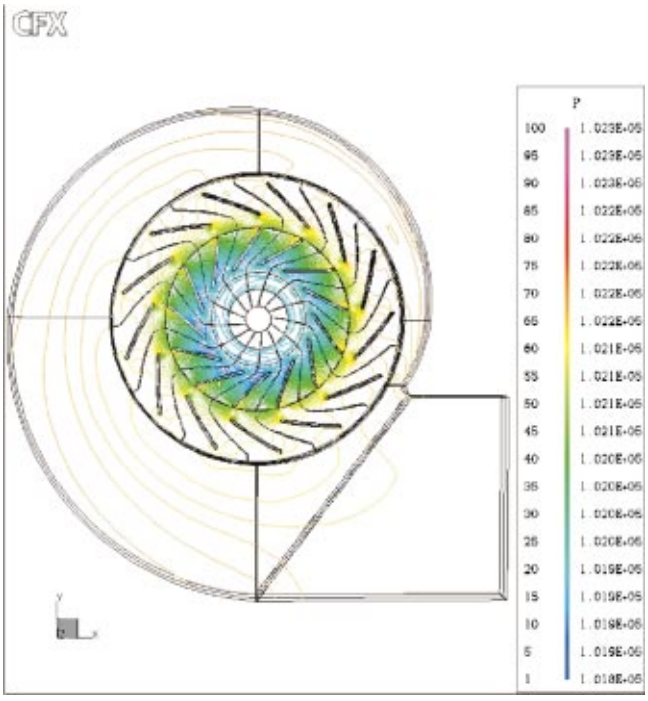

Fig. 7 The instantaneous pressure field at midspan

Since the computations are performed in a rotating frame in the impeller and in a fixed frame in the diffuser, it is natural to present the velocity field for both frames. Figure 8 shows the instantaneous relative velocity vectors in the impeller and the absolute one in the diffuser at the BEP at midspan. The evolution of the absolute velocity is viewed in a fixed frame. Conversely, the evolution of the relative velocity is viewed by an observer attached to the impeller. This gives a good overview of the rotor-stator-volute interaction mechanisms. Careful examination of velocity vectors behind the trailing edge of the impeller blade suggests vortex shedding. A low velocity region moves with the blade trailing edge in the vaneless space in the same direction of the diffuser blade. The flow in the vaneless space is very complex and this complicated flow pattern disappears beyond about 1.2 times radius of the impeller. Also, it is noted that a lower velocity region is found at the diffuser exit near the volute tongue.

3 Comparison between Experimental and Numerical Results at the Interaction Region of Impeller and Diffuser. The complexity of the impeller flow as well as the inhomogeneity of the impeller discharge flow and its interaction with the flow in the diffuser make it very difficult to bring together the whole field simulation with real flow measured by the PIV. So far, no one made a comparison between numerical and experimental unsteady flow of the whole machine because it is too complicated to model correctly and to measure experimentally in the interaction region between the impeller and the diffuser. However, some comparisons are presented here to see how well the present computation method can simulate the unsteady interaction and also to show the flow behaviors, which could not be obtained by PIV in some

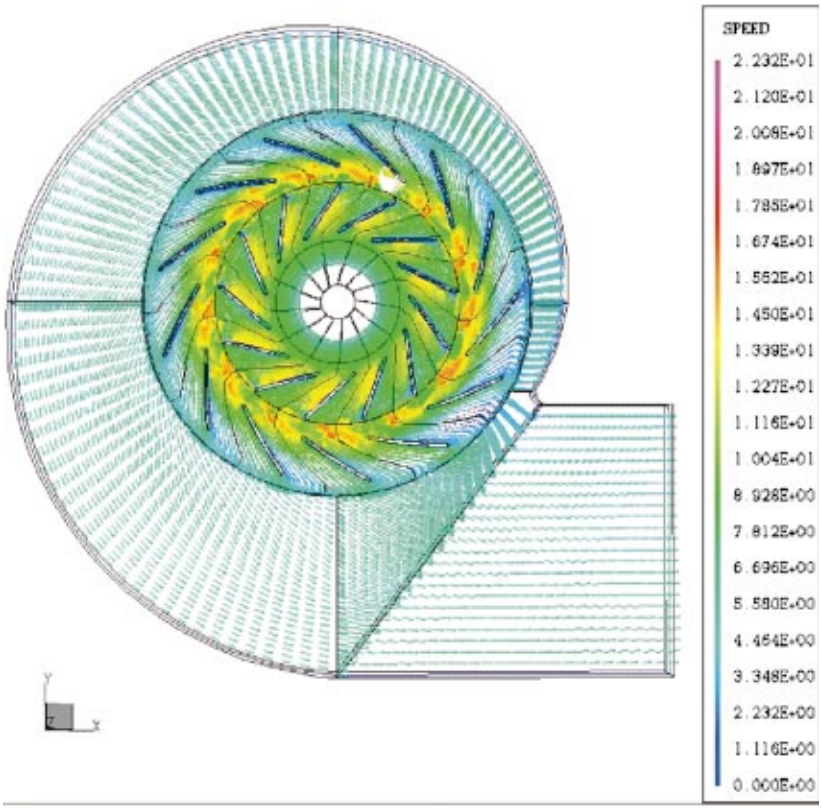

Fig. 8 The instantaneous velocity vectors at midspan

regions of the measurement area due to seeding problems or laser sheet accessing. Figures 9–11 show the comparison of the instantaneous absolute flow velocity vectors at medium flow rate at one relative position near the shroud, at midspan and near the hub, respectively. From a macroscopic point of view the agreement between experimental and numerical results is good in the sense that

1. The absolute flow velocity inside the impeller is higher than that inside the diffuser.
2. The absolute flow velocity near the shroud is a little higher than that at midspan and very small near the hub of the diffuser where a reverse flow zone pushes the flow towards the shroud.

From a microscopic point of view, it must be pointed out that there are some shortcomings of using PIV and computations. They are

1. There is a 2 mm clearance gap (which is relatively big) between impeller walls and diffuser walls along the whole circumference. This gap is a source of leakage and a highly three-dimensional flow with high axial flow velocity at the exit of the impeller along the span (from hub to shroud). The leakage of the flow with seeding in this region makes it too difficult to obtain the experimental results in this region. On the other hand, the present calculations did not consider the flow simulation in the clearance gap. The above two reasons may answer the question why the

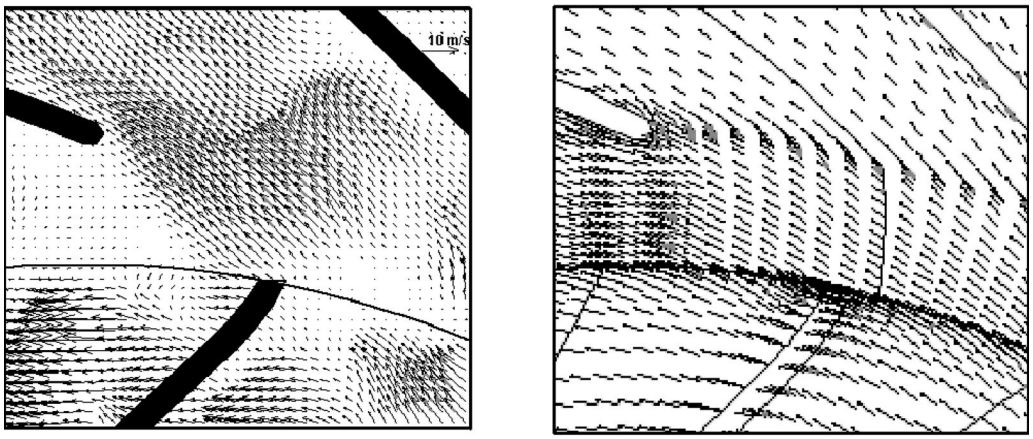

Fig. 9 Comparison of the instantaneous absolute flow velocity at design flow rate near the shroud

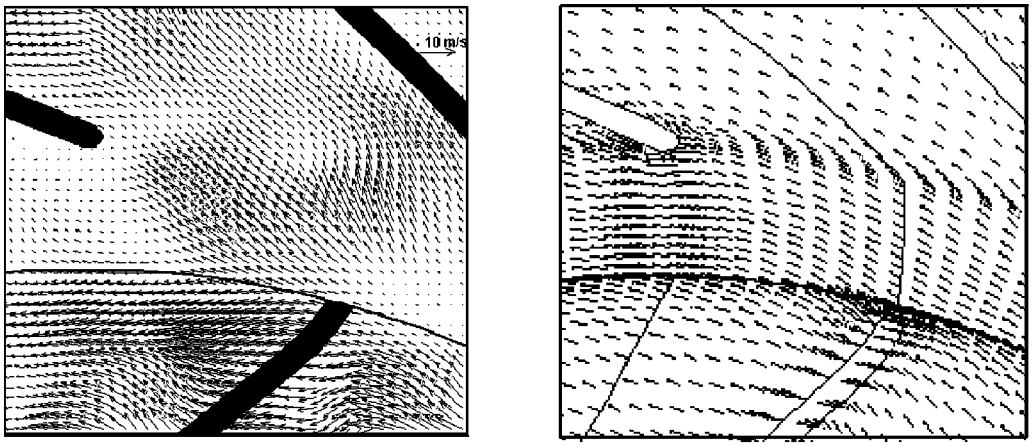

Experimental Numerical

Fig. 10 Comparison of the instantaneous absolute flow velocity at design flow rate at midspan

velocity at the exit of the impeller is low from experiment and high from numerical results.

2. The regions near walls and beside the leading edge of the diffuser vanes prevent PIV laser sheets from accessing and hence the data could not be obtained at these regions.

3. The instantaneous flow obtained from the computations is very smooth compared to the experimental results. This may be due to the turbulence model used, which is the standard K-ε model without any modifications (for example, the effect of curvature and rotation have not been taken into account). Another possible reason is that the real flow obtained by PIV is like a pulsating flow with unsteady inlet and outlet boundary conditions contrast to the steady state boundary conditions applied to the computations.

4 Performance Comparison. After applying the total pressure as inlet boundary conditions instead of applying inlet mass flow rate or inlet velocity, as mentioned in the boundary condition section, and applying the static pressure at the outlet, mass flow (or flow coefficient) rate is obtained. Using this flow coefficient the performance curve can be plotted as shown in Fig. 12. The discrepancy between the experimental and the numerical curves is due to the error in mass flow rate calculation. At design conditions ($\varphi = 0.07$), however, the discrepancy is less than 5%.

Conclusion

Unsteady flow simulations of the whole machine have been carried out by using the CFX-Tascflow code and the results are compared with the experimental results.

The following conclusions can be drawn from the present work.

1. A low velocity region behind the impeller blade is found at the suction side due to the formation of the wake at this region. A small vortex shedding can be observed and a highly distorted flow is seen at the vaneless space due to the interaction between the rotating blades and the stationary blades. Near the hub, the flow is much different from those of the other sections where the flow is highly unsteady and separated.

2. A massive recirculation zone is found near the hub and a throughflow zone near the shroud of the diffuser resulting from the inlet of the impeller. The detached flow at the diffuser extends to the volute. The transient simulation predicts a highly unsteady flow region in the vaneless space between the impeller and diffuser. The swirl flow zone in the volute is gradually attenuated from the section near the tongue to the outlet of the fan. Finally, the comparison between the measurements and the calculations showed that the rotor/stator model can predict the basic character-

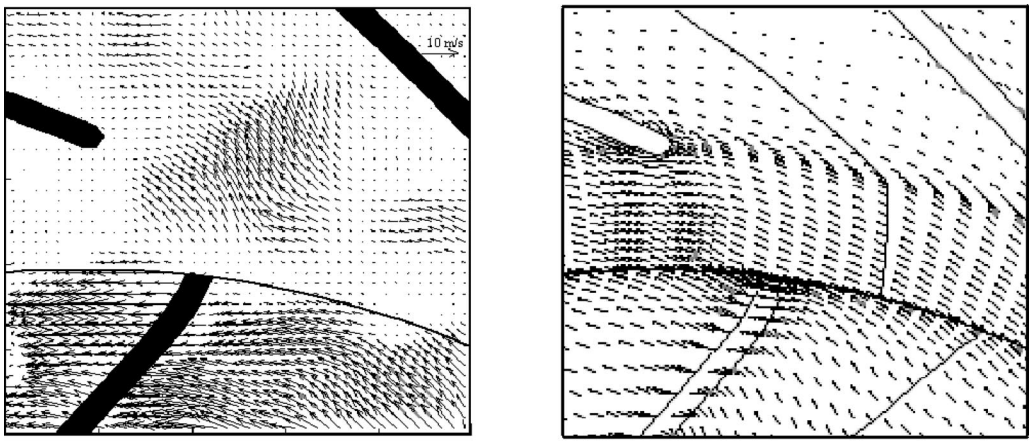

Experimental Numerical

Fig. 11 Comparison of the instantaneous absolute flow velocity at design flow rate near the hub

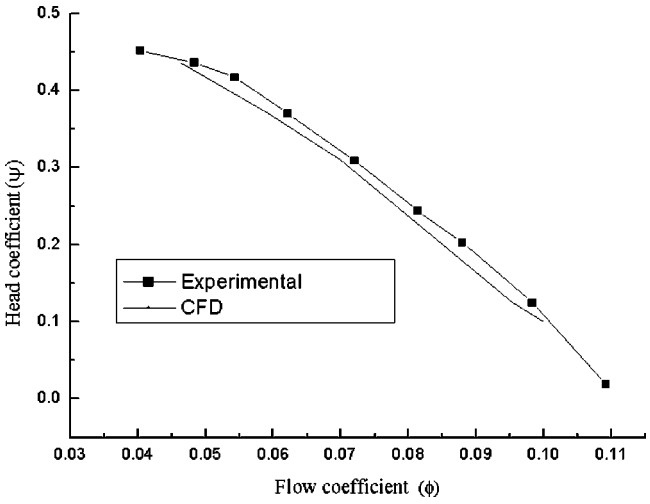

Fig. 12 Comparison between experimental and CFD results

istics of unsteady flow in centrifugal fan but still needs improvement to satisfy the true transient simulation for unsteady impeller diffuser interaction.

3. A good agreement is obtained between the experimental and CFD results for the performance.

Acknowledgment

The authors are grateful to the Brain-Korea 21 at KAIST for supporting this work.

Nomenclature

b = Impeller width
r_2 = Impeller radius
C_{mer} = Meridional velocity
C_{rad} = Radial component of velocity
C_{tan} = Tangential component of velocity
C_{ax} = Axial component of velocity
I = Streamwise direction
J = Circumferential direction
K = Spanwise direction
U_2 = Peripheral speed
PS = Pressure side
SS = Suction side
ϕ = Flow coefficient $= Q/(\pi r_2^2 U_2)$
ψ = Head coefficient $=$ Pstatic$/\rho U_2^2$

References

[1] Inoue, M., and Cumpsty, N. A., 1984, ''Experimental Study of Centrifugal Impeller Discharge Flow in Vaneless and Vaned Diffusers,'' ASME J. Eng. Gas Turbines Power, **106**, pp. 455–467.
[2] Sideris, M. T., and Van den Braembussche, R. A., 1987, ''Influence of a circumferential exit pressure distortion on the flow in an impeller and diffuser,'' ASME J. Turbomach., **109**, pp. 48–54.
[3] Arndt, N., Acosta, A. J., Brennen, C. E., and Caughey, T. K., 1989, ''Rotor-Stator Interaction in a Diffuser Pump,'' ASME J. Turbomach., **111**, pp. 213–221.
[4] Arndt, N., Acosta, A. J., Brennen, C. E., and Caughey, T. K., 1990, ''Experimental Investigation of Rotor-Stator Interaction in a Centrifugal Pump With Several Vaned Diffusers,'' ASME J. Turbomach., **112**, pp. 98–108.
[5] Paone, N., Riethmuller, M. L., and Van den Braembussche, R. A., 1989, ''Experimental Investigation of the Flow in the Vaneless Diffuser of a Centrifugal Pump by Particle Image Displacement Velocimetry'' Exp. Fluids, **7**, pp. 371–378.
[6] Hillewaert, K., and Van den Braembussche, R. A., 1999, ''Numerical Simulation of Impeller-Volute Interaction in Centrifugal Compressor,'' ASME J. Turbomach., **121**, pp. 603–608.
[7] Meakhail, T., Zhang, L., Du, Z. H., Chen, H. P., and Jansen, W., 2001, ''The Application of PIV in the Study of Impeller Diffuser Interaction in Centrifugal Fan. Part I—Impeller-Vaneless Diffuser Interaction,'' *Proceedings of The ASME Fluid Engineering Division*-IMECE2001/FED-24952 November 11–16, 2001, New York, USA.
[8] Meakhail, T., Zhang, L., Du, Z. H., Chen, H. P., and Jansen, W., 2001, ''The Application of PIV in the Study of Impeller Diffuser Interaction in Centrifugal Fan. Part II—Impeller-Vaned Diffuser Interaction,'' *Proceedings of The ASME Fluid Engineering Division*- IMECE2001/FED-24953 November 11–16, 2001, New York, USA.
[9] ASC, 1999, ''CFX-TASCflow Documentation Version 2.9.0,'' Advanced Scientific Computing, Ltd., Waterloo, Ontario, Canada.
[10] Gernot, E., Peter, D., Krain, H., Hartwig, P., Franz, A. R., and Karl, H. R., 1998, ''Analysis of the Transonic Flow at the Inlet of a High Pressure Ratio Centrifugal Impeller,'' ASME paper no. 98-GT-24.
[11] Peter, D., and Donald, H. W., 1995, ''Numerical Transonic Flow Field Predictions for NASA Compressor Rotor 37,'' ASME paper no. 95-GT-326.
[12] Mihael, S., Matija, T., and Dusan, F., 1998, ''Characteristics of One Stage Radial Centrifugal Turbine,'' ASME paper no. 98-GT-494.
[13] ASC, 1999, ''CFX-Turbogrid Documentation Version 1.4,'' Advanced Scientific Computing, Ltd., Waterloo, Ontario, Canada.
[14] Eckardt, D., 1976, ''Detailed Flow Investigations Within a High Speed Centrifugal compressor Impeller,'' ASME J. Fluids Eng., **98**, pp. 390–402.
[15] Kirtley, K. R., and Beach, T. A., 1992, ''Deterministic Blade Row Interactions in a Centrifugal Compressor Stage'' ASME J. Turbomach., **114**, pp. 304–311.
[16] Hamkins, C. P., and Flack, R. D., 1987, ''Laser Velocimeter Measurements in Shrouded and Unshrouded Radial Flow Pump Impellers'' ASME J. Turbomach., **109**, pp. 70–76.
[17] Krain, H., and Hoffman, W., 1989, ''Verification of an Impeller Design by Laser Measurements and 3D-Viscus Flow Calculations'' ASME paper no. ASME 89-GT-159.

On the Use of Five-Hole Probes in the Testing of Industrial Centrifugal Compressors

José L. Gilarranz
e-mail: jose_gilarranz@dresser-rand.com

Andrew J. Ranz

Jason A. Kopko

James M. Sorokes

Dresser-Rand Company,
Paul Clark Drive,
Olean, New York 14760

This paper addresses the use of 5-hole probes in the testing of industrial centrifugal compressors. The 5-hole probes utilized for this work are of the conical-tip type and were used in a non-nulling configuration (i.e., the probes do not need to be rotated or moved in any way during the tests). These 5-hole probes proved to be fairly robust, making them practical for a nonlaboratory setting such as an industrial multistage compressor test stand. A discussion of 5-hole probes and how they function is provided, including an overview of the mathematical formulations and calibrations required to translate the pressure data gathered from the 5 holes into static and total pressures, velocities and flow angles. A method to transform these variables from a probe-based coordinate system to a machine-based coordinate system is also presented and schematics of this process are provided to aid the reader's understanding. The testing performed on a prototype multistage centrifugal compressor using 5-hole probes is also discussed, showing that the probes provided valuable insight into the flowfield exiting the impellers and at the return bend. The hub-to-shroud velocity profile exiting an impeller was found to be more skewed than expected and was contributing to poor performance in the downstream stationary components. The measured flowfield from one of the tests is also compared against 3-D CFD results and comments are offered regarding the agreement between the analytical and measured results. Advantages and disadvantages of 5-hole probes as compared to more conventional instrumentation are presented. Finally, conclusions are drawn regarding the value of 5-hole probe data in the development and/or troubleshooting of high performance turbomachinery and in the validation/calibration of design and analysis tools. [DOI: 10.1115/1.1812319]

Introduction

Despite recent advances in computational fluid dynamics (CFD) and other sophisticated analytical methods, testing continues to play a vital role in the development of high performance centrifugal compressor stages. Compressor manufacturers are faced with demands for ever-increasing levels of efficiency and flow range while at the same time being asked to keep development costs to a minimum. Essentially gone are the days that turbomachinery designers can rely on dedicated test vehicles to acquire the much-needed component performance data [1–5]. More and more, designers must resort to gathering such data from production equipment operating in nonlaboratory environments [1,6]. Consequently, engineers have found it necessary to apply more complex instrumentation in environments that appear harsh when compared to the pristine nature of a single-stage test vehicle in a development laboratory. Still, the data is critical to confirm the viability of new designs as well as to calibrate or validate the analytical methods used to design the new components and predict their performance characteristics.

Typically, measurements on the manufacturer's production test stand are limited to instrumentation installed at the compressor inlet and discharge flanges [7]. Such probes typically measure: (a) inlet pressure (static and total); (b) inlet total temperature; (c) inlet mass flow; (d) discharge total pressure; and (e) discharge total temperature. In the case of a single-stage compressor, this may be sufficient to understand the performance of that stage. However, in a multi-stage compressor, instrumentation at the main inlet and main discharge is inadequate to obtain sufficient data to understand the performance characteristics of the individual stages.

In a quest for more detailed information, some manufacturers will install instrumentation at various locations within the compressor to gather so-called ''stage data'' [1,6]. Typical locations for this instrumentation are shown in Fig. 1. These instruments usually consist of Kiel-head total pressure probes, static pressure taps, and half-shielded or shielded thermocouples. In some instances, pressure or temperature rakes may be employed to measure the pressure or temperature distribution across the flow passage. All of this information can be very important in discerning the performance of the stages. However, if the probes are not properly aligned with the gas flow, the accuracy of the measurements may be compromised.

Typical Kiel-head probes have a range of insensitivity to incidence angle of ± 25 deg. If the gas is approaching the probe at an angle greater than ± 25 deg with respect to the probe centerline, the accuracy of the total pressure measurement will deteriorate. This limitation was normally overcome in the laboratory rig via traverse based multi-hole probes, which could be rotated automatically or manually to align the probe with the approaching flow [8–10]. However, such probes are not practical in a production multistage compressor environment.

An attractive alternative to the traverse based system is the multi-hole probe used in a non-nulling configuration and installed at a fixed position. When properly installed and calibrated, multi-hole probes are capable of acquiring very accurate pressure measurements. More importantly, these probes will provide the flow angle and velocity of the gas.

This paper describes the application of multi-hole or, more specifically, 5-hole probes in the development testing of new, high performance centrifugal stages. A detailed description of the probes and how they function is presented. Next, a case study is presented in which the probes were used to resolve the flow pro-

Contributed by the International Gas Turbine Institute (IGTI) of THE AMERICAN SOCIETY OF MECHANICAL ENGINEERS for publication in the ASME JOURNAL OF TURBOMACHINERY. Paper presented at the International Gas Turbine and Aeroengine Congress and Exhibition, Vienna, Austria, June 13–17, 2004, Paper No. 2004-GT-53375. Manuscript received by IGTI, October 1, 2003; final revision, March 1, 2004. IGTI Review Chair: A. J. Strazisar.

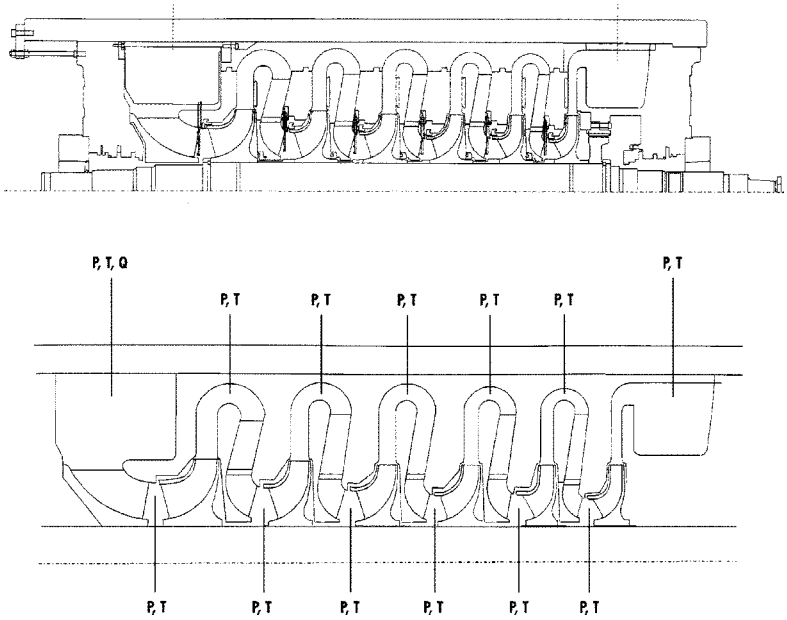

Fig. 1 Cross-section of a multi-stage test vehicle showing typical locations for instrumentation placement [1]

file downstream of a new impeller design. The measured data are also compared against CFD analyses and comments are offered regarding the agreement between the measured and analytical results. Finally, conclusions are offered regarding the use of 5-hole probes in the production test stand environment.

The 5-Hole Probe

Multi-hole pressure probes are widely used in many branches of the engineering sciences which deal with the measurement of fluid flow. Typical multi-hole probes are used in combination with the nulling technique and require auxiliary systems to either rotate or translate the probe in order to align it with at least one of the components of the flow direction. These auxiliary systems are typically either pneumatically powered or based on the use of servomotors.

When properly calibrated, 5-hole probes have the ability to measure total and static pressure as well as gas velocity and flow angle. Some types of multi-hole probes allow the user to install them at a fixed position in combination with the non-nulling technique, and are capable of measuring the above mentioned flow properties without requiring the probe to be moved or rotated during the tests. This permits the probes to be rigidly mounted at a fixed location, much like a standard Kiel-head pressure probe. Nevertheless, the probes used in this configuration require extensive calibrations that cover all of the expected flow conditions (flow angle, Mach number, etc.) that will be encountered by the probe during the tests.

The 5-hole probes utilized for the work presented herein were manufactured by the Aeroprobe Corporation, are of the conical-tip type and are used in a non-nulling configuration (i.e., the probes do not need to be rotated or moved in any way during the tests). As the name implies, 5-hole pressure probes have five pressure ports. For the probes described in this work, the pressure ports are distributed on a conical tip as shown in Fig. 2. One hole (port number 1) is located at the apex of the cone, the other holes (ports 2–5) are uniformly distributed around the central port halfway downstream of the apex. This probe geometry provides the capability of making accurate measurements for flow angles of up to 60 deg (if the probe has been properly calibrated within those limits). The three-dimensional velocity vector that is measured with these probes is expressed in the probe axis coordinate system which is shown in Fig. 3. Typically the incidence angle of the flow with respect to the probe tip is defined using one of the following angle conventions: pitch (α) and yaw (β) or cone (θ) and roll (ϕ). Hence, as shown in Fig. 3, the velocity components in the probe axis coordinate system may be expressed using one of these angle pairs as well as the velocity magnitude.

The above mentioned calibrations must be performed by inserting the probe into a specially designed calibration rig that has accurate means of measuring the flow conditions (i.e., flow velocity, total temperature, static pressure, etc.), the orientation of the probe tip (variable) with respect to the flowfield direction (fixed), and the resulting pressure existing at the five pressure ports of the probe tip. The calibration rig provides a steady uniform flowfield of known properties and fixed direction; the probe is rotated on a traversing mechanism with the aid of high-resolution stepper motors. The rotation of the probe permits us to measure the pressure

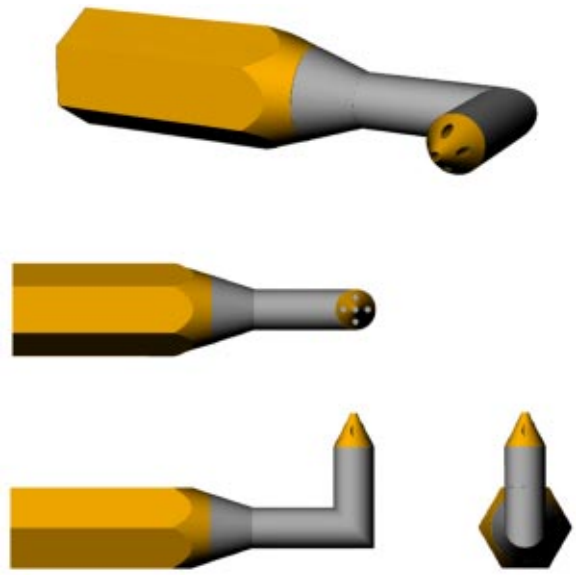

Fig. 2 L-shaped 5-hole probe with a conical tip

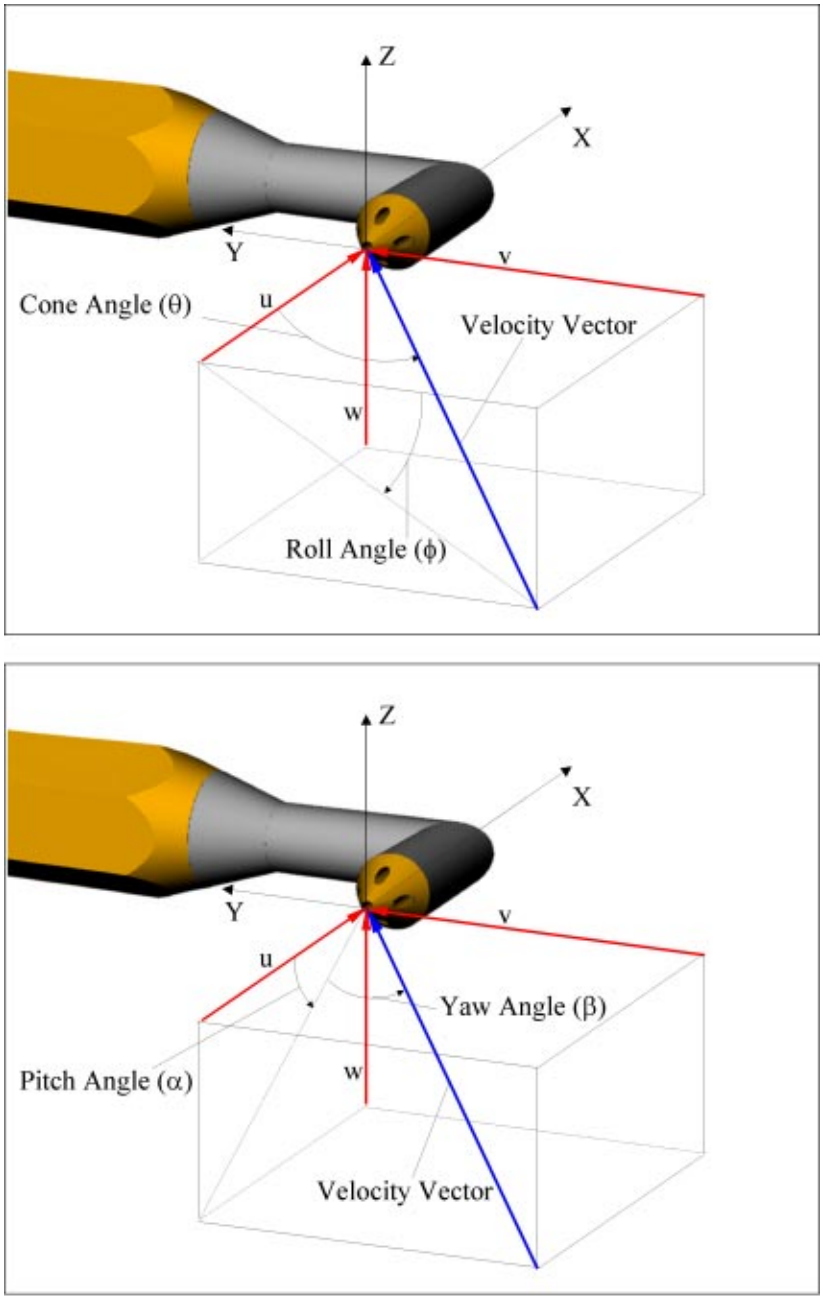

Fig. 3 Probe coordinate system and angle conventions

distribution at the tip for a previously defined set of angle combinations (pitch and yaw or cone and roll) that cover the range of incidence angles that are expected for the probe to encounter during the actual tests.

During probe calibration, a data acquisition system records the total temperature (T_t), static pressure (P_s) and velocity (or total pressure, P_t) of the reference flowfield (typically air considered as an ideal gas) as well as probe incidence angles (α and β or θ and ϕ) and the pressures at each one of the five pressure ports on the probe tip (P_1, P_2, P_3, P_4 and P_5). These measurements are taken for each data point that conforms the above mentioned matrix of incidence angles.

Typically, the port pressure data is then expressed as a group of nondimensional coefficients using equations similar to the ones presented below [11,12]. These particular equations are used for the case in which the pressure port at the apex of the probe (number 1) is highest, which occurs at low incidence angles. At higher incidence angles, one of the ports located on the periphery of the cone will measure the highest pressure, for this case, a different set of expressions is used to define the nondimensional coefficients [11,12].

pitch angle coefficient,

$$B_\alpha = \frac{p_4 - p_5}{p_1 - \frac{1}{4}(p_2 + p_3 + p_4 + p_5)} \tag{1}$$

yaw angle coefficient,

$$B_\beta = \frac{p_2 - p_3}{p_1 - \frac{1}{4}(p_2 + p_3 + p_4 + p_5)} \tag{2}$$

total pressure coefficient,

$$A_t = \frac{p_1 - p_t}{p_1 - \frac{1}{4}(p_2 + p_3 + p_4 + p_5)} \tag{3}$$

static pressure coefficient,

$$A_s = \frac{p_1 - p_s}{p_1 - \frac{1}{4}(p_2 + p_3 + p_4 + p_5)} \tag{4}$$

Once these nondimensional coefficients have been calculated, the incidence angles (α and β or θ and ϕ) and the total and static pressure coefficients (A_t and A_s) are expressed as functions of the pitch and yaw angle coefficients (B_α and B_β). This information is then saved along with other relevant calibration data in the preprocessed calibration data files for each particular probe.

The effects of the Mach (M) and Reynolds (Re) numbers over the measurement accuracy of these types of probes has been investigated by many researchers [11–15]. It has been shown that the accuracy of the measurements made with these types of probes will increase dramatically if the M and Re numbers for which the probes were calibrated coincide (or are close) to the actual values of these numbers encountered during the tests. Hence, to account for compressibility and viscous effects, probes are often calibrated over a range of Mach and Reynolds number, thus each probe can have numerous calibration files [11,12].

The probes used for this work were calibrated at the High-Speed Wind Tunnel operated by the ESM Department at Virginia Tech and used by the Aeroprobe Corporation. Details of this facility may be found in the work of Zeiger et al. [14]. Each probe was calibrated in air at Mach numbers of 0.25, 0.35 and 0.45, with corresponding Reynolds number per unit length ($\mathrm{Re/M} = \rho V/\mu$) values of 5.71×10^6, 7.8×10^6 and 9.7×10^6 [m^{-1}], respectively. The expected flow conditions existing inside the machine during the actual tests were contained between these Mach number values. Although the Reynolds numbers for the test were higher than the ones for which the probes were calibrated at, these values (test Re) were also considerably higher than 2.0×10^4. It has been shown that probe accuracy for this type of probe is not significantly influenced by viscous effects for Re numbers above this value [13,15].

Once the probes are calibrated at given M and Re numbers, the preprocessed calibration data is stored in data files that are associated to each one of the individual probes. The probes can then be inserted into an unknown flowfield and the velocity magnitude and direction with respect to the probe tip can be accurately calculated from the measurement of the pressure at the five pressure ports located at the probe tip and the total temperature of the flowfield in close proximity to the 5-hole probe. For the case at hand, these calculations were made using the data reduction software (Multiprobe V. 3.0) supplied by the Aeroprobe Corporation. This software is based on the utilization of the probe preprocessed calibration data files and the least-squares interpolation technique [11,12,16]. The algorithm uses a local interpolation scheme based on least-squares surface fitting of the pressure coefficients and the recorded angles. The algorithm accounts for compressibility effects and can therefore be applied to accurately reduce data from probes inserted into any subsonic flow field. The software was integrated as a DLL into Dresser-Rand's (D-R) proprietary data acquisition software. The Multiprobe software was initially designed for the reduction of probe measurement data performed in air as a test medium and relied heavily on the use of ideal gas relations. In view that D-R uses real gas equations of state for the calculation of gas properties and the actual tests were performed using nitrogen and carbon dioxide as test media, the original Multiprobe DLL was modified by Aeroprobe to permit the use of real gas properties as well as different test media other than air (e.g., N_2 and CO_2).

The new DLL used measured data, which included the pressures at the five holes located at the tip of the probe (P_1 through P_5) and the total temperature of the flow (T_t), measured by additional instrumentation discussed in the data reduction and coordinate transformation section this paper. The DLL also used thermodynamic properties of the gas [i.e., the molecular weight (MW), absolute viscosity (μ), compressibility ratio (Z_s) and the isentropic volume exponent (n_s or γ)] and the preprocessed calibration files that were generated for each probe to calculate the flow incidence with respect to the probe tip axis. As mentioned above and presented in Fig. 3, this incidence is typically expressed with respect to one of two coordinate systems (pitch and yaw angles or cone and roll angles). The DLL also calculated the total and static pressures of the flow (P_t and P_s, respectively) at the location of the probe tip. Once these parameters were available, the DLL proceeded to calculate the Mach number (M), the static temperature (T_s) of the flow, the speed of sound (a) for the flow conditions, the density (ρ) of the flow, and finally the velocity magnitude of the flowfield ($|\vec{V}|$). Finally, the components of the velocity vector are calculated using the flow incidence and the flowfield velocity magnitude. The data reduction sequence of calculations is summarized below.

Typically, when the probe is inserted into the unknown flowfield, the pressures at the tip of the probe (P_1 through P_5) are measured for each test condition (or test point). The five pressures are used in Eqs. (1) and (2) (for the case of low incidence angles) to calculate the pitch and yaw angle coefficients (B_α and B_β). These values are then used in combination with the preprocessed calibration data files (expressions for α, β, A_t and A_s as functions of B_α and B_β) by the DLL to calculate the values of the pitch and yaw angles as well as the total and static pressure coefficients (A_t and A_s). The total and static pressures can then be calculated using $P_1 - P_5$, A_t and A_s by rearranging Eqs. (3) and (4). For the case of high incidence angles, a similar procedure as the one described above is used but Eqs. (1)–(4) are substituted by the corresponding equations defined for this regime [11,12,16]. It is important to state that for the software used herein, the above expressions (α, β, A_t and A_s as functions of B_α, B_β) are used on a localized basis.

The equations that are used to calculate the rest of the parameters of interest (i.e., flowfield velocity magnitude and three-dimensional components) are presented below.

mach number,

$$\mathrm{M} = \left[\frac{2}{\gamma - 1}\left[\left(\frac{P_t}{P_s}\right)^{(\gamma-1/\gamma)} - 1\right]\right]^{1/2} \tag{5}$$

static temperature,

$$T_s = \frac{T_t}{1 + \left(\frac{\gamma - 1}{2}\right)\mathrm{M}^2} \tag{6}$$

speed of sound,

$$a = \sqrt{n_s g_c R T_s Z_s} \tag{7}$$

density of flow,

$$\rho = \frac{P_s}{ZRT_s} \tag{8}$$

velocity magnitude,

$$|\vec{V}| = a\mathrm{M} \tag{9}$$

Reynolds number,

$$\mathrm{Re} = \frac{\rho|\vec{V}|L}{\mu} \tag{10}$$

where L is a characteristic length (i.e., probe diameter)

velocity—x direction,

$$u = |\vec{V}|\cos(\alpha)\cos(\beta) \tag{11}$$

velocity—y direction,

$$v = |\vec{V}|\sin(\beta) \tag{12}$$

velocity—z direction,

$$w = |\vec{V}|\sin(\alpha)\cos(\beta) \tag{13}$$

As mentioned above, each probe may have several calibration files, hence the above calculations must be performed using each one of the calibration files for each given probe. The final result for each parameter (i.e., α, β, P_t, P_s, V, etc.) is calculated by interpolation of the results between the data predicted by each calibration file. The interpolation is based on weight functions which are determined by the difference between the predicted Mach and Reynolds numbers and the values of these numbers for which the calibrations were performed [11,12,16].

Description of Test Vehicle and Instrumentation

The test vehicle that was used for this work was a Dresser-Rand DATUM multi-stage centrifugal compressor. The compressor was a three-stage medium head natural gas pipeline booster, equipped entirely with prototype aerodynamic components (impellers and stationaries). The impellers were approximately 20 in. (508 mm) in diameter and the diffuser passages had a width on the order of 1 in. (25.4 mm). The first and second stages were designed with vaneless diffuser configurations, while the third stage incorporated a full passage width low solidity diffuser (LSD) with a two-dimensional profile.

The machine was instrumented internally to measure the total pressure and total temperature at each impeller eye and return bend in order to obtain stage to stage data (see Fig. 4). Three sets of probes were distributed circumferentially at each measurement station. The three sets of redundant data helped to reduce the uncertainty of the measurements. Combination probes, capable of measuring both total pressure and total temperature with a single probe, were utilized to reduce the number of probes that would be placed in the gas flowpath (see Fig. 5). The combination probes had a stem diameter of 0.250 in. (6.35 mm) but the sensor tips that were actually immersed in the gas flow were reduced down to a diameter of 0.125 in. (3.175 mm). The 0.125 in. diameter probe tips helped to reduce the blockage effects caused by the immersion of instrumentation into the gas flowpath.

In addition to the combination probes, four 5-hole probes were located in the second stage of the test compressor. Two 5-hole probes were placed at the diffuser entrance and two were located at the return bend (see Fig. 6). The second stage was selected to best represent the true flow conditions of a multi-stage compressor due to the fact that it was an intermediate stage (i.e., there was one stage located upstream and one downstream of the test-stage). Selecting the second stage of the compressor minimized the effects of the compressor inlet or volute design on the gas flow being measured.

The 5-hole probes used for this development test were L-shaped and had a 0.250 in. hex body and a 0.125 in. diameter stem and tip. Knowledge of the probe tip orientation within the machine was critical in order to obtain accurate flow angle measurements. During probe calibration the hex body was used to align the probe and therefore the exact position and orientation of the hex of the probe, and hence the tip, within the compressor was known during the tests. Since the test compressor was of the DATUM design with horizontally split internals, the probes were placed along the split-line of the internals for easy access (see Fig. 7). Slots were machined parallel to the split-line in order to accurately orient the probe tips at the desired angle. The orientation of the tip with respect to the probe hex-body was preset for this application by the probe manufacturer. In addition to the probe slots, special probe clamps were installed to secure the 5-hole probes in place and allow for immersion adjustments via set-screws (see Figs. 8 and 9).

Due to the fact that traversing mechanisms were not used in the compressor tests, the 5-hole probes were placed at two different immersion depths in the gas flowpath in order to determine the variations in gas velocity and flow angle at these locations. The ''hub side'' probes were located at an immersion depth of 33% from the hub side of the flow channel. The ''shroud side'' probes were set at a depth of 67% from the hub side of the flow channel. This naming convention for the probe immersion was used for the 5-hole probes located at both the diffuser entrance and the return

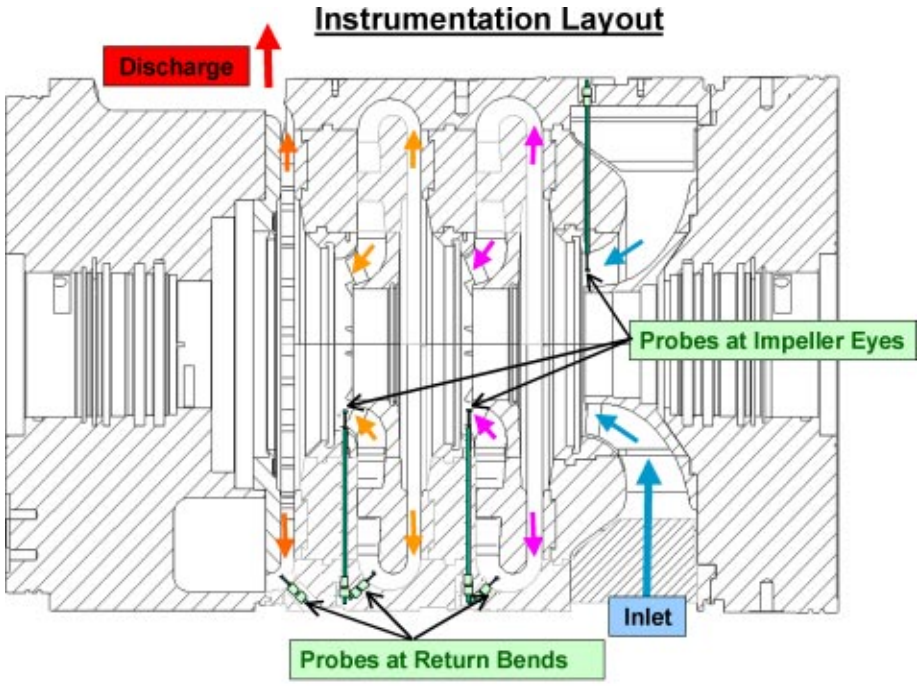

Fig. 4 Internal instrumentation layout

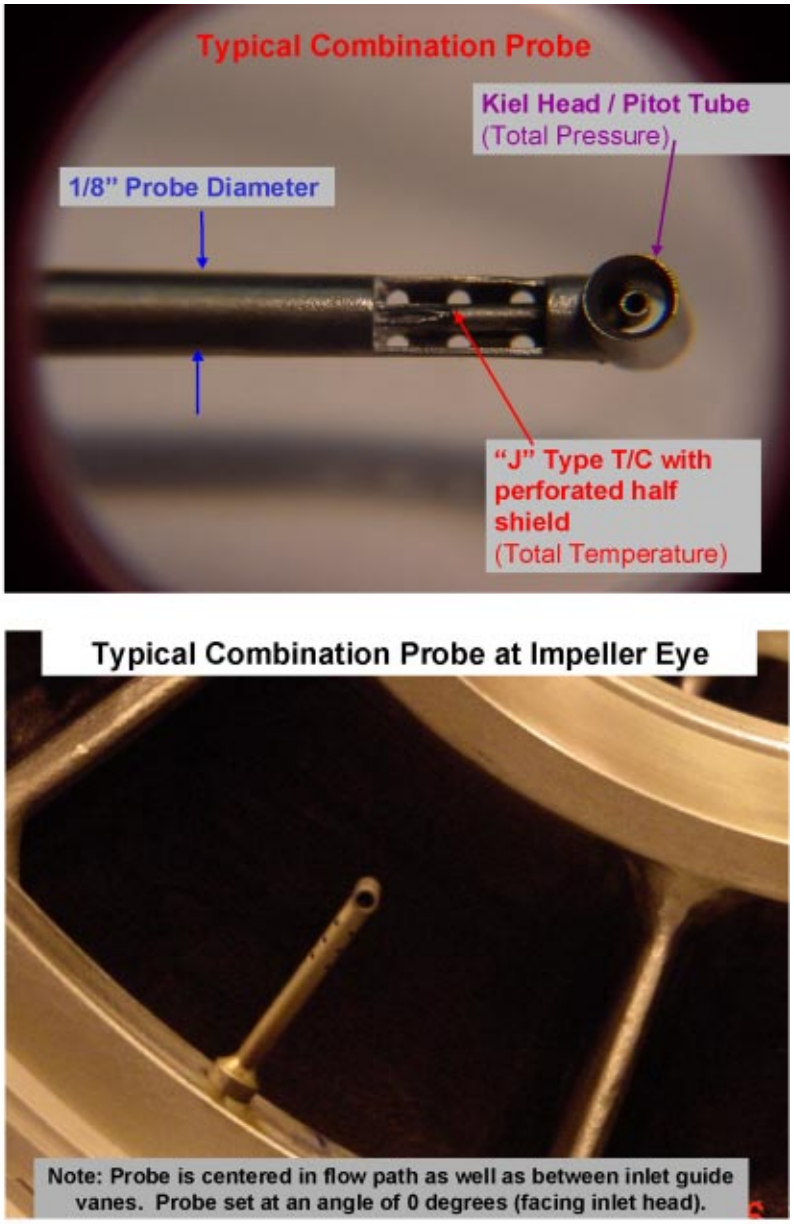

Fig. 5 Combination total pressure/total temperature probe. Probe tip detail (top), probe located at exit of IGV (bottom).

bend of the second stage of the compressor. The diffuser entrance and return bend each contained one ''hub side'' and one ''shroud side'' probe (see Figs. 8 and 9).

Test Description

The prototype compressor was operated on a closed loop test stand at Dresser-Rand's production test facility. The test configuration consisted of the prototype compressor driven by a steam turbine through a reduction gearbox (see Fig. 10). A type 2 test per ASME PTC 10 was performed to establish the performance of this pipeline booster compressor. Three speed lines were run for the test, each at a different machine Mach number (U_2/Ao), to encompass the expected operating range of the compressor (0.25 to 0.75 U_2/Ao). Nitrogen was the test medium used for the low and design machine Mach number test runs while carbon dioxide was utilized for the higher machine Mach number test. Total temperature and total pressure measurements were taken on the inlet and discharge flanges of the compressor at four circumferential locations for each station. The volumetric gas flowrate handled by the compressor was determined by means of an orifice plate. In addition to the internal measurements, the inlet and discharge flange data were utilized to determine the overall performance of the machine in order to compare with the predicted values.

The internal instrumentation (5-hole and combination probes) leads were routed out of the compressor through high-pressure seals which were installed at the non-drive end of the machine, maintaining the mechanical integrity of the compressor. The 5-hole probe pressure leads were connected to true differential pressure blocks in order to obtain high-resolution measurements of the differential pressure between the individual ports on the probe tips. In view that the static pressure at the location where the 5-hole probes were to be installed was on the order of 300 PSIG, and the magnitude of the dynamic pressure component $(1/2\,\rho V^2)$ at that location was expected to be less than 15 PSID, a special arrangement was required to accurately measure the individual pressures at the probe tip. It is important to recall that the

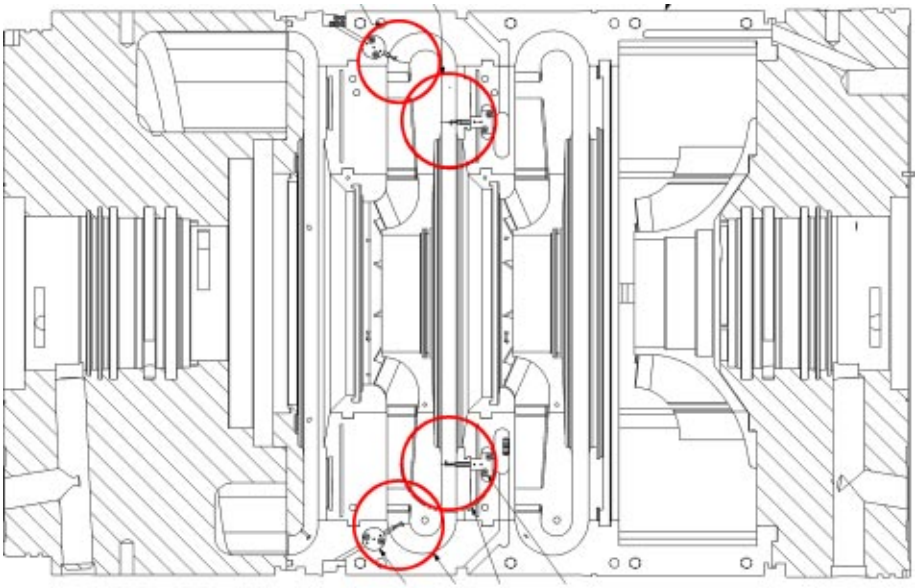

Fig. 6 Location of 5-hole probes

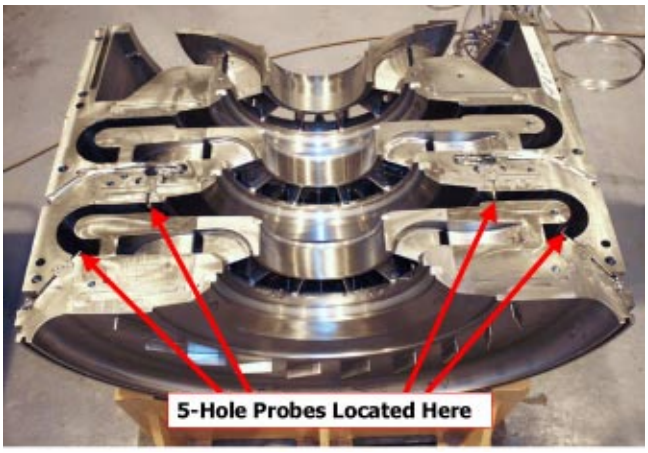

Fig. 7 Overview of 5-hole probe location

5-hole probe calculations are based on pressure differences between the individual ports of the probe, hence it is of paramount importance that the port pressures are measured as accurately as possible. If a pressure block with a 500 PSI range was used for these measurements, the accuracy of the transducers are on the order of 0.25 PSI, which would be much greater that the slight differences existing between the pressure ports of the probes, hence the measurements would be virtually useless. To circumvent this problem, true differential pressure blocks with a 45 PSID range were selected to measure the pressures at the probe tip. This selection was based both on the value of the dynamic pressure component mentioned above, as well as the fact that these pressure blocks would be used for a single-stage test rig at a later date, requiring the measurement of pressures on the order of 30 PSID.

The pressure at the central port (port 1) of each probe was used as a reference value for the measured pressure corresponding to the remaining four ports of the respective probes (via a manifold). That is, the pressure measurement for each one of the ports located at the periphery of the cone tip was referenced to the value of the pressure at the central port, hence the values for these true-differential pressures remained well below 15 PSID. This ar-

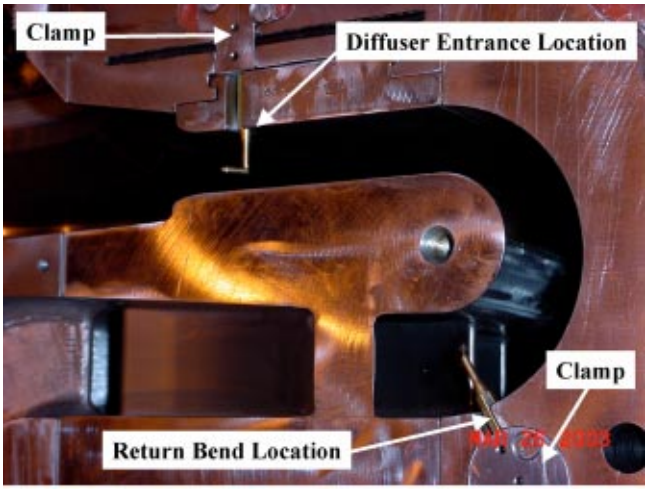

Fig. 8 Location of hub side probes

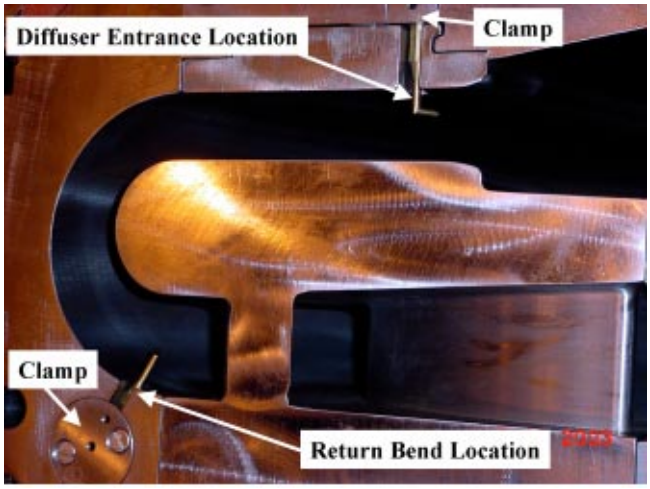

Fig. 9 Location of shroud side probes

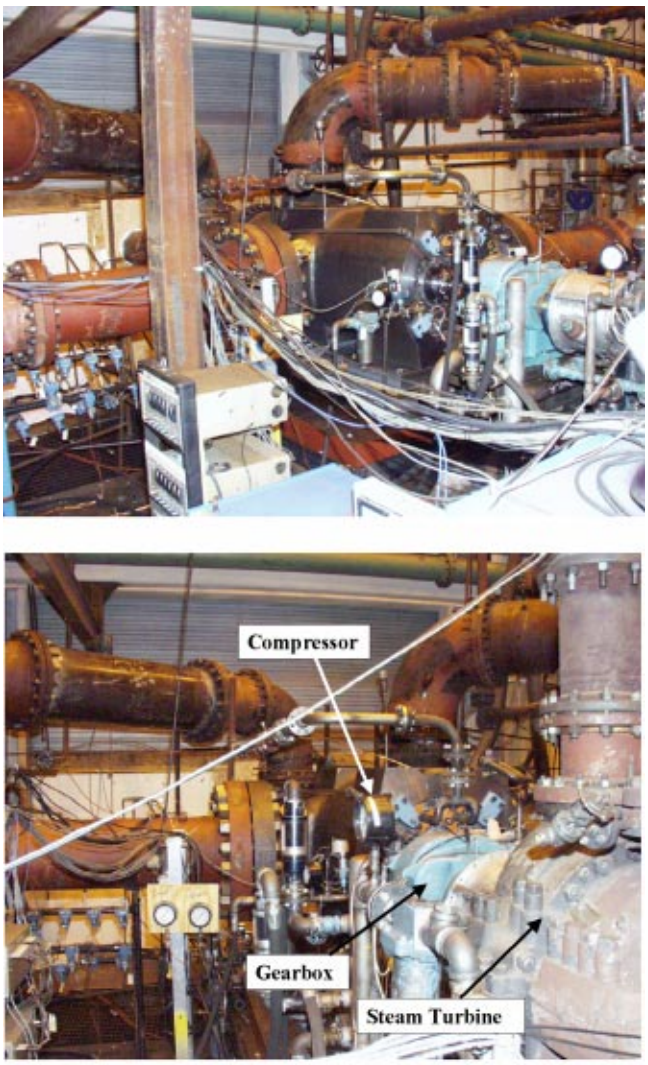

Fig. 10 Compressor test setup

rangement was only permitted by the use of true differential pressure blocks in which each individual pressure transducer (16 in total) would have their own reference pressure port. With this configuration, the pressure blocks were able to measure the pressure with a resolution which was adequate for 5-hole probe measurements. Inspection of Eqs. (1) and (2) shows that referencing the 5-hole pressures to P_1 will not affect the values of the calculated independent nondimensional coefficients used for the 5-hole probe calculation algorithms. The pressure signal of the central ports of each probe was also measured using the regular pressure blocks utilized by the main DAQ system, hence the absolute pressures of all of the pressure ports of the 5-hole probes were also available. Figure 11 shows a schematic of the connection diagram of 5-hole probes to a differential pressure block.

Data Reduction and Coordinate Transformation

The raw pressure data received from the 5-hole probes were first reduced using the modified algorithms supplied by the probe manufacturer. This software used the ''real gas'' behavior of the test media as well as each probe's calibration file. As mentioned in the previous section, the algorithm requires a measurement of the total temperature of the flowfield at (or close to) the probe tip location (point of measurement). For the case at hand, the value of the total temperature supplied to the 5-hole probe data reduction software corresponded to the value measured by the combination probes located at the second stage return bend. The software then calculated the pressures (total and static) as well as the velocity of the flow (magnitude and direction). However, this data was referenced to the coordinate system of each probe. In order to make use of the data and compare to CFD calculations, the values had to be transformed to the coordinate system of the machine.

Although it may be possible that on some occasions both the probe and machine coordinate systems may coincide due to the proper alignment of the 5-hole probes within a machine, in general this is not the case. Typically, probes must be installed at locations that require the least amount of machining and modifications to the compressor components in order to reduce the cost and effort to install instrumentation. Additionally, the probes must be installed avoiding lifting holes and alignment pins, which may be obstructing the location at which a probe would be aligned

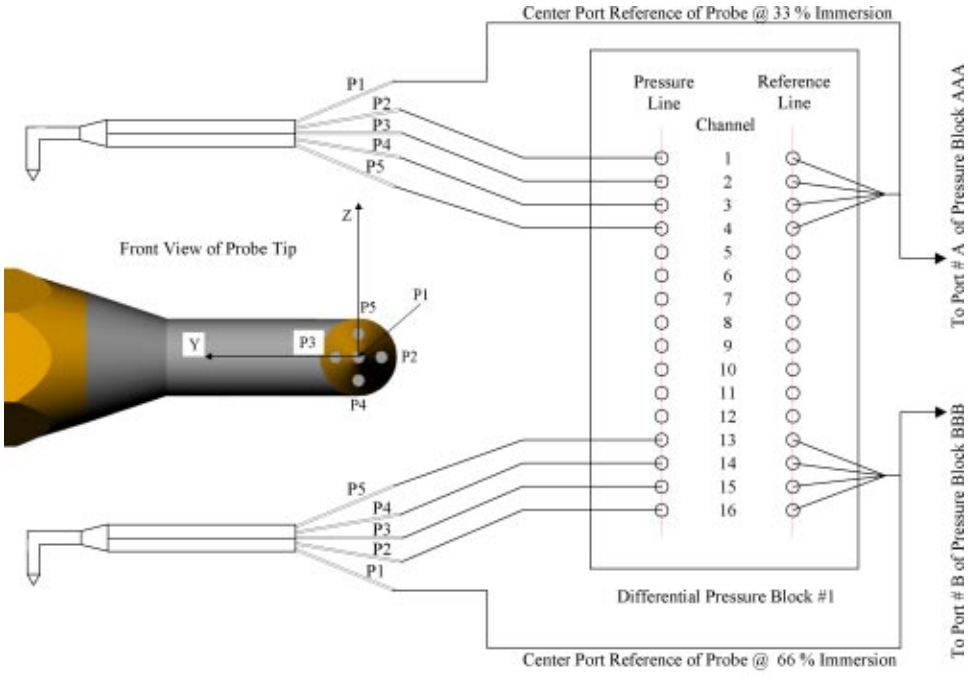

Fig. 11 Connection of 5-hole probes to pressure blocks

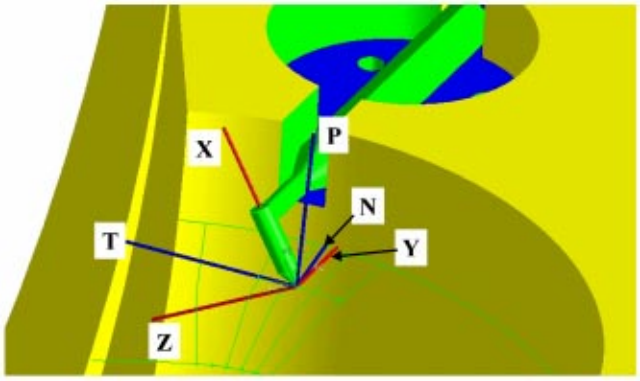

Fig. 12 Model of 5-hole probe installed in the shroud side of the compressor return bend

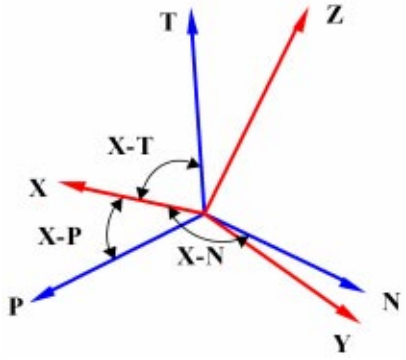

Fig. 14 Definition of direction cosines for projection of the *x*-axis from the PACS into the machine axis coordinate system (MACS)

with the machine axis. Factors such as these limit the number of applications for which the probe axis coordinate system coincides with the machine axis coordinate system. Therefore a procedure or method to transform the data from one coordinate system to the other is needed.

For the case at hand, the diffuser entrance 5-hole probes shared one axis of the coordinate system with the machine and therefore the coordinate transformations were merely two-dimensional problems. However, the 5-hole probes located at the return bend positions did not share a common axis with the machine and the coordinate transformations became three-dimensional problems.

Figure 12 presents a view of the ''shroud side'' 5-hole probe installed in the return bend of the test compressor. As may be seen in the figure, the probe axis coordinate system (PACS, shown in red) does not coincide with the machine axis coordinate system (MACS, shown in blue). Note that for the case of the MACS, one axis (**T**) is aligned with the tangential direction of the flowpath (at the location of the probe tip) on a radial plane that passes through the machine shaft centerline and through the tip of the probe. Axis **N** corresponds to the normal direction with respect to the flowpath and lays on the radial plane (**N** is perpendicular to **T**). On the other hand, axis **P** is perpendicular to the radial plane and orthogonal to both of the axes described previously. As mentioned above, the flow velocity vector must be represented in the machine axis coordinate system to simplify the comparison between the experimental and CFD data.

Figure 13 presents another view of a 5-hole probe showing both the PACS and the MACS coordinate systems that are used with the 5-hole probe measurement system. Figure 14 shows the definition of the direction cosines of the **X**-axis with respect to the machine axis coordinate system. These angles are required in order to perform the coordinate transformation from the PACS to the MACS [17,18]. The direction cosines for the **Y**-axis and **Z**-axis are defined in a similar manner and are not shown. Projecting each one of the velocity vector components from the PACS (u, v and w) into the MACS by means of the direction cosines permits the transformation. The coordinate transformation data (direction cosines) were obtained from the CAD model of the compressor, which was generated during the creation of the instrumentation layout.

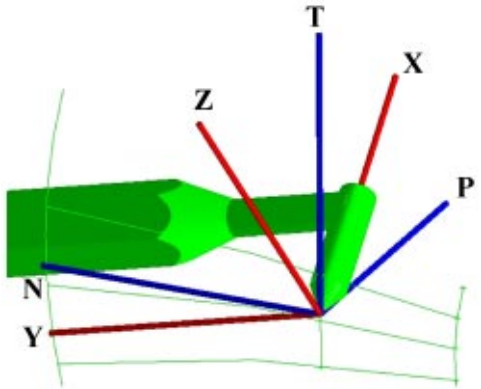

Fig. 13 View of probe showing the two coordinate systems that are used (PACS in red and MACS in blue)

The transformation of the velocity vector components from the probe axis coordinate system (**X**,**Y**,**Z**) to the machine axis coordinate system (**P**,**N**,**T**) is performed by application of the expressions shown below. For the case of the velocity component in the **X** direction (**u**), this vector is expressed in the MACS by means of $\mathbf{U_P}$, $\mathbf{U_N}$ and $\mathbf{U_T}$, which are the components of the vector in the perpendicular, normal and tangential directions, respectively. The **v** and **w** components are transformed in a similar manner.

Velocity component in the **X** direction (**u**):

$$\mathbf{P}\ \text{component:}\quad U_P = u\cos(X-P) \tag{14}$$

$$\mathbf{N}\ \text{component:}\quad U_N = u\cos(X-N) \tag{15}$$

$$\mathbf{T}\ \text{component:}\quad U_T = u\cos(X-T) \tag{16}$$

Velocity component in the **Y** direction (**v**):

$$\mathbf{P}\ \text{component:}\quad V_P = v\cos(Y-P) \tag{17}$$

$$\mathbf{N}\ \text{component:}\quad V_N = v\cos(Y-N) \tag{18}$$

$$\mathbf{T}\ \text{component:}\quad V_T = v\cos(Y-T) \tag{19}$$

Velocity component in the **Z** direction (**w**):

$$\mathbf{P}\ \text{component:}\quad W_P = w\cos(Z-P) \tag{20}$$

$$\mathbf{N}\ \text{component:}\quad W_N = w\cos(Z-N) \tag{21}$$

$$\mathbf{T}\ \text{component:}\quad W_T = w\cos(Z-T) \tag{22}$$

Following these operations, the velocity vector ($\vec{V}_M$) can be expressed in the machine axis coordinate system as:

$$V_{MP} = U_P + V_P + W_P \quad \text{perpendicular direction} \tag{23}$$

$$V_{MN} = U_N + V_N + W_N \quad \text{normal direction} \tag{24}$$

$$V_{MT} = U_T + V_T + W_T \quad \text{tangential direction} \tag{25}$$

The magnitude of the velocity vector may be expressed as:

$$|\vec{V}_M| = \sqrt{V_{MP}^2 + V_{MN}^2 + V_{MT}^2} \tag{26}$$

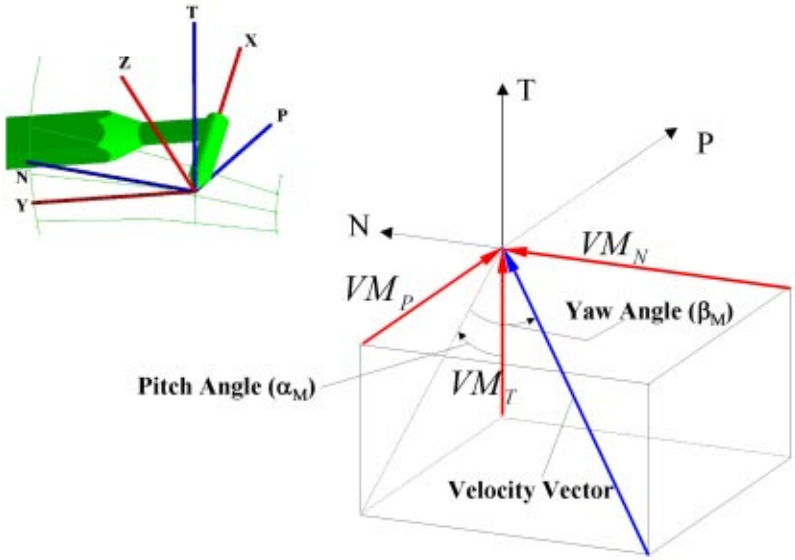

Fig. 15 Machine axis coordinate system definition

Following the angle convention shown in Fig. 15, the pitch and yaw angles in the machine coordinate system ($\boldsymbol{\alpha_M}$ and $\boldsymbol{\beta_M}$, respectively) may be expressed as:

$$\alpha_M = \tan^{-1}\left(\frac{V_{MP}}{V_{MT}}\right) \quad \text{pitch angle} \tag{27}$$

$$\beta_M = \tan^{-1}\left(\frac{V_{MN}}{\sqrt{V_{MP}^2 + V_{MT}^2}}\right) \quad \text{yaw angle} \tag{28}$$

This procedure may be used for any application in which the velocity vector components are known in one frame of reference and need to be transformed into another frame of reference that shares the origin and that has the axes rotated with respect to the known system (i.e., this coordinate transformation only includes rotation). If the origins of the coordinate systems are not coincident, then a translation must be included into the operations, this, however, is not the case at hand and hence will not be addressed herein.

Test Results and Discussion

As may be seen in Fig. 16, the prototype compressor fell short of its performance goals and was short in stability and overload capacity. Furthermore the efficiency levels were also short of expectations.

The interstage instrumentation provided stage-by-stage performance data. This data was obtained from the analysis of the information provided by the combination probes and identified the third stage as the major contributor to the performance shortfall, clearly limiting both ends of the curve (surge and overload). The first and second stage diffusers were of the vaneless type, while the third stage was equipped with a low solidity vaned diffuser (LSD). The LSD vanes had a 2D profile and were set at an angle suggested by CFD calculations. In view of the above, it was suspected that the third stage performance was being deteriorated by an improper setting of the LSD vanes.

It is important to state that although the 5-hole probes were installed at the diffuser entrance and the return bend of the second stage, flow angle measurements obtained at this stage are applicable to the first and third stages due to the fact that all of the impellers in the compressor were contour trims of one progenitor. It is well known that when impeller families are generated by contour trimming of one parent or progenitor, the resulting impellers have similar performance characteristics, such as head coefficient, efficiency, exit flowfield, etc.

Figure 17 shows the exit velocity triangle for a typical centrifugal compressor impeller. For the case at hand, the absolute flow exit angle (α_2) is measured with respect to a radial line. Figure 18 shows a schematic of the exit velocity triangle with reference to an LSD vane. Note that as the volumetric flow rate (Q) through the impeller increases, the magnitude of the relative exit velocity (W_2) also increases. This causes the flow to become more radial (i.e., the absolute flow angle decreases). As may be inferred by the figure, for the case of a fixed geometry LSD vane, the optimum incidence can not be maintained for the whole range of operation, therefore special care should be taken to match the LSD vane

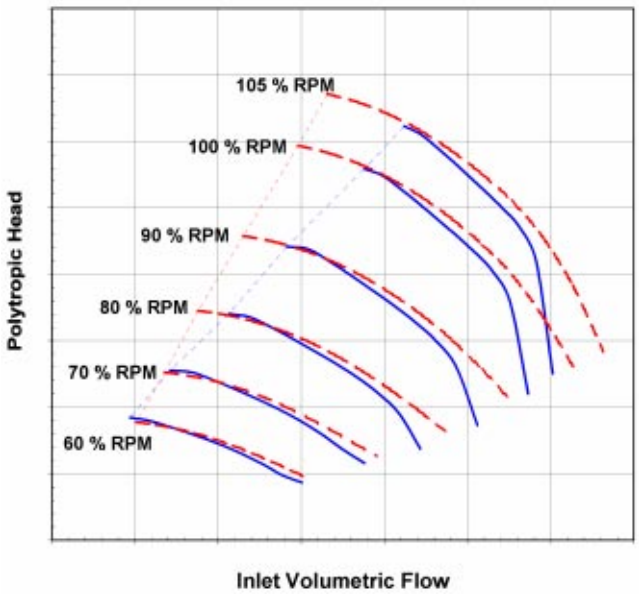

Fig. 16 Compressor polytropic head versus volumetric flow. Predicted (red-dashed) versus tested (blue-solid).

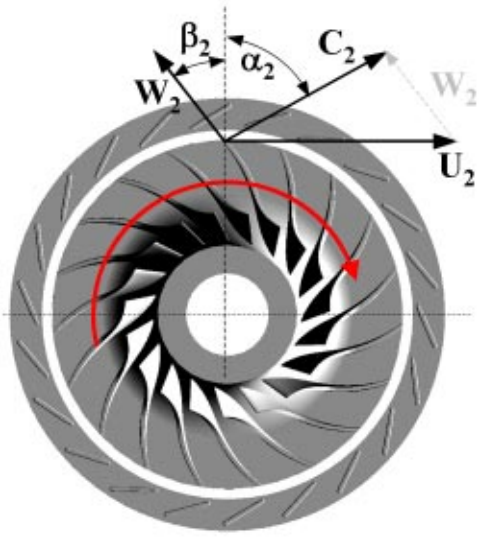

Fig. 17 Impeller exit velocity triangle

setting angle to optimize the incidence between the flow exiting the impeller and the LSD vane at the design condition.

Figures 19 and 20 show the flow angle as a function of machine flow coefficient (Q/N) at the diffuser entrance (close to the impeller exit) as measured by the 5-hole probes that were installed in the second stage of the machine. This angle is expressed as incidence with respect to the setting angle of the LSD installed at the third stage diffuser. Figure 19 corresponds to the measurements taken close to the hub side of the flow path, while Fig. 20 represents the flow close to the shroud side. These figures show data for three different values of machine Mach number (U_2/Ao), which cover the expected range of operation of the prototype stages. As may be seen in Figs. 19 and 20, the flow angle shows a steady increase as the stage flow coefficient is decreased from choke towards surge as discussed in Fig. 18.

Figure 21 shows a similar plot for the case of the 5-hole probes located at the return bend of the machine. Note that this plot shows a comparison between the flow angles measured at the hub and at the shroud side of the flowpath for the design machine Mach number (U_2/Ao). This plot shows a similar behavior as the one discussed above.

Figure 22 shows a comparison between the flow angle measured at the "hub" and at the "shroud" of the flowpath for the case of the 5-hole probes installed at the diffuser entrance. Note

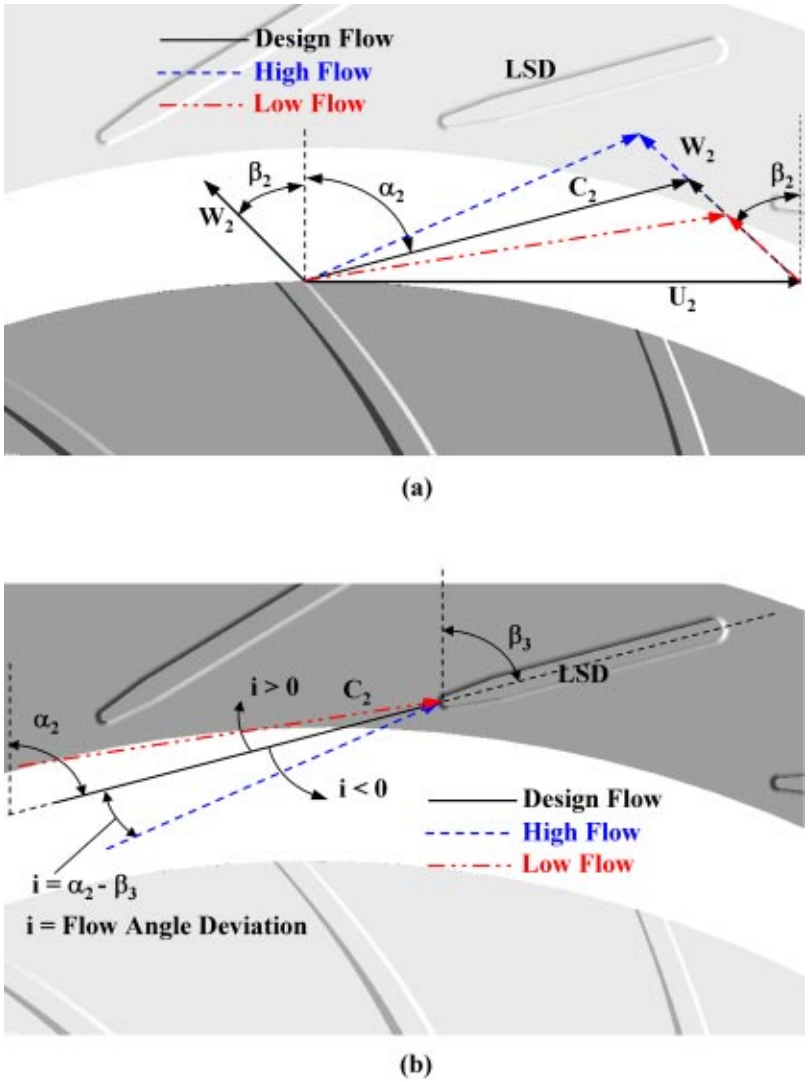

Fig. 18 (*a*) Alignment of impeller exit flow and LSD, (*b*) definition of flow angle deviation

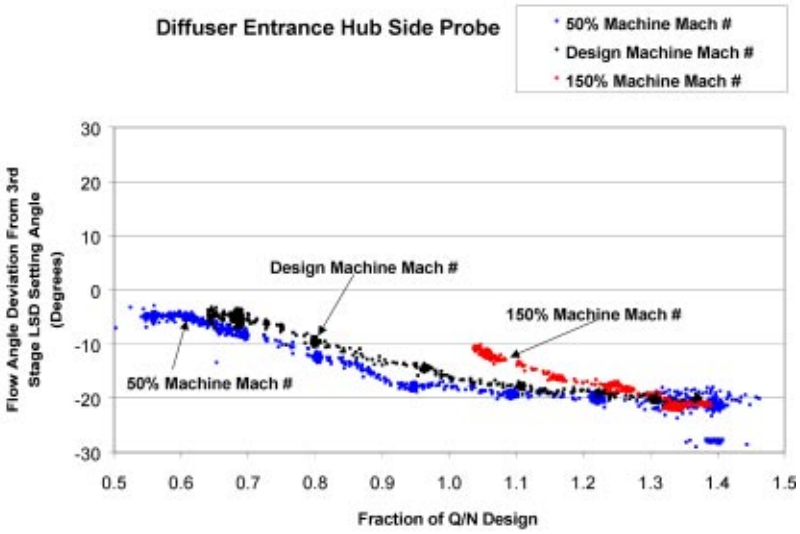

Fig. 19 Flow angle at diffuser entrance (3 values U_2/Ao)—hub side

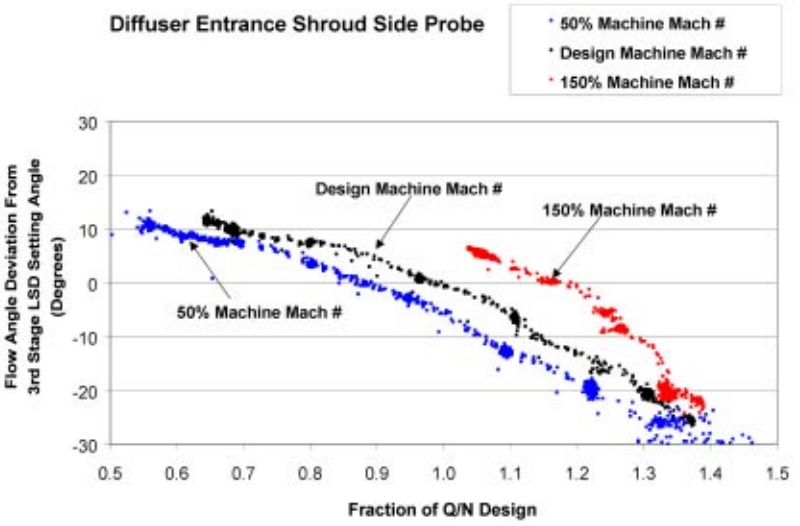

Fig. 20 Flow angle at diffuser entrance (3 values U_2/Ao)—shroud side

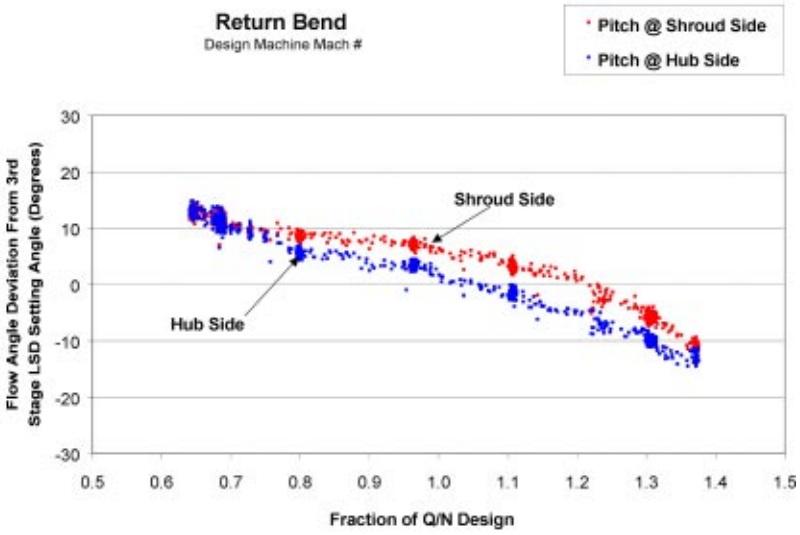

Fig. 21 Flow angle at return bend (design U_2/Ao)—hub versus shroud

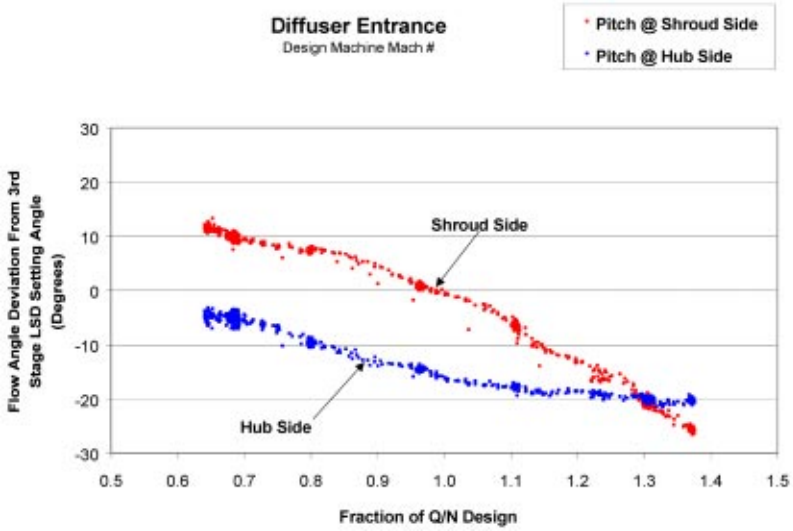

Fig. 22 Flow angle at diffuser entrance (design U_2/Ao)—hub versus shroud

that as the machine approaches surge, there is a significant difference between the measurements performed at the hub and at the shroud. This suggests that the flow exiting the impeller is skewed, being more radial close to the hub and more tangential close to the shroud. Also, the difference between the flow angularity makes it evident that the 2D profile of the LSD vane is not appropriate for this application. As may be seen in Fig. 22, the setting angle of the LSD is relatively close to the flow angle measured at the shroud side of the machine at the design flow, nevertheless at stall conditions the value of incidence is in excess of 12 deg. For the case of the flow close to the hub, it is evident that the flow never reaches the LSD setting angle, which means that there is a negative incidence on the LSD across the entire range on the hub side. Note that this behavior is also observed in Fig. 19. It is important to state that Fig. 22 corresponds to measurements taken at the design machine Mach number, nevertheless, the same behavior was observed for the off-design machine Mach numbers, hence the above discussion is valid for those conditions as well.

Returning to Fig. 21, it is important to note that for the case of the flow at the return bend, the difference between the flow angularity at the hub and at the shroud has been reduced considerably, which suggests that the skewness of the flowfield has been re-

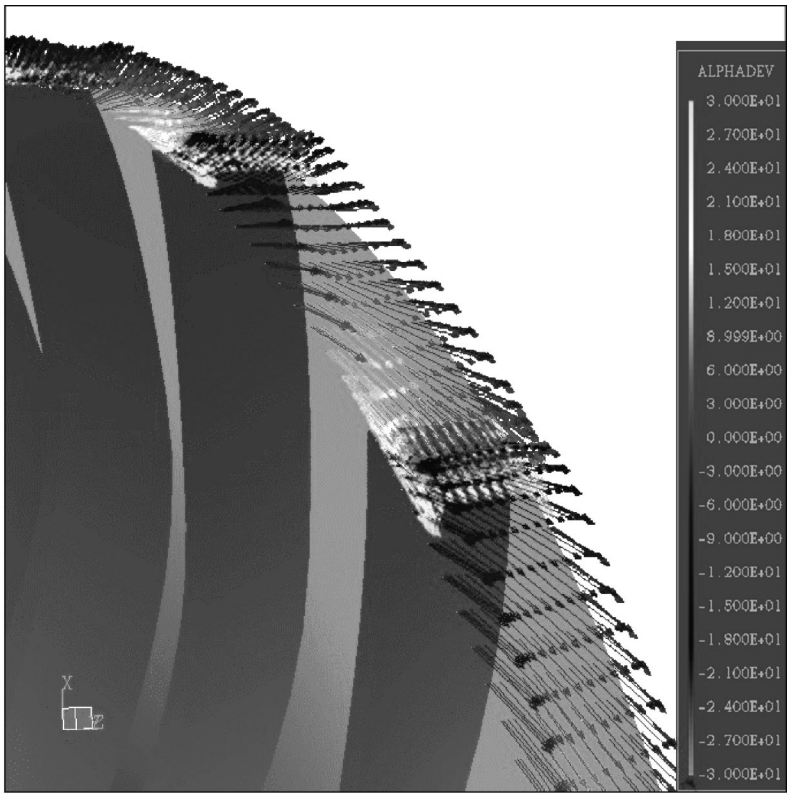

Fig. 23 Predicted impeller exit velocity

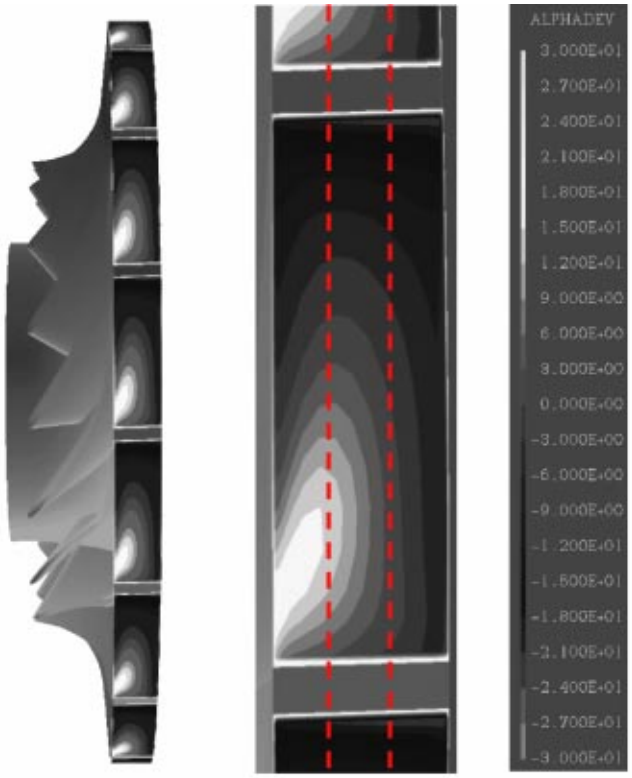

Fig. 24 Predicted impeller flow exit angle. Overall view (left) and detailed view of one flow passage (right) showing the location of the 5-hole probe measurements (dashed lines).

duced as it travels downstream of the impeller exit. This is most likely due to mixing effects and viscous dissipation caused by shear forces within the flow.

The 5-hole probes also provided the measurement of the ''yaw'' angle (perpendicular to the pitch measurement on the MACS). The test results showed that the yaw angle at all of the measured locations was negligible and remained constant throughout the operating range (surge to choke). This was a result of the 5-hole probes being installed into the machine so that their pitch angle plane (in the MACS) was aligned with the geometric flowpath.

Figure 23 shows a vector plot of the predicted impeller exit velocity for the design flowrate of the machine, operating at the design machine Mach number. The compressor was modeled using sector passages (pie slice) of the axisymmetric portion of the main inlet, all three impellers, diffusers and return channels. The discharge volute and the non-axisymmetric portion of the main inlet were not included. The overall size of the CFD model was about 500,000 nodes. The analysis was performed using CFX-TASCflow assuming steady-state conditions with a frozen rotor interface model between rotating and stationary components.

Figure 24 shows contour plots of the predicted (via CFD) impeller exit flow angle at the locations where the 5-hole probes were installed within the diffuser entrance. This figure was generated for the same operating conditions as Fig. 23. It is important to state that the CFD analysis showed a variation of about 6 deg between the predicted values at the above-mentioned locations, which were obtained by mass-averaging the exit flow angle data. This variation is within the expected range for an impeller with this type of flow-coefficient. On the other hand, for this same flow condition, the 5-hole probe data suggested that the difference between the flow exit angle reached a value of about 15 deg. This may be seen in Fig. 25 which shows a comparison between the test data and the CFD predictions (mass-averaged flow angle at the impeller exit for both immersion locations). Some possible reasons for the failure of the CFD code to completely capture the full hub to shroud flow angle variation include the effects of turbulence and interface modeling as well as the use of a coarse grid density. Additionally, it is important to mention that secondary flowpath leakage was not considered in the CFD model due to time constraints.

After the initial testing of the prototype machine, the results obtained by the use of 5-hole probes at the second stage supported the belief that the LSD installed at the third stage diffuser was the main reason for the performance shortfall. Furthermore, skewness of the flow angle between the hub and the shroud sides of the diffuser suggested that the use of a 2D profiled LSD was not appropriate for this machine. The flow near the hub was sufficiently radial and did not require the use of LSDs, while the flow close to the shroud would greatly benefit from the use of a guiding vane. In view of this, it was decided that the LSD be substituted by a rib diffuser on the shroud side with a vane immersion of

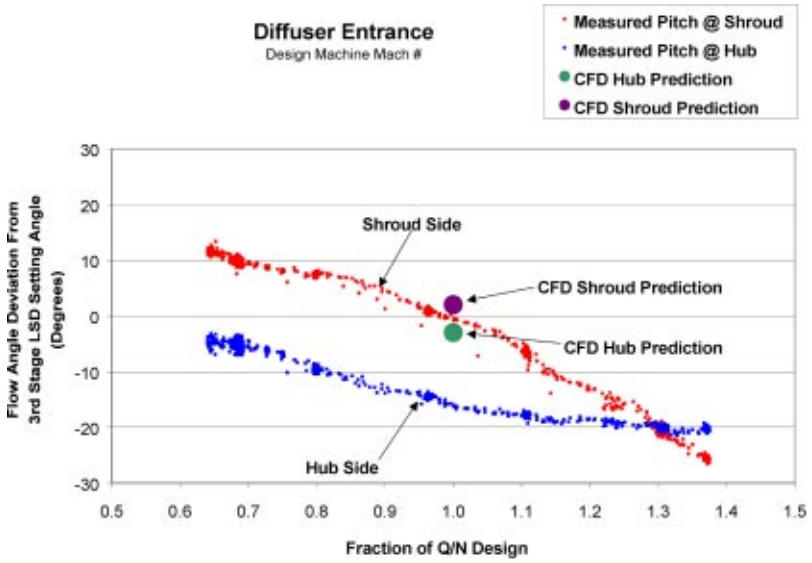

Fig. 25 Flow angle at diffuser entrance (design U_2/Ao). Comparison of test data and CFD predictions at the design flow rate.

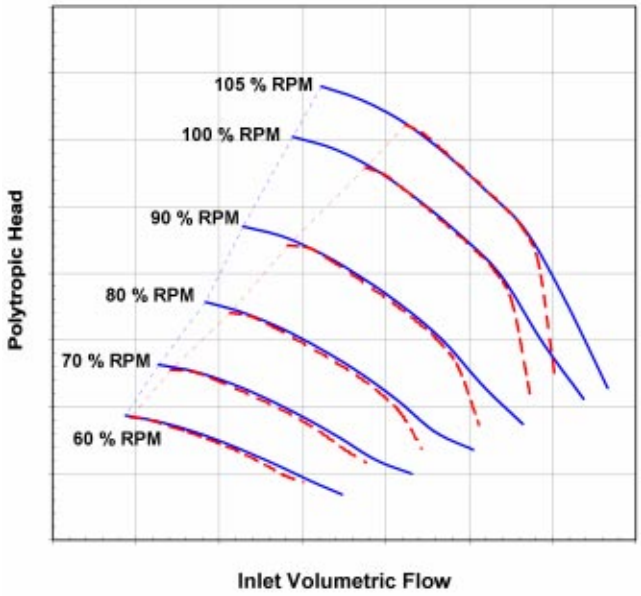

Fig. 26 Compressor polytropic head versus volumetric flow. Comparison between the performance of the original (red-dashed) and improved (blue-solid) prototype configurations.

about 30% of the flowpath height. The setting angle of the vanes was also adjusted slightly to better match the measured flow angles. It was expected that the use of this rib diffuser would increase the overload capacity and surge margin of the machine.

Figure 26 shows a comparison between the performance of the initial prototype machine configuration and the improved configuration. As may be seen in the figure, the use of rib diffusers yielded a significant improvement in performance. Both the surge margin and overload capacity were dramatically improved.

Figure 27 shows a comparison between the flow angle measured at the ''hub'' and at the ''shroud'' of the flowpath for the case of the 5-hole probes installed at the diffuser entrance for the original and the modified configuration. Note that the flow angles presented very little variation between the two tests, which suggest good repeatability of the data measurements as well as the fact that the diffuser modifications did not cause any detrimental effects on the flowfield exiting the second stage impeller. The only exception is close to surge where the downstream vanes seem to influence the flow angle measured by the probe located on the shroud side, which may be due to ''guiding'' effects that the ribs have over the flow in this region.

Comments on the Use of 5-Hole Probes

As mentioned previously, the use of multi-hole pressure probes has been limited to laboratory or research type environments under controlled conditions. The test rigs in which they are installed typically contain specially designed traverse mechanisms that allow the probes to be rotated and translated to be able to position the probe at the desired location and orientation with respect to the flowfield. These traversing mechanisms are complex and bulky and do not render themselves useful for production type testing in a multi-stage machine, as these machines do not have space to accommodate these mechanisms. The 5-hole probes used for this work were compact enough to be installed in a production multi-stage machine without major component modifications.

The present work has shown that when used in the non-nulling configuration, properly calibrated probes may be installed at fixed locations inside production type machines and can provide invaluable data regarding the flow direction at the point of measurement. Furthermore, it has been shown that these probes are robust enough to survive the harsh environment that is present in a production type test vehicle.

The 5-hole probe is less attractive than other types of simpler instrumentation due to the cost of the probes and their need for calibration at different Mach numbers. In addition, the installation requirements are certainly more complex for 5-hole probes than for more common instrumentation (i.e., Kiel head pressure probes). In spite of this, the additional data that is available from 5-hole probes (i.e., static and total pressure, velocity magnitude and direction of the flow) many times outweighs the additional resources required for their use.

For the case at hand, the use of 5-hole probes revealed the existence of a large variation between the direction of the flow exiting the second stage impeller. The magnitude of this variation was not adequately captured by the CFD simulations and hence the selection of the type and angle settings of the vaned diffuser was not appropriate for the existing flow conditions. The 5-hole

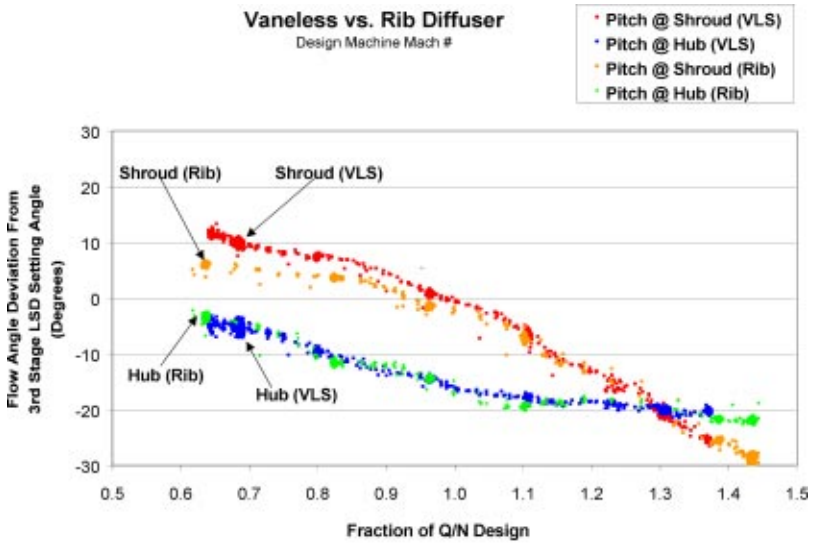

Fig. 27 Flow angle at diffuser entrance (design U_2/Ao)—hub versus shroud. Comparison between original (vaneless) and improved (rib) diffuser configurations.

probe data provided sufficient information to support hardware modifications, which resulted in improved compressor performance and a shorter redesign cycle time.

The use of this type of instrumentation in research test vehicles can provide an invaluable source of data that can be used as a benchmark to calibrate and/or validate analytical design tools such as CFD models.

The probes used for this work were made with a hexagonal stem cross-section (see Fig. 2). The tip of the probe was accurately positioned with respect to this hexagonal stem by the manufacturer. This was done to facilitate accurate orientation of the tip of the probe with respect to the flow passage when it was installed in the machine. This feature simplified the installation and alignment of the probe. When the body of the probe has a circular cross-section, the installation and accurate alignment of the probe head is very time consuming.

Besides the cost, another drawback of these probes is the lead-time for custom probe ordering and manufacturing. This may be circumvented if proper planing of the testing is permitted and sufficient time is allocated to account for this requirement.

As mentioned previously, in order to obtain accurate results with the 5-hole probes, they must be calibrated at several Mach numbers and the calibration matrices must cover the entire range of incidence angles that are expected to be encountered by the probe. The efficient use of this data for the fast reduction of the information measured during the test requires the use of complex algorithms that the user must either develop or purchase. For the case at hand, this work was performed using a site license of the Multiprobe software that is available from the Aeroprobe Corporation, and which is specifically designed for this purpose. Furthermore, the incorporation of these algorithms into D-R's proprietary DAQ system was virtually seamless. It is important to state that collaboration between D-R and Aeroprobe permitted the modification of the existing code to include the use of real gas properties as well as test data performed on gases other than air into the probe data reduction algorithms.

Finally, it should be noted that the current design of the probes and pressure tubing used to conduct the pressure signals from the probe tip to the pressure transducers are not adequate for fast response testing applications. The work reported herein corresponds to the measurement of time-mean flow quantities, which, as shown in this paper, are adequate to determine the correct setting angle of stationary components (i.e., LSD or diffuser ribs). Alternate probe designs and systems are available for fast-response type work; nevertheless, in most cases these probes would not survive the harsh environment encountered in production type testing [10,19,20].

Conclusions

The 5-hole probes provided flow angle information that was not previously available from production type testing. This data supplied invaluable insight into the impeller exit flowfield of a prototype stage.

The information from the probes enabled the identification of the source of the performance shortfall, which had not been predicted by the initial steady-state CFD simulations executed during the design of the prototype. This type of information could be used to shorten redesign cycle times for problematic or newly designed machines. Future work will investigate alternate CFD approaches and turbulence models to improve predictions.

The 5-hole probes installed at a fixed position proved to be an attractive alternative to the use of traverse based systems, specifically for the case of multi-stage production type machines, where the available space is limited.

The work presented in this paper provides evidence to support the use of 5-hole probes in an industrial setting. The 5-hole probes used for this work proved to be robust enough to survive the harsh environment frequently encountered in industrial testing applications.

Acknowledgments

The authors would like to acknowledge the contributions of Chuck Dunn, Steve Wilcox and E. ''Bruce'' Osgood from the Dresser-Rand Test Department for their help with the instrumentation of the machine, data acquisition and data reduction. Also, thanks to Gary Colby, from the Test Department, for his insight in the area of real gas analysis and calculations provided during the modifications of the probe data reduction algorithms. Thanks to Dr. Espen Johansen for the outstanding work with the data reduction algorithm modifications as well as advise in the uses of 5-hole probe data systems. Also thanks to Rick Allen, Dr. Matt Zeiger, and Dr. Othon Rediniotis from the Aeroprobe Corporation, for their help and advice in the design, manufacturing and use of the 5-hole probes used for this work. The authors would like to thank Brian Afton (formerly from the Development Engineering Group) for his help with the compressor and instrumentation drawings, as well as his invaluable insight regarding instrumentation installation techniques. Finally, the authors would like to thank Dresser-Rand for their funding of this work and permission to publish the results.

References

[1] Sorokes, J. M., and Koch, J. M., 1996, ''The Use of Single and Multi-Stage Test Vehicles in the Development of the Dresser-Rand DATUM Compressor,'' Dresser-Rand Technol. J., **2**, pp. 133–147.
[2] Sorokes, J. M., and Welch, J. P., 1991, ''Centrifugal Compressor Performance Enhancement Through the Use of Single-Stage Development Rig,'' *Proceedings of the 20th Turbomachinery Symposium*, Texas A&M, pp. 101–112.
[3] Sorokes, J. M., and Welch, J. P., 1992, ''Experimental Results on a Rotatable Low Solidity Vaned Diffuser,'' ASME paper no. 92-GT-19.
[4] Benvenuti, E., 1978, ''Aerodynamic Development of Stages for Industrial Centrifugal Compressors. Part 1: Testing Requirements and Equipment—Immediate Experimental Evidence,'' ASME paper no. 78-GT-4.
[5] Kotliar, M., Engstrom, R., and Giachi, M., 1999, ''The Use of Computational Fluid Dynamics and Scale Model Component Testing for a Large FCC Prototype Air Compressor,'' Proceedings of the 28th Turbomachinery Symposium, Texas A&M, pp. 69–76.
[6] Borer, C., Sorokes, J. M., McMahon, T., and Abraham, E., 1997, ''An Assessment of the Forces Acting Upon a Centrifugal Impeller Using Full Load, Full Pressure Hydrocarbon Testing,'' Proceedings of the 26th Turbomachinery Symposium, Texas A&M, pp. 111–121.
[7] ASME, 1997, ''PTC 10, Performance Test Code on Compressors and Exhausters,'' ASME Press.
[8] Dieter, W., 2002, ''An Optimized Pneumatic Probe for Investigation of Gas Turbine Aerodynamics in Full Scale Gas Turbines,'' ASME paper no. GT-2002-30044.
[9] Smout, P. D., and Ivey, P. C., 1997, ''Investigation of Wedge Probe Wall Proximity Effects: Part 1—Experimental Study,'' ASME J. Eng. Gas Turbines Power, **119**, pp. 598–604.
[10] Roduner, C., Köppel, Kupferschmied, P., and Gyarmathy, G., 1998, ''Comparison of Measurement Data at the Impeller Exit of a Centrifugal Compressor Measured With Both Pneumatic and Fast-Response Probes,'' ASME paper no. 98-GT-241.
[11] Johansen, E. S., Rediniotis, O. K., and Jones, G., 2001, ''The Compressible Calibration of Miniature Multi-Hole Probes,'' ASME J. Fluids Eng., **123**, pp. 128–138.
[12] Johansen, E. S., 2001, ''Development of a Fast-Response Multi-Hole Probe for Unsteady and Turbulent Flowfields,'' Ph.D. dissertation, Texas A&M University, College Station, TX.
[13] Dominy, R. G., and Hodson, H. P., 1993, ''An Investigation of Factors Influencing the Calibration of Five-Hole Probes for Three-Dimensional Flow Measurements,'' ASME J. Turbomach., **115**, pp. 513–519.
[14] Zeiger, M. D., Chalmeta, L. P., and Telionis, D. P., 1998, ''Tip Geometry Effects on Calibration and Performance of Seven Hole Probes,'' AIAA paper no. AIAA-98-2810.
[15] Lee, S. W., and Jun, S. B., 2003, ''Effects of Reynolds Number on the Non-Nulling Calibration of a Cone-Type Five-Hole Probe,'' ASME paper no. GT-2003-38147.
[16] Johansen, E. S., 1998, ''Steady and Unsteady Calibration of Multi-Hole Probes,'' M.S. thesis, Texas A&M University, College Station, TX.
[17] Brand, L., 1957, *Vector Analysis*, Wiley, New York, pp. 17–19.
[18] Spiegel, M., 1959, *Vector Analysis, and an Introduction to Tensor Analysis*, Schaum's Outline Series, McGraw Hill, New York, pp. 58–59, 76.
[19] Johansen, E. S., and Rediniotis, O. K., 2002, ''Development of Unsteady Calibration Facilities and Techniques for Fast-Response Pressure Probes,'' AIAA paper no. AIAA-2002-0689.
[20] Gossweiller, C. R., Kupferschmied, P., and Gyarmathy, G., 1995, ''On Fast-Response Probes: Part 1—Technology, Calibration, and Application to Turbomachinery,'' ASME J. Turbomach., **117**, pp. 611–617.

Experimental Investigation of Diffuser Hub Injection to Improve Centrifugal Compressor Stability

Gary J. Skoch
U. S. Army Research Laboratory,
Glenn Research Center,
Cleveland, OH 44135

Results from a series of experiments to investigate whether centrifugal compressor stability could be improved by injecting air through the diffuser hub surface are reported. The research was conducted in a 4:1 pressure ratio centrifugal compressor configured with a vane-island diffuser. Injector nozzles were located just upstream of the leading edge of the diffuser vanes. Nozzle orientations were set to produce injected streams angled at −8, 0, and +8 degrees relative to the vane mean camber line. Several injection flow rates were tested using both an external air supply and recirculation from the diffuser exit. Compressor flow range did not improve at any injection flow rate that was tested, and generally diminished as injection rate increased. Compressor flow range did improve slightly at zero injection due to the flow resistance created by injector openings on the hub surface. Resistance and flow range both increased as the injector orientation was turned toward radial. Leading edge loading and semivaneless space diffusion showed trends that are similar to those reported earlier from shroud surface experiments that did improve compressor range. Opposite trends are seen for hub injection cases where compressor flow range decreased. The hub injection data further explain the range improvement provided by shroud-side injection and suggest that stability factors cited in the discussion of shroud surface techniques are valid. The results also suggest that a different application of hub-side techniques may produce a range improvement in centrifugal compressors.
[DOI: 10.1115/1.1812779]

Introduction

Experiments to determine the causes, precursors, and control mechanisms for stall and surge in a centrifugal compressor were conducted at the NASA Glenn Research Center over the past several years. The experimental work included an evaluation of the benefits of air injection into the centrifugal compressor diffuser using nozzles employed on both the hub and shroud surfaces. The effects of bleed tubes inserted into the vaneless space through the shroud surface were also evaluated.

Spakovszky [1] had initially shown that an improvement in stable range could be obtained by injecting air through the shroud surface of the vaneless space in a direction that was tangent to impeller rotation.

Skoch [2] tested other variants of shroud-side injection. Significant results were obtained when the injectors were oriented to produce a vaneless space jet that was tangent to the impeller, but traveled in a direction that was opposite to impeller rotation. Results from shroud surface experiments proved to be very promising and showed that both a significant improvement in stable flow range as well as an ability to recover from fully developed surge could be obtained from control actions taken on the shroud surface.

Additionally, it was discovered that obstructions created by bleed tubes inserted into the vaneless space through the shroud surface provided an excellent improvement in the stable flow range when the tubes were sealed to prevent bleed. These surge control tubes provided better range improvement than air injection and caused less loss of total pressure in the diffuser.

In describing the results from shroud-side techniques, Skoch [2] concluded that the observed benefits in diffuser stability came from a reduction in the flow angle of impeller discharge fluid traveling through the vaneless space. Part of the flow angle adjustment was due to an increase in radial velocity resulting from a reduction of effective flow area in the vaneless space that was caused by the injected stream or control tube. The second part came from a reduction in tangential velocity caused by interaction with the injected jet or tube.

Hub-side injection was tested first in the same series of experiments that explored shroud-side stability control. The hub nozzles were oriented to produce jets that traveled along the vane surfaces into the diffuser passage instead of acting on flow within the vaneless space. Hub-side injection did not produce an improvement in stable flow range with the nozzle orientations that were tested. Pressure measurements collected in the diffuser indicate that injection on the hub surface did not produce the same adjustment in flow angle as shroud-side injection. The trends in diffusion and vane loading were opposite those observed with successful shroud-side techniques, as were the changes in stable flow range of the compressor.

The mere presence of the hub-side injectors did provide a minor improvement in range. That improvement was partially due to a reduction in the pressure variation between diffuser passages, as was reported by Raw [3] who demonstrated surge margin improvements in a conical pipe diffuser by using ''porous drillings'' to bleed flow from the region of the diffuser throat. Communication of pressure in the current test was through a manifold that connected the injector nozzles.

In addition to the communication noted above, the presence of hub-side injector nozzles provided some resistance to tangential flow in the vaneless space. The results indicate that turning the nozzles toward a radial orientation may have produced a higher level of resistance. Minor improvements in range occurred without any injection at nozzle orientations that were more toward radial, and diffusion trends in the diffuser matched those observed with successful shroud-side techniques.

Contributed by the International Gas Turbine Institute (IGTI) of THE AMERICAN SOCIETY OF MECHANICAL ENGINEERS for publication in the ASME JOURNAL OF TURBOMACHINERY. Paper presented at the International Gas Turbine and Aeroengine Congress and Exhibition, Vienna, Austria, June 13–17, 2004, Paper No. 2004-GT-53618. Manuscript received by IGTI, October 1, 2003; final revision, March 1, 2004. IGTI Review Chair: A. J. Strazisar.

While no significant range improvement was demonstrated, results from the hub injection experiments support the conclusions drawn from the successful shroud-side experiments and are therefore reported here. Further, the results suggest that hub injection may have shown an improvement, had the nozzles been oriented to produce a jet that opposed the swirl velocity in the vaneless region of the diffuser.

Test Compressor

The test compressor is an Allison Engine Company design that was scaled up to a flow size of 10 lbm/s (4.54 kg/s) from the original size of 3.655 lbm/s (1.658 kg/s). McKain and Holbrook [4] give complete aerodynamic and mechanical design descriptions, including impeller and diffuser geometries.

The stage (impeller with vane-island diffuser) was designed to produce a pressure ratio of 4:1 at the design mass flow. The standard day corrected speed for the design flow condition is 21,789 rev/min with an exit tip speed of 1615 ft/s (492 m/s). The mean value of the relative inflow Mach number is 0.69. The impeller contains 15 main blades and 15 splitter blades and has 50 degrees of backsweep from radial at the discharge. The splitter-blade leading edge, located at 20% of main blade chord, is offset slightly toward the main-blade suction surface in order to produce an even flow split. Both the main blades and splitter blades are formed from quasi-normal straight-line elements between the hub and tip. The inlet tip diameter is 8.264 in. (210 mm) and the inlet blade height is 2.501 in. (64 mm). The exit diameter is 16.986 in. (431 mm) and the exit blade height is 0.671 in. (17 mm). All dimensions are for hot conditions at 100% of design speed.

The vane-island diffuser contains 24 passages. The vane leading edge is at a radius ratio of 1.08 and the midpitch of the passage throat is at a radius ratio of 1.10 compared to the impeller exit radius. The diffuser exit is at a radius ratio of 1.68.

Hub Injection Apparatus

Cross sections of the centrifugal compressor test rig, a hubside injector, and the air supply system are shown in Fig. 1. Measurement stations located upstream of the impeller (Station 0), at the impeller trailing edge (Station 1), and downstream of the diffuser (Station 5) are also shown. One of eight recirculation air pickups, used in a configuration where internal air was supplied to the injectors, is shown in the same plane as the downstream (Station 5) measurement location.

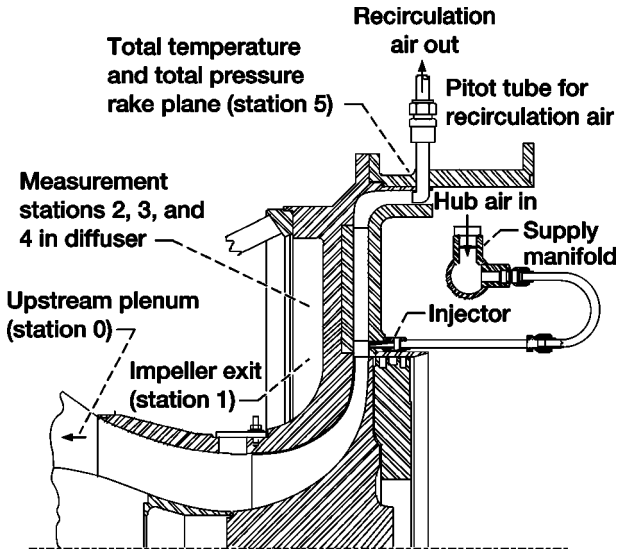

Fig. 1 Cross section of test compressor and air injection apparatus

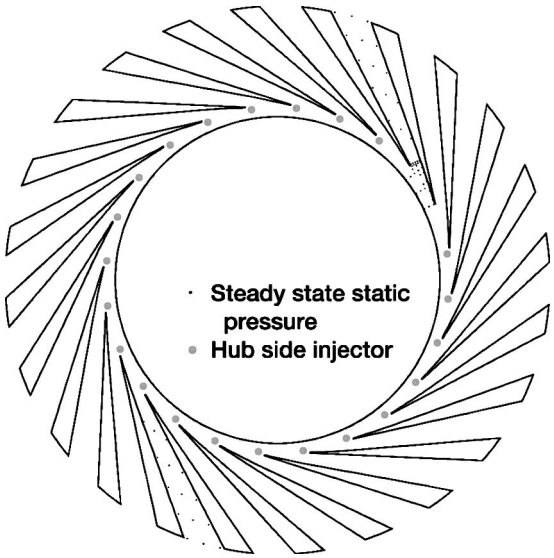

Fig. 2 Diffuser hub instrumentation and injector nozzle locations

Hub-Side Injectors

Twenty-two wall tangent injector nozzles were installed on the hub side of the diffuser as shown in Fig. 2. A nozzle was positioned directly upstream of the leading edge of each diffuser vane with the exception of two. Two passages were left without injectors in order to preserve a static pressure array in the semivaneless region of the passage. The nozzle positions were manually reset to provide the directional options shown in Fig. 3. Air was supplied to all of the 22 injection nozzles by a circumferential manifold that was inside the test-rig exhaust collector and adjacent to the diffuser hub (Fig. 1). Flow area within the air supply system was large compared to the total of throat areas from all nozzles in order to encourage a uniform air supply to each nozzle. The manifold cross section had an area that was more than five times the total of injector throat areas. The cross section of a single injector supply tube was also more than five times the throat area of a single injector. The manifold was supplied by an external air source or by Pitot tubes located at the diffuser discharge. The nozzles were sized to choke when the total injected flow rate was 0.5 lbm/s (0.23 kg/s) using air at 540°R.

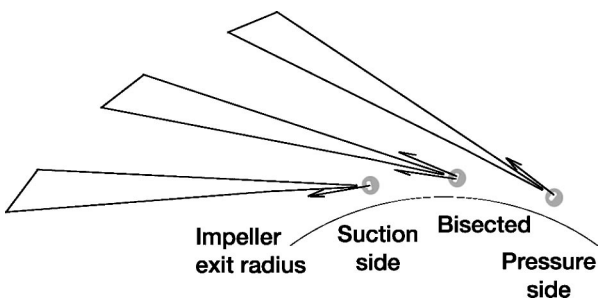

Fig. 3 Hub-side injector nozzle orientations

Test Procedure, Instrumentation

Compressor stability experiments were completed over a speed range of 60–100% of design speed and at tip clearances of 2.4%, 3.6%, and 4.8% of exit blade height. Results from tests done at 100% of design speed with a tip clearance equal to 2.4% of exit blade height are reported here. At each condition, the compressor was throttled to a starting point on the operating characteristic that was near surge and then ramped into surge by closing the throttle slowly at a constant rate. In some cases, steady-state data were first collected along a complete constant speed characteristic; in others only partial characteristics were obtained.

The flow rate where the compressor surged was determined by noting the flow rate where a significant change occurred in the sound emanating from the compressor, indicating the start of a strong surge cycle. In [2] the accuracy of the audible surge indicator was checked against a computed value that was based on a digitized measurement of pressure drop across the main flow orifice. The audible value was found to be within -0.05 and $+0.15$ lbm/s (-0.023 and $+0.068$ kg/s) of the computed value. While a digitized measurement of pressure drop was not available for these experiments, the accuracy of the audible surge indicator is assumed to be similar since both experiments were completed during a single entry into the test facility.

The surge flow rate was sensitive to changes in impeller tip clearance. Air injection changed the local metal temperature enough to change the clearance between the impeller trailing edge and the shroud. After arriving at a starting point on the characteristic that was near surge, the flow path dimensions were allowed to adjust to the temperature conditions created by air injection. The tip clearance was then adjusted to its initial value using a unique feature of the test rig that permits controlled axial movement of the impeller during operation. Tip clearance was measured during operation using a high-voltage touch-probe system.

Steady-state static pressure arrays were located in two passages on each of the hub and shroud surfaces. The hub-side static pressure arrays are shown in Fig. 2. Similar arrays were located on the shroud. Also located on the shroud were eight static pressure taps that were evenly distributed about the circumference of the impeller at its trailing edge.

The lack of static pressure measurements in the immediate region of a nozzle prevents a discussion of the localized effect of the nozzle or injected jet on the diffuser flow. However, pressure measurements collected in a region without a nozzle provide a better picture of the overall effect of injection on diffuser performance. Measurements from the static pressure arrays on the hub surface were averaged with similar arrays on the shroud to present a view of changes in the overall character of the diffuser flow field.

Stage total temperature and total pressure rise were determined from measurements collected in the upstream plenum and from rakes located in the discharge channel downstream of the diffuser. The downstream rake plane is marked in Fig. 1. Six four-element total pressure rakes and eight three-element total temperature rakes were located in the downstream plane. Rakes were distributed symmetrically about the 24 passages of the diffuser.

Five of the total temperature rakes and three of the total pressure rakes were replaced by Pitot tubes when recirculated air was used to supply injectors. The variation in measurements obtained at downstream rake locations was checked with all rakes installed to estimate the error created by replacing some rakes with Pitot tubes for recirculation experiments. The maximum deviation of measurements from individual rakes compared to the average of all rakes was less than $\pm 0.9\%$ for total pressure and $\pm 0.4\%$ for total temperature at injected flow rates of 0.15 lbm/s (0.068 kg/s) or less.

Steady-state data were collected using the test cell data system (Escort System) that records all steady-state pressure, temperature, and speed data needed to determine compressor performance. Steady-state measurement uncertainties are pressure 0.1 psi (0.1 N/cm^2), temperature 1°R (0.6°C), mass flow 0.05 lbm/s (0.023 kg/s), and pressure ratio 0.1%. The Escort System was also used to collect performance data while ramping toward surge since the throttle was being slowly closed. Data readings were taken at roughly 0.1 lbm/s (0.05 kg/s) flow increments between the ramp starting point and the surge point.

Experimental Results

The pressure rise characteristics shown in Figs. 4–6. and Figs. 9–11 are results obtained at several injected flow rates for each of the hub nozzle orientations shown in Fig. 3. All of the hub injection data were obtained with solid plugs installed in the shroud side openings used later for injection and control-tube experiments.

The plus (+) symbols are data from the baseline configuration for each nozzle orientation and were obtained using zero injected flow. The baseline characteristic for the suction-side orientation is also the baseline used to compare shroud-side injection and control-tube techniques in [2].

The other characteristics shown for each nozzle orientation were produced with various levels of air-flow injected through the hub nozzles. Some characteristics are complete (choke to surge) and others are only partial as the usual test procedure was to begin at a point close to the surge flow rate of the baseline and then ramp the throttle closed at a constant rate.

The mass flow rates of data shown in Figs. 4, 9, 10, and 11 have been adjusted to account for flow that was injected into the diffuser since it was injected downstream of the main flow measuring orifice. The uncorrected mass flow entering the compressor inlet was adjusted by adding the uncorrected injection flow rate to it and correcting the sum to standard day conditions using measurements collected in the inlet plenum. This adjustment is made in order to view the characteristics in terms of flow rate entering the diffuser while treating that flow as if it had been processed by the entire stage. Axis titles indicate ''Net'' flow where an adjustment was made.

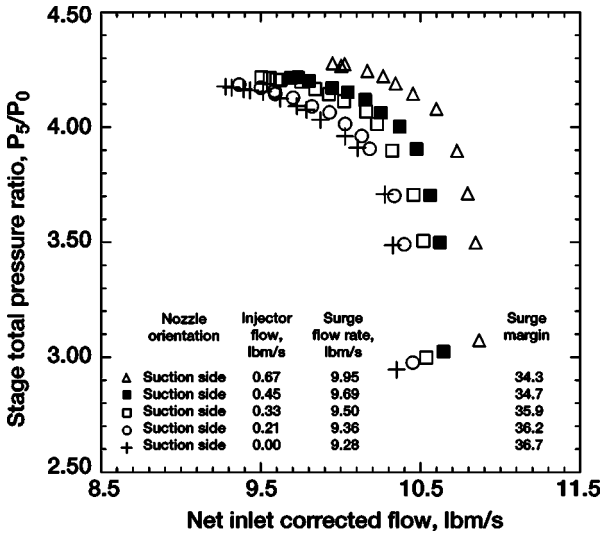

Fig. 4 Stage total pressure ratio versus net flow entering the diffuser corrected to inlet conditions at design speed and 2.4% tip clearance with hub suction-side injection

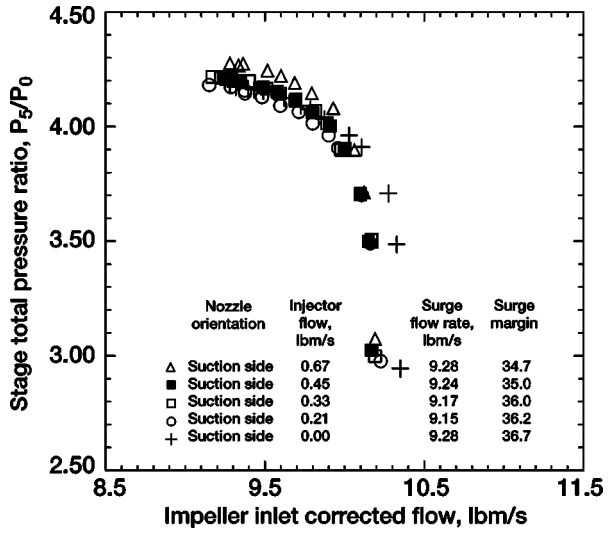

Fig. 5 Stage total pressure ratio versus impeller inlet corrected flow at design speed and 2.4% tip clearance with hub suction-side injection

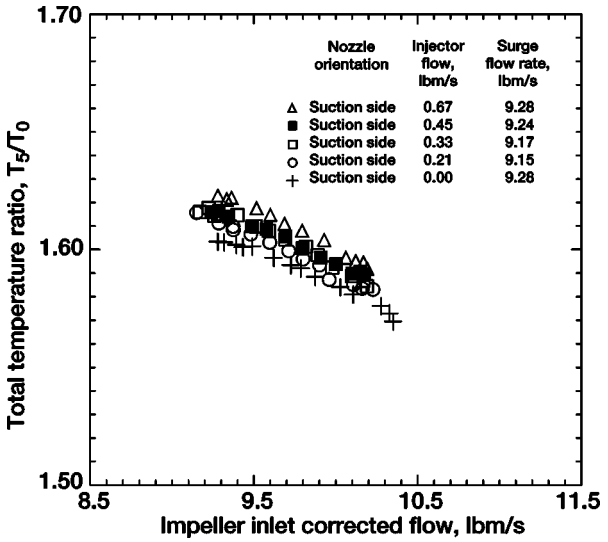

Fig. 7 Impeller total temperature ratio versus impeller inlet corrected flow at design speed and 2.4% tip clearance with hub suction-side injection

The final data point on each characteristic is at the flow rate determined from the audible surge indicator, also adjusted for injection. Mass flow at the surge point was determined from the mass flow shown on a steady-state rig performance display when the audible surge indicator was heard. Since it was difficult to observe both mass flow and pressure ratio simultaneously, the pressure ratio at surge was estimated using the mass flow at surge and first- or second-order curve fits of the last three to six steady state data points preceding surge. An estimate of surge pressure ratio from steady state data is required because there were no high response transducers in the downstream rake plane to provide a direct measurement of total pressure at surge.

The characteristics of Figs. 4–9 show that hub injection did not improve the stable flow range of the compressor and in most cases caused a decrease. Surge margins based upon the first (ref) and final (surge) points of each full characteristic are shown in the legends of each figure where surge margin is defined as

$$SM = \left(1 - \frac{\pi_{\text{ref}}}{\pi_{\text{surge}}} \cdot \frac{\dot{m}_{\text{surge}}}{\dot{m}_{\text{ref}}}\right) \times 100\% \quad \text{and} \quad \pi = \frac{P_5}{P_0} \tag{1}$$

This definition of surge margin isolates the computation to an individual characteristic by comparing the performance at surge to performance at the lowest pressure rise on the choked flow segment of the characteristic. Injection from an external source will change the position of the overall characteristic by producing offsets in through-flow and pressure ratio relative to a normal operating line. The constant speed definition of surge margin removes the influence of overall offsets if injector flow rate is held constant and each characteristic is started at the same throttle position.

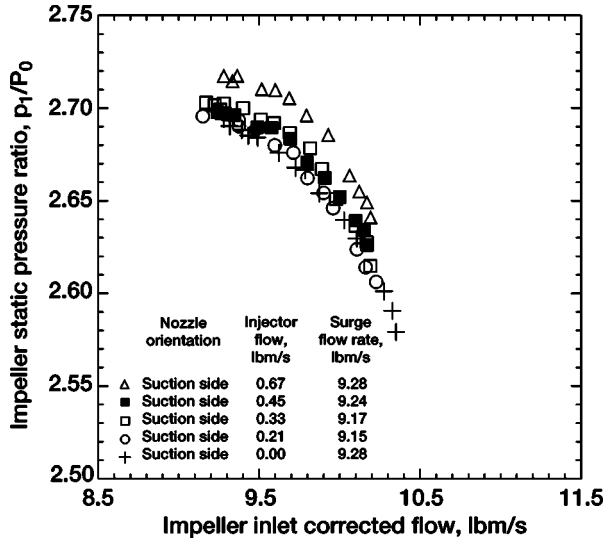

Fig. 6 Impeller static-total prerssure ratio versus impeller inlet corrected flow at design speed and 2.4% tip clearance with hub suction-side injection

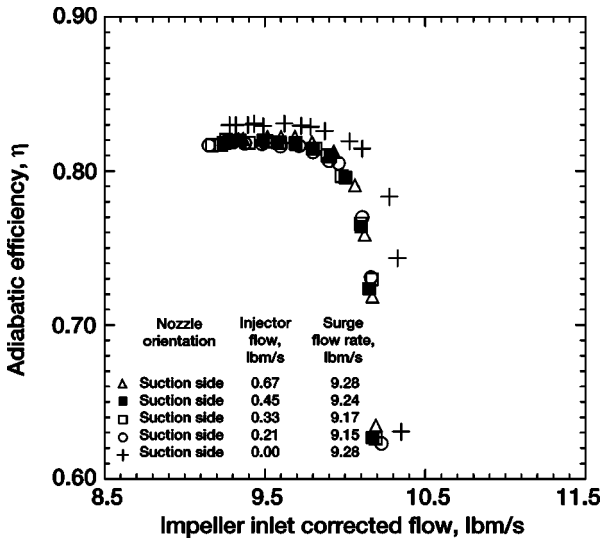

Fig. 8 Stage adiabatic efficiency versus impeller inlet corrected flow at design speed and 2.4% tip clearance with hub suction-side injection

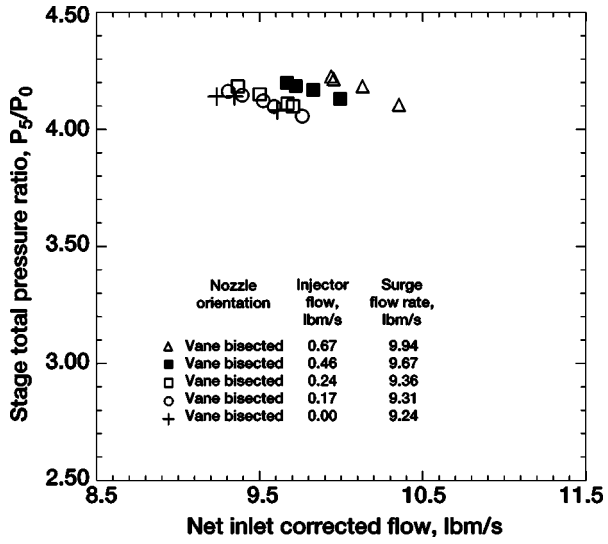

Fig. 9 Stage total pressure ratio versus net flow entering the diffuser corrected to inlet conditions at design speed and 2.4% tip clearance with hub vane-bisected injection

Diffuser Hub Suction-Side Injection

The pressure rise characteristics shown in Fig. 4 are results obtained at several injected flow rates when the hub nozzles were oriented toward the vane suction surface as shown in Fig. 3. A comparison of surge margins given in the legend of Fig. 4 shows that surge margin decreased as injected flow was increased in this case, moving from 36.7 at zero injection to 34.3 at the maximum injected flow rate of 0.67 lbm/s (0.304 kg/s).

The characteristics of Fig. 4 have been adjusted using the injector flow rate and appear to move along a constant throttle line as if speed was increasing. Speed was not increasing in this case, but air supplied from an external source was injected into the diffuser in a direction that was nearly tangential to impeller rotation. Some increase in pressure ratio resulting from the total pressure of the externally supplied injection flow is reflected in an apparent increase in compressor speed that is implied by the relative positions of the characteristics.

High injection flow rates on the hub surface did not cause the same reduction in measured impeller inlet flow that was observed in shroud-side experiments [2]. The characteristics of Fig. 4 moved significantly to the right of the baseline when injected mass flow adjustments were added to the measured inlet flow.

Figures 5 through 8 show results from hub suction-side injection plotted using only the measured flow rate at the impeller inlet. Only small through-flow reductions are seen along the choked-flow segments of the characteristics in Fig. 5, even at the highest injector flow rate.

The diffuser was able to swallow most of the additional airflow introduced by injection, preventing a substantial reduction in the flow rate entering the impeller. Part of the injected flow may have filled a blockage within the diffuser passage without creating substantial additional blockage itself.

Stage Efficiency: Suction-Side Injection

Impeller performance was influenced by at least some portion of the injected flow. Figure 6 shows impeller pressure ratio plotted against unadjusted impeller inlet flow. Impeller pressure ratio increased at a given mass flow as injector flow rate increased, indicating that injection was creating backpressure on the impeller. The impeller pressure ratio at surge increased from 2.69 on the baseline characteristic to 2.72 when the injected flow rate was increased from zero to 0.67 lbm/s (0.3 kg/s).

Impeller work input also increased with injection. Stage total temperature ratio is shown in Fig. 7 for each injector flow rate. Total temperature measurements were corrected to account for external air injection at a total temperature that differed from the local flow. The following correction was applied to the measured total temperature

$$T_5\dot{m}_{\text{impeller}} = T_{5,\text{measured}}(\dot{m}_{\text{impeller}} + \dot{m}_{\text{injector}}) - T_{\text{injector}}\dot{m}_{\text{injector}} \tag{2}$$

Stage efficiency is shown in Fig. 8. Similar levels of efficiency were maintained at the open throttle condition. The increase in work input by the impeller was not matched by a proportional increase in measured total pressure ratio when through flow was reduced, however, even though total pressure enhancement by flow entering the diffuser from an external source was still present. Efficiency decreased at low through-flow rates as a result.

Adjustments to Measured Inlet Flow

A comparison of surge margins computed for the corresponding characteristics in Figs. 4 and 5 shows that adjusting the measured inlet flow rate did not substantially change the result. The differences in surge margin between the legends of each figure result from adding a constant to both the numerator and denominator of Eq. (1) when the injector flow rate adjustment is made.

The flow rate entering the diffuser is the sum of the impeller inlet and injected flow rates. This is true even when recirculation is used to supply the injectors. Measured impeller inlet flow rates should be adjusted in all cases where injection is used in order to establish a consistent basis for comparisons between different injection rates or injector locations.

Surge margin can be computed and compared when full characteristics are available. This is not the case when working with partial characteristics. The only indication of improved surge margin, in that case, is whether the surge point on the characteristic is at equal or higher pressure ratio and at a lower flow rate. Failing to correct the data for injected flow would give a false indication of flow range improvement.

Vane-Bisected Injection and Pressure-Side Injection

Stage total pressure ratio versus net inlet corrected flow is shown in Fig. 9 for several injected flow rates using the vane-bisected orientation. Data from this configuration were collected only for partial characteristics and surge margin was not com-

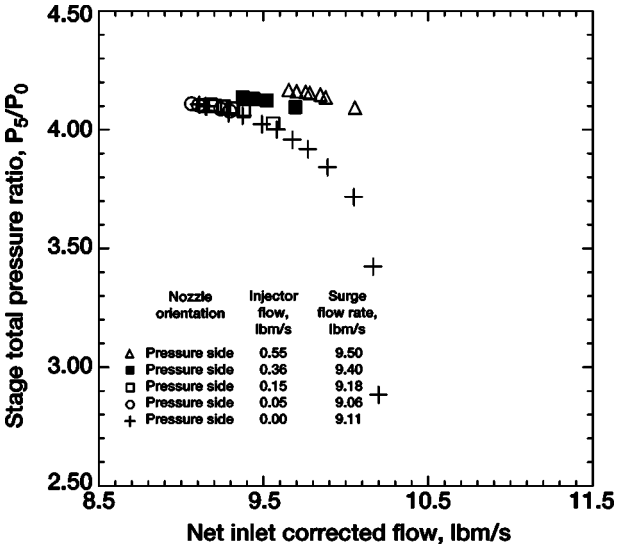

Fig. 10 Stage total pressure ratio versus net flow entering the diffuser corrected to inlet conditions at design speed and 2.4% tip clearance with hub pressure-side injection

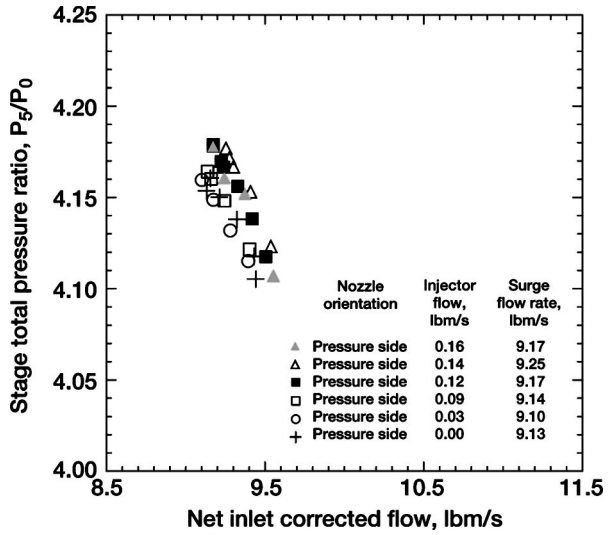

Fig. 11 Stage total pressure ratio versus net flow entering the diffuser corrected to inlet conditions at design speed and 2.4% tip clearance for the recirculation case of pressure-side injection

puted. However, there is no indication of any improvement in stable flow range from the data shown. The partial vane-bisected characteristics behave in a similar fashion to those from the suction-side configuration, where they appear to indicate increasing speed.

Figure 10 shows stage total pressure vs. net inlet corrected flow for the pressure-side configuration. A very small improvement in flow range may be indicated in data from the lowest injected flow rate of 0.05 lbm/s (0.023 kg/s). The pressure ratio of the surge point on this characteristic was estimated from a curve fit. The pressure ratio of the point immediately ahead of surge was measured and, since the pressure ratio there did not fall below that of the baseline characteristic, a small improvement in surge margin is implied for this injector flow rate. However, the remaining results from the pressure-side configuration do not indicate that there was any improvement in flow range as the injected flow rate was increased.

Figure 11 shows results from the pressure-side orientation using injection air that was supplied from within the compressor flow path. The Pitot style pickups shown in Fig. 1 were used to collect air from the diffuser exit passage which was then delivered to the hub injectors. Supply pressure was limited to the velocity head that was recovered in the diffuser and by the pickup, so the injected flow rates tested were lower than those used with an external air supply.

Lower injection rates and internal air did not make a significant difference in the performance of the pressure-side configuration as no significant improvement in flow range is generally seen in this case either. There does appear to be a small improvement in pressure ratio for the injector flow rates above 0.1 lbm/s in Fig. 11, and surge occurred at through-flow rates nearly equal to the baseline curve. The pressure-side configuration with internal air may have provided a small, but insignificant, improvement in surge margin.

Stage Efficiency: Vane-Bisected and Pressure-Side Injection

Efficiency plots are not shown for the vane-bisected and pressure-side orientations since these, like the suction-side orientation, did not produce the desired effect of flow range improvement. The trends in total temperature ratio and efficiency were similar to those shown in Figs. 7 and 8 for the suction-side nozzle orientation. Stage total temperature ratio increased faster than total pressure ratio leading to slightly lower stage efficiencies. On average, peak efficiencies for the vane-bisected and pressure-side orientations were about one point lower for the cases with injection compared to the zero injection case and this is about equal to the peak efficiency loss of the suction-side configuration with injection.

Nozzle-Only Comparison

In the discussion above, compressor stability at various hub injection rates for each nozzle orientation was compared to the performance at zero injection for the same orientation. None of the hub injector configurations tested showed a notable improvement in stable flow range or surge margin when injection was turned on or as the injected flow rate was increased. However, there was a small difference in the flow range and surge margin between the zero injection cases of each nozzle orientation.

Figure 12 compares the zero injection characteristics of the suction-side, vane-bisected, and pressure-side nozzle orientations. No adjustment to the measured through-flow rate was necessary since injection was not in use. The figure shows that there was a tendency toward improved flow range as the injector orientation was turned clockwise from the suction-side orientation to the pressure-side. Surge margin computed for the full characteristics (suction-side and pressure-side) bears this out as surge margin increased from 36.7 when the nozzle was oriented toward the suction side of the vane to 37.3 when it was oriented toward the pressure side. While surge margin was not computed for the vane-bisected configuration, its orientation was between the other two, and the vane-bisected results in Fig. 12 also lie between the results from the suction-side and pressure-side orientations.

The difference in surge flow rates between the three orientations shown in Fig. 12 are minor and lie within the error band stated earlier. However, the differences in nozzle orientation were also minor so small changes in surge flow rate are not unexpected. Confidence increases when measurements collected within the diffuser are considered (later) since the observed trends in diffuser performance are similar to those observed in [2] where the improvements in flow range were much greater.

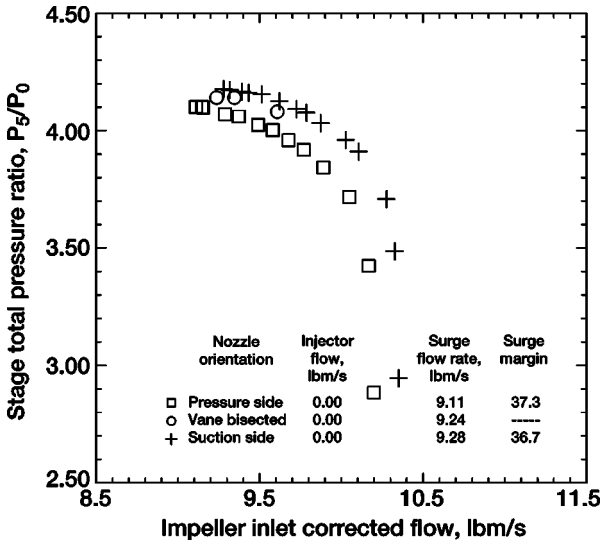

Fig. 12 Stage total pressure ratio at design speed and 2.4% tip clearance for the zero injection cases of suction-side, vane-bisected, and pressure side nozzle orientations

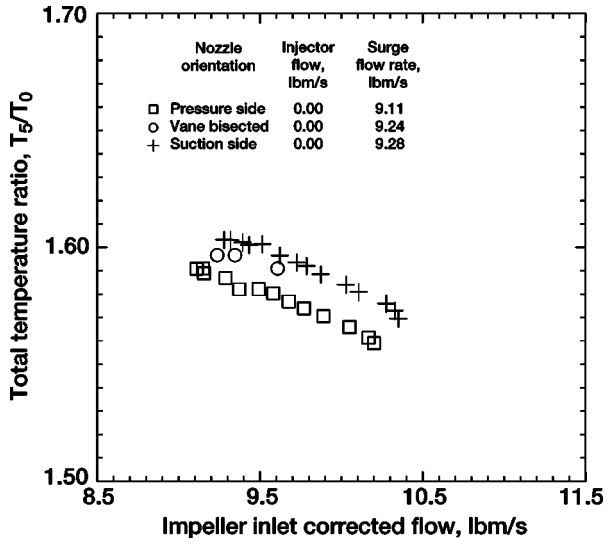

Fig. 13 Stage total temperature ratio at design speed and 2.4% tip clearance for the zero injection cases of suction-side, vane-bisected, and pressure-side nozzle orientations

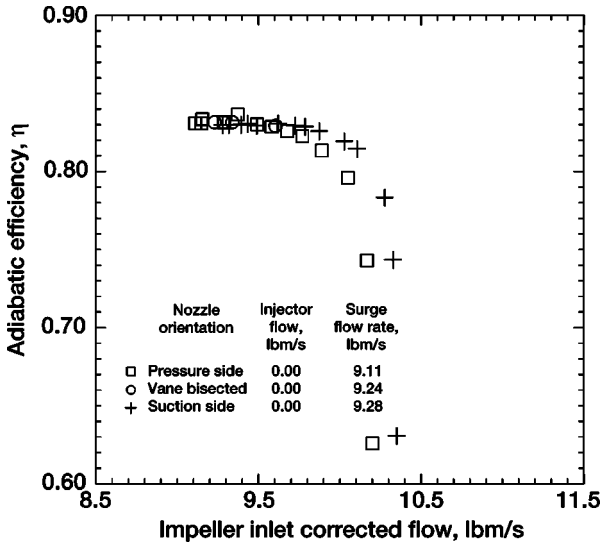

Fig. 15 Stage adiabatic efficiency at design speed and 2.4% tip clearance for the zero injection cases of suction-side, vane-bisected, and pressure-side nozzle orientations

Stage Efficiency: Nozzle-Only Configurations

Air injection into the diffuser passage caused a small increase in backpressure on the impeller and a corresponding increase in work input by the impeller. The nozzle-only data show the opposite effect, less impeller loading as the nozzles were turned toward a more radial orientation.

Figure 13 shows the stage total temperature ratio at each orientation. Turning the nozzles toward the pressure-side orientation resulted in less total temperature rise over the full range of through flow. The total temperature ratio characteristics in Fig. 13 show a step reduction in temperature ratio between the suction and pressure-side nozzle orientations, while maintaining nearly the same slope as the compressor was throttled. A reduction of impeller work input is also reflected in the reduced impeller pressure ratio seen in Fig. 14.

Flow resistance or blockage created by the hub nozzles must have altered the span-wise velocity profile of fluid discharging from the impeller. The exact mechanism is not known, but the result was either an increase in impeller through-flow velocity or an increase in slip at the tailing edge. Whatever the mechanism, it did not result in a loss of total pressure. Stage efficiency, Fig. 15, was maintained at each hub nozzle orientation. The reduction in stage total pressure ratio seen in Fig. 12 was due to reduced work input by the impeller, and was not caused by total pressure loss in the diffuser.

Diffuser Performance

In reporting results obtained from experiments done on the shroud endwall of the diffuser vaneless space, Skoch [2] concluded that stable flow range improvements provided by injection and control tubes were due to a reduction in flow angle entering

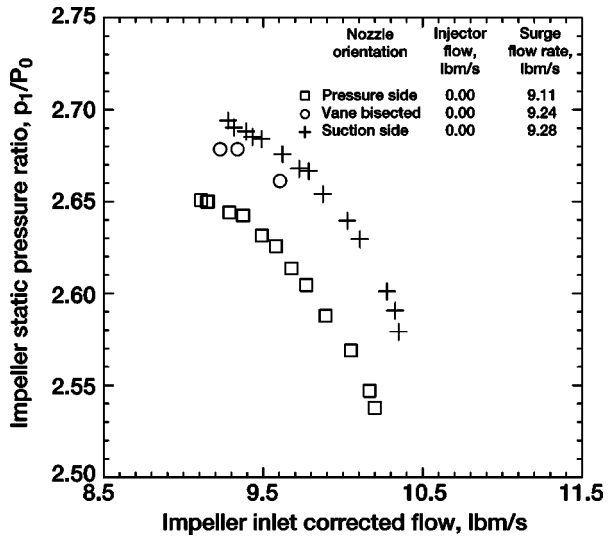

Fig. 14 Impeller static-total pressure ratio versus impeller inlet corrected flow at design speed and 2.4% tip clearance for the zero injection cases of suction-side, vane-bisected, and pressure-side nozzle orientations

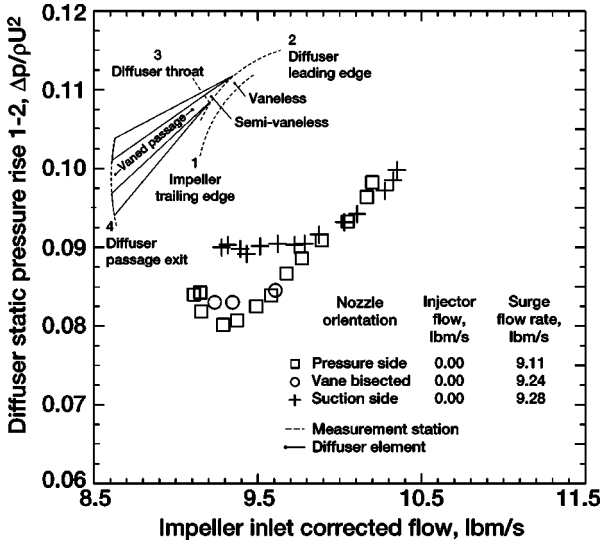

Fig. 16 Static pressure rise in the diffuser vaneless space at design speed and 2.4% tip clearance for the zero injection cases of suction-side, vane-bisected, and pressure-side nozzle orientations

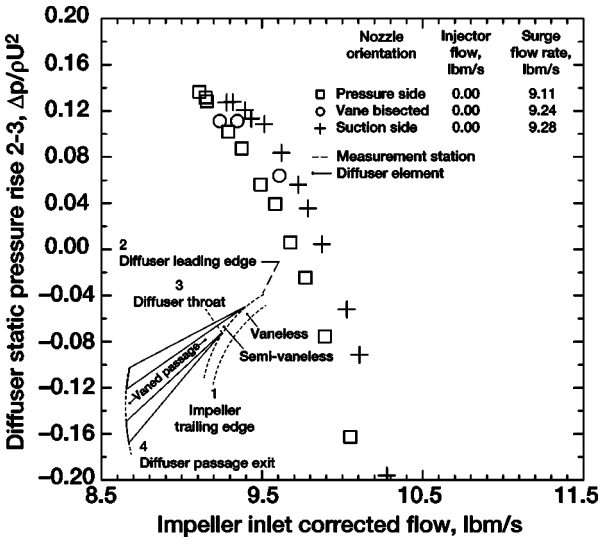

Fig. 17 Static pressure rise in the diffuser semivaneless region at design speed and 2.4% tip clearance for the zero injection cases of suction-side, vane-bisected, and pressure-side nozzle orientations

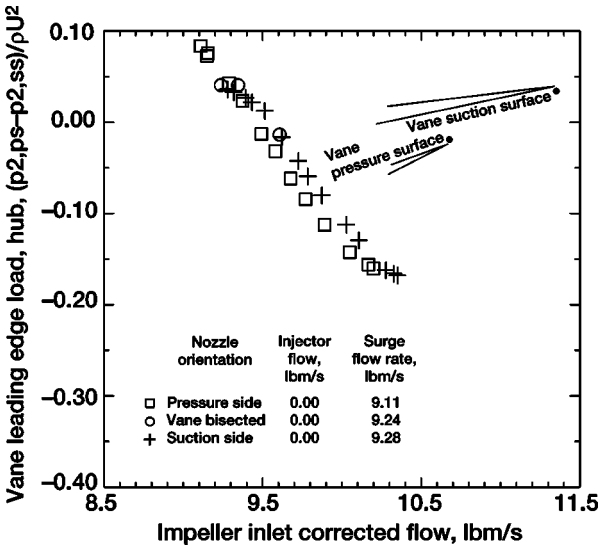

Fig. 19 Diffuser vane leading edge loading on the hub surface for the zero injection cases of suction-side, vane-bisected, and pressure-side nozzle orientations

the diffuser vane row. The conclusion was supported by evidence of reduced diffusion across the vaneless and semivaneless regions of the diffuser and by a reduction of loading on both the hub and shroud surfaces of the diffuser vane leading edge. If the pressure-side orientation at zero injection did enhance stability, then some indication of reduced diffusion and vane loading should be found in measurements collected in the diffuser.

Figures 16 and 17 show diffusion across the vaneless and semivaneless regions of the diffuser, respectively, at each of the three hub nozzle orientations. Pressure recovery decreased in the vaneless region as the compressor was throttled for all orientations. However, the decrease was greater for the vane-bisected orientation and still greater for the pressure-side orientation. Vaneless space pressure recovery decreased to a minimum and then began to increase, which is the same effect as created by shroud-side techniques that provided good range improvement. The reason for this effect is discussed later.

Pressure recovery in the semivaneless space is shown in Fig. 17. Pressure recovery measurements from the shroud-side experiments [2] showed that diffusion across this region was reduced, at a given through flow, by the successful techniques. Figure 17 shows similar behavior from the hub nozzle orientations that improved flow range.

Figure 18 and 19 show pressure loading at the leading edge of a diffuser vane. Here, the comparison to shroud-side techniques is not quite as strong. Loading at the shroud surface of the vane (Fig. 18) was reduced for a given mass flow, but it remained fairly constant at the hub (Fig. 19). However, the increase in surge margin between the tangentially oriented suction-side nozzle configuration and the pressure-side configuration was not as significant as the increase produced by shroud-side techniques. Therefore, it is not surprising that the changes in vane leading edge loading are also not as strong.

The fact that loading decreased at the shroud surface instead of at the hub, where the nozzles were located, is most likely due to a shifting of through flow toward the shroud surface as was noted earlier.

Examples of diffuser performance were not shown for the cases where injection was used. In every case, behavior in the diffuser was opposite that which has been described above. Diffusion in the vaneless and semivaneless regions increased at a given through flow as compared to the zero injection case for each orientation. The increase was roughly in proportion to the injected flow rate. Vane leading edge loading also trended in a direction opposite to that which is needed for improved stability. Leading edge loading increased at a given compressor through flow as injected flow rate was increased.

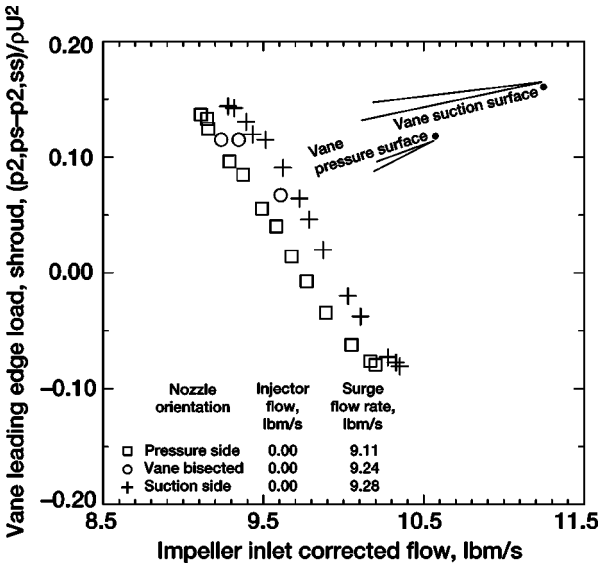

Fig. 18 Diffuser vane leading edge loading on the shroud surface for the zero injection cases of suction-side, vane-bisected, and pressure-side nozzle orientations

Vaneless Space Pressure Recovery Profile

As the compressor is throttled to lower flow rates, pressure recovery in the vaneless space (Fig. 16) follows a pattern of declining pressure recovery followed by a relatively rapid increase.

The declining portion of the pressure recovery profile seen in Fig. 16 is caused by an increasing interaction of tangential velocity with an obstruction in the vaneless space created by either a physical obstruction or an air jet that interacts with flow discharging from the impeller. As the compressor is throttled the direction

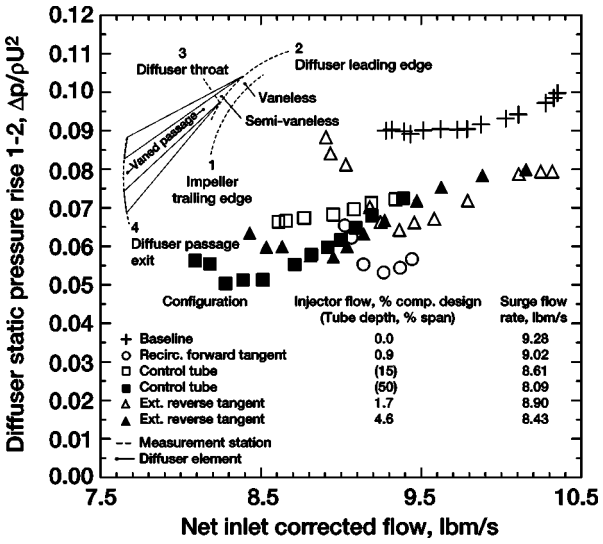

Fig. 20 Static pressure-rise in the diffuser vaneless space at design speed and 2.4% tip clearance produced by range improvement techniques applied to the shroud surface, reproduced from [2]

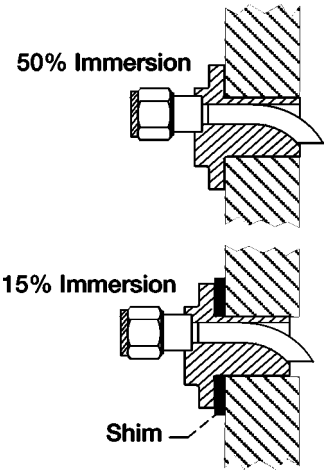

Fig. 22 Control tube immersions previously tested on the shroud surface [2]. Two immersions were achieved by placement and removal of a shim.

of impeller discharge flow becomes more tangential and the interaction with an obstruction in the vaneless space causes both a loss of tangential velocity and a turning of the absolute velocity vector toward a radial direction.

Eventually, the maximum interaction occurs as the absolute velocity vector becomes directly opposed to the obstruction and the minimum in pressure recovery occurs. As throttling continues and the absolute velocity vector at the impeller exit continues to move toward a tangential direction, fluid discharging from the impeller eventually begins to be forced into the space between the impeller trailing edge and the obstruction. At this point, the tangential velocity component within the vaneless space accelerates and diffusion resumes.

Spakovszky [1] reported an improvement in compressor range provided by tangential injection into the diffuser vaneless space through the shroud surface. Air injection was in the direction of impeller rotation and caused the tangential velocity along the shroud surface to increase. The result was an increase in effective area ratio between the impeller exit and diffuser leading edge radius that improved diffusion across the shroud surface of the vaneless space. The same effect is eventually produced by obstructions in the vaneless space with the difference being that it occurs later, after the flow turning and interaction losses have already taken place.

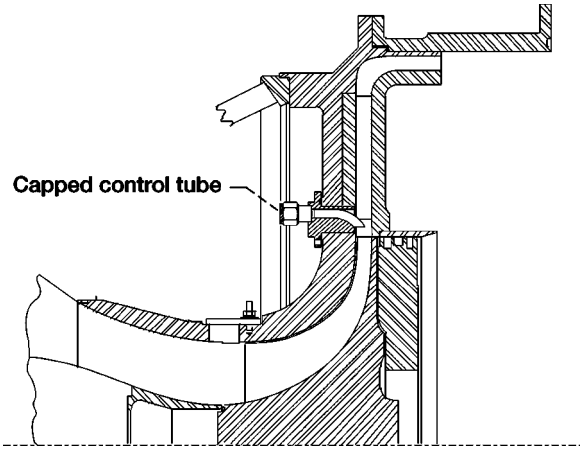

Fig. 21 Cross section of test compressor showing control tube configuration tested in [2]

Evidence to support this conclusion can be found in results from techniques that were previously tested on the shroud endwall [2]. Figure 20 is reproduced from [2] and shows the vaneless space pressure recovery for the various control-tube and injection techniques tested on the shroud endwall. Figure 21 shows one of seven control tubes that were installed in the test rig.

The vaneless space pressure recovery characteristics from shroud-side experiments (Fig. 20) have the same profile as seen in Fig. 16, decreasing then increasing for all configurations except one which was the 15% control-tube configuration (open squares). This configuration was the only one to show a continued decrease in pressure recovery as the compressor was throttled to surge without reaching a minimum, and subsequent increase in pressure recovery.

The reason for that behavior can be found in Fig. 22 which shows how the two immersions tested, 15% and 50%, were implemented. The un shimmed control tube was located at a depth within the vaneless space that was equal to 50% of the local span. The carrier plug surrounding the tube was then shimmed to achieve a 15% immersion. Movement of the carrier plug caused the plug surface that was previously flush with the flow path to move away from the flow path and increase the open volume surrounding the tube. The 15% control-tube configuration did not produce the eventual increase in vaneless space diffusion because there was more flow area between the tube and the impeller trailing edge. Conversely, the 50% control-tube configuration did not have the extra flow area and, therefore, did produce the pattern of decreasing and then increasing diffusion as the compressor was throttled.

Hub Surface Vaneless Space Obstruction

Two orientations of the diffuser hub injector nozzles, used without injection, have been shown to have an effect on diffuser performance that is similar to the obstruction (control-tube) technique that was previously tested on the shroud surface.

The question of how an obstruction was created by hub injection nozzles is now addressed. All of the nozzles were seated against machined surfaces and the nozzle surface adjacent to the vaneless space was flush with the endwall surface. The different orientations were obtained by rotating the existing nozzles and then reseating them against the same machined surfaces. If there was any error in the match between the two flow-path surfaces, it did not change for the various orientations that were tried.

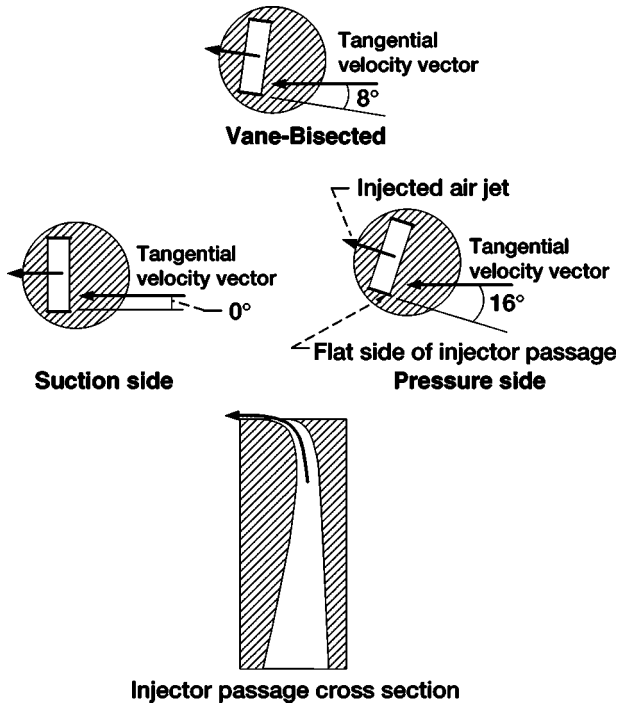

Fig. 23 Orientations of flat side of nozzle opening relative to the tangential velocity vector of impeller discharge flow within the vaneless region

The only obvious difference between the three orientations was the angle between the flat side of the injector opening and the tangential velocity vector of fluid traveling through the vaneless space. Figure 23 shows a sketch of the nozzle passage (not to scale) and the relative orientations of the three injector positions to the tangential component of velocity in the vaneless space.

When the nozzles were set to inject air on the suction side of the diffuser vanes, the side wall of the injector opening was parallel to the tangential velocity vector of fluid within the vaneless space. As the nozzles were turned toward the other two orientations, the flat side wall moved toward a radial orientation and began to oppose the tangential component of velocity in the vaneless space flow. The hub nozzles became an obstruction that was smaller in scale but still similar in effect to the control tubes previously employed on the shroud surface.

Summary

The benefits to centrifugal compressor stability provided by injecting air adjacent to the diffuser vanes through the hub surface of the diffuser were evaluated. Injectors were located just upstream of the leading edge of 22 diffuser vanes in a diffuser having a total vane count of 24. Three nozzle orientations were tested that concentrated air injection on the suction side of the vanes, on both the suction and pressure sides, and finally on the pressure side. Jets of air injected in this fashion did not provide any notable improvement in the stable flow range of the compressor or in surge margin.

Increasing the total injected flow rate did not have much effect on flow rate entering the impeller inlet. While a slight decrease was noted in flow at the inlet, it was not in proportion to additional flow being injected into the diffuser. A separation or blockage in the diffuser passage may have been responsible for the observed behavior. Injection air simply filled the separated region, but did not create additional blockage downstream of the throat.

A small improvement in stability occurred due to nozzle orientation alone and it occurred without the use of air injection. Surge margin improved by a small amount as the injector nozzles were turned from the suction-side to pressure-side orientations and stage efficiency was maintained. The suction-side position pointed the injector opening in a direction that was aligned with the tangential component of fluid flow in the vaneless space. As the nozzles were rotated toward the pressure-side orientation, a flat side of the injector passage became opposed to the tangential component of flow in the vaneless space and the nozzles became obstructions to the flow.

Diffuser data from the nozzle configurations without injection were compared to data obtained in earlier experiments [2] where control tubes inserted through the shroud surface were found to improve stability. A comparison of the change in diffuser performance between the various hub nozzle orientations and different immersions of the control tubes found that both had a similar effect. The magnitude of changes in diffuser performance caused by the nozzles was lower than that observed using control tubes, but the obstruction presented by a hub nozzle was also lower.

The results of hub injection experiments and the comparison to successful shroud-side results suggest that successful stability improvement techniques must act upon flow within the vaneless space of the diffuser. The hub nozzles were located just upstream of the leading edges of the diffuser vanes. The injected air jets traveled immediately into the diffuser passage, which proved to be an ineffective means to improve stability, at least in this compressor.

The nozzles, alone, affected the diffuser in a way that was similar to the control-tube technique previously implemented on the shroud surface and did provide a minor improvement in surge margin.

It stands to reason that if the hub nozzles had been oriented to inject flow in a tangential direction that was opposite to impeller rotation, they may have provided a range improvement similar to the reverse-tangent injection that was previously demonstrated on the shroud surface [2].

Acknowledgments

The author would like to thank Thomas Jett, Winston Johnson, and Antonio Zaldana for test cell operation; Scott Panko, Edith Parrott, and Harry Fuller for electronics support; and Mark Stevens for hardware design. Special thanks also go to Dr. Anthony Strazisar for both programmatic and technical support of the project.

Nomenclature

P = total pressure
p = static pressure
T = total temperature
T_5 = total temperature at exit rake plane after correcting for injection
$T_{5,\text{measured}}$ = measured total temperature at exit rake plane
T_{injector} = total temperature of injector flow
$\dot{m}_{\text{ref}}$ = impeller net inlet corrected mass flow on choked flow segment of pressure rise characteristic
$\dot{m}_{\text{surge}}$ = impeller net inlet corrected mass flow at surge
$\dot{m}_{\text{impeller}}$ = impeller absolute mass flow
$\dot{m}_{\text{injector}}$ = injector absolute mass flow
π_{ref} = stage total pressure ratio at lowest pressure ratio on choked flow segment of pressure rise characteristic
π_{surge} = stage total pressure ratio at surge
SM = surge margin, $(1-\pi_{\text{ref}}/\pi_{\text{surge}}\cdot\dot{m}_{\text{surge}}/\dot{m}_{\text{ref}})\times 100\%$
ρU^2 = impeller dynamic head
ΔH_{isen} = isentropic enthalpy rise
ΔH_{act} = actual enthalpy rise
η = adiabatic efficiency, $\Delta H_{\text{isen}}/\Delta H_{\text{act}}$

Measurement Station Subscripts

0 = upstream plenum
1 = impeller trailing edge
2 = diffuser vane leading edge
3 = diffuser throat
4 = diffuser exit
5 = rake plane in diffuser exit passage

References

[1] Spakovszky, Z. S., 2002, ''Backward Traveling Rotating Stall Waves in Centrifugal Compressors,'' ASME Turbo Expo, Amsterdam, ASME, New York, ASME Paper No. GT-2002-2039.
[2] Skoch, G. J., 2003, ''Experimental Investigation of Centrifugal Compressor Stabilization Techniques,'' ASME J. Turbomach., **125**, pp. 704–713.
[3] Raw, J. A., 1986, ''Surge Margin Enhancement by a Porous Throat Diffuser,'' Can. Aeronautics Space J., **32**(1), pp. 54–60.
[4] McKain, T. F., and Holbrook, G. J., 1982, ''Coordinates for a High Performance 4:1 Pressure Ratio Centrifugal Compressor,'' NASA CR-204134.

Propagation and Decay of Shock Waves in Turbofan Engine Inlets

Dilip Prasad

Jinzhang Feng

Aerodynamics Division,
Pratt & Whitney Aircraft Engines,
East Hartford, CT 06108

Numerical experiments are carried out to investigate the tone noise radiated from a turbofan engine inlet under conditions at which the relative flow past the rotor tip is supersonic. Under these conditions, the inlet tone noise is generated by the upstream-propagating rotor-locked shock wave field. The spatial evolution of this shock system is studied numerically for flows through two basic hard-walled configurations: a slender nacelle with large throat area and a thick nacelle with reduced throat area. With the flight Mach number set to 0.25, the spatial evolution of the acoustic power through the two inlets reveals that the reduced throat area inlet provides superior attenuation. This is attributed to the greater mean flow acceleration through its throat and is qualitatively in accord with one-dimensional theory, which shows that shock dissipation is enhanced at high Mach numbers. The insertion of a uniform extension upstream of the fan is shown to yield greater attenuation for the inlet with large throat area, while the acoustic performance of the reduced throat area inlet is degraded. This occurs because the interaction of the nacelle and spinner potential fields is weakened, resulting in a lower throat Mach number. The effect of forward flight on the acoustic power radiated from the two inlets is also investigated by examining a simulated static condition. It is shown that the slender nacelle radiates significantly less power at the static condition than in flight, whereas the power levels at the two conditions are comparable for the thick nacelle. The reason for this behavior is revealed to be a drastic overspeed near the leading edge of the slender nacelle, which occurs to a lesser degree in the case of the thick inlet. This has implications for ground acoustic testing of aircraft engines, which are discussed.
[DOI: 10.1115/1.1811102]

Introduction

The role of acoustics in the design of aircraft power plants has assumed significance in recent years as a consequence of stringent requirements imposed by regulatory authorities on the noise radiated during the takeoff, cutback, and approach phases of flight. Although these standards pertain to community noise, the problem of cabin noise has also become an increasingly important issue with which the engine designer must contend. Traditionally, engine acoustics has involved a great deal of expensive testing, so that the ability to predict noise assumes economic significance. Many different sources contribute to the overall noise of an aircraft propulsion system. Sources related to the turbomachinery (fan, turbine, compressor) contain both broadband and tonal components while the jet, which is usually the dominant source at takeoff, is broadband in nature. The focus of the present investigation is on the tone noise emanating from the inlet at flow conditions where the fan tip relative Mach number is supersonic. The source of the inlet noise is then the rotor-locked shock wave field propagating through the nacelle.

Most previous investigations (see, for example, [1–3]) of inlet noise have been confined to linear acoustic waves. Although these studies are applicable to fans operating at subsonic tip relative Mach numbers, their relevance to the problem at hand is questionable. The reason for this lies in the fact that the nonlinearity of shocklike disturbances causes them to evolve quite differently from their acoustic counterparts. In particular, unlike acoustic waves, shocks are dissipative in nature. This aspect of their evolution is beyond the reach of linear theory and can be expected to play an important role in determining the level and directivity of the inlet noise.

Contributed by the International Gas Turbine Institute (IGTI) of THE AMERICAN SOCIETY OF MECHANICAL ENGINEERS for publication in the ASME JOURNAL OF TURBOMACHINERY. Paper presented at the International Gas Turbine and Aeroengine Congress and Exhibition, Vienna, Austria, June 13–17, 2004, Paper No. 2004-GT-53949. Manuscript received by IGTI, October 1, 2003; final revision, March 1, 2004. IGTI Review Chair: A. J. Strazisar.

We, therefore, commence our study with a brief review of the mechanism of periodic shock decay in simple flows, which provides a basis for understanding their behavior in the more complex engine environment. With a view to simplifying the computational procedure, we employ certain idealizations to arrive at a physical model for the numerical studies described in this paper. In particular, the three-dimensional nacelle with acoustically treated inlet is replaced with a hard-walled axisymmetric geometry, while the fan blades are assumed to be identical, permitting the use of a single blade passage in the simulation. It is further assumed that the engine axis is parallel to the direction of the oncoming freestream flow.

Employing this model, we examine two basic nacelle configurations. The first is a slender nacelle with large throat area while the second is a thick nacelle with a different throat contour, which has the effect of reducing the throat area. The acoustic properties of these inlets are studied at a high-power engine setting and flight Mach number of 0.25. It is found that the reduced throat area inlet yields a significantly better acoustic performance than the large throat area inlet. This can be attributed to the higher duct Mach number in the throat region of the former configuration, which is known from previous studies of idealized periodic shock waves to enhance shock dissipation [4–6].

The effect of introducing a uniform extension just upstream of the fan is investigated next. The additional length permits further decay of the shock waves in the case of the large throat area inlet. However, this does not occur with the reduced throat area inlet because the effect of the extension is to also reduce the interaction between the potential fields associated with the spinner and inlet wall, thus lowering the throat Mach number and thereby the shock dissipation.

As a final application of the present numerical model, we investigate the effect of forward flight on the radiated acoustic power by examining a simulated static condition. Compared with the flight condition, the slender nacelle is found to significantly attenuate the radiated acoustic energy. This is caused by a drastic overspeed of the flow past the nacelle leading edge at the static

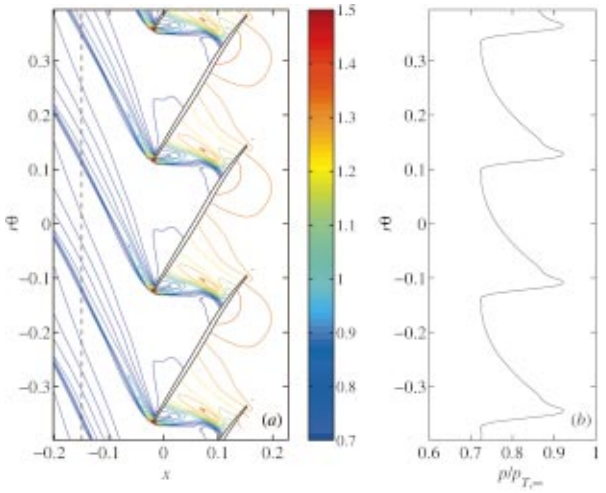

Fig. 1 (*a*) Shock structure of a supersonic blade section, illustrated using contours of static pressure normalized by freestream total pressure; (*b*) Normalized static pressure variation along the broken line in (*a*)

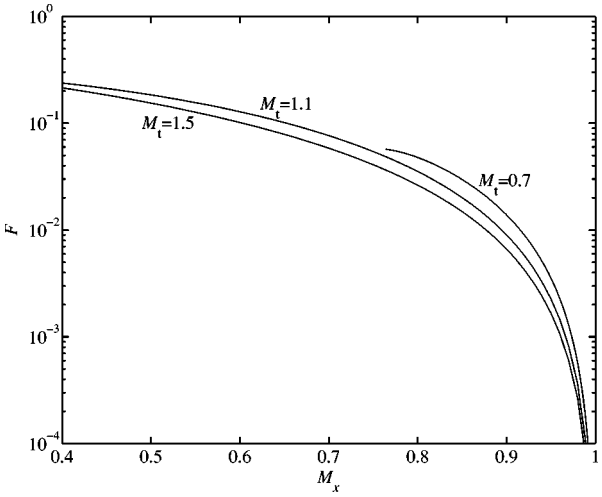

Fig. 2 Variation of F in Eq. (1) with M_x at different values of M_t

condition, which results in excessively high levels of shock dissipation. The thick nacelle, although qualitatively similar in behavior, exhibits smaller differences between the two conditions. The implications of these results for acoustic ground testing of aircraft engines are discussed.

Review of Shock Decay Mechanism

At high-power settings corresponding to the sideline (takeoff) and flyover (cutback) acoustic certification points, commercial aircraft engines are typically designed such that the outer span of the fan blade operates under supersonic relative flow conditions. The aerodynamic features of a supersonic blade section, described by Kantrowitz [7] and Ferri [8], may be understood from an examination of Fig. 1(*a*), which depicts the numerically determined blade-to-blade pressure field near the tip section of a commercial fan operating at a ''unique incidence'' condition; the pressure p is normalized by the freestream total pressure $p_{T,\infty}$. It is observed that oblique shocks are formed near the leading edge. The oblique shock on the suction side of the blade propagates away from the blade row, while that on the pressure side lies inside the blade passage. The flow immediately downstream of both shocks remains supersonic so that an expansion fan is generated over the convex part of the suction surface behind the leading edge. Further downstream, a normal shock spanning the width of the passage is formed, which merges with the pressure-side oblique shock of the adjoining blade. The static pressure variation along the broken line in Fig. 1(*a*) exhibits the behavior shown in Fig. 1(*b*), where we observe periodic shocks separated by regions of expansion. The expansion fan generated by each blade interacts with the two adjoining suction-side oblique shocks, causing the amplitude of the latter to decay upstream of the blade row.

This interaction process has been studied quantitatively by Morfey and Fisher [4], who demonstrated by means of a simplified two-dimensional model that the shock strength decays like Fd/s, where s is the axial distance upstream of the blade row, d is the blade spacing, and F is given by

$$F = \frac{(M_{\mathrm{rel}}^2 - 1)^{1/2}}{M_{\mathrm{rel}}^4}[M_x(M_{\mathrm{rel}}^2 - 1)^{1/2} - M_t]^2, \qquad (1)$$

where M_t is the tangential speed of the blade section nondimensionalized by the sonic speed, M_x is the axial (absolute) Mach number of the background flow, and $M_{\mathrm{rel}} = (M_t^2 + M_x^2)^{1/2}$ is its relative Mach number. This result can be arrived at using an alternate approach. The spatial variation of the static pressure in Fig. 1(*b*) can be regarded as the temporal variation measured at a fixed point on the broken line in Fig. 1(*a*) as the rotor moves past it. The asymptotic behavior of a nonlinear disturbance of this type propagating into an otherwise stationary fluid is to assume a sawtooth wave form that decays inversely with time owing to dissipation across the shocks [5,6]. Making use of this result in the context of the supersonic cascade flow of Fig. 1(*a*), it can be shown [4] that the spatially decaying behavior Fd/s is recovered. The function F in Eq. (1) decreases with M_x at a fixed value of M_t, as illustrated in Fig. 2. It is evident that F drops off sharply as $M_x \to 1$, a behavior that can be physically understood by observing that the larger axial Mach number prolongs the residence time of the shocks in the duct, permitting them to decay further.

The attenuated shock waves, upon leaving the inlet, are propagated to the far-field as noise. If the blades are identical, then the shock pattern repeats at the blade-passing frequency so that the radiated noise consists only of this frequency and its harmonics. However, geometric variations due to manufacturing tolerances cause the upstream-propagating shocks to vary in strength from blade to blade. Since the shock propagation speed depends on its amplitude, stronger shocks will tend to overtake their weaker counterparts, thus destroying the blade-to-blade periodicity of the flow field. Consequently, the unsteady flow is periodic at multiples of the shaft, rather than blade-passing, frequency [9–11]. This results in what is referred to as multiple pure tone noise or, more descriptively, as buzz-saw noise. In general, community noise is affected primarily by harmonics of the blade-passing frequency, while aircraft cabin noise is influenced by both harmonics of the blade-passing frequency and multiple pure tones.

Problem Formulation

Physical Model. The nacelle of a wing-mounted commercial aircraft engine is designed so that the inlet is ''drooped'' in order to accommodate the upwash induced by the circulation around the wing at the cruise condition. That is, the entrance plane is inclined at an angle to the vertical and the axis is cambered, resulting in a three-dimensional flow path as shown in Fig. 3. Moreover, at the sideline and flyover acoustic conditions, the upstream flow enters the inlet with nonzero incidence brought about by the aircraft attitude and cross-flow parallel the wing leading edge.

Thus, even if the fan blades were assumed to be identical, it is evident that the rotor flow field possesses a complete lack of symmetry and that its investigation by numerical methods would require a full-wheel unsteady simulation. Given the complexity and computational expense of carrying out a simulation of this type, it

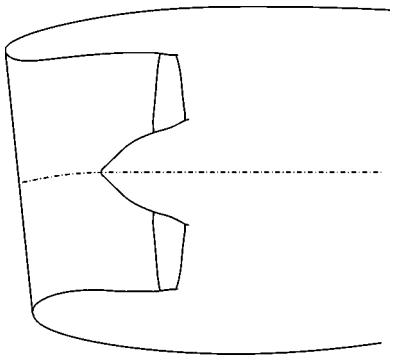

Fig. 3 Meridional section of a typical wing-mounted engine nacelle, illustrating the "drooped" entrance plane and cambered axis

is natural to inquire whether some insight may be gained by employing a simpler numerical model. To this end, the nacelle in Fig. 3 is replaced in the present study with an axisymmetric version, defined such that the flow area perpendicular to the cambered axis of the original inlet is preserved. In addition, we assume that the flow far from the nacelle is parallel to the engine axis and that the fan blades are identical, thereby permitting the simulation to be carried out using one sector corresponding to a single blade passage. Finally, in the present study, we consider the case of a hard-walled inlet; the effects of acoustic lining in the inlet will be examined in the future. Despite these simplifications, the resulting physical model captures the essential features of the flow and provides a means to develop a physical understanding of the behavior of the rotor shock field as it propagates through the inlet.

A meridional view of the model employed in the present study is illustrated in Fig. 4(*a*). It incorporates the (axisymmetric) inlet, spinner, fan rotor, splitter, and the bypass and core ducts. The fan exit guide vane and compressor inlet guide vane are not modeled. However, the study of Prasad and Prasad [12] shows that the effects of these components on the rotor flow are negligible and their omission does not affect the upstream flow field, which is of primary concern here. The tangential extent of the geometry shown in Fig. 4(*a*), including that of the upstream far field, corresponds to a single blade passage, which encompasses 15 deg along the azimuthal direction and is representative of modern wide-chord fans. The simulations presented here were run for a high-power (nominal takeoff) condition. The fan operating point is set by specifying the mechanical and corrected flows in the core and bypass regions, respectively.

Numerical Model. In the present study, the Reynolds-averaged Navier-Stokes equations for an ideal gas are solved numerically using the procedure developed by Davis et al. [13], based on the Lax-Wendroff multiple grid scheme of Ni [14]. The algorithm employs centered second-order spatial differencing and second- and fourth-order smoothing. The smoothing is applied along the flow direction and is set to a minimal level in order to limit numerical dissipation. Turbulence closure is achieved using the k-ω model of Wilcox [15] and the quasi-two-dimensional nonreflecting conditions of Giles [16] are applied at the inflow and outflow boundaries. Domain decomposition and parallel capability permit large problems to be handled. The solver has been extensively validated for numerous turbomachinery applications, details of which are to be found in the works of Ni and Bogoian [17] and Ni and Sharma [18]. A study of particular relevance to the present investigation is that of Prasad [19], who demonstrated the capability of the present solver to faithfully capture the shock decay behavior of Eq. (1) for flow past a two-dimensional supersonic compressor blade row.

In contrast to most turbomachinery flows, it is necessary in the present problem to resolve both the internal and external flows.

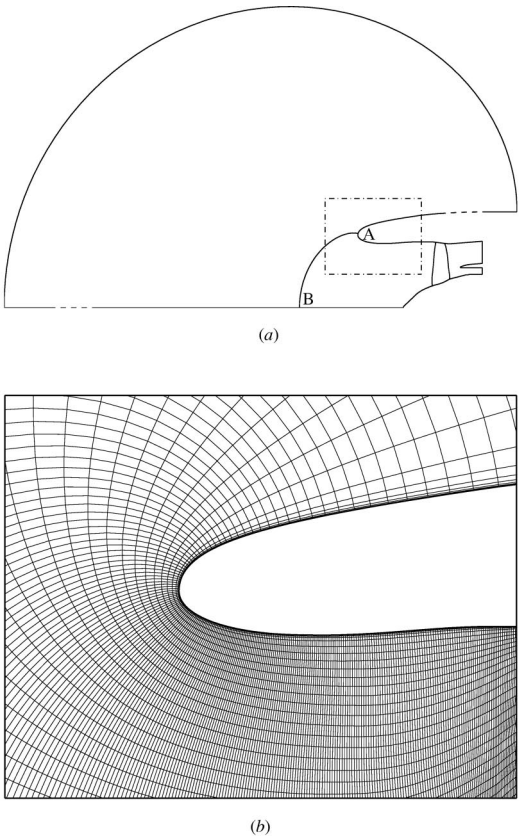

Fig. 4 (*a*) Meridional view of computational model; the outer boundary extends to about 30 engine radii from the spinner nose; (*b*) grid detail near the leading edge, with every other plane shown for clarity

For this purpose, a multiple domain grid on the geometry illustrated in Fig. 4(*a*) is employed. The exterior boundary lies at a distance of approximately 30 engine radii from the spinner nose. The nacelle grid consists of an orthogonal H-type topology, a detail of which is shown in Fig. 4(*b*).

Although, by virtue of the problem symmetry, the entire calculation can, in principle, be carried out in the reference frame of the fan rotor, numerical difficulties encountered at large radii preclude this approach. Instead, an interfacial mixing surface is inserted along the grid surface AB near the nacelle leading edge, and the steady governing equations are solved in the stationary and rotating frame upstream and downstream of this surface, respectively. The circumferentially averaged conservation variables are preserved across the interface. Furthermore, the nonreflecting conditions of Giles [16] are applied to perturbations about the circumferentially averaged quantities, thus rendering the interfacial surface effectively transparent to the disturbances emanating from the inlet. In order to verify that the interface does not cause spurious reflections, we have also carried out a fully transient simulation in which mixing does not occur at the interface. It was found that the shock behavior obtained by the two methods was essentially the same and that the spatial evolution of the acoustic power through the inlet was identical for the two simulations.

The flow around the fan blade is resolved using an O-H grid topology in order to accurately determine the flow details near the leading and trailing edges and in the boundary layers. Similarly, C-grids are employed at the spinner nose and on the splitter leading edge. Since the primary interest in the present investigation is the development of the upstream shock field, the axial grid spacing through the inlet is carefully controlled so as to minimize numerical dissipation. Specifically, the use of 481 axial and 49

circumferential planes between the nacelle and fan leading edges ensured that the axial wavelength of a disturbance was resolved by 30–40 points, with 2–4 points across shocks. This exceeds the recommendations in [19] for adequate determination of the shocks. Further, the grid was clustered in the leading edge region of the nacelle. The total number of grid points used in the present simulations was 4.7 million.

Acoustic Power. In the present study, the acoustic power is used as a means of assessing the merits of the various nacelle configurations that are investigated. The issue of determining the power carried by an acoustic disturbance propagating through a nonuniform flow is a complex one and has been the subject of much discussion [20–24]. Here, we follow Morfey [20], who defines the acoustic intensity vector **I** for a time-dependent flow as

$$\mathbf{I}=\left[\overline{\mathbf{v}}\cdot\mathbf{u}'+\frac{p'}{\overline{\rho}}\right]\left[\overline{\rho}\mathbf{u}'+\left(\frac{\overline{\mathbf{v}\rho}}{\gamma\overline{p}}\right)p'\right], \tag{2}$$

where the overbars and primes represent time-averages and perturbations, respectively. The quantities ρ, $\mathbf{v}$, p and γ represent the density, velocity, pressure, and specific heat ratio, while $\mathbf{u}'$ is the irrotational part of the velocity perturbation. This definition of the intensity reduces to that of Goldstein [21] for isentropic flow and is also consistent with the more general formulation developed by Dowling [24]. The acoustic power P crossing a surface **S** is given by

$$P=\int_{\mathrm{S}}\overline{\mathbf{I}}\cdot\mathrm{d}\mathbf{S}, \tag{3}$$

where $\overline{\mathbf{I}}$ is the time-averaged acoustic intensity. In the present instance, where temporal perturbations in the stationary frame are caused by rotor-locked disturbances, the time averages in Eq. (2) are transformed to circumferential averages in the rotating frame. The temporal perturbations themselves may be identified as the variations about the circumferential average along azimuthal lines.

For linear waves propagating through a source-free region of uniform flow, the utility of the acoustic power derives from the fact that it is a conserved quantity [20,21]. In non-uniform flows, where perturbation energy can be transferred between the acoustic, entropic, and vortical components of the unsteady flow, the acoustic power is, in general, not conserved. Moreover, when the disturbance is comprised of shocks rather than acoustic waves as in the present problem, the dissipation that occurs across the shocks will result in a decay of the acoustic power along the direction of propagation of the wavetrain. In addition to being dissipative, shocks can also generate vorticity. However, the upstream shocks are weak and become nearly plane within a short distance of the blade leading edge, as is evident in Fig. 1. Moreover, the flow varies slowly parallel to the shock surface so that the vorticity generated across the shocks is small. We may therefore replace the irrotational velocity perturbation $\mathbf{u}'$ in Eq. (2) with the total velocity perturbation $\mathbf{v}'$, thus simplifying the determination of P, with little loss in accuracy. Adopting the cylindrical polar system (x,θ,r) representing axial, azimuthal, and radial coordinates, respectively, and making use of Eq. (3), the acoustic power through an axial surface located at x is found to be

$$P(x)=B\int_0^{2\pi/B}\mathrm{d}\theta\int_{R_i(x)}^{R_o(x)}\mathrm{d}r\,r\left[\overline{\mathbf{v}}\cdot\mathbf{v}'+\frac{p'}{\overline{\rho}}\right]\left[\overline{\rho}v_x'+\left(\frac{\overline{v_x}\overline{\rho}}{\gamma\overline{p}}\right)p'\right],$$

where B is the number of blades and $R_i(x)$ and $R_o(x)$ are the local inner and outer radii.

In the present case, where the fan blades are taken as identical, P represents the sound power associated with the harmonics of the blade-passing frequency. In reality, the shocks and power associated with them can be expected to evolve differently owing to variations in the blade geometry. The behavior of P for the idealized case examined here may, nonetheless, be regarded as being qualitatively representative of the total shock noise.

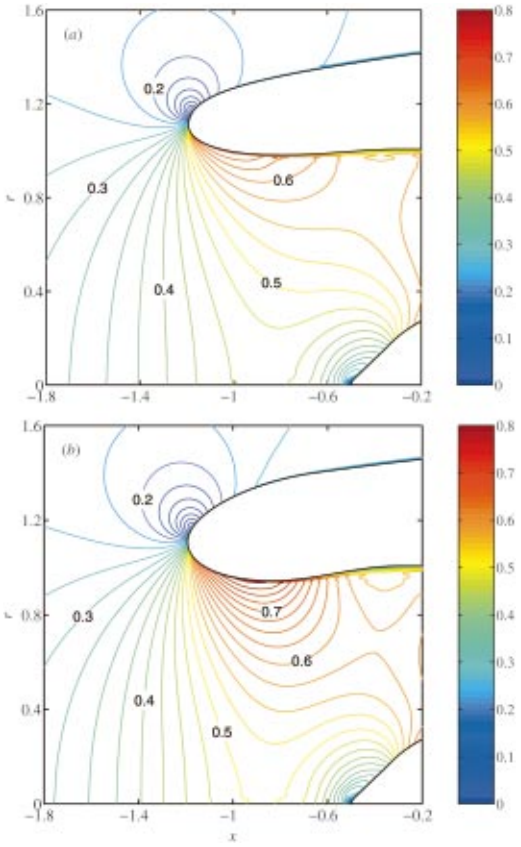

Fig. 5 Circumferentially averaged Mach number contours for (*a*) slender nacelle and (*b*) thick nacelle with reduced throat area

Numerical Results

We now describe a series of numerical experiments, wherein the behavior of the propagating shock field through various inlets is investigated. The spinner and fan geometries remain unchanged. In what follows, the coordinates are normalized by the tip radius at the fan face, with the origin of the axial coordinate placed at the leading edge of the fan tip section.

Effect of Throat Contour. We begin our study by examining two nacelles, illustrated in Figs. 5(*a*) and 5(*b*). The baseline configuration consists of a slender nacelle with a relatively large throat area. The other nacelle features a different inlet contour, which has the effect of reducing the throat area by 7.7% relative to the baseline. In addition, the external lines are such that it is thicker than the baseline nacelle. We now examine the flow through both nacelles at an engine setting corresponding to the sideline condition on a standard day, for which the parameter M_t in Eq. (1) is 1.1 at the blade tip. The flight (freestream) Mach number is set to 0.25, which corresponds to a typical takeoff speed.

The circumferentially averaged Mach number field in the meridional plane is shown in Figs. 5(*a*) and 5(*b*) for the baseline and reduced throat area inlets, respectively. It is evident that the thick nacelle features larger values of the Mach number near the throat than the slender nacelle. This is due to the smaller throat area of the former as well as the increased curvature in the neighborhood of the throat. Indeed, the potential effect of the throat contour is observed to extend well into the flow path in Fig. 5(*b*), where it

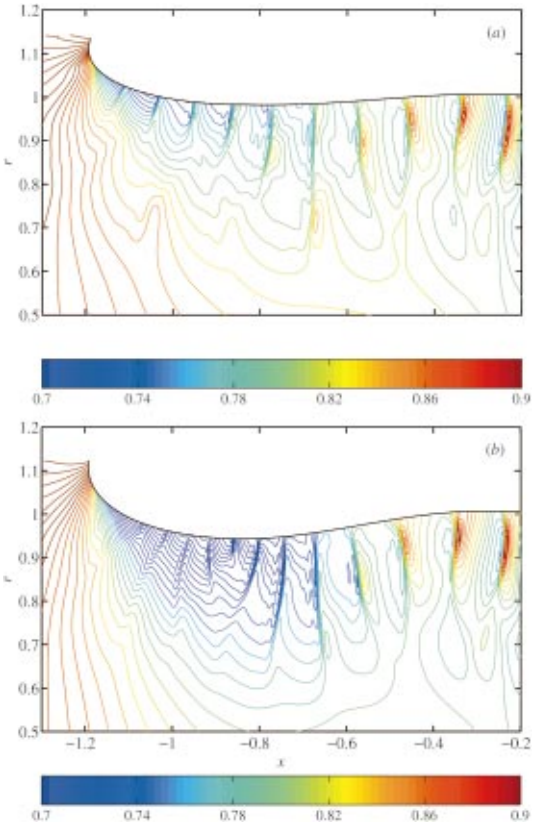

Fig. 6 Normalized pressure field on a meridional midpassage plane for (*a*) large throat area inlet and (*b*) inlet with reduced throat area

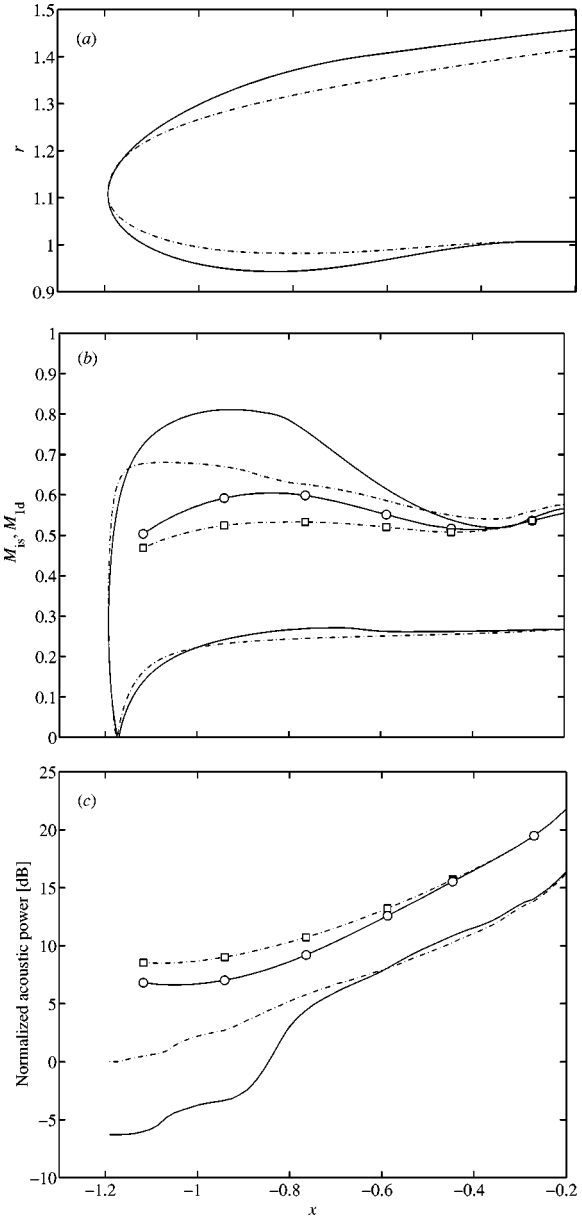

Fig. 7 (*a*) Comparison of baseline (— · — ·) and reduced throat area (—) nacelle profiles, (*b*) distributions of nacelle surface isentropic Mach number M_{is} and quasi-one-dimensional Mach number M_{1d}, (*c*) acoustic power evolution along the inlet axis. The symbols denote quasi-one-dimensional quantities for the baseline nacelle (□) and thick nacelle (○).

interacts with the upstream potential field of the spinner. There is also some potential interaction between the spinner and throat of the slender nacelle but it is significantly weaker.

We now turn our attention to the shock behavior in the two inlets, examining in Fig. 6 the normalized pressure field $p/p_{T,\infty}$ on a meridional plane lying midway between the pressure and suction surfaces of a blade passage. Focusing on the large throat area inlet, we observe from Fig. 6(*a*) that the blade shocks decay at what appears to be a nearly uniform rate as they proceed upstream. Moreover, the axial wavelength of the disturbance does not change significantly over the length of the inlet. The reduced throat area inlet exhibits a quite different behavior: the effect of the mean flow acceleration through the throat is to compress the axial wavelength of the shocks, which decay significantly faster through the throat. It is further evident from Figs. 6(*a*) and 6(*b*) that the spanwise structure of the shock field differs between the two inlets, which is likely to have a bearing on the directivity of the radiated noise.

The difference in flow behavior between the two inlets can be examined more quantitatively. To this end, we define the isentropic Mach number M_{is} on the nacelle contour as

$$M_{is}=\left\{\frac{2}{\gamma-1}\left[\left(\frac{p_{T,\infty}}{\bar{p}}\right)^{\gamma/(\gamma-1)}-1\right]\right\}^{1/2},$$

where $\bar{p}$ represents the circumferentially averaged static pressure and γ is the ratio of specific heats. The distributions of M_{is} for the two nacelles are illustrated in Fig. 7(*b*), with the nacelle contours shown in Fig. 7(*a*) for reference. The stagnation point for both nacelles occurs at on the outer wall at $x\approx-1.18$. Although the values of M_{is} differ somewhat on the outer wall owing to differences in the curvature, the freestream value of 0.25 is attained sufficiently far downstream. The isentropic Mach number differs substantially through the two inlets. In particular, there is little acceleration through the throat of the slender nacelle where the peak value of M_{is} is 0.68, while the thick nacelle causes the flow to accelerate to $M_{is}=0.81$ at its throat. Despite these differences in the two flow fields, we note that the values of M_{is} at $x=-0.2$ are almost the same, suggesting that the replacement of the slender nacelle with the thick nacelle does not alter the flow entering the fan to any significant extent. This issue is addressed in more detail later in Fig. 8.

Next, we investigate in Fig. 7(*c*) the spatial evolution of the acoustic power $P(x)$ carried by the upstream-propagating shocks. Here, and in what follows, $P(x)$ is normalized by the power radiated at the entrance plane of the baseline inlet. Focusing on the sound power in the baseline inlet, we observe that it decays monotonically with distance from the fan face at a nearly uniform rate. The small acceleration of the mean flow in the throat region ap-

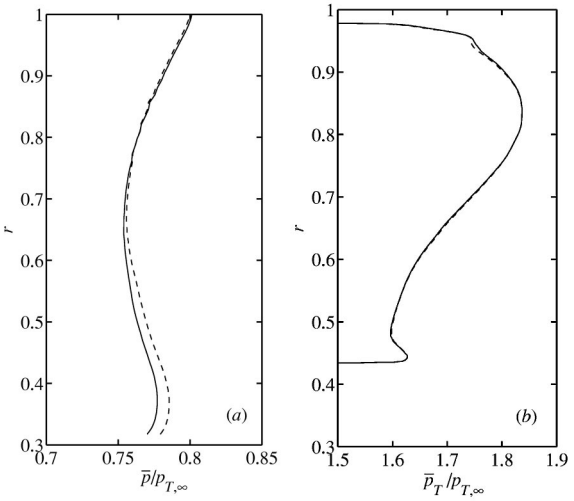

Fig. 8 Circumferentially-averaged normalized radial profiles of (*a*) fan upstream static pressure and (*b*) fan downstream total pressure for the slender (——) and thick (— — —) nacelle configurations

pears to have little effect on shock dissipation. Turning to the power evolution through the reduced throat area inlet, we observe that the behavior parallels that of the baseline inlet close to the fan, where the two curves are almost identical. As the throat is approached, however, the effect of the high-speed region is manifested in a rapid decay of the power, consistent with the qualitative observations of the shock behavior in Fig. 6(*b*). The radiated power at the entrance plane is 6.3 dB lower than the baseline case. However, the power does not decay at a uniform rate through the throat. Specifically, we note that, following the region of rapid decay in $-0.7>x>-0.9$, the decay flattens significantly for $x<-0.9$. This may be explained by observing that the rapid decay causes attenuation of the unsteady pressure field to a sufficiently small amplitudes that it behaves more like an acoustic, rather than, shock wave.

The present results may be examined in the light of predictions obtained using the model of Mathews and Nagel [25]. This model assumes a quasi-one-dimensional axially-varying mean flow, through which radially-nonuniform shocks propagate. The mean flow is determined using the one-dimensional conservation laws together with a specified axial area variation and fan face Mach number. The shock strength at the fan face varies along the span and is taken to be that of a normal shock in the rotor frame. The shock decay is calculated using the Morfey-Fisher theory [4] applied along radial strips.

The quasi-one-dimensional Mach number M_{1d} for both inlets is plotted in Fig. 7(*b*). The difference between M_{1d} and the isentropic Mach number M_{is} is least near the fan face and increases toward the throat. Further, we note that the difference is larger for the reduced throat area inlet than it is for the baseline inlet. Specifically, the maximum value of M_{1d} for the baseline inlet is 0.54, while that for the reduced throat area inlet is 0.60, which may be compared with the corresponding isentropic Mach number values of 0.68 and 0.81, respectively. This difference in behavior is to be expected, for the quasi-one-dimensional method does not take account of curvature effects, which are more significant in the latter case.

Turning now to the quasi-one-dimensional sound power,[1,2] which is plotted in Fig. 7(*c*), we observe that the levels are considerably higher than their numerical counterparts. This is not surprising in view of the normal shock assumption. The rate of decay of the quasi-one-dimensional power is nevertheless very similar to the numerical result near the fan face ($x>-0.4$). This serves to verify that the computational grid resolution is sufficient to limit the numerical dissipation to low levels. Further away from the fan, where M_{1d} differs from M_{is}, differences in the decay rate become apparent. In the case of the slender inlet, the decay rate of the acoustic power determined by the quasi-one-dimensional method is very similar to that obtained numerically. On the other hand, it is evident that the decay rate for the reduced throat area inlet is severely underpredicted by the quasi-one-dimensional approach.

These observations are qualitatively consistent with the decay rate behavior in Fig. 2. Specifically, observing from Fig. 6 that most of the shock energy is concentrated in the outer span of the blade, the behavior of the flow near the fan tip may be used to gauge the overall sound power. At $M_t=1.1$, we note that F differs by about 40% when the throat values of the isentropic and quasi-one-dimensional Mach numbers are used for the baseline inlet. In contrast, the use of the isentropic and quasi-one-dimensional throat Mach numbers for the reduced throat area inlet yields values of F that differ by a factor of about 5. The acoustic benefit provided by the reduced throat area inlet is, therefore, much higher than would be estimated using the quasi-one-dimensional approach.

We now take up the issue of the possible distortion induced by the altered nacelle contour on the fan flow. This is of crucial importance because a significant distortion can adversely impact the fan performance and thus the engine thrust. In Fig. 8(*a*), we illustrate radial profiles of the circumferentially averaged static pressure $\bar{p}$ normalized by the freestream total pressure $p_{T,\infty}$ for the two inlets at an axial station 0.3 blade tip chord lengths upstream of the tip leading edge. The potential distortion induced by the reduced throat area inlet is evident, especially near the inner radius. Nevertheless, the difference between the pressure fields associated with the two inlets is small and has virtually no effect on the total pressure rise, as is evident in Fig. 8(*b*), which depicts radial profiles of the circumferentially averaged total pressure $\bar{p}_T$ at an axial station 0.5 blade tip chord lengths downstream of the tip trailing edge. The two profiles in Fig. 8(*b*) are nearly indistinguishable, indicating that the fan work input and pressure rise are not affected by the alteration of the nacelle contour.

Effect of Uniform Extension. We now examine a variant of the two nacelle geometries, wherein a uniform cylindrical extension of length $l=0.21$ is inserted just upstream of the fan. This does not introduce slope discontinuities in the endwall since the inlet is itself cylindrical at its downstream end, as is evident in Fig. 7(*a*). The use of the extension is motivated by the observations that the increased length extends the residence time of the shocks in the inlet, permitting greater decay and that it provides additional area for acoustic treatment; only the first aspect is addressed here.

The isentropic Mach number M_{is} for the slender inlet with extension is illustrated in Fig. 9(*a*) together with the analogous distribution from Fig. 7(*b*) for the slender inlet without extension. The two distributions are more easily compared by shifting the original distribution by $x=-l=-0.21$. Upon carrying out this procedure, it is seen from Fig. 9(*a*) that the two distributions are nearly identical near the throat. This is in accord with our previous observation that the interaction between the spinner and nacelle potential fields is sufficiently weak that the axial displacement of the latter does not cause a significant change in the flow.

Next, we compare in Fig. 9(*b*) the spatial evolution of the acoustic power for the slender inlet with and without the extension. Close to the fan, where the endwall is cylindrical, the power is essentially the same for both inlets. Further upstream, the differences in the axial location of the contoured part of the inlet results in power differences but the decay rate is not significantly affected. This is in line with the Morfey-Fisher theory [4], which indicates that under the flow conditions considered here, the quan-

[1]The power determined in [25] is that corresponding to the blade-passing frequency. However, for a sawtooth disturbance, the first harmonic is dominant so that the comparison in Fig. 7(*c*) is justified.

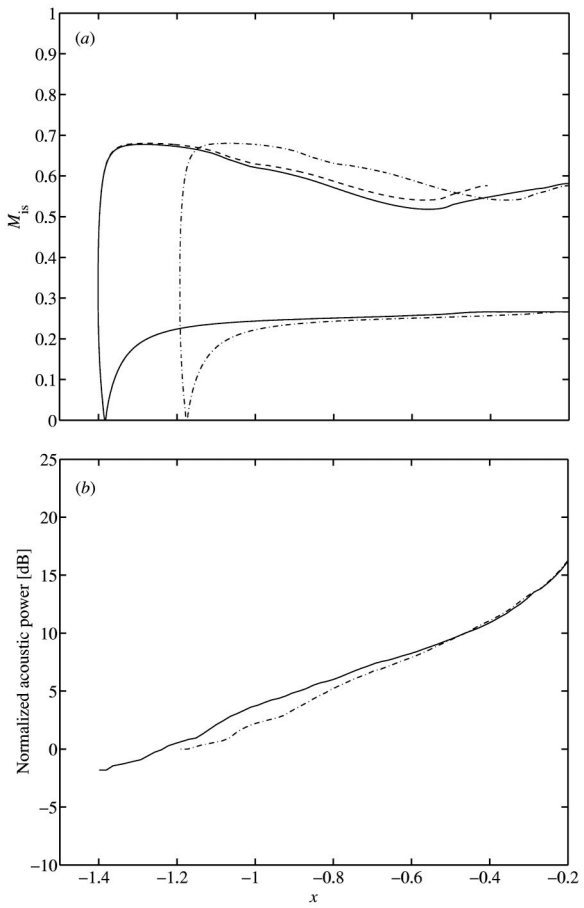

Fig. 9 (*a*) Isentropic Mach number distributions for the slender nacelle with (——) and without (— · — ·) extension of length $l=0.21$. The latter distribution shifted by $x=-l$ is also shown (— — —). (*b*) Spatial evolution of the acoustic power.

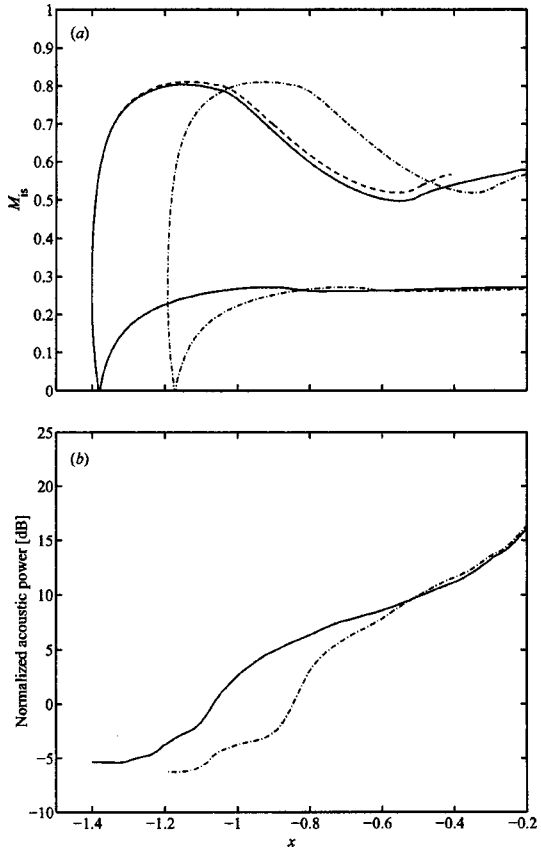

Fig. 10 (*a*) Isentropic Mach number distributions for the thick nacelle with (——) and without (— · — ·) extension of length $l=0.21$. The latter distribution shifted by $x=-l$ is also shown (— — —). (*b*) Spatial evolution of the acoustic power.

tity F in Eq. (1) is only weakly dependent on M_x, as discussed earlier. The acoustic power radiated from the extended slender inlet is found to be 1.8 dB lower than that for the slender inlet without extension. This shows that the proposed rationale for incorporating the extension so as to increase shock dissipation by lengthening their residence time in the inlet duct holds for this nacelle.

An analogous study is carried out for the thick nacelle. The isentropic Mach number distributions with and without the extension are shown in Fig. 10(*a*). As before, the latter distribution, shifted by $x=-l=-0.21$, is also illustrated for comparison. Unlike the slender nacelle, we observe that the value of M_{is} at the throat is slightly lower in the presence of the extension. This is due to the fact that the nacelle throat and spinner are now no longer in close proximity, so that the interaction between their potential fields is reduced. We have already noted that at the relatively high Mach numbers that occur near the throat of this inlet, the shock attenuation rate changes rapidly with M_x. It is therefore not surprising to find that the decay rate of the acoustic power near the throat of the extended thick nacelle is noticeably lower than near the throat of the thick nacelle without extension, as shown in Fig. 10(*b*). The effect of this lower decay rate is to increase the radiated power by 0.8 dB relative to the case where there is no extension.

Effect of Forward Flight. In the calculations discussed thus far, the flight Mach number was set to 0.25, which is representative of the takeoff condition, as noted previously. We now direct our attention to the question of whether the noise radiated in flight differs from that emitted under static conditions. This issue assumes particular significance in view of the fact that static testing forms the basis for estimating the engine noise in flight. Because this estimate is the only acoustic measure available to the engine designer until flight certification, the reliability of projections based on static tests is of crucial importance.

In carrying out numerical calculations for the static case, it would be necessary in principle to set the freestream Mach number to zero. However, this leads to numerical difficulties and, for this reason, a simulated static condition is employed, wherein the freestream Mach number is set to 0.05. We begin by examining the flow past the slender nacelle, which differs substantially between the flight and simulated static conditions. This is evident in Fig. 11(*a*) and 11(*b*), where meridional streamlines based on the circumferentially averaged velocity are shown for flight Mach numbers of 0.25 and 0.05. In the former case, the flow stagnates close to the leading edge of the nacelle. The stagnation point for the simulated static condition occurs further aft on the outer contour so that the streamlines feature a strong curvature around the leading edge. When the freestream Mach number vanishes, there is no stagnation point and the flow is drawn into the nacelle from all directions. The behavior in the neighborhood of the leading edge is however likely to be similar to that depicted in Fig. 11(*b*).

The effect of the large leading-edge streamline curvature on the circumferentially averaged Mach number field is illustrated in Fig. 12(*a*) for the case of the slender nacelle at the simulated static condition. It is observed that an overspeed region is formed on the inner side of the nacelle contour, just downstream of the leading edge, where the Mach number exceeds 0.8. Downstream of this overspeed region, the flow rapidly begins to resemble its flight counterpart in Fig. 5(*a*). The behavior of the thick nacelle at the

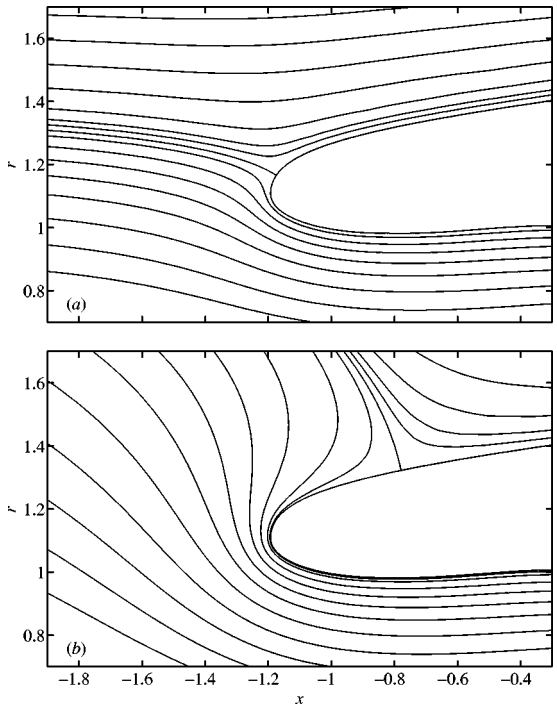

Fig. 11 Meridional streamlines for flow past the slender nacelle at (*a*) 0.25 flight Mach number and (*b*) simulated static condition

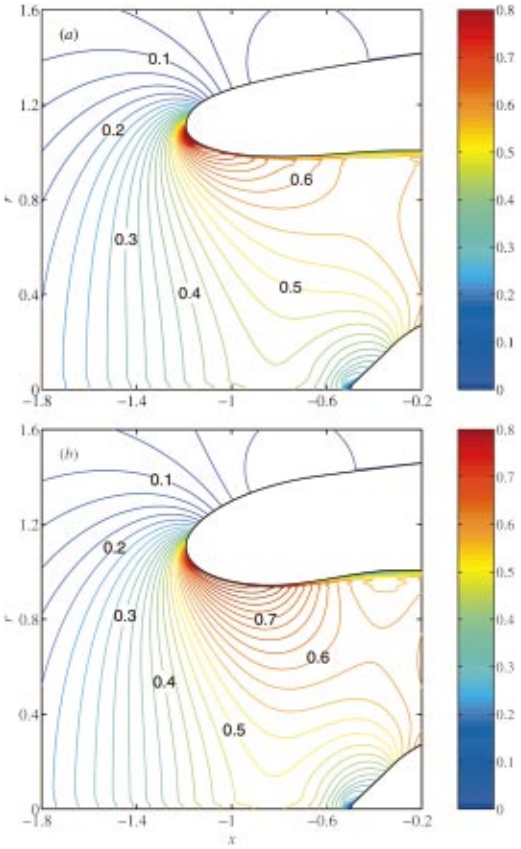

Fig. 12 Circumferentially averaged Mach number contours for (*a*) slender nacelle and (*b*) thick nacelle with reduced throat area at the simulated static condtion

simulated static condition is investigated in Fig. 12(*b*). Like the slender nacelle, an overspeed region is formed near the leading edge. However, owing to the larger leading edge radius of curvature of the thick nacelle, the flow acceleration appears to be less severe, as a comparison with Fig. 5(*b*) indicates.

The mean flow behavior is examined more quantitatively in Figs. 13(*a*) and 14(*a*) in terms of M_{is}. The isentropic Mach number distributions at the flight condition are also shown, and highlight the difference in location of the stagnation point for the two conditions. In the case of the slender nacelle, it is observed from Fig. 13(*a*) that M_{is} at the simulated static condition undergoes a rapid increase near the leading edge, assuming a peak value of 0.96. For comparison, we note that the value of M_{is} at the same location for the flight condition is about 0.6, while that at the throat is 0.68. The thick nacelle also exhibits an overspeed, as is evident in Fig. 14(*a*). It is further observed that the maximum value of $M_{is}=0.87$ exceeds the in-flight value of 0.7 at the same location and the throat value of 0.81. In both cases, the isentropic Mach number near the fan face is not affected by flight.

The effect of the nacelle flows on the duct acoustic power is shown in Figs. 13(*b*) and 14(*b*). Proceeding from the fan face to the inlet of the slender nacelle, we note that the power at the simulated static condition is almost identical to that of the flight case. As the overspeed zone near the entrance plane is encountered, the power decays dramatically, in agreement with the physical and theoretical arguments given earlier. As a consequence, the acoustic power at the entrance plane for the simulated static case is found to be 4.7 dB less than in flight. Turning to the thick nacelle, we observe that the in-duct behavior of the power in the static case is similar to that in flight. For both the flight and static conditions, the acoustic power decays in a similar manner through the throat. For $x<-0.9$, the perturbation behaves more like an acoustic, rather than shock, wave as pointed out earlier. Therefore, the effect of the overspeed is not as drastic as in the case of the slender nacelle, but is nevertheless present; the power level at the entrance plane is reduced by 0.7 dB compared with the flight case.

Discussion

In this study, we have investigated numerically the propagation of transonic fan-generated shock waves through a commercial aircraft engine inlet. These shocks are the dominant source of tone noise at high-power conditions and their speed of upstream propagation and concomitant decay are known from one-dimensional theory to be controlled by the local mean flow Mach number. This has led us to examine two basic axisymmetric hard-walled configurations: a baseline configuration consisting of a slender nacelle with large inlet throat area and a thick nacelle with a different contour, which has the effect of reducing the throat area by 7.7% relative to the baseline inlet. Considering first the case where the flight Mach number is 0.25, it was shown that the latter inlet provides a greater acoustic benefit, with the radiated acoustic power 6.3 dB less than the baseline case. This benefit was shown to be significantly higher than would have been estimated using a quasi-one-dimensional model owing to streamline curvature effects, which are not included in the latter.

With a view to increasing the duct residence time of the shocks and, thereby their dissipation, the effect of inserting a uniform extension upstream of the fan was studied. In the case of the large throat area inlet, this expectation was fulfilled and the radiated power for the extended inlet was shown to be 1.8 dB lower than the baseline configuration. However, in the case of the reduced throat area inlet, the radiated power was found to be 0.8 dB larger with the extension than without it. This behavior is caused by a weakening of the interaction between the potential fields associated with the nacelle and spinner, which lowers the throat Mach number and thus the shock dissipation. The loss of attenuation when the extension is employed does not imply that its use would be detrimental in a practical application, for, in reality, the inlet is

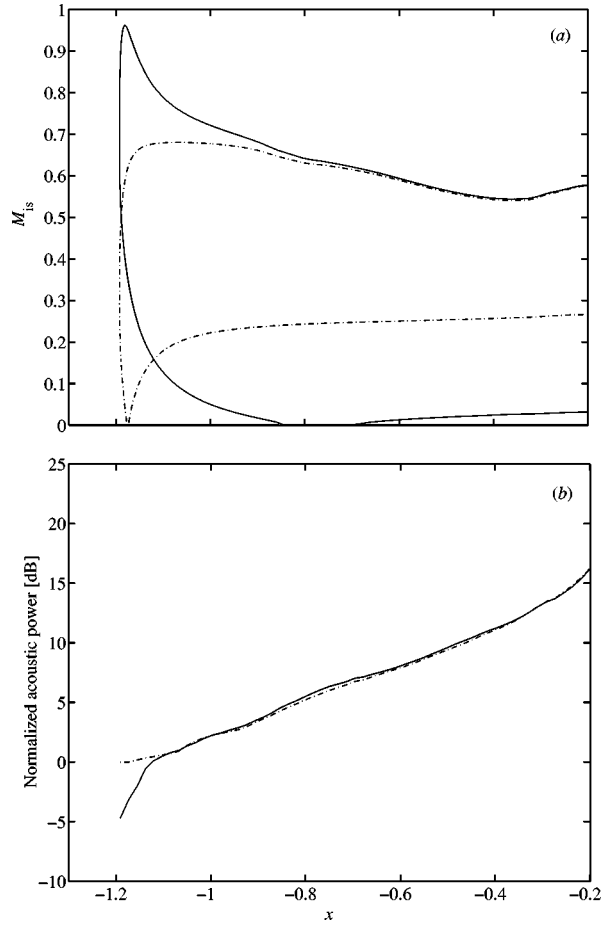

Fig. 13 (*a*) Isentropic Mach number and (*b*) acoustic power for the slender nacelle at the simulated static (——) and 0.25 flight Mach number (— · — ·) conditions.

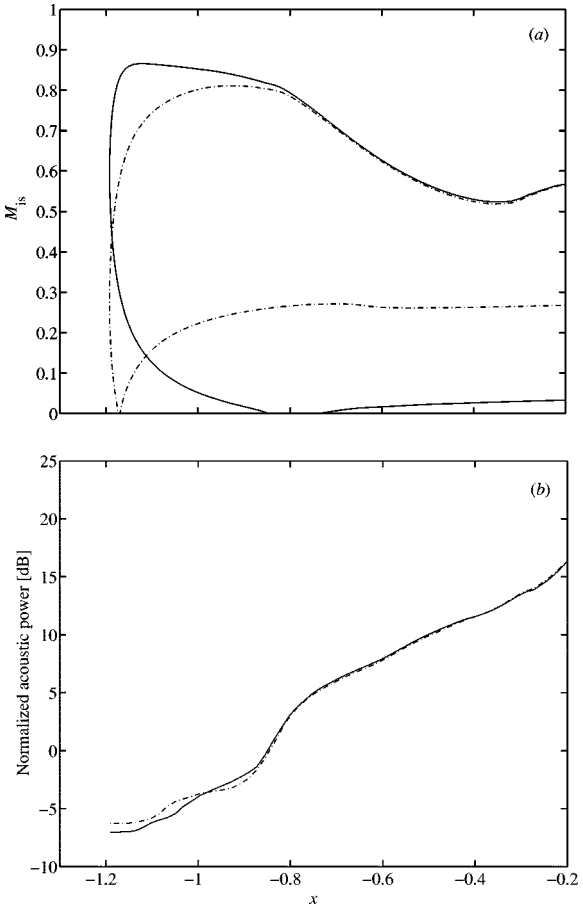

Fig. 14 (*a*) Isentropic Mach number and (*b*) acoustic power for the thick nacelle at the simulated static (——) and 0.25 flight Mach number (— · — ·) conditions

always lined and the additional acoustically treated area will invariably more than compensate for the reduced shock dissipation. This must, however, be weighed against the additional cost and weight that would be incurred and, in the present case, it would appear that the unextended inlet offers the best performance. It should be noted that, while the influence of the inlet contour in determining the acoustic behavior has been partially recognized in previous studies [25], the role of the spinner shape has not been considered. The present results suggest, nonetheless, that an optimal design from the acoustic standpoint is one in which the mutual interaction between the nacelle and spinner is accounted for and used to advantage.

The differences in noise characteristics of the engine between static and flight conditions were examined next. It was shown that the slender nacelle radiates 4.7 dB less power at the static condition than when it is in flight. This is a result of a drastic overspeed near the nacelle leading-edge under static conditions, leading to artificially large dissipation of the shocks. The thick nacelle, by virtue of its smaller leading-edge curvature and higher throat Mach numbers does not display as large a difference between the static and flight conditions.

Despite the simplifications made in this study to render an otherwise computationally expensive problem tractable, the present results have been found to be consistent with both flight and static test data. In particular, the effects of the nacelle contour and that of forward flight predicted here were borne out both qualitatively and quantitatively. However, the proprietary nature of these data precludes their presentation here.

It should be noted that although we have chosen in the present study to simulate the engine with a flight inlet at the static condition, the general practice is to fit a small bell-mouth inlet over the nacelle leading edge in order to relieve the streamline curvature. The present results demonstrate that it is crucial for this bell-mouth inlet be designed to mimic as closely as possible the flight conditions corresponding to the acoustic certification points. This is important from the point of view of obtaining noise estimates via ground testing that are representative of flight as well as in estimating the acoustic benefits of configuration changes. Thus, in the present context, we observe that the use of the slender flight inlet in ground tests would have yielded a noise estimate almost 5 dB lower than the flight level and that the acoustic benefit of the reduced throat area inlet would have been projected to be only 2.3 dB rather than the 6.3 dB obtained at the flight condition.

The relevance of the shock behavior with respect to ground tests appears not to have been emphasized in the past. Specifically, the focus for the inlet has been on ensuring that inflow nonuniformity and turbulence are minimized, motivated by the demonstration [26] that the noise generated under static conditions was higher than that in flight due precisely to larger flow nonuniformities and turbulence in ground tests. This discovery led to the development of modern inlet conditioning devices and the bell-mouth inlet alluded to earlier. On the basis of these considerations, it would appear that the use of a flight inlet in static testing would lead to conservative estimates for the forward noise level. However, this argument assumes that the inlet noise is dominated by interaction of the inflow nonuniformities with the fan, which is not true at high-power conditions.

The present study is the first of its kind, in which the rotor-locked shock-wave field through the inlet is resolved using

coupled fan-nacelle calculations. The analysis can be extended to include nonaxisymmetric inlets with the inflow at an angle of attack and nonidentical blading. Although this entails a significant increase in computational complexity, it would yield more detailed quantitative information concerning the directivity of the acoustic field and the apportioning of the acoustic energy between the multiple pure tones and harmonics of blade-passing frequency. The effects of a liner are more difficult to incorporate, in general. Qualitatively, apart from the attenuation of the pressure field, the liner can also be expected to modify the far-field directivity of the radiated noise.

Acknowledgment

The authors are grateful to Pratt & Whitney for granting permission to publish the present work. The perspicacity provided by Dr. G. F. Pickett, Dr. A. Prasad, Dr. B. L. Morin, Dr. J. S. Sabnis, Dr. O. P. Sharma, and Dr. R.-H. Ni in numerous discussions on this topic is also greatly appreciated.

References

[1] Eversman, W., and Danda Roy, I., 1993, ''Ducted Fan Acoustic Radiation Including the Effects of Nonuniform Mean Flow and Acoustic Treatment,'' NASA-CR-197449.
[2] Danda Roy, I., and Eversman, W., 1995, ''Improved Finite Element Modeling of the Turbofan Engine Inlet Radiation Problem,'' ASME J. Vibr. Acoust., **117**, pp. 109–115.
[3] Rienstra, S. W., 1999, ''Sound Transmission in Slowly Varying Circular and Annular Ducts With Flow,'' J. Fluid Mech., **380**, pp. 279–296.
[4] Morfey, C. L., and Fisher, M. J., 1970, ''Shock-Wave Radiation From a Supersonic Ducted Rotor,'' J. R. Aeronaut. Soc., **74**, pp. 579–585.
[5] Rudnick, I., 1953, ''On the Attenuation of a Repeated Saw-Tooth Shock Wave,'' J. Acoust. Soc. Am., **25**, pp. 1012–1013.
[6] Whitham, G. B., 1974 *Linear and Nonlinear Waves*, Wiley, New York.
[7] Kantrowitz, A., 1950, ''The Supersonic Axial-Flow Compressor,'' NACA Report 974.
[8] Ferri, A., 1964, ''Aerodynamic Properties of Supersonic Compressors,'' *High Speed Aerodynamics and Jet Propulsion, Volume X: Aerodynamics of Turbines and Compressors*, W. R. Hawthorne (ed.), Princeton University Press, Princeton, N.J.
[9] Hawkings, D. L., 1971, ''Multiple Pure Tone Generation by Transonic Compressors,'' J. Sound Vib., **17**, pp. 241–250.
[10] Kurosaka, M., 1971, ''A Note on Multiple Pure Tone Noise,'' J. Sound Vib., **19**, pp. 453–462.
[11] Pickett, G. F., 1972, ''Prediction of the Spectral Content of Combination Tone Noise,'' J. Aircr., **9**, pp. 658–663.
[12] Prasad, A., and Prasad, D., 2004 ''Unsteady Aerodynamics of a Fan Stage With Application to Acoustics,'' ASME J. Turbomach., **127**, pp. 64–75.
[13] Davis, R. L., Ni, R.-H., and Carter, J. E., 1986, ''Cascade Viscous Flow Analysis Using the Navier-Stokes Equations,'' AIAA Paper No. 86-0033.
[14] Ni, R.-H., 1982, ''A Multiple-Grid Scheme for Solving the Euler Equations,'' AIAA J., **20**, pp. 1565–1571.
[15] Wilcox, D. C., 1998, *Turbulence Modeling for CFD*, DCW Industries, Inc., La Cañada, CA.
[16] Giles, M. B., 1988, ''Non-Reflecting Boundary Conditions for Euler Equation Calculations,'' AIAA J., **28**, pp. 2050–2058.
[17] Ni, R.-H., and Bogoian, H., 1989, ''Predictions of 3-D Multi-Stage Turbine Flow Fields Using a Multiple-Grid Euler Solver,'' AIAA Paper No. 89-0233.
[18] Ni, R.-H., and Sharma, O. P., 1990, ''Using a 3-D Euler Flow Simulation to Assess Effects of Periodic Unsteady Flow Through Turbines,'' AIAA Paper No. 90-2357.
[19] Prasad, A., 2003, ''Evolution of Upstream Propagating Shock Waves From a Transonic Compressor Rotor,'' ASME J. Turbomach., **125**, pp. 133–140.
[20] Morfey, C. L., 1971, ''Acoustic Energy in Nonuniform Flows,'' J. Sound Vib., **14**, pp. 159–170.
[21] Goldstein, M. E., 1976 *Aeroacoustics*, McGraw-Hill, New York.
[22] Myers, M. K., 1986, ''An Exact Energy Corollary for Homentropic Flow,'' J. Sound Vib., **109**, pp. 277–284.
[23] Myers, M. K., 1991, ''Transport of Energy by Disturbances in Arbitrary Steady Flows,'' J. Fluid Mech., **226**, pp. 383–400.
[24] Dowling, A. P., 1996 ''Acoustics of Unstable Flows,'' *Theoretical and Applied Mechanics*, T. Tatsumi, E. Watanabe and T. Kambe (eds.), Elsevier, Amsterdam.
[25] Mathews, D. C. and Nagel, R. T., 1975 ''Inlet Geometry and Axial Mach Number Effects on Fan Noise Propagation,'' *Progress in Astronautics and Aeronautics* **38**, H. T. Nagamatsu (ed.), AIAA, New York.
[26] Lowrie, B. W., 1975 ''Simulation of Flight Effects on Aero-Engine Fan Noise,'' AIAA Paper No. 75–463.

Method for Analysis of Nonlinear Multiharmonic Vibrations of Mistuned Bladed Disks With Scatter of Contact Interface Characteristics

E. P. Petrov

D. J. Ewins

Centre of Vibration Engineering,
Mechanical Engineering Department,
Imperial College London,
South Kensington Campus,
London SW7 7AZ, UK

An efficient method for analysis of nonlinear vibrations of mistuned bladed disk assemblies has been developed. This development has facilitated the use of large-scale finite element models for realistic bladed disks, used hitherto in analysis of linear vibration, to be extended for the analysis of nonlinear multiharmonic vibration. The new method is based on a technique for the exact condensation of nonlinear finite element models of mistuned bladed disks. The model condensation allows the size of the nonlinear equations to be reduced to the number of degrees of freedom where nonlinear interaction forces are applied. The analysis of nonlinear forced response for simplified and realistic models of mistuned bladed disks has been performed. For a practical high-pressure bladed turbine disk, several types of nonlinear forced response have been considered, including mistuning by (i) scatter of underplatform dampers, (ii) shroud gap scatter, and (iii) blade frequency scatter in the presence of nonlinear shroud interactions.
[DOI: 10.1115/1.1812781]

Introduction

Blade mistuning is inevitable in practical bladed disks and is usually caused by small imperfections in the manufacturing and assembly processes. These imperfections result in scatter of individual blade natural frequencies and mode shapes and also in variability of the characteristics of the many contact interfaces that are present in bladed disks.

It is well known (see, e.g., [1–3]) that stress levels and vibration amplitude distributions are highly sensitive to mistuning variations even in the small ranges restricted by typical manufacturing tolerances. Because of this, the problem of analyzing mistuned bladed disks has a major practical importance and has been investigated by many authors during the past 40 years or so. Surveys of mistuning studies are given in Refs. [4] and [5]. The forced response of mistuned bladed disks has mostly been examined in these studies for cases when the vibrations of bladed disks can be considered to be linear. Moreover, forced response analysis of mistuned bladed disks was generally performed in the past using simplified models in the majority of investigations due to the large computational effort required. Recently, several techniques have been developed that are intended for use with models having large numbers of degrees of freedom in the analysis of linear vibrations of mistuned bladed disks (see [6–10]).

However, in practical bladed disk assemblies, nonlinear contact interaction forces commonly occur during service, for example, at blade-disk joints, in friction damper devices, such as underplatform dampers, and at the contact surfaces of adjacent shrouds in shrouded bladed disks, etc. These contact interaction forces can make the response of the structure strongly nonlinear, so that it exhibits phenomena that cannot be described and predicted by linearized models. Investigations of bladed disks subjected to the nonlinear interactions were restricted mostly to analysis of a single blade or a sector of the tuned bladed disk assembly, such as in Refs. [11–17].

Investigations of the effects of mistuning on forced response of nonlinear vibration of bladed disks using realistic, large-scale models of the mistuned assemblies have not been carried out to date. Moreover, scatter in the characteristics of friction contact interfaces is also inevitable, and this introduces an additional source of mistuning to that due to blade frequency mistuning into the structure. Mistuning of the contact interfaces can significantly affect forced response, stress levels, and, hence, high-cycle fatigue and reliability of bladed disks.

Because of this, the development of a method for analysis of mistuned structures, taking into account of the nonlinear effects, represents a challenging and important technical problem.

In this paper, an effective method for the analysis of essentially nonlinear vibrations of mistuned bladed disks is developed that allows large finite element models describing geometry and interaction of the bladed disk components, in detail, to be used for the first time.

Steady-state periodic vibrations are analyzed, and a multiharmonic displacement representation is used for transformation of the equations of motion into the frequency domain. The effects on the forced response levels of different types of mistuning in the bladed disk are explored, including scatter in (i) blade-alone frequencies, (ii) clearances and interferences between shrouds, and (iii) friction damper parameters and contact conditions. The influence of different causes of mistuning on the overall magnification factor is compared. A combined effect of different types of mistuning is analyzed.

Formulation of the Problem

Large-scale finite element models are now available that allow an accurate description of dynamic properties of bladed disk assemblies in wide and practically important frequency ranges. Nonlinear interactions of blades at friction contact interfaces, such as blade-disk joints, underplatform dampers, shroud contacts, and

Contributed by the International Gas Turbine Institute (IGTI) of THE AMERICAN SOCIETY OF MECHANICAL ENGINEERS for publication in the ASME JOURNAL OF TURBOMACHINERY. Paper presented at the International Gas Turbine and Aeroengine Congress and Exhibition, Vienna, Austria, June 13–17, 2004, Paper No. 2004-GT-53891. Manuscript received by IGTI, October 1, 2003; final revision, March 1, 2004. IGTI Review Chair: A. J. Strazisar.

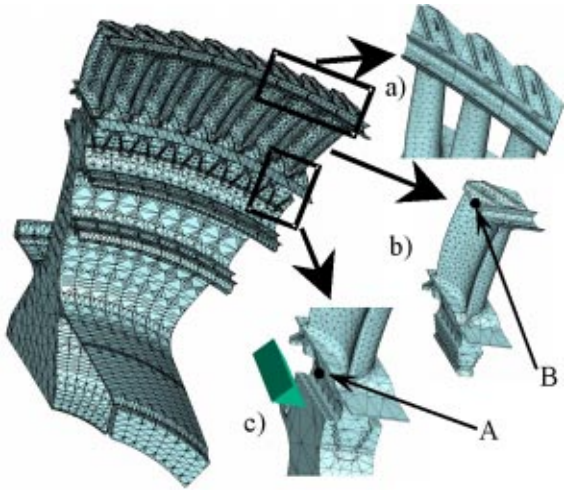

Fig. 1 Possible sources of mistuning analyzed: (*a*) scatter of shroud contacts, (*b*) individual blade mistuning, and (*c*) scatters in root contact and underplatform damper properties

others, are modeled by friction contact elements (see Fig. 1). Development of these elements was reported in Ref. [15], which provides exact expressions for the force vector and for the contact stiffness matrix describing the nonlinear contact interactions. Characteristics of the friction contact elements can be set individually for each node of the finite element model, each contact interface, and each sector of the bladed disk assembly. As a result of this, any kind of scatter of the contact interface characteristics can be modeled in addition to the customary blade frequency mistuning effects. Scatter in blade-alone frequencies and damping is modeled here by mass, stiffness, or damping elements, as shown in Ref. [7].

Complex Multiharmonic Balance Equation of Motion. A structure containing nonlinear contact interfaces between its internal components and/or interfaces at boundaries of the structure is subjected to the action of linear and nonlinear internal forces and to external excitation forces. The linear forces usually comprise inertia, elastic deformation, viscous damping, or material damping forces. Nonlinear forces are induced by nonlinear interactions at the contact interfaces. The linear forces are expressed in the finite element method through displacements using corresponding matrices (e.g., mass, stiffness, or damping). These matrices contain constant elements and are independent on the displacements for a linear system. Nonlinear forces, in general, cannot be represented in such a form and are usually described by nonlinear equations, which depend on the displacements and on design parameters of the contact interfaces. In complicated cases, the nonlinear forces cannot be defined analytically but only by using a complex algorithm.

The equation of motion for a structure with nonlinear interfaces can be written in the following form:

$$\mathbf{K}\mathbf{q}+\mathbf{C}\dot{\mathbf{q}}+\mathbf{M}\ddot{\mathbf{q}}+\mathbf{f}_{lin}(\mathbf{q})+\mathbf{f}_{nln}(\mathbf{q})-\mathbf{p}(t)=\mathbf{0} \tag{1}$$

where $\mathbf{q}(t)$ is a vector of displacements for all the degrees of freedom (DOFs) in the considered structure; $\mathbf{K}$, $\mathbf{C}$, and $\mathbf{M}$ are, respectively, stiffness, viscous damping, and mass matrices of the tuned bladed disk. For a bladed disk analyzed in a noninertial coordinate system rotating with a speed ω, the stiffness matrix can comprise not only the conventional elastic stiffness matrix $\mathbf{K}_e$, but can also include terms accounting for the rotations effects (i.e., $\mathbf{K}=\mathbf{K}_e+\mathbf{K}_g(\omega)-\omega^2\mathbf{M}_\omega$), where $\mathbf{K}_g$ is a so-called geometric stiffness matrix reflecting stiffening effects of the centrifugal forces and $\mathbf{M}_\omega$ is a spin-softening-matrix describing stiffness softening due to changing direction of the centrifugal forces under vibration. $\mathbf{f}_{lin}(\mathbf{q})$ is a vector of linear forces modeling blade frequency and/or damping mistuning; $\mathbf{f}_{nln}(\mathbf{q})$ is a vector of nonlinear interface forces, which is nonlinearly dependent on displacements; and $\mathbf{p}(t)$ is a vector of external excitation forces.

For the search of a periodic vibration response, the variation in time for displacements can be represented as restricted Fourier series, each of which can contain as many and such harmonic components as are necessary to approximate the sought solution, i.e.,

$$\mathbf{q}(t)=\mathbf{Q}_0+\sum_{j=1}^{n}\left(\mathbf{Q}_j^{(c)}\cos m_j\omega t+\mathbf{Q}_j^{(s)}\sin m_j\omega t\right) \tag{2}$$

where $\mathbf{Q}_j^{(c)}$ and $\mathbf{Q}_j^{(s)}$ $(j=1\ldots n)$ are vectors of harmonic coefficients for system DOFs using cosine and sine components marked by superscripts (c) and (s) accordingly; $\mathbf{Q}_0$ is a vector of the static components of the displacements; m_j $(j=1\ldots n)$ are specific numbers of harmonics that are kept in the displacement expansion in addition to the constant component.

It is convenient to formulate the multiharmonic equation of motion in a form using complex arithmetic as developed in Ref. [17]. In order to make such a formulation, the harmonic coefficients for displacements, excitation forces, and internal forces for each harmonic are combined into complex vectors, as follows:

$$\mathbf{Q}_j=\mathbf{Q}_j^{(c)}-i\mathbf{Q}_j^{(s)};\quad \mathbf{P}_j=\mathbf{P}_j^{(c)}-i\mathbf{P}_j^{(s)};\quad \mathbf{F}_j=\mathbf{F}_j^{(c)}-i\mathbf{F}_j^{(s)} \tag{3}$$

As a result, the following multiharmonic balance equation of motion is obtained:

$$\mathbf{R}(\mathbf{Q},\omega)=\mathbf{Z}(\omega)\mathbf{Q}+\mathbf{F}^{lin}(\mathbf{Q})+\mathbf{F}^{nln}(\mathbf{Q})-\mathbf{P}=\mathbf{0} \tag{4}$$

where $\mathbf{R}(\mathbf{Q},\omega)=\{\mathbf{R}_0,\mathbf{R}_1,\ldots,\mathbf{R}_n\}^T$ is a vector of residuals for the nonlinear multiharmonic equations formulated, which is equal to zero when a solution is found; $\mathbf{Q}=\{\mathbf{Q}_0,\mathbf{Q}_1,\ldots,\mathbf{Q}_n\}^T$ is a sought vector of harmonic coefficients of displacements; $\mathbf{P}=\{\mathbf{P}_0,\mathbf{P}_1,\ldots,\mathbf{P}_n\}^T$ is a vector of harmonic components of the excitation forces; $\mathbf{F}_{lin}(\mathbf{Q})=\{\mathbf{F}_0^{lin},\mathbf{F}_1^{lin},\ldots\mathbf{F}_n^{lin}\}^T$ is a vector of harmonic components of linear forces describing blade frequency mistuning; $\mathbf{F}_{nln}(\mathbf{Q})=\{\mathbf{F}_0^{nln},\mathbf{F}_1^{nln},\ldots\mathbf{F}_n^{nln}\}^T$ is a vector of harmonic components of non linear forces; and $\mathbf{Z}(\omega)$ is the dynamic stiffness matrix of the linear part of the system, constructed for all harmonic components. This matrix has a quasi-diagonal form, i.e.,

$$\mathbf{Z}=\mathrm{diag}[\mathbf{Z}_0,\mathbf{Z}_1,\ldots,\mathbf{Z}_n] \tag{5}$$

$$\mathbf{Z}_0=\mathbf{K};\quad \text{and}\quad \mathbf{Z}_j=[\mathbf{K}-(m_j\omega)^2\mathbf{M}]+im_j\omega\mathbf{C}+i\eta\mathbf{K}_e \tag{6}$$

where η is the material damping loss factor.

Exact Method for Condensation of the Nonlinear Mistuned Model

Harmonics in the multiharmonic balance equation of motion (4) interact through the nonlinear force vector $\mathbf{F}_{nln}(\mathbf{Q})$, which is dependent on all harmonics. Because of that, Eq. (4) represents a set of equations that has to be solved simultaneously. However, this equation has a block-diagonal matrix $\mathbf{Z}$, which allows condensation of the equations of motion to be performed for each harmonic separately. In this section, we describe a method for condensation of the multiharmonic equations of motion, which reduces number of DOFs in the resolving nonlinear equation to the number of DOFs where nonlinear forces applied. The method proposed for the condensation reduces the size of the model using matrix transformations and does not introduce any assumptions or simplifications into the model. It preserves fully the accuracy and completeness of the model, and the reduced system obtained as a result of the condensation is exact if the matrices of the original system are accurate.

Since the number of nonlinear DOFs is usually much smaller than the total number of DOFs in a mistuned bladed disk, such a

condensation gives the capability to analyze very detailed finite element models of bladed disks, as is required in real-life practical applications.

The vector $\mathbf{F}_{lin}(\mathbf{Q})$ of harmonic components of linear mistuning forces caused by linear modifications of a bladed disk can be expressed as linear combination of displacements and matrices of the mistuning modifications, i.e., stiffness matrix $\delta\mathbf{K}$, mass matrix $\delta\mathbf{M}$, viscous damping matrix $\delta\mathbf{C}$, and material damping matrix $\delta\mathbf{K}_e$ in the form:

$$\mathbf{F}_j^{lin}=[\,\delta\mathbf{K}-(m_j\omega)^2\delta\mathbf{M}+im_j\omega\delta\mathbf{C}+i\eta\delta\mathbf{K}_e]\mathbf{Q}_j=\delta\mathbf{Z}_j(\omega)\mathbf{Q}_j \tag{7}$$

Expressions for the linear mistuning given by Eq. (7) are substituted into the expressions for the jth component of the residual vector given by Eq. (4) and then they are transformed to the following form:

$$\mathbf{R}_j(\mathbf{Q},\omega)=\mathbf{Q}_j+[\,\mathbf{Z}_j(\omega)+\delta\mathbf{Z}_j(\omega)\,]^{-1}(\mathbf{F}_j^{nln}(\mathbf{Q})-\mathbf{P}_j)=\mathbf{0} \tag{8}$$

The condensation is performed for Eq. (8) in two major steps, as discussed below.

Condensation of "Passive" DOFs. At the first step, the DOFs are condensed where there are no nonlinear forces acting and there are no linear modification elements applied. These DOFs are referred to here as "passive" DOFs, and all DOFs where nonlinear or linear forces are applied are called "active" DOFs.

Introducing a matrix of dynamic compliance (or the FRF matrix) for the bladed disk mistuned by linear modifications elements, $\tilde{\mathbf{A}}_j=[\,\mathbf{Z}_j(\omega)+\delta\mathbf{Z}_j(\omega)\,]^{-1}$, the following equation can be written from Eq. (8):

$$\mathbf{R}_j=\mathbf{Q}_j+\tilde{\mathbf{A}}_j\mathbf{F}_j^{nln}(\mathbf{Q})-\tilde{\mathbf{Q}}_j=\mathbf{0} \tag{9}$$

where $\tilde{\mathbf{Q}}_j=\tilde{\mathbf{A}}_j\mathbf{P}_j$ is a vector of forced response of a mistuned structure without the nonlinear elements, but where all the linear mistuned elements are applied.

Vectors of displacements can be partitioned into active and passive parts: $\mathbf{Q}_j=\{\mathbf{Q}_j^a,\mathbf{Q}_j^p\}^T$; $\tilde{\mathbf{Q}}_j=\{\tilde{\mathbf{Q}}_j^a,\tilde{\mathbf{Q}}_j^p\}^T$. The DOFs where nonlinear forces are applied are included in the set of the active nodes, and the vector of nonlinear forces can be expressed in the form $\mathbf{F}_j^{nln}(\mathbf{Q})=\{\mathbf{F}_j^{a,nln},\mathbf{0}\}^T$. Partitioning the FRF matrix $\tilde{\mathbf{A}}_j$ of the mistuned bladed disk accordingly in Eq. (9), one can see that the passive DOFs can be excluded from Eq. (9), which gives the reduced equation:

$$\mathbf{R}_j^a=\mathbf{Q}_j^a+\tilde{\mathbf{A}}_j^a\mathbf{F}_j^{a,nln}(\mathbf{Q})-\tilde{\mathbf{Q}}_j^a=\mathbf{0} \tag{10}$$

where $\tilde{\mathbf{A}}_j^a$ is a block corresponding to the active DOFs in the matrix $\tilde{\mathbf{A}}_j$.

It was proved in Ref. [7] that the FRF matrix of a bladed disk which is mistuned by linear modification elements, and the forced response of such a bladed disk $\tilde{\mathbf{A}}_j^a$ can be calculated by considering only the active DOFs and ignoring all the passive DOFs. Moreover, from Woodbury-Sherman-Morrison formula (see [18,19]) the recurrence formulas for the calculation of the inverse of a perturbed matrix have been derived in paper [7]. These recurrence formulas take the following form:

$$\begin{aligned}
\mathbf{u}_k^T&=\frac{\delta\mathbf{z}_{jk}^T}{1+\delta\mathbf{z}_{jk}^T\tilde{\mathbf{a}}_k^{(k)}}\\
\tilde{\mathbf{A}}_j^{a(k+1)}&=\tilde{\mathbf{A}}_j^{a(k)}-[\tilde{\mathbf{a}}_k^{(k)}(\mathbf{u}_k^T\tilde{\mathbf{A}}_j^{a(k)})]\\
\tilde{\mathbf{Q}}_j^{a(k+1)}&=\tilde{\mathbf{Q}}_j^{a(k)}-(\mathbf{u}_k^T\tilde{\mathbf{Q}}_j^{a(k)})\tilde{\mathbf{a}}_k^{(k)}\\
k&=0\ldots N_{lin}-1;\quad j=0\ldots n
\end{aligned} \tag{11}$$

where superscript (k) indicates the number of the iteration in the recurrence update of the FRF matrix $\tilde{\mathbf{A}}_j^{a(k)}$ and the vector of amplitudes $\tilde{\mathbf{Q}}_j^{a(k)}$; $\tilde{\mathbf{a}}_k^{(k)}$ is the kth column of matrix $\tilde{\mathbf{A}}_j^{a(k)}$; $\delta\mathbf{z}_{jk}^T$ is the kth row of matrix $\delta\mathbf{Z}^{aa}$; N_{lin} is the number of nonzero rows in matrix $\delta\mathbf{Z}$ and $\mathbf{u}_k$ is an auxiliary vector introduced in the formulas to increase the efficiency of the calculations. N_{lin} determines the total number of iterations required for an exact calculation of the forced response amplitudes and of the FRF matrix of the mistuned structure. For the first iteration of the recurrence [i.e., for $\tilde{\mathbf{Q}}_j^{a(0)}$ and for $\tilde{\mathbf{A}}_j^{a(0)}$], the FRF matrix and the forced response of a tuned bladed disk are used.

Condensation of Linear Mistuning DOFs. For the majority of practical cases, some of the nonlinear DOFs can differ from those where linear modification elements are applied. The linear mistuning DOFs, left after the first condensation step, where there are no nonlinear forces applied, are excluded from the nonlinear equations at the second step of the multistep condensation proposed.

Appropriate ordering of the DOFs corresponding to the nonlinear and linear modification elements allows the vector of active DOFs to be partitioned $\mathbf{Q}_j^a=\{\mathbf{Q}_j^{nln},\mathbf{Q}_j^{lin}\}^T$ and, therefore, Eq. (10) to be written in the following form:

$$\mathbf{R}_j^a=\begin{Bmatrix}\mathbf{Q}_j^{nln}\\ \mathbf{Q}_j^{lin}\end{Bmatrix}+\begin{bmatrix}\tilde{\mathbf{A}}_j^{nln} & \tilde{\mathbf{A}}_j^{nln,lin}\\ \tilde{\mathbf{A}}_j^{lin,nln} & \tilde{\mathbf{A}}_j^{lin}\end{bmatrix}\begin{Bmatrix}\mathbf{F}_j^{nln}(\mathbf{Q})\\ \mathbf{0}\end{Bmatrix}-\begin{Bmatrix}\tilde{\mathbf{Q}}_j^{nln}\\ \tilde{\mathbf{Q}}_j^{lin}\end{Bmatrix}=\mathbf{0} \tag{12}$$

where superscript nln indicates components of vectors and matrices corresponding to DOFs where nonlinear and linear modification elements are applied, and superscript lin indicates the DOFs where only linear modification elements are applied. Further reduction of the size of the model can be made by eliminating from Eq. (12) those equations corresponding to the DOFs where only linear mistuning elements are applied, and this results in the following equations for each jth harmonic:

$$\mathbf{R}_j^{nln}(\mathbf{Q},\omega)=\mathbf{Q}_j^{nln}+\tilde{\mathbf{A}}_j^{nln}(\omega)\mathbf{F}_j^{nln}(\mathbf{Q})-\tilde{\mathbf{Q}}_j^{nln}=\mathbf{0} \tag{13}$$

Nonlinear Forced Response Calculation

Solution of the Nonlinear Multiharmonic Equation. There are two important points that have to be included in the solution procedure:

i. Nonlinear equations expressed by Eq. (13) can be efficiently obtained for each harmonic separately. However, these equations are coupled owing to the dependency of each harmonic of the nonlinear forces, $\mathbf{F}_j^{nln}(\mathbf{Q})$, on all the harmonic coefficients of displacements, $\mathbf{Q}$, and because of that these equations have to be solved simultaneously for all harmonics.

ii. Although the complex multiharmonic formulation is convenient for the condensation of the model and for the calculation of the residual vector, in order to use the Newton-Raphson method for the solution of the nonlinear equations they have to be formulated by real numbers. This is a necessary requirement since vectors $\mathbf{R}_j^{nln}(\mathbf{Q},\omega)$ are not analytical functions of $\mathbf{Q}$ and hence the derivatives $\partial\mathbf{R}_j^{nln}/\partial\mathbf{Q}$ needed for the solution cannot be defined.

In order to make solution of the nonlinear equations feasible, we now separate the real and imaginary parts for all vectors included in Eq. (13). These real and imaginary parts correspond to sine and cosine components of the motion. Real vectors $\hat{\mathbf{Q}}=\{\mathbf{Q}_0,\mathbf{Q}_1^{(c)},\ldots,\mathbf{Q}_n^{(s)}\}^T$ and $\hat{\mathbf{F}}^{nln}=\{\mathbf{F}_0^{nln},\mathbf{F}_1^{(c),nln},\ldots,\mathbf{F}_n^{(s),nln}\}^T$, comprising all coefficients for their multiharmonic expansion, are extracted from the vector of complex amplitudes of displacements, $\mathbf{Q}$, and of the nonlinear forces, $\mathbf{F}^{nln}$.

Accordingly, an expression for the real residual vector, $\hat{\mathbf{R}}$, can be obtained from the complex residual vectors, $\mathbf{R}_j^{nln}$, in the form:

$$\hat{\mathbf{R}}=\{\mathbf{R}_0^{nln},\mathrm{Re}(\mathbf{R}_1^{nln}),\ldots,\mathrm{Re}(\mathbf{R}_n^{nln}),-\mathrm{Im}(\mathbf{R}_n^{nln})\}^T$$
$$=\{\mathbf{R}_0,\mathbf{R}_1^c,\mathbf{R}_1^s,\ldots,\mathbf{R}_n^c,\mathbf{R}_n^s\}^T=\mathbf{0} \quad (14)$$

Iterative solution of the nonlinear equation (13) by the Newton-Raphson method and tracing of the nonlinear solution as a function of the excitation frequency ω, with predictor-corrector method (see, for example, [20,21]), requires determination not only of the vector of residuals, but also of the matrix of derivatives for the residual vector with respect to the multiharmonic amplitudes of vibration $\partial\hat{\mathbf{R}}^{(k)}/\partial\hat{\mathbf{Q}}$ and with respect to the excitation frequency $\partial\hat{\mathbf{R}}^{(k)}/\partial\omega$.

Calculation of Matrices Required for Solution of the Nonlinear Equations. Matrix $\partial\hat{\mathbf{R}}^{(k)}/\partial\hat{\mathbf{Q}}$ is determined by differentiating Eq. (13) with respect to multiharmonic amplitudes for the DOFs where nonlinear elements are applied, $\hat{\mathbf{Q}}$:

$$\frac{\partial\hat{\mathbf{R}}}{\partial\hat{\mathbf{Q}}}=\mathbf{I}+\hat{\mathbf{A}}^{nln}\frac{\partial\hat{\mathbf{F}}^{nln}}{\partial\hat{\mathbf{Q}}} \quad (15)$$

Here the identity matrix and matrix $\partial\hat{\mathbf{F}}^{nln}(\hat{\mathbf{Q}})/\partial\hat{\mathbf{Q}}$ is a matrix of tangent stiffness of the nonlinear elements. This matrix is formed from the tangent matrices of all nonlinear elements applied to the mistuned bladed disk using the standard finite element procedure. Expressions for matrices of the friction contact elements are derived analytically in paper Ref. [15], providing an exact and very fast calculation of matrix $\partial\hat{\mathbf{F}}^{nln}(\hat{\mathbf{Q}})/\partial\hat{\mathbf{Q}}$. Matrix $\hat{\mathbf{A}}^{nln}$ is formed from the FRF matrices of the linearly mistuned structure $\mathbf{A}_j^{nln}(\omega)$, determined by Eq. (11). It has the following block diagonal structure:

$$\hat{\mathbf{A}}^{nln}=\mathrm{diag}[\mathbf{A}_0^{nln},\hat{\mathbf{A}}_1^{nln},\hat{\mathbf{A}}_2^{nln}\ldots,\hat{\mathbf{A}}_n^{nln}] \quad (16)$$

where

$$\hat{\mathbf{A}}_j^{nln}=\begin{bmatrix}\mathrm{Re}(\tilde{\mathbf{A}}_j^{nln}) & -\mathrm{Im}(\tilde{\mathbf{A}}_j^{nln})\\ \mathrm{Im}(\tilde{\mathbf{A}}_j^{nln}) & \mathrm{Re}(\tilde{\mathbf{A}}_j^{nln})\end{bmatrix}$$

The vector of derivatives of the residual vector with respect to the excitation frequency $\partial\hat{\mathbf{R}}^{(k)}/\partial\omega$ takes the following form:

$$\frac{\partial\hat{\mathbf{R}}}{\partial\omega}=\frac{\partial\hat{\mathbf{A}}^{nln}}{\partial\omega}\hat{\mathbf{F}}^{nln}-\frac{\partial\hat{\mathbf{Q}}^{nln}}{\partial\omega} \quad (17)$$

where

$$\partial\hat{\mathbf{A}}^{nln}/\partial\omega=\mathrm{diag}[\mathbf{0},\partial\hat{\mathbf{A}}_1^{nln}/\partial\omega,\partial\hat{\mathbf{A}}_2^{nln}/\partial\omega\ldots,\partial\hat{\mathbf{A}}_n^{nln}/\partial\omega] \quad (18)$$

$$\frac{\partial\hat{\mathbf{Q}}^{nln}}{\partial\omega}=\left\{\mathbf{0},\mathrm{Re}\left(\frac{\partial\tilde{\mathbf{Q}}_1^{nln}}{\partial\omega}\right),\mathrm{Im}\left(\frac{\partial\tilde{\mathbf{Q}}_1^{nln}}{\partial\omega}\right),\ldots,\mathrm{Im}\left(\frac{\partial\tilde{\mathbf{Q}}_n^{nln}}{\partial\omega}\right)\right\} \quad (19)$$

Matrix $\partial\hat{\mathbf{A}}^{nln}/\partial\omega$ and vector $\partial\hat{\mathbf{Q}}^{nln}/\partial\omega$ are constructed from the complex matrices $\partial\tilde{\mathbf{A}}_j^{nln}/\partial\omega$ and vectors $\partial\tilde{\mathbf{Q}}_j^{nln}/\partial\omega$, which can be calculated separately for each of the harmonics. For the zeroth harmonic, the forced response and the compliance matrix are independent of the excitation frequency ω, and the corresponding derivatives are equal to zero.

The total number of DOFs in a mistuned bladed disk is very large, even for one harmonic. Because of that, recurrence formulas have been developed by the authors to calculate the derivatives $\partial\hat{\mathbf{A}}^{nln}/\partial\omega$ and $\partial\hat{\mathbf{Q}}^{nln}/\partial\omega$ for the active DOFs of a mistuned bladed disk using the linear mistuning matrix $\delta\mathbf{Z}_j$ and the FRF matrix and forced response amplitudes of a tuned bladed disk. These formulas are obtained by deriving expressions with respect to derivatives similar to those formulated for the FRF matrix and vector of the forced response in Eq. (11). These expressions take the following form:

$$\frac{\partial\mathbf{u}_k^T}{\partial\omega}=\frac{\partial\delta\mathbf{z}_{jk}^T/\partial\omega}{1+\delta\mathbf{z}_{jk}^T\tilde{\mathbf{a}}_k^{(k)}}-\frac{\partial\delta\mathbf{z}_{jk}^T/\partial\omega\tilde{\mathbf{a}}_k^{(k)}+\delta\mathbf{z}_{jk}^T\partial\tilde{\mathbf{a}}_k^{(k)}/\partial\omega}{(1+\delta\mathbf{z}_{jk}^T\tilde{\mathbf{a}}_k^{(k)})^2}\delta\mathbf{z}_{jk}^T$$

$$\frac{\partial\tilde{\mathbf{A}}_j^{a(k+1)}}{\partial\omega}=\frac{\partial\tilde{\mathbf{A}}_j^{a(k)}}{\partial\omega}-\tilde{\mathbf{a}}_k^{(k)}\left(\frac{\partial\mathbf{u}_k^T}{\partial\omega}\tilde{\mathbf{A}}_j^{a(k)}+\mathbf{u}_k^T\frac{\partial\tilde{\mathbf{A}}_j^{a(k)}}{\partial\omega}\right)-\frac{\partial\tilde{\mathbf{a}}_k^{(k)}}{\partial\omega}\mathbf{u}_k^T\tilde{\mathbf{A}}_j^{a(k)} \quad (20)$$

$$\frac{\partial\tilde{\mathbf{Q}}_j^{a(k+1)}}{\partial\omega}=\frac{\partial\tilde{\mathbf{Q}}_j^{a(k)}}{\partial\omega}-\left(\frac{\partial\mathbf{u}_k^T}{\partial\omega}\tilde{\mathbf{Q}}_j^{a(k)}+\mathbf{u}_k^T\frac{\partial\tilde{\mathbf{Q}}_j^{a(k)}}{\partial\omega}\right)\tilde{\mathbf{a}}_k^{(k)}-\mathbf{u}_k^T\tilde{\mathbf{Q}}_j^{a(k)}\frac{\partial\tilde{\mathbf{a}}_k^{(k)}}{\partial\omega}$$
$$k=0\ldots N_{lin}-1;\quad j=0\ldots n$$

where $\partial\delta\mathbf{z}_{jk}^T/\partial\omega$ is kth row of matrix $\partial\delta\mathbf{Z}_j/\partial\omega$, which is determined by differentiation of the matrix of linear mistuning elements defined in Eq. (7),

$$\frac{\partial\delta\mathbf{Z}_j}{\partial\omega}=m_j[-2(m_j\omega)\delta\mathbf{M}+i\,\delta\mathbf{C}] \quad (21)$$

The recurrence update starts from initial values $\partial\tilde{\mathbf{A}}_j^{a(0)}/\partial\omega$ and $\partial\tilde{\mathbf{Q}}_j^{a(0)}/\partial\omega$, calculated for the tuned bladed disk. At the end of the $(N_{lin}-1)$th recurrence, exact values for $\partial\tilde{\mathbf{A}}_j^{a}/\partial\omega$ and $\partial\tilde{\mathbf{Q}}_j^{a}/\partial\omega$ are calculated. Since nonlinear DOFs are included in the set of the active DOFs, the matrix $\partial\tilde{\mathbf{A}}_j^{nln}/\partial\omega$ and vector $\partial\tilde{\mathbf{Q}}_j^{nln}/\partial\omega$ are simply selected from $\partial\tilde{\mathbf{A}}_j^{a}/\partial\omega$ and $\partial\tilde{\mathbf{Q}}_j^{a}/\partial\omega$.

Expressions for a Whole Tuned Bladed Disk From a Sector Model

The FRF matrix $\tilde{\mathbf{A}}_j^{a(0)}$ and vector of forced response amplitudes $\tilde{\mathbf{Q}}_j^{a(0)}$ for the whole tuned bladed disk have to be calculated together with their derivatives with respect to the excitation frequencies $\partial\tilde{\mathbf{A}}_j^{a(0)}/\partial\omega$ and $\partial\tilde{\mathbf{Q}}_j^{a(0)}/\partial\omega$, in order to determine the matrices and vectors for a mistuned bladed disk using the derived expressions, (11) and (20).

The FRF matrix of a whole bladed disk cannot be determined directly by the dynamic stiffness matrix inverse $\tilde{\mathbf{A}}_j^{a(0)}=\mathbf{Z}(m_j\omega)^{-1}$ because of its prohibitively large size, and, therefore, a special method must be applied that allows an effective use of the sector model for a bladed disk. An effective method developed in Ref. [7] allows the tuned FRF matrix to be calculated exactly from the traveling wave FRF matrices calculated for one sector of the whole bladed disk. The exact expression for this matrix can be written in the following form for each m_jth harmonic:

$$\tilde{\mathbf{A}}_j^{a(0)}=\begin{bmatrix}\mathbf{H}_j^{(1)} & \mathbf{H}_j^{(2)} & \cdots & \mathbf{H}_j^{(N_B)}\\ & \mathbf{H}_j^{(1)} & \cdots & \mathbf{H}_j^{(N_B-1)}\\ & \mathrm{sym.} & \cdots & \cdots\\ & & \cdots & \mathbf{H}_j^{(1)}\end{bmatrix} \quad (22)$$

where

$$\mathbf{H}_j^{(k)}=\frac{1}{N_B}\sum_{m=-N_B/2}^{N_B/2}e^{-i\alpha m(k-1)}\mathbf{A}_m^S(m_j\omega);\quad (k=\overline{1,N_B}) \quad (23)$$

and N_B is the number of blades in the assembly, and $\alpha=2\pi/N_B$. $\mathbf{A}_m^S$ are the traveling wave FRF matrices corresponding to forward traveling (wave number $+m$) and backward traveling (wave number $-m$) waves of the engine order excitation. Because we intend to analyze a mistuned system, the traveling wave matrices for all wave numbers from $-N_B/2$ to $N_B/2$ are included in Eq. (23). The numbers of harmonics m_j selected for the multiharmonic expansion [see Eq. (2)] define here frequency values, $m_j\omega$, for which the traveling wave matrices are calculated. One can see that matrix $\tilde{\mathbf{A}}_j^{a(0)}$ is block circulant [i.e., its rows are formed by cyclic transposition of its one row formed from matri-

ces of much smaller size $\mathbf{H}_j^{(k)}$ $(k=\overline{1,N_B})$] and symmetric. The computational effort required for calculation of the FRF matrix is reduced significantly when these properties of the FRF matrix for a whole tuned disk are taken into account.

The traveling wave FRF matrices can, for example, be calculated through the complex natural modes of one sector:

$$\text{forward wave} \qquad \text{backward wave}$$
$$\mathbf{A}_m^S(\omega)=\sum_{r=1}^{n_r} c_r^m \phi_r^m (\overline{\phi}_r^m)^T; \quad \mathbf{A}_{-m}^S(\omega)=\sum_{r=1}^{n_r} c_r^m \overline{\phi}_r^m (\phi_r^m)^T \tag{24}$$

where $c_r^m=[(1+i\eta_r^m)(\omega_r^m)^2-\omega^2]^{-1}$; n_r is a number of modes used for the wave FRF matrix generation; ω_r^m and η_r^m are a natural frequency and the damping loss factor determined for the rth mode and mth wave number; ϕ_r^m are mass normalized complex mode shapes for the active DOFs; and a line over a symbol denotes the complex conjugation. In the strict sense, when the number of modes used for generation of the FRF matrix n_r is smaller than total number of DOFs in the sector, then Eq. (24) gives an approximate for the traveling wave FRF matrix. Our experience shows that a small fraction of the total number of possible modes used in Eq. (24) can provide, in many cases, the accuracy required in practical applications (see Ref. [7]).

One can see that the FRF matrix for the whole bladed disk, $\tilde{\mathbf{A}}_j^{a(0)}$, calculated for each of the multiharmonic components m_j $(j=0\ldots n)$, comprises all traveling wave matrices, $\mathbf{A}_m^S(\omega)$ $(m=-N/2\ldots N/2)$, possible for the bladed disk analysis.

Vector of amplitudes for a whole tuned bladed disk $\tilde{\mathbf{Q}}_j^{a(0)}$ are expressed through amplitudes of one sector $\mathbf{Q}_{jS}$ in the following form:

$$\tilde{\mathbf{Q}}_j^{a(0)}=\{\mathbf{Q}_{jS}, e^{i\alpha m_j}\mathbf{Q}_{jS}, \ldots, e^{i\alpha m_j(N_B-1)}\mathbf{Q}_{jS}\}^T \tag{25}$$

where $\mathbf{Q}_{jS}=\mathbf{A}_{m_j}^S(m_j\omega)\mathbf{P}_j^S$ is the vector of amplitudes of the first sector in the tuned bladed disk and $\mathbf{P}_j^S$ is the vector of excitation forces applied to this sector.

Expressions for the derivatives with respect to excitation frequency ω are obtained in a similar way. Thus, the derivatives for the traveling wave FRF matrices, introduced in Eq. (24), can be determined by the following expressions:

$$\text{forward wave} \qquad \text{backward wave}$$
$$\frac{\partial \mathbf{A}_m^S}{\partial\omega}=\sum_{r=1}^{n_r}\frac{\partial c_r^m}{\partial\omega}\phi_r^m(\overline{\phi}_r^m)^T; \quad \frac{\partial \mathbf{A}_{-m}^S}{\partial\omega}=\sum_{r=1}^{n_r}\frac{\partial c_r^m}{\partial\omega}\overline{\phi}_r^m(\phi_r^m)^T \tag{26}$$

where $\partial c_r^m/\partial\omega=2\omega[(1+i\eta_r^m)(\omega_r^m)^2-\omega^2]^{-2}$.

The derivative of the FRF matrix for the tuned whole bladed disk is expressed exactly through derivatives of the traveling wave FRF matrices in the form:

$$\frac{\partial \tilde{\mathbf{A}}_j^{a(0)}}{\partial\omega}=\begin{bmatrix} \partial\mathbf{H}_j^{(1)}/\partial\omega & \partial\mathbf{H}_j^{(2)}/\partial\omega & \cdots & \partial\mathbf{H}_j^{(N_B)}/\partial\omega \\ & \partial\mathbf{H}_j^{(1)}/\partial\omega & \cdots & \partial\mathbf{H}_j^{(N_B-1)}/\partial\omega \\ & \text{sym.} & \cdots & \cdots \\ & & \cdots & \partial\mathbf{H}_j^{(1)}/\partial\omega \end{bmatrix} \tag{27}$$

where

$$\frac{\partial\mathbf{H}_j^{(k)}}{\partial\omega}=\frac{m_j}{N_B}\sum_{m=-N_B/2}^{N_B/2} e^{-i\alpha m(k-1)}\frac{\partial\mathbf{A}_m^S(m_j\omega)}{\partial\omega} \tag{28}$$

And exact expression for the derivative of the vector of tuned forced response takes the form:

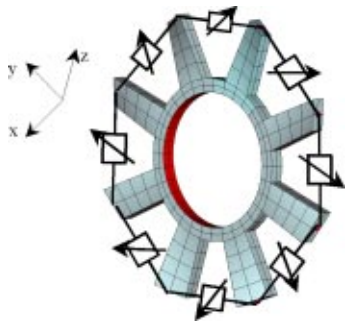

Fig. 2 A simplified model of the bladed disk

$$\frac{\partial\tilde{\mathbf{Q}}_j^{a(0)}}{\partial\omega}=\left\{\frac{\partial\mathbf{Q}_{jS}}{\partial\omega}, e^{i\alpha m_j}\frac{\partial\mathbf{Q}_{jS}}{\partial\omega}, \ldots, e^{i\alpha m_j(N_B-1)}\frac{\partial\mathbf{Q}_{jS}}{\partial\omega}\right\}^T \tag{29}$$

where, $\partial\mathbf{Q}_{jS}/\partial\omega=m_j[\partial\mathbf{A}_{m_j}^S(m_j\omega)/\partial\omega]\mathbf{P}_j^S$.

Numerical Results

The capability for calculating nonlinear forced responses for mistuned bladed disks has been added to the program code FORSE (FOrced Response SuitE) developed at Imperial College [16]. This code has been used for the investigation of a number of structures, including (i) a relatively simple model of a bladed disk used for verification purposes and for analysis of nonlinear mistuning effects, and (ii) a realistic high-pressure bladed turbine disk. Results of calculations obtained for these two systems are reported below.

Simplified Model of a Bladed Disk. A finite element model of a simplified bladed disk is shown in Fig. 2. The whole bladed disk consists of eight sectors and is modeled by hexahedral finite elements with a total number of degrees of freedom of 5760. Nonlinear interface elements are applied between adjacent blades at the middle nodes of the blade-tip faces, as illustrated in Fig. 2 by boxes with arrows. A gap-interface element was used to model the blade shroud contact when friction can be neglected, and the friction interface element was applied to model the friction forces between massless blade shrouds. Excitation by a first engine-order harmonic was considered and the damping loss factor was taken to be 0.003 (which is typical of values observed for some practical bladed disks). For the case of a tuned bladed disk, this model was used for verification by comparing results obtained by the method presented here and also by a method applying cyclic symmetry properties. Results from the comparison are identical and are reported in Refs. [17] and [22].

Examples of the influence of scatter in the characteristics of the nonlinear interface elements while the blades are perfectly tuned are shown for this bladed disk in Figs. 3 and 4. In these plots, the forced response for each blade of the bladed disk are plotted as a function of excitation frequency. Results for the tuned bladed disk with gaps 0.5 mm and for the mistuned bladed disk with random gap scatter within the range of -0.3–0.8 mm, are shown in Figs. 3(a) and 3(b), accordingly.

In Fig. 4 the forced response of the tuned bladed disk [Fig. 4(a)] with friction dampers is compared with two mistuned cases: (i) for a random scatter of the damper normal load values in the range of 1.2×10^5–2.5×10^5 N [Fig. 4(b)] and (ii) for a random scatter of the damper tangential stiffness coefficients in the range of 3.8×10^4–4.5×10^4 N/mm [Fig. 4(c)].

A significant scatter in blade amplitudes is evident in all the cases considered, although the blades themselves are tuned. It should also be noted that there is an appearance of multiple resonance peaks for the frequency range from 3.2 to 3.7 kHz in Fig. 3(b) and from 4 to 5 kHz in Fig. 4(b), which are absent for tuned systems.

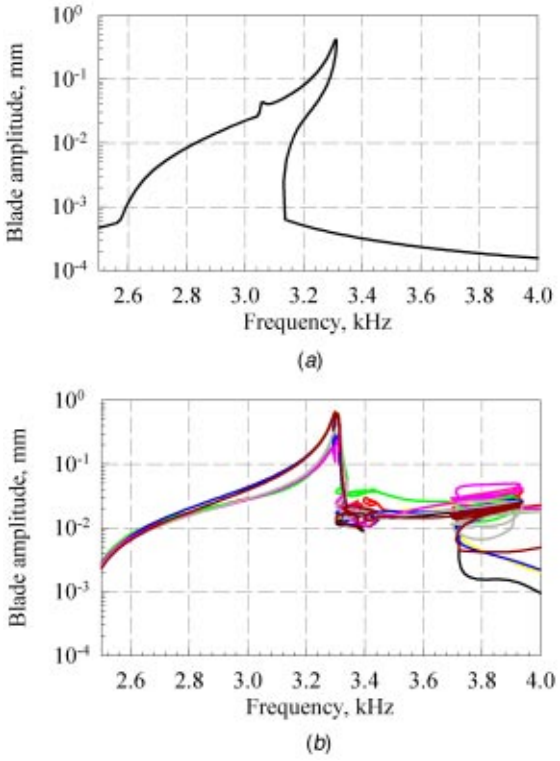

Fig. 3 Forced responses for all blades of the model with gap-type nonlinearity: (*a*) a tuned case, and (*b*) the structure is mistuned by gap alternation

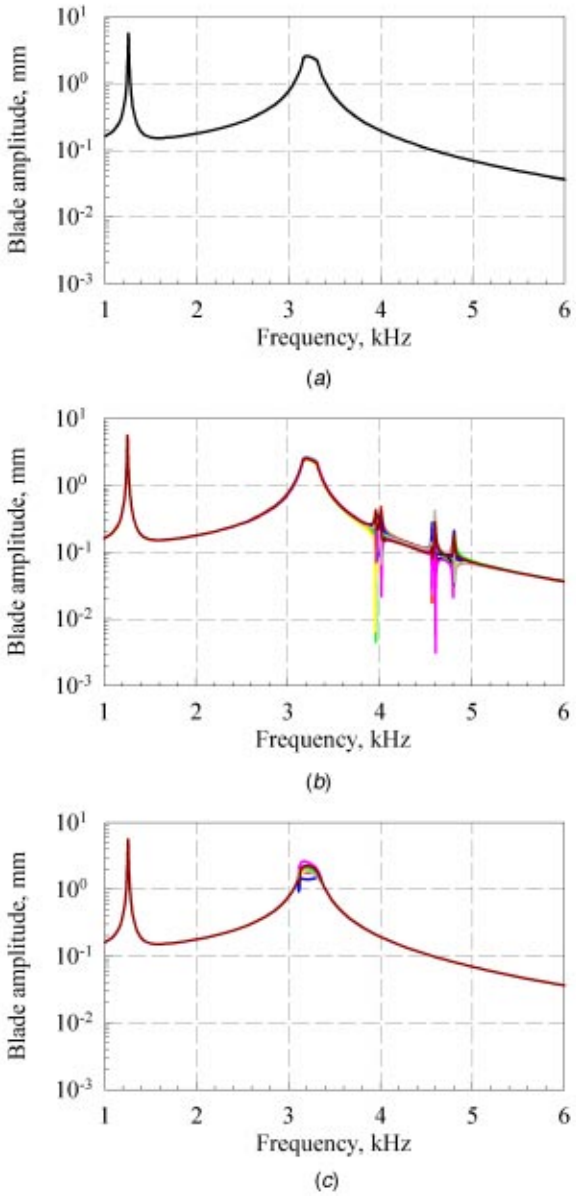

Fig. 4 Forced responses for all blades of the model with friction dampers: a tuned case (*a*), and cases of the structure mistuned by scatters of the friction dampers' stiffness (*b*) and normal load (*c*)

Large-Scale FE Model of a High-Pressure Bladed Turbine Disk. As an example of a practical application, a high-pressure turbine bladed disk is studied. The structure comprises 92 shrouded blades. A finite element model of a quarter of the bladed disk is shown in Fig. 1. The whole bladed disk FE model comprises more than 15 million DOFs. The linear damping loss factor is set in calculations to 0.003 and excitation by the 8th engine order is considered in the analysis. This model contains nonlinear interface elements and is subjected to action of nonlinear forces for all considered cases for which the forced response was calculated. Two types of nonlinear blade interaction are modeled: (i) underplatform dampers (UPD) [applied to a node marked by letter A in Fig. 1(c)] and (ii) shroud friction contacts [applied at a node marked by letter B in Fig. 1(b)]. The forced responses are calculated for a node located at the blade tip.

Mistuning by a Scatter of Parameters of Underplatform Dampers. Results of calculations for the realistic models for the bladed turbine disk, when underplatform dampers are applied between all neighboring blades, are shown in Figs. 5 and 6. Frequencies in these and other plots for the practical high-pressure bladed turbine disk are normalized by the first blade-alone natural frequency.

Two cases of mistuning for the UPD case are considered: i. a case where the UPD have a random scatter of $\pm 25\%$ of the nominal value for the normal load (Fig. 5); and ii. a case where the underplatform dampers have a $\pm 25\%$ scatter in tangential damper stiffness coefficients (Fig. 6). A frequency range including the first resonance, which corresponds to the first flap-wise (1F) mode, is examined. In the cases considered here, the blades are tuned and only the characteristics of the UPD are scattered. The forced response for all 92 blades of the mistuned bladed disk assembly is plotted by colored lines in these figures (color online). In Fig. 5(a), the forced responses of all blades of the mistuned bladed disk are compared with two extreme linear cases: i. a case without UPD, and ii. a case when all UPDs are always stuck, a situation which can happen when UPDs are too heavy so that they never slip. In Fig. 5(b), the forced responses of the mistuned bladed disk are plotted using a linear scale for amplitude so as to illustrate clearly the scatter in the amplitudes for the mistuned system. One can see a significant scatter in the peak amplitudes, but also significant differences in shape of the force response functions for different blades. To demonstrate this fact in Fig. 5(b), two extreme FRFs are also plotted for the blades specified there.

The differences in shapes of the FRFs for a bladed disk with UPDs allows the following important practical conclusion to be drawn. When damping loss factors are determined from experimentally measured blade FRFs, a significant scatter in their values can occur if the FRFs measured on different blades are used for determination of the damping loss factor. Because of that, when the forced response for only a few blades is measured in experi-

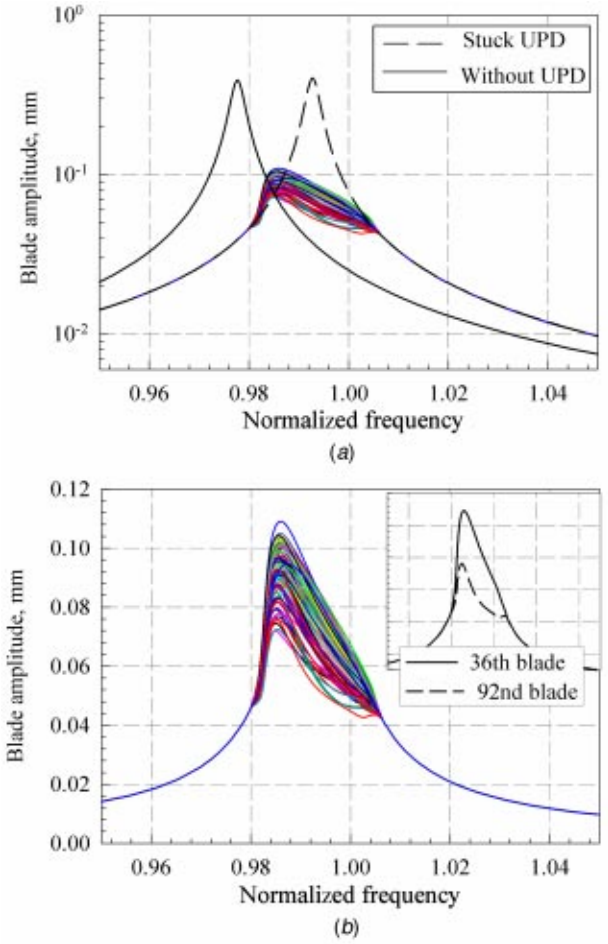

Fig. 5 Blade forced responses for the bladed turbine disk mistuned by the normal load at the UPD: (*a*) comparison with limiting linear case, and (*b*) scatter of blade FRFs

ments, there is not only a well-known danger to miss the blade with highest amplitude, but also to determine the damping loss factor incorrectly.

For the case of a bladed disk mistuned by the stiffness of the UPD, shown in Fig. 6, a significant scatter of the forced blade response levels occurs for excitation frequencies higher than the resonance frequency in the analyzed frequency range. This contrasts with the case of mistuning by the normal load variation where the maximum scatter is observed in the vicinity of the resonance frequency.

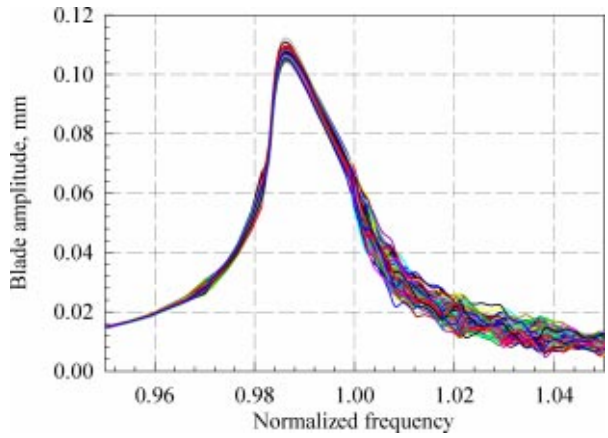

Fig. 6 Blade forced responses for the bladed turbine disk mistuned by stiffness of the UPD

Mistuning by a Scatter of Gaps Between Shrouds. The effects of scatter in the gaps between integral shrouds of the HP bladed turbine disk with tuned blades was considered by applying different gap values for the friction contact interface elements at different shroud contact surfaces. The friction contact interface elements allow not only tangential friction forces to be accounted for, but also the normal contact forces to be determined as a function of the relative displacements normal to the contact surface and of the normal stiffness coefficient of shroud contact surface, as defined in Ref. [15]. The friction forces are determined under an arbitrary variation of the normal force, including cases of separation-contact transition. Owing to this, the friction interaction of the shrouds with elastic impacts along a normal to the contact surfaces of the shrouds can be modeled. Gap values are randomly scattered in the range of 0.005–0.01 mm and are assumed to be constant over the frequency range analyzed. Normal forces emerge when the gaps are closed and the shrouds come into contact, otherwise they are equal to zero. Forced responses for all blades of the mistuned bladed disk are shown in Fig. 7(a) which illustrates a large scatter in blade amplitudes for a frequency range of 1.12–1.16. The envelope (i.e., maximum displacements found for each frequency over all blades of the assembly) of the forced response for the mistuned system is compared with the forced response of the tuned system in Fig. 7(*b*). For the tuned case, the forced response curve decreases abruptly its slopes in the vicinity of the normalized frequency 0.94 when the excitation frequency is increasing and in the vicinity of the normalized frequency 1.02, when the excitation frequency is decreasing. At these frequencies, vibration amplitudes become large enough to close clearances between shrouds and nonlinear interaction of the shrouds begins to affect resonance frequency and response levels. For the mistuned system, some shrouds come into contact at lower frequencies than for the tuned case because of scatter in the clearances. One can also see that the forced response curve for the mistuned bladed disk takes a much more complicated shape than that for the case of tuned system. The major reason for this is the multiple friction contacts and/or impacts between different shrouds of the mistuned assembly. Due to different gap values, these contacts occur at different times for different blades. The shapes of the FRFs and the presence of the unstable (and, hence, not usually realizable) solutions, indicates the possibility of chaotic motion for this system.

Amplification Factors Due to Scatters of u/p Dampers and Shroud Gaps. The effects of the mistuning due to scatter of the UPDs and the shroud gaps on amplification factors are demonstrated in Figs. 8 and 9. The amplification factor, also called normalized amplitudes, is defined as a ratio of the maximum amplitude of a mistuned bladed disk, found in the frequency range of interest, to the maximum amplitude of a tuned bladed disk. Distributions of the maximum normalized amplitudes found for each blade of the mistuned bladed disk in the frequency range comprising the first resonance frequency are shown in Fig. 8. Results for the bladed disks mistuned by normal loads at the underplatform dampers, and by gap values between blade integral shrouds, are compared here. Values of the maximum normalized amplitudes found over all blades of the assembly are shown in Fig. 9 for all scatter types of the friction contact characteristics analyzed above. In addition a maximum normalized response is plotted there for the bladed disk mistuned by blade natural frequencies. Twenty-five different mistuning patterns are randomly generated within a $\pm 5\%$ range of variation of the first blade natural frequency for the case of a bladed disk without UPDs and shroud contacts. One can see that, although effects of mistuning due to dampers and shroud gaps are significant, for the cases considered here they are significantly smaller than the effects due to blade frequency mistuning.

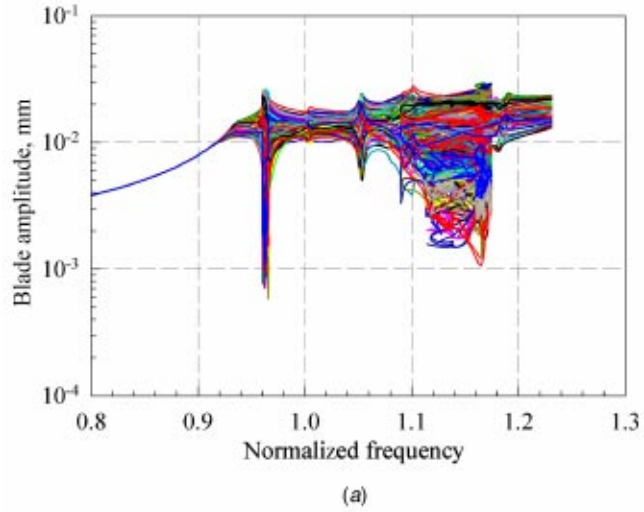

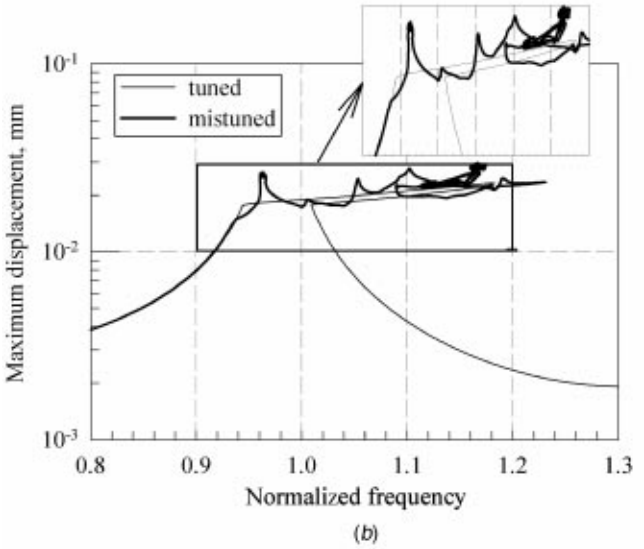

Fig. 7 Forced responses of the bladed turbine disk mistuned by shroud gaps: (*a*) FRFs for all blades, and (*b*) envelope of the FRFs and comparison with a tuned case

Bladed Disk With Tuned Shroud Interferences and Mistuned Blades. The effects of blade frequency mistuning on the forced response of bladed disks with nonlinear interfaces were also examined. An example of the nonlinear forced response of a bladed disk with frequency-mistuned blades and with small tuned shroud interferences identical for all blades is shown in Fig. 10. For comparison, the forced response levels are also shown in Fig. 10 by thin lines for two linear systems: (i) a case of tuned blades when shrouds do not come into contact due to large gaps and (ii) a case of tuned blades when shrouds are always in contact and stuck due to large interferences. One can see that for the tuned bladed disk with nonlinear shroud contacts, the resonance peak in the vicinity of the normalized frequency value of 1 is not excited. The forced response of this nonlinear tuned system is close to that of the linear system with full shroud contact over a large frequency range. Differences in the FRFs of the tuned linear and nonlinear systems occur only in the vicinity of the resonance of a frequency of 1.6 when the vibration amplitudes become large enough to cause partial separation of the shrouds. For the case of a bladed disk mistuned by blade frequencies, one can see that the forced response is radically different from that of the tuned system. This happens due to the fact that for the mistuned bladed disk, multiple resonance peaks appear at the lower bound of the considered frequency range, and, hence, the significant level of

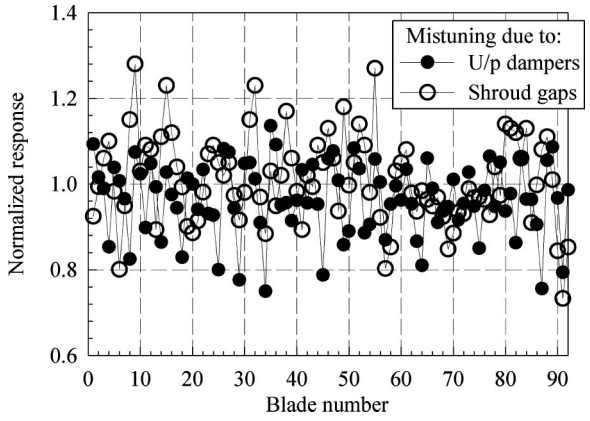

Fig. 8 Maximum normalized amplitudes for each of the blades found over the first resonance frequency range

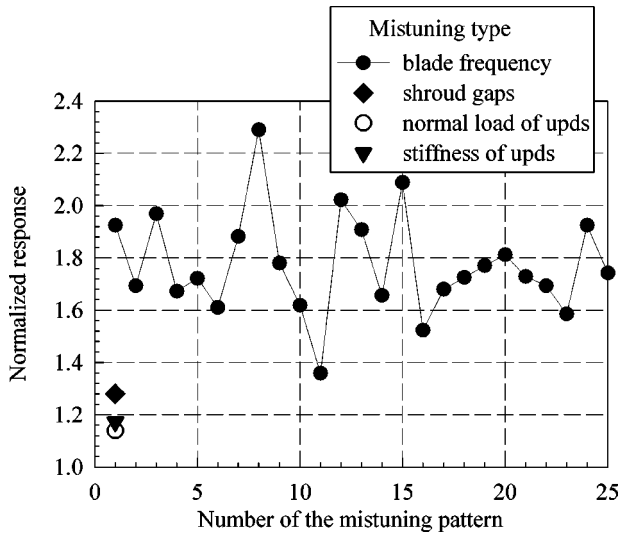

Fig. 9 Maximum amplification factors for different kinds of blade and interface mistuning

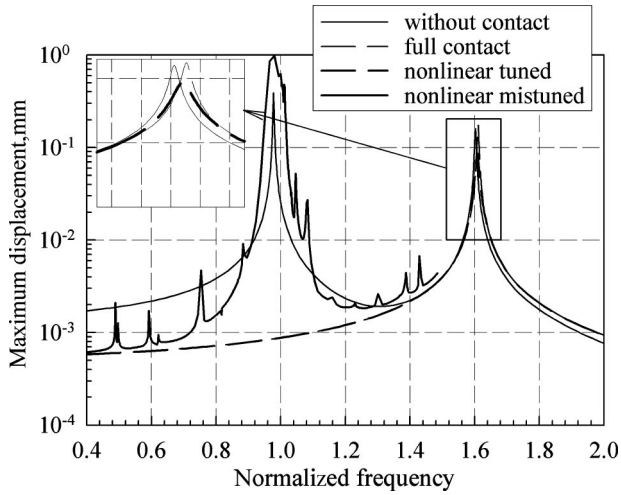

Fig. 10 Envelope of the maximum response levels of the bladed disk with frequency-mistuned blades and shroud contacts compared with the tuned responses

amplitudes causes partial separation of shrouds. The partial shroud separation at lower excitation frequencies leads to occurrence of a new major resonance peak in the vicinity of the normalized frequency value of 1, which could not be excited for the tuned system.

Conclusions

An efficient method for the analysis of nonlinear vibrations of mistuned bladed disk assemblies has been developed. The development provides a capability for the analysis of practical bladed disk using large-scale finite element models that could be used hitherto only in the analysis of linear vibrations. The method is based on the developed techniques for an exact condensation of the nonlinear finite element model of a mistuned bladed disk that reduces the size of the nonlinear equations to the number of degrees of freedom at which nonlinear interaction forces are applied.

Analysis of nonlinear forced response for simplified and realistic models of mistuned bladed disks has been performed using the new method. For a practical high-pressure bladed turbine disk, several types of nonlinear forced response were considered, including cases of mistuning by (i) underplatform damper scatter, (ii) shroud gap scatter, and (iii) blade frequencies in the presence of nonlinear shroud interactions. The effects of magnification of vibration amplitudes caused by scatter of the characteristics of underplatform dampers and shroud gaps when blades are tuned have been proved and quantified.

The magnification factors for cases of tuned blades with mistuned friction interfaces for studied systems were significantly smaller than those of a bladed disk with mistuned blades and tuned friction interfaces. For mistuned bladed disk with friction interfaces accounting for nonlinear character of interaction, forces can produce radically different forced response characteristics as compared with a tuned case.

Acknowledgment

The authors are grateful to Rolls-Royce plc. for providing the financial support for this project and for giving permission to publish this work.

References

[1] Whitehead, D. S., 1966, ''Effect of Mistuning on the Vibration of Turbomachines Induced by Wakes,'' J. Mich. Eng. , **8**(1), pp. 15–21.
[2] Dye, R. C. F., and Henry, T. A., 1969, ''Vibration Amplitudes of Compressor Blades Resulting From Scatter in Blade Natural Frequencies,'' ASME J. Eng. Power, **91**, pp. 182–188.
[3] Ewins, D. J., 1969, ''Effect of Detuning Upon the Forced Vibration of Bladed Discs,'' J. Sound Vib., **9**(1), pp. 65–79.
[4] Ewins, D. J., 1991, ''The Effects of Blade Mistuning on Vibration Response—A Survey,'' *IFToMM 4th International Conference on Rotordynamics*, Prague, Czechoslovakia.
[5] Slater, J. C., Minkiewicz, G. R., and Blair, A. J., 1999, ''Forced Response of Bladed Disk Assemblies—A Survey,'' Shock Vib. Dig., **31**(1), pp. 17–24.
[6] Yang, M.-T., and Griffin, J. H., 2001, ''A Reduced-Order Model of Mistuning Using a Subset of Nominal System Modes,'' ASME J. Eng. Gas Turbines Power, **123**, pp. 893–900.
[7] Petrov, E. P., Sanliturk, K. Y., and Ewins, D. J., 2002, ''A New Method for Dynamic Analysis of Mistuned Bladed Disks Based on the Exact Relationship Between Tuned and Mistuned Systems,'' ASME J. Eng. Gas Turbines Power, **122**(3), pp. 586–597.
[8] Bladh, R., and Pierre, C., 2002, ''Dynamic Response Predictions for a Mistuned Industrial Turbomachinery Rotor Using Reduced-Order Modeling,'' ASME J. Eng. Gas Turbines Power, **124**, pp. 311–324.
[9] Moyroud, F., Fransson, T., and Jacquet-Richardet, G., 2002, ''A Comparison of Two Finite Element Reduction Techniques for Mistuned Bladed Disks,'' ASME J. Eng. Gas Turbines Power, **124**, pp. 942–952.
[10] Feiner, D. M., and Griffin, J. H., 2002, ''A Fundamental Model of Mistuning for a Single Family of Modes,'' ASME J. Turbomach., **124**, pp. 597–605.
[11] Sanliturk, K. Y., Imregun, M., and Ewins, D. J., 1997, ''Harmonic Balance Vibration Analysis of Turbine Blades With Friction Dampers,'' ASME J. Vibr. Acoust., **119**, pp. 96–103.
[12] Berthillier, M., Dupont, C., Mondal, R., and Barrau, R. R., 1998, ''Blades Forced Response Analysis With Friction Dampers,'' ASME J. Vibr. Acoust., **120**, pp. 468–474.
[13] Chen, J. J., and Menq, C. H., 1999, ''Prediction of Periodic Response of Blades Having 3D Nonlinear Shroud Constraints,'' ASME Paper No. 99-GT-289.
[14] Szwedowicz, J., Sextro, W., Visser, R., and Masserey, P., 2003, ''On Forced Vibration of Shrouded Turbine Blades,'' ASME Paper No. GT-2003-38808.
[15] Petrov, E., and Ewins, D., 2003, ''Analytical Formulation of Friction Interface Elements for Analysis of Nonlinear Multi-Harmonic Vibrations of Bladed Discs,'' ASME J. Turbomach., **125**, pp. 364–371.
[16] Petrov, E., and Ewins, D., 2002, ''Analysis of Nonlinear Multiharmonic Vibrations of Bladed Discs With Friction and Impact Dampers,'' *Proc. 7th National Turbine Engine HCF Conference*, May 14–17, 2002, Palm Beach Gardens, Florida, 11p.
[17] Petrov, E. P., 2003, ''A Method for Use of Cyclic Symmetry Properties in Analysis of Nonlinear Multiharmonic Vibrations of Bladed Discs,'' *Proc. of ASME Turbo Expo 2003*, June, Atlanta, ASME, New York, ASME Paper No. GT-2003-38480.
[18] Sherman, J., and Morrison, W. J., 1949, ''Adjustment of an Inverse Matrix Corresponding to Changes in the Elements of a Given Column or a Given Row of the Original Matrix,'' Ann. Math. Stat., **20**, p. 621.
[19] Woodbury, M., 1950, ''Inverting Modified Matrices,'' Memorandum Report 42, Statistical Research Group, Princeton University, Princeton, NJ.
[20] Crisfield, M., 1981, ''A Fast Incremental/Iterative Solution Procedure That Handles Snap-Through,'' Comput. Struct., **13**, pp. 55–62.
[21] Cardona, A., Lerusse, A., and Geradin, M., 1998, ''Fast Fourier Nonlinear Vibration Analysis,'' Comput. Mech., **22**, pp. 128–142.
[22] Petrov, E., and Ewins, D., 2003, ''Analysis of Forced Response for Nonlinear Vibration of Mistuned Bladed Discs,'' *Proc. 8th National Turbine Engine HCF Conference*, April 14–16, 2003, Monterey, CA.

Performance Degradation due to Blade Surface Roughness in a Single-Stage Axial Turbine

Yong Il Yun
School of Mechanical and Aerospace Engineering,
Seoul National University,
Seoul 151-742, Korea
e-mail: yyoon1@snu.ac.kr

Il Young Park
Turbomachinery R&D Center,
Samsung Techwin,
Changwon 641-717, Korea
e-mail: ilyoung10.park@samsung.com

Seung Jin Song
School of Mechanical and Aerospace Engineering,
Seoul National University,
Seoul 151-742, Korea
e-mail: sjsong@snu.ac.kr

Turbine blades experience significant surface degradation with service. Previous studies indicate that an order-of-magnitude or greater increase in roughness height is typical, and these elevated levels of surface roughness significantly influence turbine efficiency and heat transfer. This paper presents measurement and a mean-line analysis of turbine efficiency reduction due to blade surface roughness. Performance tests have been conducted in a low-speed, single-stage, axial flow turbine with roughened blades. Sheets of sandpaper with equivalent sandgrain roughnesses of 106 and 400 μm have been used to roughen the blades. The roughness heights correspond to foreign deposits on real turbine blades measured by Bons et al. [1]. In the transitionally rough regime (106 μm), normalized efficiency decreases by approximately 4% with either roughened stator or roughened rotor and by 8% with roughness on both the stator and rotor blades. In the fully rough regime (400 μm), normalized efficiency decreases by 2% with roughness on the pressure side and by 6% with roughness on the suction side. Also, the normalized efficiency decreases by 11% with roughness only on stator vanes, 8% with roughness only on rotor blades, and 19% with roughness on both the stator and rotor blades.
[DOI: 10.1115/1.1811097]

Introduction

Turbine blades experience surface degradation with use, and an order-of-magnitude or greater increase in root-mean-square (rms) roughness is typical for the first stage vanes in high-pressure turbines [1–3]. Much effort has been expended to characterize the randomly distributed nature of turbine blade surface roughness and to translate their characterization into more convenient, deterministic forms (e.g., distributed cylinders, hemispherical segments, and equivalent sandgrain roughness). Taylor [2] used a stylus profilometer to measure the first-stage turbine blade roughness from two military engines. He measured several statistical quantities, such as rms, skewness, and kurtosis of the roughness height distribution, and found great variation from point to point on the blade. Bogard et al. [3] made profilometer measurements of two sample turbine vanes from military engines. Bons et al. [1] made measurements, including the centerline averaged roughness R_a, maximum peak-to-valley roughness R_t, and roughness shape/density parameter Λ_s, in many different turbines. Bons et al. [1] also categorized turbine blade surface roughnesses according to their causes—foreign deposits, pitting/erosion, and thermal barrier coating spallation. Each roughness-producing mechanism produced unique surface textures. For example, pitting and spallation had large roughness recesses below the surface mean line while deposits were characterized by peaks above the mean line.

However, since two surfaces with the same roughness height can have different aerodynamic characteristics, roughness height alone is insufficient to characterize surface roughness. Sigal and Danberg [4] have indicated that equivalent sandgrain roughness is sensitive to not only the shape, but also spacing of roughness elements. Therefore, they measured roughness shape/density parameter Λ_s as well as actual roughness k, and correlated them with equivalent sandgrain roughness k_s. Bogard et al. [3] estimated equivalent sandgrain roughness height for their measured vane surface roughness by using Sigal and Danberg's correlation. Also, to convert roughness k into equivalent sandgrain roughness k_s, Bons [5] measured c_f values for scaled replicas of ''real'' turbine surface roughness k in a wind tunnel. Then, he used Sigal and Danberg's correlation to calculate equivalent sandgrain roughness k_s, which corresponded to the measured surface roughness k and roughness shape/density parameter Λ_s. Finally, he used Schlichting's [6] correlation [Eq. (5)] to calculate c_f as a function of k_s and found good agreement between the measured and calculated c_f values in the fully rough regime. Thus, k_s was found to be an appropriate parameter for c_f prediction of ''real'' rough surfaces, and this conclusion justified previous studies that used uniform emery grains [7,8] and sand grains [9] to simulate rough surfaces in cascades and turbines. Bons [5] also attempted correlations of a number of roughness parameters and recommended a modified form of Sigal and Danberg's correlation.

Studies have been conducted to measure performance penalty due to surface roughness in turbines. Bammert and Sandstede [8] measured boundary layer parameters (momentum and displacement thicknesses) and static pressure distribution on vane surfaces in a cascade. Roughness on the blade surface caused a premature transition from laminar to turbulent boundary layers, and the roughness on the suction side increased momentum thickness two or three times more than that on the pressure side. Kind et al. [9] measured profile loss and deviation angle for flows through roughened cascade vanes. The blade-loading and deviation angle were not sensitive to surface roughness. The profile loss increased drastically due to the suction-side roughness while there was not much change due to the pressure-side roughness, reconfirming the results of Bammert and Sandstede [8]. Boyle and Senyitko [10] measured total pressure loss in a linear cascade for a wide range of Reynolds number values and proposed a roughness transition model to match their experimental results. Bammert and Sanstede [7] found that efficiency decreased by up to 14% in a four-stage turbine with all blades uniformly roughened with 580 μm emery grains. Boynton et al. [11] found that a decrease in rotor blade surface roughness from 10.16 μm (rough) to 0.76 μm (polished) increased total-to-total efficiency by 2.4% in a double-stage high-pressure fuel turbopump turbine.

Contributed by the International Gas Turbine Institute (IGTI) of THE AMERICAN SOCIETY OF MECHANICAL ENGINEERS for publication in the ASME JOURNAL OF TURBOMACHINERY. Paper presented at the international Gas Turbine and Aeroengine Congress and Exhibition, Vienna, Austria, June 13–17, 2004, Paper No. 2004-GT-53094. Manuscript received by the IGTI October 1, 2003; final revision March 1, 2004. IGTI Review Chair: A. J. Strazisar.

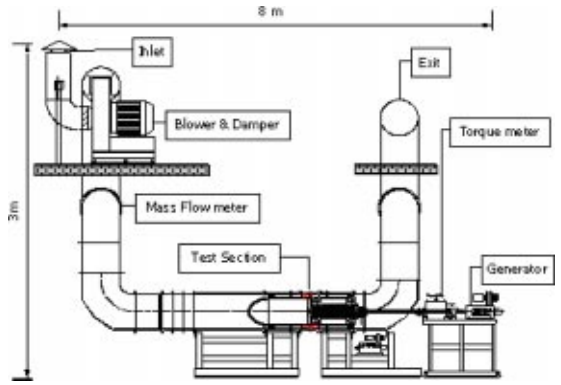

Fig. 1 Schematic of the test turbine rig

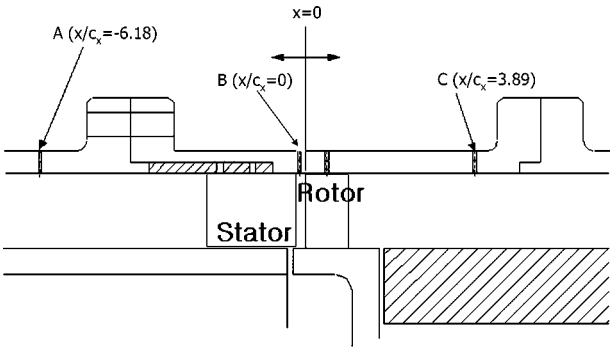

Fig. 2 Axial locations of instrumentation

Nevertheless, the influence of roughness corresponding to the ''real'' roughness [1] on turbine performance has not yet been investigated. In addition, the effects of surface roughness location on performance in rotating turbine rigs have not yet been studied. To the authors' knowledge, only the cascade experiments performed by Bammert and Sandstede [8] and Kind et al. [9] explored suction-pressure side differentiation. Therefore, this study has been conducted to measure, for the first time, the relative influence of surface roughness location—suction side versus pressure side and stator versus rotor—on turbine performance in a rotating environment.

Specifically, this paper addresses the following questions.

- How does equivalent sandgrain roughness k_s corresponding to the ''real'' blade surface roughness affect turbine performance?
- What are the relative effects of suction- and pressure-side roughness in a rotating environment?
- Is turbine performance more sensitive to stator roughness or rotor roughness?

Experimental Facility

Flow Loop. The open-loop experimental facility consists of a blower, flow conditioning section, test section, and exit. The overall view of the turbine rig is shown in Fig. 1. A 75 kW main blower provides a mass flow rate of 3.1 kg/s to the test section. Upstream of the test section, the flow passes through a mass flow meter and a flow conditioning section (honeycomb and screens) before entering the test section.

Instrumentation. Mass flow rate is determined upstream of the turbine from the pressure difference between upstream and downstream of a bank of nine calibrated venturi nozzles using pressure transducers with an accuracy of $\pm 0.25\%$ of the full scale values. The overall accuracy of the mass flow meter is $\pm 1\%$ of the measured value. The axial locations of aerodynamic instrumentation stations are shown in Fig. 2. The axial distance x is measured from the rotor leading edge and is positive in the downstream direction. The distances are normalized by the axial chord length of the rotor blade c_x. Five static-pressure taps at Station A ($x/c_x = -6.18$), another six at Station B ($x/c_x = 0$), and another six at Station C (located at $x/c_x = 3.89$) are located circumferentially to measure static wall pressure. Thermocouple-embedded pitot tubes are located at the mean radii of Stations A and B to measure total temperature and total pressure at the stage inlet and exit. The average inlet total pressure is estimated by adding average dynamic head to the averaged inlet static pressure. For static pressure data, a differential pressure transducer with an accuracy of $\pm 0.25\%$ of the full scale values is used. Torque is measured with a strain-gauge-type torque meter with an accuracy of $\pm 0.1\%$ of the measured torque. The pressure transducer signals are digitized by an A/D converter and transferred to a PC. Torque and temperature data are stored directly onto the PC via a data acquisition unit.

Test Turbine. The test turbine geometry is given in Table 1. The maximum rotating speed is 1600 rpm, and the maximum shaft power is 15 kW. The degree of reaction of this turbine is approximately 30%. At the design point, the inlet flow velocity is 20 m/s and the Reynolds number is 2.0×10^5 based on rotor chord length and relative exit velocity.

Surface Preparation. Several types of turbine blade surface roughness (e.g., foreign deposits, pitting/erosion) can be represented by equivalent sandgrain roughness k_s. However, foreign deposits affect flow in two ways—first, by increasing surface roughness and second, by reducing the blade passage area. On the other hand, pitting/erosion increases surface roughness only. This study's scope is limited to the effects of foreign deposits because foreign deposits are known to be more important in determining turbine efficiency [1]. For current investigation, the surface data corresponding to foreign deposits on the suction side, midspan, and leading edge part have been chosen (Table 2).

''Real'' roughness height cannot be directly matched with densely distributed equivalent sandgrain roughness. Previous studies have used a vague concept of the ratio of sand grain size to chord length to determine the roughness height (e.g., [7]). However, same roughness has different effects in machines operating at different Reynolds numbers. Therefore, the absolute value of roughness height alone is insufficient.

To overcome this problem, Bons [5] recommended the following correlation to estimate equivalent sandgrain roughness, taking into account the spacing of roughness elements.

Table 1 Test turbine geometry

Parameter	Stator		Rotor
Axial chord (mm)	96.01		41.04
Hub diameter (mm)		560.0	
Tip diameter (mm)		700.0	
Number of vanes/blades	38		70
Tip clearance (mm)		1.4	
Annulus area (m^2)		0.136	
Solidity	1.87		1.53
Inlet angle (deg)	0		62.3
Exit angle (deg)	77.3		74.6

Table 2 Representative turbine blade surface data (Bons et al. [1])

Region	Process	R_a (μm)	R_t (μm)	Λ_s
SS/MS/LE	Foreign deposits	14.1	168	45

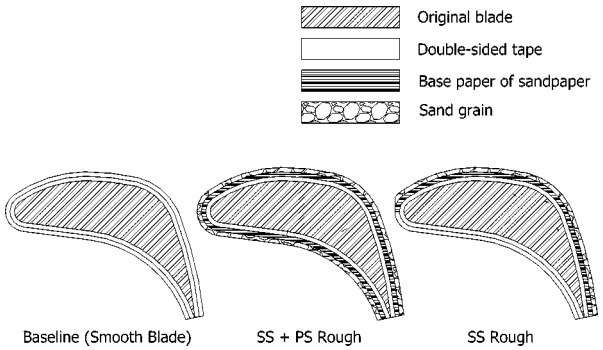

Fig. 3 Blade roughening process

Fig. 4 Roughened test turbine blade set

$$\log\frac{k_s}{k} = -0.43\log\Lambda_s + 0.82 \tag{1}$$

where, according to Sigal and Danberg [4],

$$\Lambda_s = \frac{S}{S_f}\left(\frac{A_f}{A_s}\right)^{-1.6} \tag{2}$$

The average roughness height, k in Eq. (1), is commonly estimated to be R_z, or the average of the local R_t values over the entire map [5]. According to Bons [5], R_z is approximately five times the centerline average roughness R_a. Therefore, for the case in Table 2,

$$R_z = k = 70.5\ \ \mu\text{m} \tag{3}$$

Substituting $k = 70.5\ \mu$m and $\Lambda_s = 45$ into Eq. (1), $k_s = 90.64\ \mu$m for the Bons et al. [1] case. This value is based on the blade Reynolds number Re_c of 2.0×10^6 [5], a typical value for high-pressure turbine vanes and/or blades [12]. At this Reynolds number, the roughness Reynolds number k^+ can be determined as,

$$k^+ = \text{Re}_c\frac{k_s}{c}\sqrt{\frac{c_f}{2}} = 149.2 \tag{4}$$

$$\text{where}\ \ c_f = \left[2.87 + 1.58\log\frac{c}{k_s}\right]^{-2.5}\ \ (\text{Ref. [6]}) \tag{5}$$

The chord length c is inferred to be 70 mm from the Bons [5] data. According to Nikuradse [13], $k^+ = 149.2$ is sufficiently large to be in the fully rough regime ($k^+ > 70$).

For the test facility used in this study, the blade Reynolds number is 2.0×10^5 and the true chord length of rotor blades is 60 mm. Therefore, to match $k^+ = 149.2$, the equivalent sandgrain roughness height for the fully rough test case is determined to be $k_s = 400\ \mu$m. For intermediate levels of roughness ($5 < k^+ < 70$), $k^+ = 30$ has been selected. Assuming that Eq. (5) is valid in the transitionally rough regime as well, the corresponding k_s is 106 μm.

To roughen the blades, sheets of sandpaper are attached to blade surfaces. The sandpaper is composed of 500 μm thick base paper and sand grits glued to the base paper. The effects of surface roughness have been isolated as follows. For the baseline case, the blades are wrapped with two sheets of double-sided tape with each sheet having the same thickness as the base paper of the sandpaper (Fig. 3). For rough blades, only one sheet of double-sided tape is attached to the blades, and sandpaper is attached to the double-sided tape. For roughness only on the suction side, one sheet of double-sided tape is attached to the blades, sandpaper is attached to the tape on the suction side, and another layer of double-sided tape is added on the pressure side. The roughness

Table 3 Test matrix

Baseline		Stator SS	Stator PS	Rotor SS	Rotor PS
		Smooth	Smooth	Smooth	Smooth
Fully rough	Stator SS	Fully rough	Smooth	Smooth	Smooth
	Stator PS	Smooth	Fully rough	Smooth	Smooth
	Stator	Fully rough	Fully rough	Smooth	Smooth
	Rotor	Smooth	Smooth	Fully rough	Fully rough
	Stator & Rotor	Fully rough	Fully rough	Fully rough	Fully rough
Transitionally rough	Stator	Transitionally rough	Transitionally rough	Smooth	Smooth
	Rotor	Smooth	Smooth	Transitionally rough	Transitionally rough
	Stator & Rotor	Transitionally rough	Transitionally rough	Transitionally rough	Transitionally rough

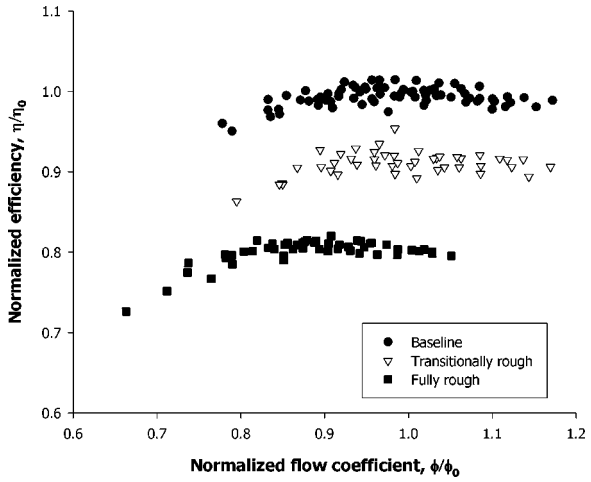

Fig. 5 Normalized efficiency degradation with transitional and full roughnesses

starts from the design stagnation point of the smooth blade. Thus, foreign deposit effects are introduced, and a roughened blade row is shown in Fig. 4.

Table 3 shows the test matrix to differentiate the effects of transitional ($k_s = 106\ \mu$m) and full ($k_s = 400\ \mu$m) roughnesses. The stator has been chosen for suction-pressure side differentiation because the roughened stator causes more performance penalty than the roughened rotor.

Experimental Results and Discussion

To evaluate surface roughness effects on turbine performance, total-to-static efficiency η_{ts} has been measured at different values of flow coefficient ϕ. The two parameters are defined as

$$\eta_{ts} = \frac{Q\omega}{\dot{m}c_p T_{t1}(1-(P_{s3}/P_{t1})^{\gamma-1/\gamma})} \tag{6}$$

$$\phi = \frac{v_{x1}}{U} \tag{7}$$

Repeatability tests have been conducted for each flow coefficient, and efficiency has been found to be repeatable to within 1%. This variation is less than the 1.4% uncertainty (95% confidence interval) in η_{ts} estimated according to the method of Kline and McClintock [14]. The turbine performance is represented by normalized efficiency η/η_0 plotted versus normalized flow coefficient ϕ/ϕ_0, where η_0 and ϕ_0 are the design efficiency and design flow coefficient of the baseline case, respectively.

Figure 5 shows the plots of normalized efficiency versus flow coefficient for the baseline, transitionally rough, and fully rough cases. As expected, blade surface roughness significantly degrades turbine efficiency. The normalized total-to-static efficiency decreases by 8% when both the stator and rotor blade rows are roughened with sandpaper of $k_s = 106\ \mu$m and by 19% with sandpaper of $k_s = 400\ \mu$m. Thus, there is more of an efficiency penalty with larger equivalent sandgrain roughness k_s. Furthermore, the flow coefficient corresponding to maximum efficiency decreases with increasing roughness.

Previously, Bammert and Sandstede [7] made measurements in a four-stage turbine with all blades uniformly roughened with the same size emery grains. Their Reynolds number based on the blade chord and exit velocity varied between 3.5×10^5 and 6.0×10^5, compared to 2.0×10^5 in the current study. Therefore, according to Eqs. (4) and (5), $k_s = 106\ \mu$m in the current study corresponds to $k_s = 60\ \mu$m in Bammert and Sandstede's turbine. As listed in Table 4, the new test results are comparable to those of

Table 4 Current test results compared with data from Bammert and Sandstede [7]

	k_s (μm)	k^+	η/η_0
Current	106	30	0.92
study	400	149	0.81
Bammert &	60	22~37	0.925
Sanstede	420	193~331	0.849

Bammert and Sandstede [7]. Differences may be due to multistage effects, which are absent in the current study.

Figure 6 shows the results of stator suction side-pressure side differentiation in the fully rough regime. The normalized efficiency decreases by 2% when the stator's pressure side is roughened and by 6% when the stator's suction side is roughened. Thus, turbine performance is more sensitive to roughness on the stator suction side than that on the stator pressure side. This result is similar to the trend found in cascades by Bammert and Sandstede [8] and Kind et al. [9]. They also found that the roughened suction side losses were about three times as large as those due to roughened pressure side.

Figure 7 shows stator-rotor differentiation results in the transitionally rough regime. The normalized efficiency decreases by approximately 4% with either roughened stator or roughened ro-

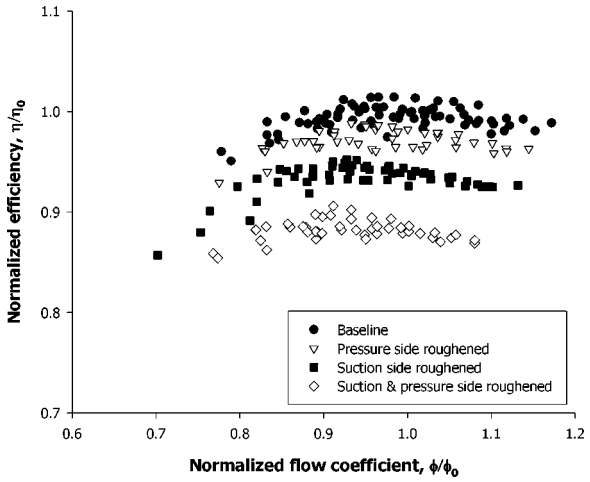

Fig. 6 Suction side-pressure side differentiation with fully roughened stator ($k_s = 400\ \mu$m)

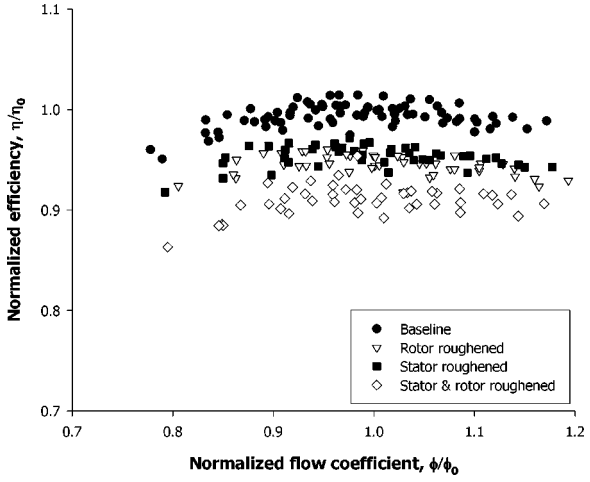

Fig. 7 Stator-rotor differentiation with transitional roughness ($k_s = 106\ \mu$m)

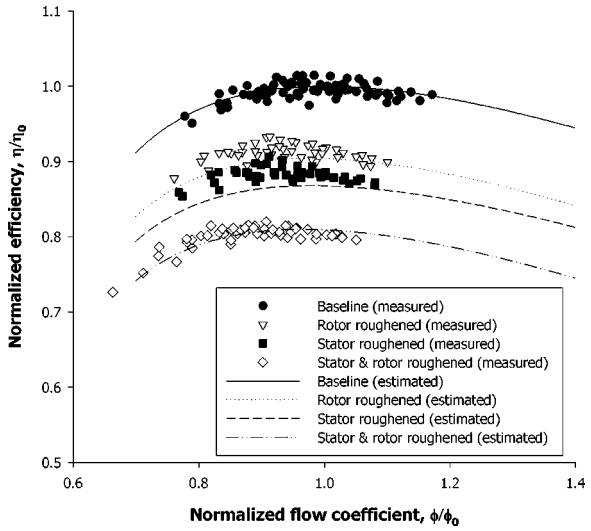

Fig. 8 Stator-rotor differentiation with full roughness ($k_s = 400\ \mu$m)

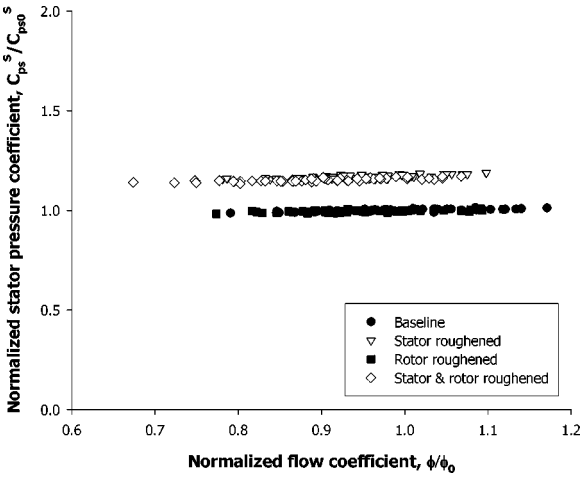

Fig. 9 Measured stator pressure coefficient

tor, and 8% with roughness on both the stator and rotor. In this case, the relative influence of stator or rotor roughness cannot be resolved because the data in both cases are within each other's uncertainty range.

However, similar data with full roughness clarify this issue. Figure 8 shows stator-rotor differentiation results in the fully rough regime ($k_s = 400\ \mu$m). The normalized efficiency decreases by 11% when stator is roughened and by 8% when rotor is roughened. When both are roughened, the efficiency decreases by 19%. Thus, compared to rotor roughness, stator roughness results in an additional 3% efficiency deterioration. This is significant because the stator of the first stage of turbines may be the most vulnerable to surface degradations. Also, the efficiency drop with a roughened stator added to the drop with a roughened rotor is approximately equivalent to the efficiency drop with both rows roughened. Furthermore, the decrease in flow coefficient corresponding to maximum efficiency also occurs here as each row is roughened.

Recently, Boynton et al. [11] measured total-to-total efficiency in a double-stage turbine. Their Reynolds number was 1.5×10^6, and they found that the total-to-total efficiency decreased by 2.4% when rotor roughness was increased from 0.76 μm rms to 10.16 μm rms. In the current study, total-to-static efficiency decreased by 4% and 8% with transitionally rough and fully rough rotor blades, respectively (Table 5). The difference can be due to several reasons. First, Boynton et al. measured total-to-total efficiency versus the total-to-static efficiency measured in the current study. Second, Boynton et al. did not report roughness shape/density parameter. Therefore, k_s and k^+ have been estimated for the Boynton et al. turbine in Table 5 by using a possible range of roughness shape/density parameter values from the Bons et al. [1] measurements. Third, multistage effects are absent in the current study. Therefore, a direct comparison is difficult.

The efficiency degradation and decrease in flow coefficient corresponding to maximum efficiency due to blade surface roughness can be explained through a mean-line analysis as follows. Figure 9 shows time-averaged stator pressure coefficient (the ratio of static pressure drop across the stator and the stator inlet dynamic head $0.5\rho v_{x1}^2$) normalized by its value at the design point of the baseline case. These results have been obtained from the casing static pressure data. The stator pressure coefficient shows a negligible change due to roughness on the rotor blades. However, roughness on the stator vanes increases the stator pressure coefficient. Based on the velocity triangles in Fig. 10, the following equation can be obtained for the stator:

$$P_{s1} + \tfrac{1}{2}\rho v_{x1}^2 = P_{s2} + \tfrac{1}{2}\rho v_2^2 + \Delta P_t^S \tag{8}$$

Here, ΔP_t^S is the total pressure loss across the stator, and because the current focus is on *steady* flow properties, total pressure change indicates loss. Equation (8) can then be nondimensionalized as follows:

$$C_{ps}^S = \frac{P_{s1} - P_{s2}}{\frac{1}{2}\rho v_{x1}^2} = \frac{1}{\cos^2 \alpha_2} - 1 + \zeta^S \tag{9}$$

Kind et al. [9] have already shown that roughness does not significantly alter flow angles. Thus, the first two terms on the right-hand side of Eq. (9) remain constant, and, consequently, the increase in stator pressure coefficient due to stator roughness (Fig. 9) must result from the increase in stator total pressure loss. Furthermore, Figure 11 shows graphs of estimated stator loss coefficient ζ^S, using Eq. (9) and the data from Fig. 9. Here, the stator loss coefficient is clearly independent of flow coefficient.

Figure 12 shows graphs of rotor pressure coefficient (the ratio of static pressure drop across the rotor and the stator inlet dynamic

Table 5 Current test results compared with data from Boynton et al. [11]

		k_s (μm)	k^+	η/η_0
Rotor roughened	Current study	106	30	0.96
		400	149	0.92
	Boynton et al.	13~72	40~280	0.976

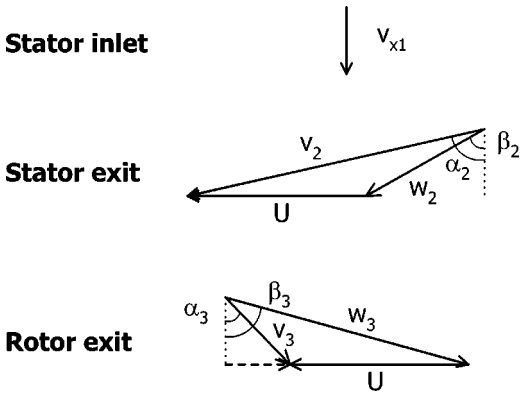

Fig. 10 Stage velocity triangles

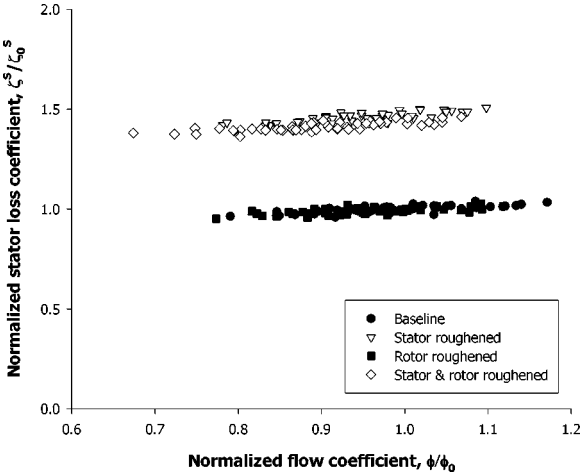

Fig. 11 Estimated stator loss coefficient

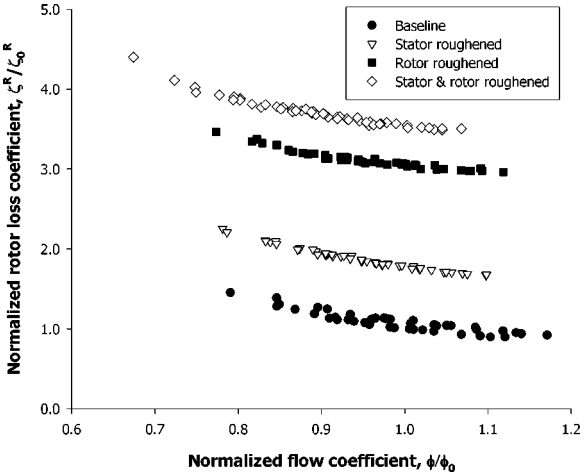

Fig. 13 Estimated rotor loss coefficient

head $0.5\rho v_{x1}^2$) normalized by its value at the design point of the baseline case. Two differences from Fig. 10 stand out. First, the rotor pressure coefficient shows dependence on flow coefficient. Second, roughness on stator vanes increases the rotor pressure coefficient even when rotor blades themselves are not roughened. Since rothalpy is conserved across the rotor and the blade's rotational speed remains constant in axial turbomachines (i.e., $U_2 = U_3$), the following equation can be obtained for the rotor:

$$C_{ps}^R = \frac{P_{s2} - P_{s3}}{\frac{1}{2}\rho v_{x1}^2} = \frac{1}{\cos^2\beta_3} - \frac{1}{\cos^2\alpha_2} - \frac{1}{\phi^2} + \frac{2\tan\alpha_2}{\phi} + \zeta^R \tag{10}$$

Again, according to Kind et al. [9], the first four terms on the right-hand side of Eq. (10) remain constant for given blade angles and flow coefficient. Therefore, the increase in the rotor pressure coefficient due to roughness on stator vanes (Fig. 12) must result from the increase in total pressure loss across the rotor blades. Thus, stator roughness increases rotor loss, and, consequently, stator roughness results in more efficiency deterioration than rotor roughness (Fig. 8).

Figure 13 shows graphs of calculated rotor loss coefficient ζ^R using Eq. (10) and the data from Fig. 12. Unlike the stator, the loss across the rotor is a function of flow coefficient because the rotor incidence angle varies with flow coefficient. Furthermore, the rotor loss coefficient increases more than the stator loss coefficient with roughness. The rotor loss coefficient can be approximated with a second-order polynomial, which can be used for efficiency estimation.

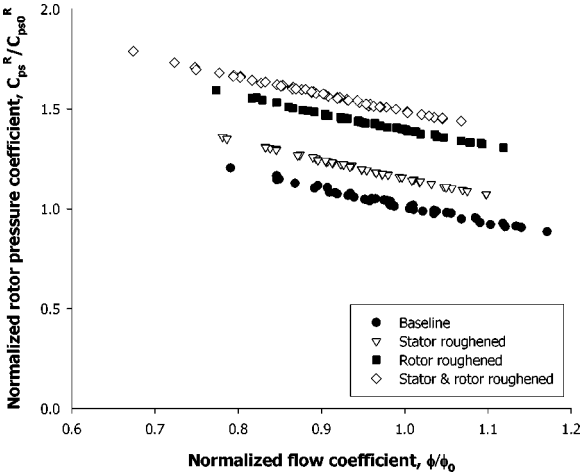

Fig. 12 Measured rotor pressure coefficient

For incompressible flows, total-to-static efficiency can be shown to have the following form:

$$\eta_{ts} = \frac{\rho U v_{x1}(\tan\alpha_2 + \tan\beta_3) - \rho U^2}{\rho U v_{x1}(\tan\alpha_2 + \tan\beta_3) - \rho U^2 + \frac{1}{2}\rho v_3^2 + \Delta P_t^S + \Delta P_t^R} \tag{11}$$

and, in terms of nondimensional parameters,

$$\eta_{ts} = \frac{2(\tan\alpha_2 + \tan\beta_3)\phi - 2}{\left(\zeta^S + \zeta^R + \dfrac{1}{\cos^2\beta_3}\right)\phi^2 + 2\phi\tan\alpha_2 - 1} \tag{12}$$

Blade angles and flow coefficient are known a priori. Stator loss coefficient ζ^S is given in Fig. 11, and rotor loss coefficient ζ^R is given in Fig. 13. Finally, Eq. (12) can be used to obtain the calculated efficiency graphs in Fig. 8.

In Fig. 8, estimated and measured efficiencies agree well with each other. The magnitudes of degradation are well captured in all cases. Stator roughness causing greater loss than rotor roughness is also captured. Also, for a given roughness, dependence on flow coefficient is well estimated. Finally, the decrease in the flow coefficient corresponding to maximum efficiency with increasing roughness is also predicted. Thus, combined with a simple mean-line analysis, efficiency data and static pressure data provide a consistent picture of the relative and cumulative effects of roughness on stator and rotor blades. According to this result, one can think of wall pressure data as indicators of performance degradation due to blade surface roughness.

Conclusions

Performance measurements have been carried out in a low speed, single-stage, axial turbine to assess the effects of blade surface roughness due to foreign deposits. New conclusions from this investigation are as follows:

1. Blade surface roughness severely degrades turbine efficiency. The normalized total-to-static efficiency decreases by 8% when both the stator and rotor blade rows are roughened with transitional roughness ($k^+ = 30$) and by 19% with full roughness ($k^+ = 149.2$). Thus, efficiency penalty increases with increasing roughness.
2. As in cascades, a rotating turbine's performance is more sensitive to roughness on the suction side of stator vanes than that on the pressure side.

3. Roughness on stator vanes increases loss through the rotor even when the rotor blades are not roughened; however, roughened rotor does not affect loss across the stator. Thus, roughened stator induces a higher performance penalty than roughened rotor.

4. Efficiency drop with a roughened stator added to the drop with a roughened rotor is approximately equivalent to the efficiency drop with both rows roughened.

5. With increasing roughness, the flow coefficient corresponding to maximum efficiency decreases, and this trend is captured with a simple mean-line analysis.

6. According to a simple mean-line analysis, wall static pressure data can be indicators of performance degradation due to blade surface roughness.

Acknowledgments

The authors gratefully acknowledge support from the EESRI (01-M-02) of the Korea Ministry of Commerce, Industry, and Energy and the Micro Thermal System Research Center of the Korea Science and Engineering Foundation.

Nomenclature

A_f = windward frontal surface area of roughness elements
A_s = windward wetted surface area of roughness elements
c = true chord length
c_x = axial chord length
c_f = skin friction coefficient
c_p = specific heat
C_{ps} = pressure coefficient ($=\Delta P_s / \frac{1}{2}\rho v_{x1}^2$)
k = average roughness height ($\approx R_z$)
k_s = equivalent sandgrain roughness
k^+ = roughness Reynolds number
$\dot{m}$ = mass flow rate
P_s = static pressure
P_t = total pressure
Q = torque
R_a = centerline average roughness
R_t = maximum peak to valley roughness
R_z = average peak to valley roughness]
Re_c = Reynolds number based on true chord length and exit velocity
S = sample surface area without roughness
S_f = total frontal surface area of sample
T_t = total temperature
U = blade rotating speed
v = absolute velocity
v_x = axial velocity
w = relative velocity
x = axial distance from rotor leading edge

Greek

α = absolute flow angle from the axial direction
β = relative flow angle from the axial direction
γ = ratio of specific heats
Δ = difference across the blade row
ϕ = flow coefficient
η_{ts} = total-to-static efficiency
Λ_s = roughness shape/density parameter
ρ = density
ω = angular velocity
ζ = total pressure loss coefficient ($=\Delta P_t / \frac{1}{2}\rho v_{x1}^2$)

Subscripts and Abbreviations

0 = baseline case design value
1 = stage inlet
2 = region between stator and rotor rows
3 = stage exit
LE = leading edge
MS = midspan
PS = pressure side
SS = suction side

Superscripts

S = stator
R = rotor

References

[1] Bons, J. P., Taylor, R. P., McClain, S. T., and Rivir, R. B., 2001, "The Many Faces of Turbine Surface Roughness," ASME J. Turbomach., **123**(4), pp. 739–748.
[2] Taylor, R. P., 1990, "Surface Roughness Measurements on Gas Turbine Blades," ASME J. Turbomach., **112**(2), pp. 175–180.
[3] Bogard, D. G., Schmidt, D. L., and Tabbita, M., 1998, "Characterization and Laboratory Simulation of Turbine Airfoil Surface Roughness and Associated Heat Transfer," ASME J. Turbomach., **120**(2), pp. 337–342.
[4] Sigal, A., and Danberg, J. E., 1990, "New Correlation of Roughness Density Effect on the Turbulent Boundary Layer," AIAA J., **28**(3), pp. 554–556.
[5] Bons, J. P., 2002, "St and cf Augmentation for Real Turbine Roughness with Elevated Freestream Turbulence," ASME J. Turbomach., **124**(4), pp. 632–644.
[6] Schlichting, H., 1979, *Boundary Layer Theory*, seventh Edition, McGraw-Hill, New York.
[7] Bammert, K., and Sandstede, H., 1972, "Measurements Concerning the Influence of Surface Roughness and Profile Changes on the Performance of Gas Turbine," ASME J. Eng. Power, **94**(3), pp. 207–213.
[8] Bammert, K., and Sandstede, H., 1980, "Measurements of the Boundary Layer Development Along a Turbine Blade With Rough Surfaces," ASME J. Eng. Power, **102**(4), pp. 978–983.
[9] Kind, R. J., Serjak, P. J., and Abbott, M. W. P., 1998, "Measurements and Prediction of the Effects of Surface Roughness on Profile Losses and Deviation in a Turbine Cascade," ASME J. Turbomach., **120**(1), pp. 20–27.
[10] Boyle, R.J., and Senyitko, R.G., 2003, "Measurements and Predictions of Surface Roughness Effects on Turbine Vane Aerodynamics," ASME Paper No. GT2003-38580.
[11] Boynton, J. L., Tabibzadeh, R., and Hudson, S. T., 1993, "Investigation of Rotor Blade Roughness Effects on Turbine Performance," ASME J. Turbomach., **115**(3), pp. 614–620.
[12] Abuaf, N., Bunker, R. S., and Lee, C. P., 1998, "Effects of Surface Roughness on Heat Transfer and Aerodynamic Performance of Turbine Airfoils," ASME J. Turbomach., **120**(3), pp. 522–529.
[13] Nikuradse, J., 1933, "Laws for Flows in Rough Pipes," VDI-Forschungsheft, **361**(B4).
[14] Kline, S. J., and McClintock, F. A., 1953 "Describing Uncertainty in Single Sample Experiments," Mech. Eng. (Am. Soc. Mech. Eng.), January pp. 3–8.

The Pulsating Flow Field in a Mixed Flow Turbocharger Turbine: An Experimental and Computational Study

D. Palfreyman[1]
CD adapco Group,
200 Shepherds Bush Road,
Hammersmith,
London, UK

R. F. Martinez-Botas
Mechanical Engineering Department,
Imperial College,
London, UK

The turbine stage of an automotive pulse system turbocharger is subjected to an unsteady pulsating flow field due to the rapid opening and closing of the reciprocating engine exhaust valves. This leads to a complex and highly disturbed flow field within the delivery volute and turbine passages, which results in an unusual "hysteresis" type performance characteristic. The aim of this paper is to investigate the flow field within the turbine stage under these representative conditions, using a computational method validated against experimental data. This paper is separated into two sections. The first deals with the validation of the numerical code and modeling approach. A mesh dependency study is undertaken with cell discretization ranging 200,000, 850,000, and 1,750,000 cells, where the accuracy is assessed through comparison with experimental performance and flow field measurements. The second part presents an investigation of the flow field under pulse conditions. Time accurate spectra of turbine performance and flow properties at various locations in the turbine stage are presented, as well as contour plots of velocity within a turbine passage at two critical positions during the pulse period.
[DOI: 10.1115/1.1812322]

1 Introduction

Turbocharging plays an important role in an automotive reciprocating engine. An improvement in the transient response (acceleration) of the engine is most acute with the addition of the turbocharger, which is particularly beneficial to the compression ignition (diesel) engine where its transient response is in general poorer to that of its counterpart, the spark-ignition engine.

Advancement of turbocharging technology, particularly pulse-type turbocharging technology which is generally the only feasible method for automotives due to under hood space constraints, is of significant importance to engine manufacturers. Pulse-type automotive turbocharger turbines are configured such that the turbine stage is coupled directly to the engine exhaust manifolds, and as a consequence are subjected to an unsteady ''pulsating'' flow field due to the rapid opening and closing of the reciprocating engine exhaust valves. Figure 1 shows inlet pressure and mass flux traces as measured from a turbocharger turbine test bed [1]. Note the time scales.

This inlet condition, consisting of 40 pulse wave forms per second, leads to a complex and highly unsteady flow field within the turbocharger turbine delivery volute and turbine passages. Under these conditions the turbocharger turbine has been shown by Dale and Watson [2], Winterbone et al. [3,4], Hakeem [5], Su [6] and Karamanis [1,7] to yield a rather unusual ''hysteresis'' type performance characteristic. Both efficiency and mass flow rate versus pressure ratio follow an enclosed curve which loops around the equivalent quasi-steady performance operating point illustrating the hysteresis type trace. A number of researchers have taken measurements of the turbine performance and the flow field under pulsating conditions; Winterbone et al. [3,4], Hakeem [5], Su [6], Karamanis [1], Karamanis and Martinez-Botas [7], Wallace and Blair [8] and Kosuge et al. [9], Winterbone and Pearson [10], Baines and Hajilouy-Benisi [11], Capobianco et al. [12–14], and Yeo and Baines [15].

Wallace and Blair [8] and Kosuge et al. [9], in the mid 1960s, were the first group of researchers to perform such measurements and determined that the turbocharger turbine behaved rather differently under pulsating conditions than under quasi-steady conditions, although it was not until 1986 that a trace of the instantaneous performance was obtained illustrating the hysteresis type loop [2]. Attempts at correlating the unsteady performance to the equivalent quasi-steady performance (Capobianco et al. [12–14], Winterbone et al. [3,4] and Baines and Hajilouy-Benisi [11]) have only shown limited success, primarily as a result of the lack of knowledge of the key aerodynamic factors influencing the unsteady turbine performance and the level of simplification employed to the correlation factors.

Measurements of the flow field during pulsating conditions are rare and as such publications are limited; Yeo and Baines [15], Baines and Hajilouy-Benisi [11], Karamanis [1] Karamanis, Martinez-Botas [7] and Su [6]. Measurements of pressure, velocity and mass flow rate within the volute and close to the leading and trailing edge of the turbine have been made, although at point locations rather than more comprehensive cross-sectional measurements, primarily due to the difficulty in performing such measurements under pulse conditions. In all cases the flow field has been shown to fluctuate substantially, generally in phase with the inlet pulse wave, leading to highly disturbed conditions far from design.

A number of researchers have modeled the turbine performance under pulsating conditions with varying degrees of success: Wallace et al. [16], Baines [11], Chen and Winterbone [17], Connor et al. [18,19], Chen et al. [20], and Lam et al. [21]. The focus of their efforts has generally been to build a tool to evaluate turbine performance rather than predict the three-dimensional structures of the flow field. With one exception, the codes generated have been one-dimensional and based upon either the filling-and-

[1]Previously of the Mechanical Engineering Department, Imperial College, London, UK.

Contributed by the International Gas Turbine Institute (IGTI) of THE AMERICAN SOCIETY OF MECHANICAL ENGINEERS for publication in the ASME JOURNAL OF TURBOMACHINERY. Paper presented at the International Gas Turbine and Aeroengine Congress and Exhibition, Vienna, Austria, June 13–17, 2004, Paper No. 2004-GT-53143. Manuscript received by IGTI, October 1, 2003; final revision, March 1, 2004. IGTI Review Chair: A. J. Strazisar.

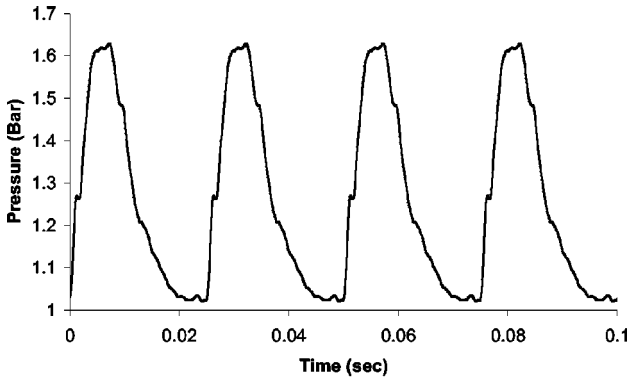

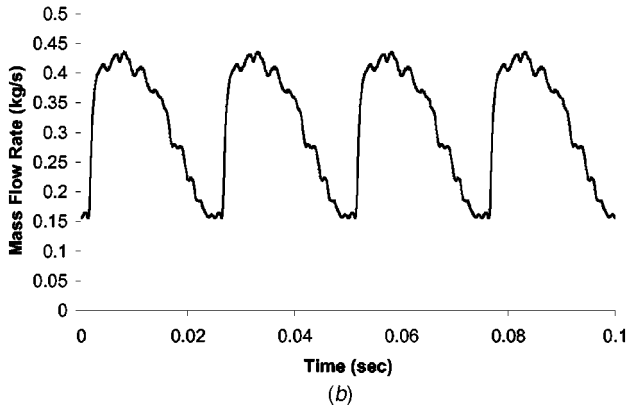

Fig. 1 Experimental data from a simulated turbocharger rig; Karamanis [1] (*a*) Inlet pressure; Karamanis [1]. (*b*) Inlet mass flow rate; Karamanis [1].

emptying models typically used in engine in-cylinder performance analysis, with the addition of gas dynamic effects to determine the conditions at the inlet to the turbocharger (Connor et al. [18,19]), or upon dedicated turbomachinery codes with the inclusion of gas dynamic effects (Chen et al. [20]); in all cases the turbine domain being treated as quasi-steady. The codes have shown little success at predicting the turbine performance, both in terms of capturing the unsteady performance trace and cycle-averaged performance. Lam et al. [21] recently (2002) applied a three-dimensional general purpose code to modeling a turbine stage under pulse conditions, taking into account the complex geometry of the volute and (radial) turbine. Lam et al. applied a multiple reference frame (MRF), or ''frozen-rotor'' approach, to the rotating frame of the turbine, and applied time varying boundary conditions to the model inlet simulating the pulse waves. The computational resources were substantial for the study; the results captured a similar hysteresis type curve for efficiency and mass flow rate, albeit with a degree of ''smoothing'' of the trace due to circumferential averaging (at each instance in time) of the flow field entering the rotating domain, a characteristic of the MRF approach. Unfortunately exact quantification of the numerical approach was not undertaken as no comparison to experimental data was made. Nevertheless, this work represented a significant step forward in the numerical modeling of the turbocharger turbine under pulse conditions.

Despite the substantial research effort undertaken over the past decades, knowledge of the flow field within the turbocharger turbine stage under pulsating conditions and an understanding of the mechanisms causing the hysteresis type turbine performance characteristic are rudimentary. This is due both to the difficulty in acquiring comprehensive and detailed experimental measurements of the flow field under the highly unsteady conditions, and the difficulty and expense of computationally modeling the three-dimensional flow field within the complete turbocharger turbine stage with sufficient temporal and spatial accuracy.

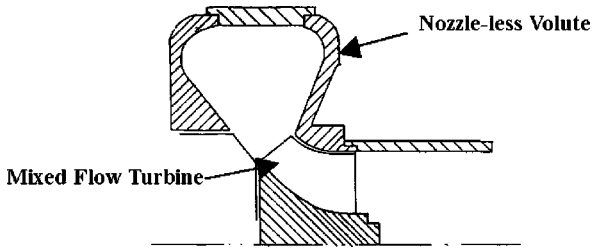

Fig. 2 Mixed flow turbine and single entry nozzle-less volute geometry, see Table 2 for dimensions

The purpose of this paper is to investigate the aerodynamic features in a medium sized mixed flow turbocharger turbine for a chosen pulsating operating condition. To this effect a three-dimensional computational model, representing the complete turbine stage (volute and turbine wheel) embodied in the commercial CFD code STAR-CD [22], will be applied with time accurate boundary conditions representing the pulsating flow condition.

The numerical model and computational methodology will be validated against experimental performance and flow field measurements, taken using laser doppler velocimetry (LDV). Following this will be a description of the transient performance of the turbine and the flow structures within the volute and turbine passages.

2 Mixed Flow Turbocharger Turbine

A mixed flow turbocharger turbine of medium size (that typical in a heavy goods vehicle) has been employed in this research. Figure 2 shows a schematic of the turbine and (nozzle-less) volute.

The design conditions and geometric details for this turbine, designed by Abidat [23], are presented in Table 1 (which includes the equivalent experimental conditions) and Table 2, respectively.

This turbine has been extensively tested under steady and pulsating conditions by Hakeem [5], Su [6] and Karamanis [1,7], and

Table 1 Design conditions

Parameter	Design condition	Equivalent experimental condition
Pressure ratio	2.91	2.91
Inlet temperature (K)	923	344
Mass flow rate (kg/s)	0.414	0.678
Rotational speed (rpm)	98,000	60,000

Table 2 Geometric details of turbine

Geometric Feature	Mixed flow turbine
Leading edge tip diameter (mm)	95.14
Leading edge span height (mm)	18.0
Trailing edge tip diameter (mm)	78.65
Trailing edge span height (mm)	25.8
Cone angle (deg)	40.0
Leading edge blade angle (deg)	Constant incidence of −20
Trailing edge blade angle at rms radius (deg)	52.0
Length of axial chord (mm)	32.5
No. of blades	12
Tip gap height (% of blade span)	3.0

Table 3 Time averaged quantities

Parameter	Value
Pr	1.327
Mass flow rate (kg/s)	0.317
$T_{0,\text{inlet}}$ (K)	334.41
N (rpm)	29403
U/C_{is}	0.562
Wact (W)	6395
Efficiency (t-s)	0.4708
P_f (Hz)	40
One pulse: time (s)	0.025

computationally modeled under steady conditions to evaluate the detailed flow features within the turbine passage (Palfreyman and Martinez-Botas [24]).

3 Experimental Apparatus and Test Condition

Test Condition. Karamanis [1,7] measured the instantaneous performance and undertook LDV measurements at the test conditions shown in Fig. 1 and Table 3.

The test condition has been scaled from the design condition, Table 1, using appropriate nondimensional parameters. This operating point represents the equivalent conditions in a six-cylinder dual turbocharged engine running at a crank shaft speed of 1600 rpm.

Experimental Apparatus. Karamanis [1] employed a dedicated turbocharger test facility consisting of the research turbine, an air supply system, a power absorber in the form of a centrifugal compressor and a data acquisition system. Approximately 1.21 m upstream of the inlet to the volute there was a pulse generator, which consisted of two counter-rotating chopper plates with special cutouts to produce a realistic engine pressure pulse profile.

The reader is referred to [1,7] for a more detailed discussion of the experimental apparatus.

Performance Measurment. The unsteady performance was evaluated by measuring the (a) instantaneous pressure at inlet, (b) instantaneous mass flux at inlet, (c) time-averaged inlet temperature, (d) exit instantaneous pressure, (e) the instantaneous speed, (f) polar moment of inertia of the rotating components and (g) the pulse frequency.

Pressure ratio, isentropic and actual work, and total-to-static efficiency are given in Eqs. (1)–(4), respectively.

$$\text{Pr}(t)=\frac{p(t)_1}{p(t)_2} \tag{1}$$

$$W(t)_{isen}=\dot{m}(t)C_pT(t)_{01}\left(1-\left(\frac{p(t)_2}{p(t)_{01}}\right)^{\gamma-1/\gamma}\right) \tag{2}$$

$$W(t)_{act}=\tau(t)\times\Omega(t) \tag{3}$$

$$\eta(t)_{t-s}=\frac{W(t)_{act}}{W(t)_{isen}} \tag{4}$$

The instantaneous torque is evaluated by Eq. (5),

$$\tau_{inst}=\overline{\tau}+\tau'=\frac{\overline{W}_{act}}{2\pi\overline{N}/60}+I\frac{\Delta W_{inst}}{\Delta t}, \tag{5}$$

that is the sum of the mean and fluctuating components. The fluctuating component of torque was evaluated by measuring the rate of change of rotational speed to derive the angular acceleration.

Velocity Measurement Using Laser Dopplier Velocimetry The laser doppler velocimetry (LDV) system comprised an argon-ion laser (spectra physics) operating at a wavelength of 0.514 μm and power of up to 1 W, an optical unit dividing the laser beam into two equal intensity parts and bringing the two beams to an intersection volume, a photomultiplier, and a frequency counter (TSI model 1995) interfaced to a microcomputer. The intersection volume was approximately 1160 μm in length and 64.0 μm in diameter, with a fringe spacing of 4.65 μm.

For measuring the flow at the rotor inlet three optical windows were used at 72, 130 and 157 deg of azimuth angle along the volute circumference. The measuring plane was parallel to the blade span at 3 mm before the leading edge. The inlet orientation of the LDV receiving optics was at a near-forward scattering angle of 60 deg to the optical axis.

Silicone oil droplets were used as seeding. The droplets were generated by an air-blast atomiser and added to the flow in a divergent portion of ducting just upstream of the volute. The atomizer produced droplets with a Sauter mean diameter of up to 2 mm, which corresponded to a maximum effective Stokes number of 0.1. This implies that the droplets, on average, followed the flow fluctuations although with occasional larger droplets, giving rise to an uncertainty considered negligible.

Laser measurements were made at (a) the mid-point of the volute cross-section at azimuth angles 40 and 130 deg, where the tangential velocity was measured and (b) 130 deg azimuth angle, 3 mm upstream and at mid-span of the turbine leading edge, where the three orthogonal velocity components were measured. Each component was measured individually via appropriate rotation of the crossing beams and correlated to the rotation of the chopper plate inducing the pulse wave forms, with one degree resolution. The digital output of the frequency counter, with a clock frequency of 1000 MHz, was fed into a microcomputer and a sample of 40,000 data points was recorded and then ensemble averaged to yield the trace for one pulse cycle.

4 Numerical Technique

The commercial computational fluid dynamics (CFD) code STAR-CD version 3.150A from CD adapco [22] was employed. This is based upon the finite volume form of the Reynolds (Favre) averaged Navier–Stokes equations which describe the conservation of mass, momentum and energy through Eqs. (6), (7), and (9).

$$\frac{\partial\rho}{\partial t}+\frac{\partial}{\partial x_j}(\rho\vec{U}_j)=0 \tag{6}$$

$$\frac{\partial(\rho u_i)}{\partial t}+\frac{\partial}{\partial x_j}(\rho\vec{u}_j u_i-\tau_{ij})=-\frac{\partial p}{\partial x_i} \tag{7}$$

where

$$\tau_{ij}=2\mu S_{ij}-\frac{2}{3}\mu\frac{\partial u_k}{\partial x_k}\delta_{ij}-\overline{\rho u_i' u_j'} \tag{8}$$

and

$$\frac{\partial(\rho h)}{\partial t}+\frac{\partial}{\partial x_j}(\rho\,\overline{u}_j h-F_{h,j})=\frac{\partial p}{\partial t}+\frac{\partial(\vec{u}_j p)}{\partial x_j}-p\frac{\partial u_j}{\partial x_j}+\tau_{ij}\frac{\partial u_i}{\partial x_j} \tag{9}$$

where

$$F_{h,j}=k\frac{\partial T}{\partial x_j}-\overline{\rho u_j' h'} \tag{10}$$

and

$$\overline{\rho u_j' h'}=-\frac{\mu_t}{\sigma_{h,t}}\frac{\partial h}{\partial x_j} \tag{11}$$

The Reynolds stress term in the momentum transport equations, Eq. 8, div($\overline{\rho u_i' u_j'}$), was resolved using the high Reynolds renormalization group (RNG) k-ε turbulence model [25]. Standard wall functions were used for the near wall boundary cells.

A proprietary formally second-order accurate spatial discretization scheme, monotone advection and reconstruction scheme

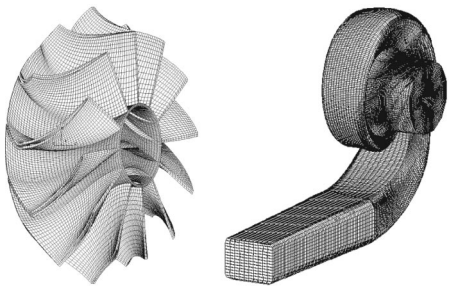

Fig. 3 Mesh of turbine wheel and complete assembly

(M.A.R.S.), was applied which employs a total variation diminishing (TVD) scheme, making it particularly well suited to capturing the sharp gradients in the flow expected during the pulse.

Euler implicit temporal discretization was employed and the pressure implicit with splitting of operators (PISO) solver of Issa [26] was used to evaluate the flow field at each time step.

Computational Model. The computational domain consisted of a portion of the test facility pipe work (0.39 m), the volute, and the turbine passages (12 in total), and extended one axial chord downstream from the trailing edge to the exit boundary. The inlet boundary was placed at the (inlet) experimental measuring location, which was located 0.82 m downstream from the two chopper plates generating the pulse waves. Modeling the full stage was felt necessary to fully capture the propagation of the pressure waves within the turbine stage.

Figure 3 shows the computational mesh for the turbine and complete assembly.

The domain was decomposed using hexahedral cells. These were body fitted to the volute and turbine blade profiles to minimize cell distortion. Three levels of discretization were employed: 198,000 (200k), 855,224 (850k) and 1,752,838 (1750k) cells. With regards to the 1750k model, the distribution of cells within the domain was 798,720 within the inlet pipe work and volute and 954,112 cells in the rotating domain, with 413,088 cells in the turbine passages. A similar distribution was employed for the 200k and 850k models.

Modeling Approach

Boundary Conditions. Figure 4 shows the inlet and exit boundary locations. A nonreflective boundary was employed at the inlet to allow (reflected) pressure waves to pass out of the domain without reflection. The boundary velocity was calculated on the basis of one-dimensional wave theory, Eq. (12), with all other variables extrapolated (zero-gradient) from the domain interior.

$$V_B = V_\infty + \mathrm{sgn}(v \cdot s)_B f(P_B)\left[\frac{P_B - P_\infty}{P_\infty}\right]\frac{V_P}{|V_P|} \qquad (12a)$$

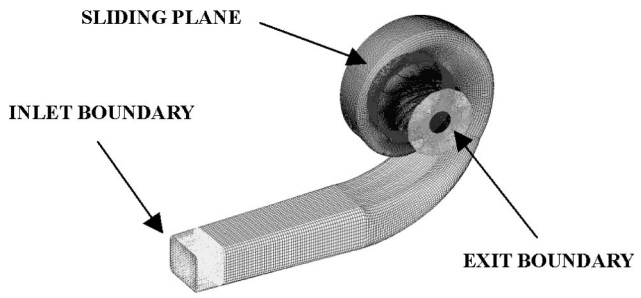

Fig. 4 Inlet, exit and sliding boundary planes

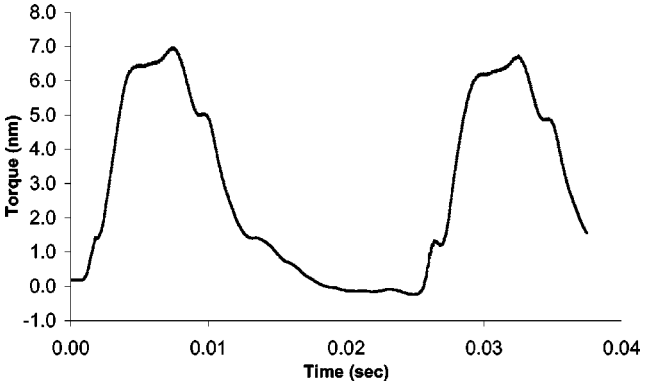

Fig. 5 Torque trace over two pulses periods

where

$$f(P_B) = \sqrt{\frac{2\gamma T_\infty}{(\gamma+1)\dfrac{P_B}{P_\infty} + (\gamma-1)}} \qquad (12b)$$

A time varying free stream pressure "$P\infty$" was applied to give a boundary pressure "P_B" trace equal to that measured experimentally. The remaining free stream (∞) conditions were kept constant in time and equal to the cyclic averaged values.

At the exit plane, a time constant pressure, varying according to radial equilibrium and equal to the experimental cycle averaged value, was prescribed.

The turbine was rotated explicitly during the calculation using built-in algorithms. These rotated the turbine mesh at the desired speed and re-coupled the domain to the stationary domain through a sliding plane (see Fig. 4) at each instance in time. The turbine domain was rotated at a constant speed, and equal to the time average experimental rotational speed. The variation during the pulse cycle was no greater than $\pm 1.0\%$, hence this was a valid approximation.

All wall boundaries including the blade surfaces were prescribed nonslip conditions.

Computational Procedure. It was felt appropriate to develop the flow field within the turbine stage to "periodic conditions" under pulse time-average boundary values, before commencing with the application of the time varying boundary conditions. To this extent the following procedure was employed.

a. A multiple reference frame (MRF) analysis was performed with the time average boundary conditions.
b. The computation was restarted from the MRF solution and run for a sufficient time to reach periodic flow conditions (12–15 full rotations of the turbine wheel were necessary), again with time average boundary conditions.
c. The computation was the restarted from the cycle averaged condition and run for a number of time steps to encapsulate the pulse cycle, with the transient inlet boundary condition applied.

In the case of the 1750k model, a computational time step of $\Delta t = 4.1.10^{-6}$ s was employed, which gave a mean Courant number of 0.8, sufficient to resolve the transient features of the flow field. The computation was run for the equivalent of $\sim$16 full turbine wheel rotations to reach fully periodic conditions, and then for a further 0.02825 s ($\sim$14 turbine rotations) to cover just in excess of one pulse period.

To assess repeatability of the prediction over more than one pulse period, the 200k model was run for two full pulse periods. The subsequent predicted torque trace is presented in Fig. 5. This

Table 4 Cycle averaged conditions

Parameter	200k	850k	1750k	Exp.
Mass flow rate (kg/s)	0.292	0.304	0.297	0.317
Pr	1.253	1.271	1.272	1.327
Wact (W)	6585	6970	6999	6395
Torque (nm)	2.142	2.264	2.273	2.077
Efficiency	0.4362	0.4992	0.5102	0.4708

shows good repeatability in the prediction and indicates that only one pulse period was necessary to adequately predict the unsteady turbine performance.

5 Comparison With Experiment

Comparison is made with (a) the cycle averaged and instantaneous performance, (b) pressure measurements around the circumference of the volute, and (c) LDV measurements within the volute and near the turbine leading edge.

Comparison With Performance. To derive the cycle average conditions, Table 4, the instantaneous conditions were integrated over the pulse period according to Eq. (14).

$$\overline{X} = \frac{1}{\lambda}\int_{\lambda} \dot{X}(t)dt \tag{13}$$

With respect to varying cell density, comparison is made upon the basis of predicted cycle-averaged performance. Referring to Table 4, the values of performance exhibit an asymptotic trend with increasing cell density indicative of the second order convergence nature of the spatial differencing scheme employed. Taking work output as an example, there is a 5.85% increase for a 4.32 multiple increase in cell density between the 200k and 850k model, and a 0.42% increase for a 2.05 multiple increase in cell density between the 850k and 1750k models. Whilst the difference in cycle-averaged performance between the 200k and 850k model is significant, that between the 850k and 1750k model is small; percentage differences are -2.5%, 0.08%, 0.41%, 0.4% and 0.01 percentage points, for mass flow rate, Pr, Wact, torque and efficiency, respectively.

Comparing the cyclic-averaged performance from the 1750k model to experiment, the percentage differences are -6.2%, -4.1%, 9.4%, 9.4% and 3.9 (percentage points) for the mass flow rate, Pr, Wact, torque and efficiency, respectively. Given that the pressure at inlet is matched to experiment, the pressure ratio differs with experiment due to a ''dampening'' effect on the exit pressure trace, caused by the close proximity to the turbine trailing edge and application of the time-constant pressure on the exit boundary plane. Figure 6 shows the experimental and predicted pressure at the turbine exit. This impacts additionally on the trace of instantaneous efficiency versus pressure ratio, Fig. 7(*a*), where the trace is shifted slightly left.

The trace of instantaneous mass flow rate versus pressure ratio, Fig. 7(*b*), shows a significant deviation from experiment. Whilst the area encapsulated by the hysteresis curve's are in reasonable agreement, the trace tends to over and under predict at the higher and lower pressure ratios respectively. The inlet boundary condition imposed a velocity, ''V_B,'' derived from one-dimensional wave theory and a function of free-steam conditions. While the free-stream velocity and temperature were constant in time and equal to the cycle-averaged experimental measurements, the free-stream pressure was varied in time to produce a boundary pressure trace, ''P_B,'' equal to experiment. The applicability of such a boundary condition is thus drawn into question. Conversely there is a degree of uncertainty over the measurement of mass flux. The experimental data appears ''capped'' at the high and low mass flow rates, a feature not observed in other published turbine maps

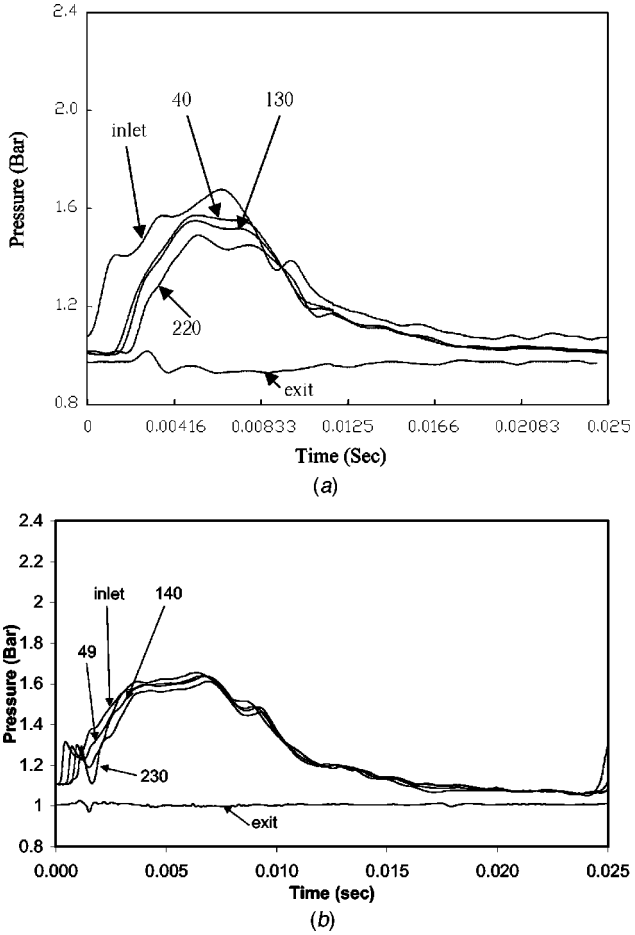

Fig. 6 Pressure at the center of the volute at given azimuth angles. (*a*) Experiment [1]. (*b*) Predicted.

under pulse conditions (Winterbone et al. [3,4] and Dale and Watson [2]), where the trace is more akin to that predicted.

The prediction of turbine torque, work output and efficiency, both on a cycle averaged basis, Table 4, and the instantaneous values, Figs. 8(*a*), 9, and 7(*a*), are in reasonable agreement with experiment. Turbine torque is derived by integrating the element torque on each blade surface, Eq. (14),

$$\tau(t) = \int_s \vec{r} \times (\vec{f}(t) \cdot \hat{n}) ds \tag{14}$$

while experimentally by evaluation of the angular acceleration of the turbocharger turbine and compressor assembly. Due to the inertia of the assembly and the compressor loading, one would expect a certain amount of ''damping'' of the experimental torque trace, which is observed in Fig. 8(*a*). The instantaneous trace of efficiency, Fig. 6(*a*), captures the hysteresis form and remains in reasonable agreement with experiment throughout the cycle.

The discrepancy with inlet mass flow rate impacts on the calculation of isentropic work, the inconsistency in the calculation of torque impacts on the calculation of work, and both impact on the evaluation of efficiency. Beyond numerical error, this ultimately leads, in part, to explain the differences with cycle-averaged and instantaneous performance to the experimental measurements.

Comparison With Flow Field Measurements. The predicted pressure trace's at inlet, four azimuth angles around the volute (measured at the center of the respective cross section), and at the exit, are compared to experiment in Fig. 6. Reasonable agreement is observed; the magnitude and variation in time, as

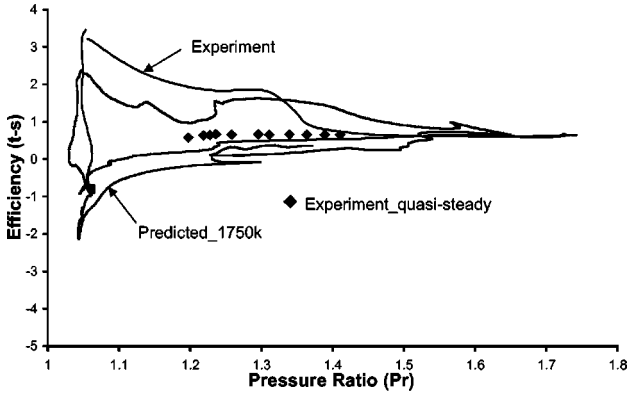

(*a*)

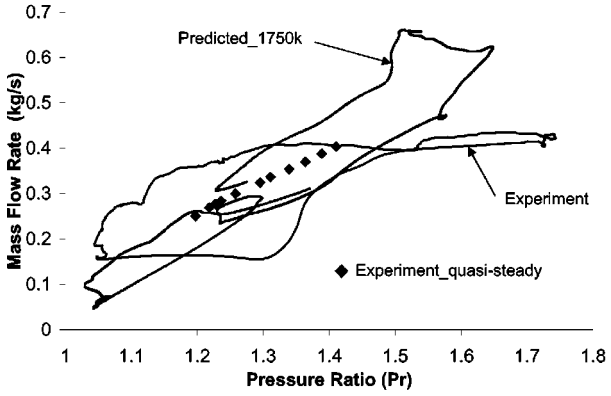

(*b*)

Fig. 7 Turbine performance maps. (*a*) Instantaneous η_{t-s} versus Pr; experimental data [1]. (*b*) Instantaneous MFR versus Pr; experimental data [1].

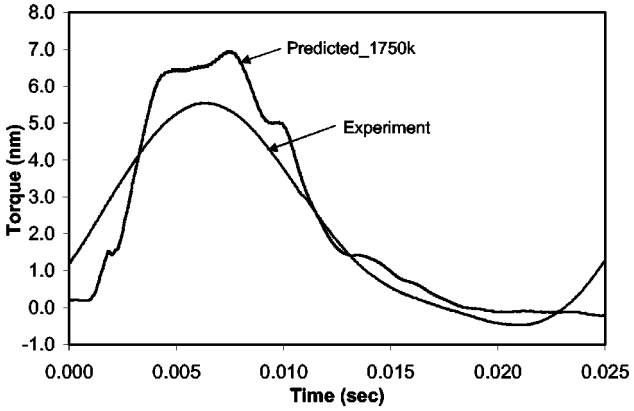

(*a*)

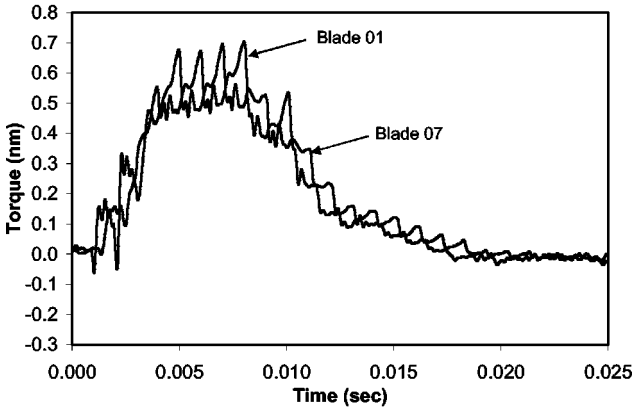

(*b*)

Fig. 8 Experimental and numerical torque data. (*a*)—Total turbine torque, experiment [1]. (*b*)—Torque on blades 01 and 07.

well as the distribution around the volute circumference, are in reasonable agreement with experiment. The noticeable exception is the trace of exit pressure, for reasons described previously.

Comparison with the (LDV) measured tangential velocity at the center of the volute for two azimuth angles is shown in Fig. 10. Again reasonable agreement is observed both in the form of the trace and its magnitude.

Figure 11 shows the measured and predicted orthogonal components of velocity at inlet to the turbine. The experimental measurement location was 3 mm upstream of the turbine leading edge, at mid span and pitch, while the numerical monitoring location was positioned at mid span and pitch, but a further 11.9 mm upstream from the leading edge. Nevertheless, the difference in location was felt small enough for a comparison to remain valid.

The tangential velocity agrees well both in form and magnitude with experiment, albeit there is a flatter trace at the point of peak velocity. The meridional and spanwise components of velocity remain fairly ''flat'' during the pulse period, as per experiment. Both components are under-predicted, a difference of $\sim$29 m/s and $\sim$17 m/s based on the time average, for the meridional and spanwise components, respectively, a degree of which can be attributed to the different monitoring locations. Towards the end of the pulse where the pressure across the stage approaches unity, the predicted velocity components fluctuate for a short period of time. This was not captured experimentally and requires further investigation.

Reasonable agreement has been observed between predicted and experimental performance. The cycle averaged performance is in reasonable agreement despite the difference in predicted mass flow rate and the difference arising due to the inconsistency in the calculation of torque. The instantaneous trace of both efficiency and mass flow parameter capture the hysteresis form, characteristic of this type of flow regime. There is some uncertainty over the trace of mass flow parameter both with regards to the numerical and experimental results. Despite this both the traces of velocity within the volute and close to the turbine leading edge, as well as the pressure trace around the circumference of the volute, agree well with experiment, giving confidence in the numerical results.

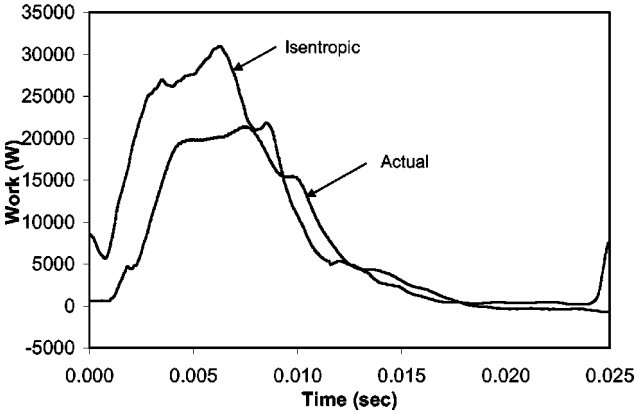

Fig. 9 Turbine work, showing isentropic and actual work

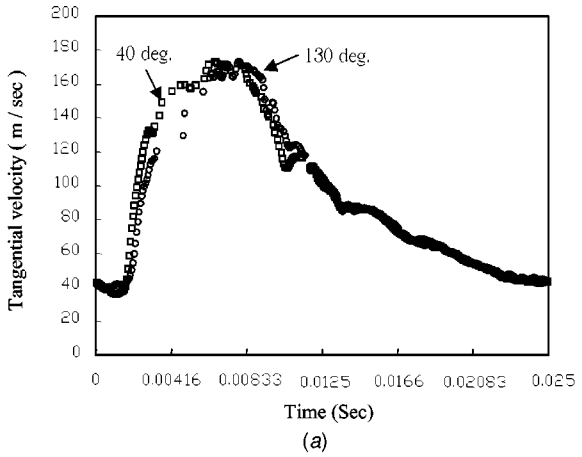

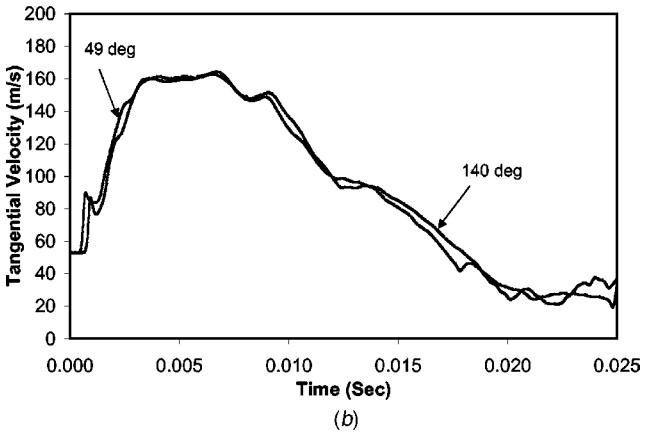

Fig. 10 Tangential velocity at the center of the volute, for two azimuth angles. (*a*) Experiment [1]. (*b*) Predicted.

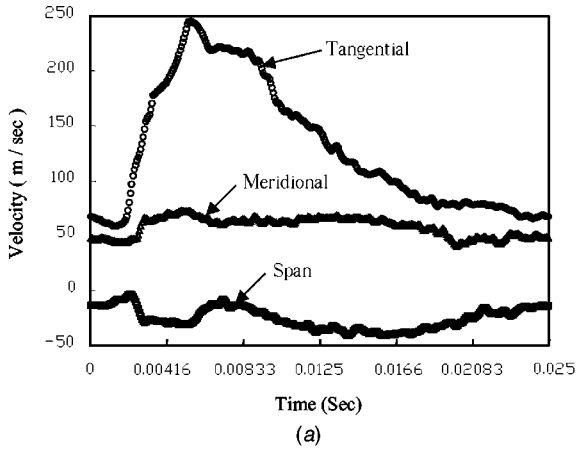

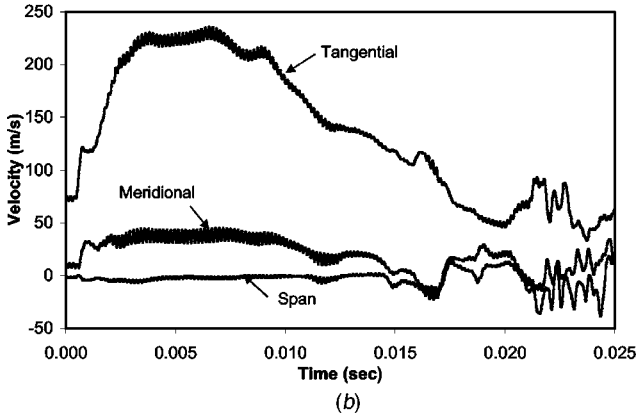

Fig. 11 Velocity at the inlet to the turbine, shown for azimuth angle 40 deg. (*a*) Experiment [1]. (*b*) Predicted.

6 Performance and Flow Field Under Pulsating Conditions

The flow field within the turbocharger turbine stage is dominated by the rapid succession of the pulse wave forms, 40 per second in this instance, at the inlet to the volute. Figure 12 shows pressure contours at a cross section through the stage, for locations ''1'' and ''2'' during the pulse period, which correspond to the points of maximum and minimum inlet pressure (see Fig. 13). The difference in pressure within the stage at the two instances is clear.

Pulsating Performance. The performance of the turbine is characterized as a hysteresis loop which encapsulates the equivalent quasi-steady value. Both the instantaneous efficiency and mass flow rate versus pressure ratio exhibit such a characteristic loop (Fig. 7). The mass flow rate exhibits such a hysteresis type loop due to the imbalance of mass flux at the stage inlet and exit during the pulse cycle (Fig. 14). The surge in mass flow accompanying the inlet pulse wave and the time taken for convection through the volute and turbine domain leads primarily to the mass imbalance. Further there is a degree of time lag associated with the ''filling and emptying'' of the volute domain as the turbine acts as a restriction (nozzle).

Efficiency is expressed as the fraction of actual to isentropic work. The trace of isentropic and actual work is shown in Fig. 9. The first point to note is that there is an offset in time between the two curves. This is a consequence of the time taken for the energy entering the domain, expressed as isentropic work, to translate with the pulse wave into the turbine wheel and be extracted as ''actual'' work. This offset results in the artificial region where efficiency exceeds unity Fig. 7(*a*), due to the actual work exceeding the isentropic work. The region of negative efficiency is caused by a negative torque which occurs towards the end of the pulse where the pressure ratio across the stage is close to unity and the turbine is in effect ''free-wheeling.'' The turbine decelerates, albeit marginally, during this condition. The flow conditions within the stage never repeat during the pulse period leading to the unique efficiency value at each instance in time.

Figure 8(*b*) shows the trace of torque from blades 01 and 07, which are separated by 180 deg. The form follows the trace of total turbine torque, Fig. 8(*a*), with the superposition of ''spikes'' due to the blade passing the tongue of the volute (a frequency of 490 Hz as opposed to the pulse of 40 Hz). It is interesting to note that the magnitude of fluctuation when passing the volute tongue is much smaller than that due to the pulse.

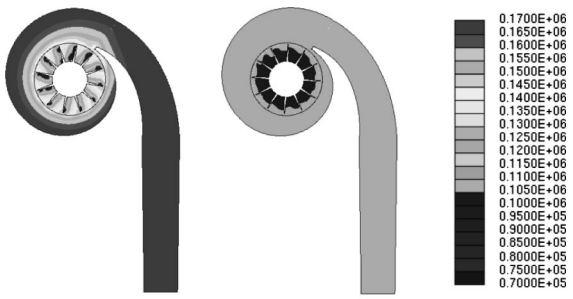

Fig. 12 Stage pressure at position "1" (left) and "2" during the pulse; see Fig. 13

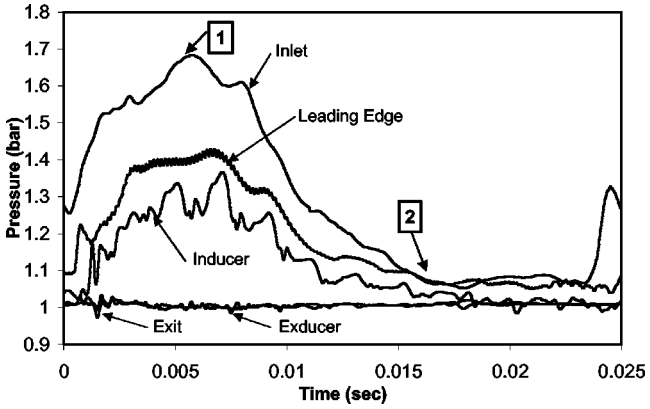

Fig. 13 Pressure distribution at given locations within the turbine stage

Pressure Field. For clarity the flow structures in the turbine passage bounded by blades 1 and 2 will be investigated in detail. Distribution of pressure within the volute and the aforementioned turbine passage is presented in Fig. 13. Five locations are considered, the stage inlet (inlet boundary plane), the leading edge (50% span and pitch, 11.9 mm upstream from the leading edge), the inducer (50% span and pitch, 25 % chord), the exducer (50% span and pitch, 82% chord) and the trailing edge (50% span and pitch, 16.7 mm downstream from the trailing edge).

Referring to Fig. 13, the form of the pressure trace at the leading edge follows closely to that at the inlet to the stage, but at a reduced pressure level due flow acceleration into the turbine passage. Superimposed on the trace are small perturbations caused by the blade passing the monitoring location. In the inducer region, again the pressure trace retains the form of that at inlet to the stage, but with additional perturbations due to the blade passing the volute tongue. In the exducer region, the pressure trace remains relatively flat across the pulse period, hardly influenced by the pressure pulse, and closely matched to that at the trailing edge. As discussed previously, a degree of damping of the exit pressure trace was observed, caused by the close proximity of the exit boundary plane. This is likely to have influenced the pressure in the exducer portion of the turbine domain, leading to the relatively flat pressure trace.

Blade Loading. The loading on blade 01 in the form of surface pressure as a function of chord, for the hub, mid and tip span locations, is shown in Fig. 15. Two positions during the pulse period are shown as highlighted in Fig. 13 as ''1'' and ''2.''

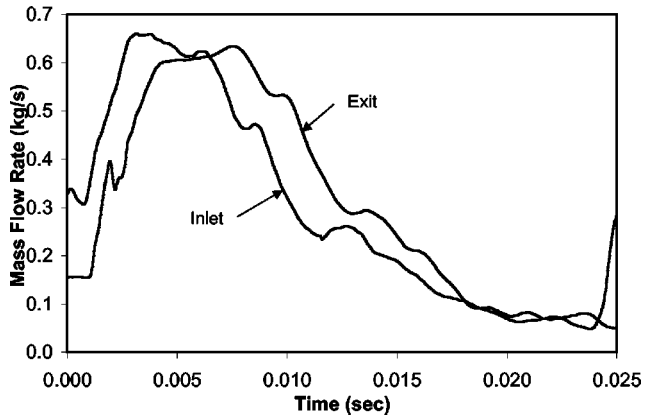

Fig. 14 Mass flow rate at the stage inlet and exit

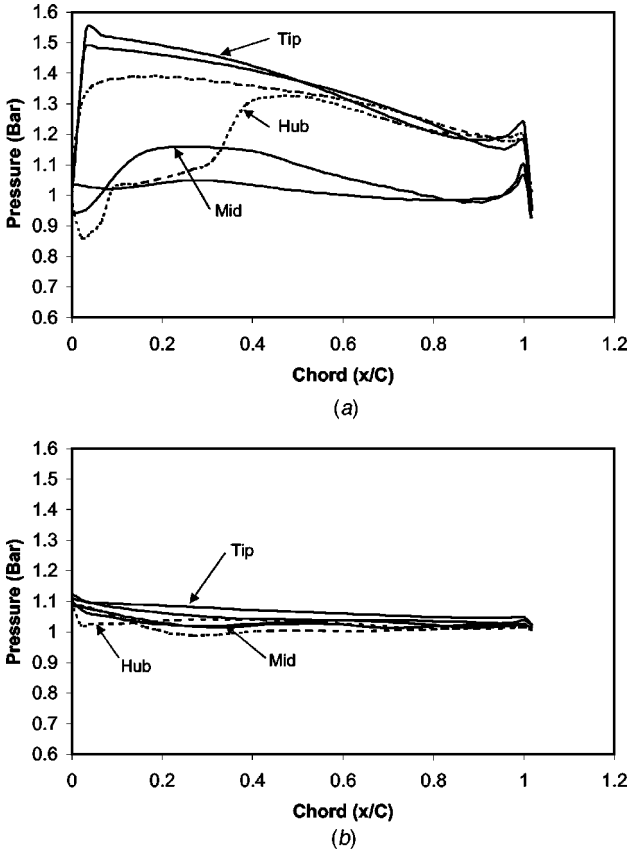

Fig. 15 Blade 01 pressure loading against chord for two locations during the pulse; see Fig. 13. (*a*) Position 01 (0.00572 s). (*b*) Position 02 (0.01955 s).

At position ''1,'' the pressure loading distribution is fairly uniform along the chord at the mid and tip span locations, while at the hub the pressure loading drops dramatically at ~44% chord. This is due to flow separation on the suction surface in the hub occurring at this location, a characteristic of the blade geometry (Palfreyman and Martinez-Botas [24]).

At position ''2,'' the pressure loading across the surface of the blade is ''lost.'' Here the torque on the blade is notionally zero and a fraction (0.0087 based on the average loading across the chord) of that at position ''1.''

Velocity Field. Figures 16–19 show the distribution of velocity during the pulse period at the leading edge, inducer, exducer and trailing edge of the turbine, at the same spatial and temporal locations as the pressure trace, Fig. 13. Figures 20 and 21 show contour plots of relative velocity on streamwise planes in the inducer and exducer regions, as illustrated in the two schematics (Fig. 22). Again the two sets of contour plots are shown corresponding to positions ''1'' and ''2'' on the pulse wave.

Turbine Inlet. Referring to velocity at the leading edge, Fig. 16(*a*) (a duplicate of Fig. 11(*b*) for clarity), the meridional and spanwise components are only marginally influenced by the pulse wave while the tangential component varies substantially, from 74 to 235 m/s, and in-phase with the pulse wave. This leads to a substantial fluctuation in the flow angles at inlet and specifically to the incidence angle, which varies from $-92°$ to $+60°$, indicating poor flow guidance throughout the pulse period, Fig. 16(*b*).

Inducer. The components of velocity within the inducer, Fig. 17, are influenced to a lesser degree by the pulse wave, with the

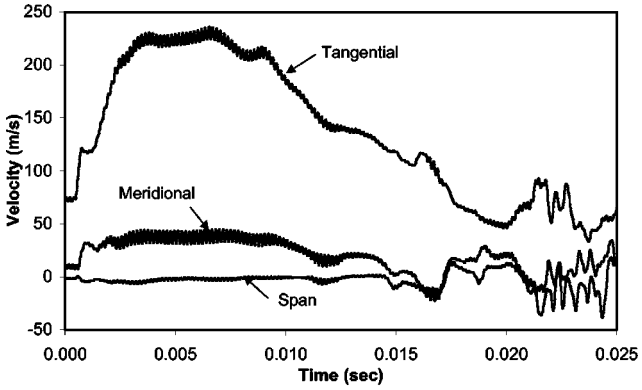

(*a*)

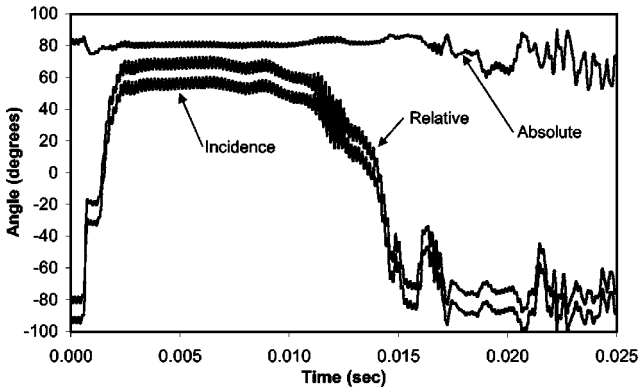

(*b*)

Fig. 16 Velocity and flow angles at the inlet to the turbine, at 40 deg azimuth angle. (*a*) Velocity. (*b*) Flow angles.

superposition of ''spikes'' due to the blade passing the tongue of the volute. This fluctuation is substantial and ~60% of that due to the inlet pulse wave.

With reference to the velocity contours on the streamwise plane; at location ''1,'' Fig. 20(*a*), on the pulse wave (Fig. 13), the region of separated flow captured on the chordwise distribution of pressure loading at the hub, Fig. 15(*a*), is clear (denoted feature ''A.'') This region stretches along the span of the suction surface and interacts with feature ''B,'' which is associated with the formation of a vortex due to tip leakage. The region of separated flow is substantial and results in a significant gradient of velocity

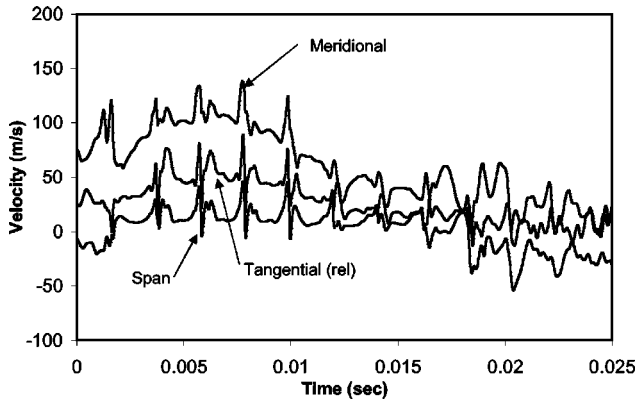

Fig. 17 Velocity components within the inducer portion of the turbine passage between blades 1 and 2, at mid span and pitch

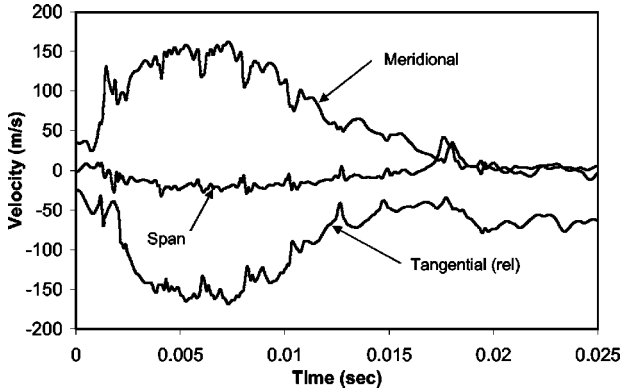

Fig. 18 Velocity components within the exducer portion of the turbine passage between blades 1 and 2, at mid span and pitch

across the passage, peaking near the passage center, feature ''C.'' Flow separation occurs only for a short period of time, 0.00345 s corresponding to 13.8% of the pulse period.

At region ''2,'' Fig. 20(*b*), on the pulse wave (Fig. 13), the structure of the velocity field is quite different. The average velocity across the passage has reduced; there is a region of low velocity in the passage center, feature ''D,'' with a positive gradient of velocity towards the suction surface hub region, resulting in a localized region of high velocity, feature ''E.''

Exducer. Referring to Fig. 19, the influence of the pulse wave is evident particularly in the trace of meridional and tangential velocity; the spanwise component remains fairly uniform across

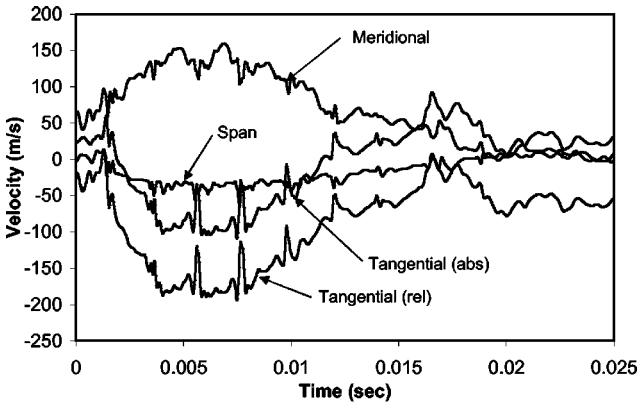

(*a*)

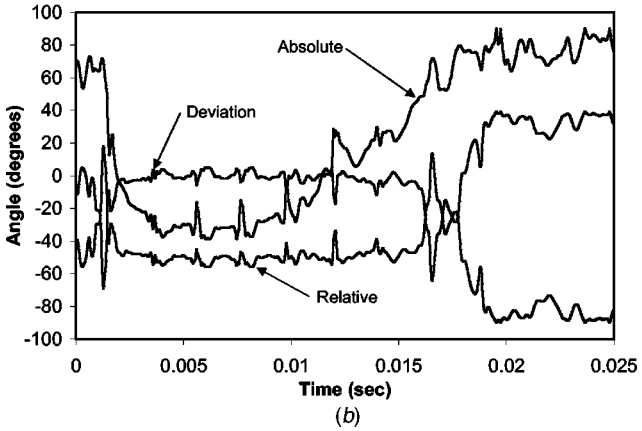

(*b*)

Fig. 19 Velocity and flow angles at the exit of the turbine, at 40 deg azimuth angle (*a*) Velocity. (*b*) Flow angles.

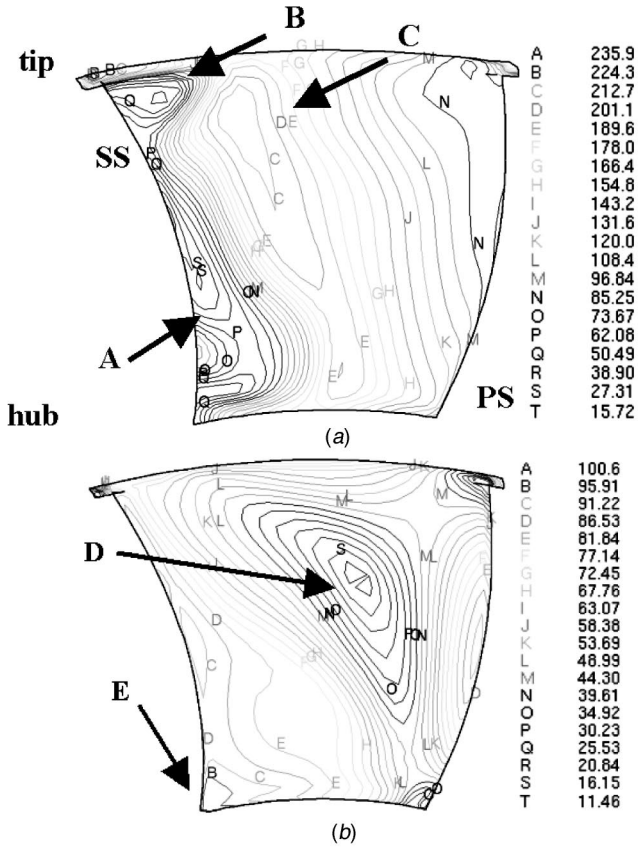

Fig. 20 Contour plots of velocity (relative) in the inducer for two positions during the pulse; see Fig. 13. (*a*) Position 01 (0.00572 s). (*b*) Position 02 (0.01955 s).

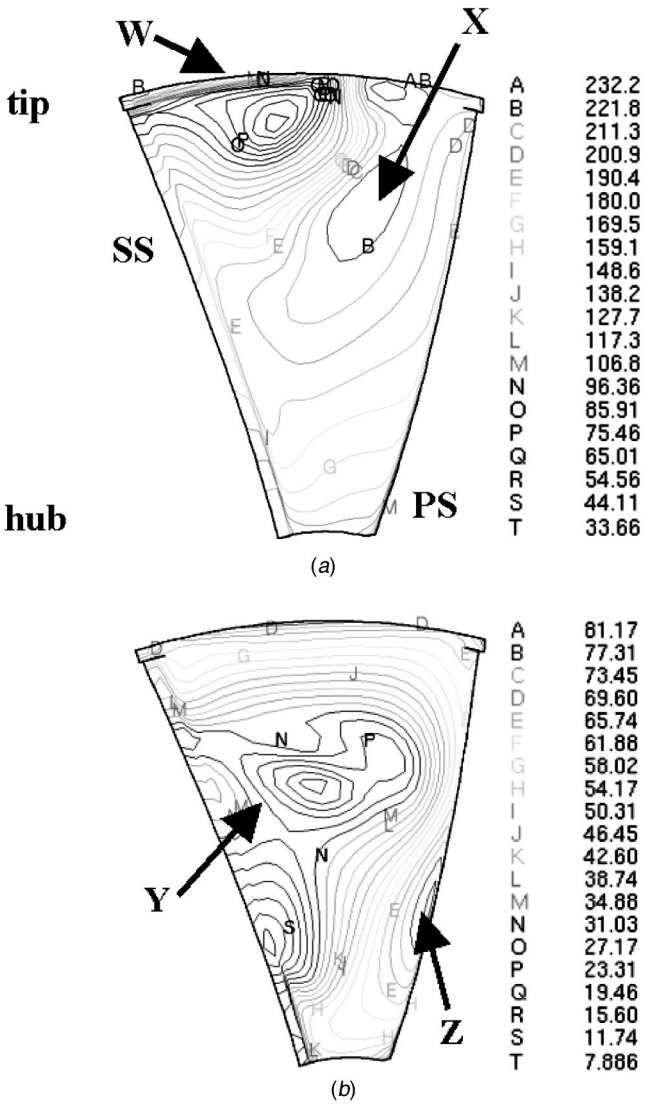

Fig. 21 Contour plots of velocity (relative) in the exducer for two positions during the pulse; see Fig. 13. (*a*) Position 01 (0.00572 s). (*b*) Position 02 (0.01955 s).

the pulse period. The ''spikes'' associated with the blade passing the tongue of the volute are interestingly still evident at this location of the passage (82% of the blade chord), although much reduced.

With reference to the contours of velocity in the streamwise plane, Fig. 21(*a*), at position ''1'' on the pulse wave (Fig. 13) the flow has reattached to the suction surface and there remains the tip leakage vortex, denoted feature ''W,'' and peak velocity region, feature ''X.'' The tip leakage vortex has propagated further into the passage upto a pitch of ~40% as measured from the suction surface.

At position ''2'' on the pulse wave (Fig. 13), Fig. 21(*b*), the region of low velocity in the center of the passage, feature ''Y,'' is observed, while a region of high velocity occurs next to the pressure surface at ~35% span, feature ''Z.''

Turbine Exit. At the turbine exit, Fig. 19, the flow velocity is still influenced by the pulse wave. The variation of the tangential velocity, coupled with the meridional velocity, produces a significant variation of the absolute flow angle. Deviation of the flow remains relatively small during the first portion of the inlet pulse wave, from 0 to 0.0175 s, but then rises rapidly to approximately 40 deg for the region of low inlet pressure, leading to poor flow guidance.

7 Conclusion

This work represents one of the first attempts at modeling the flow field within the turbine stage of a pulse system turbocharger, three-dimensionally and under realistic pulse conditions. The aim of this paper was to firstly assess the ability of a computational model to capture the pulsating performance of the turbine and specific flow properties within the stage, and secondly present principle features of the flow field under the pulsating condition. The chosen operating condition corresponds to that in a six-cylinder dual turbocharged engine running at a crank shaft speed of 1600 rpm.

The level of agreement both in terms of cycle-averaged and instantaneous performance to experiment is reasonable. There remains some uncertainty over the applicability of the inlet boundary condition and the experimental measurement of the inlet mass flux. The hysteresis type curve of mass flow rate and efficiency is captured numerically, without the degree of damping observed by Lam et al. [21]. This enforces the use of explicit mesh motion for the turbine domain to model the wheel rotation, as opposed to the ''frozen-rotor'' approach.

The predicted pressure distribution around the volute, and velocity within the center of the volute and near the turbine leading edge agree well with experiment. The general form and amplitude in each trace are captured in the numerical results with small regions of discrepancy. This indicates the code and modeling approach taken has adequately captured the details of the flow field under pulse conditions.

The flow field within the turbine stage is highly disturbed and

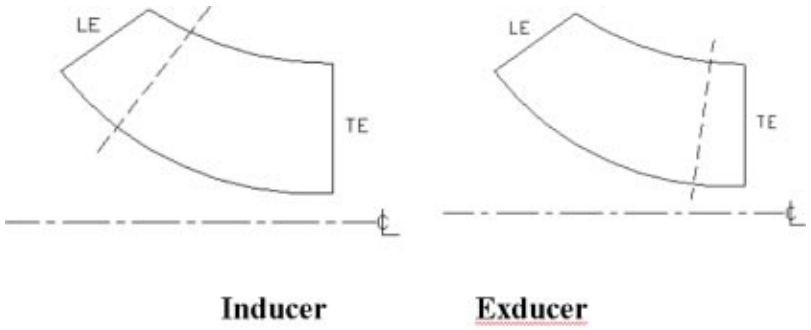

Fig. 22 Orientation perpendicular to the dotted lines

influenced primarily by the pulsating inlet condition. Blade torque, work output and loading fluctuate substantially and at the frequency of the pulse. The effect of the blades passing the tongue of the volute is observed, which is most influential in the inducer portion of the turbine. The velocity field within the turbine passage varies substantially during the pulse period where poor flow guidance is observed at the inlet and exit of the turbine. This undoubtedly diminishes the intricate design of the blade geometry, designed under quasi-steady conditions (Abidat [23]).

Computational resources for this study were substantial; over 100 Gb of data were generated with computing times certainly outside the time scales associated with today's design environment. Nevertheless modeling of the turbocharger turbine under pulse conditions has been shown to be possible, where the numerical code and methodology employed have been successful in capturing the unsteady features of the flow field.

Acknowledgments

This work was undertaken in the Mechanical Engineering Department of Imperial College London, UK, during the doctoral research work of Dean Palfreyman. The authors would wish to thank the staff at Imperial College, in particular Nick Karamanis for access to the experimental data. Furthermore, the authors would wish to thank the Engineering and Physical Sciences Research Council (E.P.S.R.C) for their financial support, Fred Mendonca of the CD adapco Group for fruitful discussion and careful review of the manuscript, and Holset Engineering for general technical support.

Nomenclature

Pf = pulse frequency (Hz)
p = pressure (Pa)
T = temperature (K)
t = time (s)
ρ = density (kg/m^3)
u_i, V = velocity (m/s)
$\dot{m}$ = mass flow rate (kg/s)
h = specific enthalpy (J/kg)
Ω = rotational speed (radians/sec)
λ = pulse period
r = radius
f = force
$\hat{n}$ = unit vector
s = unit vector normal to boundary face
A = area
S = surface
R = gas constant (287 J/kg K)
γ = ratio of specific heats; $\gamma = C_p/C_v$
C_p = specific heat at constant pressure (J/kg K)
C_v = specific heat at constant volume (J/kg K)
PS = pressure surface
SS = suction surface
LE = leading edge
TE = trailing edge
τ = torque (nm)
Pr = pressure ratio
W = work (W)
η_{t-s} = total-static efficiency

Subscripts

isen = isentropic
inst = instantaneous
i, j, k = Cartesian coordinates x, y, z, respectively
act = actual
0 = stagnation
1 = turbocharger inlet
2 = turbocharger exit
B = boundary
P = cell center
∞ = free-steam

Superscripts

$\overline{X}$ (overbar) = ensemble/cycle averaged quantity
$\vec{X}$ = vector
X' = instantaneous

References

[1] Karamanis, N., 2000, ''Inlet and exit flow characteristics of mixed flow turbines in advanced automotive turbocharging,'' Ph.D. thesis, Imperial College of Science, Technology and Medicine, London, England.
[2] Dale, A., Watson, N., 1986, ''Vaneless Radial Turbocharger Turbine Performance,'' Proc. Inst. Mech. Eng., Part C: Mech. Eng. Sci., Proceedings of IMechE C110/86.
[3] Winterbone, D. E., Nikpour, B., and Alexander, G. I., 1990, ''Measurement of the Performance of a Radial Inflow Turbine in Conditional Steady and Unsteady Flow,'' Proc. Inst. Mech. Eng., Part C: Mech. Eng. Sci., Proceedings of IMechE C405/015.
[4] Winterbone, D. E., Nikpour, B., and Frost, H., 1991, ''A Contribution to the Understanding of Turbocharger Turbine Performance in Pulsating Flow,'' Proc. Inst. Mech. Eng., Part C: Mech. Eng. Sci., Paper: C433/011.
[5] Hakeem, I., 1995, ''Steady and unsteady performance of mixed flow turbines for automotive turbochargers,'' Ph.D. thesis, Imperial College of Science, Technology and Medicine, London, England.
[6] Su, C. C., 1999, ''Flow characteristics and performance of mixed flow turbines,'' Ph.D. Thesis, Imperial College of Science, Technology and Medicine, London, England.
[7] Karamanis, N., Martinez-Botas, R. F., and Su, C. C., 2000, ''Performance and Detailed Flow Measurements at the Inlet and Exit of a Mixed Flow Turbine Under Steady and Pulsating Flow Conditions,'' ASME J. Turbomach., **123**, pp. 359–371.
[8] Wallace, F. J., and Blair, G. P., 1965, ''The Pulsating-Flow Performance of Inward Radial-Flow Turbines,'' Gas Turbine Power Division, ASME 65-GTP-21.
[9] Kosuge, H., Yamanaka, N., Ariga, I., and Watanabe, I., 1976, ''Performance of Radial Flow Turbines Under Pulsating Flow Conditions,'' ASME J. Turbomach., Paper no. 75-GT-30.
[10] Winterbone, D. E., and Pearson, R. J., 1998, ''Turbocharger Turbine Performance Under Unsteady Flow–A Review of Experimental Results and Proposed Models, Sixth International Conference on Turbocharging and Air Management Systems,'' Proc. Inst. Mech. Eng., Part C: Mech. Eng. Sci., **1998-11**, C554/031/98.

[11] Baines, N. C., Hajilouy-Benisi, A., and Yeo, J. H., 1994, ''The Pulse Flow Performance and Modelling of Radial Inflow Turbines,'' Proc. Inst. Mech. Eng., Part C: Mech. Eng. Sci., Paper no. C484/006/94.
[12] Capobianco, M., Gambarotta, A., and Cipolla, G., 1989, ''Influence of the Pulsating Flow Operation on the Turbine Characteristics of a Small Internal Combustion Engine Turbocharger,'' Proc. Inst. Mech. Eng., Part C: Mech. Eng. Sci., Paper no. C372/019.
[13] Capobianco, M., Gambarotta, A., and Cipolla, G., 1990, ''Effect of Inlet Pulsating Pressure Characteristics on Turbine Performance of an Automotive Wastegated Turbocharger,'' SAE International Congress and Exposition, Detroit, Michigan, Paper no. 900359.
[14] Capobianco, M., and Gambarotta, A., 1990, ''Unsteady Flow Performance of Turbocharger Radial Turbines,'' Proc. Inst. Mech. Eng., Part C: Mech. Eng. Sci., Proceedings of IMechE C405/017.
[15] Yeo, J. H., and Baines, N. C., 1990, ''Pulsating Flow Behavior of a Twin-Entry Vaneless Radial-Flow Turbine,'' Proc. Inst. Mech. Eng., Part C: Mech. Eng. Sci., Proceedings of IMechE C405/004.
[16] Wallace, F. J. et al., 1970, ''Performance of Inward Radial Flow Turbines Under Non-Steady Flow Conditions,'' Proc. Inst. Mech. Eng., 184.
[17] Chen, H., and Winterbone, D. E., 1990, ''A Method to Predict Performance of Vaneless Radial Turbines Under Steady and Unsteady Flow Conditions,'' Proc. Inst. Mech. Eng., Part C: Mech. Eng. Sci., Proceedings of IMechE C405/008.
[18] Connor, W. A., and Swain, E., 1994, ''Extension of the Filling and Emptying Engine Performance Simulation Method to Include Gas Dynamic Effects,'' Proc. Inst. Mech. Eng., Part C: Mech. Eng. Sci., paper no. C484/042/94.
[19] Connor, W. A., and Flaxington, D., 1994, ''A One-Dimensional Performance Prediction Method for Radial Turbines,'' Proc. Inst. Mech. Eng., Part C: Mech. Eng. Sci., Proceedings of IMechE C484/041.
[20] Chen, H., Hakeem, I., and Martinez-Botas, R. F., 1996, ''Modelling of a Turbocharger Turbine Under Pulsating Inlet Conditions,'' Proc. Inst. Mech. Eng., 210.
[21] Lam, J. K.-W., Roberts, Q. D. H., and McDonnell, G. T., 2002, ''Flow Modelling of a Turbocharger Turbine under Pulsating Flow,'' Proc. Inst. Mech. Eng., Part C: Mech. Eng. Sci., Proceedings of IMechE C602/025/2002.
[22] Star-CD Methodology Guide Version 3.150, 2001, Computational Dynamics Ltd.
[23] Abidat, M., 1991, ''Design and testing of a highly loaded mixed flow turbine,'' Ph.D. thesis, Imperial College of Science, Technology and Medicine, London, England.
[24] Palfreyman, D., and Martinez-Botas, R. F., 2002, ''Numerical Study of the Internal Flow Field Characteristics in Mixed Flow Turbines,'' GT-2002-30372, Proceesing of ASME, IGTI.
[25] Yakhot, V., Orszag, S. A., Thangam, S., Gatski, T. B., and Speziale, C. G., 1992, ''Development of turbulence models for shear flows by a double expansion technique,'' Phys. Fluids A, **4**(7), pp. 1510–1520.
[26] Issa, R. I., 1986, ''Solution of the Implicitly Discretised Fluid Flow Equations by Operator-Splitting,'' J. Comput. Phys., **62**.

Influence of Stator Clocking on the Unsteady Three-Dimensional Flow in a Two-Stage Turbine

Dieter Bohn
e-mail: post-bohn@idg.rwth-aachen.de

Jing Ren

Institute of Steam and Gas Turbines,
Aachen University,
Templergraben 55,
D-52056 Aachen, Germany

Michael Sell
ALSTOM Power,
5401 Baden, Switzerland
e-mail: michael.sell@power.alstom.com

To give insight into the influence of the clocking and the stator–rotor interaction, the unsteady three-dimensional (3D) flow through a two-stage turbine is simulated numerically, using a time marching Navier–Stokes computer code with a sliding mesh approach. A stator clocking is applied to the second stator vane over several circumferential positions. The numerical results are compared with the experimental one to check the availability of the code. Clocking effects on the turbine performance, wake trajectories, and outlet flow field are focused. A relative efficiency variation of about 0.52% is concluded among clocking positions. A link between the turbine efficiency and the wake trajectories on the midspan is shown based on the presented clocking analysis in the 3D unsteady flow field. The detailed illustration of the outlet flow field shows that the influence of the clocking at the outlet is focused on the temperature distribution.
[DOI: 10.1115/1.1812780]

Introduction

An important goal in the development of turbine bladings is to enhance their efficiency for an optimized usage of energy resources. Clocking, or indexing, is currently an attractive technique and an effective way to improve the turbine efficiency. Such a technique operates on the relative circumferential positions of fixed and rotating blade rows in consecutive stages, and aims at performance improvement. The clocking affects the interaction of the wakes and the unsteady flow field from the upstream airfoil with the downstream airfoils. The strength of these interactions can therefore affect both performance and durability of the turbines. Deep insight into the unsteady complex three-dimensional (3D) flow phenomena in multistage turbines is helpful for understanding the clocking effect.

Both experimental and numerical investigations have shown how the time-averaged turbomachinery efficiency varies periodically with stator and rotor clocking positions [1,2]. The experimental results reported by Huber et al. [3] for a two-stage HP turbine showed a 0.8% efficiency variation due to clocking of the second-stage stator. A two-dimensional (2D) numerical analysis on the midspan performed by Griffin et al. [4] for the same turbine, correctly predicted the optimum clocking positions but the estimated efficiency variation was only 0.5%. It was demonstrated that the highest efficiencies occurred when the first-stator's wake impinged on the second-stator's leading edge while the lowest were observed when the first-stator's wake convected through the mid-passage region between the second-stator's airfoils [5]. Cizmas and Dorney [6] extended this conclusion to rotor clocking and multistage clocking. They investigated the effects of full clocking (i.e., simultaneously clocking stator and rotor rows) in a three-stage steam turbine. It was found that the clocking of the second stage gives larger efficiency variations than the clocking of the third stage. The benefit of rotor clocking was almost twice that of stator clocking.

Real flow in turbines is quite complex, being viscous, unsteady and three-dimensional. 3D unsteady calculations with the sliding mesh approach make it possible to model the aerodynamic interaction between the rotor and stator. Most often, the unsteady solution that is sought in a sliding mesh simulation is time-periodic. Although enormous computer resources are needed for this modeling, it simulates real flow the best of all.

In this paper, the unsteady 3D clocking flow through a two-stage turbine is simulated numerically, using a time marching Navier–Stokes computer code with a sliding mesh approach. A stator clocking is applied to the second stator vane over several circumferential positions. The numerical results are compared with the experimental one to check the availability of the code. The complex unsteady 3D flow phenomena in multistage turbines are analyzed in detail. The investigation focuses on the clocking effects upon the 3D unsteady flow field and turbine performance.

The Turbine Stages

Investigated Configuration. The investigated configuration is a two-stage test turbine with shrouded blading built up at the Institute of Steam and Gas Turbines, Aachen University [7]. Figure 1 shows the cross section of the axial air turbine test rig. It is supplied with air from compressors at a maximum inlet pressure of 3.2 bar with a mass flow of maximum 7.4 kg/s. In order to perform changes of the configuration the turbine is constructed in a modular way.

To shield the fluid flow through the blading, the test section is framed with a perforated plate at the inlet and a torsion body at the outlet of the turbine. The geometric data of the turbine and the operating conditions during the investigations are listed in Table 1.

Clocking Series. Figure 2 shows the airfoil cascades on the midspan. The trigger position of the rotors is marked by a line which represents the stator–rotor relative position at time $t=0$. The second stator is clocked in steps of 2.5° in a range of one stator pitch. As one stator pitch refers to 7.5°, three stator–stator clocking positions are received. They are indicated in Fig. 2 as S1, S2, S3, which correspond to 0°, 2.5°, 5.0°, respectively.

Numerical Scheme

The flow through a turbine is inherently unsteady. The aerodynamic interaction between the rotating part and the stationary parts is an important contributor to the unsteadiness of the flow. In order to predict the unsteady effects resulting from the rotor–stator interaction due to their relative position change, the tran-

Contributed by the International Gas Turbine Institute (IGTI) of THE AMERICAN SOCIETY OF MECHANICAL ENGINEERS for publication in the ASME JOURNAL OF TURBOMACHINERY. Paper presented at the International Gas Turbine and Aeroengine Congress and Exhibition, Vienna, Austria, June 13–17, 2004, Paper No. 2004-GT-53511. Manuscript received by IGTI, October 1, 2003; final revision, March 1, 2004. IGTI Review Chair: A. J. Strazisar.

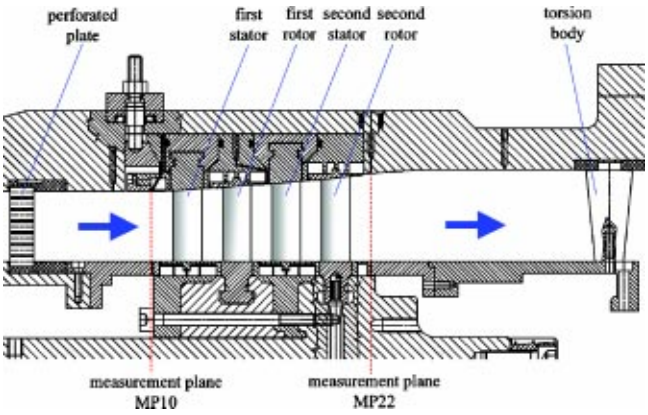

Fig. 1 Test rig

sient sliding mesh approach is implemented in the CHTflow solver, which is developed by the Institute of Steam and Gas Turbines at Aachen University. A sliding interface is used between the moving mesh of the rotor and the nonmoving mesh of the stator. During such a transient solution process, the moving mesh is forced to slide past the stationary one by a certain degree during each time step according to the defined rotation speed and the time step size. Flow information is exchanged continuously across the sliding interface. Due to the unsteady aerodynamic interaction and the coupling effects between the rotating component and the stationary ones, the flow field variation in both time and space, specifically in the circumferential direction, is fully taken into account in the transient sliding mesh approach.

The numerical scheme for the simulation of the fluid flow works on the basis of an implicit finite volume method combined with a multiblock technique for structured grids. The physical domain is divided into separate blocks, and the time-dependent, full, compressible, three-dimensional Navier–Stokes equations are solved in the fluid blocks. The governing equations for the conservative variables are developed in arbitrary body-fitted coordinates ξ, η, ζ with the fluxes in normal directions to ξ, η, ζ=const.

Table 1 Geometric data and operating conditions of the test turbine

average diameter at MP10	(mm)	410.5
average diameter at MP22	(mm)	434.5
vane height, stator, first stage	(mm)	60.5
vane height, rotor, second stage	(mm)	74.5
number of blade (rotor)	(-)	48
number of vane (stator)	(-)	48
inlet absolute pressure	(bar)	3.2
pressure ratio	(-)	1.4
inlet temperature	(K)	353.8
rotating speed	(rpm)	4763.0

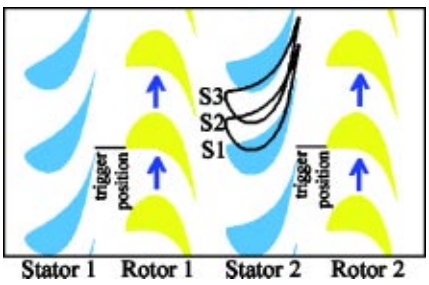

Fig. 2 Stage configurations on the midspan

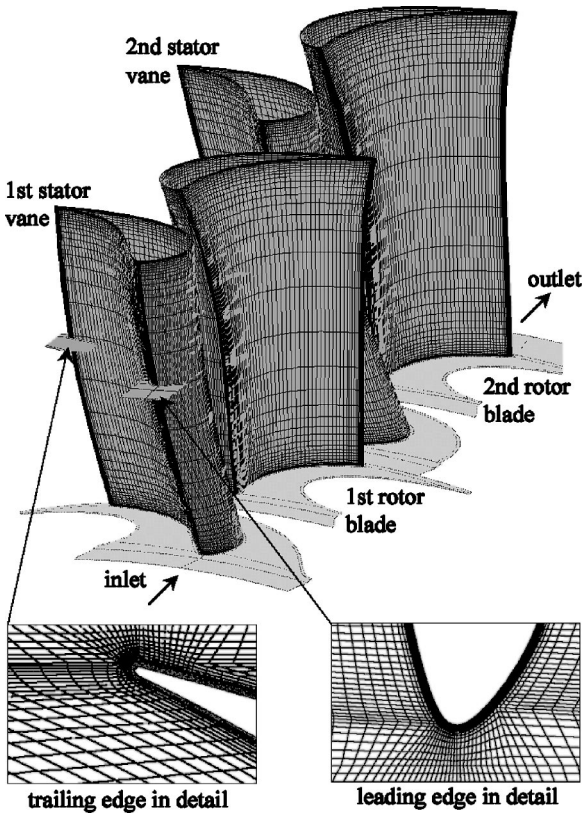

Fig. 3 Computational grid

The conservation equations are discretized implicitly first order in time using Newton's method [8]. Upwind discretization is used for the inviscid fluxes [9] and a Godunov-type flux differencing is employed for the numerical diffusion. In order to achieve third-order accuracy, van Leer's MUSCL-technique [10] is used. Since this Godunov flux is not sufficiently diffusive to guarantee stability in regions with high gradients, it is combined with a hyper-diffusive modified Steger–Warming flux. The viscous fluxes are approximated using central differences. The resulting system of linear equations is solved by a Gauss–Seidel point iteration scheme. The closure of the conservation equations is provided by the algebraic eddy-viscosity turbulence model by Baldwin and Lomax [11].

As the vane/blade number ration is 1/1, the passage between two adjacent stator vanes and two adjacent rotor blades is included in the solution domain. Figure 3 gives an impression of the numerical grids. In order to discretize the boundary layer of the blade flow, an O-block has been laid around the blade surface. For the main flow section several H-blocks have been used. The full size of the 3D grid is about 1.3 million grid points. The boundary conditions have been derived from experimental data.

Numerical Results at the Clocking Position S1 and Comparison With the Experiment

Entropy Distribution. Animation of the entropy distribution is performed in order to obtain significant information that will improve the understanding of the physical phenomena involved in the turbomachinery. The entropy generation rate comes from the blade boundary layer and the profile loss, as well as the wake region. Therefore, entropy distribution is usually used to track the wake in the flow passage.

Based on the computed flow field, the local entropy in the passage is calculated according to

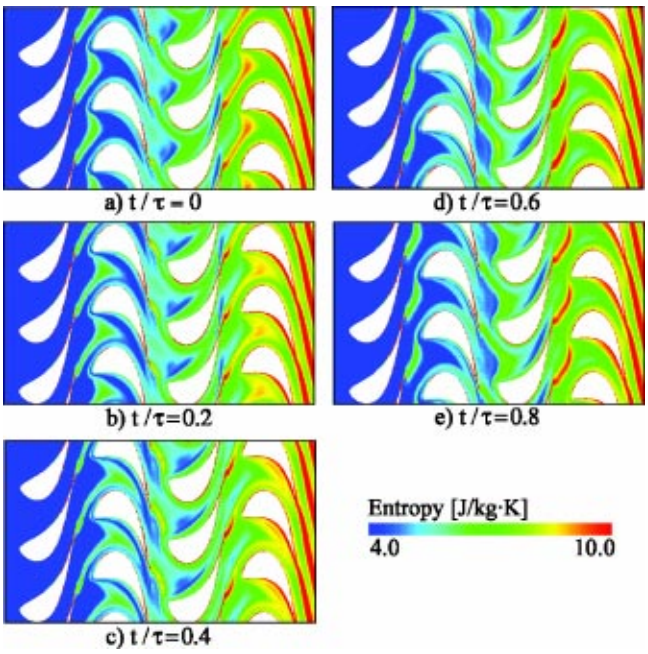

Fig. 4 Entropy distribution on the midspan section at the clocking position S1

$$\Delta s = c_p \ln\left(\frac{T}{T_0}\right) - R \ln\left(\frac{p}{p_0}\right) \tag{1}$$

where s is the entropy, T is the temperature, p is the static pressure, while T_0 and p_0 are the reference temperature and the reference pressure.

As the unsteady solution is time periodic, five dimensionless times $t/\tau(0.0,0.2,0.4,0.6,0.8)$ during one blading passing period are chosen to show the results. Here, τ is one blade passing period. Figure 4 shows the entropy distribution at the series of five predictions on the midspan at the clocking position S1.

In Fig. 4, wake trajectories are clear and distinct in the entropy contours. While the first-stator's wake enters the adjacent rotor passage, it is accelerated in an axial direction in the midpitch region between neighbored blades. It forms a bowed contour, which adapts to the profile boundary layer and further downstream to the rotor's wake. It is very similar to the 2D wake trajectories described by Arnone et al. and Dorney et al. [12,13]. The pressure gradient in the axial direction is the main source for this behavior. Wakes from other rotors and stators show a similar behavior. Wakes sweep one pitch of the next stator or rotor with different structures and magnitudes while the rotor moves. Unsteadiness of the wake trajectories is, therefore, very significant in the turbine stages. Wake losses, boundary layer losses, and the profile losses make the entropy reach the maximum value at the outlet.

Figure 5 illustrates the entropy distributions on an axial section between the first stator and the first rotor. There is a high entropy zone on the axial section, which looks like a bow bent from the hub and tip to the midspan. It is formed by the first-stator's wake on this section. The bend might be caused by the influence of the endwalls and the shape of the vane trailing edge. The corner vortex near the tip at the first-rotor's inlet is also a possible reason. Both shape and position of the bow vary with the relative movement of the first rotor. The high entropy zone reaches the highest entropy value when the leading edge of the first rotor meets the trailing edge of the first stator $[t/\tau=0.8$, see Fig. 5(e)]. At this time, the high entropy zone is bowed the most. It means the relative position between the adjacent vane and blade has a strong influence on the strength and the shape of the wake trajectories.

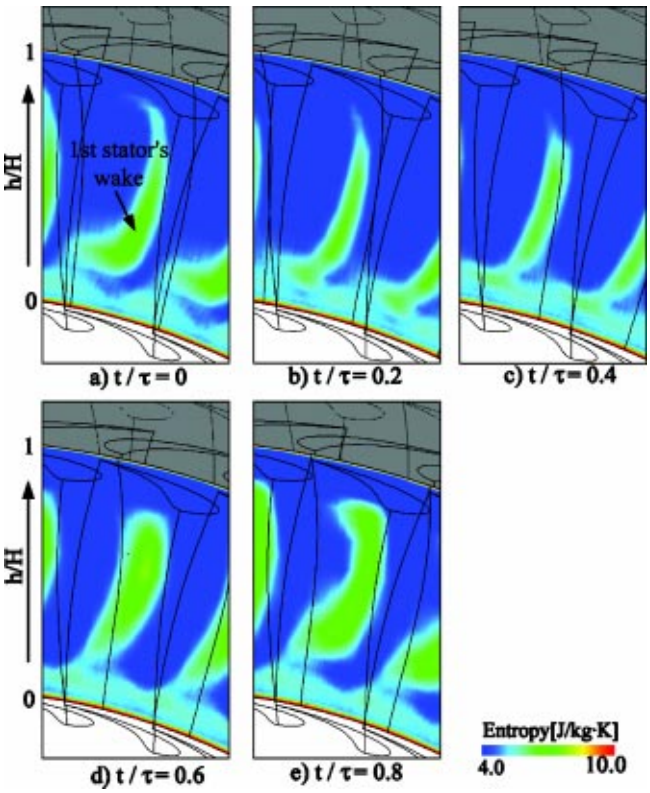

Fig. 5 Entropy distribution on an axial section between the first stator and the first rotor at the clocking position S1

Figure 6 shows the entropy distributions on an axial section between the first rotor and the second stator. There are two high entropy zones on this axial section, which are corresponding to the wakes of the first rotor and the first stator, respectively. The entropy distribution shows a strong 3D effect. Along the radial direction, the high entropy zones are bowed from hub and tip to the midspan. The first-rotor's wake is much stronger near the hub than near the tip. Meanwhile, the bowed zones also show a strong unsteadiness. Shapes and positions of both bowed zones vary while the first rotor moves. Due to the 3D shape of the blades and the interaction between the two wakes, the entropy distribution on this section is more complex than the former one in Fig. 5. The high entropy zone caused by the first-rotor's wake reaches the highest value near the hub when the second-stator's vanes near the hub meet the first-rotor's blades $[t/\tau=0.4$, see Fig. 6(c)]. The first-stator's wake is influenced by the first-rotor's wake strongly so that its behavior is not very obvious.

In order to show the 3D effect of wake trajectories more clearly, Fig. 7 gives a view on the wake transport at three different radial positions at $t/\tau=0.2$ (clocking position S1). The first-stator's wake is indicated by black arrows in Fig. 7 at different radial positions. The entropy contours reveal that the wakes show different structures and behaviors along the radius at the same time. It is mainly caused by the 3D shape of the blades/vanes. On the radial section near the hub $(h/H=15\%)$, the wake structure exhibits higher entropy values due to the endwall losses. But, it is not so evident on the radial section near the tip $(h/H=85\%)$.

Temperature Distribution. In order to have more understanding of the 3D unsteady behavior of the flow in the multistage turbine, the temperature distributions on an axial section between the first rotor and the second stator at the clocking position S1 are shown in Fig. 8.

The temperature distributions also show strong 3D and unsteady effects. The temperature near the hub is much higher than

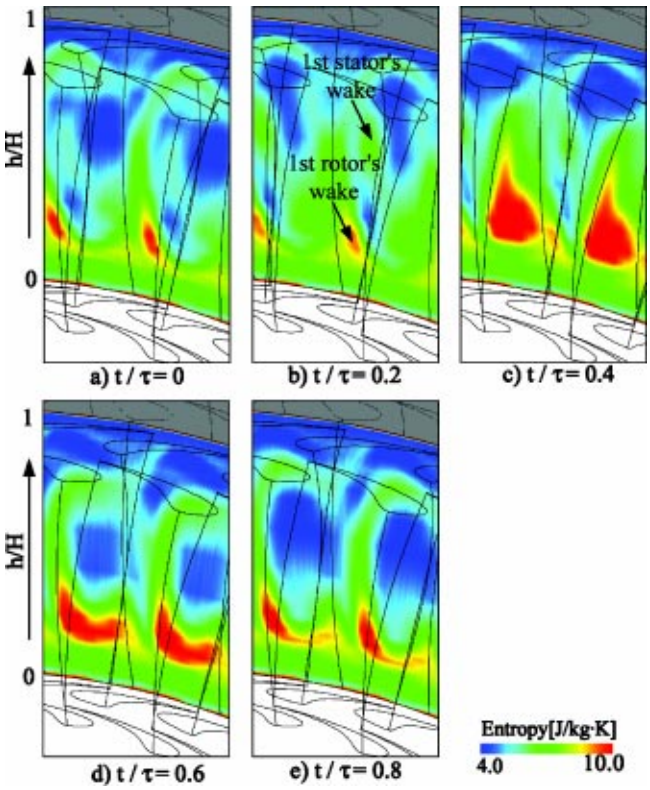

Fig. 6 Entropy distribution on an axial section between the first rotor and the second stator at the clocking position S1

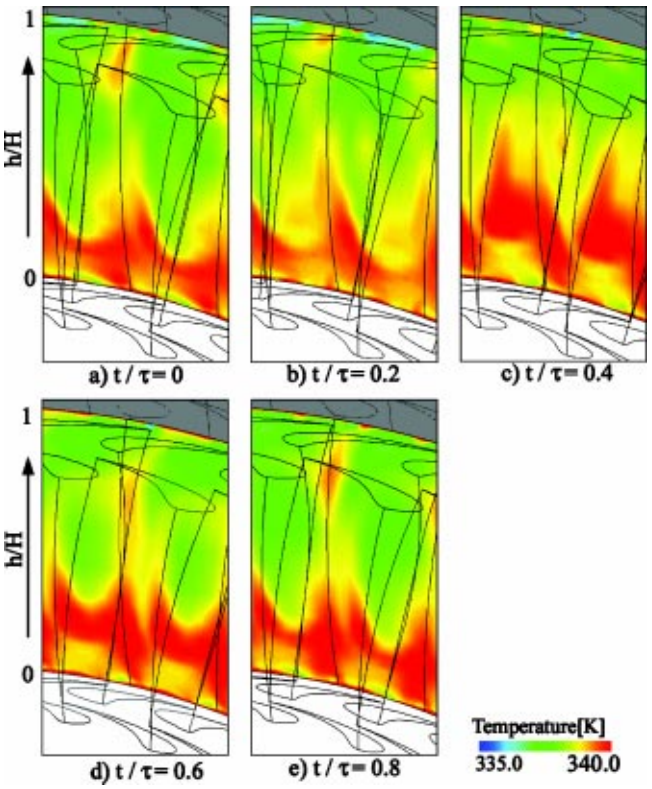

Fig. 8 Temperature distribution on an axial section between the first rotor and the second stator at the clocking position S1

the tip. It reaches the highest value near the hub when the second-stator's vanes near the hub meet the first-rotor's blades [$t/\tau = 0.4$, see Fig. 8(c)]. The temperature near the tip arrives at the highest value while the second-stator's vanes near the tip meet the first-rotor's blades [$t/\tau = 0.8$, see Fig. 8(e)]. It is very similar to what has been found in the entropy distributions in Fig. 6. It implies that the temperature has a stronger influence on the entropy than the pressure.

Comparison With the Experiment. A comparison between the numerical and experimental data of the investigated turbine at the clocking position S1 is shown in Fig. 9. The time and circumferentially averaged numerical values of the total pressure are compared to the steady probe measurements at the measurement plane MP22.

The 3D unsteady result is illustrated as a red line in Fig. 9. A corresponding steady result is shown too by a blue line, which is sourced from Bohn et al. [7]. The unsteady computed total pressure is slightly under-predicted in the middle part of the passage. But it predicts the flow features near the hub and the tip much better than the steady calculation. In particular, the unsteady result shows a peak near the tip, which has a good agreement with the experimental data. Generally speaking, the unsteady results are more consistent with the experimental results than the steady results. The improvement owes to the consideration of the stator–rotor interaction in the unsteady analysis.

Hence, the implemented 3D unsteady algorithm with the sliding mesh approach is available to analyze the clocking effects in the turbines. Further investigations will be done in the future to check the validation of the developed numerical algorithm.

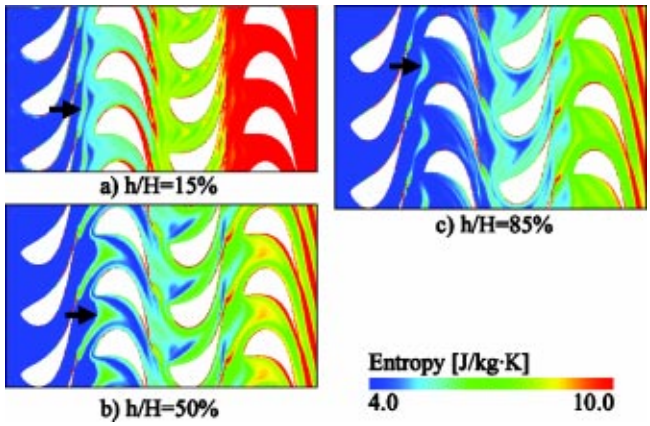

Fig. 7 Entropy distribution on three radial sections ($t/\tau = 0.2$, clocking position S1)

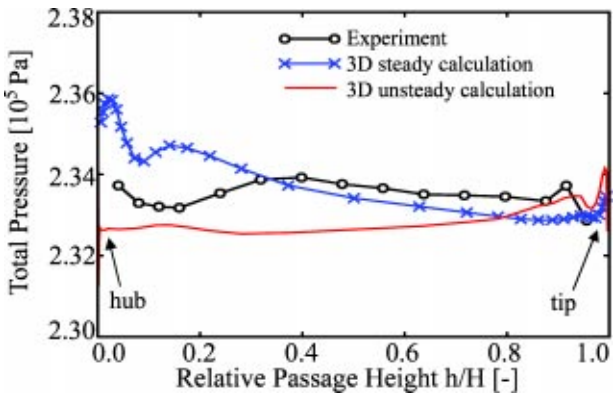

Fig. 9 Comparison of the total pressure distribution at measurement plane MP22

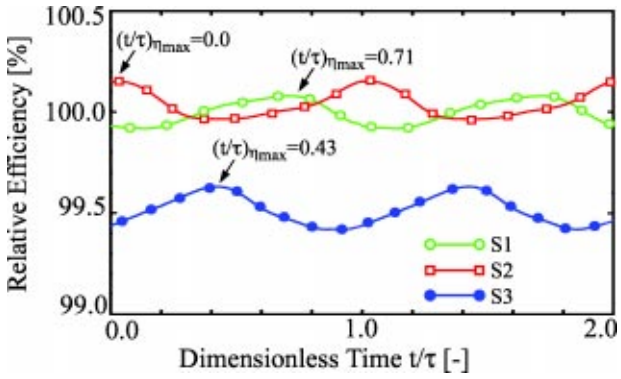

Fig. 10 Relative efficiency courses at three clocking positions

Clocking Effects

Effect on Efficiency. In the presented investigation, the total-to-total efficiency η is defined as

$$\eta = \frac{\gamma}{\gamma - 1} \frac{\ln(T_2/T_1)}{\ln(p_2/p_1)} \tag{2}$$

where T_1 and T_2 are the mass averaged temperatures at the inlet and the outlet, p_1 and p_2 are the mass averaged static pressures at the inlet and the outlet, and γ is the specific heat ratio.

As the unsteady solution is time periodic, the total-to-total relative efficiency course during two blade passing periods is presented in Fig. 10. The variation of the parameter is therefore shown more clearly. The relative efficiency is defined as

$$\eta^* = \eta / \eta_0 \tag{3}$$

where η_0 is the reference efficiency, defined as the time averaged total-to-total efficiency at the clocking position S1 in the presented work.

It is shown in Fig. 10 that clocking causes a shift of the relative efficiency course with time among three clocking positions. The maximum efficiency occurs when dimensionless time t/τ equals 0.71, 0.0, and 0.43 at the clocking positions S1, S2, and S3, respectively.

The averaged total-to-total relative efficiency η^*_{av} is calculated as the averaged value of the relative efficiency in one blade passing period. It is clear from Table 2 and Fig. 11 that the maximum efficiency occurs at the clocking position S2 while the minimum one at the clocking position S3. Therefore, clocking position S2 is the optimized clocking position considering efficiency.

Table 2 Averaged relative efficiency distributions

Clocking positions	Averaged relative efficiency η^*_{av} [%]
S1	100.00
S2	100.04
S3	99.52

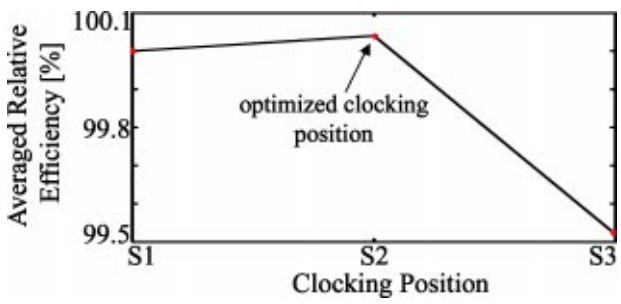

Fig. 11 Averaged relative efficiency distribution

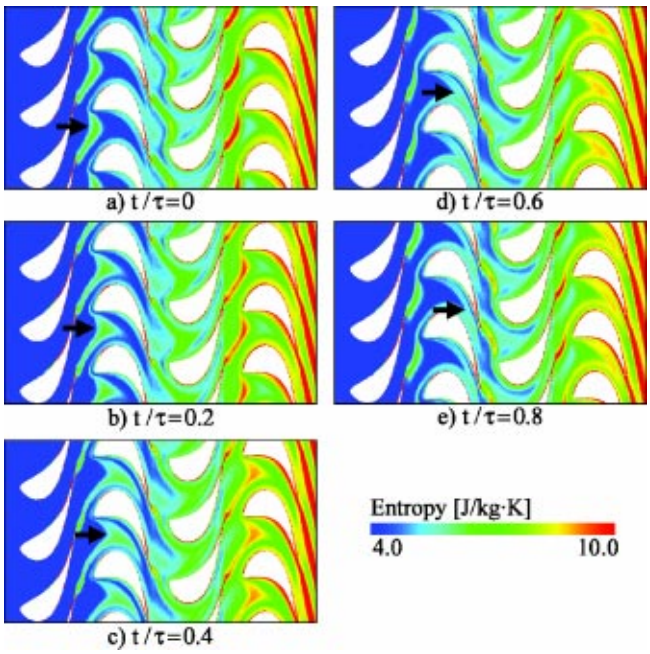

Fig. 12 Entropy distribution on the midspan at the clocking position S2 (η_{max})

The clocking effect is indicated by the averaged relative efficiency difference $\Delta\eta^*_{av}$, which is defined as

$$\Delta\eta^*_{av} = \eta^*_{av} - (\eta^*_{av})_{min} \tag{4}$$

where $(\eta^*_{av})_{min}$ is the minimum value of the averaged relative efficiency among the three clocking positions. It results from Table 2 that the maximum averaged relative efficiency difference is 0.52% in the investigated stator clocking. It is of the same order as the results in the literature [2,4,12].

Effect on Wake Trajectories. Clocking effects seem to be linked to wake trajectories in some way. Numerical results of 2D clocking analysis obtained by many authors with different numerical methods and turbulence models suggest that the maximum efficiencies can be achieved when the wake generated by a stator/rotor blade impinges on the leading edge of the next stator/rotor blade. Minimum efficiency is corresponding to a wake trajectory crossing the next stator/rotor vane's midpassage.

One explanation for the correlation between the first-stator's wake location and the efficiency is that when the first-stator's wake impinges on the second-stator's airfoils a low momentum fluid is being introduced into a region where the fluid momentum is already low, whereas when the wakes are located in the midpassage region low-momentum fluid is being introduced to a region of high-momentum fluid [13]. The latter causes higher losses and, therefore, lower efficiency.

Figures 12 and 13 give the unsteady wake trajectories by the entropy contours at the clocking positions S2 and S3, which are of the maximum and minimum turbine efficiency, respectively.

The unsteady entropy contours in Figs. 12 and 13 show how each stator's wake bows, shears, and stretches on the midspan, while being convected through the rotor vane. In the clocking position S2 (maximum efficiency position), the first-stator's wake that is indicated by the black arrows in Fig. 12 impinges on the second stator's leading edge. In the clocking position S2 (minimum efficiency position), the first-stator's wakes that are indi-

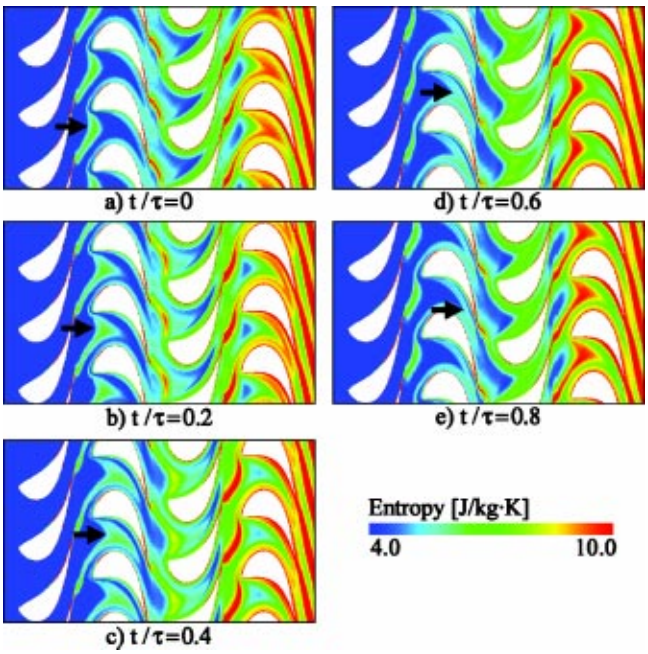

Fig. 13 Entropy distribution on the midspan at the clocking position S3 (η_{min})

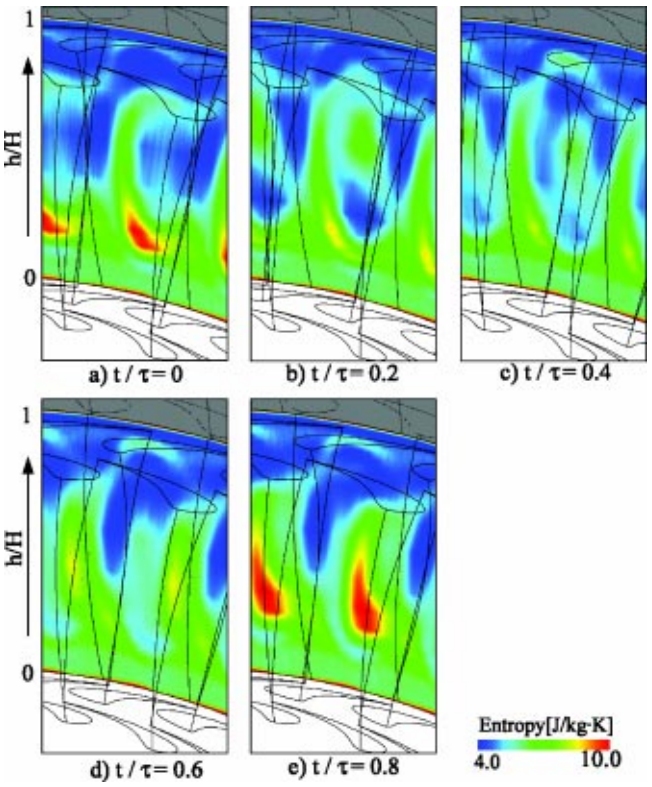

Fig. 14 Entropy distribution on an axial section between the first rotor and the second stator at the clocking position S2 (η_{max})

cated by the black arrows in Fig. 13 is convected along the mid-passage. The same situation has been observed in the rotor/rotor wake interaction.

It implies that a link between the wake trajectories on the midspan and the turbine efficiency may exist in the 3D clocking phenomena. The link which has been proved in the 2D clocking phenomenon can be extended to the 3D clocking case as: the maximum turbine efficiencies can be achieved at the clocking position in which the wake generated by a stator/rotor blade on the midspan impinges on the leading edge of the next stator/rotor blade; the minimum turbine efficiency results at the clocking position at which a wake trajectory on the midspan crosses the next stator/rotor vane's mid-passage.

But, because of the 3D shape of the blade, the wake trajectories may have different behavior from the hub to the tip, which has been shown in Fig. 7. The efficiency of the turbine should take into account the influence of the wake along the whole passage height. Therefore, such a link in the 3D clocking partly depends on the 3D shape of the blades. Further investigations are worth while to address the available scope of the link between the wake trajectories on the midspan and the turbine efficiency.

Figures 14 and 15 illustrate the entropy distributions on the axial sections between the first rotor and the second stator at the clocking position S2 and S3, respectively. The 3D and unsteady behavior of the entropy distribution are obvious in both figures.

Due to the clocking of the second stator, the maximum entropy of the first-rotor's wake shifts to $t/\tau=0.8$ [Fig. 14(e)] and $t/\tau=0.2$ [Fig. 15(b)] at the clocking positions S2 and S3, respectively. The maximum entropy of the first-stator's wake seems to occur at $t/\tau=0.2$ [Fig. 14(b)] and $t/\tau=0.6$ [Fig. 15(d)] at the clocking positions S2 and S3, respectively.

Comparing the entropy distribution in the clocking positions S2 and S3 [in the sequence: Fig. 14(e) with Fig. 15(b), Fig. 14(a) with Fig. 15(c), Fig. 14(b) with Fig. 15(d), Fig. 14(c) with Fig. 15(e), Fig. 14(d) with Fig. 15(a)], it is noticed that the entropy value at the clocking position S2 (η_{max}) is always lower than that at the clocking position S3 (η_{min}). It proves that the clocking affects the efficiency strongly by varying the wake properties.

Effect on Outlet Flow. Figures 16, 17, 18, and 19 describe the circumferentially and the time averaged static pressure, velocity magnitude, temperature, and relative efficiency distributions on the measurement plane MP22, respectively. The parameters' distributions at three clocking positions are compared with each other in every graph in order to check the influence of the clocking on the outlet flow field.

It is clear that the clocking influences the static pressure and the velocity magnitude (Figs. 16 and 17) only in the regions near the hub and the tip. In the middle part of the passage (the relative height h/H is larger than 0.2 and smaller than 0.8), clocking almost has no effect on the static pressure and velocity magnitude at the outlet.

The effect of the clocking is most evident on the temperature distribution at the outlet, which is clear and obvious in Fig. 18. The clocking position S2, the maximum efficiency clocking position, has the lowest temperature in the main part along the passage height. Meanwhile, the clocking position S3, the minimum efficiency clocking position, has the highest temperature along the whole passage height except at the hub and the tip. Correspondingly, the relative efficiency along the relative passage height in Fig. 19 shows a higher value at the clocking position S2 and a lower one at the clocking position S3.

Conclusion

In the present paper, 3D unsteady numerical investigation in a two-stage turbine has been implemented with a sliding mesh approach. The complex 3D unsteady flow fields are illustrated and analyzed in detail. Wake trajectories as well as the temperature distributions at different sections show strong 3D and unsteady effects. Wake trajectories on radial section of 3D unsteady flow field have a similar behavior to that of 2D unsteady calculation. Wake trajectories on axial section show strong 3D and unsteady behavior. The relative position of the adjacent vane and blade has

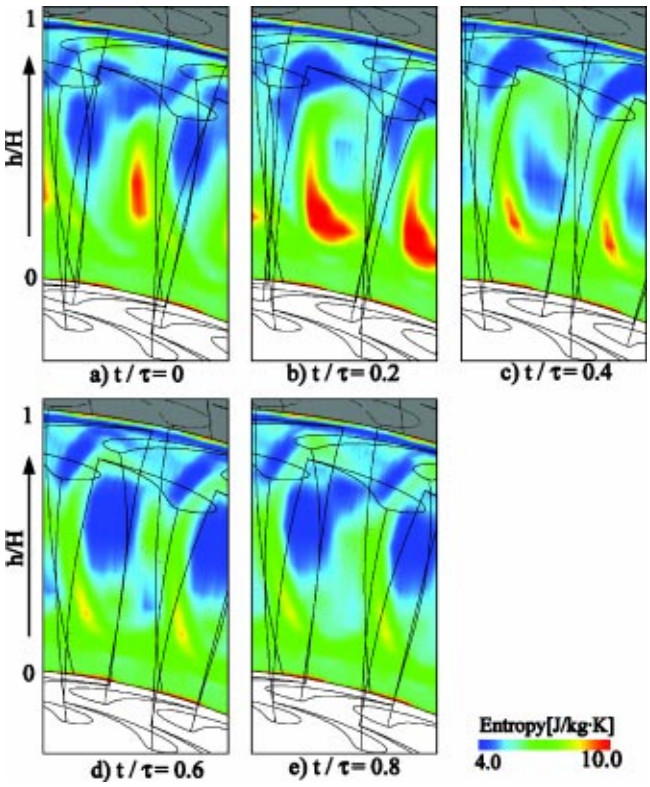

Fig. 15 Entropy distribution on an axial section between the first rotor and the second stator at the clocking position S3 (η_{min})

a strong influence on the wake strength and shape. By comparing with experimental results, the availability of the implemented 3D unsteady algorithm is shown.

A stator clocking is investigated based on the implemented 3D unsteady algorithm. Clocking effects on efficiency, wake trajectories, and the outlet flow are analyzed in detail. The efficiency estimation shows a relative efficiency variation of about 0.52% among the investigated clocking positions.

The presented investigation implies that a link between the wake trajectories on the midspan and the turbine efficiency may exist in the 3D clocking phenomena. It is described as: the maximum turbine efficiencies can be achieved at the clocking position in which the wake generated by a stator/rotor blade on the midspan impinges on the leading edge of the next stator/rotor blade;

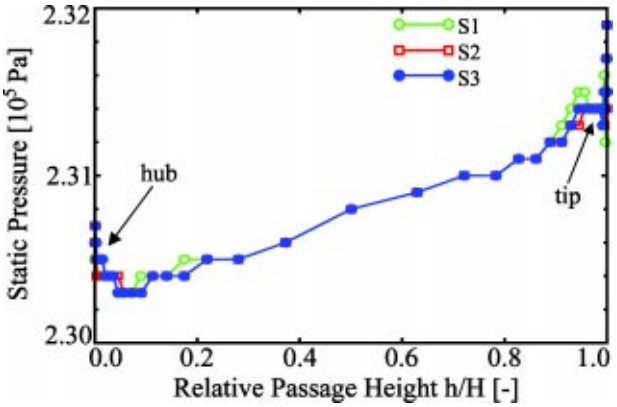

Fig. 16 Static pressure distribution on the measurement plane MP22

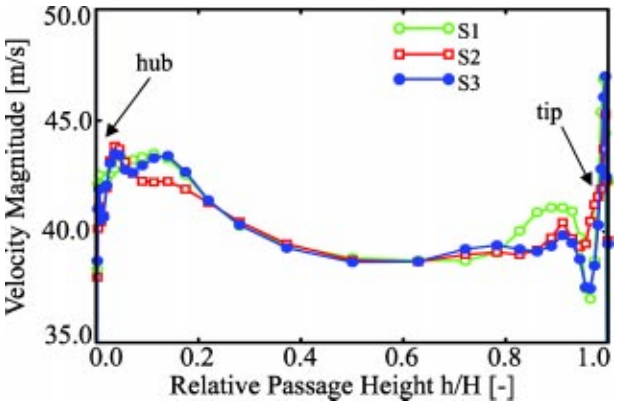

Fig. 17 Velocity magnitude on the measurement plane MP22

the minimum turbine efficiency results at the clocking position at which a wake trajectory on the midspan crosses the next stator/rotor vane's midpassage. But, because of the 3D shape of the blade, the wake trajectories may have different behavior from the hub to the tip. Therefore, such a link in the 3D clocking partly depends on the 3D shape of the blades. More investigations are worth contributing to discuss the available scope of the link between the wake trajectories on the midspan and the turbine efficiency.

The detailed illustration of the outlet flow field shows that the clocking almost has no influence on the static pressure and the velocity magnitude along the passage height, except the region

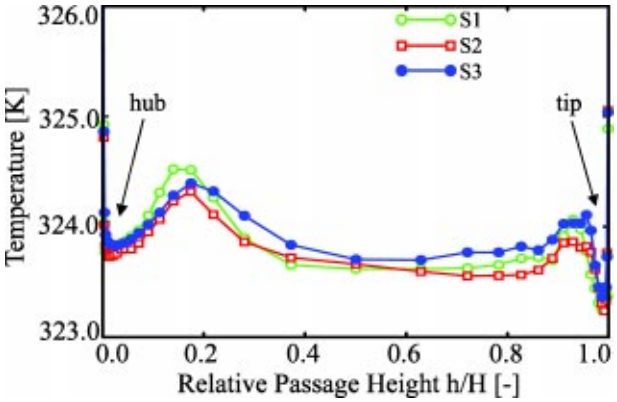

Fig. 18 Temperature distribution on the measurement plane MP22

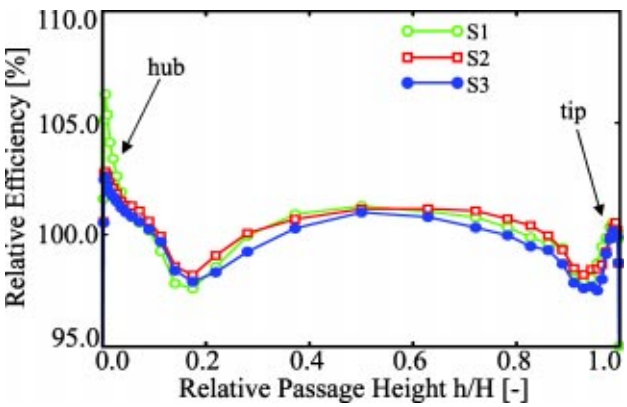

Fig. 19 Relative efficiency distribution on the measurement plane MP22

near the hub and tip. Its influence is most evident on the temperature distribution. Hence, clocking influences the efficiency of the turbines.

Acknowledgments

The investigation was performed as a part of the joint research program ''500 MW auf einer Welle (AG Turbo)''. The work was supported by the Bundesministerium für Wirtschaft (BMWI) under File No. 0327061E. The authors gratefully acknowledge AG Turbo and ALSTOM Power for their support and permission to publish this paper. Gratitude also to Christian Tümmers for his work on the numerical calculations and visualization. The responsibility for the content lies with the authors.

Nomenclature

c_p = specific heat (J/kg/K)
H = passage height (m)
h = passage height coordinate (m)
MP10 = measurement plane upstream of the first stage
MP22 = measurement plane downstream of the second stage
p = pressure (Pa)
R = gas constant
S1, S2, S3 = clocking positions
S = entropy (J/kg/K)
T = temperature (K)
t = time (s)

Greek Letters

ξ, η, ζ = arbitrary body-fitted coordinate (m)
η = total-to-total efficiency
γ = specific heat ratio
τ = blade passing period (s)

Subscripts

0 = reference
1 = inlet
2 = outlet
av = averaged
min = minimum
* = relative

References

[1] Eulitz, F., Engel, K., and Gebing, H., 1996, ''Numerical Investigation of the Clocking Effects in a Multistage Turbine,'' ASME paper no. 96-GT-26, Birminghan, UK.
[2] Reinmoeller, U., Stephan, B., Schmidt, S., and Niehuis, R., 2001, ''Clocking Effects in a 1.5 Stage Axial Turbine—Steady and Unsteady Experimental Investigations Supported by Numerical Simulations,'' *Proceedings of ASME TURBOEXPO 2001*, 2001-GT-0304, June 4–7, 2001, New Orleans, LA.
[3] Huber, F. W., Johnson, P. D., Sharma, O. P., Staubach, J. B., and Gaddis, S. W., 1996, ''Performance Improvement Through Indexing of Turbine Airfoils: Part I—Experimental Investigation,'' ASME J. Turbomach., **118**, pp. 630–635.
[4] Griffin, L. W., Huber, F. W., and Sharma, O. P., 1996, ''Performance Improvement Through Indexing of Turbine Airfoils: Part II—Numerical Simulation,'' ASME J. Turbomach., **118**, pp. 636–642.
[5] Dorney, D. J., Sharma, O. P., and Gundy-Burlet, K. L., 1998, ''Physics of Airfoil Clocking in a High-Speed Axial Compressor,'' ASME paper no. 98-GT-082.
[6] Cizmas, P., and Dorney, D., 1998, ''Parallel Computation of Turbine Blade Clocking,'' AIAA paper no. 98-3598.
[7] Bohn, D., Balkowski, I., Ma, H., Tümmers, C., and Sell, M., 2003, ''Influence of Open and Closed Shroud Cavities on the Flowfield in a 2-Stage Turbine With Shrouded Blades,'' GT2003-38436.
[8] Schmatz, M. A., 1988, ''Three-Dimensional Viscous Flow Simulations Using an Implicit Relaxation Scheme,'' *Notes on Numerical Fluid-Mechanics (NNFM)*, Vieweg, Braunschweig, Vol. 22, pp. 226–242.
[9] Eberle, A., Schmatz, M. A., and Bissinger, N., 1990, ''Generalized Flux Vectors for Hypersonic Shock-Capturing,'' AIAA paper no. 90-0390.
[10] Anderson, W. K., Thomas, J. L., and van Leer, B. A., 1985, ''Comparison of Finite Volume Flux Vector Splitting for the Euler Equations,'' AIAA paper no. 85-0122.
[11] Baldwin, B. S., and Lomax, H., 1978, ''Thin Layer Approximation and Algebraic Model for Separated Turbulent Flows,'' AIAA paper no. 78-257.
[12] Arnone, A., Marconcini, M., Pacciani, R., Schipani, C., and Spano, E., 2001, ''Numerical Investigation of Airfoil Clocking in a Three-Stage Low Pressure Turbine,'' ASME paper no. 2001-GT-0303, New Orleans, LA.
[13] Dorney, D. J., Croft, R., Sondak, D., Stand, U., and Twardochleb, C., 1998, ''Computational Study of Clocking an Embedded Stage in a 4-Stage Industrial Turbine,'' ASME paper no. 2001-GT-0509.

Heat Transfer in Two-Pass Rotating Rectangular Channels (AR=1:2 and AR=1:4) With 45 Deg Angled Rib Turbulators

Wen-Lung Fu

Lesley M. Wright

Je-Chin Han
e-mail: jchan@mengr.tamu.edu

Department of Mechanical Engineering,
Turbine Heat Transfer Laboratory,
Texas A&M University,
College Station, Texas 77843-3123, USA

*This paper reports the heat transfer coefficients in two-pass rotating rectangular channels (*AR*=1:2 and* AR*=1:4) with rib roughened walls. Rib turbulators are placed on the leading and trailing walls of the two-pass channel at an angle of 45 deg to the flow direction. Four Reynolds numbers are considered from 5000 to 40 000. The rotation numbers vary from 0.0 to 0.3. The ribs have a 1.59 by 1.59 mm square cross section. The rib height-to-hydraulic diameter ratios (e/D_h) are 0.094 and 0.078 for* AR*=1:2 and* AR*=1:4, respectively. The rib pitch-to-height ratio (P/e) is 10 for both cases, and the inlet coolant-to-wall density ratio ($\Delta\rho/\rho$) is maintained around 0.115. For each channel, two channel orientations are studied, 90 deg and 45 deg with respect to the plane of rotation. The results show that the rotation effect increased the heat transfer on trailing wall in the first pass, but reduced the heat transfer on the leading wall. For* AR*=1:4, the minimum heat transfer coefficient was 25% of the stationary value. However, the rotation effect reduced the heat transfer difference between the leading and trailing walls in the second pass.* [DOI: 10.1115/1.1791649]

1 Introduction

Advanced gas turbines operate at high temperatures to improve thermal efficiency. The high inlet temperature creates thermal stresses on the blades which can be detrimental to the operation of the engine. In order to achieve reasonable durability goals, improved cooling techniques, such as film cooling and internal cooling, are applied to turbine blades. Internal cooling is achieved by circulating compressed air in multipass flow channels inside the blade structure. To increase the heat transfer within the internal cooling channels, the internal surfaces usually are roughened by angled ribs to trip the boundary layer and increase turbulence. As the turbine blade rotates, Coriolis and buoyancy forces cause different heat transfer behavior on the leading and trailing surfaces. The typical geometry of turbine blade internal cooling passages is shown in Fig. 1. Different channel aspect ratios with roughened walls are used to achieve the cooling goals. A comprehensive review of turbine blade internal cooling can be found in the book by Han et al. [1]

Earlier studies on cooling passages were primarily based on stationary models. However, stationary models neglect the Coriolis and buoyancy effects which alter the velocity, turbulence, and temperature distributions. Metzger and Sahm [2] studied forced convection in a smooth rectangular channel by varying the divider location and the gap at the 180 deg turn. Fan and Metzger [3] extended the work by Metzger and Sahm by varying the channel width. They concluded that increasing the channel aspect ratio results in smaller azimuthal heat transfer variations and increases overall channel heat transfer. Han et al. [4] studied the local heat/mass transfer distribution in a nonrotating two-pass ribbed channel. Han and Zhang [5] studied the effect of rib-angle orientation on the local heat/mass transfer distribution in a nonrotating three-pass rib-roughened channel. It was observed that the rib angle, rib orientation, and the sharp 180 deg turn significantly affect the local heat/mass transfer distributions. The combined effects of these parameters increased and decreased the local heat/mass transfer coefficients after the sharp 180 deg turns. Han et al. [6] studied the effect of the rib-angle orientation on heat transfer distributions and pressure drop in a nonrotating square channel with opposite, in-line ribbed walls. They found that the 60 deg and 45 deg V-shaped ribs perform better than the 60 deg and 45 deg crossed ribs and 90 deg transverse ribs. Ekkad and Han [7] performed a detailed study on heat transfer characteristics in a nonrotating square channel with a sharp 180 deg turn using a transient liquid crystal technique. One wall of the channel had periodically placed rib turbulators. Four different configurations of 90 deg parallel, 60 deg parallel, 60 deg V-shaped, and 60 deg inverted V-shaped ribs were discussed. Ekkad et al. [8] repeated the same experiment, but with bleed holes placed between the ribs. They confirmed that the 60 deg V-shaped ribs performed better than the 60 deg parallel and 60 deg inverted V-shaped ribs.

Experiments with rotation have been conducted to more closely model engine cooling environments. Wagner et al. [9,10] conducted a detailed experimental study to determine the effects of rotation (buoyancy and Coriolis forces) on the local heat transfer of a multipass square channel with smooth walls. They concluded that the first pass of the coolant passage with rotation created a thinner boundary layer on the trailing surface and a thicker boundary layer on the leading surface resulting in increased heat transfer and decreased heat transfer, respectively. In the second pass the performance was different and opposite that of the first pass. The leading surface Nusselt number ratios in the second pass were higher than the trailing surface Nusselt number ratios because of the reversal of the Coriolis force direction. Taslim et al. [11,12] investigated the heat transfer distribution in square and rectangular rib roughened channels under rotation. They found that the effects of rotation were more apparent in rib-roughened channels with a larger channel aspect ratio and a lower rib blockage ratio. Johnson et al. [13] performed a parametric experiment to investigate the effects of buoyancy and Coriolis forces on the heat transfer coefficient distribution of four-pass square channels with 45

Contributed by the International Gas Turbine Institute (IGTI) of THE AMERICAN SOCIETY OF MECHANICAL ENGINEERS for publication in the ASME JOURNAL OF TURBOMACHINERY. Paper presented at the International Gas Turbine and Aeroengine Congress and Exhibition, Vienna, Austria, June 13–17, 2004, Paper No. 2004-GT-53261. Manuscript received by IGTI, October 1, 2003; final revision, March 1, 2004. IGTI Review Chair: A. J. Strazisar.

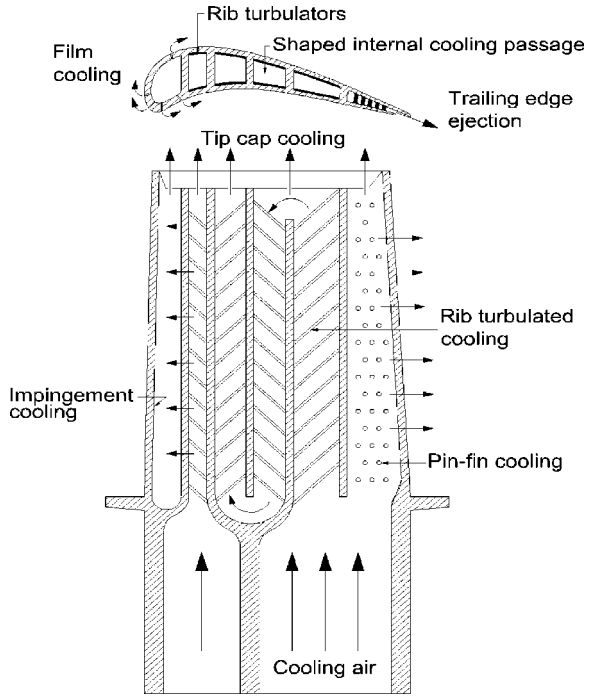

Fig. 1 Typical turbine blade internal cooling passages

deg angled ribs. Johnson et al. [14] conducted experimental work to determine the effects of channel orientation with respect to axis of rotation as well as buoyancy and Coriolis forces on heat transfer in turbine blade internal coolant passages. The experiments were conducted with rotation in both directions to simulate serpentine coolant passages with the rearward flow of coolant or with the forward flow of coolant. They concluded that both the rotation and channel orientation alter the leading and trailing surface heat transfer coefficients of the ribbed channel. Han et al. [15] investigated the uneven wall temperature effect on local heat transfer in a rotating two-pass square channel with smooth walls. They concluded that uneven surface temperatures on the leading and trailing surfaces create unequal local buoyancy forces, which alter heat transfer coefficients. Zhang et al. [16] analyzed the heating condition effects in a duct with angled rib turbulators with rotation. They found that an uneven wall temperature had a significant impact on the local heat transfer coefficients. Parsons et al. [17,18] studied the effects of channel orientation and wall heating condition on the local heat transfer coefficients in a rotating two-pass square channel with ribbed walls. They found that the effect of the Coriolis force and cross-stream flow were reduced as the channel orientation changed from the normal $\beta=90$ deg to an angled orientation of $\beta=135$ deg. Dutta and Han [19] also investigated the local heat transfer coefficients in rotating smooth and ribbed two-pass square channels with three channel orientations. Dutta et al. [20] presented experimental heat transfer results for turbulent flow through a rotating two-pass rib-roughened triangular channel for two channel orientations with respect to the axis of rotation. In addition, Park and Lau [21] and Park et al. [22] conducted experimental work using naphthalene sublimation to study the effects of the Coriolis force, 180 deg turn, channel orientation, and the different rib arrangements on local heat/mass transfer distributions on the leading and trailing walls of a two-pass square channel. Chen et al. [23] used the naphthalene sublimation method to measure the detailed mass transfer along four walls of a square duct containing a sharp 180 deg bend with normal ribs on two opposite walls under the nonrotating condition. They found that the ribbed walls have more span-wise uniformity than the smooth side walls. Al-Hadhrami and Han [24] studied the rotation effect on heat transfer in a rotating two pass square duct with five different orientations of 45 deg angled rib turbulators. They concluded that the parallel rib orientation (ribs in first and second passes are parallel and ribs on leading and trailing walls are parallel) provides a higher overall Nusselt number ratio than cross rib orientation, particularly, for the increased rotation numbers.

Liou et al. [25] studied the effect of divider thickness in a two pass nonrotating smooth square duct. They found the turn effect can extend up to eight hydraulic diameters downstream of the turn. Liou and Chen [26,27] studied the heat transfer and flow field in two pass rotating smooth duct with AR=1:1 and 1.25. They concluded that the rotation effect raises the turbulence level near the leading or trailing walls, which in turn leads to the local heat transfer enhancement. Murata et al. [28] excluded the turn effect by reversing the flow direction to obtain inward and outward flow in a one-pass square duct with rib-roughened walls. Their data showed that the 60 deg rib has better heat transfer enhancement than the 90 deg rib. The effect of the radial flow direction did not show a difference in averaged Nusselt number.

Almost all of the studies have focused on square or close to square ducts. A study of the buoyancy effect in a one-pass, high aspect ratio duct (AR=10:1) was conducted by Willett and Bergles [29]. Their duct was oriented at 60 deg to the r-z plane (150 deg respect to the rotation direction). They found the normalized Nusselt number ratio is a strong function of rotation number and buoyancy number. They also observed significant spanwise variation in the Nusselt number ratio under rotating conditions. The effect of rotation on the heat transfer distribution in a rotating, rectangular (AR=2:1), two-pass channel with ribs was investigated experimentally by Azad et al. [30]. They showed the heat transfer coefficients decrease from the leading wall and increase from the trailing wall for the first pass. They also concluded that the effect of rotation is more apparent in the channel orientated at 90 deg then the channel oriented at 135 deg with respect to the direction of rotation. Al-Hadhrami et al. [31] studied the effect of rotation on heat transfer in rotating two-pass rectangular channels (AR=2:1) with rib turbulators for two channel orientations. They found that the parallel and V-shaped ribs produce better heat transfer enhancement than the crossed and inverted V-shaped ribs. Furthermore, they confirmed the conclusion from Azad et al. [30] that the 90 deg-channel orientation produces greater rotating effect on heat transfer than a 135 deg channel orientation.

Single-pass rectangular (AR=4:1) channels were studied by Griffith et al. [32] and Lee et al. [33]. Griffith et al. [32] concluded that this narrow rectangular passage creates more heat transfer enhancement than the smaller aspect ratio channels. They also found that significant spanwise variation is present across the width of the channel, and this variation is amplified by the use of angled ribs. Lee et al. [33] investigated six different rib configurations. They found the V-shaped ribs produce the greatest heat transfer enhancement in both rotating and nonrotating channels. They found in the rib-roughened channels all surfaces undergo heat transfer enhancement with an increased effect of rotation. They also confirmed the finding of Griffith et al. [32]: Significant spanwise variation is present in the channels with angled ribs; however, this variation decreases in the channels with V-shaped ribs.

Cho et al. [34] used a mass transfer method to study the effect of rotation in a rotating two-pass rectangular channel (AR=1:2) with 70 deg angled ribs. Their results showed that the rotation effect diminished in the second pass due the 180 deg turn effect. An experimental result for a 1:4 rotating two-pass channel was reported by Agarwal et al. [35] using the mass transfer method. For a smooth surface, they found that the 1:4 channel has lower heat/mass transfer compared to square channel. For the 90 deg rib wall, the Sherwood number ratio shows a decreasing trend with increasing Reynolds number.

From the above-mentioned research, the existence of the angled

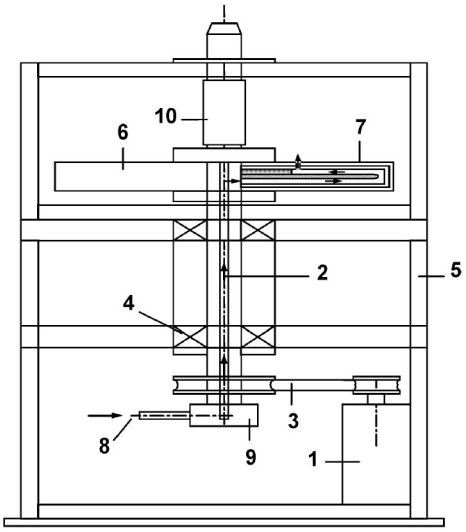

1. Electrical Motor with Controller
2. Rotating Shaft
3. Belt Drive Pulley System
4. Bearing Support System
5. Steel Table
6. Rotating Arm
7. Test Section
8. Compressor Air
9. Rotary Seal
10. Slip Ring

Fig. 2 Schematic of the test rig

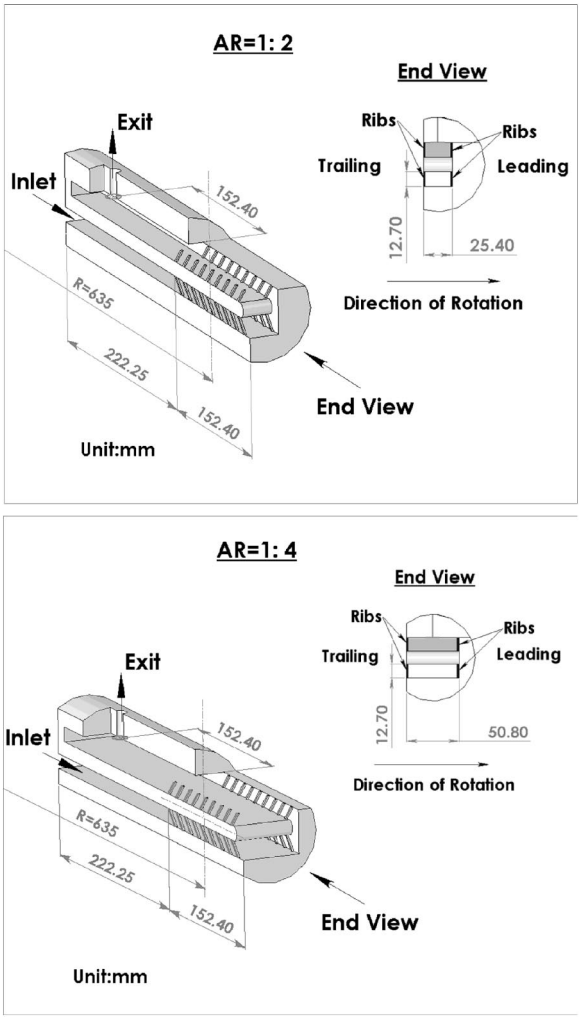

Fig. 3 Geometry of the test section

ribs (placed at an angle to the main coolant flow direction) enhances the heat transfer coefficient due to increased turbulent mixing, secondary flow, and, to some extent, due to increased surface area. Meanwhile, it has been shown in the literature that parallel ribs perform better than the crossed ribs under non-rotating conditions. Among these rib configurations, literature also showed the 45 deg and 60 deg angled ribs have a better heat transfer enhancement than 30 deg and 90 deg angled ribs. However, these results are for square or higher aspect ratio (AR=2:1 and 4:1) channels. There is very limited data available for the lower aspect ratio (AR=1:2 and 1:4) channels. The simple angled ribs would be a better choice than the V-shaped ribs for enhancing heat transfer in the lower aspect ratio channels due to the narrow width of the channel. In addition, as the secondary flows resulting from rotational effects interact with the rib-induced secondary flows and the sharp 180 deg turn, new heat transfer characteristics in the lower aspect ratio ducts with rotation are expected. Therefore, the objectives of this paper are to study:

1. The effects of 45 deg angled ribs on the heat transfer distribution in rotating two-pass lower aspect ratio channels (AR=1:2 and AR=1:4).
2. The effects of the 180 deg sharp turn on the heat transfer distribution in rotating two-pass lower aspect ratio channels (AR=1:2 and AR=1:4) with 45 deg angled rib-roughened walls.
3. The effects of the channel orientation with respect to the axis of rotation in lower aspect ratio channels.
4. The comparison of heat transfer enhancement between the lower aspect ratio ribbed channels and the published higher aspect ratio ribbed channels under rotating conditions.

2 Experimental Facility

The experimental test rig is shown in Fig. 2. This test rig was previously used by Azad et al. [30]. A variable frequency motor is connected via a gear- and-belt mesh to a hollow, rotating shaft. This shaft runs from the base of the test rig to the work platform and is attached orthogonal to the hollow, rotating arm. The test section is inserted inside the hollow rotating arm, which rotates in a plane orthogonal to the rotating shaft. A hand held optical tachometer is used to determine the rotation speed of the arm. Thermocouple and heater wires are connected to slip-ring assembly mounted to the rotating shaft. The output of the thermocouples is transferred to a data acquisition system. Power input to the heaters from the variable transformers is also transmitted through the slip ring assembly. Cooling air is pumped from a steady flow compressor, through an ASME orifice flow meter, then through the hollow rotating shaft, turning 90 deg and passing into the rotating arm, then through the test section, and is finally expelled into the atmosphere.

This experiment contains two test sections. The geometry of the test section is shown in Fig. 3. The test section of 1:2 is 12.7 $\times$25.4 mm in cross section with a hydraulic diameter (D_h) of 16.93 mm. The test section contains a 222.25 mm unheated entrance length to provide a hydrodynamic fully developed flow condition. Each pass has a 152.4 mm long heating section. The clearance of the 180 deg sharp turn is 12.7 mm from tip to end wall. The divider wall has a thickness of 12.7 mm with a 6.35 mm radius at the tip. Cooling air is expelled to the atmosphere through a 6.35 mm radius hole in the second pass. The distance from the end of the heated section in the second pass to the exit hole is 152.4 mm. The 1:4 and 1:2 test sections are identical with the exception that the 1:4 test section has a cross section of 12.7 $\times$50.8 mm with a hydraulic diameter of 20.32 mm. The mean rotating radius is 635 mm for both test sections.

A cross-sectional view of the AR=1:2 test section is shown in Fig. 4. Each pass is divided into six segments. Each segment contains six copper plates: one for the leading, one for the trailing,

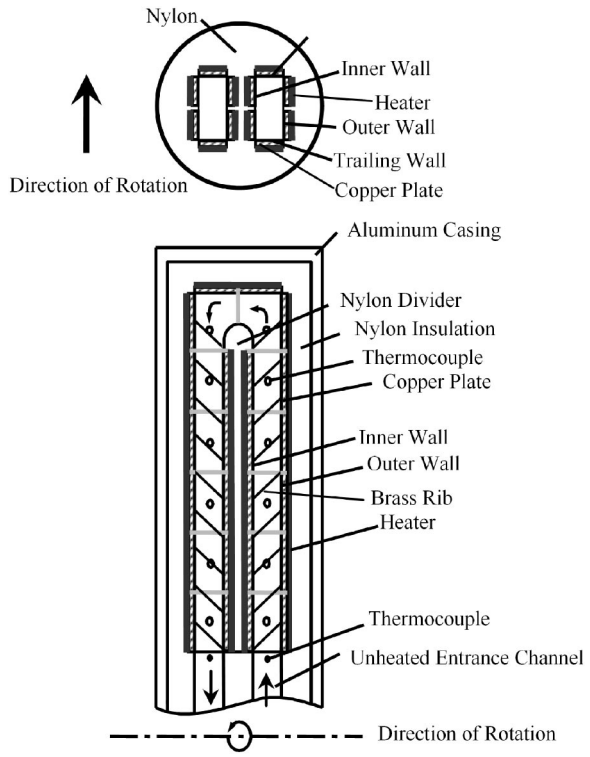

Fig. 4 Cross-sectional view of the test section (AR=1:2)

two for the outer, and two for the inner walls. The inner wall has only five segments in the flow direction because of the 180 deg turn. The copper plates are mounted in a nylon substrate, which comprises the bulk of the test section. Prefabricated flexible heaters are installed beneath the copper plates. A total of 13 heaters are used for each test section. All heaters supply steady, uniform heat flux to the copper plates. Sufficient power is supplied in order to maintain a maximum wall temperature of nearly 65°C for the corresponding section. This corresponds to an inlet coolant-to-wall density (temperature) ratio ($\Delta\rho/\rho$) of 0.115 for every test. Thermal conducting paste is applied between the heater and copper plates to promote heat transfer from the heater to the plates. Each 3.18 mm thick copper plate has a 1.59 mm deep blind hole drilled in the backside in which a copper-constantan thermocouple is installed 1.59 mm from the plate surface with thermal conducting glue. Thin nylon strips (1.59mm) between the copper plates reduce the conduction effect between the plates.

The ribs made of brass with a 1.59×1.59 mm cross section are glued on the leading and trailing walls at an angle of 45 deg to the flow direction. A thin layer of conductive glue is used so the thermal resistance between the brass ribs and the copper plates is negligible. The ratio of rib pitch-to-rib height is 10. The entire test duct is surrounded by insulating nylon material and fits in a hollow cylindrical aluminum alloy arm for structural rigidity. The AR=1:4 test section has an identical cross-sectional view except the distance between the leading and trailing walls is twice that of the AR=1:2 test section. For both test sections, the experiments were conducted for Reynolds numbers of 5000, 10 000, 25 000, and 40 000. The test section rotates at a speed of 550 rpm, resulting in a range of rotation number (Ro) of approximately 0.026–0.2 and 0.038–0.3 for AR=1:2 and AR=1:4, respectively.

3 Data Reduction

The regionally averaged heat transfer coefficient was calculated by dividing the net heat input to the coolant by the projected area and the temperature difference between the copper plate and air bulk mean temperature

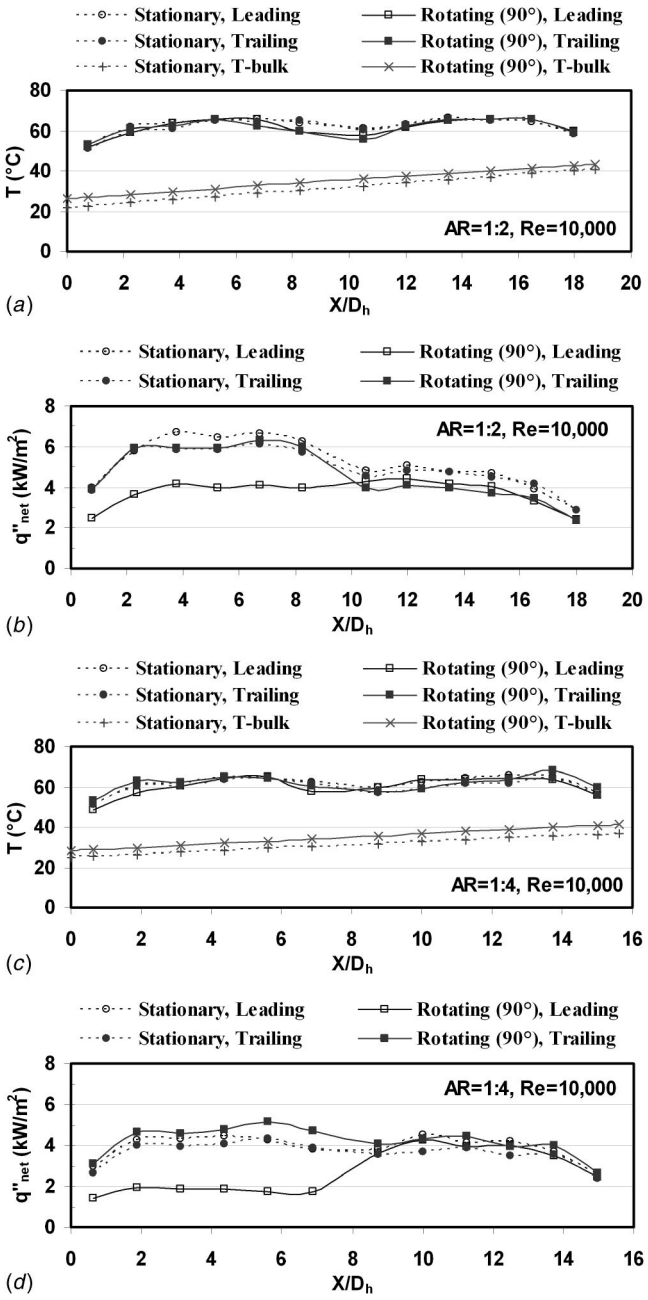

Fig. 5 Temperatures and net heat flux distributions on leading and trailing surfaces

$$h=\frac{q-q_{\text{loss}}}{A\times(T_w-T_b)} \tag{1}$$

Figure 5 shows the temperature distribution and net heat flux distribution on the leading and trailing surfaces for AR=1:2 and AR=1:4. The net heat transfer rate is the electrical power supplied to the heater ($q=VI$) minus heat losses. Heat losses were determined by supplying power to the test section until a steady state condition is achieved in a no flow condition. Fiberglass insulation was inserted into the test channel to prevent convection between the channel walls. This is done for several power inputs to obtain a relation between the total heat loss from each wall and the corresponding wall temperature. To place the results on a common basis, the heat transfer area used in Eq. (1) was always that of a smooth wall (only the projected area of the ribs). The regionally averaged wall temperature is obtained from thermocouples

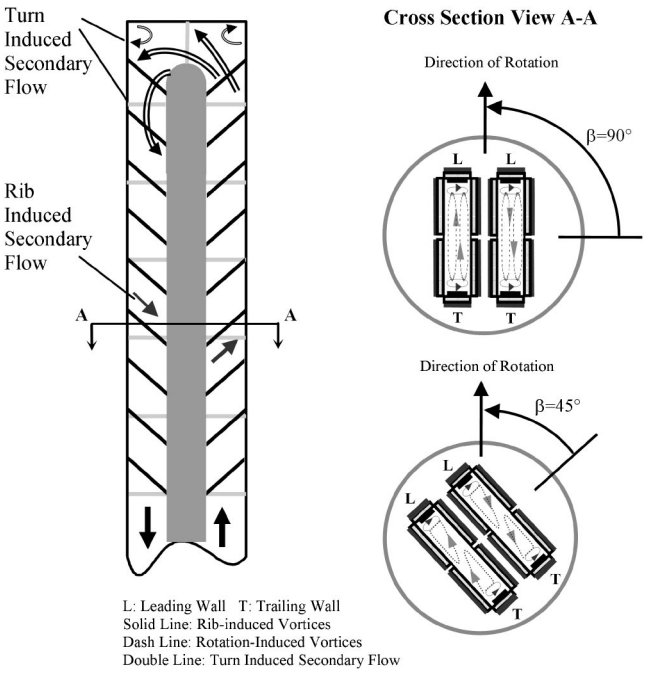

Fig. 6 Conceptual view of the secondary flow patterns (AR =1:4)

that are embedded in each copper plate. The maximum wall temperature is 65°C. The bulk mean air inlet and exit temperatures are measured by thermocouples. Because there is a long distance between leading and trailing walls, two thermocouples are placed at the exit to measure the bulk mean air temperature. The averaged value of these two measurements is used for the exit bulk mean temperature. However, the difference between these two exit measurements is less than 2°C for most cases, and the maximum difference is 5°C, which was observed in AR=1:2 under the rotating condition. The local bulk mean temperature (T_b) used in Eq. (1) is calculated from the linear interpolation between the measured inlet and exit bulk air temperatures. Another way to obtain the local bulk mean air temperature is using the energy balance through the test channel. The difference between the linear interpolation and energy balance of bulk mean temperature is 1 to 2°C in all cases.

The regionally averaged Nusselt number is normalized by the Nusselt number for fully developed turbulent flow in a smooth nonrotating circular pipe to reduce the influence of the flow Reynolds number on the heat transfer coefficient. The regionally averaged Nusselt number normalized by the Dittus-Boelter/McAdams correlation is

$$\frac{\mathrm{Nu}}{\mathrm{Nu}_o} = \frac{hD_h}{k_{\mathrm{air}}} \frac{1}{(0.023\,\mathrm{Re}^{0.8}\mathrm{Pr}^{0.4})} \tag{2}$$

The Prandtl number (Pr) for air is 0.71. Air properties are taken based on the mean bulk air temperature. The estimated uncertainty for temperature measurement is 0.5°C. Based on the method described by Kline and McClintock [36], the uncertainty of the Nusselt number ratio is about 5% for the high Reynolds number. For the low Reynolds number (Re=5000), the maximum uncertainty is about 17% on the leading wall in the first pass of AR=1:4 under the rotating condition.

4 Results and Discussion

In a two-pass rotating rectangular channel with rib roughened walls, there are five main factors affecting the heat transfer coefficient: rotation effect, turn effect, aspect ratio, buoyancy parameter, and rib induced secondary flow. The Coriolis force is known as the primary effect due to rotation. As conceptually shown in Fig. 6 (AR=1:2 has a similar flow pattern as AR=1:4), with a 90 deg channel orientation, the Coriolis force induces a pair of vortices which circulate toward the trailing wall for radial outward flow and toward the leading wall for radial inward flow. This cross-stream secondary flow pattern significantly increases heat transfer on the trailing wall in the first pass (radial outward flow) and the leading wall in the second pass (radial inward flow), but reduces heat transfer on the opposite walls (leading wall in the first pass and trailing wall in the second pass). Therefore, rotation causes a difference in the heat transfer between the leading and trailing walls. When the channel orientation is rotated to 45 deg, the effect of rotation on the heat transfer from the leading and trailing walls is reduced. The effect of rotation is evaluated by the rotation number. The buoyancy parameter due to the centrifugal force and temperature difference is important because of the high rotating speed and large temperature difference in the actual engines. For the radial outward flow, the rotation-induced buoyancy force aids the inertia force. This force opposes the inertia force in the second pass because the flow direction reversed. A buoyancy parameter, as defined by Wagner et al. [9], is used to present the combined effects of the Coriolis and buoyancy forces.

$$\mathrm{Ro} = \frac{\Omega D_h}{V} \tag{3}$$

$$\mathrm{Bo} = \left(\frac{\Delta\rho}{\rho}\right)(\mathrm{Ro})^2 \frac{R}{D_h} \tag{4}$$

When the flow passes through the 180 deg turn, the flow impinges on the outer wall due to the centrifugal force, then reattaches on the inner wall in the second pass. It creates a circulation zone right after the turn near the inner wall in the second pass. Two additional circulation zones occur in the outer corners of the turn because of the geometry. These flow structures, due to the turn, result in different heat transfer enhancements inside the turn and after the turn.

Rib turbulators break the boundary layer and increase the turbulence intensity. Therefore, they enhance heat transfer on the rib roughened walls. The angled ribs not only trip the boundary layer, but also produce secondary flows, as shown in Fig. 6, which enhance heat transfer on the walls. The angled ribs create a vortex parallel to the rib that impinges on the side wall. In this experiment, 45 deg angled ribs are placed on the leading and trailing walls (Fig. 3). The rib induced vortices impinge on the outer wall in the first pass and on the inner wall in the second pass as a result of the rib orientation. In addition to the leading and trailing walls, heat transfer enhancement is expected on the outer wall in the first pass and on the inner wall in the second pass due to the rib induced secondary flow. These flow patterns have been confirmed by earlier papers (Han et al. [4], Han and Zhang [5], Ekkad and Han [7], Park and Lau [21], Park et al. [22], Liou et al. [25], and Liou and Chen [26]).

4.1 Nusselt Number Ratio Distribution for AR=1:2

The heat transfer distributions for the 1:2 channel are shown in Fig. 7. The figure contains both nonrotating and rotating (β=90 deg and 45 deg) distributions for both the leading and trailing surfaces. The level of heat transfer enhancement created by the angled ribs remains relatively constant throughout the entire nonrotating channel, and as expected, the leading and trailing surfaces experience the same level of enhancement. It is also clearly seen that as the Reynolds number increases, the Nusselt number ratios decrease.

The effect of rotation can also be seen in Fig. 7. As one would anticipate, in the first pass, the heat transfer enhancement on the trailing surface is greater than that of the nonrotating channel, and the leading surfaces experiences a declination in heat transfer. This trend is true for both channel orientations (β=90 deg and 45 deg). However, the Nusselt number ratio trends of the second pass

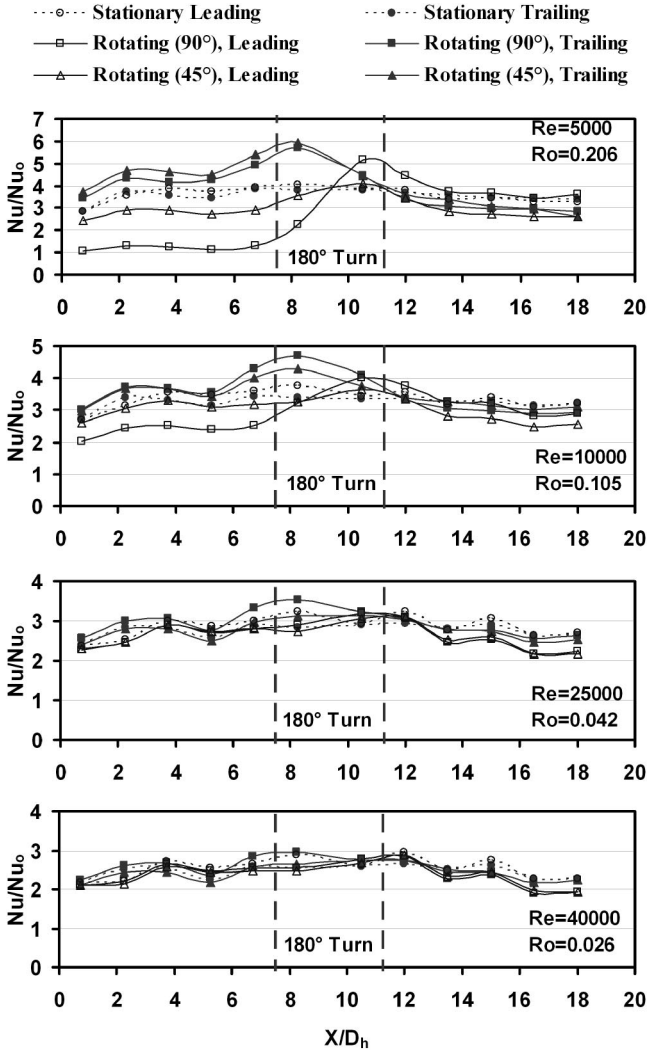

Fig. 7 Nusselt number ratio distribution for AR=1:2 with 45 deg angled ribs

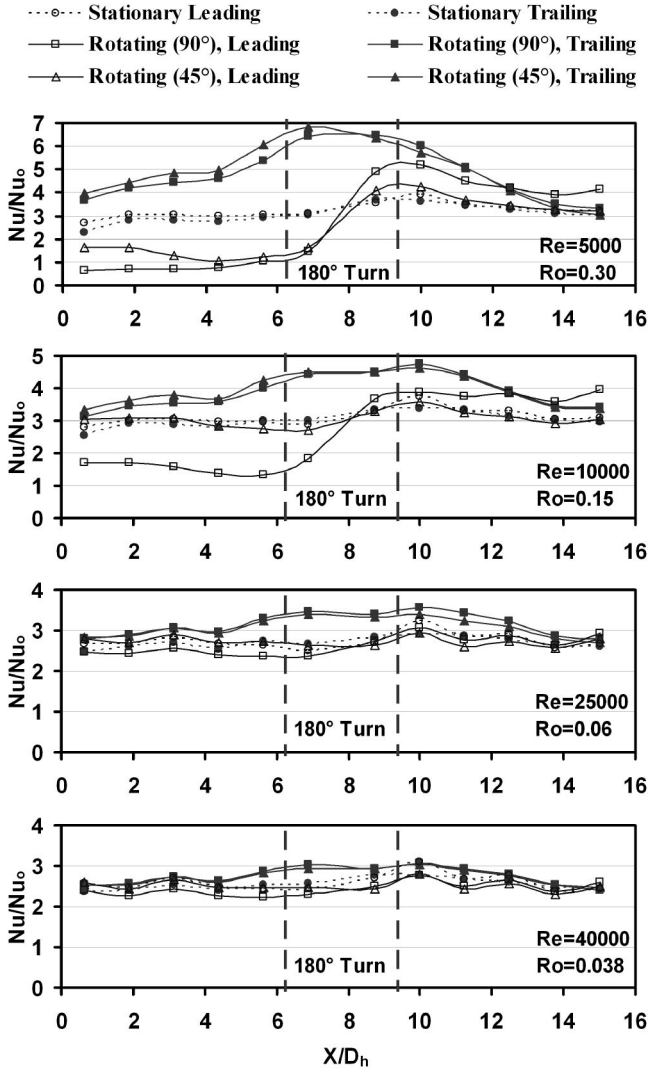

Fig. 8 Nusselt number ratio distribution for AR=1:4 with 45 deg angled ribs

are unlike those reported for square channels or channels with an aspect ratio of 2:1. In general the Nusselt number ratios for both the leading and trailing surfaces are less than those of the nonrotating channel in the present study. Again, this is true for both channel orientations. As the Reynolds number increases (rotation number decreases), the difference between the leading and trailing surfaces decreases.

Not only is the enhancement on both the leading and trailing surfaces less than that of the nonrotating channel, there is only a negligible difference between the leading and trailing surfaces of the second pass. The previous studies involving square channels indicate the leading surface of the second pass experiences heat transfer enhancement above that of a nonrotating channel, while the trailing surface experiences decreased heat transfer. For the present 1:2 channel, the difference between the leading and trailing surfaces is small due to the strong turn. The 180 deg sharp turn has a more dominant effect on the heat transfer of the second pass than rotation. Therefore, the rotation induced vortices which result in the heat transfer difference between the leading and trailing surfaces are not as strong as the secondary flow induced by the turn. The second pass is approximately nine hydraulic diameters long, and the strong turn dominates the heat transfer trends over this entire length.

4.2 Nusselt Number Ratio Distributions for AR=1:4 Figure 8 shows the Nusselt number ratio distributions for the 1:4 channel. As with the 1:2 channel (Fig. 7), the enhancement in the nonrotating channel is relatively constant throughout the entire channel. The heat transfer enhancement in the 1:4 nonrotating channel is less than that of the 1:2 channel. The height of the ribs is the same for both channels; however, the height of the 1:4 channel is twice that of the 1:2 channel. Therefore, the effect of the angled ribs is less in the 1:4 channel than the 1:2 channel. As the Reynolds number increases, the level of heat transfer enhancement decreases.

Similar to the 1:2 channel (Fig. 7), the significant effect due to rotation is observed in the first pass of the 1:4 channel. However, the difference between the leading and trailing surfaces is much greater in this 1:4 channel than the 1:2 channel. Because the rotating experiments are conducted at a constant angular velocity of 550 rpm, the rotation numbers vary between the two channel sizes (the channels have different hydraulic diameters). Therefore, the rotation numbers of the 1:4 channel are greater than those of the 1:2 channel. As the rotation number decreases (Reynolds number increases), the difference between the leading and trailing surfaces decreases for both channel orientations (β=90 deg and 45 deg).

Similar to the 1:2 channel (Fig. 7), the difference between the heat transfer from the leading and trailing surfaces decreases sig-

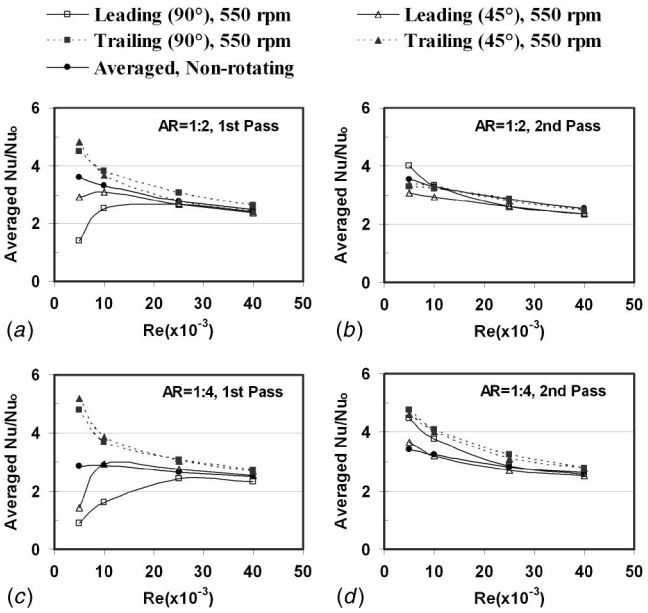

Fig. 9 Averaged Nusselt number ratio for both rotating and nonrotating cases

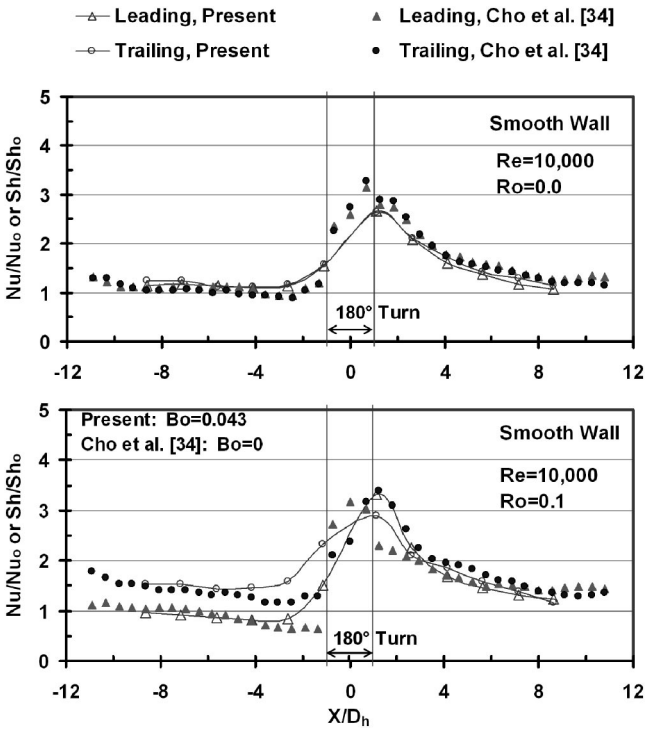

Fig. 10 Comparison of the Nusselt number ratio distributions for AR=1:2 with smooth walls

nificantly in the second pass of the 1:4 channel (Fig. 8). At the higher rotation numbers (lower Reynolds numbers), a difference between the leading and trailing surfaces can be observed, but this difference quickly diminishes as the rotation number decreases (Reynolds number increases). In this case the flow has less than six hydraulic diameters to develop downstream of the turn. This short distance is insufficient for the rotation induced vortices to overcome the dominant secondary flow induced by the 180 deg sharp turn.

It can also be observed that in general the Nusselt number ratios of both the leading and trailing surfaces are greater than those of the nonrotating channel in the second pass. This is different than the trends shown for the 1:2 channel where the ratios were less than the non-rotating channel. This offers positive information for designers in that the declination of heat transfer traditionally seen on the trailing surface of the second pass is not present in this 1:4 channel.

4.3 Averaged Nusselt Number Ratio. The channel averaged Nusselt number ratios are shown in Fig. 9 for both channel aspect ratios under nonrotating and rotating conditions. The first pass average includes all six points in the first pass. The second pass average includes all six points in the second pass. The nonrotating curves are the average of the leading and trailing surfaces in the nonrotating channels. The effect of rotation is clearly seen in the first pass of both the 1:2 and the 1:4 channels: the leading surfaces experience decreased heat transfer while the trailing surfaces experience increased heat transfer. However, the difference is significantly reduced in the second pass, and this is clearly seen for both the 1:2 and 1:4 channels in Figs. 9(b) and 9(d), respectively. As the Reynolds number increases (rotation number and buoyancy parameter decrease), the difference between the leading and trailing walls is reduced. In addition, the averaged Nusselt number ratio decreases with increasing Reynolds number.

4.4 Comparison With Previous Studies. The diminished difference between the leading and trailing surfaces of the second pass has also been observed by Cho et al. [34] in 1:2 rotating channels. Figure 10 compares the heat transfer coefficients in the smooth 1:2 channel of Cho et al. [34] to the smooth results of the present 1:2 channel. The Reynolds number of both the nonrotating and rotating channel is 10,000, and the rotation number of the rotating channel is 0.1 for both the previous study and the present study.

As shown in Fig. 10, the present study is in close agreement with the previous study for the nonrotating smooth channel. The most significant difference between the two data sets is in the 180 deg turn. The study of Cho et al. [34] is performed using mass transfer; therefore, a detailed distribution can be obtained. With the copper plate method of the present study, only two regionally averaged points are recorded for the turn, so the detailed distribution cannot be obtained to capture the slightly higher values presented in the previous mass transfer study.

The rotating results of the present 1:2 channel are also very comparable to the previous study. As shown in Fig. 10, both studies (using different experimental methods) reveal the same results for both leading and trailing surfaces of the first and second passes. This confirms the heat transfer in the second pass is dominated by the 180 deg turn. As with the current study, Cho et al. [34] reported only a negligible difference between the leading and trailing surfaces of the second pass.

Figure 11 compares the angled rib results of the present 1:2 channel to those of the 1:2 ribbed channel used by Cho et al. [34]. Although the channel geometry of both studies are similar, the rib geometry of the two studies differs. The angled ribs of the previous studies are oriented at 70 deg to the mainstream flow. The rib pitch-to-height ratio (P/e) is 7.5, and the rib height-to-hydraulic diameter ratio (e/D_h) is 0.075; for the current study P/e is 10 and e/D_h is 0.094. When comparing the nonrotating results of the current study to those of the previous study, it can be seen that Nusselt number ratios of the current study are greater than those of the previous study in both the first and second passes, but the trends of the two studies are similar. Therefore, the difference in enhancement levels can be attributed to the difference in rib geometry. It should also be reiterated, that the previous study utilizes mass transfer. The results of mass transfer experiments are traditionally lower than those of other experimental techniques because the area atop the ribs is not measured using the mass trans-

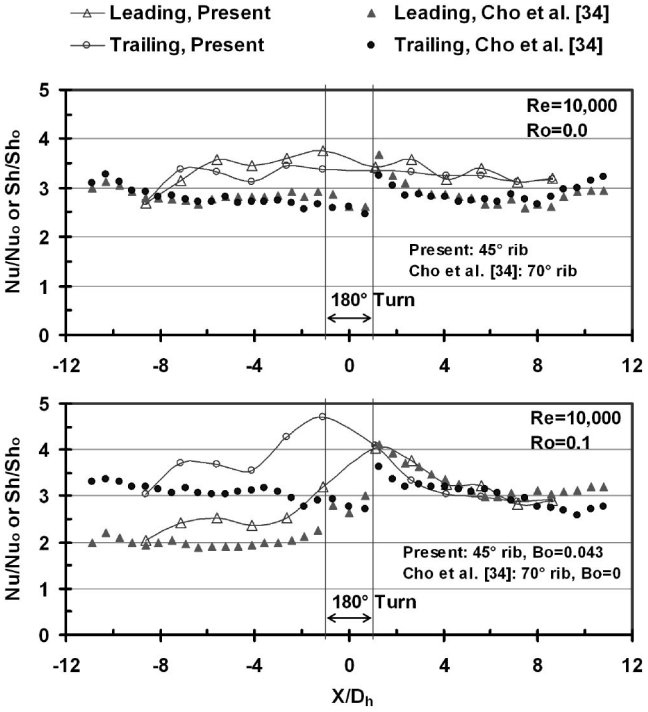

Fig. 11 Comparison of the Nusselt number ratio distributions for AR=1:2 with ribbed walls

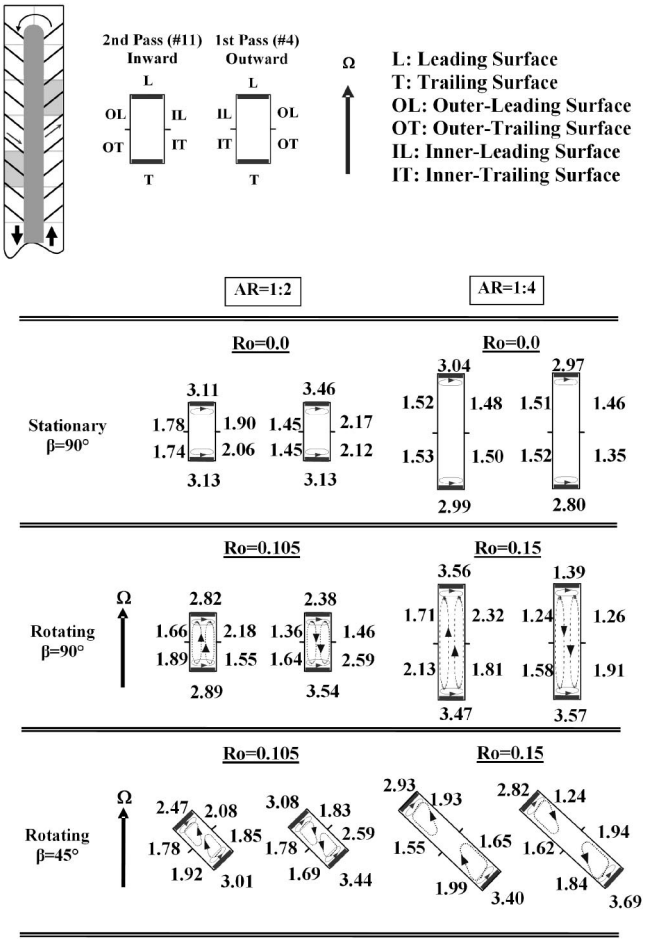

Fig. 12 Secondary flow effect on circumferential heat transfer (Re=10,000) (number represents the Nusselt number ratio)

fer method. The highest heat transfer occurs on top of the ribs, and this area of very high heat transfer is not considered using mass transfer; therefore, the average values are different between these two measurements.

The comparison of the 1:2 rotating channels with angled ribs is also shown in Fig. 11. As with the smooth channel comparison, the difference between the leading and trailing surfaces in the first pass is clearly seen. However, in both the present study and the previous study of Cho et al. [34], almost no variation exists in the second pass. The comparison confirms that the interaction between the rib induced secondary flow, rotation induced secondary, turn induced secondary flow, and the low aspect ratio result in diminished difference between the leading and trailing surfaces in the second pass.

The reduced effect of rotation in the second pass was also reported in square channels (Johnson et al. [13]) and 2:1 channels (Azad et al. [30]). Johnson et al. [13] attributed the lack of large variation in the second pass to the combined effect of the rib induced secondary flow and the secondary flow induced by the turn. Although both these studies show the effect of rotation on the second pass is less than that of the first pass, the effect of rotation in both the square and 2:1 channels is more apparent, unlike the present 1:2 and 1:4 channels.

When considering the flow structure of the coolant in the rotating two-pass channels, it has been shown that the circulation direction of the rotation induced vortices reverses in the second pass due to the reversed direction of the Coriolis force. The strength of the vortices begins growing just downstream out the turn. While the strength of the rotation induced vortices is growing, the effect of the turn is diminishing through the second pass. With a relatively large distance between the leading and trailing surfaces of the 1:2 and 1:4 channels (compared to square and 2:1 channels), more distance is required for the effect of the sharp 180 deg turn to diminish. Therefore, the length of the second pass of the present study is not long enough for the turning effect to diminish and allow the effect of rotation to become more apparent. Therefore, the effect of rotation is significantly reduced in the second pass of the low aspect ratio channels.

4.5 Secondary Flow Effect on Circumferential Walls Heat Transfer. Both the rib induced and the rotation induced secondary flows have a strong effect on the circumferential heat transfer of the channel. Figure 12 shows the angled rib induced and rotation induced secondary flow patterns, as well as the circumferential regionally averaged Nusselt number ratios at the Reynolds number of 10,000. The first pass outward flow is the right hand segment and the second pass inward flow is the left-hand segment. The circumferential distribution is shown at two locations in the channel: at the fourth point in the first pass and the fifth point in the second pass (11th point overall). The numbers marked next to each surface of the different aspect ratios, orientations, and rotation numbers are the Nusselt number ratios on these surfaces.

As shown in Fig. 12, the leading (L) and trailing (T) surfaces experience significantly greater heat transfer enhancement than the inner (IL and IT) and outer (OL and OT) walls of both the 1:2 and 1:4 nonrotating channels. This should be expected as the rib-roughened walls trip the boundary layer resulting in increased turbulence and increased heat transfer (over the smooth inner and outer walls). As is also shown for the nonrotating channels, the outer walls of the first pass experience more enhancement than the inner walls of the first pass and enhancement of the second pass inner walls is greater than that of the outer walls. This can be explained by considering the rib induced secondary flow. In the first pass, the ribs are placed so the coolant is forced from the inner wall to the outer wall. The coolant impinges on the outer wall and circulates back to inner wall. Therefore, the enhancement on the outer wall of the first pass is greater than that on the inner wall. Similarly, in the second pass, the coolant is forced from

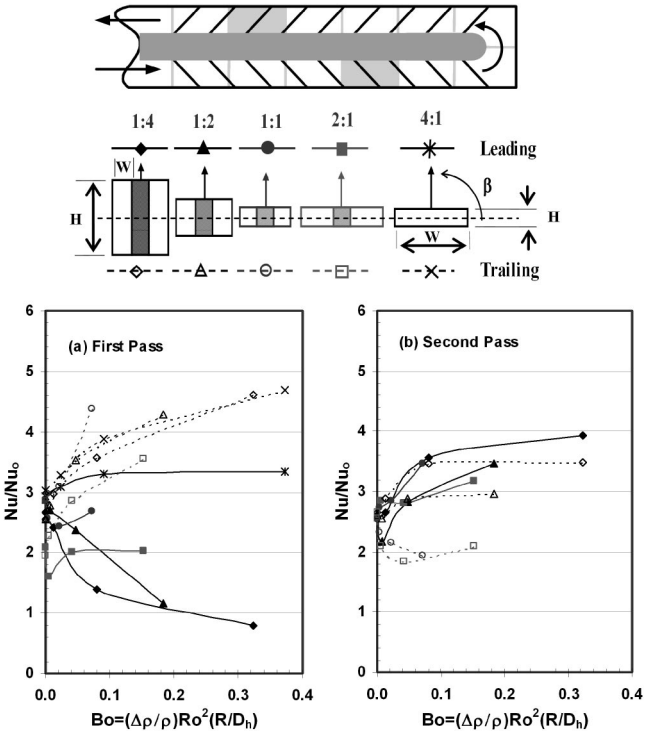

Fig. 13 Aspect ratio effect on heat transfer (β=90 deg)

outer wall to the inner wall, where it impinges on the inner wall and circulates back around to the outer wall. Therefore, in the second pass, the enhancement on the inner wall is greater than the outer wall.

When comparing the nonrotating Nusselt number ratios for the 1:2 channel to those of the 1:4 channel. It can be seen that the values in the 1:4 channel are lower than those of the 1:2 channel, especially on the inner and outer walls. The heights of the ribs are the same for both channels; therefore, the height of the ribs is less significant in the very narrow 1:4 channel than the 1:2 channel. Only a very small area of the inner and outer walls is effected by the rib induced secondary flow, and the effect is reduced due to the regional heat transfer measurements.

For the rotating channels, the constructive interaction between the rib induced secondary flow and the rotation induced secondary flow is clearly seen in the enhancement of the outer-trailing (OT) surface of the first pass and the inner-leading (IL) surface of the second pass. On both surfaces, the combined effect of the ribs and rotation result in significant enhancement above the enhancement in the non-rotating channels. This is clearly seen in both the 1:2 and 1:4 channels. This trend is also true for both channel orientations (β=90 deg and 45 deg).

4.6 Aspect Ratio Effect on Heat Transfer. A channel aspect ratio comparison is shown in Fig 13. The figure compares five channels of different aspect ratios ranging from 4:1 to 1:4; therefore, this range of channels can cover the entire cross section of an airfoil. The results of the present study (AR=1:4 and 1:2) are compared with those of Griffith et al. [32] (AR=4:1, one-pass), Azad et al. [30] (AR=2:1), and Al-Hadhrami et al. [24] (AR=1:1). All channels cover a range of Reynolds numbers varying from 5000 to 40 000. The rotation number varies with different Reynolds numbers and is different among these studies. In all of the channels being compared, the ribs are placed on the leading and trailing walls, the rib pitch-to-height ratio (P/e) is 10, and the ribs are angled at 45 deg to the mainstream flow.

The geometry of these five channels is listed in Table 1. In addition, the height of the ribs (e=1.59 mm) is the same for all

Table 1 Dimensions of Various Aspect Ratio Channels

AR	1:4	1:2	1:1	2:1	4:1
W	12.7	12.7	12.7	25.4	50.8
H	50.8	25.4	12.7	12.7	12.7
e	1.59	1.59	1.59	1.59	1.59
D_h	20.32	16.93	12.7	16.93	20.32

Unit: mm

the channels. However, because the rib height remains constant, the rib height-to-hydraulic diameter ratio changes; as the channel height (H) increases, this blockage ratio decreases. Because the channels have different hydraulic diameters but the same channel length, the comparisons are made at specific points where the flow can be considered fully developed in both the first pass and the second pass. In the first pass, data are compared at the forth copper plate, and compared at the eleventh copper plate in the second pass.

Figure 13(a) shows a comparison of the first pass of the rotating channels oriented at β=90 deg. This figure shows that the heat transfer from the trailing surface of all the channels increases with the increasing buoyancy parameter, and this should be anticipated as the core of the coolant is shifted toward the trailing surface with rotation. However, the heat transfer trends of the leading surface are more complex. For the present channels (AR=1:4 and 1:2), the Nusselt number ratios decrease with the increasing buoyancy parameter. The heat transfer from the leading surfaces of the 1:1 and 2:1 channels increases with the increasing buoyancy parameter, and the most significant increase in heat transfer with rotation is seen in the 4:1 channel.

Figure 13(b) shows the aspect ratio comparison in the second pass of the two-pass channels. The heat transfer in the second pass of the 1:4 and 1:2 channels is favorable for both the leading and trailing surfaces. In other words, the heat transfer enhancement increases on both the leading and trailing surfaces with the increasing buoyancy parameter. However, this is not the case for the 1:1 and 2:1 channels: in the second pass as the buoyancy number increases, the Nusselt number ratios on the leading surface increase, while the ratios on the trailing surface decrease with the increasing buoyancy parameter.

In the actual turbine blades, the cooling channels have different orientations in order to fit the cross section of the airfoil; therefore, the channel orientation of 90 deg is not practical for all aspect ratio channels. Figure 14 takes the channel orientation into account by comparing the heat transfer enhancement of various aspect ratio channels at various orientation angles. The square channel (AR=1:1) maintains the orientation of 90 deg, the 1:4 and 1:2 channels which would likely be located near the leading edge of the blade are oriented at 45 deg, and the 2:1 and 4:1 channels are oriented at 135 deg to fit near the trailing edge of the blade. The behavior of the first pass is shown in Fig. 14(a) and is similar to the behavior shown in Fig. 13(a). For all channels the heat transfer enhancement on the trailing surfaces is increasing with the increasing buoyancy parameter. However, the heat transfer decreases on the leading surface of the 1:4 and 1:2 channels, while increasing on the leading surfaces of the 1:1, 2:1, and 4:1 channels. However, the declination of heat transfer on the leading surfaces is much less in these channels which account for the orientation effect than in the channels orientated at 90 deg. Similar results are shown for the second pass of these channels (Fig. 14(b)) as for the orthogonal rotating channels (Fig. 13(b)): Both

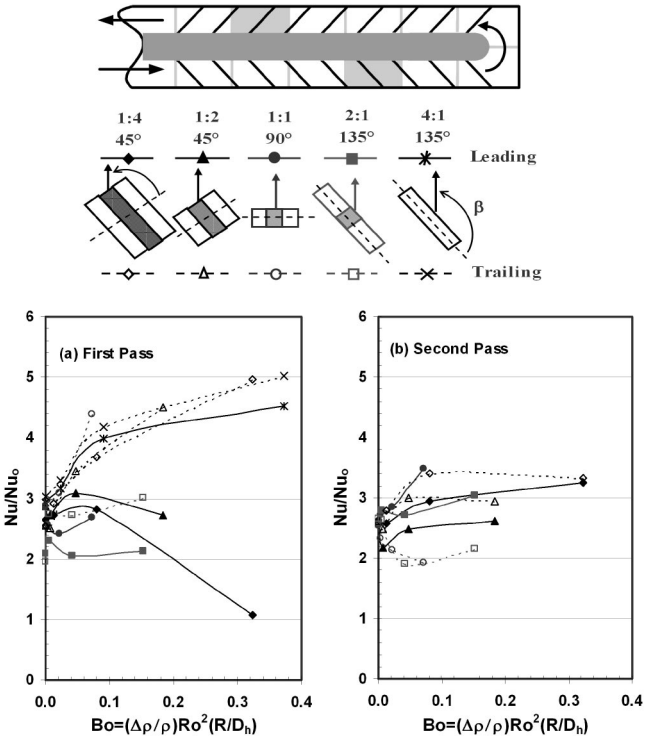

Fig. 14 Aspect ratio effect on heat transfer (β=90 deg, 45 deg, and 135 deg)

the leading and trailing surfaces of the 1:4 and 1:2 channels undergo heat transfer enhancement with the increasing buoyancy parameter, and the leading surface of the 1:1 and 2:1 channels experience enhancement while the trialing surfaces see a decrease in the Nusselt number ratios.

5 Conclusions

A limited parametric study was performed experimentally to investigate the lower aspect ratio two-pass rectangular channels under rotating conditions with rib turbulators on the leading and trailing walls. Two aspect ratio channels were tested: AR=1:2 and AR=1:4. The rotating speed was fixed at 550 rpm for all cases while the Reynolds number varied from 5000 to 40 000. The change in rotation number is dependent on the changing Reynolds number. It has a range of approximately 0.026–0.2 and 0.038–0.3 for AR=1:2 and AR=1:4, respectively. The results are comparable to the results of previous studies. The aspect ratio effect in two-pass rotating rectangular channels was considered. Based on the discussion, the main conclusions are as follows:

1. The heat transfer enhancement for the nonrotating channels (AR=1:2 and AR=1:4) due to the 45 deg angled ribs is approximately 2.5 to 3 times higher than the smooth circular pipe in the fully developed region in both radial outward and inward flows.
2. The rotation effect increased heat transfer on the trailing wall but decreased the heat transfer on the leading wall in the first pass of both the 1:4 and 1:2 channels. In the second pass, the difference of the heat transfer between the leading and trailing walls was reduced under the rotating condition when compared to the first pass.
3. The 45 deg channel orientation creates less heat transfer difference between the leading and trailing walls than the 90 deg channel orientation for both aspect ratio ducts.
4. The results of the circumferential wall heat transfer agree well with the secondary flow patterns in both the nonrotating and rotating cases. The rib induced secondary flow also enhanced heat transfer on the smooth side walls. The effect may be reduced for a regionally averaged measurement due to the large smooth side wall area in AR=1:4 duct.
5. The Nusselt number ratio decreases with increasing Reynolds number in both nonrotating and rotating channels with different aspect ratios.
6. The leading wall heat transfer has a strong dependence on the buoyancy parameter for 1:2 and 1:4 ducts in the first pass with radial outward flow, but it has a weak dependence on the buoyancy parameter for 2:1 and 4:1 ducts. Increasing the buoyancy parameter reduced the heat transfer on the leading walls for the 1:2 and 1:4 ducts in the first pass. The 1:4 duct has the largest heat transfer difference between the leading and trailing walls in the first pass.
7. Rotation has a relatively small effect in the second pass of the 1:2 and 1:4 channels. As discussed, it is due to the large width between leading and trailing walls for the lower aspect ratio channels. It was suggested that the 180 deg turn induced vortices dominate the rotation induced vortices for the low aspect ratio ducts. In the present results, the second pass has a length about nine and seven hydraulic diameters for the 1:2 and 1:4 channels, respectively. It is believed that a clear rotation effect can be observed in a longer channel or at higher rotation numbers.

Acknowledgments

This publication was prepared with the support of the US Department of Energy, Office of Fossil Energy, National Energy Technology Laboratory. However, any opinions, findings, conclusions, or recommendations expressed herein are those of the authors and do not necessarily reflect the views of the DOE.

Nomenclature

A = area of smooth wall
AR = aspect ratio, W/H
Bo = buoyancy parameter, $(\Delta\rho/\rho)\mathrm{Ro}^2(R/D_h)$
D_h = hydraulic diameter
e = rib height
h = heat transfer coefficient
H = channel height
k = thermal conductivity of coolant
Nu = local Nusselt number, hD_h/k
Nu_o = Nusselt number for fully developed turbulent flow in smooth pipe
P = rib pitch
Pr = Prandtl number
q = heat transfer rate at wall
R = mean rotating radius
Re = Reynolds number, $\rho VD_h/\mu$
Ro = rotation number, $\Omega D_h/V$
T_b = local coolant temperature
T_w = wall temperature
V = bulk velocity in streamwise direction
W = channel width
α = rib angle
β = angle of channel orientation with respect to the axis of rotation
μ = dynamic viscosity of coolant
ρ = density of coolant
$(\Delta\rho/\rho)$ = inlet coolant-to-wall density ratio, $(T_w-T_{bi})/T_w$
Ω = rotational speed

References

[1] Han, J. C., Dutta, S., and Ekkad, S. V., 2000, *Gas Turbine Heat Transfer And Cooling Technology*, Taylor and Francis, New York.
[2] Metzger, D. E., and Sahm, M. K., 1986, "Heat Transfer around Sharp 180° Turns in Smooth Rectangular Channels," ASME J. Heat Transfer, **108**, pp. 500–506.
[3] Fan, C. S., and Metzger, D. E., 1987, "Effects of Channel Aspect Ratio on

Heat Transfer in Rectangular Passage Sharp 180° Turn,'' ASME paper no. 87-GT-113.
[4] Han, J. C., Chandra, P. R., and Lau, S. C., 1988, ''Local Heat/Mass Transfer Distributions Around Sharp 180 Deg. Turns in Two-Pass Smooth and Rib-Roughened Channels,'' ASME J. Heat Transfer, **110**, pp. 91–98.
[5] Han, J. C., and Zhang, P., 1991, ''Effect of Rib-Angle Orientation on Local Mass Transfer Distribution an a Three-Pass Rib-Roughened Channel,'' ASME J. Turbomach., **113**, pp. 123–130.
[6] Han, J. C., Zhang, Y. M., and Lee, C. P., 1991, ''Augmented Heat Transfer in Square Channels with Parallel, Crossed, and V-Shaped Angled Ribs,'' ASME J. Heat Transfer, **113**, pp. 590–596.
[7] Ekkad, S. V., and Han, J. C., 1997, ''Detailed Heat Transfer Distribution in Two-Pass Square Channels with Rib Turbulators,'' Int. J. Heat Mass Transfer, **40**(11), pp. 2525–2537.
[8] Ekkad, S. V., Huang, Y., and Han, J. C., 1998, ''Detailed Heat Transfer Distribution in Two-Pass Square Channels with Rib Turbulators and Bleed Holes,'' Int. J. Heat Mass Transfer, **41**(11), pp. 3781–3791.
[9] Wagner, J. H., Johnson, B. V., and Hajek, T. J., 1991a, ''Heat Transfer in Rotating Passage with Smooth Walls and Radial Outward Flow,'' ASME J. Turbomach., **113**, pp. 42–51.
[10] Wagner, J. H., Johnson, B. V., and Kooper, F. C., 1991b, ''Heat Transfer in Rotating Passage with Smooth Walls,'' ASME J. Turbomach., **113**, pp. 321–330.
[11] Taslim, W. E., Rahman, A., and Spring, S. D., 1991, ''An Experimental Investigation of Heat Transfer Coefficients in a Spanwise Rotating Channel with Two Opposite Rib-Roughened Walls,'' ASME J. Turbomach., **113**, pp. 75–82.
[12] Taslim, M. E., Bondi, L. A., and Kercher, D. M., 1991, ''An Experimental Investigation of Heat Transfer in an Orthogonally Rotating Channel Roughened with 45 Deg Criss-Cross Ribs on Two Opposite Walls,'' ASME J. Turbomach., **113**, pp. 346–353.
[13] Johnson, B. V., Wagner, J. H., Steuber, G. D., and Yeh, F. C., 1994a, ''Heat Transfer in Rotating Serpentine Passage with Trips Skewed to the Flow,'' ASME J. Turbomach., **116**, pp. 113–123.
[14] Johnson, B. V., Wagner, J. H., Steuber, G. D., and Yeh, F. C., 1994b, ''Heat Transfer in Rotating Serpentine Passage with Selected Model Orientations for Smooth or Skewed Trip Walls,'' ASME J. Turbomach., **116**, pp. 738–744.
[15] Han, J. C., Zhang, Y. M., and Kalkuehler, K., 1993, ''Uneven Wall Temperature Effect on Local Heat Transfer in a Rotating Two-Pass Square Channel With Smooth Walls,'' ASME J. Heat Transfer, , **115**(4), pp. 912–920.
[16] Zhang, Y. M., Han, J. C., Parsons, J. A., and Lee, C. P., 1995, ''Surface Heating Effect on Local Heat Transfer in a Rotating Two-Pass Square Channel with 60° Angled Rib Turbulators,'' ASME J. Turbomach., **117**, pp. 272–280.
[17] Parsons, J. A., Han, J. C., and Zhang, Y. M., 1994, ''Wall Heating Effect on Local Heat Transfer in a Rotating Two-Pass Square Channel with 90° Rib Turbulators,'' Int. J. Heat Mass Transfer, **37**(9), pp. 1411–1420.
[18] Parsons, J. A., Han, J. C., and Zhang, Y. M., 1995, ''Effects of Model Orientation and Wall Heating Condition on Local Heat Transfer in a Rotating Two-Pass Square Channel with Rib Turbulators,'' Int. J. Heat Mass Transfer, , **38**(7), pp. 1151–1159.
[19] Dutta, S., and Han, J. C., 1996, ''Local Heat Transfer in Rotating Smooth and Ribbed Two-Pass Square Channels with Three Channel Orientations,'' ASME J. Heat Transfer , **118**, pp. 578–584.
[20] Dutta, S., Han, J. C., and Lee, C. P., 1996, ''Local Heat Transfer in A Rotating Two-Pass Ribbed Triangular Duct with Two Model Orientations,'' Int. J. Heat Mass Transfer, **39**, pp. 707–715.
[21] Park, C. W., and Lau, S. C., 1998, ''Effect of Channel Orientation of Local Heat (Mass) Distributions in A Rotating Two-Pass Square Channel with Smooth Walls,'' ASME J. Heat Transfer, **120**, pp. 624–632.
[22] Park, C. W., Yoon, C., and Lau, S. C., 2000, ''Heat (Mass) Transfer in a Diagonally Oriented Rotating Two-Pass Channel with Rib-Roughened Walls,'' ASME J. Heat Transfer , **122**, pp. 208–211.
[23] Chen, Y., Nikitopoulos, D. E., Hibbs, R., Acharya, S., and Myrum, T. A., 2000, ''Detailed Mass Transfer Distribution in a Ribbed Coolant Passage with a 180° Bend,'' Int. J. Heat Mass Transfer, **43**, pp. 1479–1492.
[24] Al-Hadhrami, L., and Han, J. C., 2003, ''Effect of Rotation on Heat Transfer in Two-Pass Square Channels with Five Different Orientations of 45° Angled Rib Turbulators,'' Int. J. Heat Mass Transfer, **46**, pp. 653–669.
[25] Liou, T. M., Tzeng, Y. Y., and Chen, C. C., 1999, ''Fluid Flow in a 180 Deg Sharp Turning Duct with Different Divider Thicknesses,'' ASME J. Turbomach., **121**, pp. 569–575.
[26] Liou, T. M., and Chen, C. C., 1999a, ''LDV Study of Developing Flows through a Smooth Duct with a 180 Deg Straight-Corner Turn,'' ASME J. Turbomach., **121**, pp. 167–174.
[27] Liou, T. M., and Chen, C. C., 1999b, ''Heat Transfer in a Rotating Two-Pass Smooth Passage with a 180° Rectangular Turn,'' Int. J. Heat Mass Transfer, **42**, pp. 231–247.
[28] Murata, A., Mochizuki, S., and Takahashi, T., 1999, ''Local Heat Transfer Measurement of an Orthogonally Rotating Square Duct with Angled Rib Turbulators,'' Int. J. Heat Mass Transfer, **42**, pp. 3047–3056.
[29] Willett, F. T., and Bergles, A. E., 2001, ''Heat Transfer in Rotating Narrow Rectangular Ducts with Heated Sides Orientated at 60° to the R-Z Plane,'' ASME J. Turbomach., **123**, pp. 288–295.
[30] Azad, G. S., Uddin, M. J., Han, J. C., Moon, H. K., and Glezer, B., 2002, ''Heat Transfer in a Two-Pass Rectangular Rotating Channel with 45-Deg Angled Rib Turbulators,'' ASME J. Turbomach., **124**, pp. 251–259.
[31] Al-Hadhrami, L., Griffith, T. S., and Han, J. C., 2003, ''Heat Transfer in Two-Pass Rotating Rectangular Channels (AR=2:1) with Five Different Orientations of 45° V-shaped Rib Turbulators,'' ASME J. Heat Transfer, **125**, pp. 232–242.
[32] Griffith, T. S., Al-Hadhrami, L., and Han, J. C., 2002, ''Heat Transfer in Rotating Rectangular Cooling Channels (AR=4) with Angled Ribs,'' ASME J. Heat Transfer, **124**, pp. 617–625.
[33] Lee, E., Wright, L. M., and Han, J. C., 2003, ''Heat Transfer in Rotating Rectangular Channels (AR=4:1) with V-shaped and Angled Rib Turbulators with and without Gaps,'' ASME paper no. 2003-GT-38900.
[34] Cho, H. H., Kim, Y. Y., Kim, K. M., and Rhee, D. H., 2003, ''Effects of Rib Arrangements and Rotation Speed on Heat Transfer in a Two-Pass Duct,'' ASME paper no. 2003-GT-38609.
[35] Agarwal, P., Acharya, S., and Nikitopoulos, D. E., 2003, ''Heat/Mass Transfer in 1:4 Rectangular Passages with Rotation,'' ASME paper no 2003-GT-38615.
[36] Kline, S. J., and McClintock, F. A., 1953, ''Describing Uncertainty in Single-Sample Experiments,'' Mech. Eng. (Am. Soc. Mech. Eng.), **75**, pp. 3–8.

The Transient Liquid Crystal Technique: Influence of Surface Curvature and Finite Wall Thickness

G. Wagner

M. Kotulla[1]

P. Ott

Laboratoire de Thermique Appliquée et de Turbomachine (LTT),
Swiss Federal Institute of Technology,
CH-1015 Lausanne, Switzerland

B. Weigand

J. von Wolfersdorf

Institute of Aerospace Thermodynamics (ITLR),
University of Stuttgart,
D-70569 Stuttgart, Germany

The transient liquid crystal technique is currently widely used for measuring the heat transfer characteristics in gas turbine applications. Usually, the assumption is made that the wall of the test model can be treated as a flat and semi-infinite solid. This assumption is correct as long as the penetration depth of the heat compared to the thickness of the wall and to the radius of curvature is small. However, those two assumptions are not always respected for measurements near the leading edge of a blade. This paper presents a rigorous treatment of the curvature and finite wall thickness effects. The unsteady heat transfer for a hollow cylinder has been investigated analytically and a data-reduction method, taking into account curvature and finite wall-thickness effects has been developed. Experimental tests made on hollow cylinder models have been evaluated using the new reduction method as well as the traditional semi-infinite flat-plate approach and a third method that approximately accounts for curvature effects. It has been found that curvature and finite thickness of the wall have, in some cases, a significant influence on the obtained heat transfer coefficient. The parameters influencing the accuracy of the semi-infinite flat-plate model and the approximate curvature correction are determined and the domains of validity are represented. [DOI: 10.1115/1.1811089]

Introduction

The demand for gas turbines with improved efficiency and higher power output has led to a continuous increase of the turbine inlet temperature. Consequently, turbine components, such as blades and platforms, are exposed to ever-higher thermal loads. To guarantee safe operating conditions and acceptable blade life, the designers have to optimize the cooling systems and to predict with sufficient precision the blade temperatures. To fulfill those tasks, detailed and accurate knowledge of the heat transfer characteristics of the blades are required.

Transient techniques have been successfully and widely used to measure the heat transfer coefficients on both internal and external surfaces of turbine blades (e.g., [1–3]). Ireland and Jones [4] used, for the first-time, liquid crystals together with the transient technique. They measured the heat transfer coefficient in blade-cooling passages with high spatial resolution and showed the importance of the method for gas turbine applications. The transient experiment is usually generated by a step change in the gas temperature. The evolution of the surface temperature during the transient test is measured and compared with the predictions of a one-dimensional heat conduction model for a prescribed heat transfer coefficient. This heat conduction model generally considers the wall of the test object as a flat, semi-infinite solid. This assumption is correct as long as the penetration depth of the heat compared to the thickness of the wall and to the radius of curvature is small. Schulz and Jones [5] evaluated that the semi-infinite model holds if the duration of the experiment is smaller than $t_{max}=d^2/16\alpha$. More recently, Vogel and Weigand [6] compared the semi-infinite model with a more complex finite model and showed that this criterion could be extended to $t_{max}<d^2/4\alpha$. Buttsworth and Jones [7] proposed a simple curvature correction based on a semi-infinite assumption and valid for $t_{max}\ll R^2/\alpha$. However, on thin and highly curved walls, such as in the leading-edge region of a film-cooled turbine blade, those limitations on t_{max} might be violated leading to incorrect heat transfer measurements. In this paper, an exact heat conduction model, taking into account the finite thickness of the wall and the curvature, is presented. The difference between the semi-infinite flat-plate approach, Buttsworth and Jones's curvature correction, and the exact solution are shown for typical experimental situations.

To verify the theoretical considerations, transient liquid crystal experiments were carried out on hollow cylinders with different wall thicknesses. Heat transfer coefficients are obtained by evaluating the measurement data with the different heat conduction models. The results are compared with recent correlations for convective heat transfer on a cylinder in crossflow [8–10]. The rigorous treatment of wall thickness and curvature effects presented in this paper should help to further improve accurate transient liquid crystal measurements.

Experimental Setup and Measuring Technique

Experimental Setup. A free-jet facility supplied by a continuously running compressor was used for this study (Fig. 1). The diameter of the free-jet nozzle was 150 mm. A square-meshed turbulence grid with a mesh size of 15 mm and a bar width of 3 mm was installed. The turbulence intensity at the location of the cylinder leading edge was about Tu=7%. The transient experiments were performed at two Mach numbers, Ma=0.11 and Ma=0.14, with a gas total temperature of 45°C. A nondimensional integral length scale of $L_x/D=0.30$ at Ma=0.14 was measured by Reiss [11] using a hot-wire probe.

A rapid insertion mechanism with a precooling box was used to generate the transient experiment. The Perspex hollow cylinder model was precooled and rapidly exposed to the hot crossflow. To investigate the influence of finite wall thickness and internal con-

[1]Present address: Institut für Luftfahrtantriebe (ILA), University of Stuttgart, D-70569 Stuttgart, Germany.

Contributed by the International Gas Turbine Institute (IGTI) of THE AMERICAN SOCIETY OF MECHANICAL ENGINEERS for publication in the ASME JOURNAL OF TURBOMACHINERY. Paper presented at the International Gas Turbine and Aeroengine Congress and Exhibition, Vienna, Austria, June 13–17, 2004, Paper No. 2004-GT-53553. Manuscript received by IGTI, December 1, 2003; final revision, March 1, 2004. IGTI Review Chair: A. J. Strazisar.

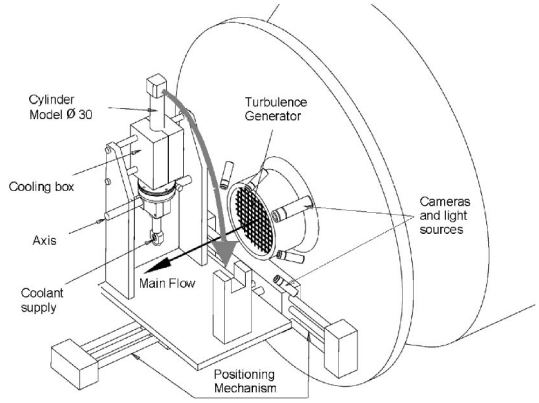

Fig. 1 Preconditioning of the cylinder model and rapid insertion mechanism

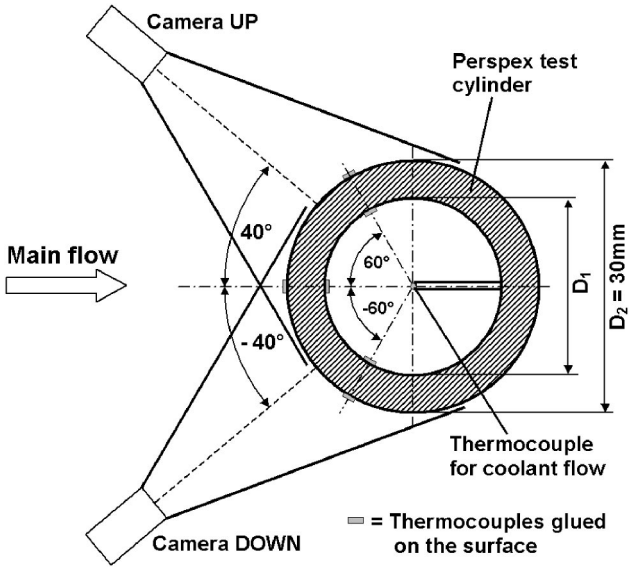

Fig. 2 Configuration of hollow cylinder model

vection on transient liquid crystal measurements, the cylinder was internally cooled. Coolant temperatures varied between 0 and 10°C. The cooling air for the preconditioning box and the internal coolant were provided by the same source of dried cold air. However, as different temperatures were required, individual mass flow and temperature regulation was possible.

Before the transient experiment, the model was in a vertical position and locked in the two-part cooling box for preconditioning the test section as shown in Fig. 1. During the preconditioning period the internal cooling was bypassed so that there was no coolant flow inside the cylinder. When the initial temperature was homogenous and at the desired level (typically −5°C), the cylinder could be inserted into the main flow for a transient test. Once the insertion mechanism was released, the preconditioning box opened and two springs pulled the cylinder, which pivoted rapidly into the free jet. At the same time, the coolant valve was triggered and the internal cooling was activated. A rubber stop locked the cylinder in the horizontal position. The time needed for the insertion (from the opening of the cooling box until the cylinder stops in its final position) was less than 0.15 s.

Three hollow cylinders with the same external diameter of 30 mm, but with different wall thicknesses of 2 mm, 5 mm, and 10 mm, were tested. The models were made out of Plexiglas XT because of its low thermal conductivity. To measure the initial temperature, thin thermocouples were glued on both the external and internal surfaces at 60 deg, 0 deg, and −60 deg (Fig. 2). Preliminary preconditioning tests have been done with a Perspex model containing eight thermocouples. It was found that the precooling setup allowed temperature uniformity of the test region within ±0.2°C. The coolant temperature during the transient test was measured with a thermocouple. At the external surface of the cylinder models, a thin and uniform liquid crystal coating was applied. The liquid crystals used for this study react at 36°C and show the whole visible spectrum in a 0.7°C temperature range.

Two 25 Hz color CCD cameras were installed for recording the color play of the liquid crystals on both sides of the cylinder. The viewing angles from the stagnation line were −40 deg and 40 deg (Fig. 2). A check of the symmetry of the results around the leading edge was then possible. Six light sources were fitted around the nozzle of the free jet in order to obtain a homogenous illumination of the test section.

Measuring Technique. In comparison to steady-state measurements, transient techniques are of short duration and allow performing many experiments in a reasonable measurement time. With the transient technique the undesirable lateral conduction inside the model is much smaller than the conduction normal to the surface and does not affect the results. Finally, no heater elements need to be fitted on the test surface, and complex geometries can be investigated. Different techniques can be used to generate the step change in the gas temperature. Ireland and Jones [4] employed fast-acting valves to suddenly activate a hot air flow through the test section, while Wang et al. [12] used electrical heater grids in the main flow. In the frame of this work, a precooled test model was rapidly exposed to a hot cross flow with a rotating insertion mechanism (Fig. 1).

Temperature evolution of the model surface is measured by a single layer of narrow-band thermochromic liquid crystals. The liquid crystal signal appears first in the area of high heat transfer, moves toward the lower heat transfer regions, and disappears when the surface temperature is higher than the reacting temperature of the liquid crystals. The video sequences of the transient tests are recorded on a digital support and transferred to a computer for the data reduction. An image processing based on a hue filtering detects the apparition time of the liquid crystal signal for every point on the two-dimensional surface. The resolution is only limited by the data acquisition system. The temperature corresponding to the liquid crystal signal is obtained by a calibration process. This hue capturing technique is further described by Ireland and Jones [13].

Data Analysis. The data analysis is based on the theory of one-dimensional heat conduction with a boundary condition of the third kind (convective heat exchange) at the outer surface. The transient experiments are usually evaluated using the model of a semi-infinite flat plate with a step change in gas temperature, for which the wall temperature response is given by

$$\Theta_w = \frac{T_w - T_i}{T_g - T_i} = 1 - \exp\left(\frac{h_{fp}^2 t}{k\rho c}\right) \mathrm{erfc}\left(\frac{h_{fp}\sqrt{t}}{\sqrt{k\rho c}}\right) \tag{1}$$

Knowing the time apparition of a specific temperature for a point on the surface, Eq. (1) can be solved in order to obtain the local heat transfer coefficient h_{fp}, where the subscript indicates the use of the flat-plate analysis. This model has the advantage of easy and time-effective evaluation.

For the semi-infinite approach the measurement time has to be limited as heat is only allowed to penetrate a small fraction of the wall thickness. The effects of finite wall thickness were evaluated by Vogel and Weigand [6] using the analytical solution of a finite flat plate with convection boundary conditions on both sides. For the investigation of heat transfer on curved surfaces with finite wall thickness, the analysis needs to be done for a hollow cylinder. Therefore, the unsteady, one-dimensional heat conduction in

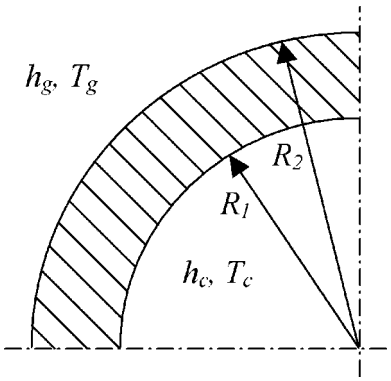

Fig. 3 Geometry under consideration

the geometry shown in Fig. 3 is investigated analytically. At the inner and the outer surface, heat is exchanged by convection.

Assuming one-dimensional transient heat conduction in the solid and under the assumption that the properties of the solid are constant, the energy equation simplifies to

$$\rho c \frac{\partial T}{\partial t} = \frac{k}{r}\frac{\partial}{\partial r}\left(r\frac{\partial T}{\partial r}\right) \tag{2}$$

with the following boundary conditions:

$$t=0: \quad T=T_i$$

$$r=R_2: \quad h_g[T_g - T(r=R_2)] - k\left.\frac{\partial T}{\partial r}\right|_{r=R_2} = 0 \tag{3}$$

$$r=R_1: \quad h_c[T_c - T(r=R_1)] + k\left.\frac{\partial T}{\partial r}\right|_{r=R_1} = 0$$

Introducing the following dimensionless quantities into Eqs. (2) and (3),

$$\tilde{r}=\frac{r}{R_1}, \quad \Theta=\frac{T-T_i}{T_g-T_i}, \quad \tau=\frac{t\alpha}{R_1^2} \text{ with } \alpha=\frac{k}{\rho c}$$
$$\mathrm{Bi}_g=\frac{h_g R_2}{k}, \quad \mathrm{Bi}_c=\frac{h_c R_1}{k}, \quad \Theta_c=\frac{T_c-T_g}{T_i-T_g}, \quad b=\frac{R_2}{R_1} \tag{4}$$

results in

$$\frac{\partial\Theta}{\partial\tau} = \frac{1}{\tilde{r}}\frac{\partial}{\partial\tilde{r}}\left(\tilde{r}\frac{\partial\Theta}{\partial\tilde{r}}\right) \tag{5}$$

$$\tau=0: \quad \Theta=0$$

$$\tilde{r}=b: \quad \frac{\mathrm{Bi}_g}{b}[1-\Theta(\tilde{r}=b)] - \left.\frac{\partial\Theta}{\partial\tilde{r}}\right|_{\tilde{r}=b} = 0 \tag{6}$$

$$\tilde{r}=1: \quad \mathrm{Bi}_c[1-\Theta_c-\Theta(\tilde{r}=1)] + \left.\frac{\partial\Theta}{\partial\tilde{r}}\right|_{\tilde{r}=1} = 0$$

The above given problem has a nonhomogeneous boundary condition for $\tilde{r}=1$. Therefore, we split the solution into two individual part as follows:

$$\Theta = \Theta_S + \Theta_T \tag{7}$$

where Θ_S denotes the steady-state temperature distribution of the problem and Θ_T describes the transient part. The steady-state part is given by

$$\Theta_S = A\ln\tilde{r} + B \tag{8}$$

with

$$A=\frac{\Theta_c}{\ln b + \frac{1}{\mathrm{Bi}_g} + \frac{1}{\mathrm{Bi}_c}}, \quad B=1-\frac{\Theta_c\left[\ln b + \frac{1}{\mathrm{Bi}_g}\right]}{\ln b + \frac{1}{\mathrm{Bi}_g} + \frac{1}{\mathrm{Bi}_c}} \tag{9}$$

For the transient problem, one has to solve the following equations:

$$\frac{\partial\Theta_T}{\partial\tau} = \frac{1}{\tilde{r}}\frac{\partial}{\partial\tilde{r}}\left(\tilde{r}\frac{\partial\Theta_T}{\partial\tilde{r}}\right) \tag{10}$$

$$\tau=0: \quad \Theta_T = 1 - A\ln\tilde{r} - B$$

$$\tilde{r}=b: \quad \mathrm{Bi}_g\Theta_T(\tilde{r}=b) + \left.\frac{\partial\Theta_T}{\partial\tilde{r}}\right|_{\tilde{r}=b} = 0 \tag{11}$$

$$\tilde{r}=1: \quad -\mathrm{Bi}_c\Theta_T(\tilde{r}=1) + \left.\frac{\partial\Theta_T}{\partial\tilde{r}}\right|_{\tilde{r}=1} = 0$$

A solution of these equations can be obtained by using the method of separation of variables. Inserting the expression

$$\Theta_T = T(\tau)R(\tilde{r}) \tag{12}$$

into Eqs. (10) and (11) results in

$$T_n = C_{n1}\exp(-\lambda_n^2\tau) \tag{13}$$

and for the eigenfunctions $R_n(\tilde{r})$, the following eigenvalue problem is obtained:

$$R_n'' + \frac{1}{\tilde{r}}R_n' + \lambda_n^2 R_n \tag{14}$$

$$\tilde{r}=b: \quad \mathrm{Bi}_g R_n(b) + R_n'(b) = 0$$
$$\tilde{r}=1: \quad -\mathrm{Bi}_c R_n(1) + R_n'(1) = 0 \tag{15}$$

Equations (14) and (15) have the solution

$$R_n(\tilde{r}) = E_n\left\{J_0(\lambda_n\tilde{r}) - \frac{\lambda_n J_1(\lambda_n) + \mathrm{Bi}_c J_0(\lambda_n)}{\lambda_n Y_1(\lambda_n) + \mathrm{Bi}_c Y_0(\lambda_n)}Y_0(\lambda_n\tilde{r})\right\} \tag{16}$$

where J_0, J_1, Y_0, and Y_1 are Bessel's functions. The eigenvalues are given by the transcendental equation

$$[\mathrm{Bi}_g J_0(\lambda_n b) - \lambda_n J_1(\lambda_n b)][\mathrm{Bi}_c Y_0(\lambda_n) + \lambda_n Y_1(\lambda_n)]$$
$$-[\mathrm{Bi}_g Y_0(\lambda_n b) - \lambda_n Y_1(\lambda_n b)][\mathrm{Bi}_c J_0(\lambda_n) + \lambda_n J_1(\lambda_n)] = 0 \tag{17}$$

The solution for the transient part of the problem is given by

$$\Theta_T = \sum_{n=1}^{\infty} D_n R_n(\tilde{r})\exp(-\lambda_n^2\tau) \tag{18}$$

with

$$D_n = -\frac{\int_1^b [B + A\ln\tilde{r}]\tilde{r}R_n(\tilde{r})d\tilde{r}}{\int_1^b \tilde{r}R_n^2(\tilde{r})d\tilde{r}} \tag{19}$$

The surface temperature $\Theta(\tilde{r}=b,\tau)=\Theta_S+\Theta_T$ is finally

$$\Theta_w(\tau) = \frac{T_w - T_i}{T_g - T_i} = A\ln(b) + B + \sum_{n=1}^{\infty} D_n R_n(b)\exp(-\lambda_n^2\tau) \tag{20}$$

The above-obtained solution can also be derived by using the Laplace transform technique and the reader is referred to Carslaw and Jäger [14] for this type of approach. Equation (20) will be used for the hollow cylinder.

Uncertainty Analysis. The uncertainties in the measurement of the temperatures T_g, T_w, T_i, and in the detection of the liquid

Table 1 Measurements errors

Quantity	Typical value	Measurement error
T_g	318.5 K	±0.15 K
T_i	268 K	±0.75 K
T_w	309 K	±0.2 K
t	15–60 s	±0.1 s
T_c	280 K	±7 K
h_c	13–80 W/m^2 K	±50%

crystal apparition time t result in an error on the obtained heat transfer coefficient. This error appears to be bigger for high heat transfer regions, such as the leading edge, which can be explained by a shorter apparition time and then a higher relative error $\Delta t/t$. Table 1 shows the measurement errors of the experiments carried out in the frame of this study.

For the semi-infinite case, an error analysis as detailed by Ireland [15] has been performed on Eq. (1). The first four errors from Table 1 together with reasonable uncertainties on the material properties indicated an error on the obtained heat transfer coefficient of 5.7% for the leading-edge region.

An analytical error analysis being too complex for the exact solution (Eq. (20)), a numerical parameter study has been performed. As internal convection is here taken into account, the uncertainties of the internal coolant temperature T_c and heat transfer coefficient h_c have to be considered. It appeared that T_c and h_c have only little influence in the obtained heat transfer coefficient. Even with large uncertainties of 7 K for T_c and 50% for h_c, the error on the heat transfer coefficient were within 5.5% for $h_g = 345$ W/m^2 K (leading-edge region) and 4.5% for $h_g = 170$ W/m^2 K. Those uncertainties are due to the errors in the measurement of the different experimental parameters, but do not include the error due to the data analysis, which are treated in the next section.

Effects of Wall Curvature, Thickness/Backside Heat Transfer

Simplified Model: Effect of Wall Curvature. For curved walls, Buttsworth and Jones [7] used Laplace transforms and provided, in similarity to Eq. (1), a simplified approximate solution valid for $\tau_R = \alpha t/R^2 \ll 1$, which is given as

$$\Theta_w = \frac{1}{1 \pm \dfrac{\sigma k}{2 h_R R}} \left[1 - \exp\left(\frac{\left(h_R \pm \dfrac{\sigma k}{2R} \right)^2 t}{k\rho c} \right) \operatorname{erfc}\left(\frac{\left(h_R \pm \dfrac{\sigma k}{2R} \right) \sqrt{t}}{\sqrt{k\rho c}} \right) \right] \tag{21}$$

where $\sigma=1$ for a cylinder, $\sigma=2$ for a sphere, the plus sign for concave surfaces and the minus sign for convex surfaces.

Using the approximate solution (Eq. (21)) for the data evaluation of the liquid crystal indications, the determined heat transfer coefficient h_R takes approximately into account the effect of wall curvature. It is the aim of this section to show the influence of curvature and the range of applicability of Eqs. (1) and (21). In the case of large radius of curvature ($R \to \infty$), Eq. (21) reduces to Eq. (1) and the determined heat transfer coefficient is $h_g = h_{fp} = h_R$.

Analyzing a transient liquid crystal experiment involves determining the heat transfer coefficient corresponding to the apparition of the dimensionless temperature Θ_w at time t. The value of the heat transfer coefficient determined from a transient experiment on a convex surface will be higher using the flat-plate model (Eq. (1)) than using Eq. (21), which is $h_R < h_{fp}$. For a concave surface one obtains $h_R > h_{fp}$. This is shown in Fig. 4 for cylindrical convex and concave surfaces. For this comparison the following procedure was applied. First the heat transfer coefficient on a curved surface h_R is prescribed, and Eq. (21) is used to evaluate the wall temperature history. Then for chosen liquid crystal indication temperatures and, therefore, different Θ_w, Eq. (1) is solved to obtain h_{fp}.

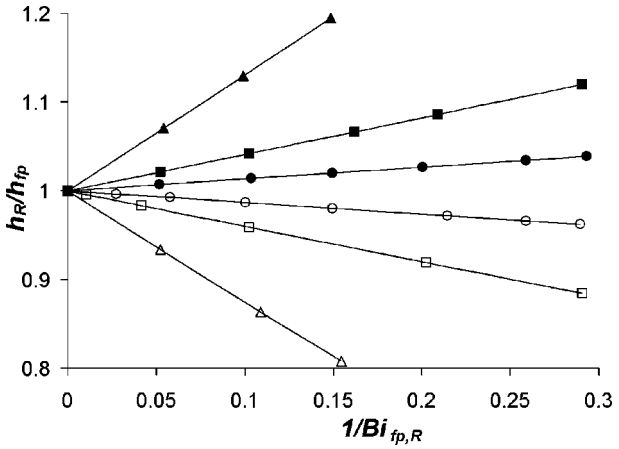

Fig. 4 Effect of surface curvature using comparison between Eqs. (1) and (21)

The ratio h_R/h_{fp} is given in Fig. 4 for different Biot numbers based on h_{fp} and R. Figure 4 shows that for Biot numbers usually found in transient experiments (typically $\mathrm{Bi}_{fp,R} > 10$), the curvature effect can lead to errors up to 10%. For shorter measurement times (lower Θ_w), the differences are smaller, which needs to be considered in the experimental layout. Analyzing some published transient experiments on cylindrical surfaces (e.g., [16–18]), the influence of curvature for the used experimental parameters was found to be less than 3%. The curvature influence needs to be considered especially for small curvature radius tests as found, e.g., in the leading-edge area of gas turbine blades using cascade heat transfer experiments.

Using the exact solution (Eq. (20)) to calculate the temperature history data for a prescribed heat transfer coefficient h_g and analyzing the data for different times with the approximate solution (Eq. (21)) in order to obtain h_R reveals the error of the approximate solution. As given by Buttswort and Jones [7], the ratio h_R/h_g can be represented versus τ_R for different Biot numbers based on h_g and R. This is shown in Fig. 5 for the convex and concave cylinders.

For the cases investigated, it is shown that the approximate solution (Eq. (21)) describes the wall temperature history with sufficient accuracy for

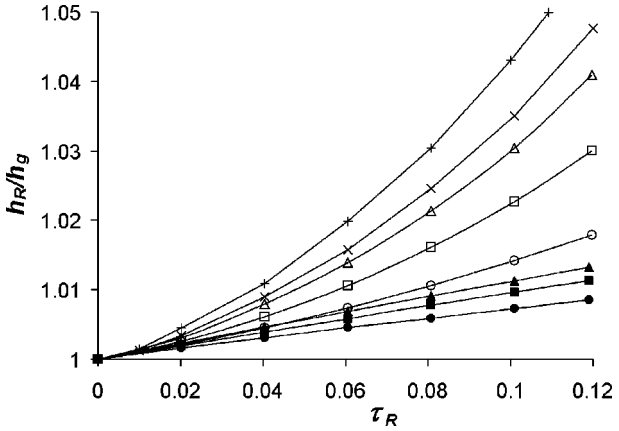

Fig. 5 Deviation of the approximate solution Eq. (21) from the exact solution Eq. (20)

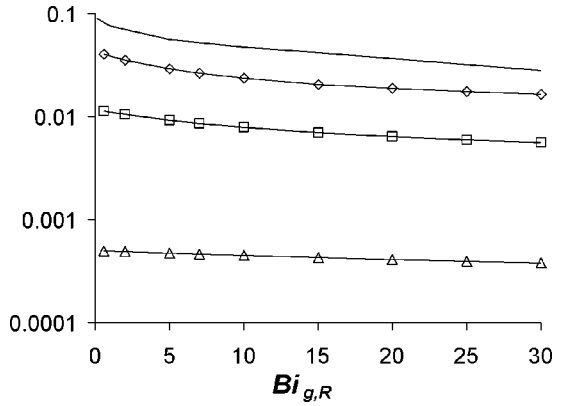

Fig. 6 Regions of validity for approximate (Eq. (21)) and flat plate (Eq. (1)) solutions depending on allowable error

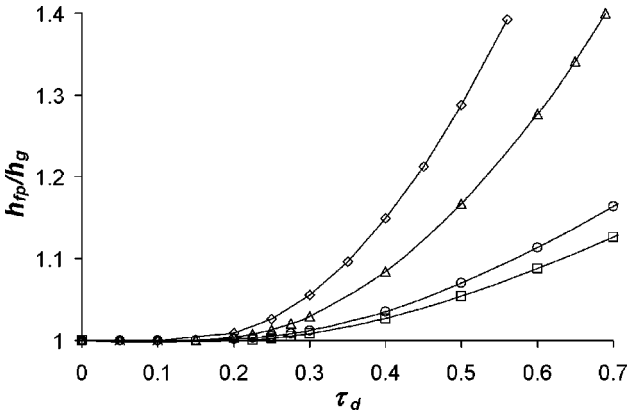

Fig. 7 Effect of finite wall thickness for flat plate

$$\tau_R = \frac{\alpha t}{R^2} < 0.02 \tag{22}$$

If Eq. (22) is respected, then the difference of the evaluated heat transfer coefficient with Eq. (21) to the prescribed value is less than 1%. This is important in data evaluation procedures of transient experiments because Eq. (21) is much easier to evaluate than the exact solution, and existing data reduction software can easily be adopted to curved walls due to the similarity of Eqs. (1) and (21). Furthermore, if experiments are made with a time-varying gas temperature, Eq. (21) can easily be adapted to this using the superposition method as usually applied for flat surfaces (e.g., [19]).

The importance to take the curvature into account and the range of validity for the flat plate and the approximate solution is illustrated in Fig. 6. This figure shows combinations of τ_R and $\mathrm{Bi}_{g,R}$ for which the differences in evaluated heat transfer coefficients are below specific errors. Below the uppermost curve (no symbols), the heat transfer coefficient evaluated from the approximate solution is within 1% to the exact value. Using the same accuracy for the flat-plate solution, the lowest curve is obtained. Increasing the allowable error in the evaluated heat transfer coefficient, the region for the flat plate solution is increased.

Effect of Wall Thickness. For film cooling experiments with showerhead cooling, the test models have to have a finite thickness to simulate the correct hole length-to-diameter ratio. This can lead to thin wall models, where the assumption of a semi-infinite solid might not be correct. Schultz and Jones [5] give a criterion for the maximum test time related to the thermal penetration distance of $\tau_d = \alpha t/d^2 = 1/16$. This criterion is very severe. As shown by Vogel and Weigand [6]; for a flat plate with typical Biot numbers, the error in the determined heat transfer coefficient is small and the semi-infinite assumption can be considered valid as long as

$$\tau_d = \frac{\alpha t}{d^2} < \frac{1}{4} \tag{23}$$

This is shown in Fig. 7. Here a wall of finite thickness with an adiabatic backside is considered. Using the analytical solution (e.g., [6,14]) with $\mathrm{Bi}_c = 0$, the time temperature history for several gas-side Biot numbers, $\mathrm{Bi}_{g,d} = h_g d/k$, and wall thicknesses can be calculated. Here the wall thickness is used in the Biot number as an appropriate dimension. Evaluating the wall temperature history using Eq. (1) leads to deviations depending on the Biot number and the dimensionless time considered.

Since the approximate solution for the curved wall (Eq. (21)) is based on the assumption that the heat penetrates only a relatively small distance into the wall, it is expected that this behavior is similar for a curved wall.

Calculating the time temperature history with the exact solution, Eq. (20), and analyzing the wall temperature evolution, using Eq. (21), reveals the influence of the wall thickness on a curved surface. For a given Biot number, the results shown in Fig. 8 are obtained.

It is seen, that the behavior is very similar to the flat plate. For thickness-to-curvature radius ratio of $d/R = 0$ the values for the flat plate are obtained. The d/R ratio shows little effect up to $d/R = 0.33$. For higher d/R, Fig. 8 indicates increasing differences between Eqs. (20) and (21) for increasing d/R. Since the semi-infinite assumption should hold better for larger d/R, this is, in the first view, somewhat unexpected. In this investigation the radius of curvature was changed keeping the wall thickness constant. Therefore, for a given time τ_d is constant but τ_R changes. The effect observed in Fig. 8 for $d/R \geq 0.33$ is the deviation of the approximate solution Eq. (21) from the exact solution (see Fig. 5). If one compares the time scales for curvature and thickness effects τ_R and τ_d and considers Eqs. (22) and (23) as limits for Eq. (21) to hold, one obtains

$$\left(\frac{d}{R}\right)_{\lim} < \sqrt{\frac{0.02}{0.25}} \approx 0.28 \tag{24}$$

This means that the deviation of Eq. (21) from the exact solution is the reason of the differences for larger d/R. Hence, the time criterion from the flat wall investigation obtained by Vogel

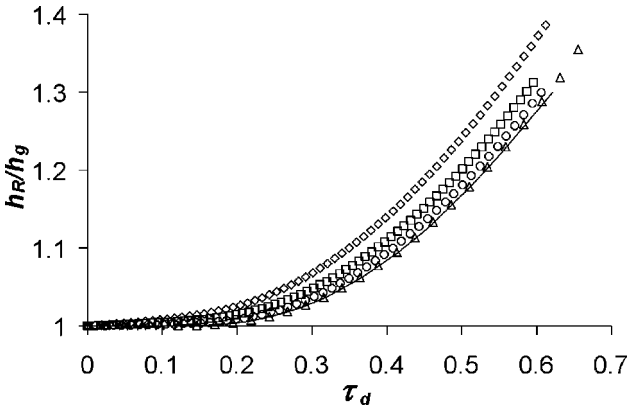

Fig. 8 Effect of finite wall thickness for convex cylinder wall for $\mathrm{Bi}_{g,d} = 5$

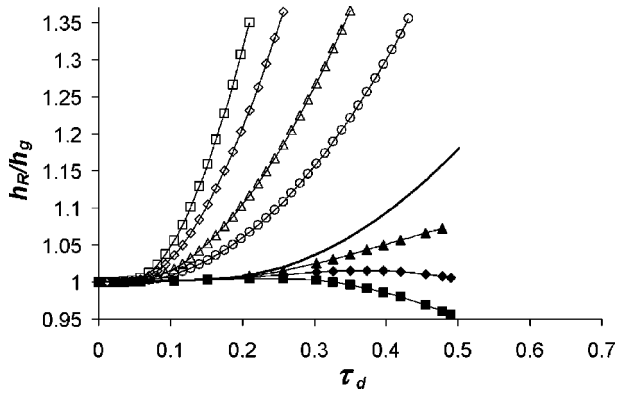

Fig. 9 Effect of backside convection for $Bi_{g,d}=5$

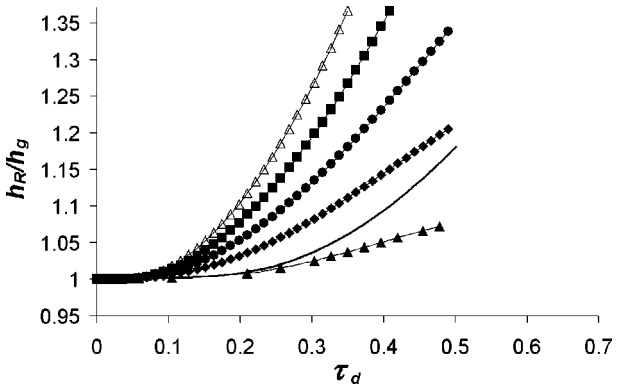

Fig. 10 Effect of backside temperature condition for $Bi_{g,d}=5$

and Weigand [6] [Eq. (23)] is also valid for curved walls if the curvature effect is taken into account using Eq. (21).

Backside Convection. For transient heat transfer experiments related to film cooling investigations, the influence of backside convection needs to be considered. Having a thin wall cylinder model heated from the outer wall, several conditions are possible for the backside.

Cooling the inner wall with a temperature equal to the model initial temperature would consider a typical film cooling experiment with a step change in hot gas temperature.

Heating the inner wall with a temperature above the initial model temperature equal to the hot gas-side temperature would relate to a heat transfer experiment with isothermal blowing, e.g., measuring the effect of film cooling blowing on heat transfer without a film-cooling effect.

Having both fluid temperatures on the outer and inner walls above the model initial temperature is a typical situation for simultaneous measurements of film-cooling effectiveness and heat transfer coefficient use (e.g., a model insertion technique [3,20]).

The effect of the backside convection is addressed for different dimensionless coolant temperatures and coolant side Biot numbers using

$$\Theta_c=\frac{T_c-T_i}{T_g-T_i}, \quad \mathrm{Bi}_{c,d}=\frac{h_c d}{k} \tag{25}$$

For heating conditions ($\Theta_c=1$), the allowable maximum test time reduces from the adiabatic case ($\mathrm{Bi}_{c,d}=0$), with decreasing values of τ_d in case of increasing coolant-side heat transfer coefficients. Cooling the backside ($\Theta_c=0$) allows the maximum test time to be extended. The results are shown in Fig. 9.

The cases with different temperatures above the model initial temperature on both sides will lie between these two limiting cases. This is shown in Fig. 10 where for a given gas-side Biot-number the value of Θ_c is varied. Using the comparison between the exact solution and the approximate solution helps in selecting the correct experimental parameters and determining uncertainties introduced using the simple Eq. (21). This equation has the advantage of being implemented straightforwardly in existing data reduction procedures and can easily be extended to more complex situations with time-varying fluid temperatures.

Experimental Results

To verify the abovementioned theoretical considerations, heat transfer measurements were carried out on a hollow cylinder exposed to a crossflow. Tests were performed at Ma=0.11 and Ma =0.14 on three hollow cylinders with the same outer diameter, but with various wall thicknesses: 2, 5, and 10 mm. Both Mach numbers show very similar values of $\mathrm{Nu}_D/\sqrt{\mathrm{Re}_D}$. For this reason, only the case Ma=0.14 is presented here. The main flow and temperature conditions are given in Table 2, while Table 3 summarizes the time duration and the dimensionless quantities of the different tests. The three heat conduction models presented above [Eqs. (1), (20), and (21)] are used to obtain the heat transfer coefficient from the wall temperature history of the transient test.

Semi-Infinite Flat Plate Model. The first approach chosen for the data reduction was to evaluate the transient tests using Eq. (1). This model, based on a flat-plate geometry is simple, time effective, and widely used for the transient liquid crystal technique. However, it does not take into account the curvature effects and the finite thickness of the wall. The $\mathrm{Nu}_D/\sqrt{\mathrm{Re}_D}$ values obtained for the different cylinders with the semi-infinite flat-plate model are compared in Fig. 11 with the correlations from Dullenkopf and Mayle [8], van Fossen et al. [9], and Oo and Ching [10].

The cylinder with a 2 mm thick wall shows a heat transfer coefficient too high in comparison to the 5 and 10 mm test models and to the correlations. For the 2 mm wall τ_d reaches 0.602 (Table 3), Bi_d being about 3.6; Fig. 7 shows clearly that the semi-infinite assumption is not valid in this case. When the heat pulse reaches the inner surface it faces a higher thermal resistance. The rise of the temperature on the outer surface becomes then faster than for a semi-infinite solid. As a result, if the solid is assumed to be semi-infinite, the heat transfer coefficient on the outer surface is overpredicted for long measurement time. For the 5 and 10 mm thick walls, τ_d reaches only 0.145, respectively 0.042 and Eq. (23) is respected. In this case, the finite thickness of the wall has no influence on the temperature evolution on the outer surface. The cylinders with 5 and 10 mm walls give then very similar heat transfer coefficients.

However, $\mathrm{Nu}_D/\sqrt{\mathrm{Re}_D}$ of the 5 and 10 mm thick hollow cylinders are still too high compared to the correlations because the curvature is not taken into account in Eq. (1). For a convex body,

Table 2 Main flow and temperature conditions

Ma (−)	Re (−)	Tu (%)	L_x (mm)	T_q (K)	T_c (K)	T_i (K)
0.14	86,600±500	7±1	9±1	318.5	~280	~268

Table 3 Time duration and dimensionless parameters for the three test models

	2 mm	5 mm	10 mm
$t_{\max}$ (s)	23	35	40
$\tau_{d,\max}(-)$	0.602	0.145	0.042
$\tau_{R,\max}(-)$	0.011	0.016	0.019
$\mathrm{Bi}_{g,d}(-)$	3.6	9	18
$\mathrm{Bi}_{g,R}(-)$	27	27	27
$d/R(-)$	0.133	0.333	0.667
$\Theta_w(-)$	0.82	0.82	0.82

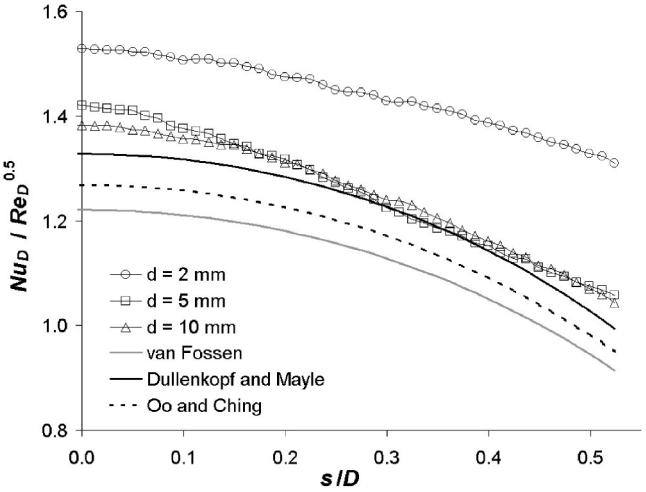

Fig. 11 Heat transfer coefficient obtained using the flat plate semi-infinite model (Eq. (1))

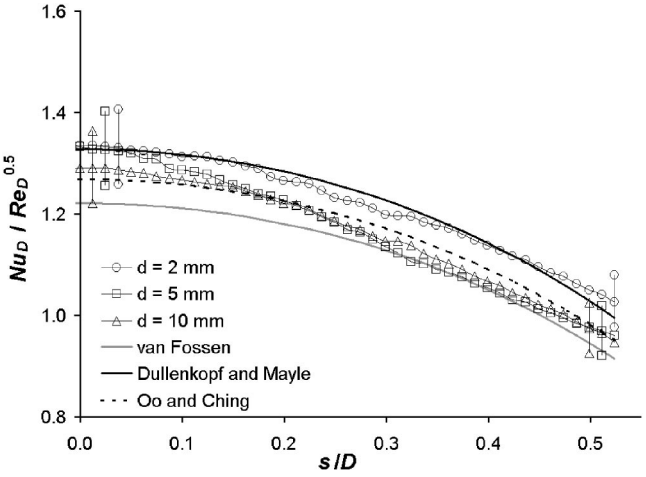

Fig. 13 Heat transfer coefficient obtained using the exact solution (Eq. (20))

the surface available for heat conduction in the direction normal to the test surface becomes smaller as the heat penetrates deeper into the solid. As a matter of fact, the thermal resistance increases and the evolution of the surface temperature during the transient test is faster than it would be on a flat body. Assuming a flat surface for a convex test model results in over-predicting the heat transfer coefficient. In the present case, according to Table 3 and Fig. 4, h_{fp} is about 7% higher than the correct value.

The errors of the experimental data showed in Fig. 11 are due to both, the errors in the measurement of the experimental parameters and non-consideration of finite thickness and curvature effects in the data analysis.

Semi-Infinite Model With Approximate Curvature Correction. The measured data was also analyzed using the simplified model from Buttsworth and Jones [7], that is to say with Eq. (21) instead of Eq. (1). The results obtained for the three test cylinders are compared in Fig. 12 with the correlations.

In comparison to the results of Fig. 11, Eq. (21) shifts the heat transfer coefficient toward smaller values and brings it closer to the correlations. The heat transfer coefficient obtained for the 5 and 10 mm thick cylinders is in good agreement with the correlations. As shown in Fig. 5, Eq. (21) accurately takes into account the curvature effects for $\tau_R < 0.02$, which is the case here. $\mathrm{Nu}_D/\sqrt{\mathrm{Re}_D}$, resulting from the measured data of the 2 mm thick cylinder, is still too high because the semi-infinite assumption is not valid for this test model. Figure 7 shows that in this case the semi-infinite assumption provides a heat transfer coefficient about 25% too high. The errors of the experimental results from Fig. 12 are due to the errors in the measurement of the experimental parameters and for the 2 mm thick cylinder to the nonconsideration of finite thickness effects in the data analysis.

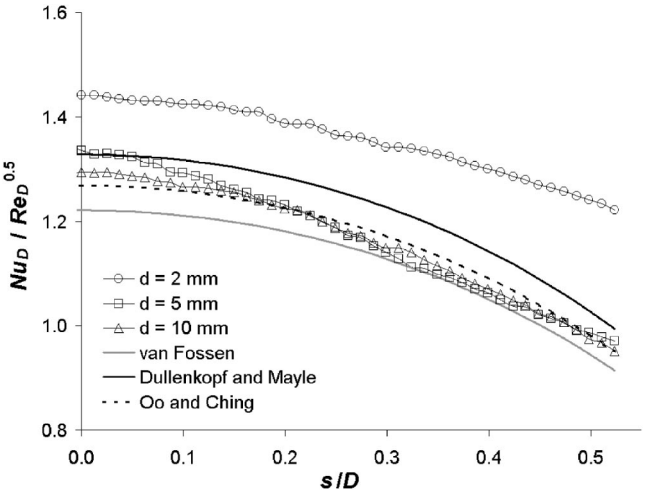

Fig. 12 Heat transfer coefficient obtained using the approximate model (Eq. (21))

Hollow Cylinder Model. Finally, the exact analytical solution (Eq. (20)) was used for the data reduction of the tests. Both curvature effects and finite wall thickness are here taken into account, but the calculations are much more time consuming than for the two models discussed above. The $\mathrm{Nu}_D/\sqrt{\mathrm{Re}_D}$ results are presented in Fig. 13 together with the correlations.

The heat transfer coefficients obtained for the cylinders with 5 and 10 mm thick walls hardly change between Fig. 12 and Fig. 13. This confirms that for those two cylinder models, both the semi-infinite assumption and the simple curvature correction from Buttsworth and Jones [7] (Eq. (21)) are correct. With the exact analytical heat conduction model, the measurements on the cylinder with a 2 mm thick wall give now reliable results that are in good agreement with the correlations. The differences between the three cylinder models are less than 10%. As both curvature and finite thickness effects are here taken into account, the data analysis is correct. The uncertainties of the experimental data are thus only due to the errors in the measurement of the experimental parameters. The measurement uncertainties are given by the error bars added at $s/D=0$ and 0.5.

For the cylinders with 5 and 10 mm thick walls, the semi-infinite model with the simple correction from Buttsworth and Jones [7] (Eq. (21)) is sufficient to give accurate results, while the exact analytical solution (Eq. (20)) is needed for the 2 mm thick wall model in order to take into account the finite wall thickness.

Conclusion

A new data analysis method for transient liquid crystal measurements is presented. The new analysis is based on the equation of heat conduction in a hollow cylinder and exactly accounts for curvature and finite wall thickness effects.

Comparisons with the classical semi-infinite flat-plate approach and with the simplified curvature correction from Buttsworth and Jones [7] showed that curvature effects and the finite thickness of the wall can have significant influence in transient heat transfer experiments.

To verify the analytical results, transient liquid crystal measurements were evaluated with the different analysis methods. The experimental results validated the analytical considerations and showed good agreement with recent heat transfer correlations.

Nomenclature

Symbols

b = radius ratio
Bi = Biot number
c = specific heat capacity
d = wall thickness
D = diameter of cylinder
h = heat transfer coefficient
h_{fp} = heat transfer coefficient from flat plate analysis Eq. (1)
h_R = heat transfer coefficient from simplified model Eq. (21)
k = thermal conductivity
L_x = turbulent length scale
Ma = Mach number
Nu = Nusselt number
r = radius
$\tilde{r}$ = dimensionless radial coordinate
R = radius of curvature
Re = Reynolds number
s = coordinate at surface from stagnation point
t = time
T = temperature
Tu = turbulence level

Greek

α = thermal diffusivity
λ = eigenvalues
ρ = density
Θ = dimensionless temperature
σ = curvature parameter (1-cylinder, 2-sphere)
τ = dimensionless time

Subscripts

c = coolant
d = based on wall thickness
fp = evaluated with semi-infinite flat-plate assumption
g = hot gas
i = initial
R = based on radius of curvature
w = wall
1 = inner wall
2 = outer wall

References

[1] Clifford, R. J., Jones, T. V., and Dunne, S. T., 1983, ''Techniques for Obtaining Detailed Heat Transfer Coefficient Measurements Within Gas Turbine Blade and Vane Cooling Passages,'' ASME Paper No. 83-GT-58.
[2] Guo, S. M., Spencer, M. C., Lock, G. D., Jones, T. V., and Harvey, N. W., 1995, ''The Application of Thin Film Gauges on Flexible Plastic Substrates to the Gas Turbine Situation,'' ASME Paper No. 95-GT-357.
[3] Drost, U., and Bölcs, A., 1998, ''Investigation of Detailed Film Cooling Effectiveness and Heat Transfer Distributions on a Gas Turbine Airfoil,'' ASME Paper No. 98-GT-20.
[4] Ireland, P. T., and Jones, T. V., 1985, ''The Measurements of Local Heat Transfer Coefficients in Blade Cooling Geometries,'' *Heat Transfer and Cooling in Gas Turbines, Propulsion and Energetics Panel 65th Symposium*, CP 390 Paper No. 28, Bergen.
[5] Schultz, D. L., and Jones, T. V., 1973, ''Heat Transfer Measurements in Short Duration Hypersonic Facilities,'' NATO Advisory Group Aeronautical RD AGARDOGRAPH 165.
[6] Vogel, G., and Weigand, B., 2001, ''A New Evaluation Method for Transient Liquid Crystal Experiments,'' National Heat Transfer Conf., NHTC2001-20250, California.
[7] Buttsworth, D. R., and Jones, T. V., 1997, ''Radial Conduction Effects in Transient Heat Transfer Experiments,'' Aeronaut. J., **101**, pp. 209–212.
[8] Dullenkopf, K., and Mayle, R. E., 1994, ''An Account of Free-Stream-Turbulence Length Scale on Laminar Heat Transfer,'' ASME Paper No. 94-GT-174.
[9] Van Fossen, G. J., Simoneau, R. J., and Ching, C. Y., 1995, ''Influence of Turbulence Parameters, Reynolds Number, and Body Shape on Stagnation Region Heat Transfer,'' ASME J. Heat Transfer, **117**, pp. 598–603.
[10] Oo, A. N., and Ching, C. Y., 2001, ''Effect of Turbulence With Different Vortical Structures on Stagnation Region Heat Transfer,'' ASME J. Heat Transfer, **123**, pp. 665–674.
[11] Reiss, H., 2000, ''Experimental Study on Film Cooling of Gas Turbine Airfoils Using Shaped Holes,'' Ph.D. thesis No. 2209, EPFL, Switzerland.
[12] Wang, Z., Ireland, P. T., Kohler, S. T., and Chew, J. W., 1996, ''Heat Transfer Measurements to a Gas Turbine Cooling Passage With Inclined Ribs,'' ASME Paper No. 96-GT-542.
[13] Ireland, P. T., and Jones, T. V., 2000, ''Liquid Crystal Measurements of Heat Transfer and Surface Shear Stress,'' Meas. Sci. Technol., **11**, pp. 969–985.
[14] Carslaw, H. S., and Jaeger, J. C., 1992, *Conduction of Heat in Solids*, Second Edition Oxford Science, Clarendon, Oxford, UK.
[15] Ireland, P. T., 1987, ''Heat Transfer in Gasturbines,'' Ph.D. thesis, Oxford University, Oxford, UK.
[16] Ekkad, S. V., Han, J. C., and Du, H., 1998, ''Detailed Film Cooling Measurements on a Cylindrical Leading Edge Model: Effect of Free-Stream Turbulence and Coolant Density,'' ASME J. Turbomach., **120**, pp. 799–807.
[17] Butler, R. J., and Baughn, J. W., 1994, ''Validation of an In Situ Heated Transient Technique With Local Heat Transfer Measurements on a Cylinder in Crossflow,'' 6th AIAA/ASME Thermophysics and Heat Transfer Conference, AIAA Paper No. 94-2009.
[18] Baughn, J. W., Ireland, P. T., Jones, T. V., and Saniei, N., 1989, ''A Comparison of the Transient and Heated-Coating Methods for Measurement of Local Heat Transfer Coefficients on Pin Fin,'' ASME J. Heat Transfer, **111**, pp. 877–881.
[19] Ekkad, S. V., and Han, J. C., 2000, ''A Transient Liquid Crystal Thermography Technique for Gas Turbine Heat Transfer Measurements,'' Meas. Sci. Technol., **11**, pp. 957–968.
[20] Falcoz, C., 2003, ''A Comparative Study of Showerhead Cooling Performance,'' Ph.D. thesis No. 2735, EPFL, Switzerland.

Turbulent Augmentation of Internal Convection Over Pins in Staggered-Pin Fin Arrays

F. E. Ames

L. A. Dvorak

M. J. Morrow

Mechanical Engineering Department,
University of North Dakota,
Grand Forks, ND 58202

The objective of this research was to investigate pin fin midline heat transfer in terms of our understanding of stagnation region heat transfer for cylinders in cross flow and turbine airfoils. An experimental investigation was conducted in a staggered-pin fin array at Reynolds numbers of 3000, 10,000, and 30,000 based on the maximum velocity between cylinders. Midline distributions of static pressure and heat transfer were acquired for rows 1 through 8 at the three Reynolds numbers. Turbulence measurements and velocity distributions were acquired at the inlet and in between adjacent pins in rows using hot wire anemometry. One-dimensional power spectra were calculated to determine integral and energy scales. Midline heat transfer distributions are reported as the Nusselt number divided by the square root of the Reynolds number as a function of angle. In these terms, heat transfer was found to increase through row 3 for a Reynolds number of 30,000. After row 3, heat transfer diminished slightly. The Reynolds number for each row was recast in terms of an effective approach velocity, which was found to be highest in row 3 due to the upstream blockage of row 2. Based on this effective velocity the Nusselt number divided by the square root of the Reynolds number increased through row 4. These data indicate that heat transfer is highest in row 3 pins due to the highest effective velocity, while heat transfer augmentation due to turbulence is highest in row 4 and beyond. Hot wire measurements show higher turbulence intensity and dissipation rates upstream of row 4 compared to upstream of row 3. Generally, pressure, heat transfer, and turbulence measurements were taken at all rows, providing a better understanding of turbulent transport from pin fin arrays. [DOI: 10.1115/1.1811090]

Introduction

Gas turbine heat transfer designers typically use empirical correlations based on bench scale testing to prescribe boundary conditions for pin fin and other internal cooling arrangements. Consequently, heat transfer engineers are constrained to a limited range of internal geometries when specifying the initial configurations. However, cooling path geometries frequently push a design outside the envelope of tested arrangements. Verification testing often takes place well after designs are committed to manufacturing. Hot section cooling engineers are in need of accurate and flexible internal heat transfer and flow predictive methods. The pin fin heat transfer and fluid dynamic research presented in this paper is part of a comprehensive study to clarify the physics of transport mechanisms in pin fin arrays. This research is expected to help lead to the development of more physically based predictive tools for designers.

Background

Research on pin fin array heat transfer and fluid flow includes measurements of average array heat transfer and pressure drop, row resolved heat transfer rates, local measurements of heat transfer on pins and endwalls, turbulence measurements, and numerical predictions. The present research studies the influence of array-generated turbulence on midline heat transfer rates and pressure distributions on pin fin surfaces. The object of this investigation is to clarify the physics of flow and heat transfer rates in internal passages. The present experimental configuration has low inlet turbulence levels and a uniform velocity field, which is typical of most pin fin array heat transfer studies.

Average Array Heat Transfer. Armstrong and Winstanley [1] reviewed staggered-array heat transfer for turbine cooling applications. They recommend the Metzger et al. [2] correlation for short pins. Metzger studied heat transfer rates from staggered arrays with short pin fins ($H/D=1$) and with a spanwise spacing of (S/D) of 2.5 in air. He correlated average heat transfer rates on Re_{Dm} and streamwise spacing (X/D).

$$\mathrm{Nu}_D = 0.135\,\mathrm{Re}_{Dm}^{0.685}(X/D)^{-0.34} \qquad 10^3 < \mathrm{Re}_{Dm} < 10^5 \tag{1}$$

Typical of most investigations, Metzger correlated his results on a pin-diameter Reynolds number, Re_{Dm}, which is based on the mass averaged velocity between the minimum pin to pin flow area, $V_{\max}$. More recently, Chyu et al. [3] studied the effects of thermal boundary conditions on average and individual row heat transfer. Chyu used naphthalene sublimation in a manner allowing the separate measurement of heat transfer from pins and the endwall. Chyu used a short pin fin array ($H/D=1$) with uniform spacing in the streamwise and spanwise directions ($X/D=S/D=2.5$). Chyu found heat transfer rates on pins were 10–20% greater than endwall values. However, Chyu found a weaker dependence on Reynolds number than Metzger, with an exponent of 0.583 versus 0.685.

$$\mathrm{Nu}_D = 0.32\,\mathrm{Re}_{Dm}^{0.583} \qquad 5\times10^3 < \mathrm{Re}_{Dm} < 2.5\times10^4 \tag{2}$$

Contributed by the International Gas Turbine Institute (IGTI) of THE AMERICAN SOCIETY OF MECHANICAL ENGINEERS for publication in the ASME JOURNAL OF TURBOMACHINERY. Paper presented at the International Gas Turbine and Aeroengine Congress and Exhibition, Vienna, Austria, June 13–17, 2004, Paper No. 2004-GT-53889. Manuscript received by IGTI, October 1, 2003; final revision, March 1, 2004. IGTI Review Chair: A. J. Strazisar.

Average Array Pressure Drop. Pressure drop across pin fin arrays is most often correlated in terms of the flow friction factor, f. The most common form of flow friction factor as given by Armstrong and Winstanley [1] is

$$f = \Delta P/(2\rho V_{\max}^2 N) \tag{3}$$

Similar to the array heat transfer correlation, $V_{\max}$ is used to determine the Reynolds number and also scale the array pressure drop. Additionally, the pressure drop is normalized by the number of rows N. Armstrong and Winstanley recommended the Metzger et al. [4] correlation for flow friction factor. Generally, Metzger found that Reynolds-number dependence changed from lower ($\mathrm{Re}_{Dm}<10{,}000$) to higher ($\mathrm{Re}_{Dm}>10{,}000$) Reynolds numbers. Metzger's correlations for S/D of 2.5 and various X/D are given below:

$$f = 0.317\,\mathrm{Re}_{Dm}^{-0.132}$$
$$10^3 < \mathrm{Re}_{Dm} < 10^4 \tag{4}$$

and

$$f = 1.76\,\mathrm{Re}_{Dm}^{-0.318}$$
$$10^4 < \mathrm{Re}_{Dm} < 10^5 \tag{5}$$

Armstrong also suggested that pressure drop in longer pin fin arrays ($H/D>2$) could be predicted well using Jacob's [5] correlation for short tubes.

$$\mathrm{f} = [0.25 + 0.1175/(\mathrm{S/D}-1)^{1.08}]\mathrm{Re}_{\mathrm{Dm}}^{-0.16} \tag{6}$$

Row Resolved Heat Transfer Rates. Chyu et al. [3] reported row average heat transfer rates for a streamwise (X/D) and spanwise (S/D) spacing of 2.5. Chyu found peak heat transfer typically occurred at the third row for Reynolds numbers above 10,000 and further back for lower Reynolds numbers. Metzger et al. [4] found that peak heat transfer depended on streamwise pin spacing (X/D).

Local Pin Heat Transfer. Heat transfer rates on pin surfaces can be substantially higher than low-turbulence heat transfer to cylinders in crossflow. Metzger and Haley [6] reported circumferential Nusselt number variation as a function of row number and pin diameter Reynolds number based on $V_{\max}$. Metzger found increases in stagnation-region heat transfer of as much as 100% between the first row and farther downstream rows at a Reynolds number of 52,800. Baughn and Saniei [7] reported local values of $\mathrm{Nu}/\mathrm{Re}_D^{1/2}$ versus angular position for a staggered-pin fin array run at a Reynolds number of 23,000. At the stagnation region for the third pin, a local value of 1.26 for $\mathrm{Nu}/\mathrm{Re}_D^{1/2}$ was reported. The array had height, span, and streamwise spacings (H/D, S/D, and X/D) all equal to 2.0.

Turbulence Measurements. The production of turbulence in pin arrays is known to be responsible for enhancing heat transfer rates on pins and endwalls. Simoneau and Van Fossen [8] acquired turbulence measurements in staggered-pin and in-line-pin fin arrays with spanwise and streamwise (S/D and X/D) spacings of 2.67. They found average local turbulence intensity levels varied from a minimum of about 15% to a maximum of 33%. Values peaked downstream from the second row and decreased slightly in subsequent rows. They acquired data at Reynolds numbers of 10,000, 50,000, and 120,000 and found higher turbulence levels at lower Reynolds numbers. Metzger and Haley acquired turbulence intensity values 4.06 cm upstream from a 5.08 cm diam pin in an array with streamwise spacings (X/D) of 1.32 and 2.19 and a spanwise spacing (S/D) of 2.5. They found the highest values occurred downstream from rows 3 and 4 with values of about 42% for the 1.32 streamwise spacing and 22% for the 2.19 streamwise spacing. Downstream values leveled out at 28% ($X/D=1.32$) and 18% ($X/D=2.19$) for the two streamwise spacings.

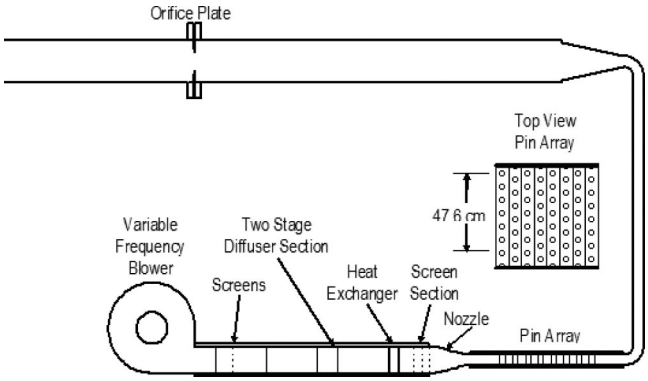

Fig. 1 UND internal heat transfer and flow facility showing staggered-pin fin array test section

Computational Predictions. Ames et al. [9] developed a well-resolved three-dimensional (3D) model of a staggered-pin fin array using FLUENT [10] with Shih's [11] realizable k-ε model. Generally, they found the steady symmetrical model underpredicted array average heat transfer, flow friction factor, and the generation of turbulence. Steinthorsson et al. [12] predicted heat transfer and pressure drop in a simulated cooling channel using GLENHT with the Baldwin-Lomax turbulence model. Using the experimental boundary conditions they found they overpredicted duct Reynolds number and underpredicted endwall heat transfer downstream of the array.

Objectives of Present Work. A significant number of previous studies have investigated heat transfer and pressure drop in pin fin arrays. These studies have documented average array heat transfer and pressure drop, row averaged heat transfer, local pin and endwall heat transfer, and turbulence intensity levels. These previous studies have examined a wide variation of relevant pin fin array geometries. However, these research investigations have not developed a quantitative link between the local fluid dynamics of the array and surface heat transfer rates. In the present study, local heat transfer rates are carefully documented and presented in terms of local fluid dynamics and turbulence conditions. Pin stagnation-region heat transfer rates are correlated for the influence of turbulence, Reynolds number, and scale.

Experimental Approach

This heat transfer research investigation is being conducted in the University of North Dakota's internal flow and heat transfer facility. The facility is shown schematically in Fig. 1. The wind tunnel is powered by a 2 kW blower, which moves up to 0.3 m^3/s of air at a static pressure rise of 2000 Pa. The blower is controlled by a variable frequency drive, which can be set to within the nearest 0.1 Hz. The blower exhausts into a two-stage multivane diffuser to distribute air across the width of the passage and recover some pressure. The diffuser is followed by a heat exchanger used to provide a steady and controllable test-section inlet temperature. The flow is conditioned downstream of the heat exchanger with a series of three screens and then takes a smooth 2.5 to 1 area-ratio contraction into the test section.

The test section is constructed from 1.2 cm acrylic sheets and consists of eight staggered rows of 7.5 pins spaced both spanwise (S/D) and axially (X/D) at 2.5 dia. The channel height is twice the 2.54 cm pin dia ($H/D=2$). Figures 2 and 3 show partial flow and top views of the pin fin array along with locations of turbulence and spectra measurements. The inlet static pressure is monitored by five static taps positioned across one pin spacing 5 dia upstream from the centerline of row 1. The exit static pressure taps are similarly located but 5 dia downstream of row 8. Both the inlet and exit have probe access ports that allow determination of inlet and exit total pressure and temperature. The inlet total pres-

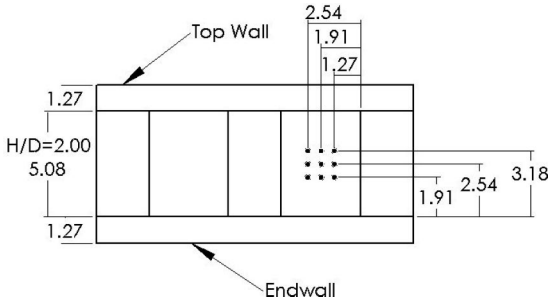

Fig. 2 Partial flow view of pin fin array showing spanwise and vertical locations of turbulence and spectra measurements

sure and temperature are monitored for all measurements as is the static-pressure drop across the array. The test section exhausts into a duct, which eventually is directed into an orifice tube. The sharp-edged orifice tube is used to determine the array mass flow rate. The heat transfer, pressure, and hot wire measurements were taken at Reynolds numbers of 30,000, 10,000, and 3000 for this investigation. The Reynolds number is based on the pin diameter and mass-averaged velocity $V_{\max}$ between adjacent pins.

Pressure Pin. Pressure distributions were acquired using a pin with 20 0.76 mm dia static-pressure taps spaced equally around the midline and were referenced to the inlet total pressure. Measurements were resolved within 6 deg increments by rotating the pin at ± 6 deg. Measurements were taken at the center pin location for each row at each Reynolds number. Pressure measurements were acquired with a custom-made pressure scanner with 4 high-side ports and 44 low-side ports.

Heat Transfer Pin. Heat transfer measurements were acquired using a constant heat flux technique. The heat transfer pin was fabricated by casting 24 equally spaced fine wire type *K* thermocouples around the midline of an epoxy pin. The pin was wrapped with a 0.023 mm Inconel foil backed with a 0.13 mm Kapton film and adhered with a 0.05 mm layer of high temperature acrylic adhesive. A constant heat flux was generated by passing a large DC current through the foil, which spanned the full 5.08 cm of the test section. Each end of the foil had a copper bus bar attached. One bus bar was soldered to the foil while the other was adhered with electrically conductive silver epoxy. The active length of the bus bar was equivalent to the circumference of the pin, but left a small unheated gap between the two bars. This experimental anomaly was circumvented by acquiring only 12 of the thermocouple readings away from the bus bar in two 180 deg oriented measurements to provide the complete boundary condition. Temperature measurements were acquired at 5 deg increments by rotating the cylinder at ± 5 deg positions. Conduction through the pin was calculated using a finite difference analysis. The net local heat flux was estimated from the electrical dissipation plus the extra heat flux due to conduction less the radiative losses. Radiation losses were estimated using the local surface temperature radiating to the inlet total temperature using a foil emissivity of 0.21 and assuming a blackbody background. The electrical dissipation in the foil was determined from the voltage across the heater times the current through. The heater current was determined using a calibrated constantan shunt resistor.

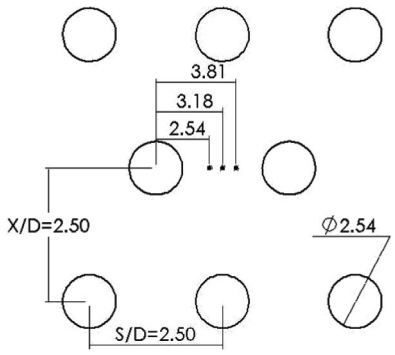

Fig. 3 Partial top view of pin fin array showing spanwise and axial locations of turbulence and spectra measurements

Data Acquisition. Thermocouple voltage measurements were acquired using an HP 3497A data acquisition unit with integral voltmeter with a 1 μV sensitivity. Thermocouples were connected to the HP 3497A through a passive constant temperature reference junction. The temperature of the junction was determined by a thermocouple immersed in an ice bath. Pressures were determined using two Rosemount Smart Pressure Transmitters. One transmitter is scaled to read 0 to 125 Pa while the other is scaled to read 0 to 1250 Pa. For a given reading, the most sensitive pressure transmitter is selected. The Rosemount pressure transmitters have a quoted accuracy of $\pm 0.1\%$ of full scale. Voltages from the pressure transmitters, heaters, and shunt resistors were also read using the HP 3497A. Hot wires were powered by a TSI ISA 300 constant temperature anemometry bridge. The TSI ISA 300 buck and gain were set to maximize the resolution of the data acquisition card. Bridge output voltages were read using a high-speed 12-bit PC-based data acquisition card. Mean velocities and turbulence intensity levels were acquired at a rate equivalent to about three integral time scales at the particular Reynolds number. Velocity time records for spectral analysis were acquired in 40 sets of 8192 samples and post processed.

Data Uncertainties. Estimates for the uncertainty in heat transfer, pressure, velocity, and turbulence measurements were determined using the root sum square method described by Moffat [13]. Heat transfer has been reported in the dimensionless terms of $\mathrm{Nu}/\mathrm{Re}_D^{1/2}$. The worst-case uncertainty occurs at the lowest Reynolds number, where the uncertainty in $\mathrm{Nu}/\mathrm{Re}_D^{1/2}$ is 6%. This includes an uncertainty in Reynolds number of 3% primarily due to the measurement of mass flow rate in the orifice tube. The uncertainty in the turbulence intensity determined with the single wire was estimated to be 3%. The largest uncertainty in the reported pressure coefficient (± 0.075) occurred at a Reynolds number of 3000. However, the uncertainty was about ± 0.025 at the two higher Reynolds numbers. The experimental error in the turbulent energy and integral scales are estimated to be $\pm 12\%$. All uncertainty estimates were quoted at a 95% uncertainty interval.

Experimental Results

Midline pin heat transfer distributions were acquired for Reynolds numbers of 30,000, 10,000, and 3000 for all eight rows of the staggered array. Data are presented for the first five rows and are supported by midline pin pressure distributions and turbulence characteristics. Pressure distributions are reported in terms of a pressure coefficient Cp, which was scaled on the dynamic pressure based on the velocity $V_{\max}$. Heat transfer data are presented in terms of both $V_{\max}$ and the local velocity V_{eff}, which is based on the pin stagnation-region velocity distribution. Heat transfer at the pin leading edge is later correlated on a turbulence parameter developed to account for the influence of flow field turbulence on stagnation-region heat transfer. All the heat transfer results presented in this paper are acquired on a single pin with no upstream heating. Therefore, the driving-force temperature difference is the local surface temperature less the local inlet total temperature. Heat transfer coefficients in pin fin arrays are typically based on the local bulk temperature.

The procedure for acquiring heat transfer, pressure distribution, and turbulence measurements involves setting the facility at a specific Reynolds number. Heat transfer and turbulence measurements require the heat exchanger recirculation system to provide a

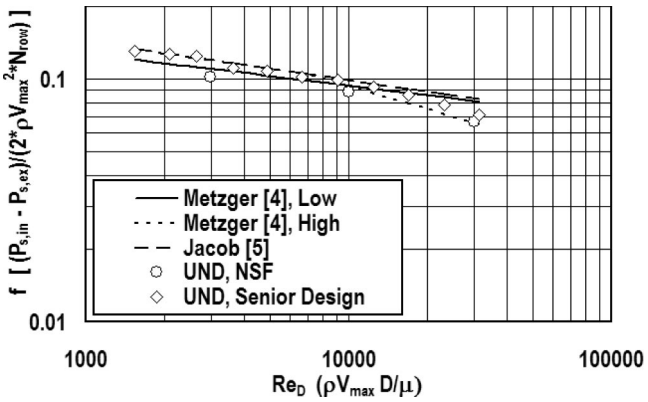

Fig. 4 Flow friction factor versus Re_{Dm} compared to prior UND [4,5]

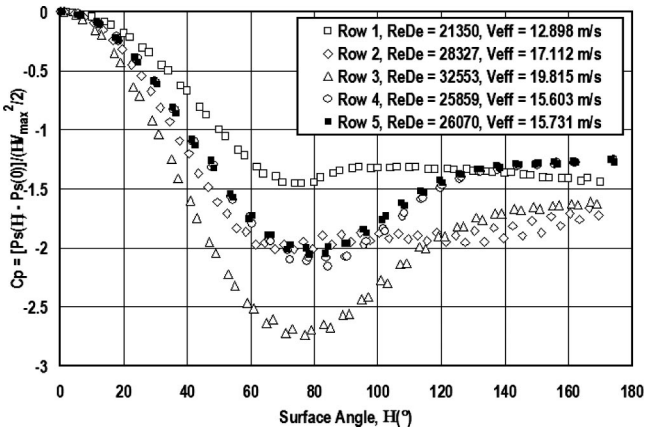

Fig. 5 Midline pressure coefficient distribution, rows 1–5, Re_{Dm}=30,000, V_{max}=18.15 m/s

steady-state inlet air temperature. As a consistency check, the flow friction factor is determined each time data are taken in the facility. Figure 4 shows flow friction factor acquired in the present facility compared with data from the constant temperature facility and the correlations of Metzger et al. [4] and Jacob [5]. Generally, the data match Metzger's low and high Reynolds number correlations.

Turbulence Characteristics. Hot wire anemometry was used to determine the characteristics of the turbulence within the array and at the inlet to the pin fin flow facility. These measurements were acquired to correlate the augmentation of heat transfer on the pins with the characteristics of the turbulence found within the array. Measurements were taken between adjacent pins, in rows 1 through 5 at the locations indicated in Figs. 2 and 3, and measurements at the inlet are presented in Table 1 for the three Reynolds numbers. Velocity time records were acquired at nine locations for each row and Reynolds number. Fast Fourier transforms (FFTs) of the acquired velocity time records were calculated to obtain the one-dimensional spectrum of u′. These 40 spectrums were then averaged and fit to a −5/3 slope in log coordinates in the inertial subrange. Ames and Moffat [14] used the following relationship to calculate the dissipation rate:

$$E_1(k_1) = 1.62(18/55)\varepsilon^{2/3}k_1^{-5/3} \tag{7}$$

This estimate for dissipation is reported in Table 1 along with the energy scale Lu. $Lu = 1.5|u'|^3/\varepsilon$ and represents the average size of the energy containing eddies in the flow. In addition to finding the dissipation rate, the averaged spectrum is used to calculate the autocorrelation in time using an inverse FFT. The autocorrelation in time is integrated to the first zero crossing to estimate the autocorrelation time scale. The autocorrelation time scale is then multiplied by the local convective velocity to develop an estimate for the integral scale Lx.

The inlet turbulence levels are low (1.5%) and at the lowest, two Reynolds numbers dissipation levels appear to be miniscule. Consequently, estimates of the energy scale have little usefulness. Typically, estimating the dissipation rate using Eq. (7) requires a well-developed inertial subrange. A relatively high turbulence Reynolds number is required to produce a spectrum with a significant −5/3 slope.

Downstream of row 1, turbulence levels climb quickly averaging 17% at row 2, 23% at row 3, 21% at row 4, and 20% at row 5. Note that the turbulence measured between pins at row 2 provides the turbulence boundary condition for the heat transfer pin in row 3. Noting that the turbulence generated in the wake of a pin will decay as it convects downstream, the following method was used to estimate the reduction in turbulence intensity from the upstream measuring station to downstream pin. Equation (8) can be developed from the free-stream kinetic energy equation assuming that U and Lu remain fixed.

$$\mathrm{Tu}(x) = 1/[1/\mathrm{Tu}(0) + x/(2Lu)] \tag{8}$$

Pin Array Reynolds Number of 30,000. The midline pressure distributions for an array Reynolds number of 30,000 are presented in Fig. 5 in terms of a pressure coefficient. The pressure coefficient Cp is based on the local- to stagnation-region pressure difference normalized on V_{max}. The pin pressure distributions change significantly from row to row as shown in Fig. 5. Initially, the inlet flow is very uniform and has a low turbulence level. Consequently, the effective velocity around the pin is relatively low and the minimum pressure coefficient is about −1.45. The flow appears to separate around 80–90 deg as evidenced by the minimal recovery and the flat pressure distribution over the aft portion of the pin. The flow approaching the second row has accelerated due to the initial row and remains relatively high due to the blockage from the row 1 pin wakes. The minimum pressure

Table 1 Pin fin array inlet and row by row turbulence characteristics

Re_{Dm} = 3000						
Location	Inlet	Row 1	Row 2	Row 3	Row 4	Row 5
U (m/s)	1.214	1.883	1.462	1.543	1.634	1.659
Lx (cm)			0.51	0.70	0.75	0.86
Lu (cm)			0.88	1.11	1.11	1.33
ε (m^2/s^3)			2.60	4.06	4.89	4.09
Tu	0.014	0.014	0.169	0.201	0.203	0.200

Re_{Dm} = 10,000						
Location	Inlet	Row 1	Row 2	Row 3	Row 4	Row 5
U (m/s)	3.71	6.06	5.22	5.20	5.47	5.36
Lx (cm)			0.40	0.74	0.68	0.68
Lu (cm)			0.82	1.22	1.26	1.26
ε (m^2/s^3)			121.2	248.3	252.6	180.9
Tu	0.014	0.016	0.165	0.243	0.235	0.215

Re_{Dm} = 30,000						
Location	Inlet	Row 1	Row 2	Row 3	Row 4	Row 5
U (m/s)	11.12	18.01	16.67	15.50	16.92	16.16
Lx (cm)	0.35	2.05	0.98	0.79	0.70	0.71
Lu (cm)	16.26	28.43	1.99	1.67	1.50	1.44
ε (m^2/s^3)	0.041	0.042	2173	5709	3562	2553
Tu	0.015	0.011	0.184	0.257	0.195	0.180

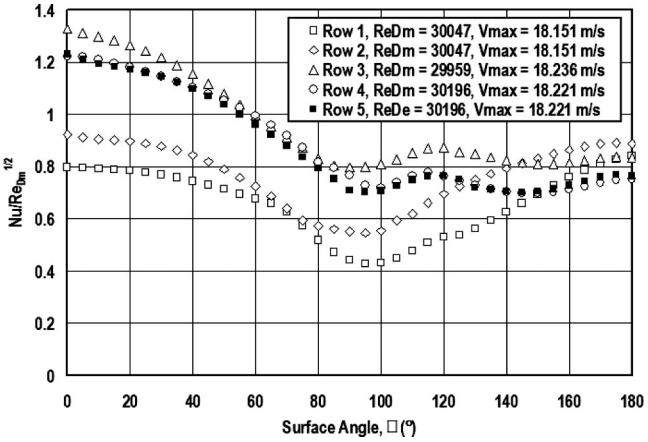

Fig. 6 Midline Nu/Re$_{Dm}^{1/2}$ distribution, rows 1–5, Re$_{Dm}$=30,000 based on V$_{max}$

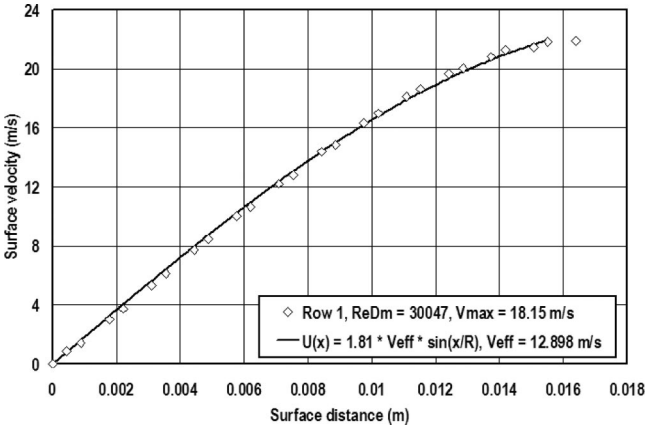

Fig. 7 Determination of V_{eff} based on pin surface velocity distribution, row 1, Re$_{Dm}$=30,000

coefficient is now less than −2. Similar to row 1 the flow appears to separate around 75–80 deg and the backside pressure distribution is flat, showing little recovery. The large separation region on the row 2 pin combined with a higher effective velocity apparently produces a very high effective velocity for row 3. The minimum pressure coefficient of −2.74 appears at 77 deg, but unlike the first two rows, 40% of the minimum pressure is recovered. This observation suggests the turbulence from the row 1 wake produces a boundary layer on pin 3 that is less susceptible to separation. The smaller separated region behind row 3 pins reduces the effective velocity seen by row 4. The pressure distributions for row 4 and beyond are quite similar in terms of both the minimum pressure coefficient, −2.1, and the backside pressure recovery.

Heat transfer distributions for a Reynolds number of 30,000 based on V_{max} are presented in Fig. 6 in terms of $Nu/Re_{Dm}^{1/2}$ versus surface angle. Row 1 heat transfer distributions are similar in character to a pin in crossflow with high levels of heat transfer in the leading edge, reducing until the point of separation. The significant backside heat transfer is the result of shedding on the rear of the pin. A $Nu/Re_D^{1/2}$ of 0.95 is typical for a cylinder in crossflow at low turbulence levels suggesting the effective velocity seen by pin 1 is lower than V_{max}. Distributions of $Nu/Re_{Dm}^{1/2}$ for row 2 are higher than row 1 due to the higher effective velocity. $Nu/Re_{Dm}^{1/2}$ levels for row 3 increase dramatically due both to the high effective velocity and turbulence generated in the pin wakes of row 1 impinging on the surface. After row 3, the level of heat transfer falls off slightly. Heat transfer on the leading pin surface is driven by the local effective velocity and turbulence. We expect turbulence to increase in the array and then plateau. The reduced heat transfer in rows 4 and beyond indicate a reduced effective velocity.

Incompressible potential flow suggests that the local velocity around a cylinder is equal to twice the approach velocity times the sine of the cylinder surface angle. However, this potential flow estimate is too high due to the growth of the displacement thickness of the boundary layer and separation off the back side of the cylinder or in this case the pin. A local velocity of 1.81 times the approach velocity times the sine of the surface angle is more appropriate. Much is happening in a staggered-pin fin array with not only boundary layer growth and separation, but also flow blockage from adjacent pins and wakes of upstream pins. However, in terms of providing an effective cylinder-approach velocity to allow comparison with cylindrical stagnation heat transfer results our 1.81 factor is appropriate as suggested by Zukauskas and Ziugzda [15]. Figure 7 presents a velocity distribution determined from the pin surface pressure distribution around row 1 compared with 1.81 times the effective approach velocity times the sine of surface angle in radians. An effective approach velocity was found for all pins by fitting the derived velocity distribution to $1.81 \times V_{eff} \times \sin\theta$ over the first 40 deg while minimizing the mean-squared error. The pin surface static pressure measurements were all referenced to the inlet total pressure. As a consequence, after row 2, the effective total pressure at the leading edge of the cylinder was also a variable used to minimize the mean-squared error. The average V_{max} for the higher Reynolds number was 18.15 m/s. Upstream of the array, the mass averaged velocity for this V_{max} would be 10.89 m/s. However, the effective approach velocity, V_{eff}, for the row 1 pin is 12.90 m/s. This difference between the average nozzle exit velocity and the effective approach velocity is due to the blockage of the adjacent pins.

Heat transfer to the leading edge of a pin or cylinder is related to heat transfer to a two-dimensional (2D) stagnation point. According to Kays and Crawford [16] wedge-flow solution for a 2D stagnation point with a Prandtl number of 0.71 (air) would be

$$Nu_x = 0.499\, Re_x^{1/2} \tag{9}$$

Assuming for small x that

$$U(x) = 1.81 \times V_{eff} \times x/R \tag{10}$$

It follows that

$$Nu/Re_D^{1/2} = 0.95 \tag{11}$$

This result is applicable to heat transfer at the stagnation region of a pin or cylinder with low flow field turbulence and a constant temperature boundary condition. However, as long as velocity is proportional to x, the heat transfer coefficient will remain constant, resulting in a constant temperature surface for a constant heat flux boundary condition.

Making heat transfer comparisons in terms of $Nu/Re_{De}^{1/2}$ as a function of surface angle allows direct comparison for the influence of flow field turbulence on pin surface heat transfer. However, because the effective velocity changes from row to row, the presentation cannot be used to make row by row comparisons in the absolute heat transfer level. Figure 8 presents midline heat transfer distributions for rows 1 through 5 in terms of this scaling for an array Reynolds number of 30,000. At the stagnation point rows 1 and 2 have values of $Nu/Re_{De}^{1/2}$ very close to 0.95. The pin fin array inlet turbulence level is about 1.5% with a very large and inactive scale suggesting results for rows 1 and 2 should compare closely with Eq. (11). This consistency between measured and theoretical $Nu/Re_{De}^{1/2}$ provides confidence in the experimental technique. Dimensionless heat transfer rates for rows 3 through 5 show that turbulent augmentation in the front half of the cylinder is higher for rows 4 and 5 compared to row 3. Considering the

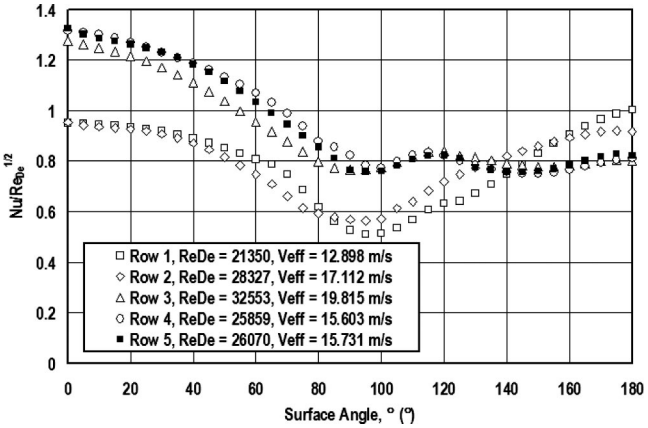

Fig. 8 Midline $Nu/Re_{De}^{1/2}$ distribution, rows 1–5, Re_{Dm}=30,000, Re_{De} based on V_{eff} (row)

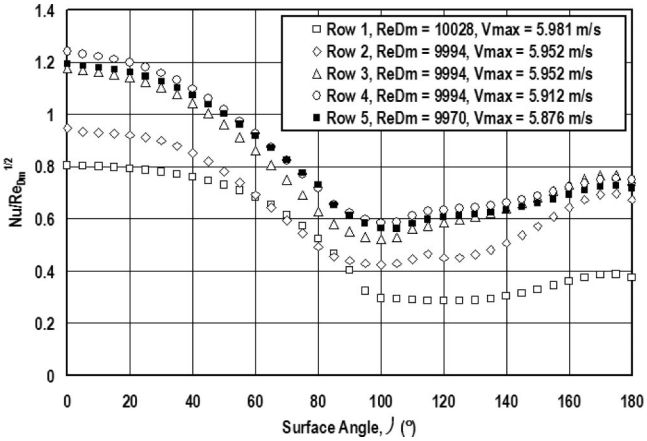

Fig. 10 Midline $Nu/Re_{Dm}^{1/2}$ distribution, rows 1–5, Re_{Dm}=10,000 based on V_{max}

higher effective Reynolds number of row 3, which is expected to increase augmentation, this comparison demonstrates that turbulent augmentation is significantly higher in rows 4 and beyond compared to row 3. This higher turbulent augmentation can be explained by the more aggressive turbulence (higher turbulence intensity and smaller energy scale) measured directly upstream of rows 4 and 5.

Pin Array Reynolds Number of 10,000. The midline pressure distributions for an array Reynolds number of 10,000 are presented in Fig. 9 in terms of a pressure coefficient. Similar to the 30,000 Reynolds number case, the minimum pressure coefficient for row 1 is −1.45 and based on the uniform backside pressure distribution separation occurs between 80 and 90 deg. Again, similar to the 30,000 Reynolds number row 2 has a minimum pressure coefficient of about −2, and the back-side pressure distribution is flat, indicating a wide area of separation. However, the minimum pressure coefficient for row 3 is only −2.34 (−2.74 at 30,000 Reynolds number), and the subsequent pressure recovery is only about 20% (40% at 30,000 Reynolds number). This difference between the present results and the results at a Reynolds number of 30,000 show that pin boundary layers are more susceptible to separation at this lower Reynolds number. The difference between pressure distributions in rows 3 and 4 is much less significant, and a consistent pressure distribution is not encountered until row 5.

Figure 10 presents distributions of $Nu/Re_{Dm}^{1/2}$ for an array Reynolds number of 10,000. Heat transfer levels in the first two rows are lowest similar to the 30,000 Reynolds number case. However, at this Reynolds number backside heat transfer levels are reduced. This observation is consistent with cylinder data, which shows the effect of shedding on backside heat transfer increases with Reynolds number. At this Reynolds number, the highest heat transfer rates occur in row 4 rather than row 3. At this Reynolds number, turbulence levels affecting rows 4 and beyond are higher, and the effective velocity seen by row 3 is comparatively much lower than in the 30,000 Reynolds number case.

Heat transfer data are presented in terms of $Nu/Re_{De}^{1/2}$ in Fig. 11. Heat transfer rates in the front half of the pin are qualitatively very similar to the 30,000 Reynolds number case. At the stagnation point values of $Nu/Re_{De}^{1/2}$ are close to 0.95 in the first two rows. In these terms the turbulence augmentation of heat transfer on pins in rows 4 and 5 are clearly higher than values for row 3. The difference in effective Reynolds between rows 1 and 2 appears to make a significant difference in the level of backside heat transfer. $Nu/Re_{De}^{1/2}$ distributions on the backside of pins in rows 3 through 5 show differences with the 30,000 Reynolds number case.

Pin Array Reynolds Number of 3000. The midline pressure distributions for an array Reynolds number of 3000 are presented in Fig. 12 in terms of a pressure coefficient. Pressure coefficients in the first two rows are quantitatively similar to values for the 10,000 Reynolds number case. In general distributions are qualitatively similar with the 10,000 Reynolds number case. However, the level of backside pressure recovery is reduced. While slight

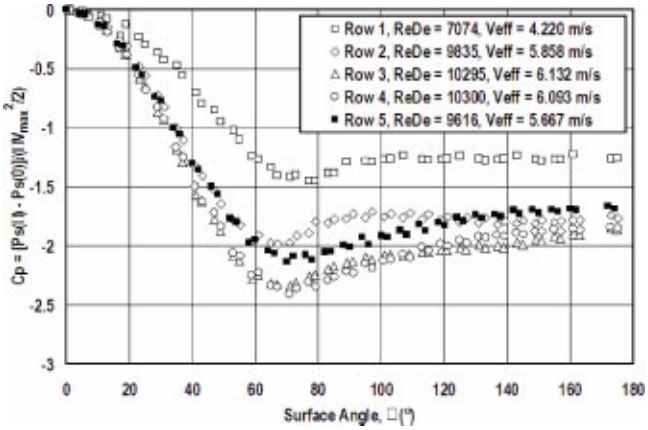

Fig. 9 Midline pressure coefficient distribution, rows 1–5, Re_{Dm}=10,000, V_{max}=5.93 m/s

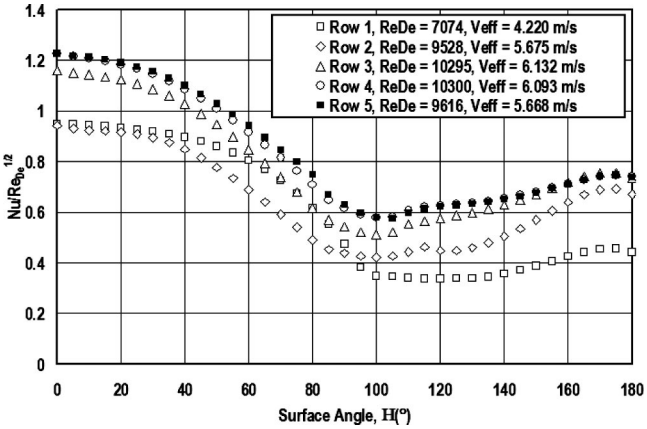

Fig. 11 Midline $Nu/Re_{De}^{1/2}$ distribution, rows 1–5, Re_{Dm} =10,000, Re_{De} based on V_{eff} (row)

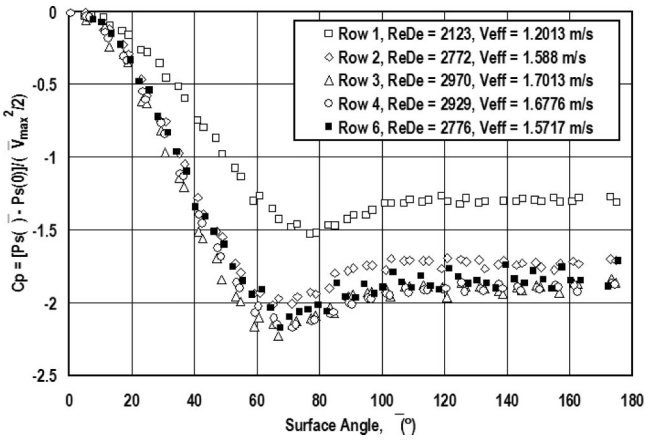

Fig. 12 Midline pressure coefficient distribution, rows 1–5, Re_{Dm}=3000, V_{max}=1.71 m/s

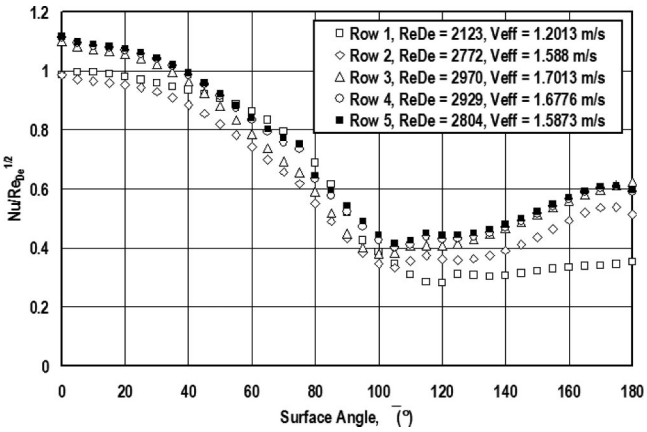

Fig. 14 Midline $Nu/Re_{De}^{1/2}$ distribution, rows 1–5, Re_{Dm}=3000, Re_{De} based on V_{eff} (row)

differences in the effective velocities exist between rows 3, 4, and 5, backside pressure coefficients are very similar.

Distributions of $Nu/Re_{Dm}^{1/2}$ for an array Reynolds number of 3000 are presented in Fig. 13. Qualitatively, these distributions are consistent with $Nu/Re_{Dm}^{1/2}$ levels displayed in Fig. 10. Differences between Fig. 13 and Fig. 10 include the level of heat transfer augmentation in rows 3, 4, and 5 and the very small variation in heat transfer coefficients for rows 3, 4, and 5 for the Reynolds number of 3000. Figure 14 presents the 3000 Reynolds number results in terms of $Nu/Re_{De}^{1/2}$. Rows 1 and 2 present values of $Nu/Re_{De}^{1/2}$ of about 0.985, which is 3.5% high but within the uncertainty band. Augmentation levels due to turbulence are clearly much lower at this Reynolds number. Based on $Nu/Re_{De}^{1/2}$ heat transfer distributions for row 3 and beyond are very consistent.

Correlation of Heat Transfer Results. At low turbulence levels our data show that the stagnation region on a pin fin is similar to the stagnation region of a cylinder in crossflow or turbine airfoil. At high levels of turbulence, heat transfer on cylinders can be significantly enhanced by the turbulent transport process. As turbulence approaches a stagnation region, eddies with axes aligned with the flow around the stagnation region are stretched by the flow field. The turbulent eddies, which are relatively small compared to the cylinder, intensify due to this straining process, penetrate into the boundary layer, and promote heat transfer. Eddies, which are relatively large, are simply blocked by the cylinder's presence and have little effect on the heat transfer process. Ames and Moffat [14] developed a parameter based on an eddy diffusivity model to correlate the influence of high-intensity large-scale turbulence stagnation-region heat transfer. The correlating parameter was a function of turbulence intensity, diameter Reynolds number, and diameter to energy scale ratio.

$$Nu/Re_D^{1/2} = f[\mathrm{Tu}\,Re_D^{5/12}(D/Lu)^{1/3}] \tag{12}$$

A good engineering approximation to this correlation can be given as

$$Nu/Re_{De}^{1/2} = 0.95\times(1+0.04\times \mathrm{TRL}) \tag{13}$$

Here, TRL is the turbulence, Reynolds number, and turbulent length scale parameter given by $\mathrm{TRL}=\mathrm{Tu}\times Re_D^{5/12}(D/Lu)^{1/3}$. In addition to correlating the influence of high-intensity turbulence on stagnation-region cylinders, this parameter has been used successfully to correlate the influence of turbulence on vane stagnation-region heat transfer [17–19].

Heat transfer acquired at the stagnation region of the heat transfer pin is presented in Fig. 15 in terms of $Nu/Re_{De}^{1/2}$ versus TRL for the five rows taken at three Reynolds numbers. The data for the first two rows are shown scattered around the correlation at a TRL less than 0.5. The remaining data for the downstream rows are spread across the TRL parameter space and tend to group by Reynolds number. The turbulence intensity used in determining TRL was adjusted for streamwise decay using Eq. (8). The decay distance was taken as the streamwise spacing between rows. Generally, 14 of 15 data points fall well within or very close to the ±6%

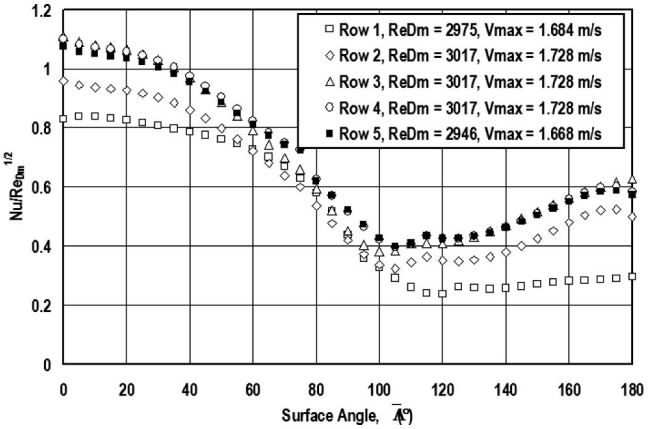

Fig. 13 Midline $Nu/Re_{Dm}^{1/2}$ distribution, rows 1–5, Re_{Dm}=3000 based on V_{max}

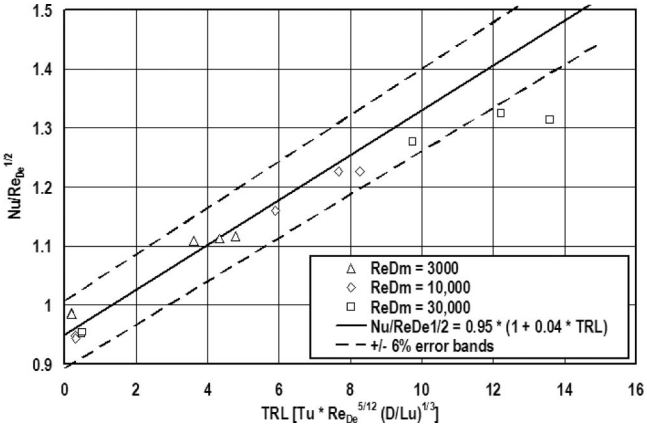

Fig. 15 Correlation of pin stagnation point heat transfer, $Nu/Re_{De}^{1/2}$ versus *TRL*

error bands, suggesting the applicability of the correlating parameter. The $Nu/Re_{De}^{1/2}$ value for row 4 of the high Reynolds number case clearly falls below the general correlation. No explanation can be given for this anomaly at this time.

Summary and Conclusions

The objective of the present research has been to advance our understanding of the influence of turbulence generated in pin fin arrays on pin fin surface heat transfer rates. The present paper has documented the 2D heat transfer rates and pressure distributions around pin fins in a staggered array as both a function of row and Reynolds number. Unlike other studies, the full characteristics of flow field turbulence, including turbulence intensity, scale, and dissipation rates, have been reported throughout the array as a function of position and Reynolds number. Using the surface-pressure distributions, an effective approach velocity has been determined for each pin and Reynolds numbers. This parametrization decouples the influence of turbulence on pin fin augmentation from the influence of the effective approach velocity and demonstrates the turbulent transport processes occurring in the pin fin array. When scaled-on diameter Reynolds number, based on the effective approach velocity, heat transfer at the stagnation region of pins in rows 1 and 2 match low turbulence values for 2D stagnation points. This rescaling has allowed the results of the present data to be compared to correlations for the influence of turbulence on stagnation-region heat transfer. Stagnation values of $Nu/Re_D^{1/2}$ in row 3 and beyond have been found to correlate well on the TRL parameter of Ames and Moffat [14]. The TRL parameter is based on an algebraic eddy diffusivity model, which accounts for the response of the turbulent spectra to the approach of the stagnation region. This result suggests that we understand the response of turbulence in this region, and that is a first step in providing physically sound turbulence models that will allow the accurate prediction of heat transfer and pressure drop in pin fin arrays. Additionally, these data have shown that the high effective approach velocity together with the significant turbulence generated by the wakes of pins from row 1 are responsible for the high heat transfer rates in row 3 for the high Reynolds number.

Acknowledgments

The present work has been funded through the National Science Foundation. The facility used in this research was developed using funding received by the North Dakota ESPCoR program. Paul Ray and Reuben Gates, while graduate students at UND, were responsible for developing the present UND pin fin heat transfer and flow facility. The authors express their appreciation for the current and previous funding and the efforts of prior students.

Nomenclature

A_{min} = minimum array flow path area, m^2
Cp = pressure coefficient, $[Ps(x)-Ps(0)]/(\rho V_{max}^2/2)$
Cp = specific heat at constant pressure, J/kg K
D = Pin or tube diameter, m
$E_1(k_1)$ = one dimensional energy spectrum function, $E_1(k_1) = UE_1(f)/2/\pi$, m^3/s^2
f = flow friction factor or pressure loss coefficient, $f = \Delta P/(2\rho V_{max}^2 N)$, Eq. (3)
f = frequency, 1/s
h = heat transfer coefficient, $W/m^2/K$
H = channel height, m
k = thermal conductivity, W/m/K
k_1 = wavenumber, $k_1 = 2\pi f/U$, m^{-1}
Lu = energy scale, $Lu = 1.5|u'|^3/\varepsilon$, m
N = number of array rows
Nu_D = Nusselt number, $Nu = hD/k$
P = Pressure, Pa
Pr = Prandtl number, $Pr = \rho Cp\nu/k$
R = pin radius, m
Re_{De} = diameter Reynolds number, based on V_{eff}
Re_{Dm} = diameter Reynolds number, based on V_{max}
S = spanwise pin spacing, m
TRL = turbulence parameter, $TRL = Tu\, Re_D^{5/12}(D/Lu)^{1/3}$
Tu = turbulence level, $Tu = u'/U_\infty$
$U(x)$ = streamwise velocity, m/s
u' = rms streamwise fluctuation velocity, m/s
V_{eff} = effective velocity given by Eq. (10), m/s
V_{max} = the average velocity through A_{min}, m/s
x = axial distance, m

Greek Symbols

ε = turbulent dissipation rate, m^2/s^3
μ = absolute viscosity, Pa s
ν = kinematic viscosity, m^2/s
ρ = fluid density, mass per unit of volume, kg/m^3

References

[1] Armstrong, J., and Winstanley, D., 1988, "A Review of Staggered Array Pin Fin Heat Transfer for Turbine Cooling Applications," ASME J. Turbomach., **110**, pp. 94–103.
[2] Metzger, D. E., Shepard, W. B., and Haley, S. W., 1986, "Row Resolved Heat Transfer Variations in Pin Fin Arrays Including Effects of Non-Uniform Arrays and Flow Convergence," ASME Paper No. 86-GT-132.
[3] Chyu, M. K., Hsing, Y. C., Shih, T. I.-P., and Natarajan, V., 1998, "Heat Transfer Contributions of Pins and Endwall in Pin-Fin Arrays: Effects of Thermal Boundary Conditions Modeling," ASME J. Turbomach., **121**, pp. 257–263.
[4] Metzger, D. E., Fan, C. S., and Shepard, W. B., 1982, "Pressure Loss and Heat Transfer Through Multiple Rows of Short Pins," Heat Transfer 1982, **3**, Hemisphere, Washington, DC, pp. 137–142.
[5] Jacob, M., 1938, "Heat Transfer and Flow Resistance in Cross Flow of Gases Over Tube Banks," Trans. ASME, **59**, pp. 384–386.
[6] Metzger, D. E., and Haley, S. W., 1982, "Heat Transfer Experiments and Flow Visualization for Arrays of Short Pin Fins," ASME Paper No. 82-GT-138.
[7] Baughn, J. W., and Saniei, N., 1990, "Local Heat Transfer Measurements on Arrays of Pin Fins in a Rectangular Duct," *Proc. Ninth International Heat Transfer Conference*, Jerusalem, Hemisphere, New York.
[8] Simoneau, R. J., and Van Fossen, G. J., 1984, "Effect of Location in an Array on Heat Transfer to a Short Cylinder in Crossflow," ASME J. Heat Transfer, **106**, pp. 42–48.
[9] Ames, F. E., Solberg, C. S., Goman, M. D., Curtis, D. J., and Steinbrecker, B. T., 2001, "Experimental Measurements and Computations of Heat Transfer and Friction Factor in a Staggered Pin Fin Array," ASME Paper No. DETC 2001/CIE-21761.
[10] FLUENT 5.3, 1999, *FLUENT 5.3 User's Guide*, Fluent, Lebanon, NH.
[11] Shih, T.-H., Liou, W. W., Shabbir, A., and Zhu, J., 1995, "A New k-ε Eddy-Viscosity Model for High Reynolds Number Turbulent Flows—Model Development and Validation," Comput. Fluids, **24**(3), pp. 227–238.
[12] Steinthorsson, E., Ameri, A. A., and Rigby, D. L., 1996, "Simulations of Turbine Cooling Flows Using a Multiblock-Multigrid Scheme," NASA CR 198539.
[13] Moffat, R. J., 1988, "Describing Uncertainties in Experimental Results," Experimental and Fluid Science, **1**, pp. 3–17.
[14] Ames, F. E., and Moffat, R. J., 1990, "Heat Transfer With High Intensity, Large Scale Turbulence: The Flat Plate Turbulent Boundary Layer and the Cylindrical Stagnation Point," Report No. HMT-44, Thermosciences Division of Mechanical Engineering, Stanford University.
[15] Zukauskas, A., and Ziugzda, J., 1985, *Heat Transfer of a Cylinder in Crossflow*, Hemisphere, Washington, DC.
[16] Kays, W. M., and Crawford, M. E., 1993, *Convective Heat and Mass Transfer*, Third Edition, McGraw-Hill, New York.
[17] Ames, F. E., 1997, "The Influence of Large Scale, High Intensity Turbulence on Vane Heat Transfer," ASME J. Turbomach., **119**, p. 23.
[18] Ames, F. E., Wang, C., and Barbot, P. A., 2003, "Measurement and Prediction of the Influence of Catalytic and Dry Low NOx Combustor Turbulence on Vane Surface Heat Transfer," ASME J. Turbomach., **125**, pp. 221–231.
[19] Ames, F. E., Argenziano, M., and Wang, C., 2003, "Measurement and Prediction of Heat Transfer Distributions on an Aft Loaded Vane Subjected to the Influence of Catalytic and Dry Low NOx Combustor Turbulence," ASME J. Turbomach **126**, pp. 139–149.

A New Method to Calculate the Coolant Requirements of a High-Temperature Gas Turbine Blade

Leonardo Torbidoni
e-mail: torbidoni@unige.it
TPG-DiMSET,
Università di Genova,
Genova, Italy

J. H. Horlock
Whittle Laboratory,
University of Cambridge,
Cambridge, UK

Earlier papers by the first author have described a computational method of estimating the cooling flow requirements of blade rows in a high-temperature gas turbine, for convective cooling alone and for convective plus film cooling. This method of analysis and computation, when applied to the whole blade chord was compared to a well-known semi-empirical method. In the current paper, a more sophisticated method is developed from the earlier work and is used to calculate the cooling flow required for a nozzle guide vane (the first blade row) of a high-temperature gas turbine, with given inlet gas temperature and coolant inlet temperature. Now the heat flux through an elementary cross-sectional area of the blade, at given spanwise (y) and chordwise (s) locations, is considered, with a guessed value of the elementary coolant flow [as a fraction $d\Psi(s)$ of the external gas flow]. At the given s, integration along the blade length gives the blade metal temperatures at the outer and inner walls, $T_{bg}(y)$ and $T_{bcl}(y)$. If the value of T_{bg} at the blade tip ($y=H$) is assumed to be limited by material considerations to $T_{bg,max}$ then the elementary coolant flow rate may be obtained by iteration. Summation along the chord then gives the total coolant flow, for the whole blade. Results using the method are then compared to a simpler calculation applied to the whole blade, which assumes chordwise constant temperatures and constant selected values of cooling efficiency and film-cooling effectiveness. [DOI: 10.1115/1.1811100]

Introduction

The cooling of high-temperature gas turbines has been the subject of intensive work over the past 40–50 years, and there is substantial literature on the subject. Useful summaries are given in a major chapter of Lakshinarayana's book [1] and by Consonni [2].

1 Semi-Empirical Approaches

In the early years of turbine cooling, engine companies relied on practical methods for determining the amount of cooling flow required to maintain blade temperatures within prescribed metallurgical limits.

One method widely used for convectively cooled blading was that devised by Halls [3] and Holland and Thake [4]. The cooling effectiveness ε_0 was defined in terms of

i. the inlet gas temperature T_g, generally assumed constant along both the span and the chord[1]
ii. a blade metal temperature T_b, also assumed to be constant along both the span and the chord, and, with thin metal walls, constant through those walls, so that $T_b=T_{bg}=T_{bcl}$
iii. a coolant inlet temperature $T_{cl,in}$

Then,

$$\varepsilon_0=(T_g-T_b)/(T_g-T_{cl,in}) \tag{1}$$

With the three temperatures T_g, T_b, and $T_{cl,in}$ known or specified, the cooling effectiveness ε_0 could be determined. Further, a cooling efficiency η_c was defined, as the ratio of the actual temperature rise (from $T_{cl,in}$ to an outlet temperature $T_{cl,\text{out}}$) to the maximum possible (from $T_{cl,in}$ to the blade temperature T_b).

Thus,

$$\eta_c=(T_{cl,\text{out}}-T_{cl,in})/(T_b-T_{cl,in}) \tag{2}$$

The nondimensional coolant mass flow w^+ was then defined as

$$w^+=m_{cl}c_{p,cl}/h_gA_{g,s}=(T_g-T_b)/(T_{cl,\text{out}}-T_{cl,in}) \tag{3a}$$

where m_{cl} is the actual coolant flow in a single blade with specific heat $c_{p,cl}$ and h_g is the mean external heat transfer coefficient over the external blade surface of area $A_{g,s}$.

Equations (1), (2), and (3*a*) may then be combined to give

$$w^+=\varepsilon_0/[\eta_c(1-\varepsilon_0)]. \tag{3b}$$

For various values of cooling efficiency a chart such as Fig. 1 then gives w^+ as a function of the prescribed effectiveness ε_0. Experimental data from convectively cooled turbine blading may be added to such charts (see, for example, [4]), implying empirical values of cooling efficiency η_c. Equation (3*a*) for w^+ may be rewritten in terms of the mean external Stanton number St_g and the mainstream gas flow m_g, of specific heat c_{pg}, through a single-blade channel of cross-sectional area A_g

$$w^+=(m_{cl}/m_g)(c_{p,cl}/c_{p,g})(A_g/A_{g,s})/S_{tg} \tag{3c}$$

so that,

$$\Psi=m_{cl}/m_g=K_{\text{cool}}w^+ \tag{4}$$

where

$$K_{\text{cool}}=\text{St}_g(c_{p,g}/c_{p,cl})(A_{g,s}/A_g)$$

For given area ratio $(A_{g,s}/A_g)$ and specific heat ratio $(c_{p,g}/c_{p,cl})$, and with the Stanton number obtained from a con-

Contributed by the International Gas Turbine Institute (IGTI) of THE AMERICAN SOCIETY OF MECHANICAL ENGINEERS for publication in the ASME JOURNAL OF TURBOMACHINERY. Paper presented at the International Gas Turbine and Aeroengine Congress and Exhibition, Vienna, Austria, June 13–17, 2004, Paper No. 2004-GT-53729. Manuscript received by IGTI, October 1, 2003; final revision, March 1, 2004. IGTI Review Chair: A. J. Strazisar.

[1]The inlet gas temperature T_g may be replaced by a gas recovery temperature or even a peak temperature in a nonuniform entry temperature distribution. But for simplicity we do not go to that degree of sophistication in the text presented here although both corrections were included in the final code.

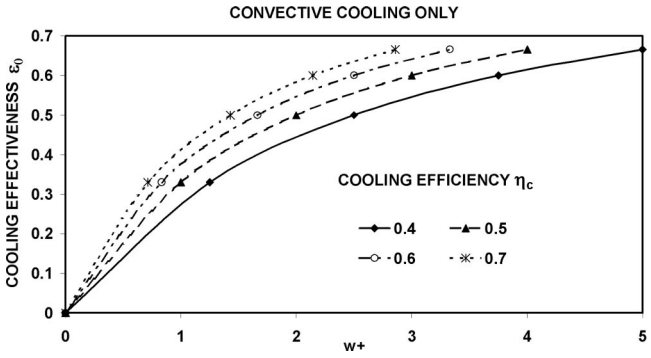

Fig. 1 Cooling effectiveness as a function of the parameter w^+ and the cooling efficiency (convective cooling only)

ventional Reynolds-number–Prandtl-number relation, the required fractional cooling flow $\Psi = m_{cl}/m_g$ can be obtained.

This general approach may be modified for blading with film cooling supplementing convective cooling, for finite thickness of the metal wall and for a thermal barrier coating (see, Wilcock, Young, and Horlock [5]). The corresponding equations they obtained are given below, without derivation,

$$\psi = \frac{m_{cl}}{m_g} = \frac{K_{\text{cool}}}{(1+B_{\text{total}})}\left\{\frac{\varepsilon_0 - \eta_{ad}[1-\eta_c(1-\varepsilon_0)]}{\eta_c(1-\varepsilon_0)}\right\} \tag{5}$$

where

$$B_{\text{total}} = \text{Bi}_{tbc} + \left(\frac{\varepsilon_0 - \eta_{ad}}{1-\varepsilon_0}\right)\text{Bi}_{bw} \tag{6}$$

Here η_{ad} is the adiabatic wall film effectiveness:

$$\eta_{ad} = (T_g - T_{aw})/(T_g - T_{cl,\text{out}}) \tag{7}$$

where T_{aw} is now the adiabatic outer wall temperature (also assumed constant along both the span and the chord) and Bi_{bw} and Bi_{tbc} are the metal blade wall and TBC Biot numbers respectively, defined by

$$\text{Bi}_{bw} = h_g t_{bw}/\lambda_{bw}, \quad \text{Bi}_{tbc} = h_g t_{tbc}/\lambda_{tbc} \tag{8}$$

in which t is the thickness and λ is the thermal conductivity of the metal or TBC.

The Holland and Thake [4] type of chart $[w^+, \varepsilon_0]$ may still be used, but now values of both η_c and η_{ad} are required. Figure 2 shows such a plot for $\eta_c = 0.7$ and varying η_{ad}, from 0 (no film cooling), to 0.5. Again experimental data may be added to such a plot to guide designers.

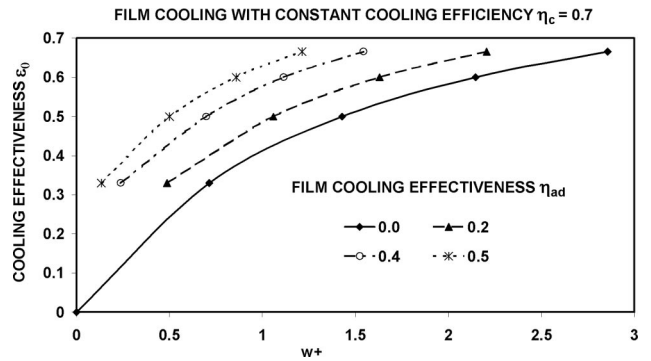

Fig. 2 Cooling effectiveness as a function of the parameter w^+, the cooling efficiency and the film cooling effectiveness (convective and film cooling)

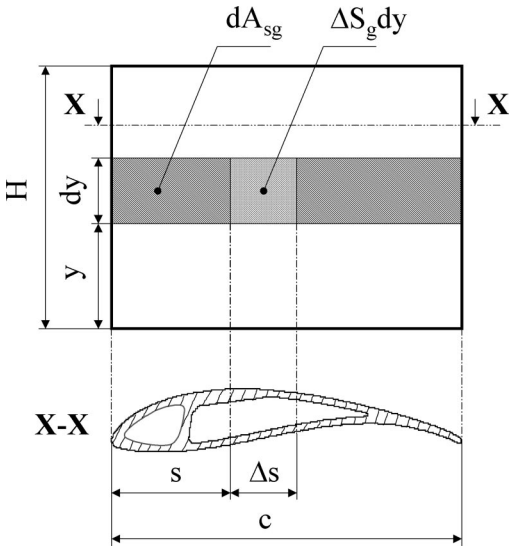

Fig. 3 Element $\Delta S_g dy$ for heat transfer through blade surface to coolant

2 Ainley's Early Work

Before considering more recent work as described in subsequent sections, it is worthwhile going back to the basic equations for the heat transfer process, as outlined originally by Ainley [6] in a classic paper in 1957. He considered an element of the full blade chord $dA_{g,s} = S_g dy = \Phi_g c dy$, at a distance y from the blade root (Fig. 3). Here S_g is the wetted external perimeter of the blade and $S_g = \Phi_g c$ with $\Phi_g > 2$ and c the full blade chord. The equations are

$$\lambda_{bw} A_m d^2 T_b/dy^2 + h_g S_g (T_g - T_b) + h_{cl} S_{cl} (T_{cl} - T_b) = 0 \tag{9}$$

$$m_{cl} c_{p,cl} dT_{cl}/dy + h_{cl} S_{cl} (T_{cl} - T_b) = 0 \tag{10}$$

Here S_{cl} denotes the *internal* heat transfer perimeter, λ_{bw} conductivity, and h heat transfer coefficient; uniform temperatures and heat transfer coefficients are assumed in the chordwise direction; the blade walls are assumed thin, so that $T_b = T_{b,g} = T_{b,cl}$. Neglecting conduction along the span (i.e., omitting the first term in Eq. (9)), Ainley rewrote these equations in terms of the parameters

$$X = h_{cl} S_{cl}/h_g S_g \quad \text{and} \quad w^+ = (m_{cl} c_{p,cl})/(h_g S_g H)$$

where H is the blade length. He succeeded in obtaining full analytical solutions for the temperature distributions $T_b(y)$ and $T_{cl}(y)$ which we do not reproduce here. But his subsequent approximations to these solutions, using a spanwise mean value of X, $\overline{X}$, and assuming constant T_g in the radial direction, are informative. They are

$$(T_g - T_b)/(T_g - T_{cl,in}) = [\overline{X}/(1+\overline{X})]e^{-k(y/H)} \tag{11}$$

$$(T_g - T_{cl})/(T_g - T_{cl,in}) = e^{-k(y/H)} \tag{12}$$

where $k = \overline{X}/[(1+\overline{X})w^+]$.

The metal and the coolant flow temperatures attain maximum values at $y = H$,

$$T_{b,\max} = T_g - (T_g - T_{cl,in})\overline{X}e^{-k}/(1+\overline{X}) \tag{13}$$

$$T_{cl,\text{out}} = T_g - (T_g - T_{cl,in})e^{-k} \tag{14}$$

Ainley showed that these equations gave quite good approximations to more detailed calculations of the temperatures distributions based on his full solutions. He found that while the variation in T_b is less than that in T_{cl}, the blade temperature is by no

means constant; the maximum blade temperature occurs at the end of the blade and it is this which must be limited by metallurgical considerations.

3 Cooling Efficiency With Blade Temperature Assumed Constant

In using the semi-empirical methods described in Section 1 the blade metal temperature is usually assumed to be constant along the blade (and set at a limiting value). This enables the second of Ainley's equations to be integrated directly to give

$$(T_b - T_{cl})/(T_b - T_{cl,in}) = \exp[-(\overline{X}/w^+)(y/H)] \tag{15}$$

from which the original definition of cooling efficiency [Eq. (2)] may be obtained as

$$\eta_c = 1 - \exp[-(\overline{X}/w^+)] \tag{16}$$

$(\overline{X}/w^+)$ may be written as $(\overline{\mathrm{St}}_{cl} A_{cl,s}/\overline{A}_{cl})$, where $\overline{\mathrm{St}}_{cl}$ is now the mean internal Stanton number, $(h_{cl}A_{cl}/m_{cl}c_{p,cl})$, and $A_{cl,s}$, $\overline{A}_{cl}$ are the surface and mean cross-sectional areas of the internal cooling flow, respectively. The Stanton number varies little with Reynolds number so it has been the general practice to take the cooling efficiency as constant for a particular range of blading, with η_c determined from experiment.

4 Consonni's More Recent Work

The new method described below in Section 5 is a development of the work of Consonni [2]. We describe his approach briefly in this section, as a preliminary to the more detailed description of the new method given later.

Like Ainley, Consonni allowed the blade temperature to increase along the span, and he closely followed Ainley's work in the determination of the heat transfer coefficients and in descriptions of the internal blading geometry, including the ''technology level'' parameter *Z*, as described in Appendix B. He also obtained analytical solutions, but not in the form of Eqs. (11) and (12). Consonni allowed for finite metal and TBC thickness [via Biot numbers] and introduced film cooling. In the illustrative brief description that follows here we consider only convective cooling without TBC, but with different metal temperatures T_{bg} and T_{bcl} on the gas and coolant sides of the metal wall, now of finite thickness t_{bw}.

Consonni adopted an ingenious approach to finding the distributions $T_{bg}(y)$, $T_{bcl}(y)$ and $T_{cl}(y)$. He regarded the whole blade (now including the metal wall and the coolant flow) as a heat exchanger subjected to a constant external temperature—which for convective cooling is the gas temperature T_g (He subsequently replaced T_g by the adiabatic wall temperature T_{aw} for film cooling.] He was then able to obtain a new form of cooling efficiency as

$$\eta_c' = (T_{cl,\mathrm{out}} - T_{cl,in})/(T_g - T_{cl,in}) = 1 - e^{-1/W^+} \tag{17}$$

for convective cooling, where $W^+ = m_{cl}\overline{c}_{p,cl}/\overline{U}_h A_{cl,s}$, and $\overline{U}_h$ is the now the overall heat transfer coefficient through the metal of finite thickness, of the form

$$U_h = \left[a_c \left(\frac{1}{h_g} + \frac{t_{bw}}{\lambda_{bw}} \right) + \frac{1}{h_{cl}} \right]^{-1} \tag{18}$$

where $a_c = A_{cl,s}/A_{g,s} = \overline{S}_{cl}/\overline{S}_g = \overline{\Phi}_{cl}/\overline{\Phi}_g$ (see Appendixes A and B, which also outline Consonni's detailed development of W^+ in terms of Stanton numbers and the internal blading parameter *Z*.)

This new cooling efficiency can be related to the form derived in Eq. (2) as follows:

$$\eta_c = \frac{T_{cl,\mathrm{out}} - T_{cl,in}}{T_{bg,\max} - T_{cl,in}} = \eta_c' \frac{T_g - T_{cl,in}}{T_{bg,\max} - T_{cl,in}} \tag{19}$$

The coolant outlet temperature $T_{cl,\mathrm{out}}$ is thus determined and Consonni finds the corresponding outlet blade temperatures simply by equating the heat fluxes at the outlet section (out)

$$\begin{aligned} h_g(T_g - T_{bg,\mathrm{out}}) &= \lambda_{bw}(T_{bg,\mathrm{out}} - T_{bcl,\mathrm{out}})/t_{bw} \\ &= h_{cl}(T_{bcl,\mathrm{out}} - T_{cl,\mathrm{out}}) \end{aligned} \tag{20}$$

With heat transfer coefficients and the necessary geometry inserted into Eqs. (17)–(20), he was able by iteration to determine the cooling flow fraction Ψ required to limit the maximum blade outlet temperature to a specified value, $T_{bg,\mathrm{out}} = T_{bg,\max}$. Consonni elaborated this approach to allow for film cooling and for thermal barrier coatings (TBCs).

In two earlier papers one of the authors (LT) developed computer codes based on Consonni's methods. In the first paper [7] comparisons were made between results obtained from the codes and from the empirical Holland and Thake method described in Section 1 (for convective cooling only). By matching the cooling flows required in the two methods it was possible to deduce values of the internal blading parameter *Z* appropriate to the two approaches. In the second paper [8], film cooling was included in the computer codes and again matching values of *Z* were obtained.

Chiesa and Macchi [9] have also used Consonni's method to study three options for turbine cooling in their study of combined cycle power plants.

5 The New Method

The new work detailed in this section involves treating successive small sections of the chord; the element $\Delta S_g dy = \Phi_g \Delta s dy$ of the blade is considered (Fig. 3) instead of the fuller element $S_g dy = \Phi_g c dy$, as used by Ainley and Consonni. The relevant equations are integrated with respect to y from $y=0$ to $y=H$, before stepping along the blade with new sections, $\Delta s = 0.1c$, to determine the full coolant flow required for the whole blade.

The equations for the (elementary) heat flux transferred are, therefore, as follows:

$$dq = h_g \Delta S_g (T_g - T_{bg}) dy \tag{21a}$$

$$dq = \frac{\lambda_{bw}}{t_{bw}} \Delta S_g (T_{bg} - T_{bcl}) dy \tag{21b}$$

$$dq = h_{cl} \Delta S_{cl} (T_{bcl} - T_{cl}) dy \tag{21c}$$

$$dq = \Delta m_{cl} c_{p,cl} dT_{cl} \tag{21d}$$

where $\Delta S_g dy$ and $\Delta S_{cl} dy$ are now the elementary areas at the external and internal sides of the blade wall, respectively equal to $\Phi_g \Delta s dy$ and $\Phi_{cl} \Delta s dy$, while the mass flow through the elementary cooling channel is Δm_{cl}. (Note that in the code, allowance is also made for a layer of thermal barrier coating on the outside of the metal blade.)

Then the sum of the first three equations yields

$$dq = \left(\frac{1}{h_g \Delta S_g} + \frac{t_{bw}}{\lambda_{bw} \Delta S_g} + \frac{1}{h_{cl} \Delta S_{cl}} \right)^{-1} (T_g - T_{cl}) dy \tag{22a}$$

If $a_c = \Delta S_{cl}/\Delta S_g = \Phi_{cl}/\Phi_g$, then

$$dq = U_h \Delta S_{cl} (T_g - T_{cl}) dy \tag{22b}$$

with U_h the overall coefficient of heat transfer of the system, as defined in Eq. (18). Equations (21*d*) and (22*b*) then yield

$$\Delta m_{cl} c_{p,cl} dT_{cl} = -U_h \Phi_{cl} \Delta s (T_g - T_{cl}) dy \tag{23}$$

The integration of this equation is then carried out along the blade length H with the elementary chordwise length Δs and the elementary coolant flow Δm_{cl} both held constant.

Hence,

$$T_g - T_{cl,\mathrm{out}} = (T_g - T_{cl,in}) e^{-\overline{U}_h H \overline{\Phi}_{cl} \Delta s / \Delta m_{cl} \overline{c}_{p,cl}} \tag{24}$$

so that Consonni's new cooling efficiency for the strip considered becomes

$$\eta_c' = 1 - e^{-(1/\Delta W^+)} \tag{25}$$

where

$$\Delta W^+ = \frac{\Delta m_{cl} \overline{c}_{p,cl}}{\overline{U}_h \Delta A_{cl,s}}$$

The above analysis refers to an elementary channel that is convectively cooled. If film cooling is introduced, then it is assumed that it begins at the beginning of the chordwise strip under consideration and continues until the end of that strip.

The adiabatic efficiency

$$\eta_{ad} = (T_g - T_{aw})/(T_g - T_{cl,\text{out}}) \tag{26}$$

is obtained from the work of Goldstein and Haji-Sheich [10], as a function principally of the distance x from the point of injection and the mass flow of coolant injected (details are given in Appendix C). In the current work Goldstein's length x is taken as the length of the strip, i.e., $x = \Delta s$, and it is assumed that the average adiabatic efficiency over the complete strip is equal to that at $x = \Delta s$. For the next small section strip, it is assumed that film cooling is started again, at the beginning of that new strip.

From the mean adiabatic effectiveness, the adiabatic wall T_{aw} temperature is obtained and substituted for T_g in the analysis leading to Eq. (24) for the coolant temperature, as described earlier in this section.

With $T_{cl}(y)$ known, all the other temperatures along the length y of the strip can be obtained, as indicated earlier. But here, after Consonni, we only need to set the prescribed maximum blade temperature $T_{bg,\max}$ at the end of the blade at $y = H$ to determine the elementary coolant flow rate Δm_{cl} for the strip considered, by iteration. We then proceed to the next small strip and repeat the process of integration with respect to y along this strip, with new values of gas-side and coolant-side heat transfer coefficients, gas temperature T_g, and effectiveness η_{ad}, but with the same internal geometry in the present calculation. In particular, the parameter ΔZ defined in the Appendix is held constant at the value for the whole blade; this implies that the ratio of the coolant surface area to the coolant flow cross sectional area is the same in the elementary cooling strip as in the whole blade.

With the cooling flow in a strip determined, there are several steps to be taken before proceeding to the next strip. These are described in the Section 6, which also involves a description of the overall flow through the blading.

6 Overall Flow Through the Blading

A relatively simple method of ''designing'' the blading is adopted, and this is used in proceeding from one strip to the next. Full details are given in Torbidoni [11] and only a brief nonanalytical description is given here, as follows:

a. The flow angle is prescribed at inlet and at exit from a blade row and it is assumed that this angle varies linearly with the chordwise distance [s] through the blades.
b. With an overall mass flow specified, it is assumed that the mean axial velocity ($\overline{C}_x$, the axial velocity that would pass the mass flow if the blades were of zero thickness) is assumed to remain constant. Nevertheless, a finite prescribed blade thickness is assumed in the present calculations, and the actual local axial velocity C_x is obtained from the continuity equation. A mean surface velocity is then obtained as $C_x/\cos\alpha$.
c. The losses in uncooled flow are first determined from the work of Kacker and Okapuu [12]. It is assumed that all the components of these uncooled losses, except those associated with shocks at the leading edge and with trailing edge thickness, vary linearly with s through the blades.
d. The change in the stagnation enthalpy and temperature of the mainstream gas across a strip is determined by using the steady flow energy equation, together with the new knowledge of the cooling flow required in the strip and the entry temperature of the coolant. This change in stagnation enthalpy is partly associated with the heat transferred across the blading and partly from the subsequent mixing of the two streams (the method described by Hartsel [13] is used).
e. Hartsel's method, based on the Shapiro relations for one-dimensional compressible gas flow, is also used to find the change in stagnation pressure associated with mixing of the film cooling air and the mainstream gas at the end of the strip.
f. The static enthalpy and temperature conditions in the mainstream are found by subtracting the known kinetic energy from the stagnation enthalpy. The static pressure is then found from the isentropic relation between the stagnation and static states, and the static density is also obtained.
g. The blade height at the end of the strip is obtained from the continuity equation and the prescribed mean axial velocity.
h. The coolant air not used in film cooling is assumed to be discharged at the blade trailing edge (after the last strip), and Hartsel's work is again used to determine the changes in flow properties due to mixing (his so-called ''Totlos'' method).
i. Losses of stagnation pressure in mixing are added to that for the uncooled flow given by Kacker and Okapuu.
j. The cooling air quantities obtained in all the strips Δs are then summed, from $s = 0$ to $s = c$, to give the total cooling air $\Sigma \Delta m_{cl}$.
k. For each strip the gas physical properties c_p, μ, W are evaluated by means of polynomials for the gas thermodynamic conditions and composition. A similar polynomial method is adopted in evaluating the specific entropy of the mainstream flow.

7 Results of Calculations of Coolant Flow Using the New Method

For a cooled turbine blade of given chord c, the method of calculation involves choosing a value of ΔZ, the number of passes for the internal flow, and the interference and enhancement factors for heat transfer Ψi and E_h. A value of the product $\Psi_d n_{ch}$ is implied by these choices, which means that the number of channels of a particular shape (e.g., ellipses with $\Psi_d = 2.24$) have been chosen.

The new method has been used to calculate the flow in a turbine nozzle guide vane row with an outlet angle of 71° as an example. The input data for the calculation, assuming 10 strips over the nozzle chord, was as in Table 1. Results of the calculation are given in Figs. 4–7.

Figure 4 gives the enthalpy-entropy diagram for the expansion through the blade row, both stagnation and static enthalpy being shown. The uncooled expansion is also shown with entropy increasing steadily through the blade row. There are several interesting features about the cooled expansion.

i. As to be expected, the expansion line heels over to the left, cooling of the mainstream gas being dominant and causing reduction in specific entropy even though there are irreversibilities due to mixing and temperature differences between mainstream and coolant.

ii. The mixing process downstream of the trailing edge leads to similar decreases in stagnation enthalpy and entropy decrease, both associated with low temperature cooling air injected into the mainstream.

Some details of the required cooling flow are shown in Figs. 5–7. Figure 5 gives the absolute and fractional cooling flow quantities for each of the ten steps used in the calculation; the total (fractional) cooling flow is close to 0.06.

Table 1 Input data for the calculation

Nozzle input data:			
m_g	140.6 kg/s (at entry section)	α_2	71 deg
		Bi_{bw}	0.25
T_g	1800 K	Bi_{tbc}	0.2
p_g	32 bar	$T_{cl,in}$	829 K
Pr_g	0.72	$T_{bg,\max}$	1125 K
K_{comb}	0.15	ΔZ	94.64 (for each strip)
	194 m/s (i.e., C_x at entry sect.)	$\Delta\alpha_h$	0.0095
$\overline{C_x}$		E_h	2
D_m	741 mm	n_p	3
Profile data	T6 profile	ψ_i	0.8
	max thickness/c=0.2	ψ_d	2.24
c	60 mm	r_{fc}	1 (0.5 for last strip)
$\sigma=c/p$	1.15		
Stagger angle	36 deg	α_{inj}	20 deg
Values ΔZ, c, Δa_h, E_h, n_p, Ψ_i, Ψ_d lead to:		External blade geometry leads to:	
d	1.9 mm	Φ_g	2.053
Δn_{ch}	1.764 (for each strip)	Mach number	0.967 (exit from nozzle)

The variation in the cooling efficiency is illustrated in Fig. 6; the efficiency drops slightly along the blade. The corresponding variation in the film-cooling effectiveness is shown in Fig. 7; again it drops slightly along the blade due to an increasing mainstream Reynolds number. The assumption of $r_{fc}=0.5$, for the last strip only, is clearly revealed in all of these three diagrams.

Table 2 gives the coolant and blade mean temperatures at blade hub and casing. Such values are close to the ones recorded at the mean section of the blade (after five steps). The limiting temperature is set for the metal temperature on the gas side at the blade tip.

In general, there is remarkably little variation in the pattern of the cooling flow from one strip to the next. This is primarily because the gas stagnation temperature T_g is not changing substantially over the blade surface, even though the static temperature is dropping sharply. Further the variation in the gas-side heat transfer coefficient is only changing slightly through the assumed Reynolds number relationship. Finally, because the local value of ΔZ for each strip is the same in this example, the internal cooling geometry (the ratio of surface area to cross-sectional area) does not change. In the future use of the code it will be possible to vary all these factors along the chord, which will lead to the optimum

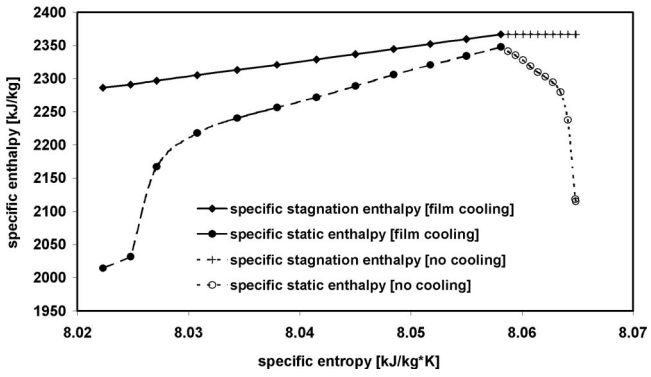

Fig. 4 Enthalpy-entropy diagrams for uncooled and cooled blading (showing both stagnation and static enthalpy)

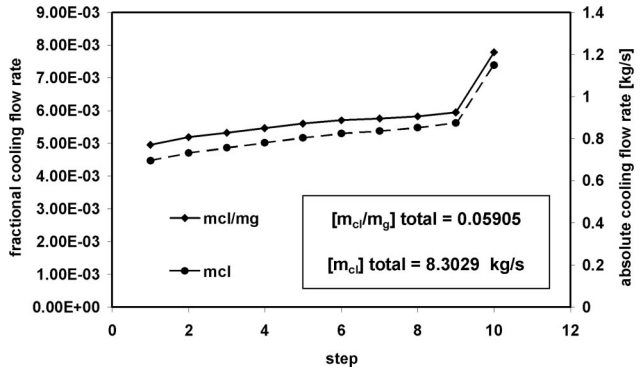

Fig. 5 Fractional and absolute cooling flow quantities required for ten steps along the blade chord

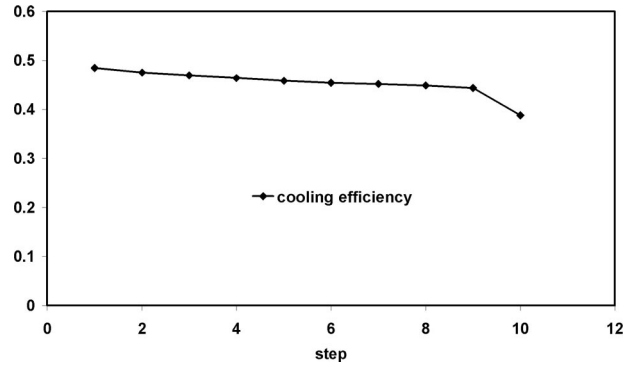

Fig. 6 Cooling efficiency for ten steps along the blade chord

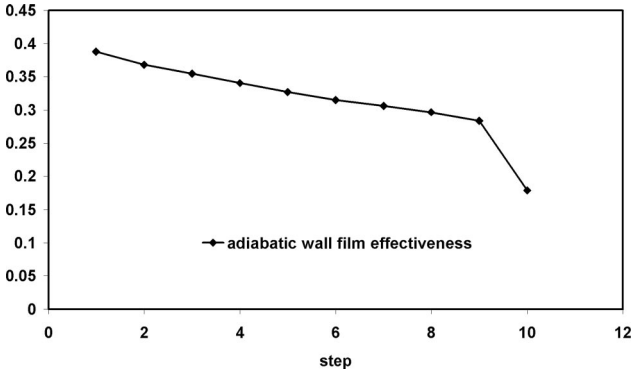

Fig. 7 Adiabatic wall film effectiveness for ten steps along the blade chord

Table 2 Coolant and blade mean temperatures at blade hub and casing

Radial location	Coolant flow	Blade coolant side	Blade gas side	TBC gas side
Hub [coolant entry]	829 K	900K	1024 K	1123 K
Casing [coolant exit]	963 K	1022K	1125 K	1208 K

distribution of the cooling flow with chordwise distance s, and may enable the total cooling flow to be minimized.

Finally, we have validated the code by comparing the results with those obtained using the ''mean flow'' method of Wilcock, Young and Horlock [5], which leads to Eq. (5). Those authors chose values of the parameters K_{cool}, η_c, and η_{ad} based on practical engine experience, and obtained coolant fractional flows in line with such practice. The results of the new code gave the following values of the parameters for the example of the turbine nozzle guide vanes

$$K_{\text{cool}}=0.01921, \quad \eta_c=0.456, \quad \eta_{ad}=0.320$$

Substitution of these values into Eq. (5), together with the cooling effectiveness resulting from the input data, gave a coolant mass flow fraction of $\Psi=0.0604$, compared to $\Psi=0.0590$, resulting from the code. This served to validate the code, the small remaining difference in ψ probably resulting from the different assumptions on blade wall metal temperature (which is assumed to be constant in Ref. [5], but is allowed to vary along the span in the new code). It should, however, be noted that these values of ψ are low compared with those obtained in [5] where, in particular, a higher value of K_{cool} was employed in order to obtain coolant mass flows used in real engines.

8 Conclusions

A new method of calculating the coolant flow requirements has been developed. It describes how the cooling flow in each chordwise strip may be calculated, assuming a particular internal cooling geometry (associated with the Ainley/Consonni parameter Z). Comparisons with a simplified method of calculation, assuming constant blade temperature along the span, indicate broad agreement.

However, the full potential of the code lies in its ability to respond to variation of input data (heat transfer coefficient, blade internal geometry, etc.) along the blade chord. This feature has yet to be exploited and will be the subject of a later paper.

The new method presented should then give more reliable evaluations than the semi-empirical methods, particularly for the study of innovative cycles, where conventional fluids and operating conditions cannot be assumed in the performance calculations. It is hoped that such full development of the code will provide a useful design tool for the turbine designer faced with the necessity of blade cooling.

Acknowledgments

The authors wish to thank Professor Aristide Massardo of the University of Genoa, Italy, for his excellent and significant work in the completion of this paper. His technical contributions were of major assistance, particularly in the selection of the project and the development of the program. The authors are also grateful for help received from Professor R. Singh and P. Pilidis for the provision of facilities at Cranfield University, UK. Professor J. B. Young and Professor J. D. Denton, of the Engineering Department, Cambridge University, UK, both gave useful technical advice.

Nomenclature

- A = area
- A_g, A_{cl} = for cross-sectional area of gas flow (single-blade channel), and coolant flow (single blade), respectively
- $A_{g,s}$, $A_{cl,s}$ = for wetted heat transfer areas of gas flow (single blade) and coolant flow (single blade), respectively
- A_m = cross-sectional metal blade area
- a_c = $A_{cl,s}/A_{g,s}$
- Bi = Biot number
- c = chord
- c_p = specific heat at constant pressure
- d = cooling channel hydraulic diameter
- D_m = mean diameter of blading
- E_h = parameter that considers increased surface of cooling channels due to turbulators
- h = heat transfer coefficient
- H = blade height
- k = $X/[(1+X)w^+]$
- K_{comb} = combustion pattern factor
- K_{cool} = $\text{St}_g(c_{p,g}/c_{p,cl})(A_{g,s}/A_g)$
- M = injection rate
- m = mass flow rate (for a single blade channel or blade)
- n_{ch} = number of the cooling channels inside the blade
- n_p = number of cooling channel passes
- NTU = number of transfer unite
- p = pressure, also blade pitch or spacing
- p_{ch} = cooling channel perimeter
- Pr = Prandtl number
- q = rate of heat transferred (heat flux)
- Re = Reynolds number
- r_{fc} = fraction of the coolant flow used for film cooling
- s = coordinate along chord line (such that $ds\cos\alpha=dx$)
- S = surface per unit length, i.e., perimeter (subscripts g and cl for gas and coolant)
- St = Stanton number
- t = blade thickness
- T = temperature
- U = overall heat transfer coefficient, also velocity
- w^+, W^+ = nondimensional mass flow rates
- W = molecular weight
- w = injection slot width
- x = axial co-ordinate, also distance in downstream direction from film injection location
- y = radial (span-wise) coordinate
- X = $h_{cl}S_{cl}/h_gS_g$
- Z = blade cooling system technology level parameter

Greek

- α = flow angle (measured from axial direction), film injection angle (plus subscript -inj)
- α_h = ratio, (empty blade cross sectional area)/c^2
- Δ = referring to blade ''strip''
- ε_0 = cooling effectiveness
- η_c = cooling efficiency
- η_{ad} = adiabatic wall film effectiveness
- λ = conductivity
- μ = dynamic viscosity
- ρ = density
- σ = c/p solidity
- Ψ = m_{cl}/m_g coolant fraction
- ψ_i = heat transfer interference parameter

Ψ_d = $p_{ch}/\pi d$ shape parameter for coolant channels
Φ = $\Delta S/\Delta s = S/c$

Subscripts

2 = exit from blade row
ad = referring to film cooling effectiveness
aw = adiabatic wall (temperature)
b = blade
bw = blade wall
cl = coolant, cooling side
ch = referring to coolant channels
g = gas, gas side
in = inlet
inj = injection
max = maximum
out = outlet
s = surface
tbc = thermal barrier coating
total = total
w = related to the film injection slot

Superscript

$\bar{}$ = mean or average (specific heats, heat transfer coefficients, etc.)

The parameters β, ξ, C_{g1}, C_{f1}, C_{f2} appear in complex equations and are as defined in the Appendixes.

Appendix A: Relations for the Heat Transfer Coefficients

A1 External Stanton Number. The external Stanton number is obtained from an empirical relationship for turbulent flow

$$\mathrm{St}_g = 0.285\,\mathrm{Re}_g^{-0.37}\,\mathrm{Pr}_g^{-2/3} \tag{A1}$$

where

$$\mathrm{St}_g = \frac{h_g}{c_{p,g}(m_g/A_{g,2})}$$

$$\mathrm{Re}_g = \frac{m_g c}{A_{g,2}\mu_g}$$

and where m_g is now the mass flow through a single blade channel of exit area $A_{g,2}$ (at station 2), given by

$$A_{g,2} = \pi D_m H_2 \cos\alpha_2/z = cH_2\cos\alpha_2/\sigma.$$

Here the outlet angle is α_2, the mean diameter is D_m, the blade height is H_2, z is the number of blades in the row, and σ is the solidity, the blade chord divided by the blade pitch.

The constant of 0.285 in Eq. (A1) is obtained from Chiesa and Macchi [9] who quoted experimental data of Louis et al. [14].

A2 The Internal Stanton Number. For the internal flow, the Colburn empirical correlation is used

$$St_{cl} = E_h 0.023\,\mathrm{Re}_{cl}^{-0.2}\,\mathrm{Pr}_{cl}^{-2/3} \tag{A2}$$

where E_h ($E_h \geq 1$) is an enhancement factor associated with the use of "turbulators" within the internal flow passages. However, it is difficult to express this correlation in a useful form for the calculation of coolant flow because of the complex geometry.

Consider the geometry of one of the (noncircular) internal cooling passages, of area A_{ch} and with a perimeter p_{ch}. Then the hydraulic diameter is $d = 4A_{ch}/p_{ch}$, and the perimeter is $p_{ch} = \Psi_d \pi d$, where Ψ_d is a factor that would be unity for a circular channel, but is greater than unity for a noncircular channel. The cross-sectional area of the channel may be written

$$A_{ch} = p_{ch}\frac{d}{4} = \Psi_d \pi \frac{d^2}{4}$$

If there are n_{ch} coolant channels in the whole blade and for each channel there are n_p "passes" (each of length H), then the total area occupied by cooling channels within the blade cross-section is

$$n_{ch} n_p A_{ch} = n_{ch} n_p \left(\Psi_d \pi \frac{d^2}{4}\right) = \alpha_h c^2$$

However, the cross-sectional area available for the flow of coolant is only

$$A_{cl} = n_{ch}\left(\Psi_d \pi \frac{d^2}{4}\right) = \frac{\alpha_h c^2}{n_p}$$

and the total effective coolant heat transfer surface area is $A_{cl,s} = \Psi_i n_{ch} n_p (\Psi_d \pi d H)$, where, after Consonni [2], Ψ_i is a factor that allows for heat transfer between channels.

We shall consider the strip of the blade which carries a coolant flow Δm_{cl}, and assume that the number of coolant channels in this strip is Δn_{ch}. It is implied that $\Delta n_{ch}/n_{ch} = \Delta\alpha_h/\alpha_h$. But the number of passes in the strip is unchanged at n_p, and the area available for flow of coolant in the strip is

$$\Delta A_{cl} = \Delta n_{ch}\left(\Psi_d \pi \frac{d^2}{4}\right) = \frac{\Delta\alpha_h c^2}{n_p}$$

where

$$\Delta\alpha_h = \Delta n_{ch} n_p \left[\Psi_d \pi \frac{(d/c)^2}{4}\right]$$

The Reynolds number of the internal flow within the strip can now be obtained as

$$\mathrm{Re}_{cl} = \frac{\rho_{cl} U_{cl} d}{\mu_{cl}} = \frac{\Delta m_{cl} d}{\Delta A_{cl}\mu_{cl}} = \frac{n_p \Delta m_{cl} d}{\Delta\alpha_h c^2 \mu_{cl}}$$

which can be inserted into Eq. (A2) to give

$$\mathrm{St}_{cl} = E_h 0.023\left(\frac{n_p \Delta m_{cl} d}{\Delta\alpha_h c^2 \mu_{cl}}\right)^{-0.2}\mathrm{Pr}_{cl}^{-2/3} \tag{A3}$$

After some algebra, this expression may be developed in terms of the ratio of coolant to mainstream gas flow through a single-blading channel and the corresponding Reynolds numbers to give

$$\mathrm{St}_{cl} = \frac{0.023 E_h}{C_{g1}^{0.2} C_{f1}}\left[\left(\frac{c}{d}\right)\left(\frac{\Delta\alpha_h}{n_p}\right)\right]^{0.2}\left(\frac{\Delta m_{cl}}{m_g}\right)^{-0.2} \tag{A4}$$

where

$$C_{g1} = \frac{(H_2/c)}{\sigma}$$

$$C_{f1} = \mathrm{Pr}_{cl}^{2/3}\left[\mathrm{Re}_g \cos\alpha_2\left(\frac{\mu_g}{\mu_{cl}}\right)\right]^{0.2}$$

Appendix B: Determination of Number of Transfer Units [NTU] for the Strip

The number of transfer units for the strip may be written

$$\mathrm{NTU} = 1/\Delta W^+ = \frac{\bar{U}_h H \bar{\Phi}_{cl}\Delta s}{\Delta m_{cl}\bar{c}_{p,cl}} \tag{B1}$$

where the effective surface heat transfer area of Δn_{ch} channels with n_p passes is

$$\Delta A_{cl,s} = H\bar{\Phi}_{cl}\Delta s = \Psi_i(\Delta n_{ch} n_p \Psi_d \pi d H)$$

the coolant thermal capacity is

$$\Delta m_{cl}\bar{c}_{p,cl} = \Delta n_{ch}\left(\rho_{cl} U_{cl}\Psi_d \pi \frac{d^2}{4}\right)\bar{c}_{p,cl}$$

and the overall heat transfer coefficient is

$$U_h=\left[a_c\left(\frac{1}{h_g}+\frac{t_{bw}}{\lambda_{bw}}\right)+\frac{1}{h_{cl}}\right]^{-1}$$

Hence Eq. $(B1)$ becomes

$$\mathrm{NTU}=1/\Delta W^+ = \frac{\Delta n_{ch}\Psi_i n_p \Psi_d \pi d H}{\left[a_c\left(\frac{1}{h_g}+\frac{t_{bw}}{\lambda_{bw}}\right)+\frac{1}{h_{cl}}\right]\left[\Delta n_{ch}\left(\rho_{cl}U_{cl}\Psi_d\pi\frac{d^2}{4}\right)\overline{c}_{p,cl}\right]}\cdot\frac{h_{cl}}{h_{cl}} \qquad (B2)$$

But the internal Stanton number may be written

$$\mathrm{St}_{cl}=\frac{h_{cl}}{\left[\left(\rho_{cl}U_{cl}\Psi_d\pi\frac{d^2}{4}\right)\Big/\left(\Psi_d\pi\frac{d^2}{4}\right)\right]\overline{c}_{p,cl}} \qquad (B3)$$

so that

$$\mathrm{NTU}=1/\Delta W^+=\frac{4\mathrm{St}_{cl}\Psi_i n_p (H/d)}{1+\left(a_c\frac{h_{cl}}{h_g}\right)(1+Bi_{bw})} \qquad (B4)$$

With Eq. $(A4)$ for the Stanton number obtained in Appendix A it follows, after some algebra, that

$$\mathrm{NTU}=1/\Delta W^+=\frac{0.092\frac{H}{c}\Delta Z\left(\frac{\Delta m_{cl}}{m_g}\right)^{-0.2}}{C_{g1}^{0.2}C_{f1}\left[1+\left(a_c\frac{h_{cl}}{h_g}\right)(1+\mathrm{Bi}_{bw})\right]} \qquad (B5)$$

where ΔZ is the so-called technology level parameter referred to the single strip

$$\Delta Z=\Psi_i\Delta\alpha_h^{0.2}n_p^{0.8}E_h(c/d)^{1.2}$$

and

$$\mathrm{Bi}_{bw}=h_g\frac{t_{bw}}{\lambda_{bw}}$$

$$C_{g1}=\frac{(H_2/c)}{\sigma}$$

$$C_{f1}=\mathrm{Pr}_{cl}^{2/3}\left[\mathrm{Re}_g\cos\alpha_2\left(\frac{\mu_g}{\mu_{cl}}\right)\right]^{0.2}$$

while

$$a_c\frac{h_{cl}}{h_g}=\frac{0.092C_{g1}^{0.8}C_{f2}\Delta Z(\Delta m_{cl}/m_g)^{0.8}}{0.285\Phi_g(\Delta s/c)}$$

and

$$C_{f2}=\mathrm{Re}_g^{0.17}(\overline{c}_{p,cl}/c_{pg})(\mu_{cl}/\mu_g)^{0.2}(\mathrm{Pr}_g/\mathrm{Pr}_{cl})^{2/3}(\cos\alpha_2)^{0.8}$$

Appendix C: The Goldstein and Haji Expressions for Adiabatic Effectiveness in Film Cooling

The adiabatic wall film effectiveness η_{ad}, is defined as

$$\eta_{ad}=\frac{T_g-T_{aw}}{T_g-T_{cl,\mathrm{out}}} \qquad (C1)$$

The value of η_{ad} may be calculated by means of the semi-empirical correlation proposed by Goldstein and Haji-Sheikh [10], for the injection of the film cooling air through a continuous slot over flat plates

$$\eta_{ad}=\frac{1.9\mathrm{Pr}_g^{2/3}}{1+0.329\left(\frac{c_{p,g}}{c_{p,cl}}\right)\left(\frac{\mu_g}{\mu_{cl}}\right)^{0.2}\xi^{0.8}\beta} \qquad (C2)$$

in which

$$\xi=\left(\frac{x}{wM}\right)\mathrm{Re}_w^{-0.25},$$

$$\beta=1+0.00015\,\mathrm{Re}_w\left(\frac{\mu_{cl}}{\mu_g}\right)\left(\frac{W_g}{W_{cl}}\right)\sin\alpha_{inj}$$

and where x is the distance in downstream chordwise direction from the injection location; w is the injection slot width; $M=(\rho_{cl}U_{cl})_{inj}/(\rho_g U_g)_{inj}$ is the injection rate at the injection location in which $(U_{cl})_{inj}$ is the coolant velocity as it is injected to feed the film; $\mathrm{Re}_w=(\rho_{cl}U_{cl})_{inj}w/\mu_{cl}$ is the Reynolds number referred to the injection velocity $(U_{cl})_{inj}$ and the slot width w; and W_g and W_{cl} are molecular weights of the two streams.

The β term takes into account an injection angle α_{inj} different from zero for the coolant film. When α_{inj} is equal to zero, β is equal to unity, and the coolant is injected in the direction parallel to the blade surface.

Taking the injection geometry into account, it is then possible to translate the semi-empirical correlation $(C2)$ into the more useful form

$$\eta_{ad}=\frac{1.9\mathrm{Pr}_g^{2/3}}{1+0.329\left(\frac{c_{p,g}}{c_{p,cl}}\right)\mathrm{Re}_{g,inj}^{0.8}\left(\frac{x}{c}\right)^{0.8}\left[\left(\frac{m_g}{\Delta m_{cl}}\right)\left(\frac{2H_{inj}\mu_g}{m_g r_{fc}}\right)+0.00015\frac{W_g}{W_{cl}}\sin\alpha_{inj}\right]}$$

where r_{fc} is the ratio between the coolant mass flow that feeds the film and the total coolant mass flow entering the blade strip; m_g is the gas flow through one blade channel; $\mathrm{Re}_{g,inj}$ is the mainstream Reynolds number at the injection point; Δm_{cl} is the mass flow through the strip on one blade.

References

[1] Lakshminarayana, B., 1996, *Fluid Dynamics and Heat Transfer in Turbomachinery*, Wiley, New York.

[2] Consonni, S., 1992, "Performance Prediction of Gas/Steam Cycles for Power Generation," MAE Dept. Princeton Univ., Ph.D. thesis No. 1983-T.

[3] Halls, G. A., 1969, "Air Cooling of Turbine Blades and Vanes," AGARDograph No. 120.

[4] Holland, M. J., and Thake, T. F., 1980, "Rotor Blade Cooling in High Pressure Turbines," Am. Ind. Hyg. Assoc. J., **17**, 412–418.

[5] Wilcock, R. C., Young, J. B., and Horlock, J. H., 2005, "The Effect of Turbine Blade Cooling on the Cycle Efficiency of Gas Turbine Power Plants," ASME J. Eng. Gas Turbines Power, **127**, pp. 109–120.

[6] Ainley, D. G., 1957, "Internal Air Cooling for Turbine Blades: A General Design Survey," Aeronautical Research Council Reports and Memo. 3013.

[7] Jordal, K., Torbidoni, L., and Massardo, A. F., 2001, "Convective Blade Cooling Modelling for the Analysis of Innovative Gas Turbine Cycles," *ASME Turboexpo 2001*, ASME, New York, ASME Paper No. 2001-GT-0390.

[8] Torbidoni, L., and Massardo, A. F., 2002, "Analytical Blade Cooling Model for Innovative Gas Turbine Cycle Evaluations Supported by Semi-Empirical

Air Cooled Blade Data,'' ASME J. Eng. Gas Turbines Power, **126**, pp. 498–506.
[9] Chiesa, P., and Macchi, E., 2002, ''A Thermodynamic Analysis of Different Options to Break 60% Electric Efficiency in Combined Cycle Power Plants,'' ASME, Paper No. GT-2002-30663.
[10] Goldstein, R. J., and Haji-Sheikh, A., 1967, ''Prediction of Film Cooling Effectiveness,'' *Proc. 1967, Semi-Int. Symp.* (Tokyo), pp. 213–218, JSME, Tokyo.
[11] Torbidoni, L., 2004, PhD thesis, University of Genoa, Italy.
[12] Kacker, S. C., and Okapuu, U., 1982, ''A Mean Line Prediction Method for Axial Flow Turbine Efficiency,'' ASME J. Eng. Power, **104**, pp. 111–119.
[13] Hartsel, J. E., 1972, ''Prediction of Effects of Mass-Transfer Cooling on the Blade-Row Efficiency of Turbine Airfoils,'' *AIAA, 10th Aerospace Sciences Meeting*, San Diego, Paper No. AIAA-72-11.
[14] Louis, J. F., 1977, ''Systematic Studies of Heat Transfer and Film Cooling Effectiveness,'' AGARD CP 229.

Surface Roughness Effects on External Heat Transfer of a HP Turbine Vane

M. Stripf

A. Schulz

S. Wittig

Lehrstuhl und Institut für Thermische Strömungsmaschinen, Universität Karlsruhe (TH), Kaiserstr. 12, 76128 Karlsruhe, Germany

External heat transfer measurements on a highly loaded turbine vane with varying surface roughness are presented. The investigation comprises nine different roughness configurations and a smooth reference surface. The rough surfaces consist of evenly spaced truncated cones with varying height, diameter, and distance, thus covering the full range of roughness Reynolds numbers in the transitionally and fully rough regimes. Measurements for each type of roughness are conducted at several freestream turbulence levels (Tu_1=4% to 8.8%) and Reynolds numbers, hereby quantifying their combined effect on heat transfer and laminar-turbulent transition. In complementary studies a trip wire is used on the suction side in order to fix the transition location close to the stagnation point, thereby allowing a deeper insight into the effect of roughness on the turbulent boundary layer. The results presented show a strong influence of roughness on the onset of transition even for the smallest roughness Reynolds numbers. Heat transfer coefficients in the turbulent boundary layer are increased by up to 50% when compared to the smooth reference surface. [DOI: 10.1115/1.1811101]

Introduction

In recent gas turbines, sophisticated cooling concepts are utilized to allow turbine inlet temperatures far beyond the blade material's melting temperature, thereby reaching high thermodynamic efficiency. To predict blade life in such a severe environment and to optimize cooling, it is necessary to have an exact knowledge of the heat transfer distribution on the blade's surface. Various factors influence heat transfer, e.g., pressure distribution, free-stream turbulence, surface curvature, wakes, secondary flows, and surface roughness. While the first five factors do not change remarkably during an airfoil's lifetime, the surface roughness is not constant, but it increases due to particle deposits, erosion, and corrosion. Several recent experimental studies at different levels of abstraction show a considerable increase in heat transfer with elevated surface roughness.

Flat plate experiments with zero pressure gradient were conducted by Barlow et al. [1] and Hosni et al. [2] using deterministic rough surfaces with different element shapes and densities. The measurements showed an increase in heat transfer by up to 120% compared to the smooth plate, depending on element shape and distribution.

Bogard et al. [3] used regular arrays of truncated cones on a flat plate to simulate two real vane surfaces, both near or in the fully rough regime. They also varied the free-stream turbulence intensity and found an additive effect of roughness and turbulence level. Bons [4] investigated almost 100 land-based gas turbine components from different manufacturers and selected six characteristic inservice turbine surfaces, which he reproduced in a scaled-up version using a three-dimensional (3D) printer. By varying the freestream turbulence level, he found a synergistic effect on heat transfer between roughness and turbulence, which is higher than the additive effect.

In another study, Bons and McClain [5] investigated the combined effect of roughness and pressure gradient on a flat plate. Again they found a synergistic effect, which, for an adverse pressure gradient, is lower than the additive effect and, for a favorable pressure gradient, is higher than the additive effect. Other flat plate studies that included the effect of pressure gradient were performed by Coleman et al. [6]. They introduced an acceleration parameter for use with rough wall flow and found that for constant values of this parameter, the rough wall boundary layer is in an equilibrium state.

Pinson and Wang [7] conducted flat plate transition experiments and used strips of different sandpapers at the leading edge of the plate. They found that the onset of transition is shifted toward the leading edge when roughness size is increased. Another interesting result was that leading-edge roughness causes a pretransitional region, where the momentum and thermal transport in the boundary layer behave like laminar flow, but the wall heat transfer is already significantly increased. In a consecutive study [8], the effect of a step change in roughness was investigated. The step height turned out to have a major effect on the location of transition onset. Gibbings and Al-Shukri [9] investigated the combined effect of surface roughness and turbulence intensity on the laminar boundary layer and its transition. They correlated the momentum thickness Reynolds number at the start of transition with the freestream turbulence intensity and the roughness Reynolds number. The length of transition was correlated in a similar way.

The flat-plate investigations with and without pressure gradient give a better understanding of the effects of roughness on heat transfer, they are, however, not directly transferable to a rough airfoil. A further step toward a realistic turbine environment has to be taken, most often, with the drawback of less detailed instrumentation and less flexibility when choosing the surface roughness. Most of the cascade experiments with rough airfoils have been conducted during the last decade. Turner et al. [10] glued abrasive powders on a rotor blade and measured the midspan heat transfer distribution around it. They found that suction-side transition moved toward the leading edge and pressure surface heat transfer increased uniformly when roughness height was increased. Hoffs et al. [11] used unpolished liquid crystals as surface roughness with a maximum peak-to-valley height of 25 μm. The measurements were performed in a linear cascade with five airfoils and an inlet turbulence intensity of 10%. On the pressure side the roughness had little to no effect on heat transfer coefficients, whereas on the suction side the transition started earlier. Using a three vane linear cascade with a chord length of 48 mm,

Contributed by the International Gas Turbine Institute (IGTI) of THE AMERICAN SOCIETY OF MECHANICAL ENGINEERS for publication in the ASME JOURNAL OF TURBOMACHINERY. Paper presented at the International Gas Turbine and Aeroengine Congress and Exhibition, Vienna, Austria, June 13–17, 2004, Paper No. 2004-GT-53114. Manuscript received by IGTI, October 1, 2003; final revision, March 1, 2004. IGTI Review Chair: A. J. Strazisar.

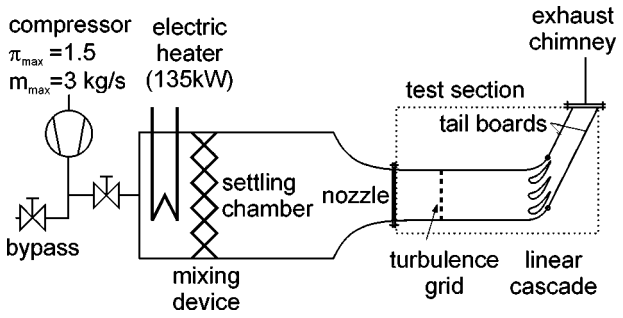

Fig. 1 Schematic view of the hot wind tunnel

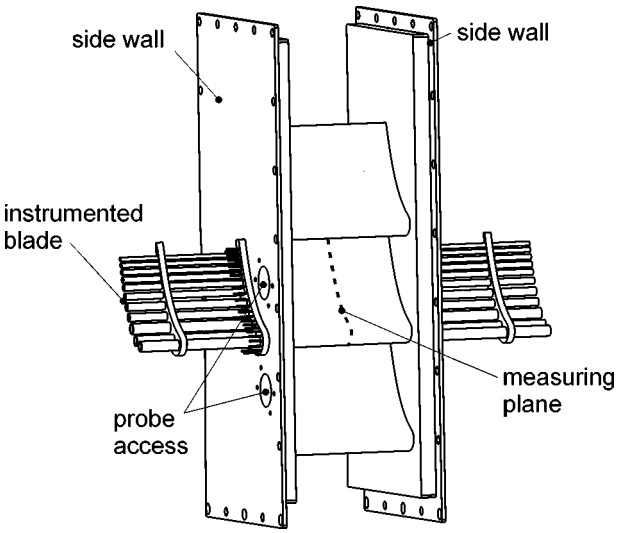

Fig. 2 Three vane linear cascade

Abuaf et al. [12] investigated the influence of roughness due to different levels of surface finish. The inlet turbulence intensity was constantly 14%. A centerline average roughness (CLA) of 1.03 μm showed a considerably earlier transition and a higher heat transfer coefficient on the entire suction surface when compared to the lowest roughness with 0.81 μm CLA. Bunker [13] obtained airfoil heat transfer distributions for three different surface roughnesses with a maximum peak-to-valley height of 27.8 μm, using a transonic linear vane cascade with a chord length of 127.5 mm. Varying Tu from 4% to 13%, he found that the higher roughness levels tend to dominate turbulence in most regions. Boyle et al. [14] used a three vane linear cascade, with an instrumented middle airfoil that consisted of a foam material. A roughness height of 111 μm was achieved by not smoothing the foam surface. At a turbulence level of 10%, heat transfer on the suction surface was higher than would be expected for a smooth surface by almost a factor of two. For $Tu=1\%$ this factor was smaller.

Full span measurements were conducted by Blair [15] using a smooth and two different rough blade surfaces with a peak-to-valley height of 51 μm and 660 μm, respectively. Roughness was achieved using black paint or grit. Midspan heat transfer was augmented by up to 100% for the roughest case in comparison to the smooth case. The roughness also had important augmentation effects in the near-hub and near-tip regions of the suction surface.

All rough surfaces in the cascade experiments known to the authors were created either by using liquid crystals, grit, or by not smoothing the natural surface. Hence, no systematic variation in roughness density, height, and shape could be performed. The present study will therefore provide heat transfer data of a high-pressure turbine vane with well-defined deterministic rough surfaces.

Experimental Setup and Measuring Technique

Test Facility. The measurements are conducted on a highly loaded linear turbine cascade in a hot wind tunnel, illustrated in Fig. 1. The compressed air enters the wind tunnel and is heated up to 350 K by an electric heater. After passing a settling chamber, the flow is guided through a nozzle into the test section with rectangular cross section (100 mm wide and 250 mm high).

The cascade geometry is the same that was previously investigated experimentally and numerically by Schiele et al. [16] for a smooth vane surface. However, for the sake of a higher measurement resolution and higher inlet chord Reynolds numbers $Re_1 = u_1 \cdot c/\nu$, the cascade was scaled up by a factor of 1.5, which leads to a chord length of 93.95 mm in the present study. While the upper and lower airfoils of the three vane cascade in Fig. 2 are only used to guide the flow, the middle airfoil is instrumented either for heat transfer or pressure distribution measurements. The upper and lower channel boundaries are shaped according to the streamlines and pass into adjustable tail boards that allow fine-tuning of periodic flow conditions. Periodicity is assured by measuring and matching the pressure distributions on the side wall over the two neighboring flow channels of the middle airfoil. In addition, the measured pressure distribution around the middle airfoil is consistent with measurements conducted by Schiele et al. [16] on a five vane cascade.

Two different turbulence grids consisting of square rods can be placed 350 mm upstream of the cascade, leading to freestream turbulence intensities of 5.1% and 8.8% at the cascade entry. The turbulence intensity without grid is 4%. The turbulence dissipation length scale L_ε is determined for each grid by measuring the decay of turbulence with a single hot wire constant temperature anemometer at eight locations between the grid and the cascade. Using simplified versions of the k-ε-transport equations, L_ε is calculated from the decay of turbulence intensity [16]. Turbulence intensities and dissipation length scales were found to be independent of Reynolds number. Other common turbulence length scales, such as the viscous dissipation length scale λ and the integral length scale Λ, are obtained using relations developed by Mayle et al. [17]. Turbulence Reynolds numbers Re_λ range from 83 to 302, thus covering typical values found in gas turbine engines [17]. Table 1 gives an overview of the turbulence parameters that are used in the experiments.

Roughness. A deterministic roughness that consists of evenly spaced truncated cones and that is uniformly distributed on the vane surface is chosen for the experiments because of several reasons. First, numerous surface roughness measurements on gas turbine blades performed by Taylor [18], Bons et al. [19], and Tarada and Suzuki [20] show that the type of roughness varies considerably with the location inside the machine, the place of operation, coatings, and cooling configuration. There seems to be

Table 1 Turbulence parameters

grid	Tu_1 (%)	$Re_1 \cdot 10^5$ (-)	$L_{\varepsilon,1}$ (mm)	η_1 (mm)	$Re_{\lambda,1}$ (-)	λ_1 (mm)	Λ_1 (mm)
		0.9		0.174	182	4.6	41.0
—	4.0	1.4	100.0	0.125	226	3.7	39.4
		2.2		0.089	284	3.0	38.2
		2.5		0.081	302	2.8	37.9
		0.9		0.092	83	1.7	8.3
1	5.1	1.4	16.9	0.066	104	1.3	7.7
		2.2		0.047	130	1.1	7.3
		2.5		0.043	139	1.0	7.2
		0.9		0.070	144	1.7	12.3
2	8.8	1.4	29.3	0.050	180	1.3	11.7
		2.2		0.036	225	1.1	11.3
		2.5		0.033	240	1.0	11.2

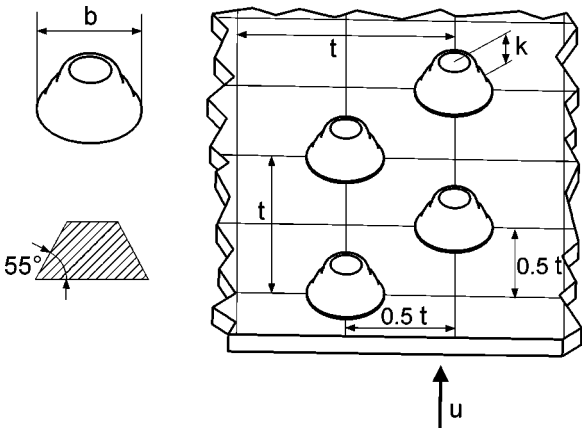

Fig. 3 Roughness model

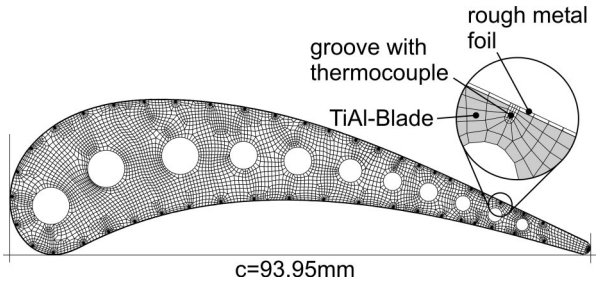

Fig. 4 Finite element mesh

nothing like a typical gas turbine blade roughness that could be used for the experiments. Second, the experimental data is used to develop new numerical methods, and the roughness used should be accurately defined in order not to introduce more uncertainties. Third, using a deterministic model, specific parameters, such as roughness height and distance, can be set independently and their separate effects on heat transfer can be investigated.

The rough surface is produced using a photolithography process where the pattern of roughness elements is transferred from the mask to a metal foil, which is coated with a photoresist. The base shape and distance of the elements are defined in this step. In a subsequent etching process, the element height k is set by adjusting the etching time. Measurements with a laser profilometer show that the resulting truncated cones have an angle of approximately 55 deg (Fig. 3). Element heights up to 80 μm are produced using a metal foil of 100 μm thickness. While any base shape and distribution is possible, the investigations in this paper use circular base shapes and a uniform distribution as shown in Fig. 3.

A common quantity to describe the surface roughness in fluid dynamics is the equivalent sand grain roughness k_s introduced by Schlichting [21]. For fully rough surfaces, i.e., roughness Reynolds numbers Re_{ks} greater than 70, Waigh and Kind [22] provide a correlation between the regular deterministic roughness geometry and the equivalent sand grain roughness. The correlation distinguishes between a dense regime, in which the roughness elements are closely packed and k_s increases with the distance between the elements, and a sparse regime, where k_s decreases with the distance between the elements. In the present paper, the correlation is also used for smaller Re_{ks} to characterize the roughness geometry. Table 2 shows a summary of the different surfaces that are investigated. The extension -s in the roughness name signifies that the roughness is in the sparse regime, -m means that the distance between the roughness elements is selected so that k_s attains its maximum value for the given roughness element height and base diameter.

Table 2 Surfaces used in the experiments

roughness name	k (μm)	b (μm)	t (μm)	$k/c \cdot 10^{-4}$ (-)	k_s (μm)
000-0			hydraulically smooth		
r10-m	10	25	55	1.06	48
r10-s	10	25	70	1.06	25
r20-m	20	50	110	2.13	96
r20-s	20	50	140	2.13	51
r30-m	30	75	165	3.19	144
r40-m	40	100	220	4.26	192
r40-s	40	100	300	4.26	89
r50-s	48	100	300	5.32	106
r80-s	80	200	600	8.52	177

Heat Transfer Measuring Technique. For the heat transfer measurements, the rough metal foil is glued on an instrumented airfoil using a highly heat conductive adhesive and a vacuum bagging technique. The thermal transmittance of the adhesive joint was measured and found to be about 15,000 W/m^2/K. The scatter in thermal transmittance on different probes is small because the vacuum bagging technique ensures good reproducibility of the bonding procedure due to the constant atmospheric pressure that is applied while the adhesive is cured.

The heat transfer measuring airfoil is made of titanium alloy (TiAl6V4) with a thermal conductivity of $\lambda \approx 7.0$ W/m/K. It is convectively water-cooled by 11 cylindrical cooling channels, which results in an average airfoil surface temperature of 300 K. The temperature distribution around the airfoil is measured by 46 thermocouples, with a diameter of 0.25 mm, which are embedded in its surface. The tips of the thermocouples all end precisely at midspan, giving a defined measuring plane. The airfoil material was selected as a result of a one-dimensional error analysis following the method of Kline and McClintock [23] and taking into account the uncertainties of the materials' thermal conductivities, the thermal transmittance of the adhesive joint, the positioning of the thermocouples, the heat transfer coefficients in the cooling channels, and the temperature measurement. Thus errors for the heat transfer coefficients were estimated in a range of 5% to 10% for most of the vane surface and up to 15% near the trailing edge, where the airfoil is thin and positioning uncertainties of the thermocouples have a notable effect.

The method described by Turner [24] and Wittig et al. [25] is used for the measurements and is adapted to account for the thermocouple grooves, adhesive joint, and metal foil. For each cooling channel the water temperature at the inlet and outlet of the airfoil, as well as the coolant mass flow have to be determined experimentally. With a correlation for turbulent flow in pipes the heat transfer coefficient in the coolant channels can be determined using the mass flow and mean temperature. The temperature distribution around the airfoil underneath the metal foil and adhesive joint is measured by the 46 thermocouples, and the total temperature at the inlet is obtained using a thermocouple in a pitot tube.

In contrast to [24,25] the temperature distribution around the airfoil is only known underneath the metal foil and not on its outer surface. Hence the following iterative procedure is applied to obtain the heat transfer distribution $h(s)$:

1. $h(s)$ around the airfoil surface is estimated.
2. With a finite element method, the equation for heat conduction within the compound airfoil is solved and the temperature field is calculated. The boundary condition on the airfoil surface is the estimated $h(s)$ together with $T_{\mathrm{tot},1}$ as the reference temperature. In the cooling channels the heat transfer coefficients with the mean water temperatures are used as boundary conditions. As can be seen from Fig. 4, the finite

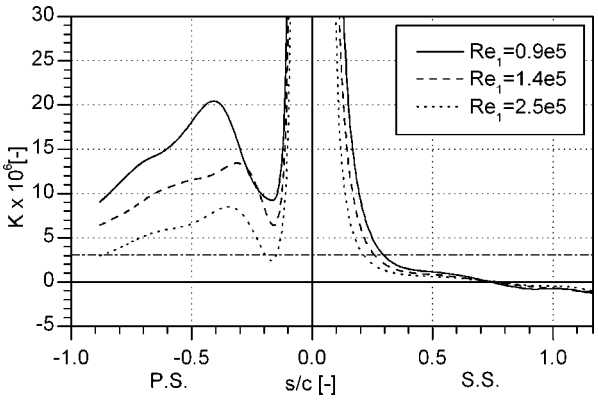

Fig. 5 Distribution of acceleration parameter K

element model includes the thermocouple grooves and the metal foil. The thermal transmittance of the adhesive joint is modeled as well.

3. The temperatures measured at the 46 locations of the thermocouples are compared with the calculated ones and if they differ, $h(s)$ is adjusted appropriately.
4. If the temperature differences calculated in step 3 are not satisfyingly small, a new temperature field is calculated in step 2 using the new $h(s)$. Otherwise the iteration is stopped. Normally, after 15–20 iterations, a converged solution is achieved.

Since the average thickness of the metal foil changes with the roughness that was etched into it, a different finite element model with adjusted foil thickness is used for each roughness.

Results and Discussion

Before heat transfer data are discussed in detail, some characteristics of the airfoil are considered. As a typical aft-loaded profile, it has an extended region of accelerated flow on the suction side. The maximum velocity is attained at about 70% chord. On the pressure side the flow is accelerated throughout the whole surface, leading to very high acceleration parameters $K=\nu/u^2 \cdot du/ds$ (Fig. 5). In case of a smooth surface a laminar boundary layer can be expected on the whole pressure side because K is always greater than the minimum value required for relaminarization ($K=3.0\text{e-}6$, [26]). On the suction side, transition is expected to occur close to the velocity maximum.

Heat transfer distributions are reported in form of Nusselt or Stanton numbers. The Nusselt numbers are calculated using the local heat transfer coefficient, the chord length and a constant thermal conductivity $k=0.03$ W/m/K

$$\mathrm{Nu}=\frac{h\cdot c}{k}=\frac{q}{T_{\mathrm{tot},1}-T_w}\cdot\frac{c}{k} \tag{1}$$

The Stanton numbers are calculated by relating the local wall heat flux to a characteristic local enthalpy flux density,

$$\mathrm{St}=\frac{q}{\rho c_p(T_{ad}-T_w)u} \tag{2}$$

To calculate the enthalpy flux density, the difference between local adiabatic and real wall temperature is used because it is the appropriate measure for the driving temperature difference. The adiabatic wall temperature

$$T_{ad}=T_{\mathrm{stat}}+r\frac{u^2}{2c_p} \tag{3}$$

is calculated using a constant recovery factor of $r=0.892$.

Nusselt number distributions for nine rough surfaces and the smooth reference surface are shown in Fig. 6 for three different Reynolds numbers and two turbulence intensities. The results for the smooth case are in accordance with the findings of Schiele et al. [16] and were thoroughly discussed there. The major findings can be summarized as follows:

- When Reynolds number is increased, heat transfer along the entire blade surface rises and laminar-turbulent transition moves upstream.
- Increasing turbulence intensity leads to an earlier transition on the suction side. The boundary layer on the pressure side remains laminar in all cases.
- The highest heat transfer in the stagnation region is slightly shifted toward the suction side because of the extremely high flow acceleration at the beginning of the suction side in all cases. This behavior was observed in other research on different airfoil geometries and cannot be addressed to positive or negative incidence or vane misalignment.
- Stagnation-point and pressure-side heat transfer increase remarkably with increasing turbulence intensity (between 4% for $\mathrm{Re}_1=0.9\text{e}5$ and 10% for $\mathrm{Re}_1=2.5\text{e}5$ when increasing Tu_1 from 4% to 8.8%)
- At low freestream turbulence and Reynolds number the transition takes place via a short laminar separation bubble. In the other cases the transition is of the bypass mode.

Effect of Roughness on Suction Side Transition. All nine rough surfaces cause the laminar-turbulent transition on the suction side to move upstream (with one exception, as described below). The influence of roughness is more pronounced at the higher Reynolds numbers because the laminar boundary layer on the suction side is thinner and the acceleration parameter is smaller (Fig. 5). To get an impression of the laminar boundary layer thickness δ_{99} in relation to the roughness height, values for δ_{99} on a smooth surface are calculated with the numerical code ALFA [27]. For $\mathrm{Re}_1=0.9\text{e}5$, δ_{99} increases from 130 μm at $s/c=0.07$ to 620 μm at $s/c=0.9$. The corresponding values for $\mathrm{Re}_1=1.4\text{e}5$ and $\mathrm{Re}_1=2.5\text{e}5$ are 120–490 μm and 90–380 μm, respectively.

In general, two modes of transition are observed: a bypass transition, which occurs at high Reynolds numbers, high freestream turbulence, and/or high roughness, and a transition that takes place via a separation bubble. The latter one causes a decrease in heat transfer before it rises quickly to the turbulent level. Because this decrease is difficult to see in Fig. 6, the heat transfer distributions are presented exemplarily for the $\mathrm{Re}_1=0.9\text{e}5$ and $Tu_1=4\%$ case as Stanton numbers over chord Reynolds numbers (Fig. 7). The lower dashed line in Fig. 7 shows the Kays and Crawford [28] correlation for laminar heat transfer on a smooth flat plate:

$$\mathrm{St}_{\mathrm{taminar}}=0.332\cdot\mathrm{Pr}^{-2/3}\,\mathrm{Re}_s^{-1/2} \tag{4}$$

The upper dashed line represents the correlation from the same authors for turbulent heat transfer:

$$\mathrm{St}_{\mathrm{turbulent}}=0.0287\cdot\mathrm{Pr}^{-2/5}\mathrm{Re}_s^{-1/5} \tag{5}$$

For the lowest Reynolds number and the low turbulence level, only the two roughest surfaces r50-s and r80-s cause a bypass transition close to $s/c=0.5$. For all other surfaces, the transition takes place via a separation bubble (Fig. 7). It was found and assured by multiple measurements that the separation bubble is considerably longer for the roughness r30-m than it is for all other surfaces, including the smooth case. This leads to a laminar-turbulent transition that is even downstream of the smooth case (Fig. 6(*a*)). At high freestream turbulence ($Tu_1=8.8\%$, Fig. 6(*b*)) the onset of transition moves slightly upstream for all surfaces and the exceptional behavior for the roughness r30-m disappears.

For the $\mathrm{Re}_1=1.4\text{e}5$, $Tu_1=4\%$ case (Fig. 6(c)), the three roughest surfaces (r40-m,r50-s,r80-s) cause a bypass transition, whereas on all other surfaces a separation bubble is present. The transition on the r80-s surface even occurs in a region where the accelera-

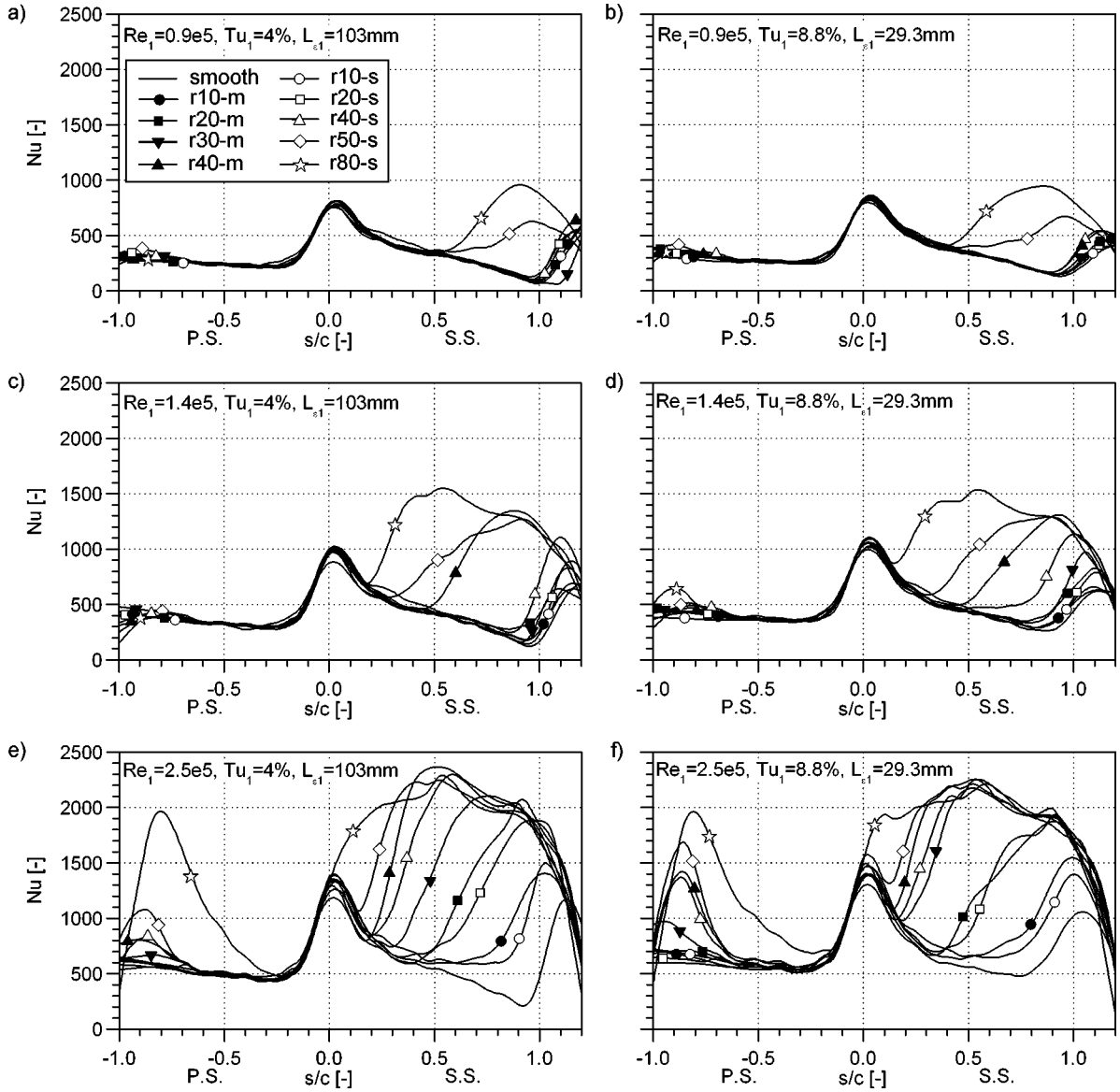

Fig. 6 Influence of roughness on Nusselt number distribution for different Re_1 and Tu_1

tion parameter is greater than 3e-6 and turbulent fluctuations are normally damped. Increasing the turbulence intensity to 8.8%, the transition for roughness r40-s switches to the bypass mode and thereby moves considerably upstream (Fig. 6(*d*)).

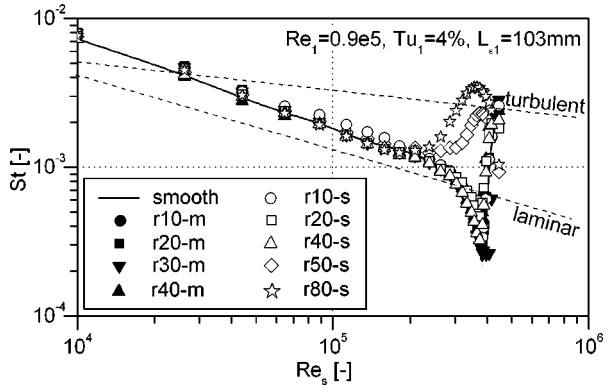

Fig. 7 Stanton numbers over surface length Reynolds numbers

At the highest Reynolds number (Figs. 6(*e*) and 6(*f*)); all but the smooth surface cause a bypass transition. The onset of transition moves upstream as the roughness height and density are increased. For the greater roughnesses again the transition takes place in regions where $K > 3e\text{-}6$. With increasing turbulence level, the separation bubble that was present on the smooth surface disappears and the laminar-turbulent transition for all roughnesses moves slightly upstream (Fig. 6(*f*)).

From Fig. 6 it can be seen that the influence of roughness for a given Reynolds number and turbulence intensity depends primarily on the roughness height and secondarily on the roughness density (open symbols represent sparse roughness configurations). The higher the roughness, the earlier the transition occurs. For a given roughness height the transition moves upstream if the roughness density is increased. Looking at the equivalent sand grain roughness k_s of the surfaces (Table 2), it can be seen that the denser roughness has a higher k_s than the comparable sparse one. However, if k_s is the appropriate quantity to describe the effect on transition, surfaces r10-m and r20-s should have about the same effect, as well as r20-m and r40-s. Since this is not the case, it is apparent that k_s is not suitable for this purpose.

Looking at Fig. 6, a dual slope behavior in the Nusselt number

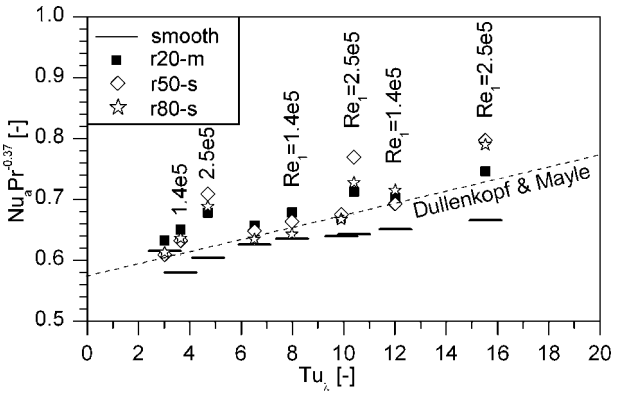

Fig. 8 Stagnation point heat transfer

distribution during the laminar-turbulent transition can be observed for the following test cases: surfaces r50-s at $Re_1=0.9e5$, r40-s at $Re_1=1.4e5$ and $Tu_1=8.8\%$, and r10-m at $Re_1=2.5e5$. This behavior was also found by Pinson and Wang [7] who conducted flat plate heat transfer measurements with different leading edge roughnesses. With detailed boundary layer measurements, they found an extended pretransitional region that occurred with some rough surfaces.

Effect of Roughness on Pressure Side Transition. Due to the high acceleration on the pressure side, the boundary layer stays laminar at the lowest Reynolds number for all surface roughnesses. For the medium Reynolds number, transition occurs only at high turbulence intensity and only for the r80-s surface. At the highest Reynolds number all rough surfaces that have an onset of transition on the suction side in a region with $K>3e\text{-}6$ cause a laminar-turbulent transition on the pressure side. For the other surfaces, the boundary layer stays laminar.

Effect of Roughness on Stagnation Point Heat Transfer The heat transfer in the stagnation region of a smooth airfoil depends mainly on the Reynolds number, the velocity gradient, the turbulence intensity, and the turbulence length scale. Dullenkopf and Mayle [29] propose a correlation which is based on the idea

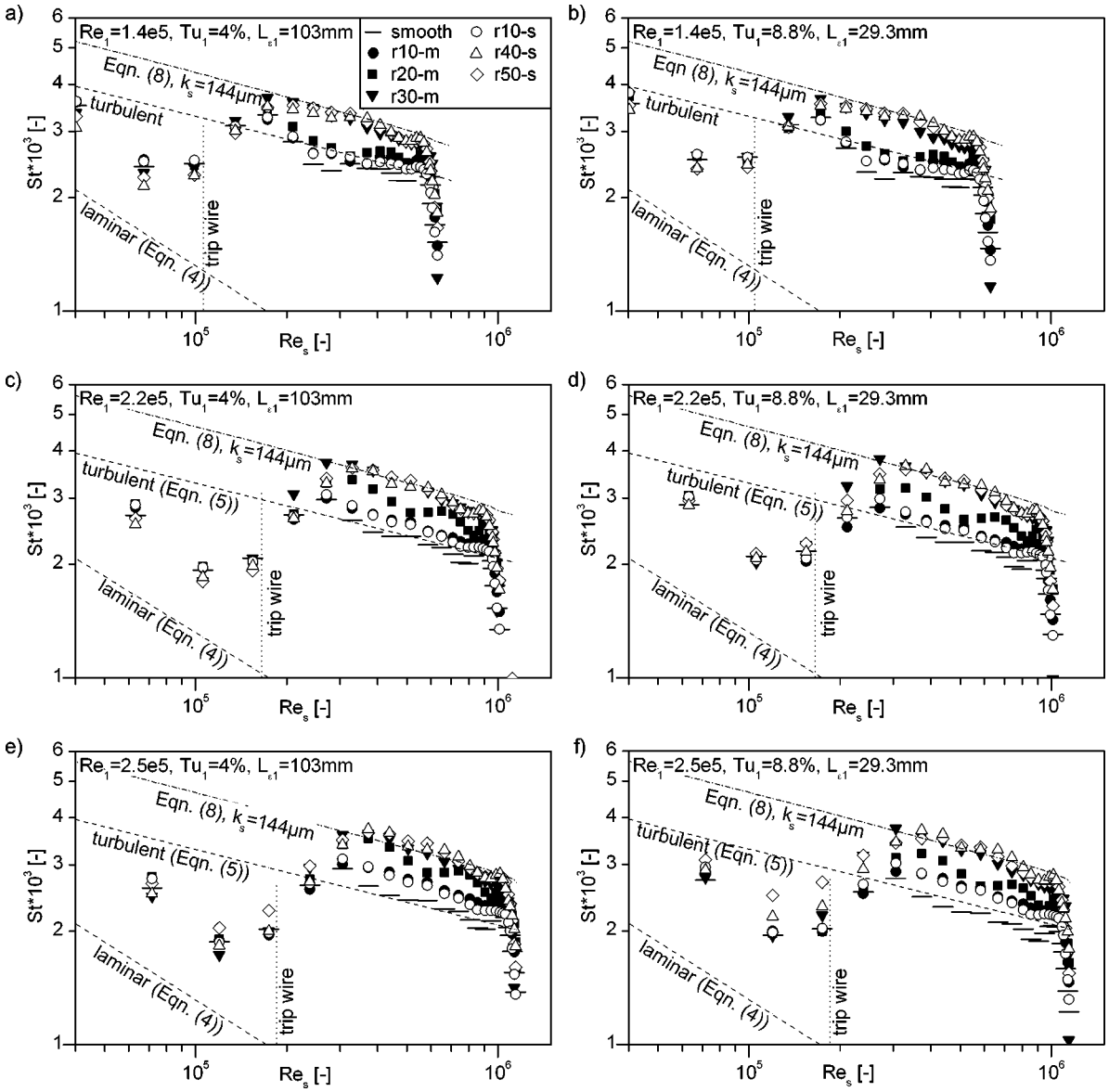

Fig. 9 Suction-side Stanton number distributions with trip wire at $s/c=0.24$

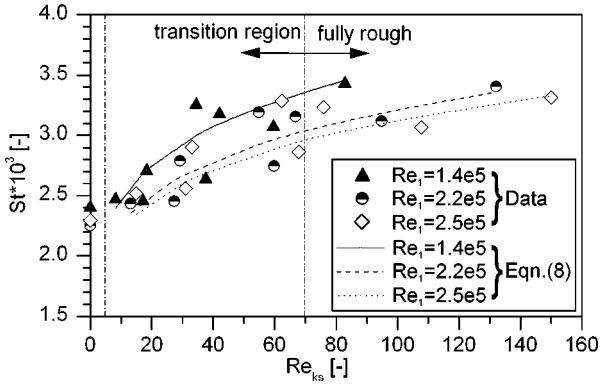

Fig. 10 Stanton number data at $s/c=0.6$ for $Tu_1=4\%$ and correlations from Kays and Crawford

that the boundary layer reacts only on perturbations within a specific frequency band. To account for this, they introduce an effective turbulence parameter

$$Tu_\lambda = \frac{Tu_a\sqrt{\Lambda_a}}{[1+0.004\Lambda_a^2]^{5/12}} \tag{6}$$

The two parameters $\Lambda_a=\Lambda/\sqrt{\nu/a}$ and $Tu_a=Tu_1u_1/\sqrt{a\nu}$ depend on the acceleration parameter $a=du/dx$. For a constant acceleration parameter, Dullenkopf and Mayle [29] suggest the following correlation for the stagnation area heat transfer,

$$\mathrm{Nu}_a\,\mathrm{Pr}^{-0.37}=0.571+0.01Tu_\lambda \tag{7}$$

The Nusselt number $\mathrm{Nu}_a=h\sqrt{\nu/a}/k$ in Eq. (7) again incorporates the acceleration parameter. Measured stagnation point heat transfer coefficients for different surface roughnesses are plotted in Fig. 8 together with the dashed line that represents Eq. (7). The effective turbulence parameters between 3 and 15.5 arise from three Reynolds numbers (Re_1=0.9e5, 1.4e5 and 2.5e5) and from three turbulence levels ($Tu_1=4\%$, 5.1% and 8.8%).

Figure 8 reveals that the smooth surface values are slightly below the Dullenkopf and Mayle [29] prediction. The rough surfaces consistently cause a higher heat transfer in the stagnation region. The augmentation effect is bigger at higher Reynolds numbers. A similar augmentation behavior can be seen in the data of Turner et al. [10] and Bunker [13].

It is interesting to note, that the laminar regions on the pressure side do not show an increase in heat transfer with increasing roughness height (Fig. 6). This is probably due to the smaller acceleration compared to the stagnation region.

Effect of Roughness on Turbulent Heat Transfer. From the measurements presented above, the effect of roughness on the turbulent part of the boundary layer can hardly be quantified, because the turbulent regions differ in length and experience different acceleration due to the varying onset and length of transition. To overcome this issue, the measurements are repeated with a trip wire placed on the suction side at $s/c=0.24$. At this point the acceleration parameter K drops below 3.0e-6 for Reynolds numbers greater than 1.4e5 (see Fig. 5) and it can be expected that the boundary layer stays turbulent after it is tripped. The measurements with trip wire also take into account that on many turbine airfoils, cooling air is ejected in the leading-edge region, thereby tripping the boundary layer.

Figure 9 presents the resulting suction-side Stanton number distributions for six rough surfaces and the smooth reference surface. Data for three Reynolds numbers (Re_1=1.4e5, 2.2e5 and 2.5e5) and two turbulence levels ($Tu_1=4\%$ and 8.8%) are shown. As can be seen from the steep increase in Stanton numbers, the trip wire causes a clearly defined onset of transition for all surfaces, independent of their roughness height. Furthermore, the length of transition seems to be unaffected by surface roughness. Hence it is now possible to compare the turbulent heat transfer caused by different rough surfaces.

At the low Reynolds number (Re_1=1.4e5, Figs. 9(*a*) and 9(*b*)) and small roughness heights (smooth, r10-m, r10-s, r20-m), Stanton numbers are slightly decreasing again below the turbulent level after the laminar-turbulent transition has completed. This is due to the high acceleration, which is damping the turbulent fluctuations in the boundary layer. In contrast, this damping cannot be observed for the bigger roughness heights. Here, the turbulent fluctuations that are constantly produced by the roughness elements seem to be the governing factor. With increasing Reynolds number, the boundary layer gets thinner and the smaller roughnesses (r10-m, r10-s) do not show this decrease in Stanton number anymore (Figs. 9(*c*)–9(*f*)). Interestingly, surface r20-m still shows this behavior even at the highest Reynolds number. Further investigations are necessary to give an explanation for this effect.

In general, the heat transfer augmentation by the roughness is more pronounced at higher Re_1. This is most notable for the smaller roughnesses, as they move from the transitional rough ($5<\mathrm{Re}_{ks}<70$) towards the fully rough ($\mathrm{Re}_{ks}>70$) regime when Re_1 is increased. The rough surfaces, which are already close to or in the fully rough regime, show only a small effect of Reynolds number on Stanton numbers.

The Stanton data in Fig. 9 are compared with a standard flat plate correlation from Kays and Crawford [28] that is valid for fully rough flow:

$$\mathrm{St}=\frac{c_f/2}{\mathrm{Pr}_t+\sqrt{c_f/2}\,\mathrm{Re}_{ks}^{0.2}\,\mathrm{Pr}^{0.44}/C} \tag{8}$$

For the constant C a value of 0.35 is chosen, following the suggestion of Bons [4]. While he used this value to correlate data he obtained on real surface roughness, it also yields good results on the deterministic roughness used in this study. The friction coefficient in Eq. (8) is calculated with a correlation from White [30], which again is valid for fully rough flat plate boundary layers:

$$c_f=\left(1.4+3.7\log\frac{s}{k}\right)^{-2} \tag{9}$$

Roughness Reynolds numbers Re_{ks} are determined using the friction coefficients from Eq. (9):

$$\mathrm{Re}_{ks}=\frac{u_\tau k_s}{\nu}=\sqrt{\frac{c_f}{2}}\frac{uk_s}{\nu} \tag{10}$$

For the rough surface with the biggest sand grain roughness height (r30-m with $k_s=144\,\mu$m), correlation (8) is presented as a dash-dotted line in Figs. 9(*a*)–9(*f*). It shows good agreement with the data at all Reynolds numbers.

Further comparison with Eq. (8) for all roughnesses and for $Tu_1=4\%$ is presented in Fig. 10 for one location at $s/c=0.6$. This location is chosen, because here the acceleration is small and should have little effect on heat transfer. The overall agreement between the data at $s/c=0.6$ and the Kays and Crawford correlation (Eq. (8)) is good. For $\mathrm{Re}_{ks}>80$ the average deviation is less than 1.6% with a maximum of 3.1%. The deviations are bigger at lower Re_{ks} (average 6.4%, max. 13.4%). This is not surprising, since all correlations were developed for fully rough flow conditions.

A curious effect is observed when increasing the freestream turbulence intensity. While Stanton numbers in the laminar region on the pressure side and at the stagnation point increase remarkably as expected (Fig. 6, $s/c\leq 0$), they slightly decrease in the turbulent regions on the suction side when Tu_1 is raised. This peculiar behavior is seen at all Reynolds numbers and on all surfaces (rough and smooth) when the trip wire is present (Fig. 9). It also occurs without trip wire, when the roughness elements are big enough to cause a transition in the highly accelerated region on the suction side (Figs. 6(*e*) and 6(*f*), Re_1=2.5e5, r40-m, r40-s,

r50-s, r80-s). Similar effects are found in the data of Turner et al. [10] and partially in the data of Boyle et al. [14]. At present, there is no coherent explanation for this effect known to the authors. Further boundary layer investigations have to be conducted to get a better understanding of the underlying mechanisms.

Summary and Conclusion

The effect of surface roughness on the external heat transfer distribution of a highly loaded turbine vane has been investigated experimentally. Even the smallest roughness causes the laminar-turbulent transition to move considerably upstream and increases stagnation point and turbulent heat transfer. Both roughness height and density show an influence. While the equivalent sand grain roughness is found to be a suitable measure to describe the turbulent heat transfer, it is not appropriate to describe the onset of transition. Heat transfer in the laminar region on the pressure side is unaffected by roughness. Finally, an unexpected effect of turbulence on the boundary layer on the suction side is found when it is tripped in the highly accelerated stagnation region: turbulent heat transfer decreases when freestream turbulence level is increased.

Acknowledgments

This work was performed within a joint project of the AG-TURBO research program, which is partly funded by the German Federal Ministry of Economics and Labor. The permission for publication is gratefully acknowledged by the authors.

Nomenclature

a = acceleration parameter, du/ds (l/s)
b = roughness element base diameter (m)
c = chord length (m)
c_p = specific heat at constant pressure (J/kg/K)
h = heat transfer coefficient, $q_w/(T_{\mathrm{tot},1}-T_w)$ (W/m^2/K)
k = turbulent kinetic energy (m^2/s^2)
k = roughness element height (m)
k = thermal conductivity (W/m/K)
k_s = equivalent sand grain roughness height (m)
K = dimensionless acceleration parameter
L_ε = dissipation length scale, $k^{3/2}/\varepsilon$ (m)
Nu = Nusselt number
Pr, Pr$_t$ = Prandtl number, turbulent Prandtl number
q = heat flux (W/m^2)
r = recovery factor
Re = Reynolds number
Re$_{ks}$ = roughness Reynolds number, $u_\tau k_s/\nu$
Re$_\lambda$ = turbulence Reynolds number, $\sqrt{\overline{u'^2}}\lambda/\nu$
s = surface length (m)
St = Stanton number
t = distance between roughness elements (m)
T = temperature (K)
Tu = turbulence intensity (%)
Tu_λ = effective turbulence parameter
u = free-stream velocity (m/s)
u' = stream wise velocity fluctuation (m/s)
u_τ = friction velocity (m/s)

Greek

δ_{99} = boundary layer thickness (m)
ε = dissipation of kinetic energy (m^2/s^3)
η = Kolmogorov's length scale (m)
λ = viscous dissipation length scale (m)
Λ = integral length scale (m)
ν = kinematic viscosity (m^2/s)
ρ = density (kg/m^3)

Subscripts

1 = at cascade inlet
ad = adiabatic
stat = static
tot = total
w = wall
a, k_s, ε, λ, s = see definition above

References

[1] Barlow, D. N., Kim, Y. W., and Florschuetz, L. W., 1997, "Transient Liquid Crystal Technique for Convective Heat Transfer on Rough Surfaces," ASME J. Turbomach., **119**, pp. 14–22.
[2] Hosni, M. H., Coleman, H. W., and Taylor, R. P., 1998, "Rough-Wall Heat Transfer in Turbulent Boundary Layers," Int. J. Fluid Mech. Res. **25**(1–3), pp. 212–219.
[3] Bogard, D. G., Schmidt, D. L., and Tabbita, M., 1998, "Characterization and Laboratory Simulation of Turbine Airfoil Surface Roughness and Associated Heat Transfer," ASME J. Turbomach., **120**, pp. 337–342.
[4] Bons, J. P., 2002, "St and c_f Augmentation for Real Turbine Roughness With Elevated Freestream Turbulence," ASME Turbo Expo, Amsterdam, Netherlands, ASME Paper No. GT-2002-30198.
[5] Bons, J. P., and McClain, S. T., 2003, "The Effect of Real Turbine Roughness With Pressure Gradient on Heat Transfer," ASME Paper No. GT-2003-38738.
[6] Coleman, H. W., Moffat, R. J., and Kays, W. M., 1981, "Heat Transfer in the Accelerated Fully Rough Turbulent Boundary Layer," ASME J. Heat Transfer, **103**, pp. 153–158.
[7] Pinson, M., and Wang, T., 1994, "Effects of Leading-Edge Roughness on Fluid Flow and Heat Transfer in the Transitional Boundary Layer Over a Flat Plate," ASME Turbo Expo, The Hague, The Netherlands, ASME Paper No. 94-GT-326.
[8] Pinson, M. W., and Wang, T., 1999, "Effect of Two-Scale Roughness on Boundary Layer Transition Over a Heated Flat Plate: Part 1—Surface Heat Transfer," ASME Turbo Expo, Indianapolis, Indiana, ASME Paper No. 99-GT-158.
[9] Gibbings, J. C., and Al-Shukri, S. M., 1997, "Effect of Sandpaper Roughness and Stream Turbulence on the Laminar Layer and Its Transition," Aeronaut. J., **101**, pp. 17–24.
[10] Turner, A. B., Tarada, F. H. A., and Bayley, F. J., 1985, "Effects of Surface Roughness on Heat Transfer to Gas Turbine Blades," Paper No. 9, AGARD-CP-390.
[11] Hoffs, A., Drost, U., and B̃olcs, A., 1996, "Heat Transfer Measurements on a Turbine Airfoil at Various Reynolds Numbers and Turbulence Intensities Including Effects of Surface Roughness," ASME Turbo Expo, Birmingham, UK, ASME Paper No. 96-GT-169.
[12] Abuaf, N., Bunker, R. S., and Lee, C. P., 1997, "Effects of Surface Roughness on Heat Transfer and Aerodynamic Performance of Turbine Airfoils," ASME Turbo Expo, Orlando, Florida, ASME Paper No. 97-GT-10.
[13] Bunker, R. S., 1997, "Separate and Combined Effects of Surface Roughness and Turbulence Intensity on Vane Heat Transfer," ASME Turbo Expo, Orlando, Florida, ASME Paper No. 97-GT-135.
[14] Boyle, R. J., Spuckler, C. M., Lucci, B. L., and Camperchioli, W. P., 2000, "Infrared Low Temperature Turbine Vane Rough Surface Heat Transfer Measurements," ASME Paper No. 2000-GT-0216.
[15] Blair, M. F., 1994, "An Experimental Study of Heat Transfer in a Large-Scale Turbine Rotor Passage," ASME J. Turbomach., **116**, pp. 1–13.
[16] Schiele, R., Sieger, K., Schulz, A., and Wittig, S., 1995, "Heat Transfer Investigations on a Highly Loaded, Aerothermally Designed Turbine Cascade," *ISABE 95-7100, 12th Int. Symp. on Air Breathing Engines*, Melbourne, Australia, pp. 1091–1101.
[17] Mayle, R. E., Dullenkopf, K., and Schulz, A., 1998, "The Turbulence That Matters," ASME J. Turbomach., **120**, pp. 402–409.
[18] Taylor, R. P., 1990, "Surface Roughness Measurements on Gas Turbine Blades," ASME J. Turbomach., **112**, pp. 175–180.
[19] Bons, J. P., Taylor, R. P., McClain, S. T., and Rivir, R. B., 2001, "The Many Faces of Turbine Surface. Roughness," ASME Paper No. 2001-GT-0163.
[20] Tarada, F., and Suzuki, M., 1993, "External Heat Transfer Enhancement to Turbine Blading Due to Surface Roughness," ASME Turbo Expo, Orlando, Florida, ASME Paper No. 93-GT-74.
[21] Schlichting, H., 1936, "Experimentelle Untersuchungen zum Rauhigkeitsproblem," Ingenieur-Archiv, Arch. Appl. Mech. **7**(1), pp. 1–34.
[22] Waigh, D. R., and Kind, R. J., 1998, "Improved Aerodynamic Characterization of Regular Three-Dimensional Roughness," AIAA J., **36**(6), pp. 1117–1119.

[23] Kline, S. J., and McClintock, F. A., 1953, ''Describing Uncertainties in Single-Sample Experiments,'' Mech. Eng. (Am. Soc. Mech. Eng.), **75**, pp. 3–8.
[24] Turner, A. B., 1970, ''Heat Transfer Instrumentation,'' AGARD-CP-73.
[25] Wittig, S., Schulz, A., and Bauer, H.-J., 1985, ''Effects of Wakes on the Heat Transfer in Gas Turbine Cascades,'' AGARD-CP-390.
[26] Jones, W. P., and Launder, B. E., 1972, ''The Prediction of Laminarization With a Two-Equation Model of Turbulence,'' Int. J. Heat Mass Transfer, **15**, pp. 301–314.
[27] Rodi, W., and Scheuerer, G., 1985, ''Calculation of Laminar-Turbulent Boundary Layer Transition on Turbine Blades,'' Heat Transfer and Cooling in Gas Turbines, AGARD-CP-390.
[28] Kays, W. M., and Crawford, M. E., 1993, *Convective Heat and Mass Transfer*, Third Edition, McGraw-Hill, New York.
[29] Dullenkopf, K., and Mayle, R. E., 1995, ''An Account of Free-Stream-Turbulence Length Scale on Laminar Heat Transfer,'' ASME J. Turbomach., **117**, pp. 401–406.
[30] White, F. M., 1974, *Viscous Fluid Flow*, McGraw-Hill, New York.

Investigation of a Novel Secondary Flow Feature in a Turbine Cascade With End Wall Profiling

Grant Ingram

David Gregory-Smith

School of Engineering,
University of Durham,
South Road,
Durham DH1 3LE, UK

Neil Harvey
Rolls-Royce plc,
Derby, DE24 8BJ UK

A novel secondary flow feature, previously unreported for turbine blading as far as the authors are aware, has been discovered. It has been found that it is possible to separate part of the inlet boundary layer on the blade row end wall as it is being over-turned and rolled up into the passage vortex. This flow feature has been discovered during a continuing investigation into the aerodynamic effects of non-axisymmetric end wall profiling. Previous work, using the low speed linear cascade at Durham University, has shown the potential of end wall profiling for reducing secondary losses. The latest study, the results of which are described here, was undertaken to determine the limits of what end wall profiling can achieve. The flow has been investigated in detail with pressure probe traversing and surface flow visualization. This has found that the inlet boundary locally separates, on the early suction side of the passage, generating significant extra loss which feeds directly into the core of the passage vortex. The presence of this new feature gives rise to the unexpected result that the secondary flow, as determined by the exit flow angle deviations and levels of secondary kinetic energy, can be reduced while at the same time the loss is increased. CFD was found to calculate the secondary flows moderately well compared with measurements. However, CFD did not predict this new feature, nor the increase in loss it caused. It is concluded that the application of non-axisymmetric end wall profiling, although it has been shown to be highly beneficial, can give rise to adverse features that current CFD tools are unable to predict. Improvements to CFD capability are required in order to be able to avoid such features, and obtain the full potential of end wall profiling. [DOI: 10.1115/1.1812321]

Introduction

Three-dimensional non-axisymmetric end wall profiling has been shown to reduce secondary loss using a number of different geometries. Sieverding [1] and later Langston [2] have provided excellent reviews of secondary flows, the fundamentals of which are not discussed in this paper. Harvey et al. [3] and Hartland et al. [4] described the design and testing of a profiled end wall (PEW) geometry for a low speed linear cascade (the so-called Durham cascade). They showed a reduction in overall loss of some 20% of the planar value. Ingram et al. [5] describe detailed testing of two generations of PEWs that reduce secondary loss by up to 31%. Brennan et al. [6] and Rose et al. [7] designed and tested three-dimensional non-axisymmetric end walls for the HP turbine of the Rolls-Royce Trent 500 in an engine representative rig. They reported a stage efficiency improvement of 0.59%. More recently Harvey et al. [8] validated end wall profiling in a multiple blade row environment and Ingram et al. [9] examined the reasons behind the improvement in performance. PEWs are now making their way onto the next generation of aeroengines.

The aim of non-axisymmetric end walls is simple: profiling works by reducing the cross passage pressure gradient at the end wall by means of streamline curvature. Convex curvature accelerates the flow and reduces the local static pressure, concave curvature retards the flow and increases the local static pressure. Therefore, to reduce the cross passage pressure gradient convex curvature (a ''hump'') is applied to the pressure side of the passage and concave curvature (a ''dip'') is applied to the suction side of the passage. This reduced pressure gradient then results in less secondary flow and therefore loss.

In reality the picture is complicated by the fact there are multiple vortical structures in even cascade secondary flow (see Sieverding [1] and Langston [2]) and the flow is transitional (Moore and Gregory-Smith [10]). However, more recent work such as Ingram et al. [5] suggests that the reduced cross passage gradient may not be the only factor in play and changes made to the horseshoe vortex may be equally important. This work may have important parallels with work conducted by Zess and Thole [11] and Sauer et al. [12] who altered the leading edge in an attempt to change the horseshoe vortex.

This paper describes the experimental investigation of an ''aggressive'' PEW design (see the next section) which introduced a novel flow feature on the end wall. The reason for the introduction of this flow feature and the lack of prediction by the CFD based design system is discussed. This should be seen in the context of designs which produced secondary loss reductions of up to 31%.

Design for Maximum Loss Reduction

The aim of the PEW design described in this paper was to produce the best reduction in loss possible in the Durham cascade within the constraints of profile manufacture. The ''aggressive'' profiling of this end wall is therefore greater than that encountered in previous designs. The ''peak'' to ''dip'' amplitude has been increased to 40 mm (previous designs used 30 mm). Since the curvature is generated using sine waves in the pitchwise direction the curvature has increased in proportion in that direction. However, the previous profiles had the peak approximately twice that of the dip ($+20$ to -10 mm) while this profile has an equal peak and dip value ($+20$ to -20 mm). Thus the streamwise curvature

Contributed by the International Gas Turbine Institute (IGTI) of THE AMERICAN SOCIETY OF MECHANICAL ENGINEERS for publication in the ASME JOURNAL OF TURBOMACHINERY. Paper presented at the international Gas Turbine and Aeroengine Congress and Exhibition, Vienna, Austria, June 13–17, 2004, Paper No. 2004-GT-53589. Manuscript received by the IGTI, October 1, 2003; final revision, March 1, 2004. IGTI Review Chair: A. J. Strazisar.

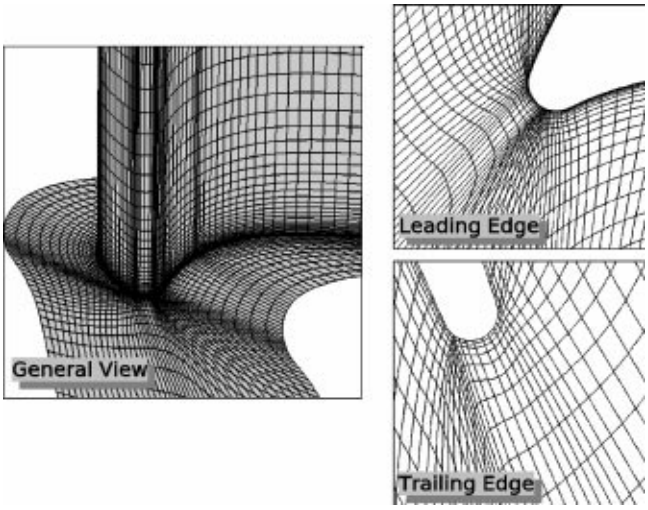

Fig. 1 CFD grid

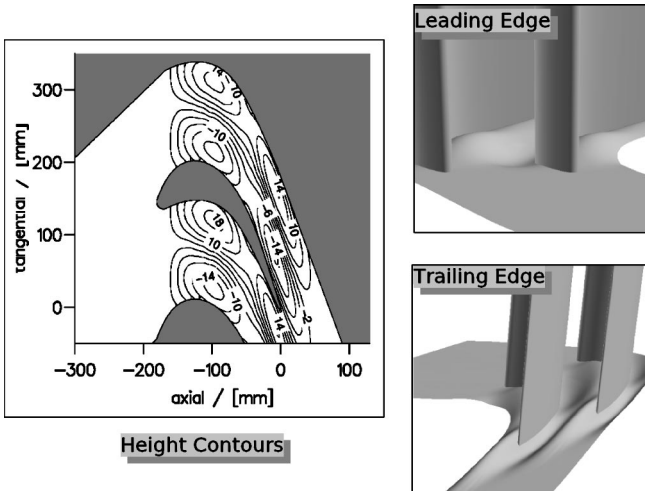

Fig. 2 New design of end wall

around the dip is approximately doubled. These limits are governed by the thickness of material available to be machined for the cascade; in real machines stress considerations are likely to govern the maximum amplitudes obtainable.

The design process used to define the end wall is a developed version of the system used to design end walls as described in Harvey et al. [3]. In this case profiling has been restricted to after the leading edge of the blade and to around 130% of axial chord, the rationale being that in turbine blades a trailing edge platform is present so this is more representative of machine design. Essentially a representation of the end wall shape is made using splines passing through a number of control points on the end wall surface. Each control point is perturbed in six ways and computations done on the effect of each perturbation. For six control points this means that 36 fully viscous calculations need to be made to obtain sufficient information to design a profile. An acceptable shape is extracted from each run without further fully viscous calculations; this is done by using linear superposition on the flow fields and the geometries.

The computational fluid dynamics solutions presented in this paper were conducted at Rolls-Royce and the post-processing described above and analysis were conducted at Durham University. The CFD solution does not represent the ''state-of-the-art'' in fluid mechanics, rather it represents a typical grid size and configuration usually used in design work. The CFD solution used 280,000 grid points and the whole cascade is modeled rather than just the half span and the measurements of the inlet boundary layer are used as boundary condition for the CFD solution. Some views of the grid are provided in Fig. 1. The planar reference case was recomputed for the design of this aggressive PEW to give a benchmark against which to measure. The code used was a steady flow solver using the pressure correction algorithm of Moore [13]. For the initial design the boundary layers are treated as fully turbulent everywhere with an algebraic mixing length model and wall functions.

The design aim of the profile was to produce a large loss reduction. However, since loss prediction from CFD is unreliable, a different method such as examining exit angles deviations has to be adopted. Previous work (Ingram [14]) has suggested that there is a correlation between reduction of secondary kinetic energy and loss, so this can be used as an alternative parameter. The geometry of the new end wall is shown in Fig. 2. As can be seen, the end wall features a ''conventional'' hump and dip arrangement in the early part of the passage followed by two extended peaks and troughs that perturbate the end wall downstream of the blade trailing edge.

Throughout this paper an emphasis is made on comparing CFD results with those found by experiment and highlighting the differences between the two. Without CFD the design of PEWs is impossible, but it is only by understanding the limitations of the tools available to the designer that they can be used effectively.

Experimental Method

The Durham cascade is a low speed, large scale linear cascade of six rotor blades taken from a high pressure rotor design. A grid of bars mounted 1.4 m in front of the blades gives a turbulence intensity of around 5% at inlet. A boundary layer bleed is provided before the cascade is reached. The design data for the cascade is given in Table 1. The Reynolds number obtained in the cascade is not much less than that found in some HP and IP turbines (see Harvey et al. [8]). Concerns that the slightly lower Reynolds number might be causing significant differences in transition were dispelled by Ingram et al. [9]. Further details on the Durham cascade may be found in Ingram [14] and Hartland et al. [4].

Experimental Results

Experimental measurements were conducted on the new design of PEW. The measurements firstly consisted of conventional five hole probe traverses at a number of axial locations within the blade row. The technique used in this case is similar to that described in Ingram et al. [9] with the exception that only one traverse rather than three was carried out to obtain quantitative results.

Figure 3 shows the pitch averaged loss results for both the planar case and the new aggressive design at 128% C_{ax}. This figure shows clearly that although the loss core for the new design is closer to the end wall it is not noticeably smaller than that for the planar reference case. Close to the end wall the new design appears to generate more loss than for the planar case. Also shown in Fig. 3 are the results from an earlier design of profiled end wall (labeled ''Old PEW''). This design has a reduced amplitude of

Table 1 Design data for the Durham Cascade

Inlet flow angle	42.75°
Blade exit angle	−68.7°
Blade chord	224 mm
Blade axial chord	181 mm
Blade pitch	191 mm
Blade half-span	200 mm
Reynolds no. (C_{ax} and exit velocity)	4.0×10^5

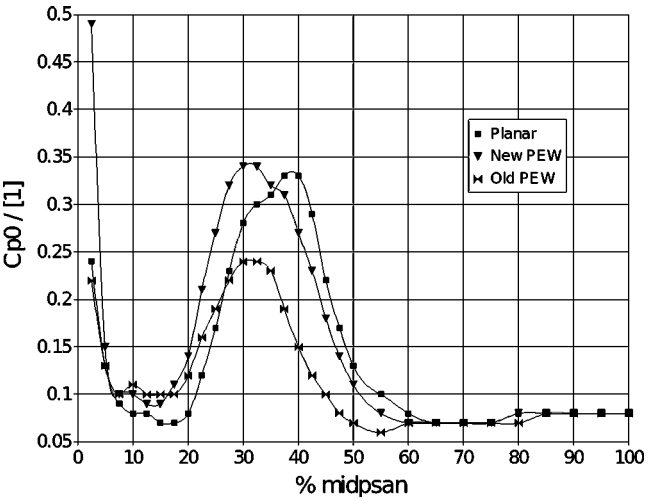

Fig. 3 128% C_{ax} loss results

"peak" to "dip" compared to the current design. From Fig. 3 it is clear that the old profiled end wall reduces the size of the passage loss core—this allows the reader to put the current design in context. The "old" profiled end wall is described in Ingram et al. [9].

Table 2 shows the result of mass averaging the flow over the 128% plane. This shows that the secondary loss for the new design is around 109% of the planar value although there is a very large reduction in secondary kinetic energy, down to 57%. The unexpected gain in loss in spite of a significant secondary kinetic energy reduction and the failure to meet the design intent lead to an investigation to determine the cause of the design–experiment mismatch. Also shown in Table 2 are results from an older design of profiled end wall (also shown in Fig. 3) which successfully reduces secondary loss by around 31%.

A useful tool for this investigation is oil/dye surface flow visualization which has been carried out successfully in the past in the Durham cascade. This was carried out on the new end wall, and in order to provide more information about the flow two colors were used. Yellow oil/dye was used on the blade surface and red oil/dye was used on the end wall. The blade surface was black and the end wall surface was painted white. Therefore, on the aerofoil, dark regions represent an absence of dye and on the end wall light regions represent an absence of dye. A general view of the flow visualization of the new design and the planar end wall is shown in Fig. 4.

The most striking feature is the behavior of the suction surface horseshoe vortex rising up the suction surface of the aerofoil. This feature is not present on the planar case. Figure 5 shows the region of interest in more detail. Particularly noticeable is the migration of red (end wall) oil/dye up the blade surface compared to the planar case at the same location. Another point is that in the previous successful end walls the pressure side leg of the horseshoe vortex migration across the passage is much less visible than

Table 2 Experimental results at 128% C_{ax}

	Planar end wall	Profiled end wall	Old profiled end wall
Total net loss	0.1531	0.1599	0.1289
Mid-span loss	0.0779	0.0779	0.0772
Secondary loss	0.0751	0.0821	0.0517
% Planar sec. loss	100.0%	109.2%	69.0%
Secondary k.e.	0.0205	0.0117	0.0092
% Planar s.k.e.	100.0%	57.1%	45.0%

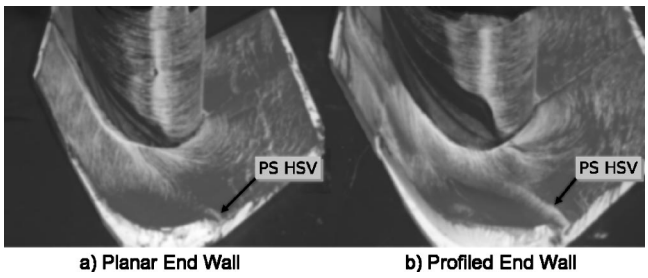

Fig. 4 Flow visualization

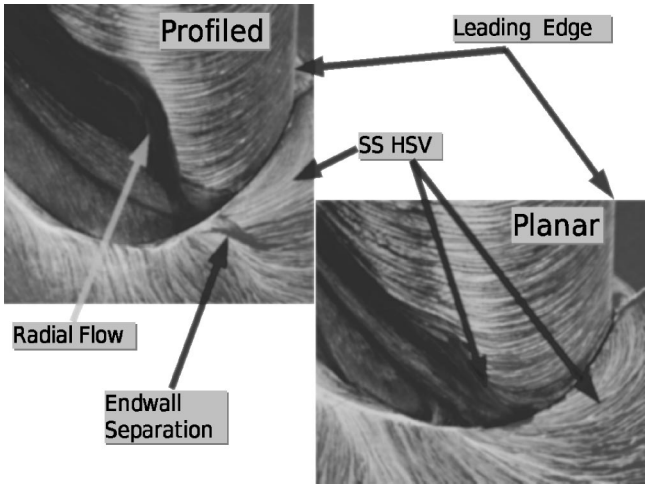

Fig. 5 Region of interest

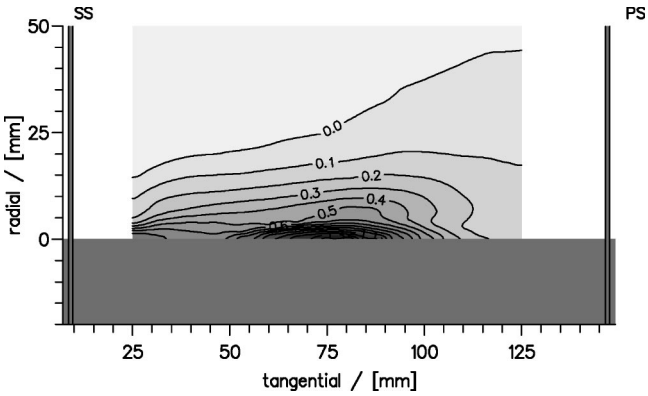

Fig. 6 Cp0 near wall at 38% C_{ax}—planar

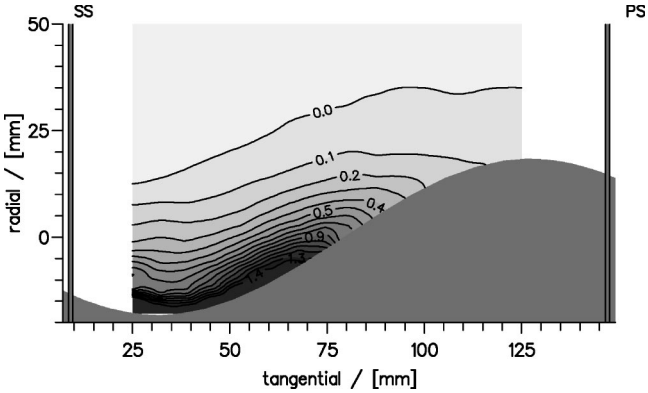

Fig. 7 Cp0 near wall at 38% C_{ax}—profiled

is seen with a planar end wall (see Ingram et al. [9]). For the design in the current paper the pressure side horseshoe migration is again visible in the oil/dye traces.

Three-Dimensional Separated Region. Having identified a region of new interest on the end wall the next step was to determine whether or not this feature actually produced loss. Previous end wall flow visualization studies have shown features on the end wall that appear to have no deleterious effect on overall performance (Ingram et al. [9]). A three hole probe traverse was therefore conducted immediately downstream of the region of interest (at 38% C_{ax}) to see if the feature results in increased loss. Figure 6 shows the planar reference case and Fig. 7 shows the profiled case. It is immediately apparent that there is a large increase in loss for the PEW at this position.

This region was further analyzed with the aid of wool tufts taped onto the surface of the end wall in the region of interest. For the planar case the tufts were relatively quiescent but for the new design of the end wall the tufts exhibit much more unsteady behavior.

Thus it was concluded that the feature represented a three-dimensional separation which caused the increased loss.

CFD Prediction of Separated Flow Region

Clearly the original design CFD did not predict the three-dimensional separated region on the end wall. Once this region had been identified a key question is whether or not there was information in the CFD that could have predicted the separated region but was not routinely used in the analysis of candidate geometries. In order to examine this possibility the CFD for the design was examined in more detail.

Firstly the flow around the region of interest is examined using a post-processing CFD tool. Figure 8 shows apparently benign flow around the region of interest. The vectors and loss contours in Fig. 8 are projected onto the same axial plane as the measurements taken in Figs. 6 and 7. Also shown are streamlines that pass through points of interest which demonstrate that the CFD does not predict the dramatic (near vertical) movement that occurs in the profiled case, although the CFD does predict some increased radial movement of flow.

CFD post-processing tools also allow surface streamlines to be calculated. This has been carried out and is shown in Fig. 9. As can be seen, the calculations for the PEW do not pick up the near radial flow seen in the flow visualization, though the CFD does predict a slight increase in migration of fluid up the end wall suction surface.

Modifications to the CFD. Given that there is little information in the original solution that could predict this region of separation, a number of things were varied in the CFD solution to see if separation could be predicted. It is expected that the turbulence model may be significant; a too active turbulent viscosity might suppress separation. Two significant CFD solutions from this work are described here, first the influence of free stream turbulence on the mixing length was altered (this solution is labeled *mlmod*) and second the turbulent viscosity was altered to model the transitional flow on the suction surface aerofoil surface (this solution is labeled *vismod*).

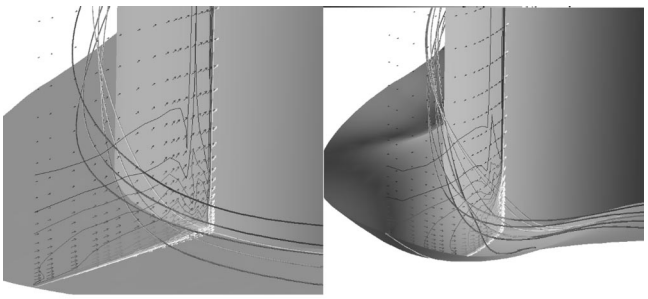

a) Planar End Wall b) Profiled End Wall

Fig. 8 Sample CFD of separated region

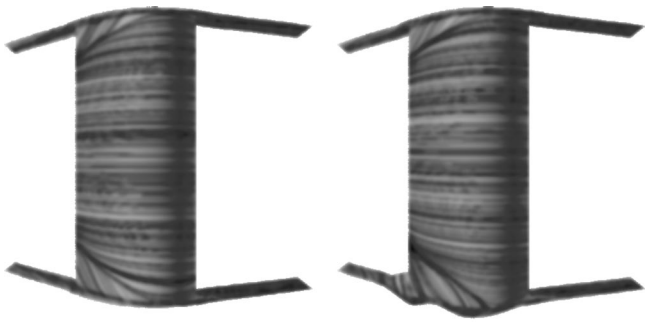

a) Planar End Wall b) Profiled End Wall

Fig. 9 CFD surface flow viz. datum CFD calculation

During the analysis of the CFD it became apparent that earlier end wall designs used a series of input parameters to the CFD that matched the experimental results and CFD results well. Specifically, it was found using a free stream mixing length scale of 0.936 mm gave good agreement but the default value in routine design calculations is much higher than this (2.97 mm). Moore [15], who conducted extensive turbulence measurements on the Durham cascade, concluded that the CFD code (the same as the one used in the design process for the end wall under consideration in this paper) was oversensitive to the influence of free stream turbulence.

As discussed earlier, the boundary layers on the end wall and blade surfaces were modeled as fully turbulent throughout. The work of Moore [15] and Moore and Gregory-Smith [10] clearly showed that the boundary layers on the blade and end wall surface were transitional in nature. More recent work by Ingram [14] showed that end wall profiling did not dramatically change the transitional flow pattern on the suction surface or the end wall. In order to see if a properly specified transitional boundary layer would predict the separated region on the PEW, the results of Moore and Gregory-Smith [10] were used to alter the turbulent viscosity on the end wall in order to model the transitional flow. The effects of these two modifications can be seen in Fig. 10, which shows the surface flow visualizations for the PEW. Although some increase in radial flow is evident (compare Fig. 9) at the point where the suction side leg of the horseshoe vortex meets the blade surface, neither modification produces a picture with as much radial flow as seen in the measured flow visualization, Fig. 4*b* or 5.

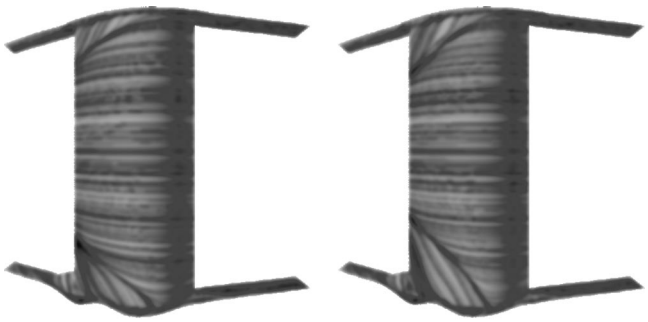

a) Profiled mlmod b) Profiled vismod

Fig. 10 CFD surface flow viz. modified CFD calculations

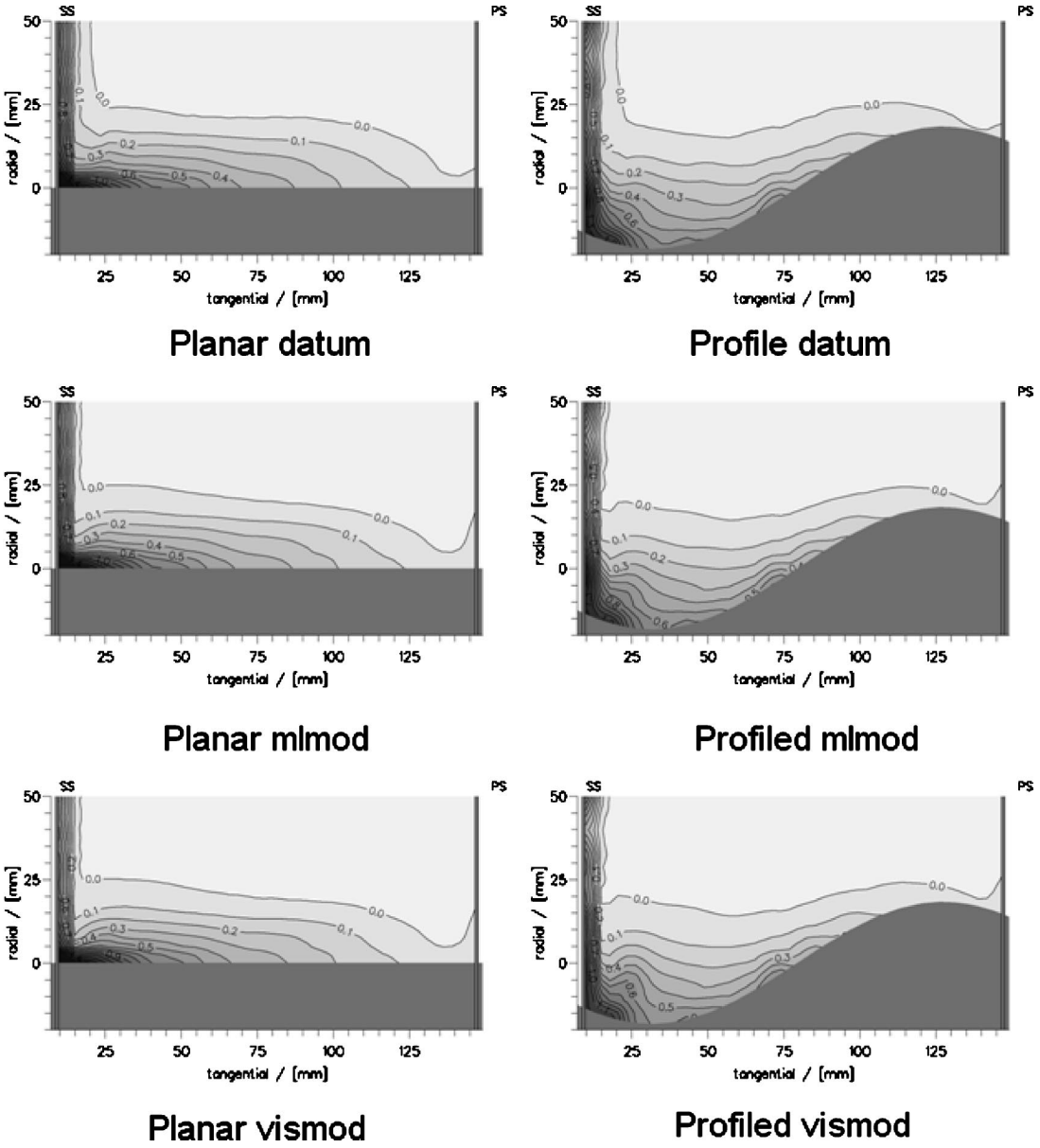

Fig. 11 38% C_{ax} CFD loss coefficient (Cp0)

The changes in the CFD methodology produced little change in static pressure fields on the end walls, with no evidence of a separated region. In the absence of separation the static pressure field should be fairly insensitive to the turbulence model used.

Figure 11 shows the results of the three CFD solutions for the loss contours at 38% C_{ax} and these may be compared to Figs. 6 and 7. The qualitative differences in loss prediction are not great for the same end wall, and the large experimental difference that was found experimentally with the PEW is not seen with any of the CFD predictions.

Table 3 shows a comparison of the loss and secondary kinetic energy from the three different CFD computations. The overall loss is too high compared to the experiment (Table 2), and this is due to the overprediction of mid-span loss. However, these values

Table 3 CFD results at 128% axial chord

	Planar CFD	Profiled CFD	Planar mlmod	Profiled mlmod	Planar vismod	Profiled vismod
Total net loss	0.2603	0.2574	0.2255	0.2237	0.1813	0.1808
Mid-span loss	0.2087	0.2055	0.1816	0.1776	0.1381	0.1356
Secondary loss	0.0516	0.0519	0.0439	0.0461	0.0432	0.0451
% Planar sec. loss	100%	100.6%	100%	105.0%	100%	104.4%
Secondary k.e.	0.01164	0.00988	0.02299	0.01608	0.02183	0.01482
% Planar s.k.e.	100%	84.9%	100%	70.2%	100%	87.0%

are lower for mlmod, which allows for the influence of free stream turbulence, and even lower for vismod, which allows for regions of laminar flow on the blade surfaces. The secondary loss values are then smaller than those measured, and the PEW gives a slightly higher loss than the planar in all cases, although not as much as the increase in loss in the experiment. The two modified CFD calculations give similar secondary kinetic energy significantly larger than the original CFD. They show some reduction with the PEW, but not as big a reduction as experimentally observed (Table 2). The less active turbulence viscosity in the two modified CFD computations gives less loss and more secondary flow. However, the computations give only modest quantitative agreement with the experimental data, although they are somewhat better than the original computation.

Conclusions

Some specific conclusions may be drawn:

- An aggressive design has found a limit for PEW application. This limit is a three-dimensional separated flow feature stemming from the strong convex/concave curvature in the early part of the passage near the suction surface. This separation is accompanied by a strong flow locally up the suction surface, driven by the spanwise pressure gradient due to higher pressure near the end wall caused by the profiling.
- This work should be seen in the context of PEW design which can produce loss reductions of up to 31% of secondary loss.
- This feature resulted in an increase in secondary loss despite a large reduction in secondary kinetic energy, which in previous profiles resulted in significant loss reduction.
- The three-dimensional separation was not picked up by the CFD. Although the modified CFD computations with a less active turbulent viscosity gave slightly better quantitative results and some slight indication of some of the surface flow features, the separation was still not clearly seen.
- The question naturally arises of where the limits in the design of PEW's lies, and this is obviously of concern to designers. It had been hoped that less active turbulent viscosity modeling in the CFD might have been more liable to indicate a separation. Perhaps this indicates a limitation of a steady RANS code with an algebraic turbulence model and this level of grid definition. The previously reported successful designs, Ingram et al. [5], showed poor CFD predictions of the loss reductions, so it perhaps not surprising it is difficult to get accurate separation predictions in this complex flow situation.
- These results highlight the importance of, and need for, experimental validation of new concepts and design methodologies.

Acknowledgments

This work has been carried out with the support of Rolls-Royce plc and DTI CARAD. The authors would like to thank them for funding it and their permission to publish this paper. Thanks are also due to David Bagshaw for help in carrying out some of the flow visualization and in the preparation of the script.

Nomenclature

C_{ax}	=	Axial chord
Cp0	=	Total pressure coefficient (upstream-local)/inlet dynamic head
Cp	=	Static pressure coefficient (upstream-local)/inlet dynamic head
CFD	=	Computational fluid dynamics
Expt	=	Experimental
mlmod	=	CFD solution with mixing length modified
vismod	=	CFD solution with turbulent viscosity modified
PEW	=	Profiled end wall

References

[1] Sieverding, C. H., 1985, ''Recent Progress in the Understanding of Basic Aspects of Secondary Flows In Turbine Blade Passages,'' ASME J. Eng. Gas Turbines Power, **107**, pp. 248–252.

[2] Langston, L. S., 2001, ''Secondary Flows in Axial Turbines-a Review,'' *Heat and Mass Transfer in Gas Turbine Systems*, Trenie Iznos, **943**, pp. 11–26.

[3] Harvey, N. W., Rose, M. G., Shahpar, S., Taylor, M. D., Hartland, J., and Gregory-Smith, D. G., 2000, ''Non-Axisymmetric Turbine End Wall Design: Part I Three-Dimensional Design System,'' ASME J. Turbomach., **122**, pp. 278–285.

[4] Hartland, J., Gregory-Smith, D. G., Harvey, N. W., and Rose, M. G., 2000, ''Non-Axisymmetric End Wall Design: Part II Experimental Validation,'' ASME J. Turbomach., **122**, pp. 286–293.

[5] Ingram, G. L., Gregory-Smith, D. G., Rose, M. G., Harvey, N. W., and Brennan, G., 2002, ''The Effect of End-Wall Profiling on Secondary Flow and Loss Development in a Turbine Cascade,'' ASME paper no. GT-2002-30339.

[6] Brennan, G., Harvey, N. W., Rose, M. G., Fomison, N., and Taylor, M. D., 2001, ''Improving the Efficiency of the Trent 500 HP Turbine Using Non-Axisymmetric End Walls: Part 1 Turbine Design,'' ASME paper no. 2001-GT-0444.

[7] Rose, M. G., Harvey, N. W., Seaman, P., Newman, D. A., and McManus, D., 2001, ''Improving the Efficiency of the Trent 500 HP Turbine Using Non-Axisymmetric End Walls: Part 2: Experimental Validation,'' ASME paper no. 2001-GT-0505.

[8] Harvey, N. W., Brennan, G., Newman, D. A., and Rose, M. G., 2002, ''Improving Turbine Efficiency Using Non-Axisymmetric End walls: Validation in the Multi-Row Environment and with Low Aspect Ratio Blading,'' ASME paper no. GT-2002-30337.

[9] Ingram, G., Gregory-Smith, D. G., and Harvey, N. W., 2003, ''Quantification of the Benefits of End-Wall Profiling in a Turbine Cascade,'' *XVI International Symposium on Air Breathing Engines (ISABE)*, AIAA paper no. AIAA-2003-1101.

[10] Moore, H., and Gregory-Smith, D. G., 1996, ''Transition Effects on Secondary Flows in a Turbine Cascade,'' ASME paper no. 96-GT-100.

[11] Zess, G. A., and Thole, K. A., 2002, ''Computational Design and Experimental Evaluation of Using a Leading Edge Fillet on a Gas Turbine Vane,'' ASME J. Turbomach., **124**, pp. 167–175.

[12] Sauer, H., Muller, R., and Vogeler, K., 2000, ''Reduction of Secondary Flow Losses in Turbine Cascades by Leading Edge Modifications at the End-wall,'' ASME paper no. 2000-GT-0473.

[13] Moore, J. G., 1985, ''Calculation of 3D Flow without Numerical Mixing,'' AGARD-LS-140, *3D Computation Techniques applied to Internal Flows in Propulsion Systems*, pp. 8.1–8.15.

[14] Ingram, G. L., 2003, ''End Wall Profiling for the Reduction of Secondary Flow in Turbines,'' Ph.D. thesis, University of Durham.

[15] Moore, H., 1995, ''Experiments in a Turbine Cascade for the Validation of Turbulence and Transition Models,'' Ph.D. thesis, University of Durham.

Sean C. Jenkins
e-mail: sjenkins@mail.utexas.edu

David G. Bogard
e-mail: dbogard@mail.utexas.edu

Mechanical Engineering Department,
The University of Texas at Austin,
Austin, TX 78712

The Effects of the Vane and Mainstream Turbulence Level on Hot Streak Attenuation

This paper discusses the effects of varying pitch position on the attenuation of a simulated hot streak in a vane cascade under conditions of low and high turbulence. Measurements describe the effect of both small and large changes in pitch away from the stagnation line as evidenced by hot streak variations in the wake and at the trailing edge. Under both turbulence conditions, the vane serves to increase or decrease the attenuation rate depending on the location of the hot streak relative to the vane due to isolating of the hot streak core by the vane wall. Additional attenuation resulted due to the action of the wake on the hot streak. [DOI: 10.1115/1.1812777]

Introduction

Appropriate positioning of the temperature non-uniformities, or ''hot streaks,'' exiting the combustor relative to the first-stage nozzle guide vane has been a concern for engine designers for some time. Modern gas turbine engines have been refined such that appropriate positioning of the exit of the combustor with respect to the vanes or passages between vanes is possible. ''Clocking'' of the hot streak involves aligning the hot streak with respect to the guide vanes in engines where an integer multiple of combustors to first-stage nozzle guide vanes makes this possible. Previous researchers have studied the effects of ''clocking,'' but the results are limited and the literature is somewhat contradictory. Effects of the vane on the hot streak are complex and depend not only upon the hot streak position, but also on the turbulence field parameters. In general, realistic turbulence conditions of both intensity and length scale have not been simulated, and where studied, a range of pitch positions have not been investigated. Furthermore, those studies that investigated the effect of vane impingement versus non-impingement focused on surface measurements of the downstream rotor, and therefore do not directly address the attenuation of the hot streak itself.

The most relevant experimental study, by Roback and Dring [1], investigated hot streaks seeded with CO_2 as a trace gas. Though not given, it may be inferred that the mainstream turbulence levels were very low by the facility description. In general, the results were presented as rotor surface trace gas concentrations from which surface heat transfer values could be inferred. However, concentration profiles taken across the span of the rotor leading edge showed both the shape and peak levels were roughly the same for an impinging and non-impinging hot streak.

In contrast, the computational results given by Gundy-Burlet and Dorney [2] showed that clocking the hot streak so that it is positioned at the vane leading edge results in a diminishing effect of the hot streak on the downstream rotor as evidenced by decreased pressure side rotor surface temperature ratios on the order of about 40%. This was attributed to the deceleration and increased mixing of the hot streak as it interacted with the vane and vane wake. Inlet mainstream turbulence levels were not mentioned, so presumably these levels were nominally zero.

A more recent computational study by Gundy-Burlet and Dorney [3] studied heat transfer effects for a three-dimensional hot streak by using a non-adiabatic vane. This study noted that full impingement of the hot streak on the vane resulted in relatively low levels of heat transfer for the majority of the vane with higher levels at the leading edge. However, the computational results do not compare the effects of an impinging and a non-impinging hot streak. In addition, since the values are taken at the vane surface, the effect of the vane on the hot streak itself is unclear. Again, inlet turbulence conditions were not indicated in the paper.

In the experimental results by Jenkins et al. [4], comparisons were made between a simulated hot streak impinging the stagnation line of the vane versus passing through the mid-passage at $0.4P$. Little difference was seen between the two hot streak pitch positions under conditions of high mainstream turbulence.

It is clear that the current incomplete picture of the role of the vane in hot streak attenuation must be addressed. Conflicting results, largely due to a lack of information regarding inlet conditions, imply a need for a more rigorous investigation of the details of vane/hot streak interactions. Engine designers should benefit from a clearer understanding of the effects of the placement of the hot streak relative to the first-stage nozzle guide vane.

In the present study, experiments were conducted to determine the ideal position of the hot streak relative to an uncooled first-stage nozzle guide vane, and the effects of the range of positions between the stagnation line and the mid-passage.

Facilities and Experimental Conditions

The test facility was a closed-loop, low-speed wind tunnel, driven by a 50 hp, variable pitch, variable speed fan. The test section, shown in Fig. 1, was a simulated three-vane, two-passage cascade with adjustable bleed and adjustable walls to maintain the proper flow around the test airfoil. A full description of the facility is given in Polanka [5].

The test airfoil was a scaled up model of a first-stage turbine guide vane with the Reynolds number matched to actual engine operating conditions. The vane had a chord length of $C = 594$ mm, a span of $S = 550$ mm, and the pitch between airfoils was $P = 460$ mm. The mainstream approach velocity was $U_0 = 5.8$ m/s for all experiments resulting in a Reynolds number of $\mathrm{Re} = 1.2 \times 10^6$ based on chord length and exit velocity. The test vane was constructed of polyurethane foam selected for strength and low thermal conductivity, with a value of $k = 0.048$ W/m K.

The hot streak generator section was installed upstream of the test section as shown in Fig. 1. The exit of the hot streak generator was located $1.7C$ upstream of the vane leading edge and was designed to provide a nominal temperature ratio of $T/T_\infty = 1.1$ under both low- and high-turbulence conditions at a location $0.21C$ upstream of the vane, noted as Position A in Fig. 1. It was designed to be continuously adjustable across the pitch of the vane

Contributed by the International Gas Turbine Institute (IGTI) of THE AMERICAN SOCIETY OF MECHANICAL ENGINEERS for publication in the ASME JOURNAL OF TURBOMACHINERY. Paper presented at the International Gas Turbine and Aeroengine Congress and Exhibition, Vienna, Austria, June 13–17, 2004, Paper No. 2004-GT-54022. Manuscript received by IGTI, October 1, 2003; final revision, March 1, 2004. IGTI Review Chair: A. J. Strazisar.

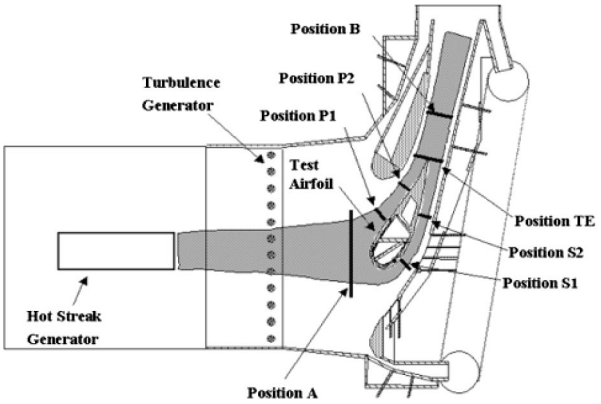

Fig. 1 Simulated vane cascade with hot streak generator

cascade. The construction and adjustment of the hot streak generator section is fully described in Jenkins et al. [4].

The velocity profile was nominally uniform with no hot streak and followed the relation $V_{hs}=V_{\infty}^{*}(T_{hs}/T_{\infty})^{1/2}$ with the hot streak activated, consistent with a conserved total pressure.

Turbulence intensity and integral length scales were established using hot-wire anemometer measurements at Position A. For the low-turbulence condition, the turbulence intensity was Tu=3.5% and the integral length scale was large, between $\Lambda_f=19$ and 30 mm. High mainstream turbulence was generated using an array of 38-mm-diam vertical rods, spaced 85 mm apart, and located 0.88 C upstream of the stagnation point as shown in Fig. 1. The turbulence generator produced a turbulence intensity of Tu=20% with an integral length scale of $\Lambda_f=33$ mm at Position A. This level of turbulence intensity has been shown to be representative of actual engine operating conditions [6]. The turbulence generation rods were constructed of a material with very low thermal conductivity to avoid interference with the hot streak. It should be noted that measurements were made in the facility by previous researchers showing that the turbulence field was isotropic at Position A. Additional details regarding the turbulence field and turbulence generator are available in Cutbirth [7].

The hot streak temperature profiles were measured using a thermocouple rake consisting of 22 K-type thermocouples spaced 7.8 mm apart. Measurements were taken normal to the flow direction as shown in Fig. 1 as measurement planes at Position A, S1, S2, P1, P2, T, and B. Temperature readings from the thermocouple rake and thermocouples placed in the mainstream were acquired using a National Instruments multiplexer and A/D module, and LABVIEW software and time-averaged over a 6 s time span. For some results, the temperature data were normalized by the mainstream temperature to produce temperature ratios, T/T_{∞}, where T_{∞} was the mainstream temperature. For other results, the use of a normalized temperature ratio, Θ_R, was found to be more appropriate. The normalized ratio, Θ_R, was defined based on the peak hot streak temperature, $T_{0,hs}$, measured at the standard reference Position A, shown as follows:

$$\Theta_R=\frac{T_{hs}-T_{\infty}}{T_{0,hs}-T_{\infty}} \tag{1}$$

For all tests, the thermocouple rake was positioned at midspan, $0.5S$, where the hot streak was centered.

An order of magnitude conduction analysis was conducted to determine the possible effect of conduction of the hot streak into the vane. The vane was constructed of a very low conductivity material in order to reduce the possibility of conduction error and was designed to simulate an adiabatic wall. For the largest temperature differential across the vane surface, i.e., the hot streak at the stagnation line $(0.0P)$, a maximum decrease in the near wall temperature of $\Delta T=0.2$ K was estimated. Clearly this temperature reduction applies only for the portion of the hot streak in close proximity to the vane, and in this region may have the effect of reducing the hot streak by no more than $T/T_{\infty}=0.001$, or $\Theta_R=0.007$. For the results presented in this paper, differences in hot streak peak temperature ratio differed by much more than this amount. It should also be noted that the total attenuation of the hot streak from Position A to Position T was about $\Delta T=12.5$ K, so compared to this significant decrease in temperature due to turbulence effects, the conduction error was diminishingly small.

To eliminate bias uncertainty of the measurements for the thermocouple rake, the equipment was tested against a known standard, i.e., an ice bath, and repeatable bias errors were computed. The bias errors between thermocouples were eliminated by adjusting the raw data according to the bias error previously determined. In this way, biases between thermocouples and thermocouple channels could be removed leaving only random or precision error. Based on statistical analysis of the temperature measurements, the precision uncertainty (95% confidence interval) of the time-averaged temperature values ranged between ± 0.1 K at the mainstream temperature to ± 0.4 K at the peak hot streak temperature. This error was random error resulting from the data acquisition system. Based on the temperature uncertainties, the uncertainty in the temperature ratio, T/T_{∞}, was calculated to be ± 0.001 and the uncertainty in the normalized temperature ratio, Θ_R, was calculated to be ± 0.02.

Results

The effect of the vane on the hot streak was investigated under low and high mainstream turbulence conditions to determine if the vane serves to increase or decrease the attenuation rate of the hot streak. Under both turbulence conditions, the vane can either increase or decrease the level of decay depending on the proximity of the hot streak peak to the vane surface. For both turbulence conditions, the vane acts to split the hot streak, isolating the peak and preventing heat loss across the vane. Also, the suction and pressure sides of the vane affect the hot streak differently due to the difference in streamline length around the pressure and suction sides of the vane. The effect of the wake was investigated by comparing profiles taken at Position T, at the trailing edge, with those observed $0.32C$ downstream at Position B. The effect of the wake was to smooth out the sharp temperature gradient present at the trailing edge, and to further attenuate the hot streak both due to the mainstream turbulence and the turbulent wake.

Effects of the Vane at Low Mainstream Turbulence. Experiments to determine the effect of the pitch position of the hot streak on the attenuation of the hot streak were performed by positioning the hot streak generator in varying pitch increments to both the pressure and suction sides of the test vane. The nominal position of the hot streak was a position such that the center of the hot streak impacted the stagnation line of the vane, i.e., $0.0P$. Positions of ± 10 mm, ± 20 mm, ± 30 mm, ± 40 mm, and ± 46 mm, representing pitch changes of $\pm 0.022P$, $\pm 0.043P$, $\pm 0.065P$, $\pm 0.087P$, and $\pm 0.1P$, were chosen to determine the effect of fine scale pitch position changes. To determine the effect of larger pitch position changes, the hot streak generator was adjusted between the stagnation line $(0.0P)$ and $\pm 0.5P$ to both sides of the test vane in increments of $0.1P$. For pitch position comparisons, the rake was positioned at midspan, where the hot streak peak occurred.

Under conditions of low turbulence, a sharp temperature gradient was produced for pitch positions on either side of the stagnation line. This is demonstrated in Fig. 2(*a*) for the hot streak positioned at $\pm 0.1P$ where it is evident that a very sharp temperature gradient exists at Position T (at the trailing edge) between the two parts of the hot streak that have passed on either side of the vane. These sharp temperature gradients can be attributed to the interruption of the hot streak dispersion by the wall of the vane. The schematic in Fig. 2(*b*) indicates the splitting line and how the two regions of the hot streak attenuate differently. The ''tail'' re-

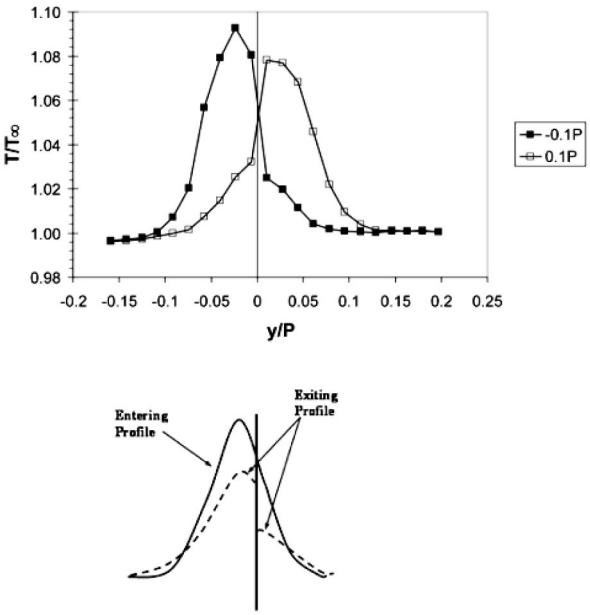

Fig. 2 (*a*) Temperature profiles of the hot streak at Position T with hot streak position at $-0.1P$ and $+0.1P$, Tu=3.5%. (*b*) Schematic of entering (stagnation line) and exiting (trailing edge) temperature profiles.

gion of the hot streak, i.e., the part that does not include the peak, attenuated more quickly because it was isolated from the peak region of the hot streak that would normally transport high temperature hot streak fluid toward the outer "tail" region. On the other hand, the peak region of the hot streak attenuated less because hot fluid from the core of the hot streak toward the right tail side was blocked by the vane. Consequently the difference in hot streak temperature between the two sides of the hot streak split by the vane was accentuated resulting in a sharp temperature gradient in the center of the hot streak at the trailing edge of the vane. The peak temperature ratio was higher for the hot streak on the pressure side than the suction side since the longer distance traveled along the suction side causes a greater level of attenuation. The difference in streamline lengths is shown in Fig. 3, where the pressure-side streamline shown measured 660 mm, or $1.11C$, and the suction side was 895 mm, or $1.51C$, more than 35% longer. Presumably this difference in streamline length caused the tail region passing around the suction side to attenuate more than the corresponding tail region passing around the pressure side.

Comparing the hot streak positioned to impact the stagnation line to intermediate positions between those shown in Fig. 2 ($\pm 0.1P$), it is evident that the greatest attenuation level occurred

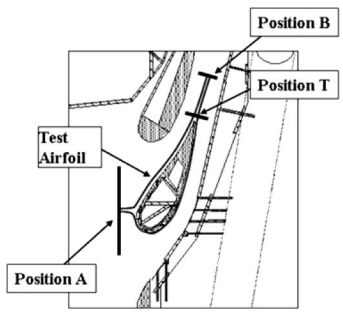

Fig. 3 Comparison of the length of streamlines from Position A to Position T passing along the suction and pressure sides of the vane

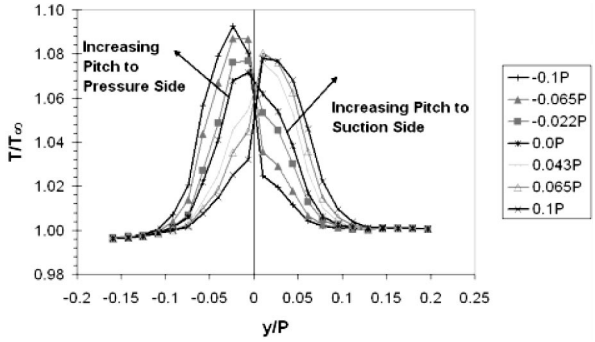

Fig. 4 Temperature profiles of the hot streak at Position T with hot streak position varying from $-0.1P$ to $+0.1P$, Tu=3.5%

at the stagnation line position ($0.0P$). In Fig. 4, temperature ratio profiles for pitch positions between $-0.1P$ and $+0.1P$ indicate that splitting of the hot streak resulted in a higher hot streak peak temperature ratio for all pitch positions to either side of the stagnation line. In general, as indicated above, pitch positions to the suction side resulted in lower peaks than those to the pressure side. Since the hot streak positioned to impact the stagnation line was split equally to either side, heat loss was maximized from the core toward the tail region on both sides, and the hot streak peak was minimized.

The variations of the hot streak temperature profiles downstream of the vane for hot streaks positioned laterally from $-0.5P$ to $0.5P$ upstream of the vane are shown in Fig. 5. Immediately apparent was a lower level of peak temperatures for the hot streak positioned on the suction side of the vane, i.e., $y>0.0P$, compared to the pressure side of the vane, $y<0.0P$. This distinct difference in the strength of the hot streak can be attributed to the longer length of streamlines in the mid-passage passing around the suction side relative to the pressure side up to the measurement plane at Position T, which was normal to the flow direction. The difference in streamline length is illustrated in Fig. 6. The streamlines at the mid-passage positions of $-0.5P$ and $+0.5P$ had different streamline path lengths because of the orientation of the downstream measurement plane and were 465 mm ($0.78C$) and 915 mm ($1.54C$) for the pressure and suction side, respectively. To confirm that equivalent hot streak strengths would be obtained at mid-passage if measurements were made at the equivalent streamline length, measurements of the hot streak were made at the upstream position on the suction side as indicated on Fig. 6. It should be noted that the positions indicated in Fig. 6 are along a constant axial plane. Results from these measurements, shown in Fig. 7, confirmed that the hot streak peak temperature ratio was the same at mid-passage through both passages if measured at equivalent distances. However, as seen in the figure, the

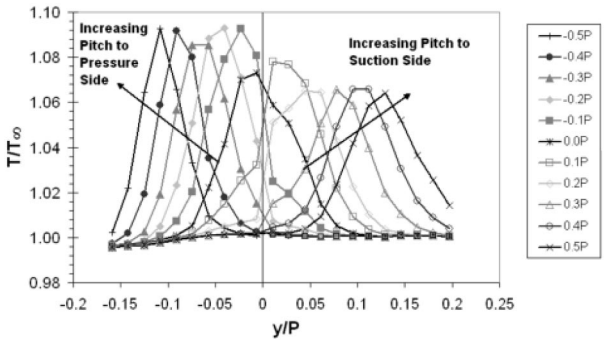

Fig. 5 Temperature profiles of the hot streak at Position T with hot streak position varying from $-0.5P$ to $+0.5P$, Tu=3.5%

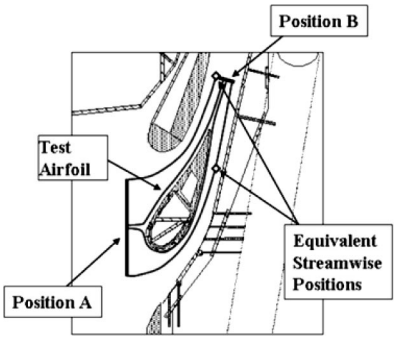

Fig. 6 Comparison of the length of streamlines from Position A to Position B passing through the mid-passage on the suction and pressure sides of the vane

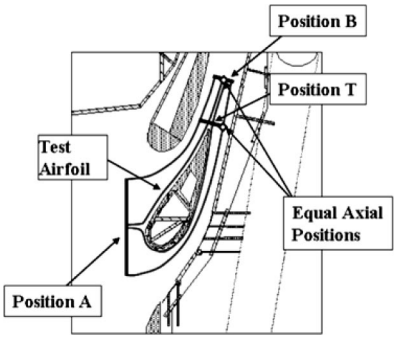

Fig. 8 Tunnel schematic showing positions along an axial plane for hot streak positions of 0.0*P* and +0.5*P*

hot streak was slightly wider passing through the suction-side passage. This may be attributed to the boundary condition present for the suction side, where, as seen in Fig. 6, the hot streak was bounded by the test vane and the outer wall as compared to the pressure side passage which was bounded by the partial vane and the wake.

Comparing the peak hot streak temperature at Position T for the hot streak impacting at various positions on the suction side of the vane as shown in Fig. 5, the peak temperature for the hot streak positioned at 0.1*P* was clearly greater than for the hot streak positioned from 0.2*P* to 0.5*P*. This may be attributed to the decrease in attenuation of the peak hot streak temperature because of the splitting of the hot streak by the vane as discussed previously. Another factor that may be involved is the possible reduction of the large scale mainstream turbulence by the close proximity of the vane. This would also lead to a decreased attenuation of the hot streak peak temperature.

In order to address the issue of impinging versus non-impinging hot streak strength, measurements were taken at equal axial positions, shown in Fig. 8, for the hot streak impacting the stagnation line and passing through the suction-side mid-passage at +0.5*P*. The comparison, shown in Fig. 9, indicates that the hot streak had the same peak temperature ratio, although the hot streak passing over the vane was slightly wider. It is clear that under conditions of low turbulence, the hot streak was not diminished more greatly due to vane interaction.

Effects of the Vane at High Mainstream Turbulence. Hot streak temperature profiles measured at Position T for conditions of high mainstream turbulence ($Tu_0 = 20\%$) are shown in Figs. 10(*a*) and 10(*b*) for hot streaks positioned to the suction and pressure side of the vane, respectively. Immediately obvious from these figures is the much greater spread of the hot streak relative to the profiles shown for the low mainstream turbulence case in Fig. 5. On the suction side at mid-passage (0.5*P*) the high mainstream turbulence caused an essentially uniform temperature profile from the surface of the vane to the outer wall of the test section located at $y/P = 0.2$. For hot streaks positioned closer to

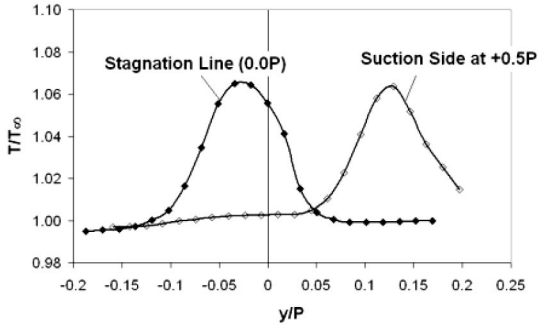

Fig. 9 Comparison of hot streak profiles impacting the vane at 0.0*P*, and passing through the mid-passage at +0.5*P* at equal axial positions, Tu=3.5%

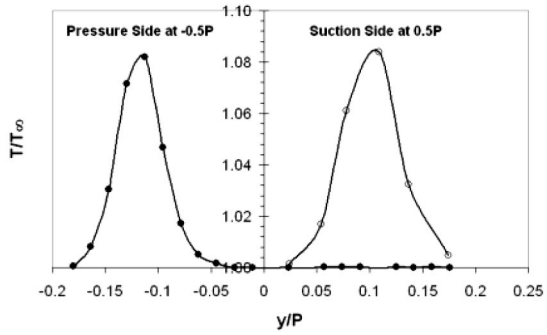

Fig. 7 Comparison of hot streak profiles at equivalent streamwise distances shown in Fig. 6

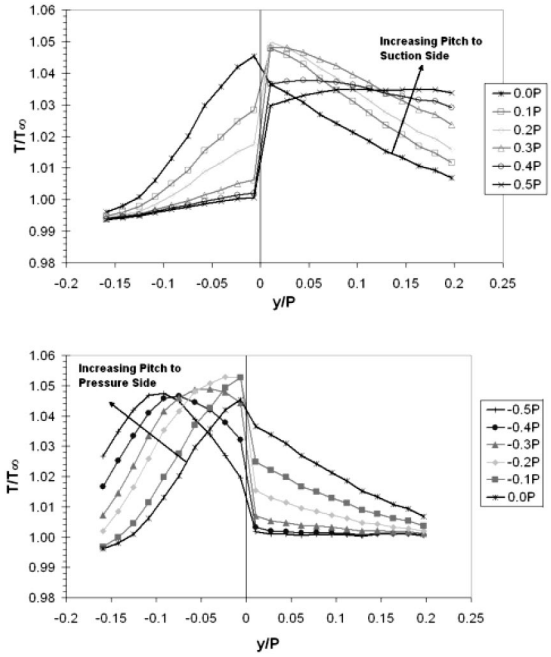

Fig. 10 (*a*) Temperature profiles of the hot streak at Position T with hot streak position varying from 0.0*P* to +0.5*P*, Tu =20%. (*b*) Temperature profiles of the hot streak at Position T with hot streak position varying from −0.5*P* to 0.0*P*, Tu=20%

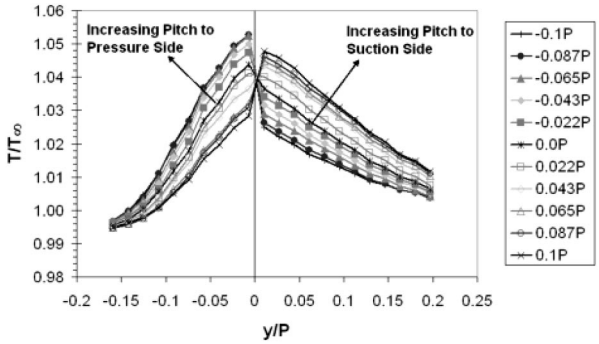

Fig. 11 Temperature profiles of the hot streak at Position T with hot streak position varying from $-0.1P$ to $+0.1P$, Tu=20%

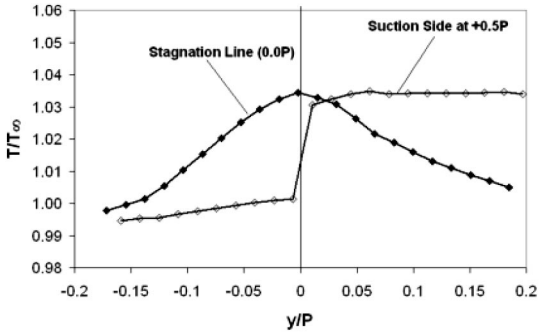

Fig. 12 Comparison of hot streak profiles impacting the vane at $0.0P$, and passing through the mid-passage at $+0.5P$ at equal axial positions, Tu=20%

the vane on the suction side, there was an increase in the peak temperature of the hot streak at Position T [Fig. 10(a)]. This may be attributed to the decreased attenuation of the hot streak peak temperature because of the interaction with the vane similar to that discussed previously for the low mainstream turbulence case. This interaction with the vane is evidenced by the sharp temperature gradient that occurs at $y/P=0.0$ for every hot streak positioned on the suction side of the vane.

The hot streak temperature profiles at Position T for hot streaks positioned on the pressure side of the vane, Fig. 10(b), also show large temperature gradients at $y/P=0.0$ indicating interaction with the vane for all profiles except the mid-passage profile ($-0.5P$). Unlike the mid-passage profile on the suction side, this hot streak profile was not uniform. Recall that the mid-passage measurement position on the pressure side was significantly farther upstream relative to the suction side (see Fig. 6), so the $0.5P$ profile in Fig. 10(b) can be viewed as an intermediate stage in the dispersion of the hot streak that would ultimately become uniformly dispersed.

As is evident in Figs. 10(a) and 10(b), there was a significant decrease in the hot streak temperatures for the hot streak positioned at $0.0P$ relative to either $+0.1P$ or $-0.1P$. Consequently the hot streak was moved with finer resolution about the stagnation line position of $0.0P$. Hot streak temperature profiles measured at Position T are shown in Fig. 11. This figure shows a systematic decrease in the hot streak peak temperature for hot streak positions approaching $0.0P$, but the minimum peak temperature occurred for the hot streak positioned at $0.022P$ on the suction side. For a pitch position of $0.022P$ to the suction side, the greater attenuation on the suction side due to streamline length was balanced by the higher incoming temperature profile so that the profile at Position T was nearly the same on both sides of the vane. Due to this effect, at Position T this hot streak position had the lowest peak temperature ratio.

Comparing hot streak temperature ratio profiles for equal axial positions under conditions of high turbulence in Fig. 12, the peak temperature ratio was the same for the hot streak positioned at the stagnation line versus passing through the mid-passage. However, in contrast to the result under low turbulence conditions, the hot streak shape was significantly different. Although the peak level was the same, the hot streak passing over the stagnation line was dispersed over a two-pitch width, while the hot streak passing through the mid-passage was constrained between vanes and ultimately also by the tunnel outer wall, as seen in Fig. 8. Presumably, without the constraining outer wall, the outside portion of the hot streak would decrease somewhat, spreading through the vane wake, but the hot streak profile near the center vane would likely remain the same since it was constrained by the vane wall.

Evolution of the Temperature Profile. For the hot streak positioned to impact the stagnation line on the vane, the effects of the difference in flow around the pressure and suction side were apparent from measurements at Position T presented in previous sections of this paper. Further temperature profile measurements were made at Positions S1, S2, P1, and P2 along the vane corresponding to 1/3 and 2/3 of the total length along the surface of the vane as shown in Fig. 1. Immediately upstream of the vane, at Position A, the hot streak had a peak temperature of $T/T_\infty=1.084$ for high mainstream turbulence (Tu=20%). Recall that by definition the normalized temperature at this upstream position is $\Theta_R=1.0$. The changes in the Θ_R profiles on both sides of the vane are shown in Fig. 13. At Positions S1 and P1, 1/3 of the distance downstream from the stagnation line to the trailing edge, the hot streak peak temperature ratio dropped by 39% to $\Theta_R=0.61$ on the suction side (Position S1) and 25% to $\Theta_R=0.75$ on the pressure side (Position P1). Between the 1/3 and 2/3 positions the decay of the hot streak was much less; a 17% decrease on the suction side to $\Theta_R=0.50$, and a 9% decrease on the pressure side to $\Theta_R=0.68$. Finally from the 2/3 position to the trailing edge there was a 12% decay on the suction side to $\Theta_R=0.44$, and a 19% decrease on the pressure side to $\Theta_R=0.55$. Clearly there was a much greater attenuation of the hot streak during the first 1/3 of the distance around the vane. This may be attributed to the higher levels of relative turbulence intensity in the mainstream over this range. As shown by Radomsky and Thole [8], the mainstream turbulence intensity decreases substantially beyond the first 1/3 of the passage length. The much greater attenuation around the suction side of the vane over the first 1/3 distance may be due to the strong acceleration in this region which would result in a substantial decrease in the width of the hot streak and hence increases in the temperature gradients.

A first look at the effect of the wake is also shown in this figure, where measurements at Position B appeared as a smoothing of the sharp temperature gradient present at Position T, $0.32C$ upstream. Additional attenuation of the hot streak coming off the pressure side was seen in the relaxing of the temperature gradient as it

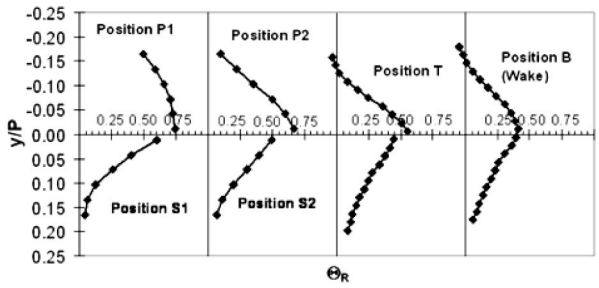

Fig. 13 Temperature profiles of the hot streak for the hot streak aligned with the stagnation line, Tu=20%

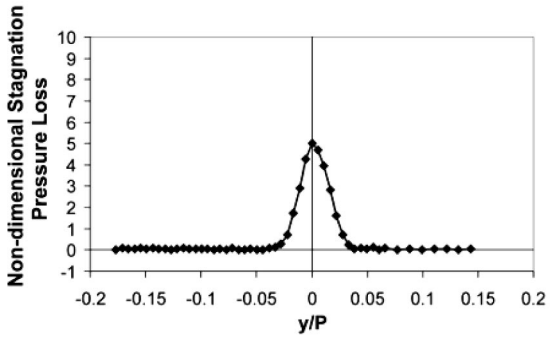

Fig. 14 Stagnation pressure loss profile taken in the wake of the vane at Position B, Tu=3.5%

mixed with the suction side fluid. A similar sharp temperature gradient was seen at the trailing edge (Position T) for the low mainstream turbulence condition, Tu=3.5%, as shown in Figs. 4 and 5.

Effects of the Wake. The effects seen in the wake downstream of the vane pertaining to hot streak attenuation are twofold. As seen previously, the sharp temperature gradient present at the trailing edge (Position T) was dissolved and the temperature profile became smooth. This effect is strongly dependent on the strength of the gradient, i.e., a higher gradient undergoes a stronger attenuation for the discontinuity to disappear. The second effect was simply a general attenuation of the hot streak overall, due to action of turbulent transport over the distance traveled downstream, so it is not truly a wake effect, but an effect of downstream distance. This effect was the same as that seen away from the vane through the passage.

A measure of the width of the wake at Position B downstream of the vane was obtained by measuring the stagnation pressure loss profile as shown in Fig. 14. Here the non-dimensional stagnation pressure loss was defined as $(P_{0,\mathrm{Pos\,A}} - P_{0,\mathrm{Pos\,B}})/P_{\mathrm{dyn,Pos\,A}}$. This measurement showed that the wake profile had a width of about $0.07P$, which was about 1/3 of the width of the hot streak at the same position downstream of the vane. Therefore, the wake of the vane was expected to cause a greater dispersion of the hot streak in the range $y/P=\pm 0.035$.

The profiles shown in Fig. 15 demonstrate the effect of the wake in eroding the sharp temperature gradient present at Position T for a pitch position of $0.1P$, which resulted from splitting the entering hot streak profile as discussed previously. This gradient was eroded by the mixing process in the wake of vane near $y/P=0$. The drop in peak temperature ratio was substantial, going from $T/T_\infty=1.053$ at Position T to $T/T_\infty=1.042$ at Position B, $0.32C$ downstream, a drop of about 20%. Not only did the wake

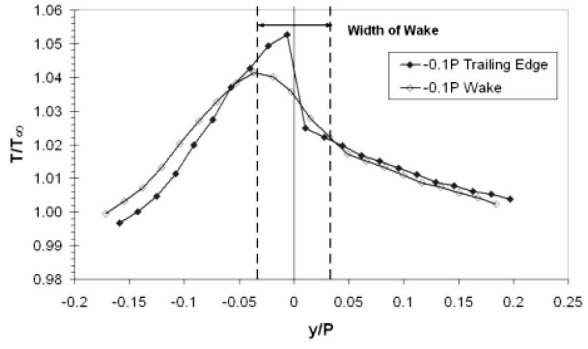

Fig. 15 Comparison of temperature ratio profiles at Position T (trailing edge) and in the wake at Position B for the hot streak at −0.1*P*, Tu=20%

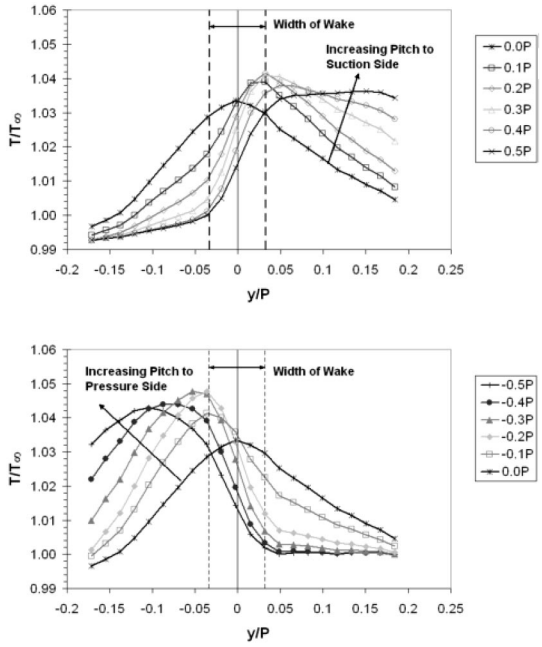

Fig. 16 (*a*) Temperature profiles of the hot streak at Position B with hot streak position varying from 0.0*P* to +0.5*P*, Tu =20%. (*b*) Temperature profiles of the hot streak at Position B with hot streak position varying from −0.5*P* to 0.0*P*, Tu=20%

erode the peak in this region of high gradients, but as a result, the peak was shifted about $0.03P$ to the pressure side. At the position of the peak at Position T ($y/P=-0.006$), the drop was larger at about 25%.

The effect of the wake in eroding the sharp temperature gradients occurred for all pitch positions, as seen in Figs. 16(*a*) and 16(*b*), showing suction-side and pressure-side pitch positions, respectively. Here, the sharp temperature gradients present at the trailing edge disappeared, resulting in smooth profiles at Position B, $0.32C$ downstream. These profiles may be compared to those in Figs. 10(*a*) and 10(*b*), where the sharp temperature gradients were present at Position T. Note that for the suction side, although the peak temperature ratios for positions on the stagnation line ($0.0P$) and through mid-passage ($+0.5P$) were similar, peak temperature ratios for intermediate positions at $+0.2P$ and $+0.3P$ were somewhat higher. On the pressure side, intermediate positions ($-0.2P$ and $-0.3P$) also had higher values than those found on the stagnation line ($0.0P$) and through the mid-passage ($-0.5P$).

The effect of attenuation over the distance downstream from Position T to Position B is seen in Fig. 17, for the hot streak profiles at $-0.5P$ to the pressure side. Here the sharp temperature gradient at the trailing edge was less of an issue since the approaching temperature profile was mainly on the pressure side. Still, the tail region of the hot streak was attenuated more greatly, resulting in a flat profile at Position T. Shifting focus to the peak on the pressure side, the more sharply peaked profile at Position T was flattened during its progress downstream to Position B due to mainstream turbulence effects. The drop in peak temperature ratio was about 9% over the $0.32C$ traveled. This compares with a much greater level of attenuation for the hot streak affected by the wake. As shown in the figure, for a pitch position of $0.022P$, the profile at Position T did not have a sharp temperature gradient and the drop in peak temperature ratio was about 18% from Position T to Position B. The significant difference between the attenuation rates for these two pitch positions confirms that the wake has a separate effect from that of the turbulence in the mainstream since turbulence levels are much higher in the vane wake.

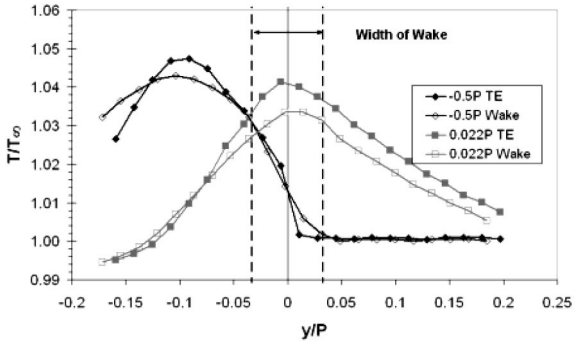

Fig. 17 Comparison of temperature ratio profiles at the trailing edge and in the wake at Position B for the hot streak at +0.022*P* and −0.5*P*, Tu=20%

Conclusions

Depending on the position of the hot streak relative to the stagnation line of the vane, the vane may serve to increase or decrease the attenuation of the hot streak. Furthermore, parts of the hot streak that pass along the suction side of the vane are attenuated more than parts of the hot streak passing around along the pressure side. This appears to be due to the longer distance traveled along the suction side of the vane, and due to the high acceleration around the suction side leading edge of the vane. The effects of the vane on the hot streak were investigated for low and high mainstream turbulence levels, Tu=3.5% and 20%, and trends were found to be similar. Comparisons between the hot streak impacting the vane at the stagnation line and passing through the mid-passage showed the peak hot streak temperature was the same for an impinging and non-impinging hot streak. This was true for both low and high turbulence, although for the high-turbulence condition, the non-impinging hot streak had a much flatter profile due to being constrained by the vane walls.

A major factor in the vane influence on the hot streak attenuation is the interruption of the hot streak dispersion caused when a hot streak impacts the vane and is split into two parts. This effect is most pronounced when the peak of the hot streak passes to either side of the vane so that a lower temperature outer edge, or ''tail,'' of the hot streak is split from the core. The core of the hot streak is then attenuated less because dispersion of heat from the core is blocked on one side by the vane. However, the outer edge of the hot streak that is split from the core is attenuated more because it is isolated from the peak. This interaction with the adiabatic vane causes very sharp temperature gradients in the hot streak at the trailing edge of the vane, resulting in an increase or decrease in hot streak peak strength depending on pitch position. Additional attenuation of the hot streak occurs due to the wake, also dependent on the hot streak pitch position.

Acknowledgments

We are most grateful to the sponsors of this work, the U.S. DOE National Energy Technology Laboratory through the South Carolina Institute of Energy Studies at Clemson University, and Pratt & Whitney. We would also like to thank Pratt & Whitney for supplying the turbine vane geometry.

Nomenclature

C = vane chord length, 594 mm
k = thermal conductivity
P = pitch between vanes, 460 mm
S = span length of vane, 550 mm
T_{hs} = hot streak temperature at a point in the flow
$T_{0,hs}$ = upstream peak hot streak temperature at the reference location
T_∞ = mainstream temperature
Tu = turbulence intensity, $u_{rms}/U \times 100\%$
U_0 = approach velocity to the vane
y = flow normal coordinate originating at the trailing edge or vane wall (positive toward suction side of test vane, negative toward pressure side of test vane)

Greek Symbols

Λ_f = turbulence integral length scale
Θ_R = normalized temperature ratio, $T_{hs}-T_\infty/T_{0,hs}-T_\infty$

Subscripts

hs = hot streak value
R = normalized
rms = root-mean-square
∞ = mainstream
0 = approach condition

References

[1] Roback, R. J., and Dring, R. P., 1993, ''Hot Streaks and Phantom Cooling in a Turbine Rotor Passage. 1. Separate Effects,'' ASME J. Turbomach., **115**, pp. 657–666.
[2] Gundy-Burlet, K. L., and Dorney, D. J., 1997, ''Three-Dimensional Simulations of Hot Streak Clocking in a 1-1/2 Stage Turbine,'' Int. J. Turbo Jet Engines, **14**, pp. 123–132.
[3] Gundy-Burlet, K., and Dorney, D., 1997, ''Influence of 3D Hot Streaks on Turbine Heat Transfer,'' *Proceedings of the 1997 International Gas Turbine & Aeroengine Congress & Exposition*, June 2–5 1997, Orlando, FL.
[4] Jenkins, S. C., Varadarajan, K., and Bogard, D. G., 2003, ''The Effects of High Mainstream Turbulence and Turbine Vane Film Cooling on the Dispersion of a Simulated Hot Streak,'' International Gas Turbine and Aeroengine Congress and Exposition, Atlanta, ASME Paper no. GT-2003-38575.
[5] Polanka, M. D., 1999, ''Detailed Film Cooling Effectiveness and Three Component Velocity Field Measurements on a First Stage Turbine Vane Subject to High Freestream Turbulence,'' Ph.D. dissertation, The University of Texas at Austin.
[6] Kuotmos, P., and McQuirk, J. J., 1989, ''Isothermal Flow in a Gas Turbine Combustor—a Benchmark Experimental Study,'' Exp. Fluids, **7**, pp. 344–354.
[7] Cutbirth, J. M., 2000, ''Turbulence and Three-Dimensional Effects on the Film Cooling of a Turbine Vane,'' Ph.D. dissertation, The University of Texas at Austin.
[8] Radomsky, R. W., 2000, ''High Freestream Turbulence Studies on a Scaled-Up Stator Vane,'' Ph.D. dissertation, University of Wisconsin–Madison.

Hector Iacovides

Diamantis Kounadis

Brian E. Launder

Department of Mechanical,
Aerospace and Manufacturing Engineering,
UMIST,
Manchester M60 1QD, UK

Jiankang Li
British Energy,
Barnwood, UK

Zeyuan Xu
Department of Mechanical,
Aerospace and Manufacturing Engineering,
UMIST,
Manchester M60 1QD, UK

Experimental Study of the Flow and Thermal Development of a Row of Cooling Jets Impinging on a Rotating Concave Surface

The paper reports an experimental study of impingement cooling in a rotating passage of semi-cylindrical cross section. Cooling fluid is injected from a row of five jet holes along the centerline of the flat surface of the passage and strikes the concave surface. The cooling passage rotates orthogonally about an axis parallel to that of the jets. Tests have been carried out, using water, both within the passage and as the jet fluid, at a fixed Reynolds number of 15,000, for clockwise and counter-clockwise rotation. Local Nusselt number measurements, using the liquid-crystal technique, show that under stationary conditions a high Nusselt number region develops around each impingement point, with secondary peaks half-way between impingement points. Rotation reduces heat transfer, leads to the disappearance of all secondary peaks and also, surprisingly, of some of the primary peaks. Flow visualization tests suggest that these changes in thermal behavior are caused because rotation increases the spreading rate of the jets. LDA and PIV measurements are also presented. They show that under stationary conditions the five jets exhibit a similar behavior, with their cores remaining intact up to the point of impingement at the top dead center. The LDA and PIV studies help explain the rather surprising thermal behavior under rotating conditions. [DOI: 10.1115/1.1812778]

Introduction

The leading-edge region of modern gas-turbine blades experiences particularly high temperatures, due to the normal impingement on the blade of the hot gas stream leaving the combustion chamber. To preserve the integrity of the blades they must be cooled both internally and externally, with protection being especially needed in the stagnation-point region. Using relatively cool by-pass air, effective strategies are being sought to achieve as high heat transfer coefficients as possible on the interior surface of the blade. The most popular route to achieve this is to adopt ''impingement cooling'' in which a row of jets is directed to the inside of the blade surface, just opposite the external stagnation point.

Until now the design of the interior of the blade has been based on measurements of mean heat-transfer coefficients beneath an impinging jet row. These data are usually obtained on a plane (rather than a concave) surface and invariably in a stationary rig. Thus, the contributions of blade rotation to the heat-transfer coefficient are unexamined as are, likewise, the detailed effects of the coolant flow, particularly the character of the fluctuating velocity field. Experimental information on impingement cooling under rotating conditions has only recently started to emerge with studies such as those by Akella and Han [1], Parsons and Han [2], and Hsieh et al. [3]. These studies focused on impingement cooling in rotating rectangular channels and provided measurements of the side-averaged Nusselt number. They showed that rotation can reduce the cooling effect of impingement by as much as 20%. Perhaps the study closest to the present one, in terms of both geometry and mode of rotation, is the mass transfer study of Mattern and Hennecke [4]. They also focused on a row of jets impinging on a concave surface, with the angle between the axis of rotation and that of the jets ranging from 0° (the same as in the present study) to 90° and for rotation numbers up to 0.02. Under stationary conditions, the local mass transfer data suggest that, as expected, each jet produces a peak in Nusselt number, due to impingement and that secondary peaks also appear half-way between the impingement points. In common with other researchers they showed that rotation, especially for the 0° case, reduces the levels of wall heat transfer. Moreover, the results for the 0° case also indicate that the secondary peaks in Nusselt number start to diminish.

Here the first detailed thermal and flow measurements are reported, for a simplified model of the impingement-cooling cavity, shown in Fig. 1, installed in UMIST's unique rotating facility. The data cover local Nusselt number, flow-field visualizations, and detailed LDA measurements over the full range of rotation numbers encountered in blade cooling. For the stationary case, detailed PIV mappings on some planes are also included. The experimental results will help to guide the blade designer and also serve to provide the detailed data that are required to validate CFD models for such complex flows.

Apparatus and Instrumentation

The measurements have been undertaken in the rotating flow test rig described in Iacovides et al. [5]. The particular test section to be examined is mounted on a horizontal circular table that may be driven over a range of rotational speeds up to 250 rpm by an electric motor. The table is housed within a stationary, circular, 1.2-m-diam tank. Water, the working fluid, is circulated in a closed-loop system being first metered in a straight section containing an orifice plate, before arriving, through a vertical pipe, at the center of the rotating table. From there water is fed to a chamber within the rotating table below the experimental model and it is injected into the cooling passage through the five jet holes. Electrical power is supplied to the rotating test section through slip rings as are likewise the data-output channels providing details of the electrical power supply.

A sketch of the test section under examination is shown in Fig. 1. It comprises a transparent perspex chamber, semi-circular in

Contributed by the International Gas Turbine Institute (IGTI) of THE AMERICAN SOCIETY OF MECHANICAL ENGINEERS for publication in the ASME JOURNAL OF TURBOMACHINERY. Paper presented at the International Gas Turbine and Aeroengine Congress and Exhibition, Vienna, Austria, June 13–17, 2004, Paper No. 2004-GT-53244. Manuscript received by IGTI, October 1, 2003; final revision, March 1, 2004. IGTI Review Chair: A. J. Strazisar.

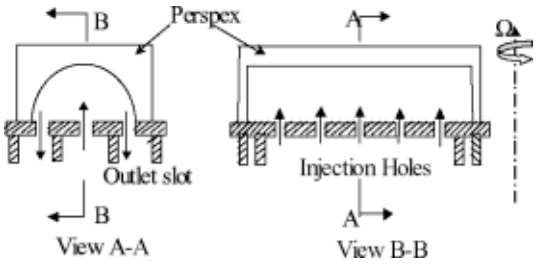

Fig. 1 Experimental model

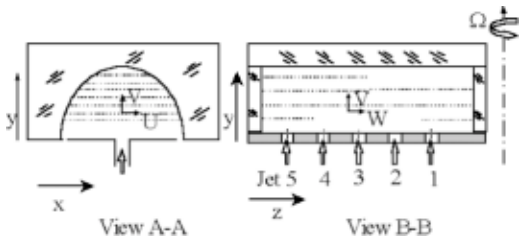

Fig. 4 LDA traverses for stationary case

cross section beneath which is a horizontal plate with five holes each 11.2 mm in diameter and spaced 44.8 mm apart. Water flows through the holes forming circular jets, which, for zero rotation, impinge symmetrically on the curved surface 35 mm above the holes. The jet fluid leaves the semi-circular cavity as shown. Two identical test sections have been made, one for heat transfer and the other for measuring the velocity field. In the former, the semi-circular surface has first been coated with thermo-chromic liquid crystals (TLCs), which are then covered by double-sided adhesive tape. As shown in Fig. 2, five thin steel foil strips were affixed to the other side of the adhesive tape. By passing electrical current through these, they provided the heat input to the cavity surface, under uniform-wall-heat-flux thermal boundary conditions. The temperatures on the curved surface were determined by recording the color play of the TLCs on a video camera mounted externally to the cavity but rotating with it, as documented in Iacovides et al. [5]. In order to transform the liquid crystal data to Nusselt numbers considerable image and data processing was necessary to identify the coordinates of the contour line of the selected (yellow) color, which is also a contour of a constant heat transfer coefficient. It was also necessary to correct for the effects of the surface curvature and to combine the information from different heating rates to produce a set of Nusselt number contours, Iacovides et al. [5].

The gathering of flow field data started with a flow visualization study, aiming to establish qualitatively how the jet trajectories were modified by rotation. As shown in Fig. 3, a stationary fiber-optic probe was placed above the center of the rotating platform. The vertical laser beam from the stationary probe struck a rotating mirror inclined at 45°. A horizontal rotating beam was thus reflected from the mirror. The rotating beam then passed through a glass rod fixed on the rotating platform, which generated a rotating light sheet. This light sheet was used to illuminate the central plane of the rotating passage that bisects the five jet holes. The trajectory of seeding particles within the illuminated plane could then be monitored. Still pictures were recorded using a high-resolution digital camera and moving pictures using a CCD camera, both of which rotated with the experimental model. The digital camera was operated through a remote control unit. The CCD camera was connected to a transmitter fixed on the rotating platform. The transmitter signal was sent to a stationary receiver that was connected to a TV monitor and also a video recorder.

The LDA investigations have been carried out for both the stationary and the rotating cases. The same two-channel fiber-optic probe employed in the flow visualization studies has been used. A TSI IFA750 unit was used for data acquisition and initial processing. For the stationary case, see Fig. 4, traverses have been carried out at a number of heights, both across and along the passage. The main focus has been on the three central jets that for no rotation exhibit a similar behavior. For the rotating case, as can be seen in Fig. 5, the stationary fiber-optic probe was placed along the side of the rotating platform. A beam expander was used to extend the focal length of the beam, so as to be able to access the entire length of the experimental model. As the experimental model rotates past the probe, instantaneous velocity readings are recorded along circumferential traverse lines such as those shown in Fig. 5. The exact position of the measuring volume relative to the rotating passage was determined by a rotary encoder mounted on the shaft that had a resolution of 2000 bins (discrete angular segments) per revolution. At the location of jet 3 this resulted in 45 data bins across the passage. The LDA data collected were then indexed with the corresponding bin number, so as to identify the location of the instantaneous flow measurements. As the rotating flow data were collected over circumferential traverse lines, interpolation for three and sometimes four traverses at only slightly different radii was used to create profiles along straight-line traverses. The minimum number of data points in each bin was 500.

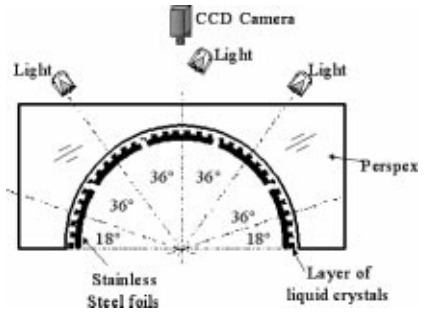

Fig. 2 Heating and viewing arrangements

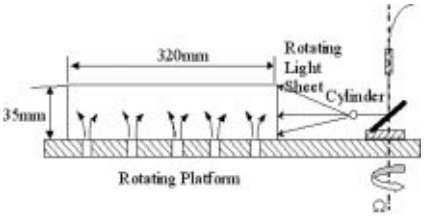

Fig. 3 Flow visualization setup

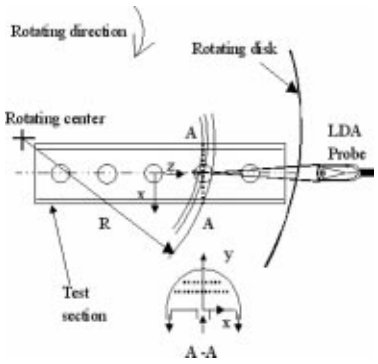

Fig. 5 LDA traverses for rotating case

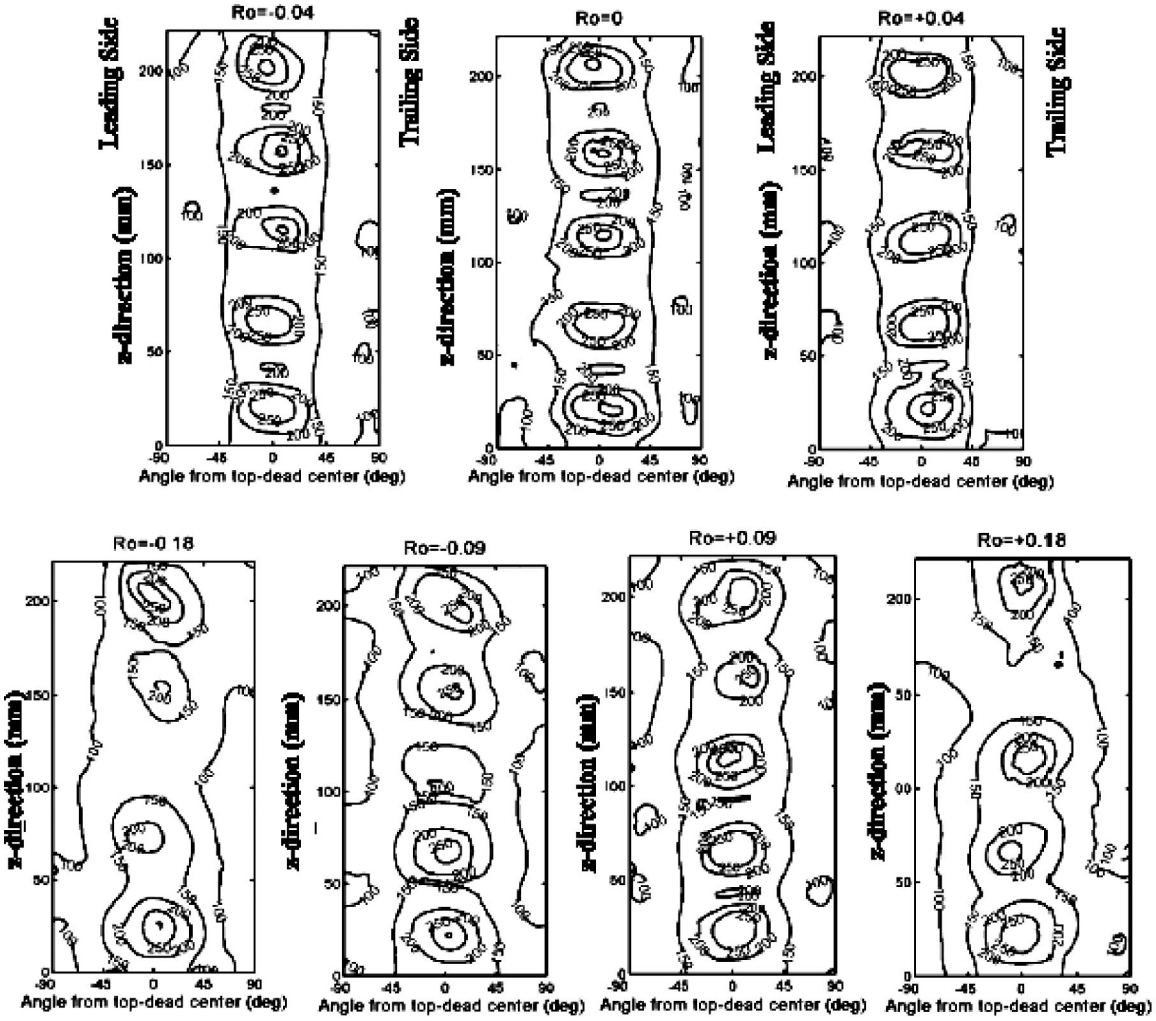

Fig. 6 Nusselt number contours for Re=15,000 and Pr=6.09

Finally PIV images have also been recorded using a DANTEC system. These images show snapshots of the flow within cross sections of the passages for which LDA traverses are also available for stationary and rotating conditions.

Results

Heat Transfer Measurements. All heat transfer tests have been carried out at a mean flow Reynolds number of 15,000 based on the jet exit velocity V_J and diameter d_j and for rotation numbers ($\mathrm{Ro}/\Omega d_j/V_j$) ranging from 0 (stationary) to 0.18, the latter being typical of engine conditions. Both clockwise and counter-clockwise rotation has been considered, with rotation numbers for counter-clockwise rotation denoted as positive and for clockwise rotation as negative. All fluid properties are evaluated at the fluid film temperature, defined as the average between the jet inlet and the wall temperatures. The appropriate wall temperature in this case is the yellow color temperature for the liquid crystals, determined by calibrating the crystals under the same heating, viewing, and illumination conditions as in the actual experiment. The Nusselt number is defined in terms of the difference between the wall and the jet inlet temperature.

The local Nusselt number measurements are summarized in the contour plots of Fig. 6. For the non-rotating case ($\mathrm{Ro}=0.0$) it is noted that the imprint of the impingement of the five jets is very clear giving rise to roughly concentric elliptic rings of uniform Nu. There is only a small difference between the contours created by one jet and the others: in most cases the contour of $\mathrm{Nu}=300$ is just reached at the impingement point, while for the second jet from the bottom in the figure it is just absent (though the $\mathrm{Nu}=250$ contour for this jet is similar in size to the others). The major axis of the roughly elliptic contours is horizontal, which is probably because the flow around the concave surface is unimpeded, while in the z direction the jets from adjacent holes collide, thus reducing the velocity. Weak secondary peaks in Nu are evident midway between the jet-impingement zones. These arise from the collision of the radially outward wall jets following the jet impingement. As noted earlier, they have also been reported in the mass transfer study of Mattern and Hennecke [4].

At the low rotation number of $\mathrm{Ro}=\pm 0.04$ a slight reduction in Nusselt number is evident. Fewer of the jets exhibit a contour for $\mathrm{Nu}=300$ and the inter-jet peaks have reduced. If the flow were perfectly symmetric, one would expect the effect of a counter-clockwise rotation to be an inverted mirror image of that for an anti-clockwise rotation of the same magnitude.

As the rotation rate is further raised, besides a progressive reduction in the mean levels of Nu, two notable changes to the contour pattern are evident. First, the major axis of the ''ellipses'' of the jet-impingement contours are no longer horizontal (or in compass terminology E–W). For counter-clockwise rotation the contours have a distinct NE–SW orientation while for clockwise rotation the orientation is NW–SE. The second notable change is that in each case one of the jets produces a significantly lower level of heat-transfer coefficient than the others. For counter-clockwise rotation (positive Ro's) the jet in question is the second

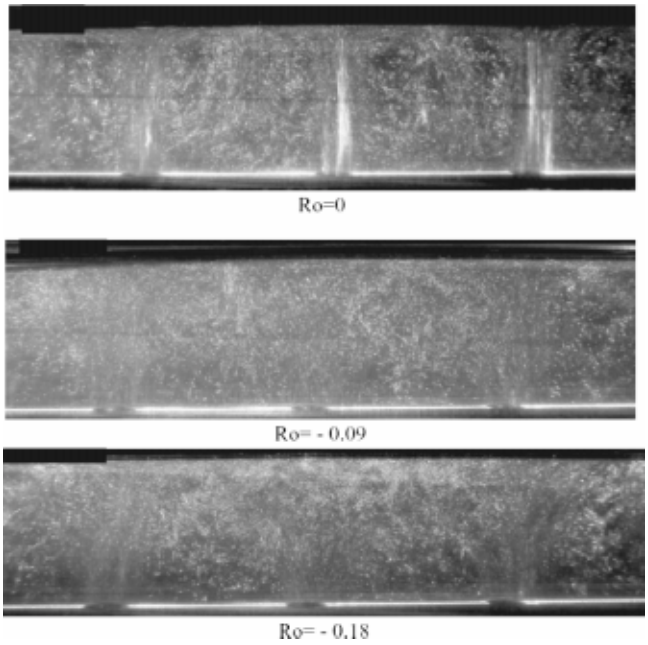

Fig. 7 Flow visualization for the three central jets

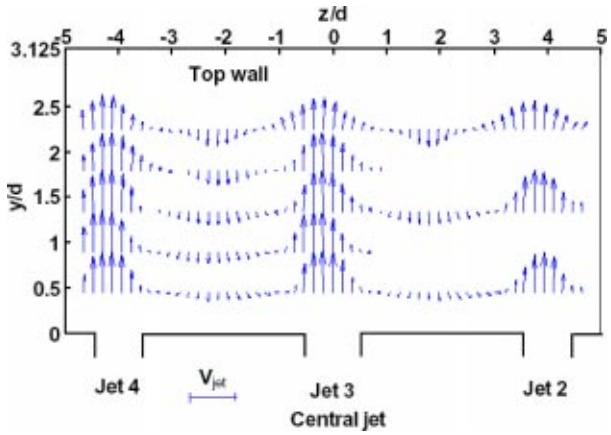

Fig. 8 Axial traverses along the central plane for the three middle jets. Stationary conditions.

from the top while for negative rotation it is the central jet. This selective diminution is quite evident at $Ro=\pm 0.09$ while for $Ro=\pm 0.18$ the imprint of the two jets has entirely disappeared. Now, the fact that in each case just a single jet should be so affected is surprising, doubly so since it is a different jet (that is, the location of the jet affected for one rotation rate is not the mirror image of the other case). This strongly implies that what is observed is some sort of instability provoked by very small differences between one jet and another and amplified by equally small differences due to rotation.

It is salutary to note that in an actual turbine blade the manufacturing tolerances will inevitably be much larger than in the present experiment where the hole diameter is an order of magnitude larger than in an actual blade. Moreover, due to the extreme temperature ranges to which it is subjected in use, even if a turbine blade is perfect at the start of its life, it will quickly develop small imperfections due to depositions, etc. Thus, while the mean effects of rotation on overall heat-transfer coefficients uncovered in this exploration are consistent with earlier studies and are thus an expected outcome, the effects on *local* Nusselt number at the levels of blade rotation occurring in an actual gas turbine are found to be quite profound, resulting in changes that would lead to local hot spots with serious implications for blade cooling.

Flow Visualization. As a start to an extensive examination of the quantitative effects of the rotation on the flow field, a series of flow-visualization studies was first made. As noted earlier, a sheet of laser light illuminates the flow movement in the plane of the jets' axes. Here attention is focused on the three central jets. The comments provided in what follows are based not just on the still photographs reproduced in Fig. 7 but also, as noted earlier, on the video recordings of the events. The figure shows clearly that there is a noticeable effect of the rotation on the jets. For the stationary case, the jet core remains intact up to the point of impact (as would be expected, since the distance from discharge to the impingement surface is only just over three jet diameters) and the resultant radial wall jets collide, giving rise to a noticeable, though highly unsteady, jet ''fountain.'' This vigorous unsteadiness where the wall jets collide is what leads to the secondary peaks in Nusselt number noted above. Successively raising the rotation rate appears to make the potential core shrink and disappear while the jets appear to spread more quickly: thus, at their point of impact, they are more diffuse, a development which could be responsible for the diminution in Nu. At the highest rotation rates examined ($Ro=-0.09$ and -0.18) it appears that the central jet may be spreading more rapidly than the ones on either side. This would seem to be consistent with the heat transfer data that show a complete disappearance of the central jet imprint at $Ro=-0.18$.

Stationary Flow Measurements. Figures 8 and 9 present some of the results of the first part of the LDA and PIV investigations, focused on the stationary case. Figure 8 shows the flow development along the symmetry plane of the passage, for the three central jets. As also seen in the flow visualization tests, all three jets show a similar behavior. The jet cores do remain distinct up to the top wall. Another feature present in the flow visualization images is the formation of the fountain regions between the jets, as a result of the collision of adjacent jets along the top (concave) wall. The fountain regions are characterized by the strong downward motion that expands along the downward direction, to eventually occupy most of the space between the jets. Figures 9(*c*) and 9(*d*) show comparisons between LDA and PIV measurements of the mean flow over the cross-sectional plane above Jet 3 and also [(a) and (b)] provide PIV data of the mean flow over the cross-sectional plane above Jet 5 and the plane half-way between Jets 3 and 4. The LDA traverses show that, as already suggested by the Nu contours, the flow is symmetric. The center-line velocity diminishes in the flow (vertical) direction, but the jet core remains distinct for the first two and a half diameters. The core disappears only over the last half diameter from the top dead center, where the jet is deflected symmetrically on either side of the stagnation point. Another important feature of the jet development is that the predominant flow direction over the cross section is upward. Downward flow is confined to only a thin layer along the curved wall, Fig. 9(*c*), the post-impact velocity being greatest about one jet diameter from the stagnation point. The upward flow is clearly not balanced by the downward flow. The reason for this apparent mass imbalance is the three-dimensionality of this flow. As the jet moves upwards fluid is deflected on either side of it, along the longitudinal (z as denoted in Fig. 4) direction, a feature confirmed by Figs. 8 and 9(*b*). The PIV measurements for the plane of Jet 3 are consistent with the corresponding LDA data, showing the same flow development. The only differences are in the near wall regions, where it was found impossible to eliminate the glare from the wall within the short time that the PIV system was at our disposal. Thus it was not possible to collect reliable velocity data within these regions. If we compare the PIV data for Jets 3 and 5, differences in the measured fields above Jets 3 and 5 are small. PIV data for the other two inner jets, Jets 2 and 4, not included here, show that under stationary conditions the flow development of these jets is similar to that of Jet 3. At the location halfway

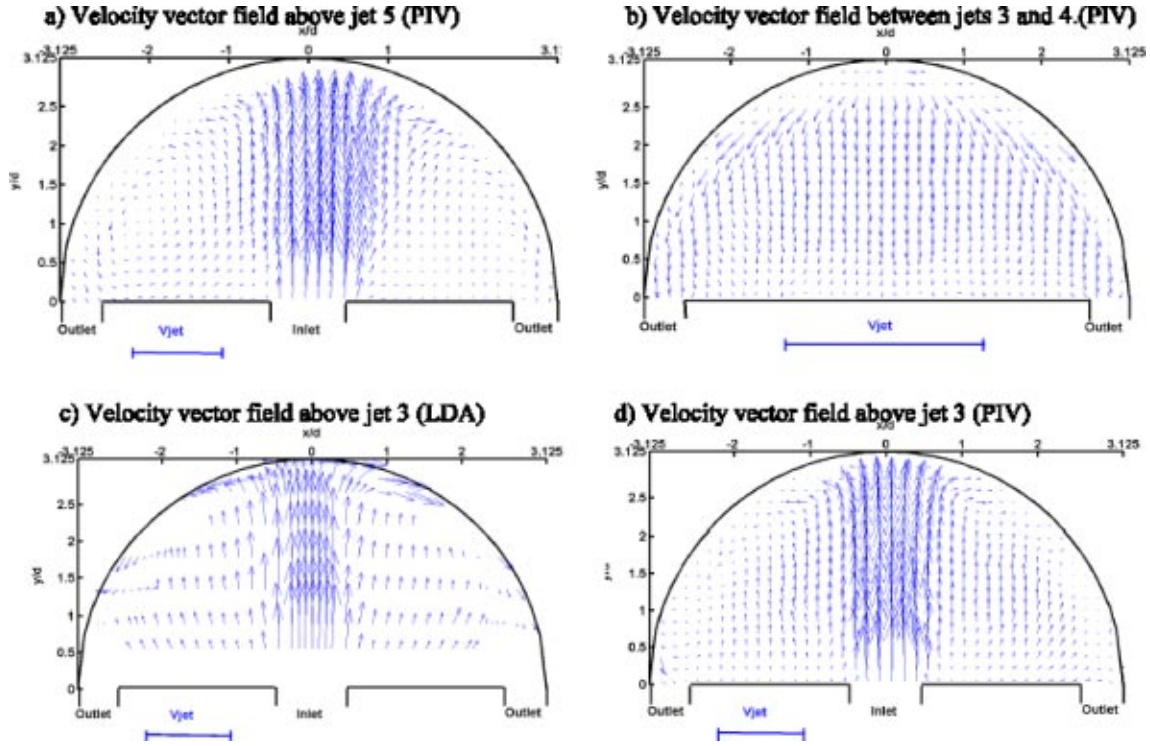

Fig. 9 Flow field LDA and PIV measurements, above and between jet exits, for stationary conditions

between Jets 3 and 4 the fountain phenomenon leads to a downward motion over the entire cross section. A similar behavior has been observed at the other half-way locations.

Figure 10 shows the development of the rms fluctuating velocities, under stationary conditions. Close to the jet exit (half a diameter) the levels of turbulence intensity are high even near the jet axis. This must be due to the fact that, in order to represent what happens in blade-cooling passages, the length of the jet pipes was kept short (about one diameter). Another feature present near the jet exit ($y/d=0.55$) is that at the edges of the jet the turbulence intensity along the flow direction, v, is higher than that along the radius of the jet, u. This must be due to the effects of the pipe walls, which would selectively damp turbulence fluctuations in the wall normal direction, in this case the u fluctuations. As the flow progresses upwards, the levels of the turbulence intensities continue to increase and the location of the maximum levels gradually moves from the edges to the center of the jet. Moreover the anisotropy also increases, with the turbulence intensities in the jet axial direction (y) being higher than those in the radial direction of the jet (x). Closer to the top wall, the distribution of the turbulence intensities across the jet becomes more uniform. At the traverse location closest to the wall, the turbulence intensities along the axis of the jet, which are normal to the top wall, become lower than those in the radial jet direction.

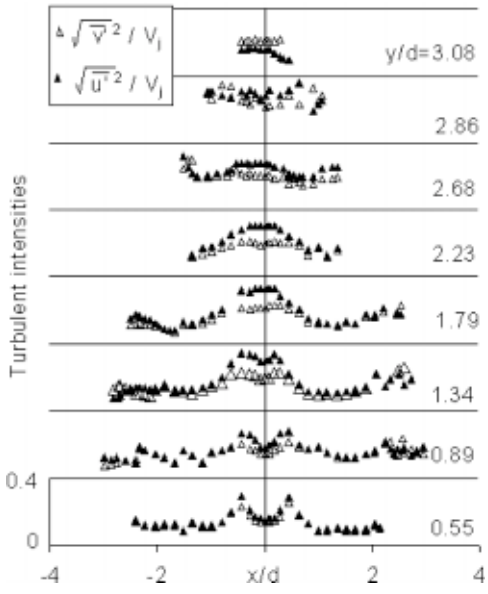

Fig. 10 Turbulence intensity profiles for Jet 3, under stationary conditions

Rotating Flow Measurements. Here, the first question we sought to answer was what causes the reduction or disappearance of some of the Nusselt number peaks above the internal jets (2, 3, and 4) at high rotation numbers. To address this question we first look at spanwise traverses of the vertical velocity at 1.3 jet diameters above each jet exit, for $\mathrm{Ro}=-0.18$, shown in Fig. 11. This is the case for which, as shown in Fig. 6, the peak in Nusselt number above the central jet, Jet 3, disappears, while those for Jets 2 and 4 are considerably reduced. In comparison to the corresponding stationary profiles (not shown here), the two outer jets (1 and 5) are almost unchanged, in Jets 2 and 4 the center-line velocity is reduced by a factor of almost 2 and Jet 3 has practically disappeared. While the complete disappearance of the central jet, 1.3 diameters above the injection hole, would suggest that rotation has reduced the mass flow rate of the central jet, the flow visualization images would suggest that the increase in the jet spreading rates is more likely to be the cause. In order to confirm this, additional traverses have been carried out above Jet 3 under rotating conditions, moving progressively closer to the jet exit. As can be seen in Fig. 12, the traverse closest to the jet exit shows that Jet 3 is still present and suggests its mass flow rate is not diminished at high speeds of rotation. The rapid disappearance of the core of Jet 3 after only 1.3 diameters from its exit, suggests that its spreading rate is strongly increased by rotation. This finding provides un-

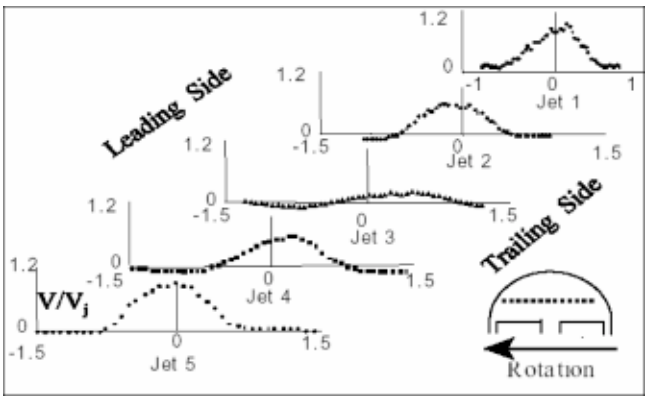

Fig. 11 Axial velocity profiles along spanwise traverse lines at 1.3 diameters above each jet center, for rotating conditions. Re=15,000 and Ro=−0.18.

equivocal qualitative support for the indication of the flow visualization explorations. As shown in Mattern and Hennecke [4], under these rotating conditions, as the jet begins to spread radially, the Coriolis force, due to the interaction between the radial velocity component of each jet and the rotation vector which is parallel to the axis of the jet, will generate a swirl velocity within each jet. This would then further increase the jets' spreading rates. Indeed an earlier numerical study, Iacovides and Chew [6], of the simpler case of flow in an axi-symmetric rotating cavity with a central impinging jet also showed a similar jet development at high rotation numbers. The question of why the two outer jets (1 and 5) are not as strongly affected by rotation as the three central ones, still remains to be answered. One possible explanation might be that for the three inner jets (2, 3, and 4) there is interference (from neighboring jets) on both sides. Under rotating conditions, the increase in the jet spreading rates will enhance jet interaction and this is bound to preferentially reduce the cooling effectiveness of the inner jets.

More information on the effects of rotation on the mean flow development is provided by the vector plots of Figs. 13 and 14, for the cross-sectional planes above Jet 4 and halfway between Jets 3 and 4, respectively. For Jet 4, while the effects of negative rotation are not as strong as for Jet 3, there is nevertheless a significant reduction of the jet center-line velocity with rotation and, in contrast to the stationary case, outside the jet core there is also a significant downward flow that becomes stronger at the higher rotation rate. At the halfway plane between Jets 3 and 4,

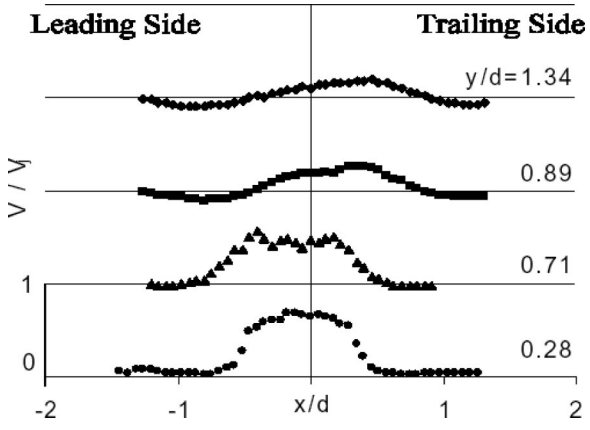

Fig. 12 Axial velocity profiles along spanwise traverse lines at 1.3 diameters above Jet 3, for rotating conditions. Re=15,000 and Ro=−0.18.

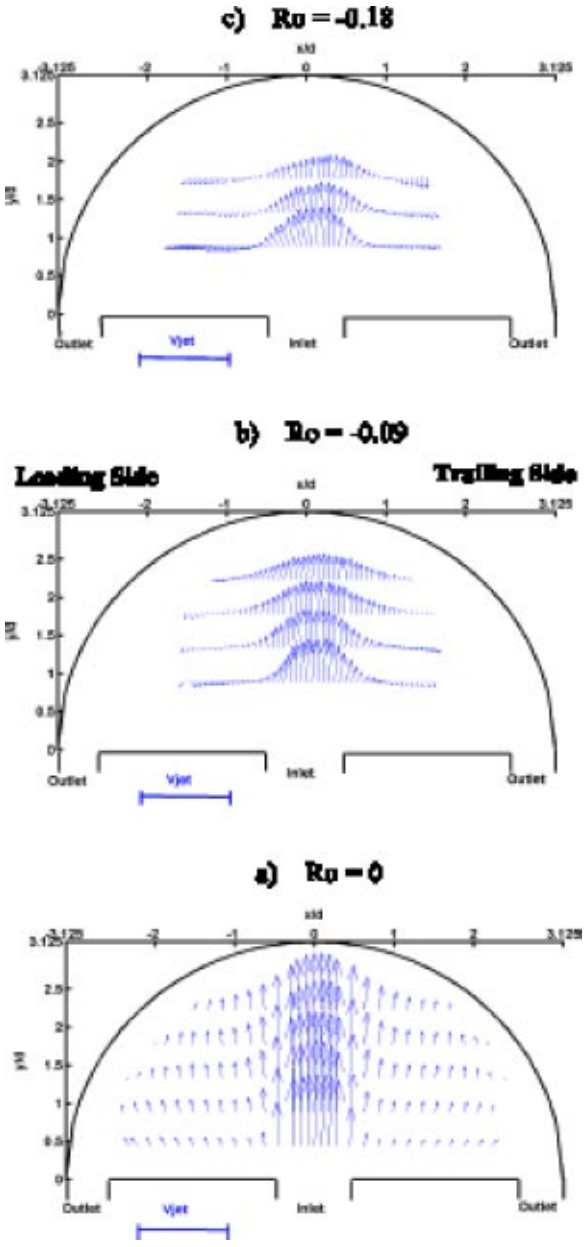

Fig. 13 LDA measurements in the cross-sectional plane above Jet 4

Fig. 14, it is clear that rotation leads to the disappearance of the fountain region, which is consistent with the disappearance of the secondary Nusselt number peaks. This is because, due to the increase in the jet spreading rate, there is no longer strong wall impingement which generates the fountain feature.

As shown in Fig. 1, the cooling fluid exits symmetrically from two longitudinal slots on either side of the jet plate. In order to explore how influential exit conditions are, a set of heat transfer tests were carried out with the initial exit slots blocked and the cooling fluid allowed to leave the passage from a 20-mm-radius exit hole in the end wall facing the center of rotation. The resulting liquid crystal images, not included here, show only minor differences from those obtained with the original exit arrangements. This suggests that, at least for a row with several jets as examined in this study, the effect of the exit arrangement on the flow and thermal development is not significant.

Finally Figs. 15 and 16 show some of the effects of rotation on the turbulence. Starting with Jet 4, shown in Fig. 16, as far as the

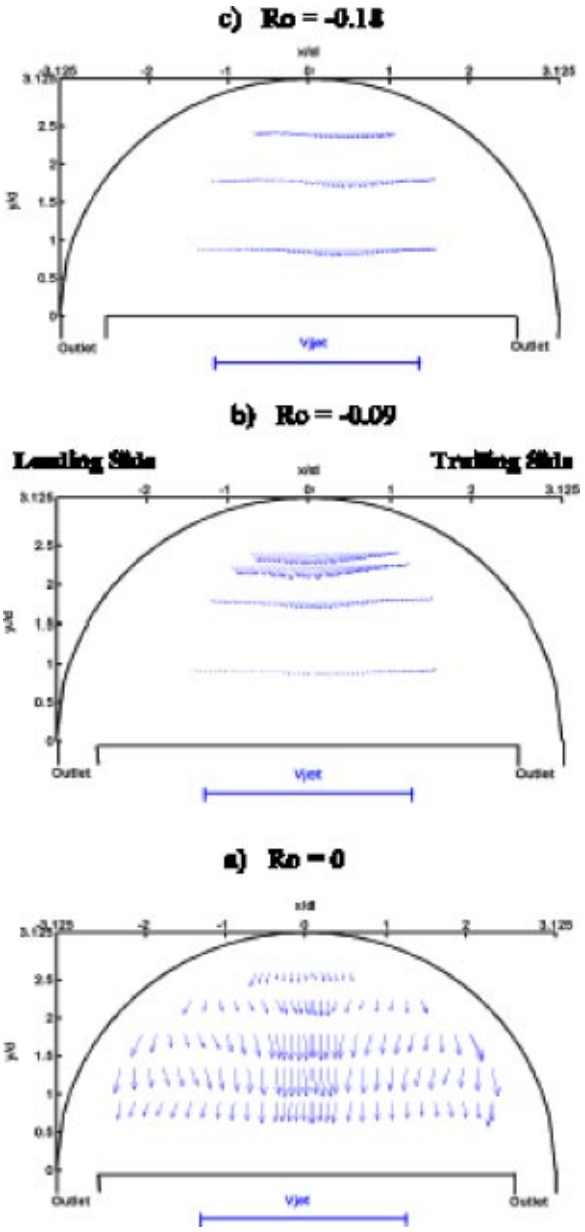

Fig. 14 LDA measurements in the cross-sectional plane between Jets 3 and 4

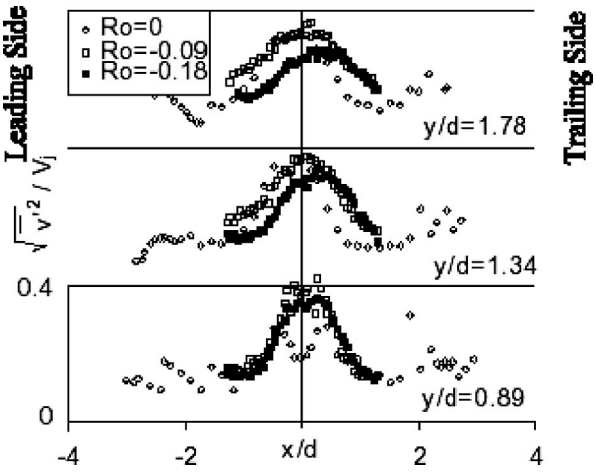

Fig. 15 Axial component of turbulence intensity above Jet 3

axial turbulence intensity is concerned, the main effect of rotation appears to be an increase in turbulence levels in the jet core. Outside the jet core, initially (close to the jet exit) rotation has a far weaker effect on the levels of turbulence intensity, but further downstream there is a more noticeable increase in intensity levels with rotation outside the jet core. This is probably related to the development of down flow outside the jet core under rotating conditions. For Jet 3 initially (close to the jet exit) rotation has a similar effect on turbulence intensities as for Jet 4. At locations further from the jet exit, however, intensity levels at higher rotational speeds start to reduce relative to those for the stationary case. This is probably because, as seen in Fig. 12, under rotating conditions Jet 3 disappears after the first jet diameter from the jet exit.

Conclusions

Measurements of the local Nusselt number have been presented that for the first time show in detail the effects of rotation on impingement cooling. As also shown by some recent studies, rotation has been found to reduce the overall effects of impingement cooling. Moreover, the local Nusselt number data produced in this study show that rotation can lead to strong non-uniformity in wall heat transfer, with some regions of high Nusselt number, due to impingement, disappearing completely. This feature has great practical significance for the design of blade-cooling passages. The local thermal data also show that reversing the direction of rotation does not lead to a mirror-image Nusselt number distribution.

The flow visualization studies suggest that rotation increases the spreading rate of the cooling jets and, at the higher rotation numbers, this leads to variations in the spreading rates of different jets. These flow observations are consistent with the thermal measurements.

LDA and PIV measurements for the stationary case are consistent with both the Nusselt number measurements and the flow visualization tests. They show that under stationary conditions all the jets undergo a similar flow development which is symmetric about the longitudinal plane of geometrical symmetry, that the central jet core remains distinctive until about half jet diameter from the top wall, and that there are source regions of strong downward motion in the space between adjacent jets. Moreover, as the jets develop, the anisotropy in the turbulence field along the axial and radial direction of the jets, initially confined to the edges of the jet, spreads over the entire jet core and increases in magnitude.

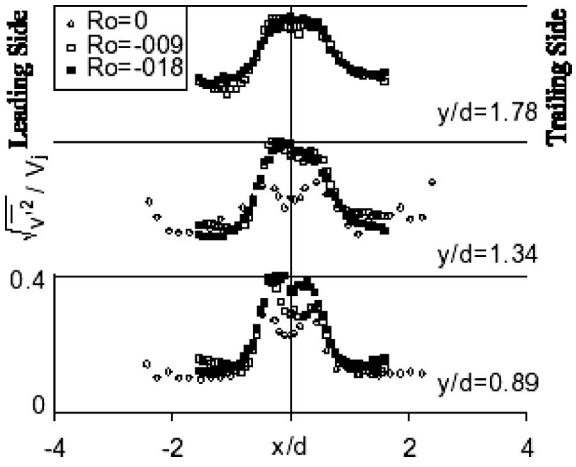

Fig. 16 Axial component of turbulence intensity above Jet 4

These flow observations are consistent with the thermal measurements. Rotation is shown to have a very strong effect on the spreading rate of the interior jets, causing some to spread so rapidly that their core completely disappears within the first diameter from the jet exit. A possible cause is the generation of swirl by the Coriolis force, as the jets expand.

Acknowledgments

The research reported here is sponsored by the UK Science and Engineering Research Council, under Grant No. GR/R03433. Rolls Royce plc and Alstom plc have provided helpful input on the spacing and relative size of the injection holes. Mr. D. C. Jackson and Mr. D. Cooper provided expert technical advice, which is also gratefully acknowledged. Finally the authors thank Dantec Dynamics Ltd., UK Bristol, for the loan of their PIV system and for the cooperation and technical assistance received from Mr. G. Hasell, Mr. R. Jaryczewski, and Mr. P. Jones. The authors' names are listed alphabetically.

Nomenclature

d = diameter of injection holes
k = fluid thermal conductivity
Nu = Nusselt number $(q_W d_J/(T_W - T_J)k)$
Pr = Prandtl number
R = distance from axis of rotation
Re = Reynolds number $(V_J d_J/\nu)$
Ro = rotation number $(\Omega d_J/V_J)$
T_j = fluid inlet temperature
T_W = local wall temperature
q_W = rate of wall heat transfer per unit area
U = velocity component along the spanwise direction
u = fluctuating velocity component in spanwise direction
V = velocity component along the jet axial (vertical) direction
v = fluctuating velocity component in jet axial direction
V_j = jet exit velocity
W = velocity component along the length of the passage
ν = fluid kinematic viscosity
Ω = speed of angular rotation

References

[1] Akella, K. V., and Han, J.-C., 1998, "Impingement cooling in rotating two-pass rectangular channels," J. Thermophys. Heat Transfer, **12**, pp. 582–588.
[2] Parsons, J. A, and Han, J.-C., 1998, "Rotation effect on jet impingement heat transfer in smooth rectangular channels with heated target walls and radially outward cross flow," Int. J. Heat Mass Transfer, **41**, pp. 2059–2071.
[3] Hsieh, S. S., Huang, J. T., and Liu, C. F., 1999, "Local heat transfer in a rotating square channel with jet impingement," ASME J. Heat Transfer, **121**, pp. 811–818.
[4] Mattern, Ch., and Hennecke, D. K., 1996, "The influence of rotation on impingement cooling," ASME paper no. 96-GT-161, International Gas-Turbine and Aero Congress, Birmingham, UK.
[5] Iacovides, H., Jackson, D. C., Kelemenis, G., Launder, B. E., and Yuan, Y.-M., 2001, "Flow and heat transfer in a rotating U-bend with 45 degree ribs," Int. J. Heat Fluid Flow, **22**, pp. 308–314.
[6] Iacovides, H., and Chew, J. W., 1993, "The computation of convective heat transfer in rotating cavities," Int. J. Heat Fluid Flow, **14**, pp. 146–154.

P. M. Byvaltsev
Researcher,
First Department,
Mechanical Engineering Research Laboratory,
Hitachi, Ltd.,
502 Kandatsu, Tsuchiura,
Ibaraki 300-0013, Japan
e-mail: petr@merl.Hitachi.co.jp

K. Kawaike
Chief Researcher,
Gas Turbine Department,
Power and Industrial Systems R&D Laboratory,
Hitachi, Ltd.,
832-2 Horiguchi, Hitachinaka,
Ibaraki 312-0034, Japan
e-mail: kazuhiko_kawaike@pis.Hitachi.co.jp

A Comparative Study of Two Transition Zone Models in Heat Transfer Predictions

A comparative study of two transition zone models was carried out to assess their ability to simulate boundary layer laminar-turbulent transition. Transition modeling is based on the use of an algebraic equation for the intermittency distribution. The crucial difference between the models lies in the nondimensional breakdown rate formulation. A two-dimensional marching code was used to combine these models with the modified Johnson and King turbulence model and the algebraic "nonturbulence" model developed earlier. Flat plate and various turbine blade heat transfer measurements were used in the comparison. One model gave reasonably accurate results for most of the test cases considered. [DOI: 10.1115/1.1731446]

1 Introduction

Predicting laminar-turbulent transition is one of the remaining difficulties encountered in computing boundary layer flows. It is well known that transition has a dominant effect on the distributions of boundary layer (BL) characteristics along solid surfaces. The distributions of wall shear stress and surface heat transfer are significantly affected by transition behavior. Boundary layer transition phenomena and transition modeling have been comprehensively discussed by Narasimha [1]. The role and practical significance of transition in gas turbine engines has been discussed in detail by Mayle [2].

A widespread approach to predicting transitional flows is the direct use of low Reynolds number turbulence models. The use of the current models to predict bypass transition induced by freestream turbulence was investigated by Westin and Henkes [3]. The ability of large variety of different models to predict a number of T3-series transition flow experiments was tested. The results showed that none of the models could correctly predict both the location and length of transition for a range of flow conditions. The authors concluded that the existing models were inadequate for predicting flow transition.

An alternative approach is transition modeling based on the use of the intermittency factor, γ, (the probability that flow will be turbulent at a certain position). BL flow quantities in the transition zone are represented by a combination of turbulent and pseudo-laminar (nonturbulent) quantities in accordance with the intermittency factor, [2]. The value of γ can be obtained either by integrating a partial differential equation for γ, as is done in a number of papers, [4–6], published recently, or by using an algebraic equation for the intermittency distribution. In the latter case, we define the intermittency distribution formula coupled with additional relationships for its variables as a transition zone model (TZM), following Solomon et al. [7]. Two TZMs are assessed in this paper.

Emmons' statistical theory, [8], for turbulent spots and the concentrated breakdown hypothesis of Narasimha [9] created the basis for further development of TZMs. Chen and Thyson [10] subsequently used Emmons' theory and Narasimha's hypothesis to develop a transition model that supposedly allowed for the influence of the pressure gradient on a turbulent spot convection. Using the model to simulate pressure-gradient transitional flows showed that the Chen-Thyson model was not able to correctly predict a transition length. Even significant corrections of the model made in accordance with the experimental correlations of Gostelow et al. [11] do not satisfactorily resolve the problem of inadequate prediction of transition behavior in cases when the pressure gradient changes considerably throughout the region of intermittent flow.

This problem has been attributed to the significant influence of the local pressure gradient on turbulent spot propagation. The experiments of Gostelow et al. [12] confirmed this assumption and enabled the authors to obtain tentative correlations for spot growth parameters from the experimental data that they had assembled.

One of the TZMs examined in the present work is a model developed by Solomon, Walker and Gostelow [7] (hereafter referred to as SWGM). The authors used the correlations for spot propagation parameters of Gostelow et al. [12], together with correlations for the spot generation rate from Gostelow et al. [11] and Fraser et al. [13], to produce a new model by modifying the original Chen and Thyson model.

The other transition zone model examined here is the model suggested by Byvaltsev and Nagashima [14] (hereafter referred to as BNM). It was used by the authors for heat transfer predictions for turbine blade surfaces. A zero pressure gradient version of the model was proposed earlier by the same authors, [15]. It was developed by a simple reformulation of the original model of Chen and Thyson for the intermittency distribution so that the terms of the distribution formula relating to dimensions of length and time became non-dimensional. This rearrangement of terms gave rise to a nondimensional combination containing the spot generation rate, which was assumed to be constant. This assumption avoids the need to estimate the spot generation rate at transition inception and makes the prediction of transition length less sensitive to errors in computing the location and flow parameters for transition onset.

In the cited work, [14], the zero pressure gradient transition model was modified by using the correlations of Gostelow et al. [12] for spot propagation parameters and was then used for heat transfer predictions for the suction surface of turbine blades, while the zero pressure gradient version of the model was applied to heat transfer calculations for the pressure surface. In the present work, BLs at both the suction and pressure surfaces were calculated using the same model, BNM (as defined above) employed by Byvaltsev and Nagashima [14] for suction surface BL simulations. This model, like its counterpart, SWGM, incorporates the correlations of Gostelow et al. [12] for the spot propagation parameters which react to changes in the local pressure gradient through the transition zone.

The algebraic eddy-viscosity ''nonturbulence'' model proposed

Contributed by the Turbomachinery Division of THE AMERICAN SOCIETY OF MECHANICAL ENGINEERS for publication in the JOURNAL OF TURBOMACHINERY. Manuscript received by the Turbomachinery Division, October 15, 2003; revised manuscript received, November 9, 2003. Editor: D. Wisler.

by Byvaltsev and Nagashima [15] is used to simulate pretransitional (pseudo-laminar) BLs subjected to freestream turbulence (FST). The model takes into account, in a simple form, intensity, length scale of FST, and favorable pressure gradient. Very satisfactory results were obtained for the nonturbulent portions of BLs for turbine blades considered in the cited paper.

A simulation of the turbulent portions of BLs was carried out using the Johnson and King turbulence model, [16]. The model falls between algebraic and one-equation turbulence models and employs more physics than algebraic eddy-viscosity models. It requires the solution of an additional one-dimensional equation for the maximum Reynolds stress. Therefore, it can easily be incorporated and then modified if necessary. In addition, the eddy-viscosity formulation of the model combines well with the algebraic nonturbulence model in laminar-turbulent ''overlapping'' (transitional) regions. This is why we adopted it for our purposes. In this paper, we suggest modifications to the model to adapt it for predictions of heat transfer to convectively cooled turbine blades.

The objective of the present work was to carry out a comparative study of the two transition zone models, the SWGM and BNM, by examining their ability to simulate the laminar-turbulent transition of boundary layers on flat-plate and turbine-blade surfaces. Since transition behavior has a dominant effect on the distribution of surface heat transfer, it is practicable to use heat transfer experiments to compare the transition zone models. Heat transfer measurements for a flat plate by Rued and Wittig [17] and for turbine blades by Ames [18], Consigny and Richards [19], Arts et al. [20], and Arts et al. [21] were used in evaluating the models. A two-dimensional finite volume marching code was utilized to produce numerical results. Modeling of BL flows is described in Section 2, which also includes subsections on problem formulation, and descriptions of the nonturbulence (pre-transition) model, the Johnson and King turbulence model (with our proposed modifications), and the transition zone models used in the study. The results of the comparative study of the two TZMs in flat plate and turbine blade test cases are discussed in Section 3.

2 Modeling of Boundary Layer Flows

2.1 Governing Equations and Numerical Method. External two-dimensional compressible BL flows around turbine blades were considered. ''Steady'' perfect gas flows (with a constant Prandtl number) were described using a system of two-dimensional time-averaged boundary layer conservation equations, [22], (the continuity, streamwise momentum, and stagnation enthalpy equations). No-slip and thermal (specified temperature) boundary conditions were imposed at the smooth impermeable wall. The freestream conditions, for streamwise velocity, $\overline{U}$, and total enthalpy, $\overline{H}$, were specified at an appropriate distance from the wall. The equations were integrated along the suction and pressure surfaces from the stagnation point located at the blade leading edge. The initial conditions at this point were specified for $\overline{U}(=0)$ and iteratively computed for $\overline{H}$. The detailed formulation of the problem is given in the previous papers, [14,15].

Before the governing equations could be solved, we had to incorporate a model for the Reynolds stress terms, $\overline{\rho u' v'}$ and $\overline{\rho v' t'}$, which were present in the equations as a result of the time-averaging process. To estimate these terms, the eddy-viscosity formulation described in the previous papers, [14,15], was adopted as follows:

$$-\overline{\rho u' v'} = [(1-\gamma)\mu_{nt} + \gamma\mu_t]\frac{\partial \overline{U}}{\partial y} \tag{1a}$$

$$-\overline{\rho v' t'} = \left[(1-\gamma)\frac{\mu_{nt}}{\mathrm{Pr}_{nt}} + \gamma\frac{\mu_t}{\mathrm{Pr}_t}\right]\frac{\partial \overline{T}}{\partial y} \tag{1b}$$

where γ is the intermittency factor (the probability that a BL flow at the streamwise x position is turbulent), $\overline{U}$ is the mean velocity, $\overline{T}$ is the temperature, and the subscripts t and nt are used to denote the turbulent and ''nonturbulent'' (pseudo-laminar) portions of the flow within the transitional BL.

The eddy-viscosity terms could then be determined by using appropriate turbulence and ''nonturbulence'' models. The value of Pr_{nt} was taken to be equal to its turbulent analogy ($\mathrm{Pr}_{nt}=\mathrm{Pr}_t=0.9$). The conventional approaches to simulating transitional BLs neglect the nonturbulent terms in Eqs. (1*a*)–(1*b*). However, they may be important for adequate modeling of laminar BLs affected by FST. For some of the turbine blades considered below, an accelerating BL on the pressure surface and the front part of the suction surface remains in a pseudo-laminar state, which was successfully predicted using the nonturbulent terms only.

BL equations written in the conservative form were solved using an implicit and forward marching finite-volume iterative procedure (50 iterations were made at each $x=$ const. position). The numerical scheme has a first-order accuracy in the x direction and a second order in the normal, y, direction. For flows with separation, a special procedure, [23], was used to overcome the stability problem associated with a negative $\overline{U}$ velocity. This procedure ignores the longitudinal convection terms in the momentum and energy equations, and works satisfactorily provided the region of separated flow is small. As the size of the recirculation region increases, this approximation becomes less accurate, [24].

In the x,y plane a geometric progression with a coefficient of the order of 1.05–1.08 was used to refine a computational grid in the wall direction. To ensure grid-independent solutions, 80 grid points were used in that direction. The grid point adjacent to the wall did not exceed a value of $y^+=0.6-1.0$ in all calculations. In the case of flat plate tests, the grid in the x direction was refined exponentially to the leading edge. In turbine blade test cases, the distribution of the points in the x direction coincided with the distribution of the nodes of the mesh for external flow calculations (approximately 50 and 30 points on the suction and pressure sides, respectively).

2.2 Nonturbulence Model. Nonturbulent BLs affected by FST were simulated using the simple algebraic model proposed by Byvaltsev and Nagashima [15]. It is a semi-empirical one-layer eddy-viscosity model, in which μ_{nt} is given by

$$\mu_{nt}=[1-\exp(-\zeta)]\overline{\rho}\ell_{nt}^2\left|\frac{\partial \overline{U}}{\partial y}\right| \tag{2}$$

where

$$\zeta = C_\zeta Tu_e/100F_L(z_o)(2+\Lambda^+/6) \tag{3}$$

$$\ell_{nt}=[1-\exp(-y^+/(2+\Lambda^+/6))]\kappa y.$$

In the above expressions, $y^+=\rho_w u_{\tau m} y/\mu_w$ and $u_{\tau m}=\max_y(\mu_\Sigma|\partial\overline{U}/\partial y|)^{1/2}/\overline{\rho}$, the values of κ and C_ζ are 0.41 and 1.07, respectively, and $\mu_\Sigma=\mu+(1-\gamma)\mu_{nt}+\gamma\mu_t$. The FST level, Tu_e, is assumed to vary along the blade surface as $Tu_e=Tu_\infty\overline{U}_\infty/\overline{U}_e$, where the inlet (oncoming freestream flow) and BL-edge quantities are denoted by the subscripts ∞ and e, respectively. The function $F_L(z_o)$ was proposed by Dullenkopf and Mayle [25] to account for the FST length scale on heat transfer for stagnation flows. In the model, its value is computed at the stagnation point and then used to calculate the developing BL as an invariable FST length scale factor as follows:

$$F_L(z_o)=1/2z_o^{1/2}/[1+0.0281z_o^2]^{5/12},$$

where z_o is the ratio of the streamwise integral length scale of turbulence L_∞ and the BL thickness δ_o at the stagnation point of a blade: $z_o=L_\infty/\delta_o$. Here and hereafter, δ is the 99% of the BL thickness: $\overline{U}_{y=\delta}=0.99\overline{U}_e$. When there is no data for L_∞, the streamwise dissipation length scale of turbulence Lu, defined as $Lu=-u_e'^3/(\overline{U}_e du_e'^2/dx)$, can be used for the approximate estimation of L_∞: $L_\infty=2/3Lu_\infty$.

The last factor (in parentheses) on the right side of Eq. (3) represents the coefficient of the Pohlhausen polynomial velocity profile, [22], for laminar BLs with zero and favorable pressure gradients, where

$$\Lambda^+ = (|\Lambda| + \Lambda)/2, \quad \Lambda = \rho_e \delta^2 / \mu_w d\overline{U}_e / dx.$$

The boundary layer measurements of Westin et al. [26] for flows over a flat plate and the heat transfer data of Ames [18] and Arts et al. [20] for gas turbine vanes were used by the authors of the model to evaluate the capabilities of the nonturbulence model. In all the cases described, very satisfactory agreement between the computed and measured data was obtained for the nonturbulent portions of BLs. The model demonstrated remarkable properties, corresponding well to the experimental data given by Westin et al. [26]. In particular, it showed that the presence of FST did not significantly affect the development of the displacement thickness, δ_1, in the region upstream of the transition onset. In contrast, FST had a noticeable influence on the development of the BL and momentum thickness, δ and δ_2. The model captured the decrease of the shape factor H_{12} ($H_{12} = \delta_1 / \delta_2$) in linear proportion to the square root of the Reynolds number.

2.3 Turbulence Model. The half-equation Johnson and King turbulence model (JKM), [16], is composed of an eddy viscosity formulation and an ordinary differential equation to describe the streamwise development of the maximum Reynolds shear stress. The equation is used to scale the eddy viscosity in the outer region of the BL. The JKM was designed to simulate flows with strong adverse pressure gradients or separated flows. The model takes into account "nonequilibrium" flow development, when a BL changes rapidly and turbulence production no longer equals the turbulent dissipation of energy. Here, modifications to the model are suggested to enable it to be used for heat transfer predictions for convectively cooled turbine blades. In describing the modified Johnson-King model (JKMM) we follow the notation of Neel et al. [27].

For the Johnson-King model, the kinematic eddy viscosity is defined as

$$\nu_t = \nu_{to}[1 - \exp(-\nu_{ti}/\nu_{to})] \tag{4}$$

where ν_{to} and ν_{ti} are the outer and inner viscosities, respectively, and are defined by

$$\nu_{to} = 1.20\,\sigma_\nu(x) K_C \overline{U}_e \delta_1 \gamma_K \tag{5}$$

$$\nu_{ti} = [1 - \exp(-y u_D \sigma_D / \nu A^+)]^2 \kappa y u_s \tag{6}$$

where $\gamma_K = 1/[1 + 5.5(y/\delta)^6]$, $u_D = \max[u_*, (-\overline{u'v'_m})^{1/2}]$, $u_s = u_*(1-\gamma_S) + (-\overline{u'v'_m})^{1/2}\gamma_S$, $\gamma_S = 1 - \exp(-y/[u_* y_m/(u_* + (-\overline{u'v'_m})^{1/2})])$, and u_* is the wall shear velocity. The value of K_C is 0.0168, κ is 0.41, and A^+ is 15. This value of A^+ was adjusted by Johnson and King [16] for the van Driest damping term in their model. The same value of A^+ was also used by other researchers, in particular, by Neel et al. [27]. No pressure-gradient corrections for A^+ were applied in the above-cited works, [16,27], as well as in the present work. The subscript m indicates that the variable is evaluated at the y location where Reynolds shear stress is maximum, $\tau_m = (\overline{\rho}\nu_t \partial\overline{U}/\partial y)_m$. The location of τ_m varies in a streamwise direction. At each x location, a value of σ_ν is used to scale the outer viscosity, Eq. (5), such that the relationship $\sigma_\nu \cong \tau_m / \tau_{m,eq}$ is satisfied. The variable $\tau_{m,eq}$ represents the equilibrium value of the maximum Reynolds shear stress and is found by setting $\sigma_\nu(x) = 1$.

Modifications made to the original JKM relate to the expressions (5) and (6). A factor of 1.20 was added to the definition of outer viscosity (5). This coefficient was determined by the requirement for agreement with the experimental data used in the present work and the heat transfer results computed using the Cebeci and Smith turbulence model, [28]. An additional factor σ_D was incorporated into the damping term for inner viscosity (6). The purpose was to improve the results for regions characterized by adverse pressure gradients and located behind laminar-separation/turbulent-reattachment zones. The equality $\sigma_D = \sigma_\nu(x) \geqslant 1$ is adopted in these cases, while $\sigma_D = 1$ for all other cases. Using this modification in BL calculations leads to a decrease in the viscous sublayer and, as a consequence, to an enhancement of heat fluxes at walls in the regions following reattachment. At present, there is no exact criterion for replacing the equality $\sigma_D = 1$ with the other equality $\sigma_D = \sigma_\nu(x)$ during computation. If taking this equality into account in computations of BLs for turbine blade pressure surfaces generally leads to improved results, then it is not quite right for suction surfaces. For instance, a calculation of heat transfer rates in the zone of the interaction of a separated laminar BL with a shock wave can produce significantly overestimated results (not shown).

The JKM requires the solution of an ordinary differential equation (ODE) for the maximum Reynolds shear stress τ_m:

$$\frac{L_m \overline{U}_m}{a_1 \tau_m} \frac{\partial \tau_m}{\partial x} = \left(\frac{\tau_{m,eq}}{\rho_{m,eq}}\right)^{1/2} - \left(\frac{\tau_m}{\rho_m}\right)^{1/2} - \frac{\rho_m L_m D_m}{\tau_m} \tag{7}$$

where the turbulent diffusion term D_m is defined by

$$D_m = \frac{0.5(\tau_m/\rho_m)^{3/2}}{a_1 \delta[0.7 - (y/\delta)_m]} |1 - \sigma_\nu(x)^{1/2}|.$$

Here, the value of a_1 is 0.25 and L_m is a dissipation length scale with the following values: $L_m = 0.41 y_m$ when $y_m/\delta \leqslant 0.22$ and $L_m = 0.09\delta$ for $y_m/\delta > 0.22$.

The eddy-viscosity model (4) is used to determine the actual shear stress, and the differential Eq. (7) is then employed to control the level of the actual shear stress through the σ_ν parameter. At each x location the following relationship must be satisfied:

$$\tau_{m,\mathrm{ODE}} = (\overline{\rho}\nu_t \partial\overline{U}/\partial y)_{m,\mathrm{actual}}.$$

2.4 Transition Zone Models. In transition zones, the nonturbulence model is combined with the modified Johnson-King turbulence model (JKMM) using the intermittency factor γ (see Eqs. (1*a*)–(1*b*)). The location of the onset of transition is estimated using the empirical correlation suggested by Mayle [2]

$$\mathrm{Re}_{2tr} = 400 Tu_e^{-5/8} \tag{8}$$

provided that the acceleration parameter $K = (\nu_e/\overline{U}_e^2) d\overline{U}_e/dx \leqslant 3\times 10^{-6}$. In the above expression, Re_{2tr} is the Reynolds number based on the momentum thickness at the start of transition and Tu_e is the turbulence intensity (percent). Although obtained for zero pressure gradient flows, Eq. (8) also remains valid for flows with variable pressure gradients at $Tu_e \geqslant 3\%$ (cf. Fig. 16 in paper [2]). This is usually the case for transitional BLs on the pressure surface of turbine blades. In contrast, being high generally in the oncoming flow, the turbulence levels on the suction surface locally reduce to levels of 1% to 3% or even less than 1% because of flow acceleration. At these levels, Eq. (8) ceases to be valid. In addition, neglecting turbulence decay in the computation of Tu_e ($Tu_e = u'_\infty/\overline{U}_e$) must generally lead to the earlier transition (which is actually observed in some turbine-blade calculations presented below). In other words, the onset of transition on the suction surface is not determined accurately. Such a situation is common for turbulence models, [3], that is, they experience significant difficulties to correctly predict the onset of transition. Therefore, Eq. (8) was used to estimate the onset of transition in all the turbine test cases considered, and the two transition zone models were compared with the same transition onset conditions.

In the present work, if flow separation occurs, instantaneous transition is imposed immediately behind the separation point. Non-separated-flow transition is modeled by using the intermittency factor γ based on Emmons' statistical theory, [8], of turbulent spots and the concentrated breakdown hypothesis of Narasimha [9].

Assuming a triangle turbulent spot platform, Chen and Thyson [10] derived an expression for the intermittency factor, the two-dimensional form of which reads as follows:

$$\gamma = 1 - \exp\left[-n\sigma \int_{xtr}^{x} dx \int_{xtr}^{x} \frac{dx}{\overline{U}_e} \right] \tag{9}$$

where n is the spot generation rate at transition onset and σ is the nondimensional propagation parameter, which is assumed to be constant through the transition zone. The quantities at the transition point are denoted by the subscript tr. The quantity of σ can be represented as $\sigma = \tan\alpha(b^{-1} - a^{-1})$, where α is the spot spreading half-angle, and a and b are the ratios of the propagation velocities for the leading and trailing edges of the turbulent spot, respectively, to the freestream velocity: $U_{LE} = aU_e$ and $U_{TE} = bU_e$.

The unexpectedly large influence of the local pressure gradient on turbulent spot propagation clearly invalidates the assumption that spot propagation characteristics should not vary significantly with the pressure gradient through the transition zone. The following tentative correlations for variations of α and σ with the pressure gradient parameter λ_θ were obtained from the experimental data assembled by Gostelow et al. [12]:

$$\alpha = 4 + (22.14/(0.79 + 2.72\exp(47.63\lambda_\theta))) \tag{10}$$

$$\sigma = 0.03 + (0.37/(0.48 + 3.0\exp(52.9\lambda_\theta))). \tag{11}$$

Based on these correlations and assumptions allowing the spreading rate of turbulent spots to vary continuously through the transition zone in response to changes in the local pressure gradient parameter λ_θ, Solomon et al. [7] proposed a new transition zone model (SWGM)

$$\gamma = 1 - \exp\left[-n \int_{xtr}^{x} \tan\alpha dx \int_{xtr}^{x} \frac{\sigma}{\tan\alpha} \frac{dx}{\overline{U}_e} \right] \tag{12}$$

The spot generation rate n is computed at the onset of transition using the correlations suggested, [11,13], for Narasimha's breakdown parameter $N = n\sigma\delta_{2tr}^3/\nu$. This method was used by the authors of the model.

To simulate laminar-turbulent transition for turbine blade surfaces, Byvaltsev and Nagashima [15] modified the Chen-Thyson model (9) so that the terms of the intermittency distribution formula relating to dimensions of length and time became nondimensional:

$$\gamma = 1 - \exp\left[-\varphi \int_{xtr}^{x} \frac{dx}{x_{tr}} \frac{\overline{U}_{etr}}{x_{tr}} \int_{xtr}^{x} \frac{dx}{\overline{U}_e} \right] \tag{13}$$

where the coefficient $\varphi = n\sigma x_{tr}^2/\overline{U}_{etr}$.

Using the simple equality $\varphi = 1$ produced surprisingly good agreement with the experimental data reported by Rued and Wittig [17] and Arts et al. [20]. The intermittency distribution formula (13) enables laminar-turbulent transition in BLs with mild pressure gradients to be described and can be considered as a zero-pressure-gradient TZM.

A modified version of the model (BNM) has recently been used by the same authors for turbine blade heat transfer predictions, [14]. The correlations (10)–(11) for spot propagation characteristics were incorporated into the intermittency distribution formula (13) which took into account the influence of the local pressure gradient on turbulent spot propagation

$$\gamma = 1 - \exp\left[-\varphi \int_{xtr}^{x} \tan\alpha \frac{dx}{x_{tr}} \frac{\overline{U}_{etr}}{x_{tr}} \int_{xtr}^{x} \frac{\sigma}{\sigma_o \tan\alpha} \frac{dx}{\overline{U}_e} \right] \tag{14}$$

where, as previously, $\varphi = n\sigma_o x_{tr}^2/\overline{U}_{etr}$ with $\sigma_o = \sigma_{\lambda_\theta = 0}$. The breakdown coefficient φ is a function of the local conditions at transition inception (turbulence intensity, pressure gradient, etc.). As in previous work, [14], the equality, $\varphi = 1$, was also adopted in the present work for predicting transition zones.

The SWGM was tested with good results on cases that reported both intermittency and surface pressure distribution data. The model showed a much reduced sensitivity to errors in predicting the start of the transition zone in comparison with models based on the assumption that spot propagation characteristics do not vary through the transition zone. The remaining degree of sensitivity to errors in predicting transition onset is mainly associated with the requirement for the model to estimate the spot generation rate n at the start of transition. The correlations of n with Tu_e and λ_θ, [11,13], incorporated into the model seem to be sensitive to the values of Tu_e and λ_θ being calculated at the transition onset.

A somewhat different approach is used in the BNM to estimate n at transition inception. This parameter is included in a nondimensional combination which has a constant value. This results in a reduced sensitivity to errors in predicting the location and flow parameters for transition onset. The only parameters needed for the model at transition onset are $\overline{U}_{etr}$ and x_{tr}. According to Eq. (8), x_{tr} is defined by the freestream conditions and BL development.

It is worth noting that Eqs. (12) and (14) are mathematically equivalent. The only, but crucial difference between the BNM and the SWGM is the nondimensional formulation used for estimating the breakdown parameter n. The BNM, in its present form, uses the equality $\varphi = n\sigma_o x_{tr}^2/\overline{U}_{etr} = 1$, whereas the SWGM incorporates the correlation of N with Tu_e and λ_θ, [11,13]. The expression for φ used in the BNM can be rewritten as $N = \varphi\sigma/\sigma_o \, \mathrm{Re}_{2tr}^3/\mathrm{Re}_{xtr}^2$. This expression can significantly be simplified for the case of zero-pressure-gradient flows. Using the Blasius boundary layer relationship, $\mathrm{Re}_2 = 0.664\mathrm{Re}_x^{1/2}$, and correlation (8) in the above expression for N gives the following relationship, $N = 0.49 \times 10^{-3} Tu_e^{5/8}$. This value of N differs from the correlation of Gostelow et al. [11] used in the SWGM by the factor of $0.57 \times Tu_e^{1.189}$.

The correlations (10)–(11) used by the models assume finite positive values of $\alpha(\alpha \geq 4°)$ and $\sigma(\sigma \geq 0.03)$ for all values of λ_θ. This means that neither of the transition zone models, SWGM and BNM, can describe reverse transition (''relaminarization'') in rapidly accelerating BLs. Therefore, noticeable, if not considerable, deviations of the computed boundary layer characteristics from the measured ones can be expected for transition and post-transition zones, in which the acceleration parameter, K, attains values ($K > 3 \times 10^{-6}$) high enough to cause reverse transition.

3 Results and Discussion

In all the turbine blade test cases considered below, the pressure distributions along the turbine blade surfaces required for BL simulations were obtained from external flow predictions based on the two-dimensional full-potential formulation, [29]. Sufficiently good agreement between the computed and measured pressure/velocity distributions has been demonstrated previously, [14,15]. For conciseness, comparisons of calculated and measured pressure distributions are not shown for most test cases.

3.1 Flat-Plate Test Cases—Rued and Wittig [17]. An experimental study of heat transfer in a flat plate reported by Rued and Wittig [17] was used in the present work to verify the modified Johnson-King turbulence model (JKMM) as well as to compare transition-prediction capabilities of the transition zone models of Solomon et al. [7] (SWGM, Eq. (12)) and Byvaltsev and Nagashima [14] (BNM, Eq. (14)).

Three different distributions of the acceleration parameter K ($K = 0$, $K =$ var. with $K_{\max} = 3.2 \times 10^{-6}$ and $K \approx 1.2 \times 10^{-6}$) were used in the experiments to examine the effects of FST and pressure gradient on heat transfer and boundary layer development in

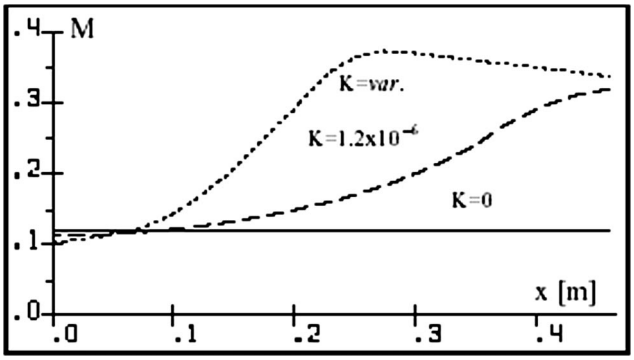

Fig. 1 Mach number distributions in flat-plate test cases

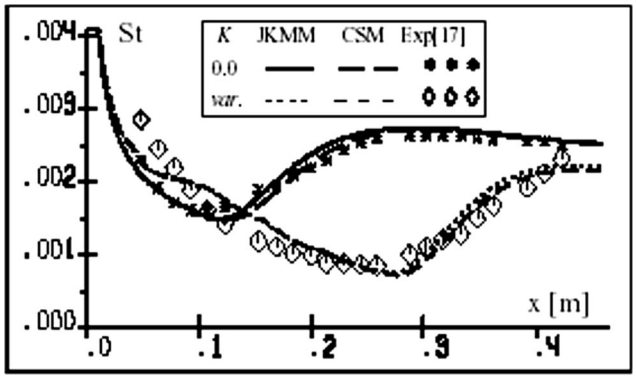

Fig. 3 Flat plate: $Tu_\infty = 2.3\%$, $K = 0$ and $K = \text{var}$. Predictions corresponding to the JKMM and CSM.

highly cooled surfaces ($T_w/T_o = 0.64$). The freestream Mach number distributions along a flat plate for each of the cases are depicted in **Fig. 1**.

The measured and computed Stanton numbers, St, at a high level of turbulence, $Tu_\infty = 8.7\%$, for zero pressure gradient flow ($K = 0$) are shown in **Fig. 2**. The distributions of St were predicted using different turbulence models: the algebraic Cebeci-Smith model, [28], (CSM), the original Johnson-King model, [16], (JKM), and the JKMM. In the calculations, the onset of transition was determined by using Eq. (8). Although they slightly underestimated St values, all the models satisfactorily reproduced the experimental data. In the turbulent portion of the BL, the JKM gives slightly lower and equally deviated values of St in comparison with the values provided by the CSM and JKMM, which show little difference in the distribution of St. Almost the same tendency (not shown) is observed in the turbine blade test cases considered.

A comparison of the numerical results corresponding to the CSM and JKMM along with the experimental data for transitional BLs with $K = 0$ and $K = \text{var.}$ at a moderate level of turbulence ($Tu_\infty = 2.3\%$) is depicted in **Fig. 3**. A clear difference in the computed results can be observed in the transition zones, where the JKMM shows slightly higher levels of St compared to those for the CSM. This difference is due to a deviation of the BL in the JKMM from the "equilibrium" state, when the quantity of σ_ν in Eq. (5) takes values appreciably higher than those for equilibrium flows ($\sigma_\nu \approx 1$) and attains the maximum value of 1.18 in the middle of the transition zone for both cases.

The data in **Figs. 2** and **3** clearly demonstrate that the CSM and JKMM produce almost the same results for the equilibrium and near-equilibrium portions of the boundary layers; however, a difference in results can be expected for the nonequilibrium portions of the BLs.

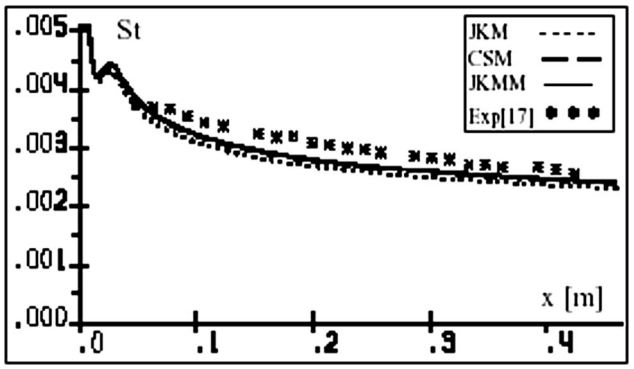

Fig. 2 Flat plate: $Tu_\infty = 8.7\%$, $K = 0$. Computed and measured Stanton number distributions.

The flat-plate test cases corresponding to transitional BLs were used to verify the ability of the TZMs to follow the experimental data. In each case, the onset of transition was selected manually and independently for each of the transition zone models in order to obtain the best agreement with the measurements. The computed and measured distributions of St at $Tu_\infty = 2.3\%$ are shown in **Figs. 4–5**. The lines in **Figs. 4** and **5** correspond to predictions made by the JKMM using the transition zone models, the SWGM and BNM, respectively. For test cases with $K = 0$ and $K = \text{var.}$, both models produced almost the same results. In the case of $K \approx 1.2 \times 10^{-6}$, the BNM demonstrates better agreement with the experimental data than the SWGM. Conversely, the SWGM produced slightly better agreement with the experimental results than the BNM in the case of a zero pressure gradient flow. In general, both models produced similar results, although the location of transition onset in some corresponding cases differed considerably (cf. **Figs. 4**(***b***) and **5**(***b***)). This means that in cases with the same

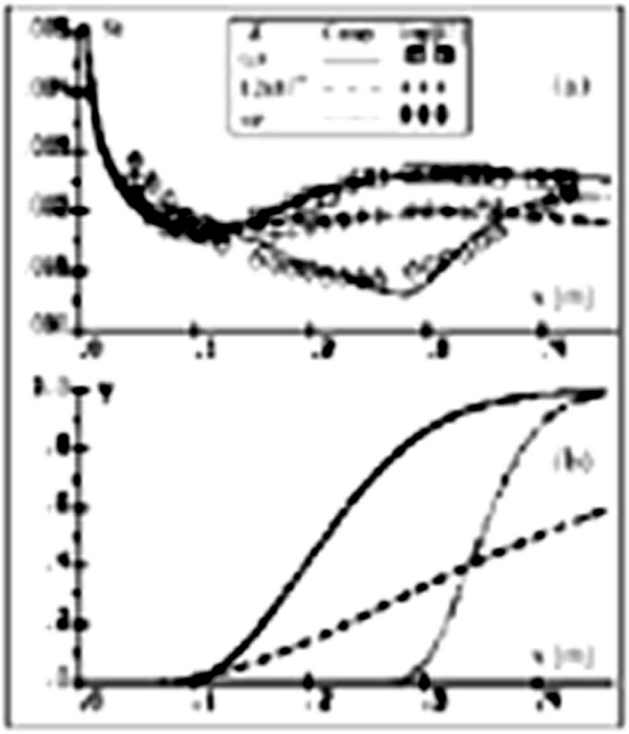

Fig. 4 Flat plate. Predictions made by the SWGM.

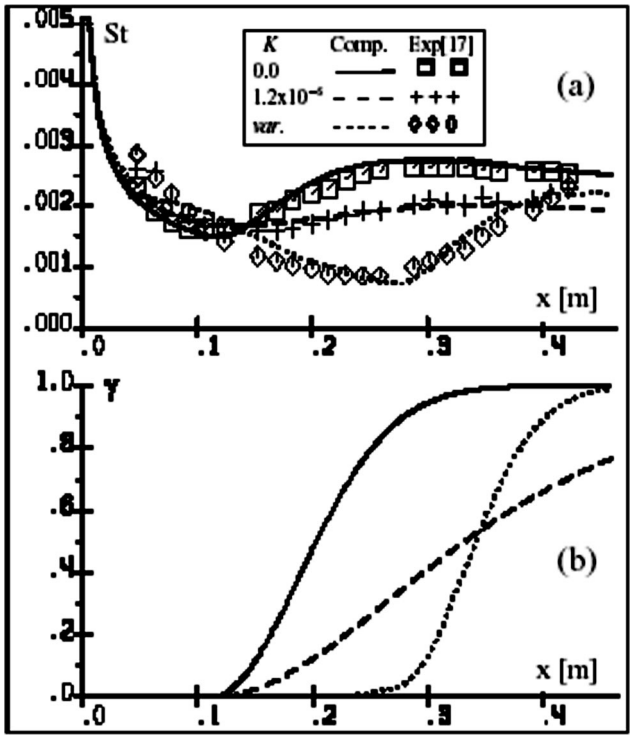

Fig. 5 Flat plate. Predictions made by the BNM.

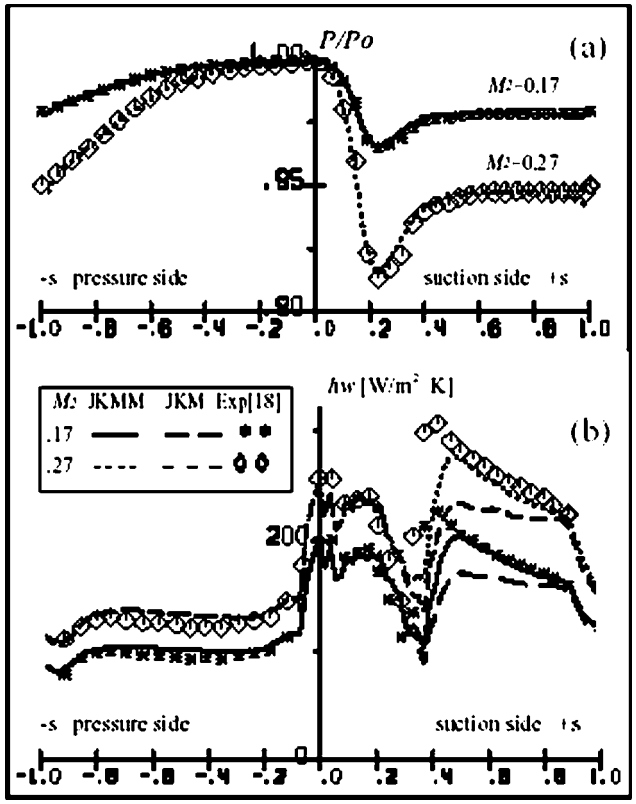

Fig. 6 C3X vane. Comparison of results obtained using the JKM and JKMM.

onset of transition, the SWGM and BNM can give different transition lengths, as can be seen in some of the turbine blade tests discussed below.

3.2 C3X Vane—Ames [18]. The following two test cases were chosen for the calculations (the run numbers correspond to those used by Ames [18]): $M_2=0.271$, $Re_{C2}=0.779\times10^6$, $Tu_\infty=7.75\%$, and $Lu_\infty=0.0136$ m (run HTG100); and $M_2=0.170$, $Re_{C2}=0.506\times10^6$, $Tu_\infty=7.5\%$, and $Lu_\infty=0.011$ m (run HTG200). The measurements were used to compare the performance of the TZMs and the turbulence models, the JKM and JKMM, in heat transfer predictions for essentially ''nonequilibrium'' BLs.

The nondimensional pressure distributions for the two basic exit Mach numbers are given in **Fig. 6**(***a***). The predictions are compared with the measurements denoted by the symbols. The comparison shows good agreement between the computed and measured data.

The predicted and measured heat transfer coefficients, h_w, are compared in **Fig. 6**(***b***). Over the whole of the pressure surface and the favorable pressure gradient portion of the suction surface the BLs remain ''laminar'' due to a strong main-flow acceleration. On these parts of the blade surface the nonturbulence model demonstrates good agreement with the experimental data. Flow separation was experimentally observed in the region of a strong adverse pressure gradient on the suction surface. In contrast to the experiments, flow separation was not predicted, presumably because of the effect of nonturbulence viscosity on BL development and the earlier start of transition predicted by Eq. (8). Nevertheless, due to the correlations (10)–(11), both transition zone models naturally reproduced fast laminar-turbulent transition in the ''separation region'' in complete accord with the experiments (the SWGM gave a quicker transition, not shown).

The turbulence models, the JKM and JKMM, started showing different levels of h_w immediately after the onset of transition. A comparison of the numerical results with the experimental data for the region following transition inception clearly demonstrates the superiority of the JKMM compared to the JKM in the heat transfer prediction for this region. This is primarily due to the modification of the damping factor in the JKMM model, that is, the incorporation of the factor σ_D into the expression for the inner viscosity (6) of a region with an adverse pressure gradient, where $\sigma_D=\sigma_\nu$. In this region, σ_ν attains the values ($\sigma_{\nu,\max}\approx1.5-1.6$), which are significantly above its ''equilibrium'' level, $\sigma_\nu\approx1$.

As was mentioned in the description of the JKMM, at present there is no exact criterion for using the equality $\sigma_D=\sigma_\nu$ in the damping factor instead of $\sigma_D=1$ for the ''equilibrium'' flows. Currently, this equality is used in the subsonic regions of BLs characterized by adverse pressure gradients and located behind the laminar-separation/turbulent-reattachment zones.

3.3 VKI Turbine Blade—Consigny and Richards [19]. Heat transfer measurements, [19], on a VKI (von Karman Institute) turbine blade were used in the present work for testing the SWGM and BNM. The ''C3'' test cases chosen for the calculations were: $M_2=0.92$, $Re_{C1}=7.231\times10^5$, $Tu_\infty=3.0$, 3.8 and 5.2%. The value of the dissipation length scale $Lu_\infty=0.02$ m was accepted for all the calculations described in this subsection.

The computed data corresponding to the BNM and SWGM are shown in **Figs. 7** and **8**, respectively. The JKMM was used to simulate the turbulent portions of the BLs.

On the suction surface, the numerical results corresponding to the BNM, **Fig. 7**(***a***), follow the experimental data quite well, whereas the distributions of h_w predicted by the SWGM, **Fig. 8**(***a***), are considerably lower than those measured, except for when $Tu_\infty=3\%$. The calculated distributions of the intermittency factor, γ, are shown in **Figs. 7**(***b***) **and 8**(***b***). It can be seen that the TZMs produce different distributions of γ and therefore different transition lengths.

On the pressure surface, the SWGM gives slightly better results than the BNM, primarily due to the quicker transition. The quicker transition generates larger values of σ_ν. The latter may

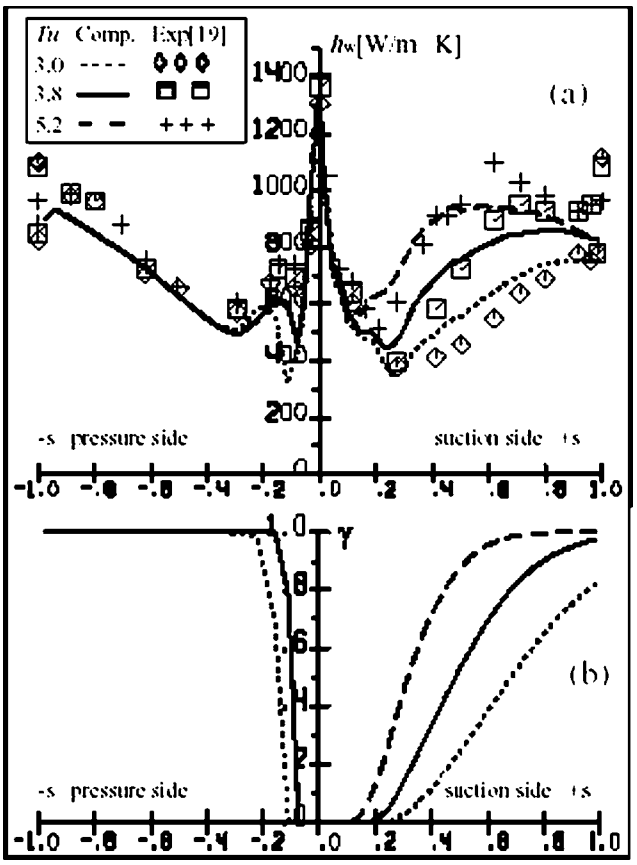

Fig. 7 VKI blade. Predictions made by the BNM.

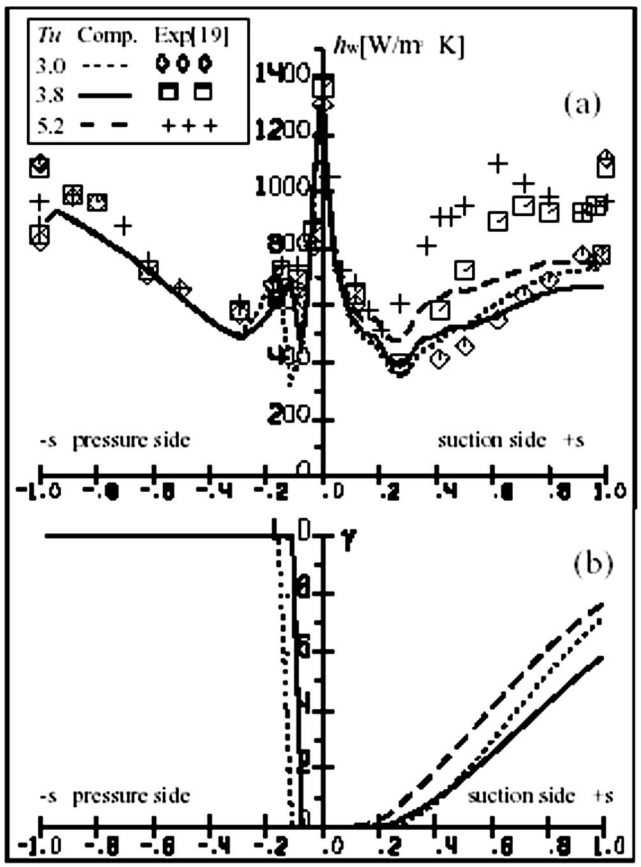

Fig. 8 VKI blade. Predictions made by the SWGM.

then be used in the damping factor for inner viscosity as $\sigma_D = \sigma_\nu$. In all the cases shown in **Figs. 7** and **8**, BL separation was not predicted, presumably due to the effect of the nonturbulence model prior to the onset of transition and errors in the predicted pressure distribution. According to the experimental data, as BL develops along the pressure surface, the transition seems to occur immediately behind the leading edge via a separation bubble. This suggests that the equality $\sigma_D = \sigma_\nu$ should be used in calculations of BLs along the pressure surface for regions with adverse pressure gradients, regardless of the absence of flow separation in calculations.

3.4 VKI Turbine Vane—Arts et al. [20]. Heat transfer measurements on a VKI turbine vane have been carried out under a wide range of operating conditions, [20]. Two test cases were chosen for the assessment of the transition zone models (the run numbers correspond to those used by Arts et al. [20]): $M_2 = 0.78$, $Re_{C2} = 1.01 \times 10^6$, and $Tu_\infty = 6\%$ (run 237); and $M_2 = 0.92$, $Re_{C2} = 2.14 \times 10^6$, and $Tu_\infty = 6\%$ (run 239). The value of Lu_∞ was accepted as being equal to that used by Byvaltsev and Nagashima [15] for these test cases, $Lu_\infty = 0.01$ m.

The experimental and calculated heat transfer coefficients, h_w, are compared in **Fig. 9**(***a***). The corresponding distributions of the intermittency factor, γ, are given in **Fig. 9**(***b***).

At the Reynolds number $Re_{C2} = 10^6$, the BL on the pressure surface and the front part of the suction surface remains in a "laminar" state due to a strong main-flow acceleration. In these pseudo-laminar flow regions, the nonturbulence model produces distributions of h_w that agree quite well with the experimental data. On the suction surface, both transition zone models, the SWGM and BNM, in combination with the JKMM, show very similar h_w–distributions, which are in satisfactory agreement with the experimental results. The computed distributions of γ for this case (**Fig. 9**(***b***)) follow each other quite well.

The same trend is observed on the suction surface at the increased $Re_{C2} = 2 \times 10^6$. In this case, most of the discrepancies between the SWGM and BNM relate to the pressure surface. The SWGM failed to predict transition on the pressure side correctly and produced an intermittency factor with values near zero, while the BNM gave an intermittency distribution that increased with distance and produced values of h_w that agreed satisfactorily with the measurements.

3.5 SNECMA RS1S Profile—Arts et al. [21]. Heat transfer measurements on an RS1S profile of the SNECMA high-turning rotor blade have recently been performed in the VKI facility by Arts et al. [21]. The flow conditions corresponding to the chosen test cases were $M_2 = 1.12$, $Re_{C2} = 1.05 \times 10^6$ and 1.84×10^6, $Tu_\infty = 4\%$, and I (incidence angle) $= -5$ deg. The value of Lu_∞ was taken to be equal to that in the previous subsection ($Lu_\infty = 0.01$ m).

A comparison of the measured and predicted h_w along with the calculated distributions of γ are presented in **Figs. 10**(***a***) and **10**(***b***), respectively.

On the pressure side, both transition models produced a fast transition as a result of strong adverse pressure gradients in the short-length region located immediately behind a leading edge. In the experiments, transition seems to occur via a separation bubble. As in the previous cases, separation has not been shown in calculations. This occurs when we meet strong accelerating BL-flows ($K > 3 \times 10^{-6}$) on the pressure surface in the large region located some distance behind the points where the models showed the completion of laminar-turbulent transition. As was mentioned above in the description of the TZMs, the models are not able to

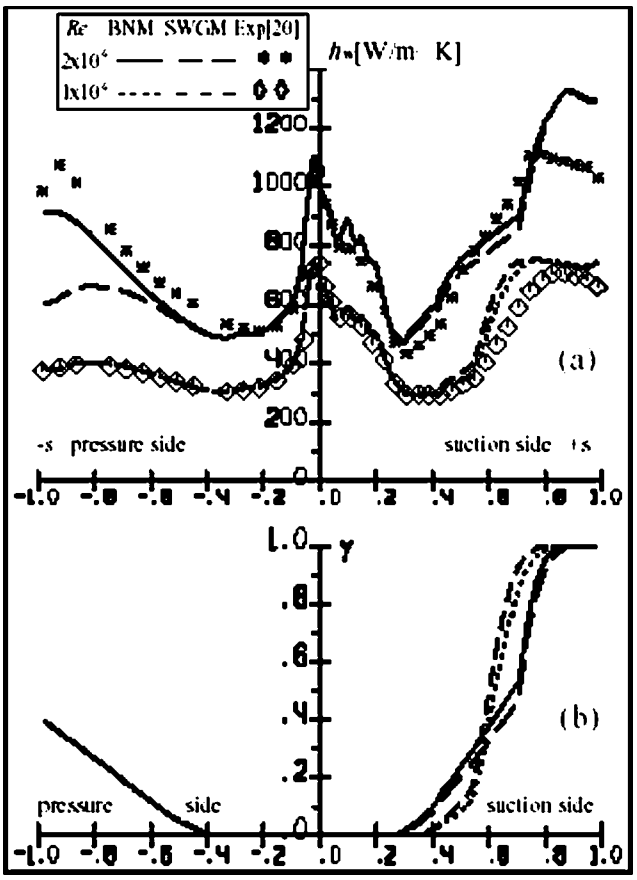

Fig. 9 VKI vane. Predictions made by the SWGM and BNM.

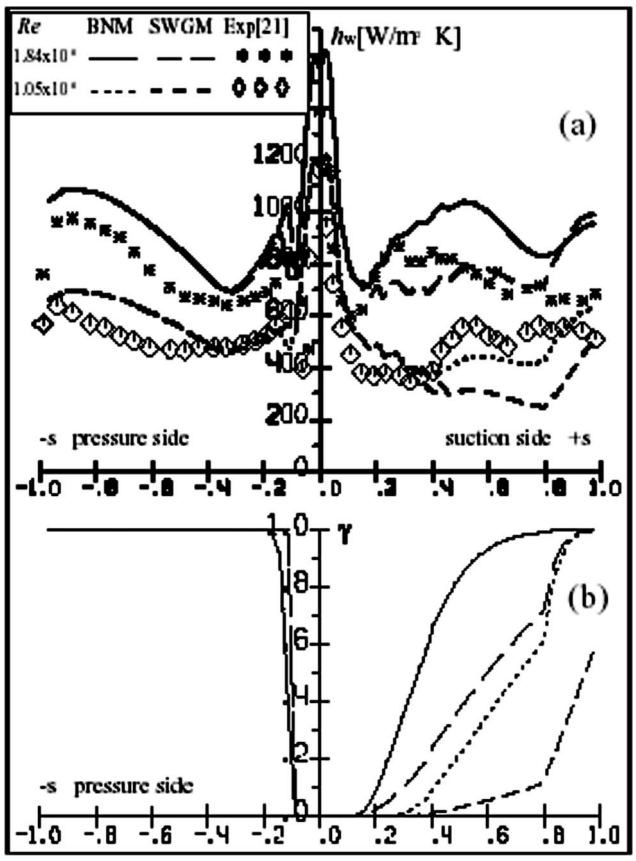

Fig. 10 SNECMA RS1S profile. Predictions made by the SWGM and BNM.

predict reverse transition. A noticeable disagreement between the computed and measured h_w on the pressure side can be attributed to this deficiency.

On the suction surface, the SWGM and BNM demonstrate considerably different transition behavior (**Fig. 10**(***b***)). Both models show significant deviations from the experimentally determined values of h_w. In the case of a higher Reynolds number, the SWGM performs better than the BNM. In the case of a lower Re_{C2}, quite the opposite is found: the prediction made by the BNM is better than that made by the SWGM. These test cases clearly show that the TZMs require some corrections to enable them to better simulate boundary layer transition. Note that including the Mach number (compressibility) effect in the models would not improve the agreement between computations and measurements on the suction surface. According to different correlations (see, for example, Steelant and Dick [5]), the compressibility effect would lead to an increase in transition length, thereby reducing the predicted levels of h_w and generally adversely affecting the existing accord between the computed results and the experimental data.

4 Conclusions

A comparative study of the transition zone models (TZMs) of Solomon et al. (SWGM) and Byvaltsev and Nagashima (BNM) was performed to examine their ability to simulate boundary layer laminar-turbulent transition. Both models incorporate the correlations of Gostelow et al. for turbulent spot propagation parameters which react to changes in the local pressure gradient through transition. A marching two-dimensional code based on solving the boundary layer equations for compressible gas flows was used in the study. The code was used to combine the transition zone models with the modified Johnson and King turbulence model and the algebraic nonturbulence (pre-transition) model developed earlier by Byvaltsev and Nagashima to simulate the influence of free-stream turbulence on a boundary layer flow prior to transition. Heat transfer experiments on a flat plate, turbine blades, a C3X vane, a VKI turbine blade, a VKI turbine vane, and a SNECMA RS1S profile were used to compare the computed results. The following conclusions can be drawn from the study.

Flat-plate test cases with different distributions of the acceleration parameter were used to verify the ability of the transition zone models to follow the experimental data. The onset of transition in each case was selected manually and independently for each transition zone model in order to obtain the best agreement with the measurements. For transitional boundary layer flows, both models produced almost the same results. In the location of transition onset for some cases the models differed considerably.

In all turbine blade test cases, the location of transition onset was estimated using the empirical correlation provided by Mayle [2]. In the VKI turbine blade and vane test cases, the BNM reproduced the experimental data satisfactorily, while the SWGM in some cases did not follow the measured data. In the SNECMA RS1S profile test cases, neither of the models agreed well with the experimental data. These test cases clearly show that the TZMs require some corrections to enable them to better simulate boundary layer transition.

In summary, the BNM appears to be preferable to the SWGM for engineering use in calculating boundary-layer flows on axial turbine blades. In its present form the BNM does not require the direct estimation of the turbulent spot characteristics at transition inception. This results in a reduced sensitivity to errors in predicting the location and flow parameters for transition onset.

In the C3X vane test cases, the modified Johnson and King turbulence model performed better than the original one in heat

transfer predictions for turbine blade regions characterized by adverse pressure gradients and located behind laminar separation/turbulent reattachment zones. It should be noted that, as yet, there is no criterion for using the modification to the damping factor for the inner viscosity of the model.

Acknowledgments

The authors gratefully acknowledge the invaluable contribution of Prof. T. Nagashima of The University of Tokyo to this work. The assistance of Dr. M. Ikegawa is thankfully appreciated.

Nomenclature

h_w = heat transfer coefficient, W/m^2/K
K = acceleration parameter$=(\nu_e/\overline{U_e}^2)d\overline{U}_e/dx$
L = streamwise integral length scale of turbulence, m
Lu = streamwise dissipation length scale of turbulence, m
M = Mach number
N = Narasimha's breakdown parameter$=n\sigma\delta_{2tr}^3/\nu$
n = spot generation rate, $(\mathrm{m\,s})^{-1}$
P = pressure, Pa
Pr = Prandtl number
Re_2 = Reynolds number$=\overline{U}_e\delta_2/\nu_e$
Re_{C1} = Reynolds number based on blade chord and inlet conditions
Re_{C2} = Reynolds number based on blade chord and exit conditions
Re_x = Reynolds number$=\overline{U}_e x/\nu_e$
s = normalized arc length along blade surface
T = temperature, K
t' = temperature fluctuation, K
Tu = turbulence level, percent$=100u'/\overline{U}_e$
U = velocity component in x direction, m/s
u',v' = fluctuating velocity components in x and y directions, m/s
u_* = wall shear velocity, m/s
x = surface coordinate in streamwise direction, m
y = coordinate normal to surface, m
y^+ = dimensionless distance from the wall

Greek Symbols

α = spot spreading half-angle, deg.
γ = intermittency factor
γ_K = Klebanoff's intermittency function$=1/[1+5.5(y/\delta)^6]$
δ = boundary layer thickness: $\overline{U}(y=\delta)=0.99\overline{U}_e$, m
δ_1 = displacement thickness$=\int_0^\delta(1-\overline{\rho U}/\overline{\rho}_e\overline{U}_e)dy$, m
δ_2 = momentum thickness$=\int_0^\delta\overline{\rho U}/\overline{\rho}_e\overline{U}_e(1-\overline{U}/\overline{U}_e)dy$, m
κ = von Karman's constant$=0.41$
Λ = Pohlhausen parameter$=\delta^2\rho_e/\mu_w d\overline{U}_e/dx$
λ_θ = pressure gradient parameter$=\delta_2^2\rho_e/\mu_e d\overline{U}_e/dx$
μ = dynamic viscosity, kg/(m s)
ν = kinematic viscosity, m^2/s
ρ = density, kg/m^3
σ = spot propagation parameter
σ_ν = ratio of actual to equilibrium τ_m
τ = Reynolds shear stress, $(-\rho\overline{u'v'})$, N/m^2
φ = nondimensional breakdown coefficient in Eqs. (13), (14)

Subscripts

e = edge of a boundary layer
eq = equilibrium conditions
i = inner part of boundary layer
m = values of quantity where τ is a maximum
nt = nonturbulent
o = stagnation or reference conditions
t = turbulent
tr = transition
w = wall
∞ = inlet or freestream conditions

Superscripts

$^-$ = time-averaged or ensemble-averaged quantity

Abbreviations

BL = boundary layer
BNM = Byvaltsev-Nagashima TZM
CSM = Cebeci-Smith turbulence model
FST = freestream turbulence
JKM = Johnson-King turbulence model
JKMM = modified Johnson-King model
SWGM = Solomon-Walker-Gostelow TZM
TZM = transition zone model

References

[1] Narasimha, R., 1985, "The Laminar-Turbulent Transition Zone in the Boundary Layer," Prog. Aerosp. Sci., **22**, pp. 29–80.
[2] Mayle, R.E., 1991, "The Role of Laminar-Turbulent Transition in Gas Turbine Engines," ASME J. Turbomach., **113**, pp. 509–537.
[3] Westin, K.J.A., and Henkes, R.A.W.M., 1997, "Application of Turbulence Models to Bypass Transition," ASME J. Fluids Eng., **119**, pp. 859–866.
[4] Cho, J.R., and Chung, M.K., 1992, "A k-ε-γ Equation Turbulence Model," J. Fluid Mech., **237**, pp. 301–322.
[5] Steelant, J., and Dick, E., 2001, "Modeling of Laminar-Turbulent Transition for High Freestream Turbulence," ASME J. Fluids Eng., **123**, pp. 22–30.
[6] Suzen, Y.B., and Huang, P.G., 2000, "Modeling of Flow Transition Using an Intermittency Transport Equation," ASME J. Fluids Eng., **122**, pp. 273–284.
[7] Solomon, W.J., Walker, G.J., and Gostelow, J.P., 1996, "Transition Length Prediction for Flows With Rapidly Changing Pressure Gradients," ASME J. Turbomach., **118**, pp. 744–751.
[8] Emmons, H.W., 1951, "The Laminar-Turbulent Transition in a Boundary Layer—Part I," J. Aerosp. Sci., **18**, pp. 490–498.
[9] Narasimha, R., 1957, "On the Distribution of Intermittency in the Transition Region of a Boundary Layer," J. Aerosp. Sci., **24**(9), pp. 711–712.
[10] Chen, K.K., and Thyson, N.A., 1971, "Extension of Emmons' Spot Theory to Flows on Blunt Bodies," AIAA J., **9**, pp. 821–825.
[11] Gostelow, J.P., Blunden, A.R., and Walker, G.J., 1994, "Effects of Free-Stream Turbulence and Adverse Pressure Gradients on Boundary Layer Transition," ASME J. Turbomach., **116**, pp. 392–404.
[12] Gostelow, J.P., Melwani, N., and Walker, G.J., 1996, "Effects of Streamwise Pressure Gradient on Turbulent Spot Development," ASME J. Turbomach., **118**, pp. 737–743.
[13] Fraser, C.J., Higazy, M.G., and Milne, J.S., 1994, "End-Stage Boundary Layer Transition Models for Engineering Calculations," Proc. Inst. Mech. Eng., Part C: J. Mech. Eng. Sci., **208**, pp. 47–58.
[14] Byvaltsev, P.M., and Nagashima, T., 2001, "Heat Transfer Prediction for Transitional Boundary Layer Flows at the Turbine Blade Surface," *Some Aero-Thermo-Fluid Aspects in Airbreathing Propulsion*, Proceedings of Japan-Russia Seminars on Specialized Aspects in Aerospace Propulsion Research, University of Tokyo and CIAM (1995–1998), T. Nagashima and M. Ivanov, eds., Central Institute of Aviation Motors, Moscow, pp. 204–226.
[15] Byvaltsev, P.M., and Nagashima, T., 1998, "Correlation of Numerical and Experimental Heat Transfer Data at the Turbine Blade Surface," JSME Int. J., Ser., **41**(1), pp. 191–199.
[16] Johnson, D.A., and King, L.S., 1990, "A Mathematically Simple Turbulence Closure Model for Attached and Separated Turbulent Boundary Layers," AIAA J., **28**(11), pp. 2000–2003.
[17] Rued, K., and Wittig, S., 1985, "Free-Stream Turbulence and Pressure Gradient Effects on Heat Transfer and Boundary Layer Development on Highly Cooled Surfaces," ASME J. Eng. Gas Turbines Power, **107**, pp. 54–59.
[18] Ames, F.E., 1997, "The Influence of Large-Scale High-Intensity Turbulence on Vane Heat Transfer," ASME J. Turbomach., **119**, pp. 23–30.
[19] Consigny, H., and Richards, B.E., 1982, "Short Duration Measurements of Heat-Transfer Rate to a Gas Turbine Rotor Blade," ASME J. Eng. Gas Turbines Power, **104**, pp. 542–551.
[20] Arts, T., Lambert de Rouvroit, M., and Rutherford, A.W., 1990, "Aero-Thermal Investigations of a Highly Loaded Transonic Linear Guide Vane Cascade," VKI Technical Note 174.
[21] Arts, T., Duboue, J.-M., and Rollin, G., 1998, "Aerothermal Performance Measurements and Analysis of a Two-Dimensional High Turning Rotor Blade," ASME J. Turbomach., **120**, pp. 494–499.
[22] Schlichting, H., *Boundary-Layer Theory*, McGraw-Hill, New York.
[23] Reyhner, T.A., and Reyhner, T.A., 1968, "The Interaction of a Shock Wave With a Laminar Boundary Layer," Int. J. Non-Linear Mech., **3**(2), pp. 173–199.
[24] Cebeci, T., 1988, "Parabolic System: Finite-Difference Method II," *Handbook of Numerical Heat Transfer*, W.J. Minkowycz et al., eds., John Wiley and Sons, New York, pp. 117–154.
[25] Dullenkopf, K., and Mayle, R.E., 1995, "An Account of Free-Stream-

Turbulence Length Scale on Laminar Heat Transfer,'' ASME J. Turbomach., **117**, pp. 401–406.
[26] Westin, K.J.A., Boiko, A.V., Klingmann, B.G.B., Kozlov, V.V., and Alfredsson, P.H., 1994, ''Experiments in a Boundary Layer Subjected to Free Stream Turbulence—Part 1: Boundary Layer Structure and Receptivity,'' J. Fluid Mech., **281**, pp. 193–218.
[27] Neel, R.E., Walters, R.W., and Simpson, R.L., 1998, ''Computations of Steady and Unsteady Low-Speed Turbulent Separated Flows,'' AIAA J., **36**(7), pp. 1208–1215.
[28] Cebeci, T., and Smith, A.M.O., 1974, *Analysis of Turbulent Boundary Layers*, Academic Press, San Diego, CA.
[29] Byvaltsev, P.M., 1992, ''A Method of Calculating the Flow Around and Aerodynamic Design of the Profiles of Turbomachinery Blade Rows,'' Comput. Maths Math. Phys., **32**(4), pp. 509–519.